Characterization of arterial hemodynamics using mouse models of atherosclerosis and tissue-engineered artery models

Charakterisierung arterieller Hämodynamiken in atherosklerotischen Mausmodellen und tissue-engineerten Arterienmodellen

Doctoral thesis for a doctoral degree

at the Graduate School of Life Sciences,

Julius-Maximilians-Universität Würzburg,

Section: Biomedicine

submitted by:

Kristina Andelovic

From Essen

Würzburg 2022

Submitted on:

Members of the Thesis Committee

Chairperson: Prof. Dr. Keram Pfeiffer

Primary Supervisor: Prof. Dr. Alma Zernecke

Supervisor (Second): Prof. Dr. Dr. Wolfgang Bauer

Supervisor (Third): Prof. Dr. Jan Hansmann

Date of Public Defence:

Date of Receipt of Certificate:

TABLE OF CONTENTS

LIST OF FIGURES

LIST OF SUPPLEMENTARY FIGURES

LIST OF TABLES

LIST OF SUPPLEMENTARY TABLES

AIMS AND MOTIVATION

Atherosclerosis is a chronic disease of the arterial system, characterized by the development and growth of atherosclerotic lesions (plaques) and typically remains undetected for decades, until occlusion of the artery, rupture or erosion of these plaques occur. The consequent atherosclerotic cardiovascular disease (CVD), which includes myocardial infarction and stroke, remains the leading cause of death worldwide [1]. Atherosclerosis is initiated and modulated by altered hemodynamics, associated with inflammatory processes in the vascular wall, and results in changes in arterial elasticity due to plaque growth. These plaques preferentially develop at inner curvatures of arteries, branch points, and bifurcations, where the wall shear stress (WSS), which is proportional to the friction force of the blood flow acting on the vessel wall, is low and oscillatory. In conjunction with other processes such as lipid deposition, these altered hemodynamics lead to local vascular inflammation and plaque growth. There is also evidence that low and oscillatory shear stress contribute to arterial remodeling, entailing reduced arterial elasticity and therefore an increased arterial pulse wave velocity (PWV). Therefore, altered shear stress profiles, elasticity and inflammation are closely intertwined and are critical factors responsible for plaque development and growth [2]. However, how these parameters exactly correlate with plaque development, composition, and vulnerability in advanced atherosclerosis, still remains to be defined. At this point, magnetic resonance imaging (MRI) has been demonstrated to be an excellent tool to provide insights into a large range of biological parameters, enabling the evaluation of the dynamic process of atherosclerotic lesion formation without the need for harmful radiation [3]. In particular flow-sensitive MRI provides the possibility to quantify hemodynamic parameters such as WSS [4-8] or PWV [6, 9-15], which may eventually replace invasive and radiation-based techniques for imaging vascular function and characterize atherosclerotic plaques. However, preclinical and clinical investigations mostly focus on the investigation of only one of these parameters due to the experimental and / or technical limitations or only provide 2-dimensional (2D) information about these parameters. Moreover, the investigation of aortic hemodynamics in particular in murine models is still rare due to the requirement of both, high spatial and temporal resolution as well as due to curved geometry of the aortic arch and the associated difficulties in slice positioning. Therefore, a method for the three-dimensional acquisition of hemodynamics with sufficient temporal and spatial resolution, covering the complete aortic arch in reasonable scan times is of great importance. Consequently, there is also still a lack of longitudinal studies investigating the role of altered hemodynamics and the influence on plaque development and progression in preclinical atherosclerosis models in particular in the aortic arch using high-resolution 4D-flow MRI. Although mouse models of atherosclerosis like the low-density lipoprotein-deficient (*Ldlr*$^{-/-}$) and the apolipoprotein E-deficient (*Apoe*$^{-/-}$) mouse are well established and frequently used for the investigation of fundamental processes in atherosclerosis, they only offer a limited possibility to investigate hemodynamic-related disease development and their influence on specific biologic parameters in a controllable manner. At this point, tissue engineering could serve as a promising new alternative for *in vivo* studies, as they could help to reduce animal experiments, while simultaneously offering a fully controllable hemodynamic environment as well as complete freedom in choosing biological variables like cell sources and cell types. Consequently, tissue-engineered *in vitro* artery models could serve as promising test models for hemodynamic-related atherosclerosis research. Taken together, this results in the following goals:

- The establishment of a fast acquisition method for the simultaneous assessment of hemodynamic parameters like the WSS and PWV via high-resolution 4D-flow MRI in the complete murine aortic arch in reasonable scan times
- The investigation of aortic hemodynamics during early and progressive atherosclerosis in atherosclerotic mouse models
- The establishment of artery models for the targeted investigation of fundamental flow-related processes of atherogenesis in a fully controllable environment

Driven by these demands, this thesis aims to investigate the role of hemodynamics, in particular the WSS and PWV and their influence on plaque development, progression and composition, during early and late atherosclerosis. For this, two approaches were taken into account: 1) The utilization of established atherosclerotic mouse models for the investigation of hemodynamics in early and late atherosclerosis via serial *in vivo* measurements using high-resolution 4D-flow MRI and 2) the creation of suitable artery models and bioreactor systems for the application of a fully controllable biologic and hemodynamic environment, enabling the targeted investigation of the hemodynamic impact on biological factors *in vitro*.

Accordingly, this thesis can be divided into six major parts:

Chapter 1 provides an overview of the development and progression of atherosclerosis, including brief summary about the most frequently used mouse models for atherosclerosis research. Moreover, current imaging methods and strategies for the characterization of hemodynamics and vascular function as well as characterization of atherosclerotic plaques via MRI are discussed, highlighting in particular the role of WSS and arterial elasticity via measurements of the PWV [3]. In addition, the potential and current strategies of vascular tissue engineering for flow-related atherosclerosis research are discussed.

As mentioned above, most studies investigating hemodynamic-related atherosclerosis development and progression mostly focus on only one hemodynamic parameter or only provide 2D information, despite many indications of a close relationship of altered WSS and arterial stiffening. Therefore, the aim of **Chapter 2** was to establish a fast technique for the simultaneous *in vivo* measurement of 3D WSS and aortic PWV in the murine aortic arch [16], which is based on the previously developed method for fast, self-navigated wall shear stress measurements in the murine aortic arch using radial 4D-phase contrast cardiovascular magnetic resonance at 17.6 T [4]. A post-processing algorithm using flexible reconstruction frameworks permits the simultaneous quantification of global PWV and 3D-WSS in a single acquisition, therefore enabling the acquisition of both parameters in only 35 minutes. This work is the basis for the following *in vivo* studies, enabling the fast assessment of all relevant parameters describing altered hemodynamics in atherosclerosis development and progression in the complete murine aortic arch in only one session, markedly accelerating and improving the analyses and information content of *in vivo* measurements.

Nevertheless, a detailed analysis of the spatial and temporal hemodynamic changes over time in healthy and diseased mice is essential to unravel the relationship between hemodynamics and plaque progression as well as composition. Therefore, **Chapter 3** aimed for the investigation of global and local hemodynamics during ageing and atherosclerosis progression in the complete murine aortic arch [5] using the previously established 4D-flow MRI methods [4, 16] to simultaneously assess all relevant hemodynamic parameters like the WSS, oscillatory shear index (OSI) and the PWV. Additionally, another aim was to statistically analyze and visualize these spatiotemporal differences over time and between healthy and diseased subjects at a glance through generation of spatially resolved 2D projection maps of the complete aortic arch, allowing for the pixel-wise statistical analysis of inter-group and intra-group differences. Atherosclerotic plaque composition is furthermore strongly influenced by the local hemodynamic conditions. Therefore, the second aim of this chapter was to analyze this influence on the cellular and extracellular matrix composition of advanced atherosclerotic plaques in a spatially resolved manner. The 2D projection maps were proven to be a promising and powerful tool to enable spatially resolved correlations of hemodynamics with plaque and vessel wall characteristics, identifying the circumferential WSS as a potential marker for advanced plaque composition and the radial strain as a potential marker for vascular elasticity.

However, the description of hemodynamic profiles during late atherosclerosis is not sufficient to unravel the basic mechanisms flow and plaque development in early stages of atherosclerosis. Moreover, another big gap in hemodynamic-related atherosclerosis research are the missing studies incorporating *Ldlr*$^{-/-}$ mice or even the simultaneous investigation and comparison of both most popular atherosclerotic mouse models, namely *Ldlr*$^{-/-}$ and *Apoe*$^{-/-}$ mice. Interestingly, both models show the same regions of plaque development in the aortic arch and distinct differences in plasma lipoproteins, but differences in hemodynamic profiles using preclinical flow-sensitive MRI at baseline levels and during early atherosclerosis development were not performed up to now. Therefore, the aim of **Chapter 4** was to characterize hemodynamics at baseline levels and during early atherosclerosis development in both atherosclerotic mouse models, revealing distinct baseline flow, WSS and OSI profiles in both models. Interestingly, among other factors like the blood pressure and blood viscosity, the WSS strongly depends on the arterial geometry [17, 18] and is also influencing the LDL lumen surface concentration [19], pointing out a close relationship between lipid accumulation and local WSS patterns. Therefore, the second aim was to fully characterize the aortic geometry, lipid profiles and WSS profiles in the atherosclerotic *Ldlr*$^{-/-}$ and *Apoe*$^{-/-}$ mouse models during early atherosclerosis progression.

Taken together, atherosclerotic mouse models are very suitable for the investigation of fundamental processes causing atherosclerosis development and progression, as they offer a complex environment with all important factors influencing disease development, but a reduction of animal experiments should be promoted according to possibility for reasons of animal welfare. Moreover, mouse models are very expensive and time-consuming - and most importantly, the determination of local hemodynamic effects for the examination of the influence on distinct biological parameters is challenging due to the high complexity of a living organism. Controlling hemodynamic parameters *in vivo* is only very limited through complicated operations [20, 21] or the utilization of drugs [22]. At this point, vascular tissue engineering offers a potential alternative to conventional *in vivo* mouse studies, as they can resemble the biomechanical properties and cellularity of native arteries while allowing the study of the role of hemodynamics during disease development and progression in a fully controllable environment when cultured in suitable bioreactor systems [23].

Therefore, **Chapter 5** aimed to establish a tissue engineered artery model for hemodynamic-related atherosclerosis research, which is based on decellularized scaffolds obtained from porcine carotid arteries. Despite the large amount of literature describing the generation of decellularized vascular scaffolds, there is still a lack of fast and gentle decellularization methods for arteries, as most published protocols include extensive chemical, enzymatic or physical, treatment, leading to the loss of mechanical stability and cell adhesion [24-26]. Consequently, the first aim was to develop a gentle but fast decellularization method, which efficiently removes all cells and cellular remnants from the scaffold, while simultaneously maintaining the complex mixture of structural and functional proteins comprising the natural extracellular matrix (ECM) for an excellent cell adhesion and growth [27] and the minimization of effects on the mechanical stability. The *in vitro* artery model based on decellularized porcine carotid artery scaffolds showed complete acellularity while maintaining the overall ultrastructure, extracellular matrix composition and mechanical strength, and simultaneously offering good cellular adhesion and proliferation. After the successful generation of a tissue-engineered artery model, the second aim was to develop an MRI-suitable bioreactor system to non-invasively assess high-resolution 4D hemodynamics in tissue-engineered artery models, including all parameters relevant for flow-related disease research like WSS, OSI and PWV as well as morphological analysis in tissue-engineered artery models.

In **Chapter 6**, the aim was to develop an alternative biomimetic artery model, including bifurcations and curvatures mimicking the geometric properties of the aortic arch, which is based on biomaterials in order to overcome the issues of the native artery model described in Chapter 5. These include the lack of design freedom (e.g., curved arteries or bifurcations) and the missing smooth muscle cell layers, which are a prerequisite for a good atherosclerosis model. The field of biofabrication provides several techniques to create artery models with a multi-layered structure, but most of these methods need special and / or expensive equipment or even complex multi-step procedures to create complex geometries like bifurcations or even the aortic arch. Moreover, to investigate the important role of flow dynamics in atherosclerosis, a functional and design-specific perfusion chamber for a fully controllable, dynamic cultivation of these models is of great importance. Therefore, the second aim of this work was to develop a custom-fit perfusion chamber for the controlled application of flow and pressure during dynamic cultivation. However, the generation of the artery model should be easy-to-prepare at low cost and fully customizable. This was achieved by the utilization of thermoresponsive sacrificial scaffolds, generated with the technique of Melt Electro Writing (MEW) and the utilization of a simple gelatin-hydrogel, crosslinked with bacterial transglutaminase, making it an excellent basis for the development of *in vitro* disease test systems for e.g., atherosclerosis research.

In **Chapter 7**, the established methods and results of the thesis are summarized, and future perspectives of the presented work are discussed.

CHAPTER 1

Introduction:

Evaluation of plaque characteristics and inflammation using magnetic resonance imaging

&

Vascular tissue engineering as potential tool for atherosclerosis research

Parts of Chapter 1 (Chapter 1.3 – 1.6) were published in a scientific journal as a review article (Kristina Andelovic, Patrick Winter, Wolfgang Rudolf Bauer, Peter Michael Jakob, Volker Herold and Alma Zernecke: "Evaluation of plaque characteristics and inflammation using magnetic resonance imaging" in the special issue of Biomedicines: Molecular imaging of inflammation and immunity, Biomedicines 2021, 9(2), 185, reproduced from [3] as open access article distributed under the Creative Commons Attribution License which permits unrestricted use, distribution and reproduction in any medium.

The original text was extended substantively and modified to improve readability.

The author contributions to the original review article are as follows:

Contributor	Contributions
Kristina Andelovic	Conceptualization, original draft preparation, review and editing, visualization
Patrick Winter	Original draft preparation, review and editing, visualization
Peter Michael Jakob	Review and editing
Wolfgang Rudolf Bauer	Funding acquisition, review and editing
Volker Herold	Funding acquisition, visualization, review and editing
Alma Zernecke	Funding acquisition, conceptualization, original draft preparation, review and editing

1.1 ATHEROSCLEROSIS

Atherosclerosis is a chronic, inflammatory disease of the vessel wall, characterized by intimal lesions (atherosclerotic plaques) in the vascular system and typically remains undiagnosed for the first decades of development and progression until complications occur. Rupture or erosion of these plaques can trigger life-threatening diseases such as myocardial infarction and stroke, the leading causes of morbidity and mortality worldwide [1]. Despite the improvements in prevention, diagnosis, and medical treatment, too many people still die of the acute complications or suffer from impaired cardiac function. Therefore, the investigation of new effective therapies as well as novel diagnostic tools is highly prioritized.

However, despite the continuous progress in cardiovascular medicine, our understanding of the basic mechanisms underlying atherogenesis is still incomplete. For example, one of the remaining puzzles is still the focal distribution of atherosclerotic lesions, implicating area-specific susceptibility to disease development within the vasculature, which may be an important target for the development of new therapies. In the next chapters, the basic mechanism of atherosclerosis development and progression will be explained, including the connection of arterial hemodynamics to local lesion development and current strategies in non-invasive magnetic resonance imaging (MRI) methods.

1.1.1 ROLE OF LIPID METABOLISM IN THE PATHOGENESIS OF ATHEROSCLEROSIS

The basic mechanisms underlying atherosclerosis development are of multifactorial nature, including genetic predisposition, lipid metabolism, oxidation processes, inflammation, and hemodynamics, therefore involving multiple cell types, cellular mediators and signaling pathways. Atherosclerotic plaque development is initiated by the intimal accumulation of lipoproteins and leukocytes at predilection sites. The recruitment of inflammatory cells and the subsequent foam cell formation within atherosclerotic plaques is hereby triggered by an early endothelial dysfunction and lipid deposition. In addition to monocytes / macrophages, also other immune cells, including T and B cells, contribute to the cellular plaque infiltrate, resulting in a continuous inflammatory process and steady plaque growth. Next to other risk factors like smoking, diabetes and hypertension, hypercholesterolemia is one of the main triggers in atherosclerosis development [28, 29]. The serum cholesterol is carried by several lipoproteins - dietary lipids are mainly transported by chylomicrons, whereas endogenous lipids are mainly carried by very low density lipoproteins (vLDL), low density lipoproteins (LDL), and high density lipoproteins (HDL). The vLDL particles, which are synthesized in the liver, are triglyceride-rich and contain apolipoprotein E (ApoE) and apolipoprotein B-100 (ApoB^{100}). The main role is the transportation of fatty acids from the liver to peripheral tissue like muscles and adipose tissue, where triglycerides are removed. Parts of the remaining vLDL remnants are then metabolized to LDL particles, which only contain ApoB^{100}, a small proportion of triglycerides and a high proportion of cholesterol and cholesterol-esters, which they transport to peripheral tissues by receptor-mediated endocytosis through the LDL receptor (LDLR), recognizing the N-terminal domain of ApoB^{100}. Once ingested into the cell, LDL particles are degraded completely, where unesterified cholesterol is e.g., integrated into membranes, used for steroid synthesis or converted to cholesterol esters and stored in intracellular lipid droplets [28]. The uptake-rate through the hepatic LDL receptor pathway hereby determines the level of circulating LDL, as seen in patients with homozygous familial hypercholesterolemia, which lack functional LDL receptors and consequently massively accumulate LDL [30]. Intracellular cholesterol levels are hereby controlling the expression of LDL receptors and other genes involved in cholesterol metabolism by regulating the activation of sterol regulatory element-binding protein (SREBP) transcription factors [30].

Furthermore, LDL-cholesterol plays a major role in atherosclerosis development, as evidenced by the fact that statins, which are indirectly inhibiting endogenous cholesterol synthesis reduce the risk for cardiovascular events. Through the decrease in intracellular cholesterol, SREBP transcription factors are activated, and LDL receptor expression is upregulated, therefore reducing LDL plasma concentration [30]. HDL is also synthesized in the liver, but their major role is the reverse cholesterol transport from extrahepatic tissue to the liver, where cholesterol is degraded. HDL is able to bind to LDL particles in order to take over the cholesterol and cholesterol esters as well as triglycerides, therefore acting as a counterplayer to LDL [28]. Triglycerides, LDL and HDL levels are independent predictors of atherosclerosis [31].

1.1.2 INITIATION OF ATHEROSCLEROSIS

1.1.2.1 Endothelial Cell Activation and LDL Accumulation

The development of “fatty streaks” at predilection sites of the vasculature is the earliest stage of atherogenesis, characterized by the intimal accumulation of LDL and presenting the earliest morphological change of the arteries. Interestingly, these predilection sites are characterized by regions, where laminar flow is disturbed and therefore low and oscillatory WSS predominates - a hemodynamic condition triggering endothelial dysfunction, leading to a decreased barrier function [32]. Endothelial cells in atheroprone regions show a disordered alignment, a cuboidal morphology and increased cell senescence and apoptosis as well as decreased nitric oxide (NO) expression, whereas in atheroresistant regions, alignment, proliferation, migration and survival are maintained [28]. Moreover, in these regions, expression of endothelial nitric oxide synthase (eNOS) is enhanced, therefore promoting barrier integrity. In atheroprone regions, the nuclear factor kappa B (NF-kB) pathway is activated, leading to endothelial cell activation and therefore upregulation of adhesion molecules like the vascular cell adhesion protein 1 (VCAM-1), intercellular adhesion molecule 1 (ICAM-1) and P-selectin, increased expression of proinflammatory receptors, cytokines like the monocyte chemoattractant protein-1 (MCP-1) and reactive oxygen species (ROS) [28, 32, 33]. Reduced expression of NO in atherosusceptible regions therefore compromises endothelial barrier integrity and dysregulates transendothelial flux of lipoproteins, which causes an abnormal accumulation of cholesterol-carrying LDL in the subendothelial intima. However, there is also evidence that hypercholesterolemia could directly cause an endothelial dysfunction by changing the permeability, therefore facilitating the uptake of LDL particles into the subendothelial space [29]. However, recent work from Huang et al. showed that the accumulation of LDL particles into the subendothelial space is mediated by the scavenger receptor class B type 1 (SR-B1), which is furthermore increased in human atherosclerotic arteries and atheroprone regions in murine aortas. Therefore, the accumulation of LDL seems not to be driven by a passive movement through a leaky endothelium, but rather an active transport of these particles [34].

The retained lipoproteins in the subendothelial space are furthermore modified by lipases and proteases, which in turn leads to an increased inflammation process, in particular through the modification of LDL to oxidized LDL (oxLDL) through lipoxygenase, myeloperoxidase and ROS [28]. Oxidized LDL has strong proinflammatory and proatherogenic properties, acting as chemo-attractant to monocytes and vascular smooth muscle cells and cannot be recognized by LDL receptors. However, scavenger receptors expressed on macrophages and smooth muscle cells can bind and engulf oxLDL [35].

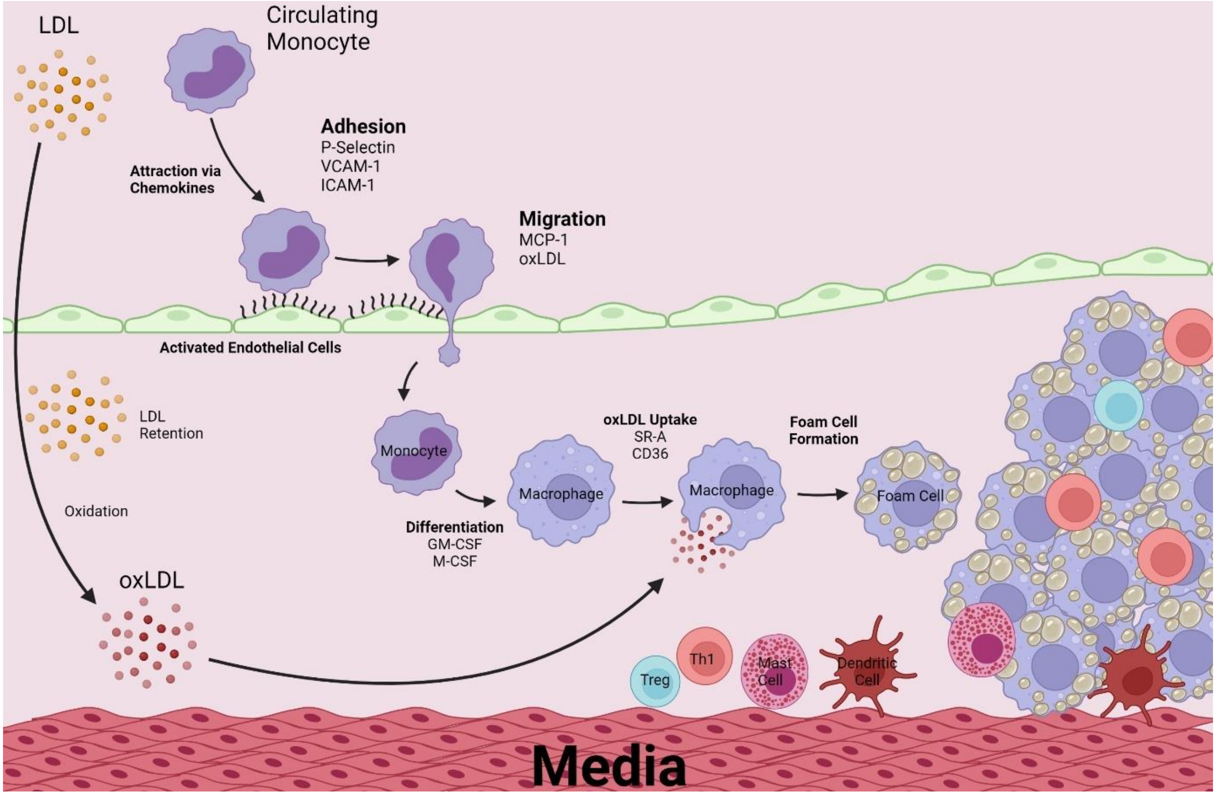

Figure 1: Initiation of Atherosclerosis. LDL is retained in the subendothelial space, leading to endothelial cell activation and increased expression of adhesion molecules. Circulating monocytes are adhering and transmigrating into the intima, where they differentiate into macrophages. LDL and oxLDL are engulfed by macrophages, leading to the formation of foam cells, which accumulate in the subendothelial space and form the fatty streak. Next to monocytes and macrophages, also T-cells, B-Cells, dendritic cells and mast cells contribute to the cellular plaque infiltrate. Image recreated and adapted from [28] with BioRender.com.

1.1.2.2 Immune Cell Recruitment and Foam Cell Formation

The recruitment and subsequent differentiation of monocytes into macrophages may be a protective function in order to remove proinflammatory and cytotoxic oxLDL particles as well as apoptotic cells. However, the increased macrophage accumulation and oxLDL engulfment leads to the progression of the fatty streak development and therefore atherosclerosis [35]. The retention and modification of the trapped lipoproteins hereby further increases the expression of adhesion molecules on the activated endothelium, which stimulates the recruitment of circulating monocytes including rolling, adhesion and transendothelial migration into the subendothelial space through selectins (in particular P-selectin), mediating the rolling process of monocytes on the endothelium, whereas adherence is mediated by adhesion proteins like VCAM-1 and ICAM-1 [36]. Final transmigration of monocytes is promoted by chemoattractants, in particular MCP-1 and interleukin 8 (IL-8) before differentiation into macrophages, stimulated by the secretion of macrophage-colony stimulating factor (M-CSF) and granulocyte–macrophage colony stimulating factor (GM-CSF) [28]. Next to monocytes, also T-cells and other immune cells are recruited, where they recognize LDL as antigen and produce proinflammatory mediators like tumor necrosis factor (TNF) and interferon-γ (IFNγ) [37]. Intraplaque macrophages then accumulate intracellular cholesterol through uptake of native and oxLDL through scavenger receptors (SR) like SR-A and cluster of differentiation 36 (CD36). Interestingly, in contrast to LDL receptors, no downregulation of scavenger receptors occurs in response to intracellular cholesterol levels. After lysosomal degradation of the lipoproteins, the free cholesterol is transported to the endoplasmatic reticulum, esterfied to cholesteryl esters and stored into lipid droplets [28], giving these foam cells their characteristic morphology. Moreover, reverse cholesterol transport pathway components like the ATP binding cassette (ABC) transporter, ABCA1, is downregulated in macrophages in atherosclerosis, impairing the metabolization and export of lipids to carriers for hepatic recycling [38].

However, next to their continuous recruitment and differentiation, monocytes / macrophages furthermore proliferate, making them the most abundant cell population in atherosclerotic plaques [28]. Interestingly, murine monocytes can be divided into inflammatory Ly6C^{hi} and patrolling Ly6^{lo} monocytes [28, 39] and an increase in Ly6C^{hi} monocytes was observed in hypercholesteremic *Apoe*$^{-/-}$ mice, additionally being the major population infiltrating atherosclerotic plaques [40]. There is also evidence that macrophages can also be divided into two main subsets, consisting of a more inflammatory M1 phenotype, induced *in vitro* by IFNγ and LPS and a less inflammatory, pro-healing M2 phenotype, inducible by IL-4 or IL-13 [41]. In atherosclerotic plaques, these two subsets were further found to have differences in location and lipid content, with M2 macrophages having less lipid enrichment and being further from the necrotic core than M1 macrophages [42], which are likely derived from infiltrating Ly6C^{hi} monocytes [39].

Due to triggering of macrophage inflammatory pathways, oxidative stress and cytokine secretion is further enhanced, increasing endothelial cell activation, monocyte recruitment and foam cell formation and consequently leading to continuous plaque growth [28].

1.1.3 PROGRESSION OF ATHEROSCLEROSIS

The formation of fatty streaks is still reversible and therefore can undergo regression until lesions become more advanced (see Figure 2). The hallmark of these advanced lesions is the infiltration of vascular smooth muscle cells (vSMCs) from the media into the intima due to proliferative and migratory stimuli from inflammatory macrophages [38], like platelet-derived growth factor (PDGF), fibroblast growth factors (FGFs), epidermal growth factor (EGF) and matrix metalloproteinases (MMPs), whereas HDL acts as an proliferation and chemokine secretion inhibitor [28]. Moreover, macrophages produce transforming growth factor β (TGF-β), which in turn stimulates the production and secretion of ECM like collagen. The core of foam cells is then covered with a fibrous cap, consisting of mainly collagen produced from the migrating and proliferating SMCs (see Figure 2). Interestingly, intimal SMCs seem to differ from medial SMCs in terms of phenotype, proliferation, and ECM secretion [38], with the latter having a protein expression related to the contractile phenotype by expression of smooth muscle myosin heavy chain (SM-MHC) or α-smooth muscle actin (αSMA). In contrast, intimal SMCs show higher proliferation rates, express less contractile phenotype proteins, but are more related to the synthetic phenotype by showing increased production and secretion of ECM (25 – 46x higher), cytokines, proteases and a higher migration capacity than contractile, medial SMCs [38]. Various atherogenic stimuli are proven to induce the switch between the contractile and synthetic phenotype, including e.g., shear stress, ROS, various cytokines and lipids [38]. Interestingly, this subset of SMCs is also able to accumulate lipids through expression of CD36, vLDL-, LDL- and SR-receptors [28, 38], downregulates the expression of typical SMC markers and in turn expresses macrophage markers like CD68, F4/80 and Macrophage-1 antigen (Mac-2) [28, 38, 43]. Interestingly, expression of the cholesterol transporters ABCA-1 and ATP-binding cassette sub-family G member 1 (ABCG-1) is first upregulated, but with continuing lipid accumulation downregulated again, promoting the transdifferentiation of SMCs to macrophages and consequently foam cell formation [38]. Around 30% of smooth muscle cells in atherosclerotic plaques express macrophage markers and therefore undergo transdifferentiation, as evidenced by fate mapping studies of vascular smooth muscle cells [44]. A co-expression of SMC and macrophage markers was also observed, indicating the existence of a chimeric cell type [45]. Moreover, cholesterol-rich extracellular lipids from apoptotic foam cells accumulate in the advancing lesions and are engulfed by other macrophages as well as SMCs, which show a reduced cholesterol efflux compared to macrophages due to less expression of ABCA-1 and inefficient cholesterol trafficking - but in advanced plaques, also macrophages show a comprised lysosomal function and therefore impaired cholesterol clearance [28].

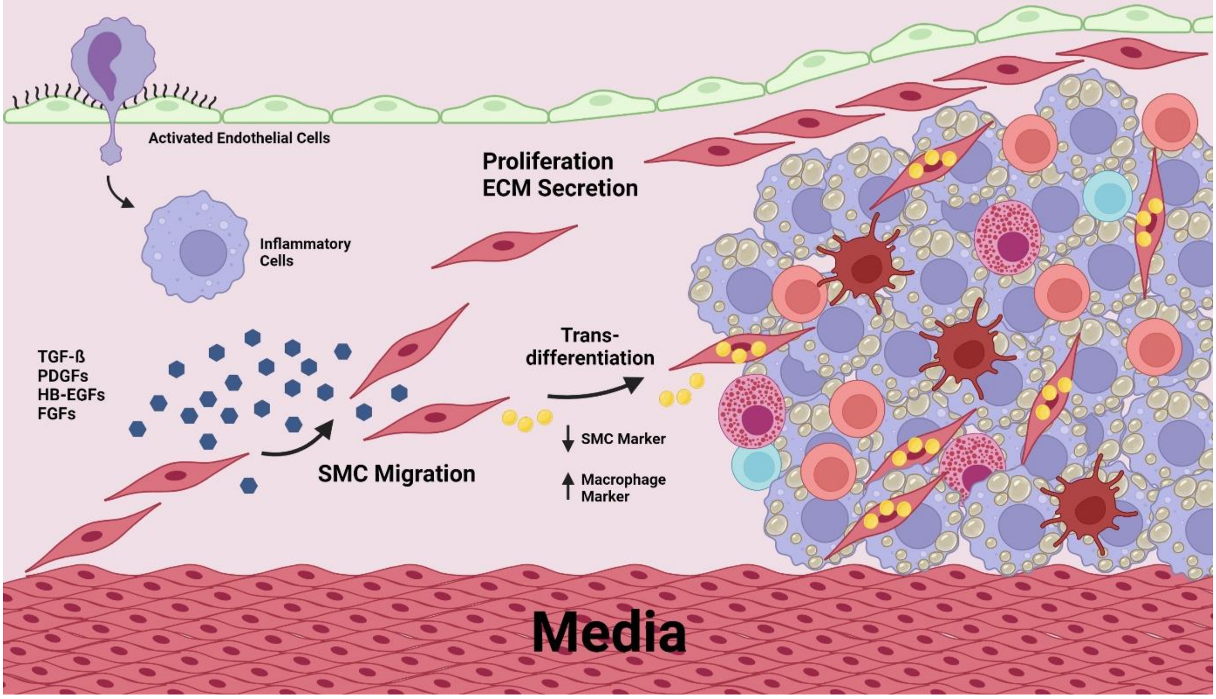

Figure 2: Progression of Atherosclerosis. Inflammatory signaling from activated endothelial cells and foam cells leads to a continuous recruitment of immune cells, which are infiltrating the subendothelial space. Moreover, these cells produce proliferation factors and chemoattractants like fibroblast growth factors (FGFs), heparin-binding epidermal growth factor (HB-EGF), platelet-derived growth factors (PDGF) and transforming growth factor-β (TGF-β), leading to the infiltration and proliferation of medial smooth muscle cells, marking the transition from a fatty streak to a fibrofatty lesion. SMCs migrate to the luminal side of the plaque to form the fibrous cap, where they proliferate and secrete ECM. Through expression of macrophage receptors and internalization of the intimal lipoproteins, a subset of SMCs transdifferentiates to macrophages and become foam cells. Image recreated and adapted from [28] with BioRender.com

While a steady growth of the plaque occurs due to the continuous recruitment of immune cells, foam cell formation and SMC migration and proliferation, and the plaque becomes more complex, vascular remodeling takes place in order to lessen the lesion protrusion into the lumen and simultaneously allowing the preservation of the arterial flow [46]. However, increased apoptosis and necrosis of foam cells leads to the formation of a necrotic core, consisting of cellular debris, lipids, and cholesterol crystals. These crystals furthermore act proinflammatory and result in the release of IL1-β and in turn IL-6 through SMCs. When a stable plaque is formed, the fibrous cap consists of many layers of SMCs with a dense network of collagen and other extracellular matrix components, creating a stable barrier between the plaque content and the vascular lumen, therefore preventing plaque rupture. Moreover, they show decreased extracellular lipid content and a small necrotic core. TGF- β and IL-10, produced by regulatory T-cells (T_{regs}) hereby decrease together with the consequentially reduced activation of Th-1 cells and IFNγ production the proinflammatory macrophage phenotype. This in turn leads to decreased apoptosis, more effective efferocytosis and increased production of the anti-inflammatory cytokines like TGF-β, which in turn stimulates the collagen production of SMCs and extracellular collagen maturation [28, 43, 47].

1.2.1.1 Plaque Rupture and Plaque Erosion

When a vulnerable plaque is formed, plaque rupture can occur, which leads to clinical events like stroke or myocardial infarction due to thrombus formation through exposure of prothrombotic factors from the lipid core to procoagulant factors and platelets in the blood, consequently occluding arteries. A vulnerable plaque is hereby characterized by a thin (≤65 µm) fibrous cap, rich in T-cells and other inflammatory immune cells like macrophages and a large necrotic core, resulting from the non-resolving inflammatory condition and the steady apoptosis and necrosis of foam cells, which release their lipids. In contrast to the stable plaque, the production of IFNγ through activation of Th-1 cells is enhanced, which has a destabilizing effect on the fibrous cap through inhibition collagen production and maturation as well as inhibitory effects on SMC proliferation and differentiation. Moreover, an enhanced extracellular matrix degradation occurs through the secretion of MMPs, which are activated through proteases released by mast cells, but also macrophages, endothelial cells and smooth muscle cells secrete MMPs [43, 47]. Other common features include a large plaque size, the presence of spotty microcalcifications in atherosclerotic plaques, which further contribute to the instability of the plaque, whereas larger areas of calcification provide stability as well as expansive remodeling, neovascularization and intraplaque hemorrhage [43, 47]. The combination of all these factors make these thinned areas of the fibrous cap prone to rupture, in particular when arterial hemodynamics change.

Interestingly, the increased usage of statins, leading to changes in plaque biology, led to a decline of ruptured vulnerable plaques being the cause for most CVDs and plaque erosion becoming the predominant reason for thrombus formation. In contrast to plaque rupture, plaque erosion describes the thrombus formation on plaques with intact fibrous caps, but areas of endothelial denudation, exposing the underlying intima with its smooth muscle cells and extracellular matrix which is rich in proteoglycans and glycosaminoglycans. Moreover, autopsy studies revealed that eroded plaques are different from ruptured plaques, containing more ECM and SMCs while showing less inflammatory cell and lipid content. Furthermore, in contrast to ruptured plaques, which feature a red thrombus, the thrombus of an eroded plaque is rich in platelets and therefore referred to as white thrombus [48]. Changes in WSS profiles, in particular high oscillatory WSS, hereby account for the main reason for plaque erosion. These changes lead to the activation of the Toll-like receptor 2 on endothelial cells and an innate immune response, which together with type IV collagenases like e.g., MMP2 lead to a state of endothelial-to-mesenchymal transition, cytoskeletal reorganization and all together to the degradation of the basement membrane, endothelial cell death and therefore denudation [48].

Therefore, local hemodynamics as well as the plaque geometry seem to play an important role in plaque erosion and plaque rupture (see Chapter 1.3.3 for a detailed discussion of the role of hemodynamics on plaque rupture and erosion).

1.2 MOUSE MODELS OF ATHEROSCLEROSIS

Atherogenesis and progression is of multifactorial nature, which includes altered hemodynamics, lipid metabolism, chronic inflammation processes and oxidative stress acting together, therefore involving a complex network of different cell types and signaling pathways. Hence, the investigation of these mechanisms requires suitable animal models, which meet certain criteria to model different disease stages for studying the underlying basic mechanisms and to reveal potential new targets for therapeutic approaches. These common requirements for good animal models of human atherosclerosis include the ability to monitor atherosclerosis in a reasonable period, a good compatibility with human physiology and anatomy and therefore a good translational potential. Most importantly, these models need to resemble the human lesion topography and to share crucial aspects of the disease with humans. The necessary accelerated plaque formation is achievable by different approaches, including cholesterol-rich diets, modifications of genes involved in lipid metabolism and application of additional risk factors of atherosclerosis. Especially mouse models of atherosclerosis are widely used, in particular since the *Apoe*$^{-/-}$ mouse model was independently introduced by Zhang *et al.* and Plump *et al.* in 1992 [49, 50] and the *Ldlr*$^{-/-}$ mouse model by Ishibashi *et al.* shortly after [51]. Mouse models have a high reproduction rate, a short life cycle, are easy to maintain at relatively low costs, can be easily crossbred and manipulated genetically, making their use convenient for atherosclerosis modelling. Despite all these advantages, they show some differences with human atherosclerosis, including less coronary plaque formation, no intraplaque neovascularization and hemorrhage as well as rare plaque rupture and thrombosis. However, lack of these features can be circumvented by creating more appropriate mouse models like the Apolipoprotein E-deficient Fibrillin-1 mutant (*Apoe*$^{-/-}$ *Fbn1*^{C1039G}) mouse model [52].

1.2.1 THE APOLIPOPROTEIN E DEFICIENT (*APOE*$^{-/-}$) MOUSE

The Apolipoprotein E-deficient (*Apoe*$^{-/-}$) mouse is one of the most used mouse models in atherosclerosis research. ApoE is a glycoprotein synthesized mainly in the liver and the brain and can be associated with all lipoprotein particles except LDL [53, 54]. Deficiency of ApoE, a major ligand for receptors with function to clear vLDL and chylomicron remnants by hepatic uptake through LDL receptors (LDLR) and the LDLR related protein 1 (LRP-1), leads to an increase in total plasma cholesterol mainly due to increased vLDL and chylomicrons. Therefore, *Apoe*$^{-/-}$ mice are hyperlipidemic (with plasma cholesterol levels between 300 and 500 mg/dl) even when fed a normal chow diet and complex, cellular vascular lesions, being comparable to human ones, are developed spontaneously, without the need for a high fat, high cholesterol diet. However, this process can be accelerated by applying a Western type diet (WD) with enriched fat and cholesterol, resulting in plasma cholesterol levels of > 1000 mg/dL and lesions enriched in foam cells [55]. Depending on the diet duration and type, atherosclerotic lesions develop in the aortic root, aortic arch, innominate artery, carotid arteries, and other arteries [56], in contrast to human lesion development, which occurs more frequently in the carotids, coronary arteries and peripheral vessels.

However, the *Apoe*$^{-/-}$ mouse also features some disadvantages. While in humans, plasma cholesterol is carried by LDL, which plays the major role in human atherosclerosis, cholesterol in the *Apoe*$^{-/-}$ mouse is mainly carried by lipoprotein remnants. Moreover, an influence on atherosclerosis independent of plasma lipid levels cannot be excluded due to other functions of ApoE, for example in reverse cholesterol transport in macrophages, smooth muscle cell migration and proliferation and immune function [54, 57].

1.2.2 THE LOW-DENSITY LIPOPROTEIN RECEPTOR-DEFICIENT (*LDLR*$^{-/-}$) MOUSE

Another commonly used atherosclerotic mouse model is the LDL receptor-deficient (*Ldlr*$^{-/-}$) mouse. The LDL receptor is a plasma membrane protein responsible for the hepatic uptake and clearance of plasma lipoproteins, which contain ApoB^{100} or ApoE. However, these ApoB^{100}/ApoE-containing lipoproteins are primarily cleared by the hepatic LDL receptor and its absence results in an accumulation of ApoB^{100} -containing LDL particles in this atherosclerotic mouse model [39]. Therefore, deficiency of this receptor leads to high increase of total plasma cholesterol through impaired clearing of the cholesterol-rich LDL particles, better reflecting the human lipoprotein profile than the *Apoe*$^{-/-}$ mouse. Moreover, vLDL and remnants are taken up by other pathways, leading to a milder lipoprotein profile alteration in comparison to the *Apoe*$^{-/-}$ mouse model, resulting in a plasma cholesterol level around 250 - 300 mg/dL on regular chow [54]. Therefore, these mice develop no or only mild atherosclerosis without dietary induction. However, feeding a high-fat, high-cholesterol diet results in a remarkable change of the lipoprotein profile and plasma cholesterol levels rising above 1000 mg/dL due to an increase in vLDL remnants and mainly LDL and consequently accelerated atherosclerosis development [39]. In these animals, atherosclerotic lesions also develop in a time-dependent manner, from the proximal aorta to other arteries [58].

1.2.3 THE *APOE*$^{-/-}$ VS. THE *LDLR*$^{-/-}$ MOUSE MODEL

The *Apoe*$^{-/-}$ and the *Ldlr*$^{-/-}$ mouse models are the most used atherosclerotic mouse models. However, there are some specific differences between these models regarding the ability to develop atherosclerotic lesions spontaneously as well as the blood lipid profile. While the *Apoe*$^{-/-}$ mouse develops a faster and more advanced phenotype than the *Ldlr*$^{-/-}$ mouse and does not necessarily need a special diet for the development of complex, atherosclerotic plaques, *Ldlr*$^{-/-}$ mice offer a more human-like lipid profile, as the cholesterol is mainly carried by LDL particles. Furthermore, in contrast to ApoE, deficiency of the LDL receptor does not affect inflammation processes and macrophage function. Therefore, atherosclerosis in *Ldlr*$^{-/-}$ mice is not induced by other functions linked to the LDL receptor, but by elevated plasma lipid levels. Another advantage of the *Ldlr*$^{-/-}$ mouse is the similarity to human familial hypercholesterolemia, caused by the absence of functional LDL receptors [39, 54, 55, 59].

However, despite all the differences in the underlying mechanisms causing atherosclerosis initiation and progression, both models are described to develop plaques at the same positions in the vascular tree, namely the inner curvature of the aorta, branch points and bifurcations. These positions share the same hemodynamic characteristics: Regions of low and oscillatory WSS, pointing out the importance and major role of hemodynamics in atherosclerosis development and progression.

1.3 THE ROLE OF SHEAR STRESS IN THE DEVELOPMENT AND PROGRESSION OF ATHEROSCLEROSIS

Vascular inflammation is intricately linked to the biophysical forces acting on the vessel wall through the blood flow, which exerts a tangential force vector, causing a shearing deformation of the vessel wall and leading to regionally different hemodynamic characteristics and therefore spatiotemporal changes in shear forces [32].

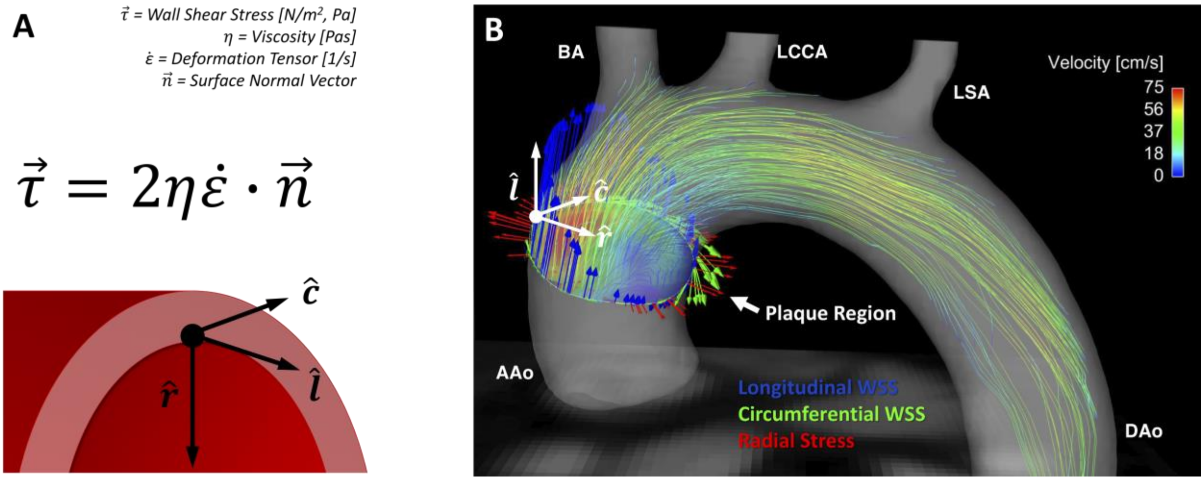

Figure 3: Scheme of the three WSS components. **A** WSS can be calculated from the spatial velocity gradient with the blood viscosity η, the deformation tensor $\dot{\varepsilon}$ and the surface normal vector $\vec{n}$ and can be separated into three components: the longitudinal component $\hat{l}$, the circumferential component $\hat{c}$ and the radial component $\hat{r}$. Redrawn from [8]. **B** Streamline visualization of the flow and WSS components in a ring segment in the ascending aorta of a murine aortic arch with longitudinal WSS in blue, circumferential WSS in green and radial strain in red. Image slightly adapted from [5].´

The hereby-generated WSS, which is dependend on the fluid frictional force acting at the apical surface of endothelial cells is proportional to the spatial velocity gradient at the vessel wall and can be separated into three components (Figure 3): a longitudinal component $\hat{l}$ along the main direction of the flow and a circumferential component $\hat{c}$, which can be attributed to helical flow. Furthermore, a radial strain component $\hat{r}$, perpendicular to the other components is pointing towards the center of the vessel. [8, 60]. The wall shear stress, expressed in N/m^2 or Pa, is a vector quantity – therefore, the strength and the direction are crucial [60].

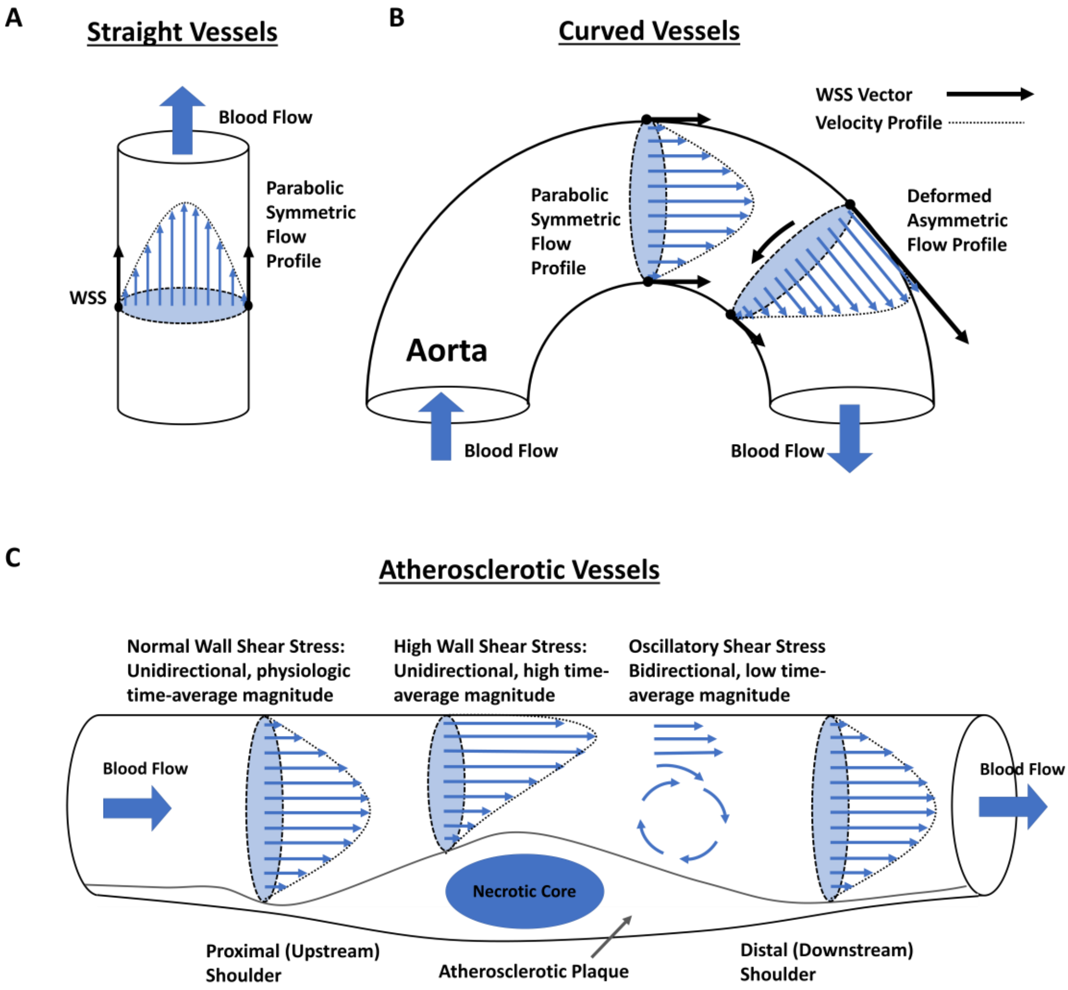

Figure 4: WSS is highly dependent on the vessel geometry. **A** In straight vessels, a parabolic, symmetric flow profile is present. **B** In curved vessels, the flow profile is asymmetric, leading to low WSS values in the inner curvature and high WSS values in the outer curvature of the vessel. **C** In atherosclerotic vessels, the growing plaque further disturbs flow patterns leading to regions exposed to a high WSS gradient at the proximal plaque region as well as bidirectional, oscillatory shear stress with a low time-average magnitude in the distal region. Redrawn and adapted from [61].

Moreover, WSS is highly dependent on the vessel geometry (see Figure 4). In straight vessels, the flow profile is symmetric (parabolic) and the longitudinal WSS component predominates (Figure 4A). However, in curved vessels, the flow profile is getting deformed, leading to an asymmetric flow profile and therefore a high WSS gradient with low WSS values at the inner curvature and high WSS values at the outer curvature of the vessel as well as increased circumferential WSS values (Figure 4B). Especially at predilection sites like the inner curvature of arteries, bifurcations and branchpoints, the resulting shear stress is low and oscillatory, favoring inflammation and remodeling processes and therefore plaque development and growth [62, 63]. The growing plaque further disturbs flow patterns (see Figure 4C), leading to regions exposed to even lower and higher WSS as well as oscillations in the direction of flow, which can be characterized via the oscillatory shear index (OSI), describing the temporal variability of the WSS waveform. A minimal OSI value (OSI = 0) is obtained when no changes in the direction of shear stress occur (unidirectional). However, strong periodic variations due to recirculative flow at the distal region of atherosclerotic plaques or during the diastolic cardiac phase, leading to sign changes (bidirectional magnitude), let the OSI approximate to its maximal value (OSI = 0.5). Both, low WSS magnitude and a high OSI are furthermore known to favor plaque development and progression [64].

1.3.1 ATHEROGENIC EFFECTS OF SHEAR STRESS

Numerous effects of shear stress are described, as summarized in Figure 5 [65-67]. Shear stress is sensed by luminal endothelial mechanoreceptors, which trigger a complex network of intracellular pathways to control endothelial cell homeostasis. In particular, low wall shear stress disrupts nitric oxide-dependent vascular protection, triggering endothelial cell activation, low-density lipoprotein (LDL) cholesterol uptake, and endothelial permeability, which simplifies LDL and monocyte migration into the subendothelial space. Activated endothelial cells upregulate adhesion molecules like VCAM-1, ICAM-1 and E-selectins as well as cytokines like TNF-α, IL-1 and IFNγ and chemokines like MCP-1 to drive leukocyte recruitment to the vessel wall and therefore inflammation processes [65-68].

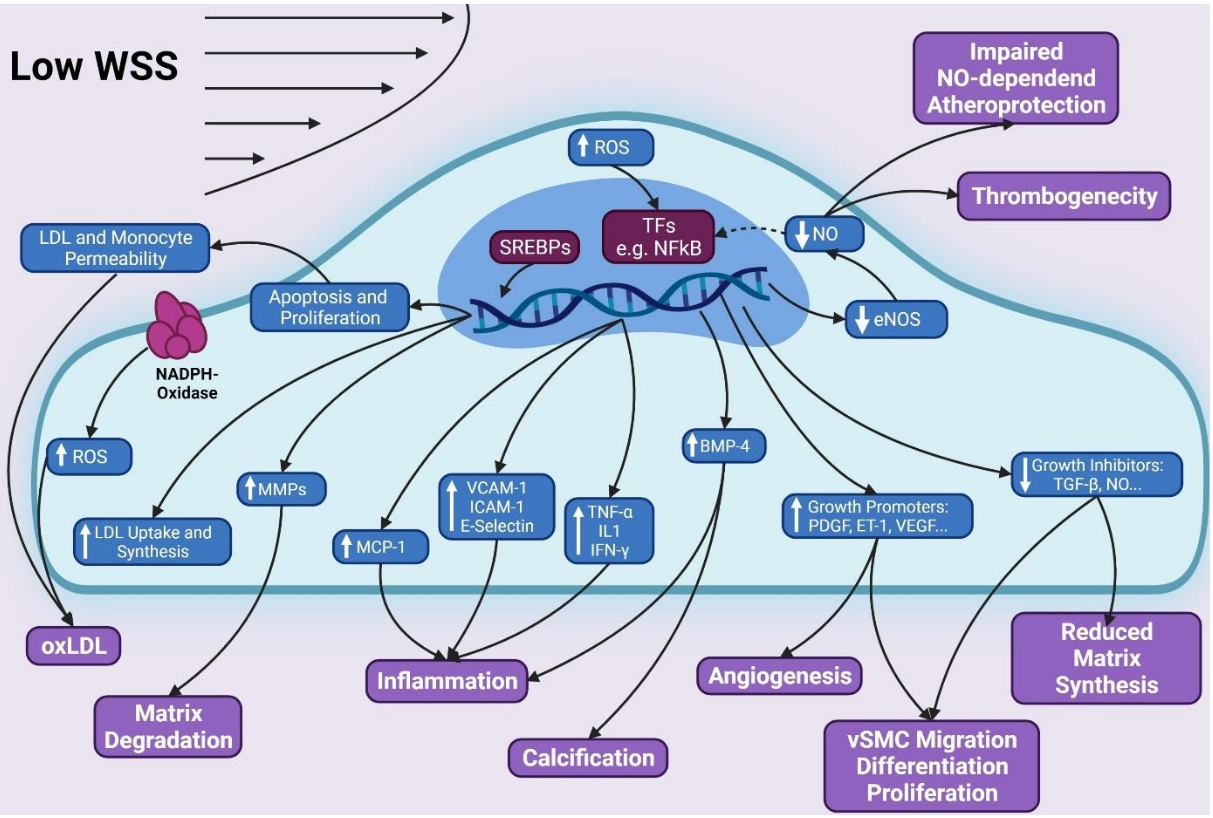

Figure 5: Atherogenic effects of WSS. WSS has various effects on endothelial gene expression through activation of transcription factors like SREBPs and NFκB, faciliating LDL insudation and driving inflammation processes as well as vSMC differentiation, migration and proliferation. A decreased production of eNOS and therefore NO furthermore decreases NO-dependent atheroprotection and increases thrombogenicity. Further consequential effects are an increased matrix degradation, and a reduced matrix synthesis are as well as calcification processes and angiogenesis. Image reproduced and adapted from [65]. Created with BioRender.com

The production of reactive oxygen species is augmented by low WSS, which can cause LDL particles deposited in the vascular wall to undergo oxidative modification to further potentiate their proinflammatory impact on endothelial cells and other vascular and immune cells accumulating in the artery wall. Low endothelial shear stress is also known to sensitize endothelial cells towards interleukin-1β [69], a process that could further amplify local inflammatory processes. Monocytes recruited to the vessel wall differentiate into macrophages, which ingest lipids and transform into foam cells. In the context of ongoing inflammation, vascular smooth muscle cell (SMC) mitogens are produced, promoting SMC dedifferentiation, and SMC migration from the media into the intima and their proliferation, a key process that controls the formation of a fibrous cap [65]. Low WSS has been correlated to a reduction in SMC and collagen production, and an increased matrix metalloproteinase (MMP) activity [69], contributing to a degradation of the extracellular matrix [65].

1.3.2 MOUSE MODELS AND THE ROLE OF WSS

Mouse models of atherosclerosis confirmed the determinant role of low wall shear stress for atherosclerotic lesion size and vulnerability, whereas effects of oscillatory shear stress may be more complex and conflicting results have been reported. A perivascular shear stress modifier placed around murine carotid arteries to investigate effects of fluid shear stress on plaque formation and composition revealed that low shear stress induced larger lesions with a vulnerable plaque phenotype, whereas vortices causing oscillatory shear stress induced stable lesions [70]. Lesions in lowered WSS regions furthermore showed more outward vascular remodeling, an increased lipid content and matrix metalloproteinase activity compared to oscillatory shear stress lesions [70], which seems to be regulated by an increased expression of multiple chemokines [71]. In another study using cuff-induced atherosclerosis, computational fluid dynamics (CFD) suggested that shear stress magnitude contributes to the formation of advanced plaques with a vulnerable phenotype, whereas variations in both magnitude and direction promoted the formation of plaques with stable features [72]. In a study investigating the temporal and spatial changes in WSS over a growing plaque and a potential correlation of WSS and plaque composition, lumen narrowing was observed in all mice after cuff placement. As the plaque developed and intruded into the lumen, absolute WSS significantly decreased and the proximal part of the plaque exposed to relatively lower WSS was small and eccentric, and harbored a greater accumulation of macrophages in histological sections [73]. Interestingly, low WSS seemed to induce pro-inflammatory M1 macrophage polarization in murine thin-cap atherosclerotic plaques induced by cast placement. In macrophage-rich areas of low shear stress-induced lesions, inflammatory M1 markers were highly expressed, while pro-healing M2 markers were elevated in lesions exposed to oscillatory shear stress [74]. Another study conducted in apolipoprotein E-deficient (*Apoe*$^{-/-}$) mice using cuff placement found a significantly higher MMP-2 and MMP-9 activity in the upstream region of the cuff exposed low shear stress, whereas a more stable plaque phenotype was reported in the region of oscillatory shear stress [75], pointing out the connection of wall shear stress and vascular remodeling processes through MMP activity.

Transglutaminase activity may contribute to regulate plaque composition by controlling monocyte recruitment, as investigated in another cuff model of atherosclerosis. *Apoe*$^{-/-}$ mice treated with a transglutaminase inhibitor showed a significant reduction in lipid and macrophage content in the distal region of the cast, where the shear stress is oscillatory. Interestingly, in these regions the lesion size was increased due to an augmented smooth muscle cell content [76]. In *in vitro* experiments of bovine

SMCs exposed to oscillatory shear stress, an increased vascular smooth muscle cell proliferation and activation of the PI3K-Akt signal transduction pathway was observed [77], whereas laminar shear inhibited SMC proliferation [78]. In endothelial cells, however, oscillatory shear leads to endothelial dysfunction and altered lipid uptake as investigated by in different *in vitro* and *in vivo* studies [79-82], pointing out the ambiguous role of oscillatory shear stress in the context of atherosclerosis.

Interestingly, WSS is influenced by systemic blood pressure. CFD demonstrated that ivabradine-induced heart rate reduction enhanced the WSS in the aorta, accompanied by an induction of eNOS and a suppression of VCAM-1 at the inner curvature of the aorta [22]. In a rabbit model of atherosclerosis, it was reported that the heart rate reduction with ivabradine was furthermore associated with a more stable plaque phenotype with decreased macrophage content, plaque microvasculature flow and permeability [83]. Moreover, it was shown that lowered blood pressure and improved left ventricular function induced by docosahexaenoic acid supplementation reduced oscillatory shear at ostia in the descending aorta, which led to decreased plaque endothelial IL-1β expression and a reduction in lesion burden in distal aortas and in brachiocephalic arteries of atherosclerosis-prone mice [84].

1.3.3 PLAQUE CHARACTERISTICS, CARDIOVASCULAR RISK AND THE ROLE OF WSS

Plaque characteristics have also been evaluated in different studies in patients. MRI of carotid artery plaque burden and characteristics were analyzed in a cohort of 1,256 participants from the Atherosclerosis Risk in Communities (ARIC) Carotid Magnetic Resonance Imaging sub study. In this study, the presence of a lipid core was independently associated with incident cardiovascular disease events when adjusted for traditional cardiovascular disease risk factors and carotid artery wall thickness in asymptomatic individuals, and improved risk prediction of incident cardiovascular disease events over traditional cardiovascular risk factors [85]. Of note, the majority of acute coronary syndrome culprit lesions display a ruptured fibrous cap, and only 25% display an intact fibrous cap, as revealed by optical coherence tomography. Culprit lesions with intact fibrous caps displayed a lower lipid content, less calcification, a thicker fibrous cap and were largely localized near coronary bifurcations. Moreover, they also showed an enrichment in $CD4^+$ and $CD8^+$ T cell, providing insights into a pathogenesis mechanism involving cells of the adaptive immune system and their effector molecules [86].

1.3.3.1 High shear stress and plaque vulnerability

How WSS affects advanced atherosclerosis and plaque vulnerability in patients, however, is still unclear and both high and low WSS have been suggested to play a detrimental role and to associate with aspects of plaque progression and vulnerability in clinical imaging studies. In different studies, for instance, it was reported that plaques rupture predominantly in the upstream region of the plaque shoulder [87, 88], where plaques are exposed to an increased WSS, suggesting that an elevated WSS promotes plaque vulnerability in coronary atherosclerosis [89]. In line, increased shear stress was reported to cause vulnerable plaque formation by inducing angiogenesis [90]. Furthermore, focal elevations of high WSS have been associated with plaque rupture and future myocardial infarctions [69, 91]. In a three-dimensional intravascular ultrasound study, Fukumoto et al. also found a relation of localized elevations in the shear stress and coronary plaque rupture. In this study, however, absolute

WSS values were demonstrated to not directly provoke mechanical destruction of the fibrous cap, but to play a triggering role in fibrous cap rupture [91]. A recent study from Kojima et al. has also shown the association of high maximum wall shear stress and plaque rupture in aortic atherosclerosis [92]. High WSS values were furthermore associated with high-risk atherosclerotic plaque characteristics in coronary artery disease patients independently of stenosis severity [93]. A high WSS gradient was moreover associated with plaque rupture and erosion, whereas a high oscillatory shear index correlated with plaque erosion, as revealed by intracoronary optical coherence tomography [94].

1.3.3.2 Low shear stress and plaque vulnerability

However, both in humans [95-100] and porcine models of atherosclerosis [101, 102], plaque vulnerability was also linked to low WSS, which may predict lesion progression to require percutaneous coronary intervention and to be associated with future angiographically driven revascularization and non-culprit major adverse cardiac events [103]. In an intracoronary 3D optical coherence tomography study, Chatzizisis et al. found local, low WSS and expansive lumen remodeling to be associated with the presence of high-risk plaques. Furthermore, they introduced a shear stress score, a global metric of the portion of the artery exposed to the lowest WSS rates. An increased shear stress score was linked to an increased frequency of high-risk plaques [96]. Moreover, a larger lipid burden, a thinner fibrous cap and a higher prevalence of thin cap fibroatheroma in regions exposed to low shear stress was observed in a combined optical coherence tomography and computational fluid dynamics study [97]. Low WSS furthermore predicted the localization of high-risk plaques in an intravascular ultrasound and histopathology study in diabetic, hypercholesterolemic pigs. The complexity and heterogeneity of these lesions was determined by the magnitude of low shear stress [101], which seems to favor the focal evolution of thin-capped atheroma by promoting an imbalance of decreased collagen synthesis and increased collagen breakdown [102]. Also in humans, atherosclerotic plaque burden, composition, and distribution was linked to low WSS in patients with coronary artery disease, as revealed by virtual histology intravascular ultrasound and doppler velocity measurements for computational fluid dynamics modeling [98]. Moreover, local low shear stress was shown to have a critical effect on the de novo eccentric plaque development and progression [99]. In another study, it was observed that artery segments exposed to low WSS showed total plaque progression. In contrast, exposure to low and oscillatory WSS caused total plaque area regression but was associated with a phenotypic transformation towards a more vulnerable phenotype due to a decrease in fibrous tissue and an increase in necrotic core and calcium deposition. This may indicate that low in combination with oscillatory WSS to be the dominant flow characteristic affecting plaque progression and vulnerability [100].

1.3.4 MRI MEASUREMENTS OF WALL SHEAR STRESS AND OSCILLATORY SHEAR INDEX

These in part contradictory reports of the role of WSS in plaque development, progression and rupture emphasize the need for further studies to resolve causality. Most of the studies aiming at a local plaque characterization, however, rely on invasive intra-artery measurements, such as intracoronary optical coherence tomography or intravascular ultrasound, which can cause severe complications, including ventricular fibrillation or vessel dissection, or harbor limitations such as the investigation of only a localized area of the artery. The exploration of alternative and non-invasive methods is such warranted.

Flow sensitive MRI provides the non-invasive assessment of time-resolved 3-dimensional velocity fields and high-resolution morphological information simultaneously in all places of the vascular tree. Especially, a combination of time-resolved 3D spatial and velocity encoding (4D-phase contrast) MRI is considered to drastically improve non-invasive diagnostics, since it allows flow measurements at arbitrary locations and does not depend on the positioning of predefined 2D slices, which may help to reduce the inter-observer variability. MRI could thus be a potential tool for *in vivo* measurements of WSS and OSI, and by allowing a 4-dimensional view of the cardiovascular hemodynamics help to better understand and characterize the pathology of atherosclerosis. It may also present a possible surrogate for inflammation imaging since no contrast agents or tracers are required.

1.3.4.1 Combination of Computational Fluid Dynamics (CFD) and MRI

Moore et al. conducted one of the first MRI-based *in vivo* WSS measurements in humans in 1994 [104]. Since then, 4D MR techniques for WSS quantification have become increasingly important for clinical applications in the aorta [105-108]. In 2006, 2D PC-MRI and CFD using the Navier Stokes equation were used for the first time for investigating the WSS in mice and other mammals [109]. In this work, an allometric scaling law for the WSS of the form WSS ~ M^b (M: body mass, b= -0.38) was found empirically. Weinberg et al. subsequently stated that the WSS inversely depends on body mass to the 3/8th power and predicted 20-fold higher WSS values in mice relative to men [110]. However, early computational models did not take pulsatile flow into account. Therefore, recent models considering more physiological oscillating flow predicted a men-to-mouse-ratio of only 1:8 [111] and therefore lower WSS values. CFD-aided computations of murine WSS were also used by Feintuch et al. [17]. Here, 2D MRI flow measurements were compared with ultrasound measurements. It was observed that ultrasound flow quantification overestimates flow and stated that the MRI flow measurements were slightly more accurate. Furthermore, the CFD simulations revealed that the asymmetry of the WSS distribution across the arch is dependent on the Reynolds number of blood. Subsequently, MRI and CFD were utilized by Doormaal et al. [18] using 2D flow measurements in the aortic root as input function for the CFD simulation. Furthermore, a combination of 4D flow MRI and CFD was recently introduced for detailed WSS studies in the aortic arch of rabbits [112]. While CFD models used for WSS calculations provide valuable information about the complex hemodynamics in the mouse, they still exhibit some limitations. For instance, CT scans of 3D casts of the aorta, which required sacrificing of the animal [17, 18] were used to assess the geometry information for the simulations. Thus, CFD models often neglect lumen area changes and aortic compliance and therefore can overestimate the WSS [2, 7].

1.3.4.2 Direct measurements of WSS using 2D-flow MRI

An alternative approach to assess WSS are direct measurements using flow MRI. These techniques provide unmediated flow and geometry information from the magnitude and phase data. However, as demonstrated in a study in humans [60] and in a flow phantom [113], direct WSS measurements are highly dependent on the spatial and temporal resolution, making the development of preclinical techniques challenging.

First, 2D techniques using triggered radial phase-contrast (PC)-MRI [7] or Cartesian flow cine MRI [114] were developed to study WSS in the abdominal aorta of wild type, *Apoe*$^{-/-}$ and Low density lipoprotein receptor deficient (*Ldlr*$^{-/-}$) mice. WSS was also assessed in the carotids of mice with unstable plaques using Gd-enhanced 2D flow MRI [115] and in the carotids of rats [116]. Furthermore, 2D flow MRI was used to determine WSS at different locations along the vascular tree in arteries and veins in wild-type mice, revealing significant sex- and age -related differences of the WSS and flow values [117].

1.3.4.3 Direct measurements of WSS using 4D-flow MRI

A first 4D PC MRI technique for direct WSS measurements in the mouse was presented in 2011 [8]. Janizcek et al. used 3D spiral MRI with an isotropic spatial resolution of 170 µm and a scan time of 60 minutes to study the longitudinal and circumferential WSS as well as the OSI in the aortic arch of 24 weeks old *Apoe*$^{-/-}$ mice. A highly asymmetric distribution of longitudinal WSS was observed, yielding the lowest values near the inner radius of the arch, where atherosclerotic plaques predominantly manifest. An opposed relation was shown for the circumferential WSS, yielding the highest values near the inner radius. For preclinical WSS measurements in mini pigs, a retrospectively triggered radial 4D PC MRI technique was developed by Wentland et al. [6]. This method enabled simultaneous measurements of WSS and PWV in the abdominal aorta. In 2017, Braig et al. presented a triggered Cartesian 4D PC MRI technique using a cryogenic surface coil for WSS measurements in the murine aortic arch [118]. In this work, dummy scans were used to maintain a close to steady state condition of the longitudinal relaxation in order to reduce image artifacts. For the first time, streamline presentations of aortic flow in the murine aorta were presented. The presented 4D-flow technique featured scan times of 40 minutes and a moderate spatial resolution (300x320x280 µm^3). Therefore, to accelerate the measurement and increase spatial resolution, a retrospectively triggered radial 4D PC MRI technique and compressed sense image reconstruction were introduced to further improve the measurement [119].

1.3.4.4 ECG-free acquisition of WSS and OSI with 4D-flow MRI

Most imaging techniques for wall shear stress quantification rely on an electrocardiogram (ECG) based synchronization of the measurement with the animal's cardiac motion, which can be prone to interferences with the imaging gradients. Furthermore, 4D flow measurements are still very time-consuming. Therefore, accelerated techniques are needed in order to assess arterial WSS values in reasonable measurement times. In 2019, we presented a radial PC MRI sequence that uses self-navigation and retrospective cine reconstruction for 4D flow measurements in the murine aortic arch, which was developed and validated as part of the work on this thesis [4]. Due to the strong signal enhancement of blood and suppression of undersampling artifacts, a scan time reduction to 35 minutes and high spatial resolution (100 µm isotropic) were achievable. The new technique was used to study the 3D distribution of WSS values across the aortic arch (see Figure 6A), temporal changes of WSS over the cardiac cycle and the OSI. However, in addition to shear stress, other factors such as local wall architecture and compliance will have to be considered to fully characterize atherosclerotic lesions in the aorta [2].

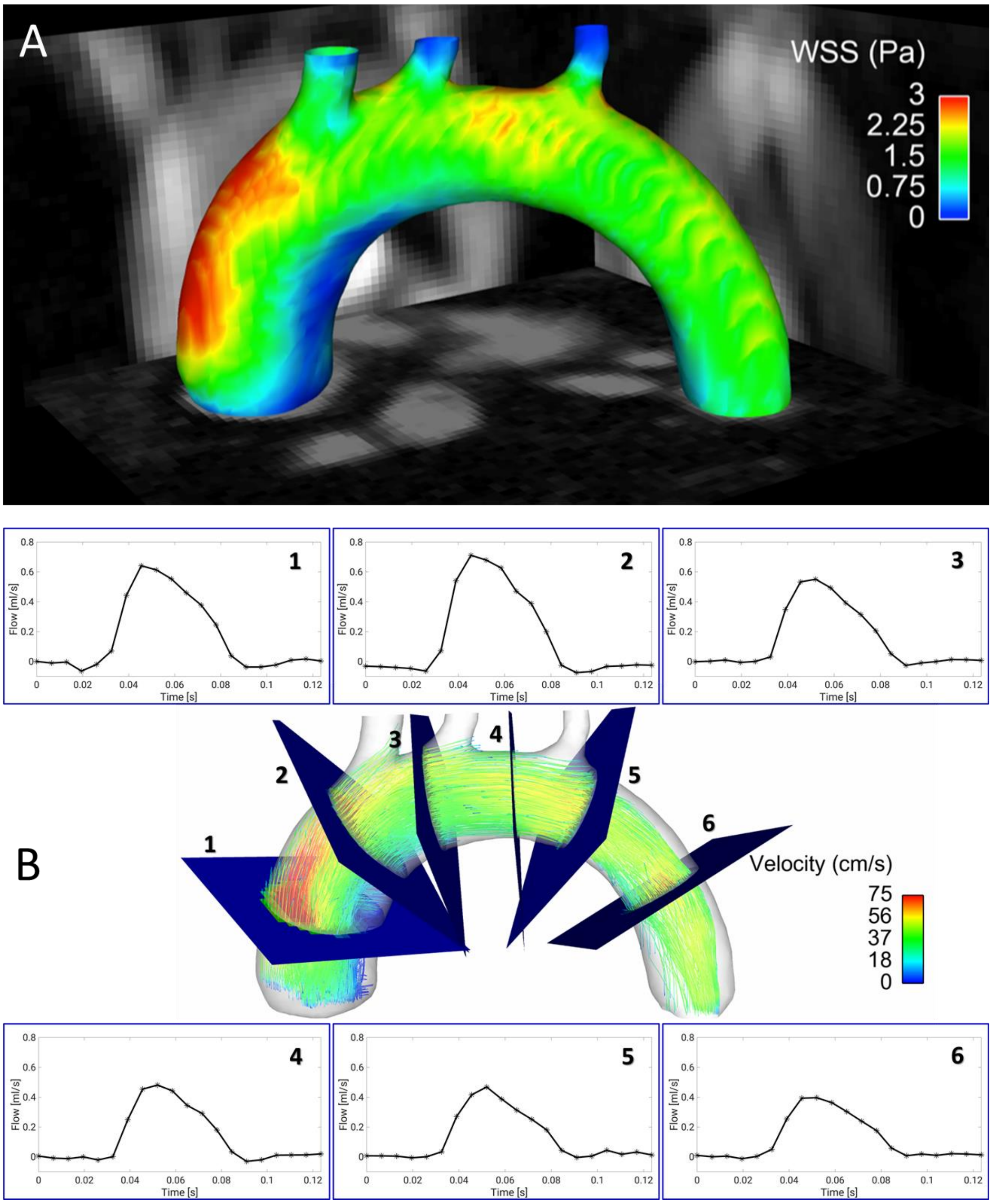

Figure 6: 4D Flow and WSS measurements in the murine aortic arch. **A** Wall shear stress map of the aortic arch of an *Apoe*$^{-/-}$ mouse fed a Western diet, assessed with a self-gated radial 4D PC MRI sequence *[4]*. Especially in the ascending aortic arch, a large region of low WSS can be observed in the inner curvature. This area is known to be prone to plaque development. **B** Streamline presentation of the measured flow and through plane flow for 6 exemplary analysis planes, obtained from the 4D flow measurement [4].

1.4 ARTERIAL WALL STIFFNESS IN ATHEROSCLEROSIS

During atherosclerosis progression, the vessel wall shows structural and morphological adaptions to vascular stress and inflammation. Compensating for a higher circumferential stress due to hypertension, an augmentation in collagen content and number of SMCs is observed, leading to an increased wall thickness [120]. Especially circumferential stress was shown to stimulate the NADPH-Oxidase Isoform

1 (Nox1)-dependent formation of reactive oxygen species (ROS) [121], resulting in a dysfunction of SMCs and the dedifferentiation from the contractile to the synthetic and migratory phenotype as well as in an increase in MMP activity [122] (see also Figure 5). Chesler *et al*. have also shown an increased production and activation of matrix-degrading MMP-2 and MMP-9 in *ex vivo* porcine carotid arteries as a consequence of elevated transmural pressure [123]. Hypertension and a decreased aortic compliance due to reduced elastin content, however, does not seem to affect atherosclerotic plaque burden in atherosclerosis-prone mice [124], suggesting that reductions in the aortic wall compliance may not directly promote atherosclerosis, but rather function as indicators of the disease. However, it has also been shown that estrogen-dependent inhibition of arterial stiffening provided protection against atherosclerosis in females. In this study, oxidized LDL stimulated the secretion of MMP12 in macrophages, which was antagonized by estrogen. Reduced MMP12 expression led to reduced aortic stiffness and inhibited atherosclerosis [125].

1.4.1 IMPORTANCE OF PWV MEASUREMENTS FOR THE EARLY DETECTION OF ATHEROSCLEROSIS

Several human studies investigated the correlation between atherosclerosis and the stiffness of the aortic arch and the carotid artery, and therefore the importance of PWV for early detection of cardiovascular disease. In 2000, the Rotterdam study showed that a high intima media thickness causes an increased arterial stiffness, which in turn lead to an increased plaque burden. They further found a connection between peripheral artery disease and an increased stiffness of the aorta and carotid arteries [126]. Interestingly, in MESA (Multi-Ethnic Study of Atherosclerosis) including 3,527 participants, aortic arch PWV measured by MRI at baseline and when patients were free of overt cardiovascular disease predicted cardiovascular disease events among middle-aged (45-54 years old) individuals during a 10-year follow-up period, whereas the aortic arch PWV was not associated with cardiovascular disease among elderly [127]. At early stages of atherosclerosis, when lumen narrowing is still absent or minimal, the measurement of the PWV may thus function as a surrogate marker for early atherosclerosis. This notion was also supported in a study in atherosclerosis-prone mice, revealing an increased PWV before morphological vessel wall changes and wall thickening occurs [9]. However, measuring the PWV may also be useful in characterizing atherosclerotic plaques. For example, Harbaoui et al. developed a method for measuring the coronary PWV (coPWV) to investigate the effect of local coronary stiffness and found a significant difference in coPWV values in stable and unstable coronary vessel diseases. Furthermore, the coPWV showed an association with acute coronary events in contrast to the aortic PWV (aoPWV) [128]. The local and cell-specific biological responses of the arterial wall and how these are linked to plaque inflammation and vulnerability, however, are not fully understood in detail.

1.4.2 MEASUREMENTS OF PULSE WAVE VELOCITY

Local elasticity (Et) is related to the pulse wave velocity c (PWV) through the Moen-Korteweg-equation [129]:

$$c = Eth / (\rho D), \qquad (1)$$

where h is the vessel thickness, D the vessel diameter and ρ the blood density. During atherosclerosis progression, the vessel wall thickness (h) increases and the diameter decreases (D), consequently leading to an increase in PWV (c, see Figure 7). Therefore, the PWV represents an important physical parameter to characterize the mechanical properties of arteries. The gold standard and most accurate method for measuring the pulse wave velocity are invasive methods with catheter-based flow or pressure probes. These have the highest accuracy and can therefore show new insights into cardiovascular diseases. However, as the use of catheters imply a surgical procedure, the invasive PWV assessment is complicated and laborious due to the intravascular placement of probes, limiting the use in human and animal studies. Besides the use of invasive pressure probes, Applanation Tonometry [130] and Doppler Ultrasound (US) are the most common and established methods for PWV estimation in clinics.

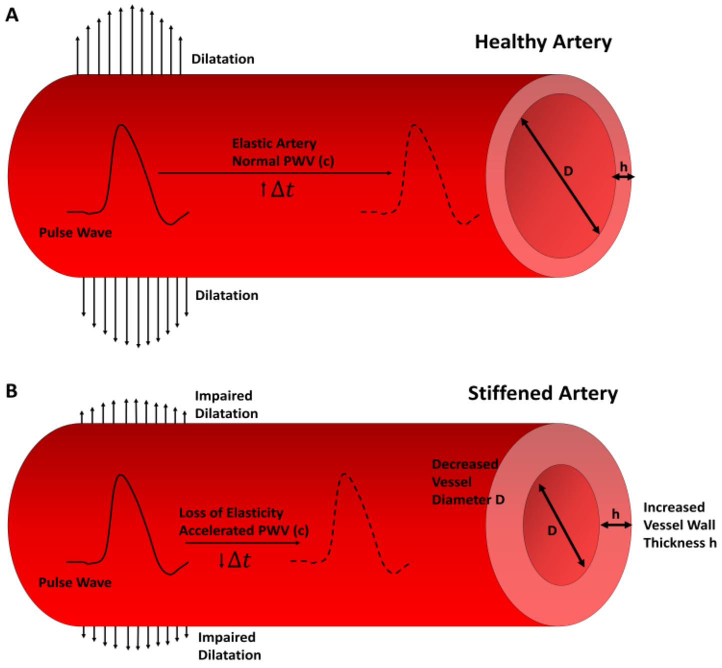

Figure 7: Scheme of the pulse wave velocity in healthy and stiffened arteries. A Healthy, elastic arteries are dilatating and buffering the pulse wave. **B** In stiffened arteries, this dilatation is impaired due to an increased vessel wall thickness h and the decreased vessel diameter D. Consequently, the pulse wave is accelerated through the stiffened artery and the time between two pulse waves Δt is decreased, leading to an increased PWV (c).

1.4.2.1 Ultrasound-based PWV measurements

In US-based PWV acquisitions, ultrasonic waves are used to measure flow. Two probes with a known distance are placed on the target arteries, where one ultrasonic wave is transmitted in direction of the flow and one against the flow. The difference in transit time is directly proportional to velocity and by dividing the measured distance by the difference in transit time of the two waveforms, the PWV can be calculated. An alternative ultrasound-based method is pulse wave imaging (PWI), which uses the detection of vessel wall motion [131]. In the clinic, however, the evaluation of the carotid-femoral PWV (cfPWV) and the brachial-ankle PWV (baPWV) are most common [132]. Ultrasound is furthermore used to characterize plaques in carotid artery disease patients *in vivo* [133] and to determine the local PWV in the human ascending aorta [134]. Also, for preclinical research of cardiovascular disease in animal models, new methods are constantly being developed. For example, Wang *et al.* developed a new methodology for PWV quantifications in the rat abdominal aorta, which was further validated using invasive measurements [135]. Furthermore, micro-ultrasound measurements revealed alterations of the PWV in *Apoe*$^{-/-}$ mice fed a high-fat diet [136].

1.4.2.1.1 Ultrasound-based PWV measurements vs. MRI-based PWV-measurements

Ultrasound based PWV measurements offer many advantages: they are non-invasive, inexpensive and do not require ionizing radiation. Moreover, as US provides flow measurements with a very high temporal resolution, it enables real-time measurements of pressure and flow waves in the vasculature. Not only the PWV but also the WSS [137, 138] and the vessel wall thickness [139] can be assessed with ultrasound-based methods, enabling a good characterization of the flow and the vessel morphology in one session. However, the estimation of the measured vessel distance is prone to inaccuracies. A small error in the distance measurement can already lead to high inaccuracies in PWV estimation with up to 30% error [140]. Furthermore, cfPWV and baPWV only provide global information about the vessel properties. Many studies have already indicated that local PWV measurements are needed to provide a more precise evaluation of the artery conditions [141, 142]. Assessing the local stiffness in a vessel segment may be important to identify plaque formation, but also to characterize the hemodynamic environment of progressive (vulnerable) plaques. The local determination of PWV with ultrasound in various target arteries was already described [132, 134, 143, 144]. However, its wide use in the clinic is still limited. Di Lascio et al. described an ultrasound-based method for the determination of the local PWV in the murine abdominal aorta and found significant differences between younger and older wild-type mice [145]. Moreover, a good correlation between regional transit-time (TT) and local flow-area (QA) method of ultrasound-based PWV assessment was found [146], proving the feasibility of determining the global and local PWV in the murine system with ultrasound. Despite all the advantages, ultrasound-based PWV measurements also entail some detrimental characteristics like the error-prone distance measurements [147]. Therefore - especially in comparison to MRI - ultrasound is very user-dependent [148]. In addition, ultrasound has a limited penetration depth, making some vessels difficult to reach. Furthermore, it only provides a comparably poor soft tissue contrast in comparison to MRI, which not only provides flow information but also high-resolution morphological images. Ultrasound flow measurements also tend to overestimate the peak flow values [17]. For that reason, the development of MRI based PWV measurements is of great interest.

1.4.2.2 MRI-based PWV measurements

The quantification of the PWV with MRI was firstly described in 1989 by Mohiaddin [149]. Today, its determination using phase contrast cine MRI and transit time methods is already established for clinical *in vivo* measurements. In contrast to MRI based elastography measurements [150], PWV quantification provides aortic stiffness values without the need of additional hardware. PWV is regarded as a potential predictor of cardiovascular events, which is used for the assessment of aortic stiffness in aortic stenosis [151] and of the carotid arteries [152]. Recent technical advancements also enable real-time PWV measurements, which can be applied during exercise stress testing [153]. In preclinical atherosclerosis research, mouse models are of great relevance to reveal the pathophysiological mechanisms underlying atherogenesis and plaque progression, and to characterize the therapeutic effects of new drugs.

Therefore, there is a need for developing methods for the indirect measurement of vascular elasticity and function in mice. The adaption of these methods to the murine system is challenging due to the small vessel dimensions, the high heart rates (cardiac periods ~ 120ms) and the small aortic arch dimensions (around 2mm diameter and 30mm length), requiring both, high temporal and spatial resolution methods. Consequently, the needed scan time is markedly increased in order to compensate for the loss of signal-to-noise ratio SNR in comparison to standard PC-MRI sequences.

1.4.2.2.1 Global PWV measurements

Zhao et al., who presented a method based on radial phase-contrast MRI to determine the global PWV and WSS in the murine abdominal aorta [7], described the first *in vivo* implementation of PWV measurements with MRI in atherosclerotic mice. Simultaneously, Parczyk et al. have developed a high-field MR-method for assessing the global PWV in a vessel segment based on travel-time-measurements of the pulse wave [13]. In a swine model with familial hypercholesterolemia, the global PWV was assessed with an undersampled radial 4D-PC cine sequence with retrospective ECG gating. Here, it was shown that the obtained values correlated well with invasive pressure probes measurements. Moreover, it was demonstrated that one single 4D-PC MRI measurement was sufficient to determine both PWV and WSS in only 10 minutes [6].

1.4.2.2.2 Local PWV measurements

The evaluation of the vessel wall, e.g. for the identification of initial atherosclerosis requires a technique to determine the local vascular elasticity as an early biomarker. Through the interrelation between vascular wall elasticity and intravascular hydrodynamic, the local PWV can be calculated through the local temporal behavior of the vessel cross section A and the corresponding volume flow Q with the equation:

$$c = \Delta Q / \Delta A. \tag{2}$$

This MRI-based method of assessing the local PWV was shown for the first time in humans by Vuillémoz et al. [154]. As the mouse represents a good model for longitudinal studies of arterial elasticity and plaque development in atherosclerosis research, the determination of the local PWV was further adapted for the first time to the murine system [11]. With an accuracy of 5-10%, changes in vascular elasticity were observed in *Apoe*$^{-/-}$ mice in comparison to wild type mice. Moreover, a significant increase in the PWV in the ascending aorta was shown even before a visible thickening of the vessel wall. Interestingly, this early loss of elasticity also correlated with an increased elastin fragmentation [9]. A direct comparison of local and global PWV values, however, revealed no significant correlation between global and local PWV values in *Apoe*$^{-/-}$ mice, pointing out the heterogeneous distribution of arterial stiffening in early atherosclerosis and proving the importance of local PWV measurements [10].

Due to the long measurement time and the required consistency of the heart cycle, the measurement of the local PWV is possible in only a few (2-3) locations. Therefore, a correlation of plaque-morphology with PWV is not possible in the whole aorta with conventional techniques. With a modified kt-BLAST method, the measurement time could be reduced to 1/8, allowing measurements of the PWV profile with the vessel morphology with a sampling density of 500µm. With this technique, the measurement of the elasticity profile of the murine abdominal aorta could be realized for the first time, revealing a more heterogeneous distribution of PWV values in *Apoe*$^{-/-}$ mice and pointing out the local character of lesion development [12]. Conventional cartesian imaging techniques are prone to disturbances due to motion and flow and therefore require synchronization with ECG- and respiratory probes. In contrast, radial k-space trajectories are more resistant to motion, as navigation signals of heart and breathing motion can be extracted from the radial k-space data, enabling an ECG-free retrospective reconstruction of dynamic image series (cines) and a more flexible data analysis, where also arrhythmias can be considered. This method was implemented on small animal MRI systems [15, 155] and compared with conventional triggered measurement methods. By measuring the local PWV, the local vascular elasticity of the abdominal aorta could be assessed for the first time without additional heart- or breathing signals (see Figure 2B) [15].

1.4.2.2.3 3D PWV measurements

In the aortic arch, however, a complete profile is not obtainable due to the relatively high slice thickness and the curved geometry, especially in regions with high plaque susceptibility. Moreover, most of the flow velocity measurements are based on 2D-cine acquisition of single planes and the corresponding measurement of the velocity component perpendicular to it [7, 9, 10, 12, 15]. For a full determination of the flow dynamics in arteries, there is a need for 3D measurements with high temporal and spatial resolution, but in an adequate measurement time. In humans, 4D flow-sensitive MRI for the assessment of global aortic pulse wave velocity is already far advanced [14, 156] and was validated *in vitro* [157]. Furthermore, it is already used in several clinical applications, for example in patients with aortic atherosclerosis [158]. Recently, it was also shown that the estimation of aoPWV with 4D flow MRI can be obtained and reproduced using a full 3D coverage in the human aortic arch. The results were compared and significantly associated with standard PWV acquisition [159]. 4D PC MRI was also used to determine PWV and wall shear stress in the aortic arch at the same time [160].

1.4.3 THE GOLDEN GOAL: SIMULTANEOUS MEASUREMENTS OF WSS AND PWV

4D-PC-MRI can overcome the limitations of conventional 2D-PWV measurements such as slice positioning in curved vessels like the aortic arch and through-plane susceptibility artifacts. One major bottleneck of 4D flow measurements, however, is the long acquisition time, which usually results in a compromise between spatial and temporal resolution. On the other hand, 4D PC MRI provides a variety of advantages. For example, in certain vessels, global, regional, and local PWV can be assessed at the same time. Furthermore, other hemodynamic parameters such as WSS, pressure gradients, OSI and vessel geometry can be determined from the same measurement [161]. Therefore, 4D flow MRI and 3D PWV quantification are promising tools for preclinical research, especially when applied in mouse models of cardiovascular diseases. These murine disease models are used to advance our mechanistic understanding of atherosclerosis - thus, there is a need to adapt these methods to the murine system. In 2019, our group presented a self-gated radial 4D flow MRI sequence that enabled high-resolution WSS measurements in 35 minutes [4]. However, combined measurements of both WSS and PWV are challenging since both parameters have different requirements for the temporal and spatial resolutions [6]. In order to circumvent this issue, a new post-processing algorithm was introduced that allows the reconstruction of 4D flow cine datasets at variable temporal and spatial resolutions and the assessment of both PWV and WSS from the same MRI dataset [162] (see Figure 6 and Figure 8A) This method was validated by *in vivo* measurements in wildtype and *Apoe*$^{-/-}$ mice, showing good accordance with results for the PWV values in comparison to triggered methods [10].

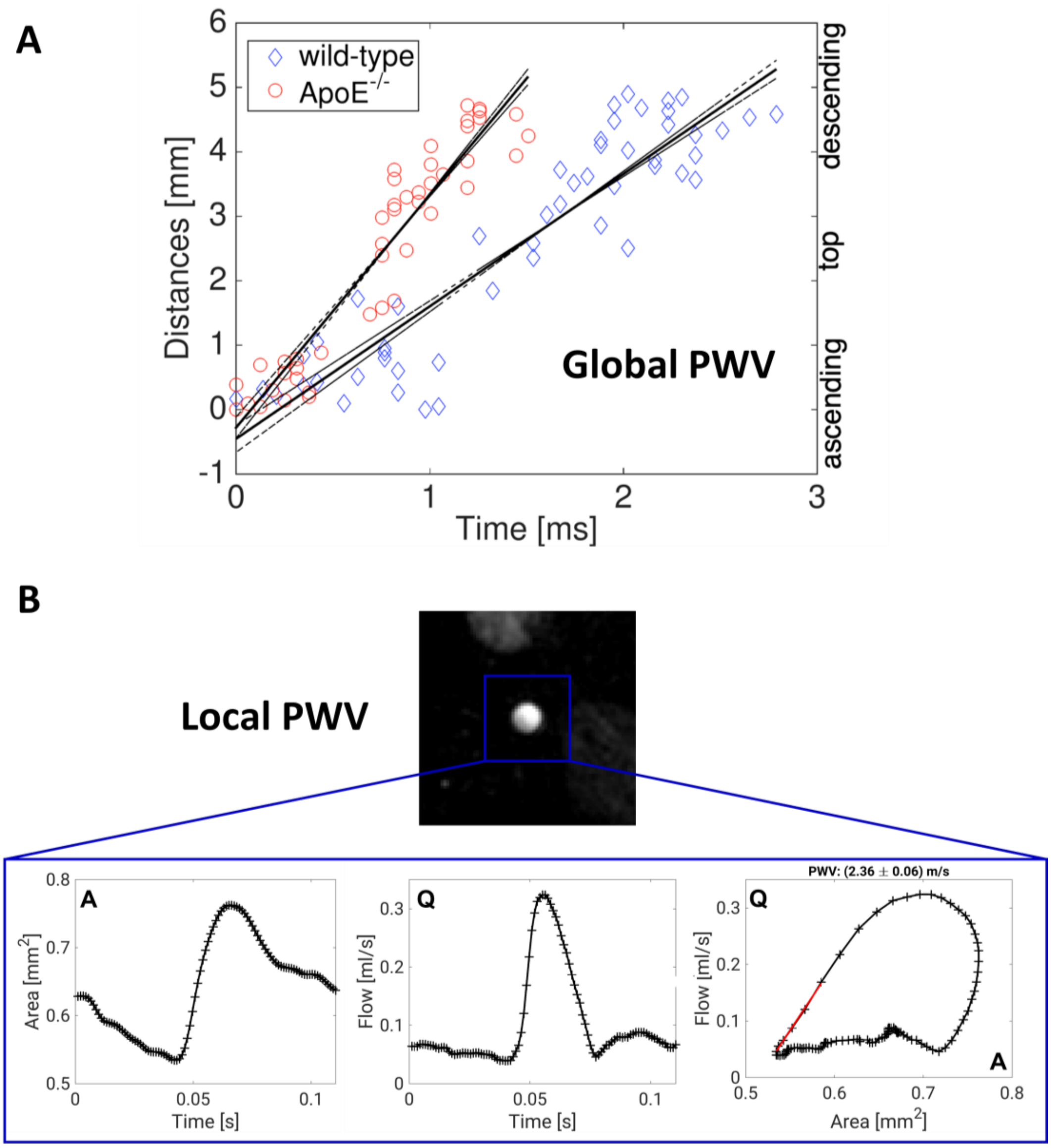

Figure 8: Global and local measurements of pulse wave velocity in murine vessels. **A** Assessment of global PWV for exemplary measurements in the aortic arch of a wild-type and an *Apoe*$^{-/-}$ mouse. For determination of the global PWV values, the time points of the early systolic upstrokes were measured for multiple planes along the aortic arch (see Figure 6B) and plotted against the locations of the planes. The PWV is derived from the slope of a line fitted to the data points [162]. **B** Exemplary measurement of the local PWV in the abdominal aorta of a wild-type mouse using a retrospectively navigated PC-Cine MRI technique [15]. The through-plane flow (Q) and the cross-sectional areas (A) were determined. The local PWV is derived from the Q-A curve by fitting a line to the early systolic data points.

1.5 WSS AND PWV INTERACT TO PROMOTE VASCULAR INFLAMMATION

WSS and PWV are not separate factors with distinct functions; rather, there are mutual interactions that influence biological factors in the vessel wall. Various studies support the hypothesis that within the vascular microenvironment, a signaling cross talk occurs between arterial WSS and vascular stiffness (see Figure 9). An alteration in the architecture and composition of the ECM, namely the increased secretion and deposition of collagen and the fragmentation of elastin as well as the increased smooth muscle cell proliferation and differentiation are distinctive for arterial stiffening [163] – processes, which are also influenced by the local shear stress conditions influencing EC signaling (Figure 5). Studies already showed various indications that vascular remodeling is influenced by pathologic hemodynamic conditions on cellular level. Hu *et al.* investigated the influence of hypertonia, leading to higher circumferential stress, *ex vivo* in the in the porcine *arteria basilaris* and observed structural and morphological adaptions of the vessel wall through increased number of smooth muscle cells and therefore collagen content, consequently leading to an increased wall thickness [120]. Moreover, Gotschy et al. observed an increased elastin fragmentation and elevated PWV values even before morphological changes in the vascular wall were observable [9]. The local character of lesion development, leading to locally stiffened arteries, was demonstrated in following studies [10, 12].

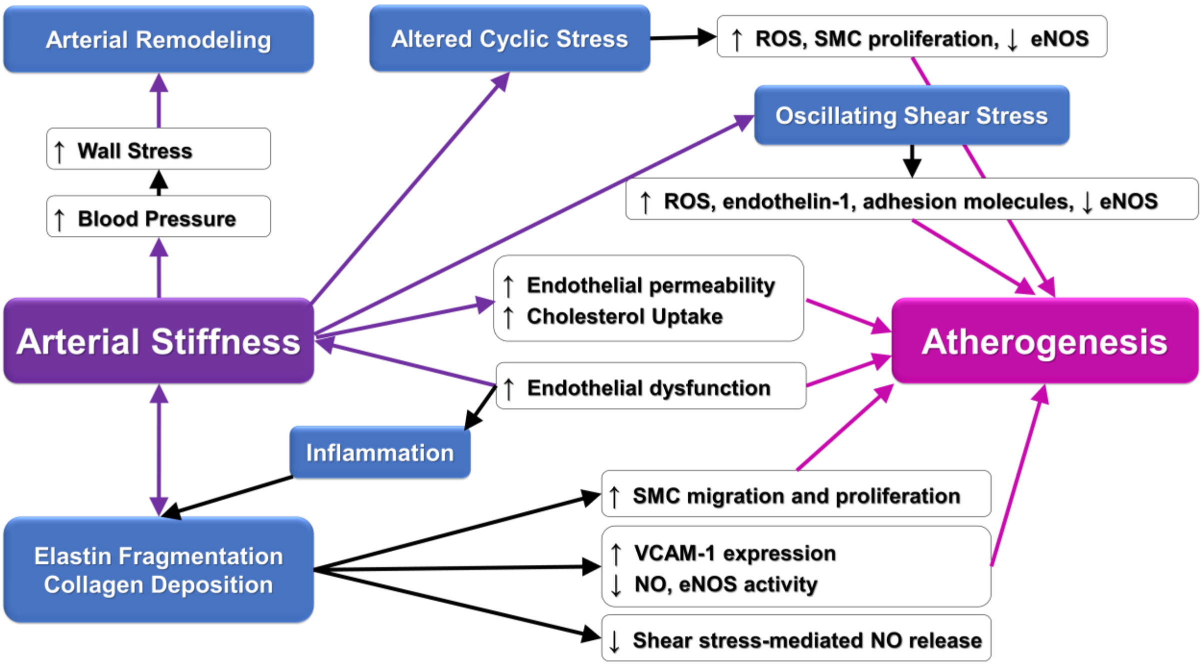

Figure 9: Mechanisms linking arterial stiffness and atherosclerosis. Arterial stiffness, atherogenesis and inflammation processes are closely intertwined and influence each other to promote vascular disease. Image recreated and adapted from [163].

Interestingly, in a minipig model of carotid stenosis by Millon *et al.*, low WSS induced intimal thickening, while large WSS variations and inflammation induced medial thinning [164], pointing out the close relationship and interaction of altered WSS profiles with arterial elasticity.Therefore, the knowledge of the correlation between arterial PWV as a marker of vascular elasticity and local WSS is of great relevance to understand the interaction of arterial stiffness with pathologic flow patterns [3]. In a study using bovine aortic endothelial cells cultured on hydrogels, the cooperative effects of WSS and matrix stiffness were investigated. Hydrogels matching the elasticity of compliant (young) or stiff (aging) arteries were exposed to laminar WSS and revealed that endothelial cells grown on more compliant matrices displayed increased elongation and tighter endothelial cell junctions, decreased activation but enhanced nitric oxide production, suggesting that elastic matrices promote atheroprotective signaling [165]. Furthermore, disturbed flow not only drives endothelial cell activation, but it also causes arterial stiffening through factors released from endothelial cells, e.g. thrombospondin-1, which cause activation of profibrotic signaling pathways, leading to collagen deposition in murine and human arteries [166]. In addition, microcalcifications which are frequently detected within atherosclerotic lesions could bidirectionally affect WSS and PWV. By using a finite element analysis, it was found that even small microcalcifications can elevate the wall stress locally [66]. Interestingly, disruptions in the elastic fibers concomitantly observed with increased PWV [9] can feature a predisposition for the mineralization with calcium and phosphor [167].

However, for an even deeper insight into the processes causing atherogenesis, the heterogeneous distribution of plaques and elasticities needs to be considered [10]. Therefore, the ultimate goal of 4D PC-MRI is the acquisition of the local 3D PWV. The retrospectively gated radial 4D PC MRI sequence described above [162] may allow the assessment of local PWV values at certain locations of the aortic arch (proximal ascending aorta, distal descending aorta). The combined measurement of local PWV, global PWV, WSS and imaging of plaque characteristics and vessel wall inflammation may result in a better understanding of flow-related parameters with the loss of elasticity due to the continuous inflammation process during atherosclerosis progression. In the next chapter, a variety of different imaging techniques for visualization of plaque components and inflammation is described, which may be used in combination with the aforementioned flow-based MRI techniques in order to clarify the interrelation between hemodynamics, plaque composition and inflammation.

1.5.1 VISUALIZATION AND DIFFERENTIATION OF STRUCTURAL PLAQUE COMPONENTS WITH CONTRAST WEIGHTING TECHNIQUES

Atherosclerotic plaques can contain different components, such as a lipid rich necrotic core or intraplaque hemorrhage. The visualization and differentiation of these plaque components is possible with a variety of MR imaging techniques through the use of multiple contrast weightings, including T_1-, T_2-, , T_2*- or proton density- weighted contrast in *ex vivo* [168-171] and *in vivo* imaging applications [172-175], providing complementary information on the plaque composition and morphology. For example, lipid has hyperintense contrast in T_1 weighted and proton density –weighted images and hypointense in T_2 weighted images, while calcified tissue has hypointense contrast in all acquisition techniques, as shown for an *Apoe*$^{-/-}$ mouse fed a western diet in Figure 3A [176]. In *ex vivo* measurements of intracranial atherosclerotic plaques, Jiang et al. could classify different plaque types with an overall accuracy of 80.7% compared with histology through the assessment of the relaxation times (T_2 and T_2*) of the different plaque components [168]. In another *ex vivo* study using intracranial atherosclerotic plaque specimens, T_1-, T_2-, T_2*- and proton density- weighted MRI at 7T was used in combination with histopathological validation for quantitative plaque characterization [171]. Here, significantly different relaxation times and proton density values were observed for different plaque components, with best results for T_1-weighted imaging for plaque characterization. Furthermore, intraplaque hemorrhages in coronary arteries of fixed human hearts were studied with T_1- weighted MRI [169], while T_1- and T_2*-mapping was used to classify the components of surgically resected carotid plaques of patients [170]. MRI data were in good agreement with the corresponding histological sections. Quadratic discriminant analysis of the T_1/T_2* maps, however, resulted in a higher degree of misclassifications of plaques with inflammation or hemorrhage.

For *in vivo* applications, fast T_1- weighted spin echo techniques with compressed sensing were developed, enabling a faster and better visualization of the carotid artery wall and atherosclerotic plaques in patients [172]. Furthermore, T_2 mapping was used to accurately quantify the lipid rich core in atherosclerotic carotid arteries, which was greater in symptomatic plaques than in asymptomatic plaques despite similar volume and luminal stenosis [173]. Moreover, carotid plaque lipid depletion after high-intensity statin treatment was successfully quantified in a following study [174]. For preclinical *in vivo* applications, atherosclerotic plaque stabilization was studied in rabbits using T_1- and T_2- weighted MRI in combination with ^{18}F-FDG positron emission tomography/ computed tomography (PET/CT) [175].

1.5.2 INFLAMMATION IMAGING IN ATHEROSCLEROSIS

Increasing evidence supports a critical role of inflammation and the immune system in atherosclerosis in preclinical mouse models of atherosclerosis and in patients, as reviewed in detail in [177-180]. Clinical trials evaluating the therapeutic targeting of the inflammatory cytokine interleukin-1β (CANTOS trial) or low-dose therapy with anti-inflammatory Colchicine in patients with chronic coronary disease demonstrated a reduction in the risk of developing adverse cardiovascular events [181, 182]. However, the tools to detect inflammation and processes in the vessel wall that could indicate disease progression, or the immanent risk of plaque erosion or rupture are still limited, and subject of continuous research and improvements based on e.g., the technical advancement of imaging tools, which help to increase the diagnostic quality and minimize the burden caused by diagnostic procedures on patients and laboratory animals. Imaging of inflammation for clinical and preclinical applications has been achieved using various probes for Positron Emission Tomography (PET) imaging or combined PET/Computed Tomography (PET/CT) scanning. In a PET study using ^{18}F-fluorocholine (^{18}F-FCH), a strong correlation was found between the uptake of the tracer and the macrophage infiltration, as revealed by histological analysis of carotid endarterectomy specimens [183].

Other examples of PET/CT include ^{68}Ga-DOTATATE PET/CT to image somatostatin receptor–expression, initially developed for imaging of tumors, as a tool to detect inflammation of large arteries [184], 18F-4V for imaging of VCAM-1 expression in atherosclerosis [185], or CD80-targeting PET Tracers [186]. These techniques offer non-invasive detection of inflammation at high spatial resolution but impose a high radiation burden. In addition, PET in combination with magnetic resonance imaging (PET/MRI) has been tested in animal models of atherosclerosis and in humans, as reviewed in [187]. For instance, P-selectin was targeted by gallium-68-labeled fucoidan PET for noninvasive characterization of vulnerable plaques in Apolipoprotein E-deficient (*Apoe*$^{-/-}$) mice [188], and an integrated ^{18}F-FDG-PET and DCE-MRI imaging protocol was applied to noninvasively quantify lesion inflammation, neovasculature, permeability, and plaque burden in a rabbit model of atherosclerosis [175].

Moreover, large-scale multiterritorial PET/MRI demonstrated ^{18}F-Fluorodeoxyglucose uptake in plaque-free arterial segments as an indicator of early stages of atherosclerosis [189]. PET/ MRI offers a good soft tissue contrast; however, patients are still exposed to radiation due to PET tracer. Therefore, the development of completely non-invasive imaging techniques is still of high relevance in order to reduce the examination burden on the laboratory animals and to increase the patient comfort. Flow sensitive MRI is an excellent imaging modality as it provides the assessment of functional cardiovascular parameters such as PWV and WSS without the use of ionizing radiation. Due to its non-invasiveness, it is also well suited for long-term research studies to examine the morphological and functional changes involved during atherosclerotic plaque development.

1.5.2.1 USPIO-based inflammation imaging

Another approach to identify and visualize vascular inflammation sites during the progression of atherosclerosis is the use of ultrasmall superparamagnetic iron oxide particles (USPIOs) as a surrogate marker of macrophage accumulation and activity. These particles are engulfed by macrophages, showing their infiltration in the vascular wall through a rapid signal decline and therefore signal cancellations in T2* weighted images.

To quantify the degree of the particle accumulation and therefore inflammation, pre- and post-contrast agent measurements need to be acquired and compared. Functionalized USPIOs against various targets were also successfully used in different human [190, 191] and animal studies to visualize vascular inflammation. For example, imaging of *Apoe*$^{-/-}$ mice with lipid-coated USPIOs targeting oxidation-specific epitopes or oxLDL targeted iron oxide nanoparticles in the carotid arteries of *Apoe*$^{-/-}$ mice demonstrated the successful imaging of atherosclerotic lesions [192, 193]. Also, Scavenger receptor-AI–targeted iron oxide nanoparticles were able to detect atherosclerotic lesions in *Apoe*$^{-/-}$ and *Ldlr*$^{-/-}$ mouse models [194]. Furthermore, it is possible to image carotid plaque inflammation with Ferumoxytol, which is selectively taken up by atherosclerotic plaques [190]. Especially in early atherosclerosis, VCAM-1 is known to play a critical role. This adhesion molecule is overexpressed on the surface of inflamed ECs in atherosclerosis and mediates the recruitment and adhesion of immune cells to vascular inflammation sites. The use of functionalized USPIOs targeting VCAM-1 therefore enables the visualization of these areas of arterial inflammation in atherosclerosis in animals [195] and in humans [191]. Moreover, dual-targeted microparticles of iron oxide (DT-MPIO) to detect VCAM-1 and P-selectin have furthermore been probed in mice [196]. Our group has demonstrated that USPIOs functionalized against VCAM-1 accumulated in the inflamed vessel wall, leading to a signal loss in T_2* weighted images and enabling the visualization of early inflammation in the aortic arch [197].

Nevertheless, true imaging of vascular inflammation with MRI is still desirable since it would provide complete coverage of complex vessel geometries such as the aortic arch in contrast to 2D slices. Conventional methods to visualize these signal cancelations are based on triggered 2D FLASH measurements [197] and are usually limited to a few previously selected locations along the aorta, making a whole coverage of the vessel unfeasible. A further problem of 2D measurements is the usually large slice thickness, since objects with large susceptibility differences outside the image slice (e.g., lung tissue) can lead to misleading signal voids in the 2D image.

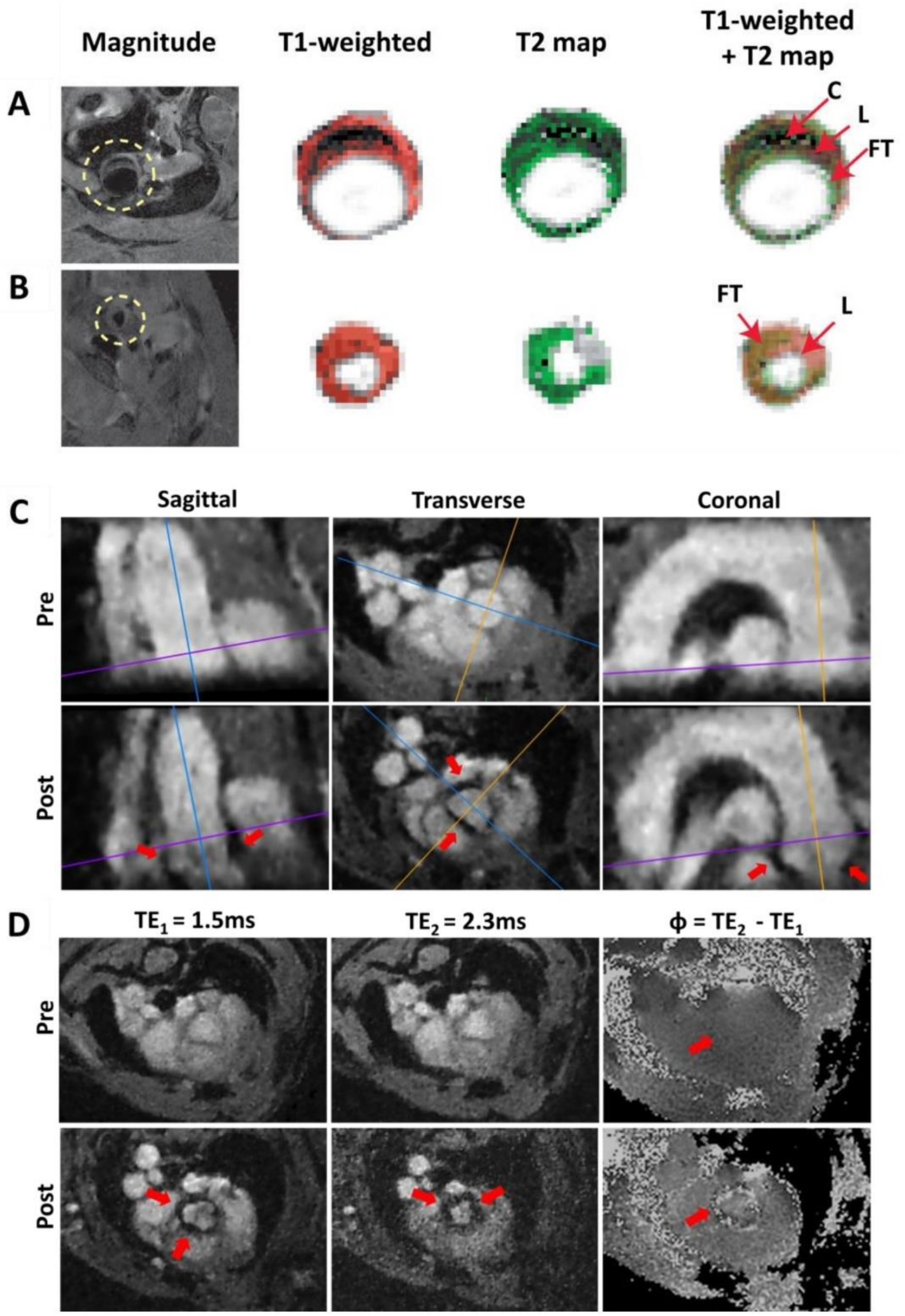

Figure 10: Morphology and inflammation imaging in murine atherosclerotic vessels. **A** Multispin Multi Echo (MSME) imaging of the ascending aorta (A) and the carotid artery (B) of an *Apoe*$^{-/-}$ mouse fed a western diet. FG: Fibrotic tissue. L: Lipid rich core. C: Calcified tissue. **C, D** 3D VCAM-1 Measurement [198]. **C** Sagittal, transverse, and coronal orientation of the aorta extracted from the radial 3D-Cine measurement (TE_1=1.5 ms) before administration of the contrast agent (pre) and after administration of the contrast agent (post). The lines mark the slice orientations. Areas of signal cancellation due to iron particles are marked with arrows. **D** Measurement of the aortic arch at one exemplary position (see purple line in Figure 10C). Measurement with TE_1=1.5 ms, TE_2=2.3 ms and map of the phase differences $\Phi = TE_2 - TE_1$. No significant phase jumps can be found in the aortic vessel wall in the pre-contrast agent measurement (pre), whereas in the phase difference map of the post-CA measurement (post), significant phase jumps are observable.

1.5.2.1.1 3D USPIO-based inflammation imaging

As a proof of principle, the detection of USPIOs, based on an ECG-free radial multi-echo 3D-Cine measurement of the complete aortic arch (see Figure 10C) was further advanced as a part of the work on this thesis [198] and was published as a part of [3]. The cine reconstruction enables the tracking of the nanoparticles during the complete cardiac cycle and the measurement of two different gradient echoes provides the calculation of phase difference maps. These phase difference maps provide more detailed structure information when combined with magnitude maps to better assign the areas of VCAM-1 accumulation. The post-CA measurement indicated significant signal losses in the aortic root and the ascending aorta due to the presence of the iron particles. In contrast, in the phase difference map from the baseline measurement, no significant local phase differences were detectable (see Figure 10D). This demonstrates that the coverage of the complete aortic arch at high spatial resolution and the detection of functionalized USPIOs is feasible with an ECG-free radial 3D-Cine acquisition [198]. Especially when combined with mouse models of vulnerable plaques (e.g. cast models or the insulin-like growth factor-1 knockout model, resulting an unstable plaque phenotype in *Apoe*$^{-/-}$ mice [199], the 3D visualization of USPIOs to detect inflammation could provide the possibility to correlate the localization of inflammation sites with measurements of endothelial WSS and PWV in order to study its potential causal relations and to characterize plaque vulnerability.

1.6 SUMMARY - MRI IS A VIABLE TOOL FOR ATHEROSCLEROSIS RESEARCH

Atherosclerosis is a chronic disease, initiated and modulated by blood flow characteristics, inflammatory processes in the vessel wall, and vessel wall elasticity [3]. Low WSS has been shown to promote arterial inflammation in multiple cell types to promote lesion formation and plaque vulnerability, whereas the role of oscillatory WSS seems more complex. There is also evidence that low and oscillatory WSS contribute to arterial remodeling, entailing a loss in arterial elasticity and therefore an increased PWV [3]. Moreover, arterial wall stiffening is regulated by inflammatory processes and may in addition contribute to the inflammatory load. Although altered shear stress profiles, elasticity and inflammation are closely intertwined and critical for plaque growth, preclinical and clinical investigations for atherosclerosis mostly focus on the investigation of one of these parameters due to the experimental limitations. However, how these parameters correlate with disease and plaque vulnerability, remains to be defined. In this regard, MRI as a non-invasive technique - which does not use ionizing radiation - has been demonstrated to be a potent tool to provide insights into a large range of biological parameters in one experimental session. It enables the non-invasive evaluation of the dynamic process of atherosclerotic lesion formation without the need for harmful radiation [3]. Flow sensitive MRI provides the assessment of hemodynamic parameters regarding altered hemodynamics like WSS [4, 16], PWV [13, 15, 16, 200] as well as changes in the vascular morphology [201] and inflammation processes [197, 198], which may replace invasive and radiation-based techniques for imaging vascular function and characterize early plaque development. The analyses and correlations of these parameters could not only significantly advance basic preclinical investigations of atherosclerotic lesion formation and progression, but also the diagnostic clinical evaluation for the early identification of high-risk plaques, which are prone to rupture [3].

1.7 VASCULAR TISSUE ENGINEERING AS POTENTIAL ALTERNATIVE TO *IN VIVO* EXPERIMENTS IN ATHEROSCLEROSIS RESEARCH

Although the assessment of important parameters of hemodynamics and vascular function via MRI *in vivo* are challenging due to the limited spatiotemporal resolution and the long measurement times, this technique, however, is mainly used in humans and rodents. Another disadvantage is the limited control of hemodynamics like e.g., flow, WSS, PWV and blood pressure *in vivo*. At this point, tissue engineering poses a potential alternative to *in vivo* measurements, as tissue-engineered arteries can indeed meet the elastic properties of a native artery, but until now, only a few studies were reporting the utilization of artificial vessels in combination with MRI measurements [13, 202]. Moreover, when using tissue-engineered arteries, long measurement times are not an issue anymore and consequently enable measurements with higher spatiotemporal resolutions. Most importantly, the utilization of tissue engineered arteries, cultured in suitable bioreactors, offers a fully controllable environment and therefore the possibility, to selectively control hemodynamics and study their effects on vascular cells in a simplified environment. Nevertheless, the utilization of native artery models for flow-related disease research using high-resolution 4D-flow MRI hat not been reported yet. In the next chapters, the basic principle of tissue engineering will be explained, including the utilization of native, decellularized and artificial, biofabricated scaffolds as well as the generation and application of tissue-engineered arteries for *in vitro* atherosclerosis research.

1.7.1 TISSUE ENGINEERING AND REGENERATIVE MEDICINE

Tissue Engineering (TE) describes interdisciplinary process of life sciences and engineering for creating biological tissue by isolation and cultivation of host cells together with biomolecules (e.g., growth factors) in 2D or 3D cell culture combined with a matrix (scaffold, see Figure 11) to replace or regenerate diseased tissue in patients or to establish functional *in vitro* test systems [203]. Tissue engineering and regenerative medicine are closely intertwined and can be divided into three major strategies: i) Cell transplantation from a healthy donor to a diseased recipient or from healthy tissue to injured tissue, ii) the targeted injection of biomolecules, which induce tissue regeneration and iii) the three-dimensional seeding and cultivation of cells on an appropriate matrix prior to implantation or in order to create functional *in vitro* models. In general, there are four different kinds of implants described: i) from the patient himself (autologous) like skin transplantations or autologous stem cell transplantations [204], ii) from an individual of the same species (allogenic) like kidney transplants or stem cell transplantations, iii) from genetically identical individuals (twins, syngen) and iv) from other species (xenogenic), e.g., heart valves [205]. The basic principle of tissue engineering is depicted in Figure 11. Cells are usually isolated from a donor and expanded *in vitro*. Scaffolds of biological or synthetic nature are prepared and combined with the isolated cells in order to create a three-dimensional cell-matrix construct, which is cultured *in vitro* together with appropriate biomolecules, supporting the formation of the new tissue. Afterwards, the construct is either used as an *in vitro* test system or transplanted back into the host or another recipient [203]. In particular, the development of three-dimensional (3D) tissue models is of great interest for various scientific research fields like biology, pharmacy and medicine, by creating a more realistic cell environment through mimicking natural cell-cell and cell-matrix interactions compared to conventional 2D cell culture. The increasing understanding of the signal response and interaction of individual cells with their environment and the hierarchical organization of tissues and organs paved the way for the targeted manipulation of these processes in order to replace damaged tissues or create functional *in vitro* tissue models. These 3D tissue models act as a more accurate bridge to the *in vivo* situation [206, 207] and could therefore help to gain new insights into disease development and progression by offering a simplified *in vivo* situation and consequently reduce animal experiments. The two main approaches for scaffold-based TE using either natural, decellularized scaffolds or synthetic, biomaterial-based scaffolds, are described in the following.

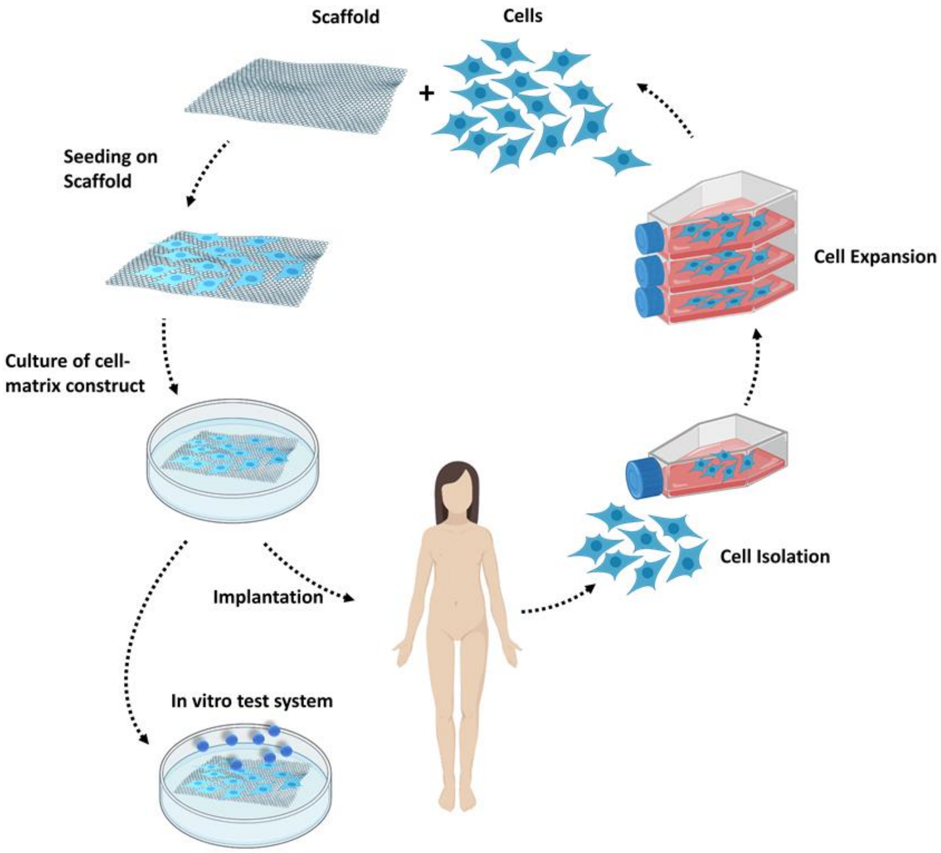

Figure 11: Principle of Tissue Engineering. Cells are isolated from the host and expanded before seeding onto an appropriate scaffold or hydrogel matrix. After cultivation, the cell-matrix construct, is either transplanted back into the host or used as an *in vitro* test system. Redrawn and adapted from [208]. Subimages were taken from biorender.com and modified.

1.7.1.1 Decellularized Scaffolds for Tissue Engineering

A promising approach to generate organs and tissues for replacement of diseased host tissue and the generation of functional *in vitro* test systems is the decellularization of native tissue, resulting in a natural, acellular three-dimensional ECM scaffold and the subsequent reseeding with the appropriate cell types. In preclinical studies as well as clinical applications in humans, a successful utilization of these biological scaffolds has already been reported, e.g., heart valves [209], blood vessels [210] and skin [211]. Moreover, host tissue (like human tissue discarded during operations) can be used for scaffold preparation, and customized autologous or allogenic tissue can be generated when reseeding the scaffolds with host cells, which lowers the risk for rejection by the immune system.

The decellularization itself is the process of removing cells from a donor organ or tissue, with either physical, chemical, enzymatic methods or a combination of these methods, leaving behind a composite of different structural and functional extracellular matrix proteins. In general, the cell membranes from the donor tissue are lysed using physical methods or ionic solutions and cytoplasmic and nuclear components are solubilized in a first step, followed by an enzymatic treatment for the separation of cellular components and digestion of residual host deoxyribonucleic acid (DNA) and complete removal of all remaining cellular debris and decellularization agents through extensive washing, before sterilization of the scaffold for further use [24, 25]. Coupling with mechanical agitation further increases the effectiveness of these steps. However, there are a lot of variations and methods described in literature regarding the species used for scaffold generation, the original organ or tissue, from where the scaffold is obtained, different approaches for the decellularization and the final sterilization [24, 25]. For small, simple tissues like heart valves, the tissue is harvested and submersion decellularization is performed, meaning that the tissue is simply submersed in decellularization agents to enable intimate contact of the decellularization agents to all cells. Such tissues are processed as two-dimensional scaffolds and are not connected to the host vasculature upon implantation. The vascular network, however, develops over time and the seeded and infiltrating cells rely on diffusion of nutrients and oxygen until the vascular network is formed. A breakthrough enabling the immediate creation of more complex and hierarchically structured tissues and even organs was the invention of perfusion decellularization, which uses the existing vasculature of the donor tissue to perfuse the decellularization agent and therefore enable the removal of cells throughout the complete complex tissue or organ [24, 25, 212]. This technique furthermore offers the advantage to maintain the complete vascular scaffold of the donor tissue for the subsequent recellularization with e.g., endothelial cells, to create a functional, vascularized tissue which can overcome the limitations based on the diffusion distance in 3D cell culture [213-215] and the corresponding size limitation.

Most importantly, every single decellularization step affects the ultrastructure and the extracellular matrix composition and - after eventual implantation - also an eventual immune-mediated rejection of the tissue from the host. An ineffective decellularization can also cause a strong inflammatory response in transplantation studies [216], but is also affecting cell adhesion, proliferation and survival and, due to excessive ECM damage and loss of ultrastructure, also causing a loss in mechanical stability. However, when creating *in vitro* test systems, the response to certain allogeneic and xenogenic antigens is negligible. Nevertheless, decellularization affects the mechanical behavior of the tissue – therefore, the decellularization protocol needs to be efficient in cell removal, but simultaneously minimize the effects on the three-dimensional architecture, the biological activity of the scaffold, the ECM composition, the ultrastructure and the mechanical integrity [24, 25].

The mechanical behavior of a tissue is hereby determined by the complex mixture of tissue-specific functional and structural extracellular matrix components like collagen, elastin, glycoproteins and proteoglycans, and arranged three-dimensionally, affecting a variety of cellular activities and allow the tissue to fulfill biological as well as structural functions. However, the metabolic activity of the resident cell population, influenced by the mechanical demands of the tissue and the microenvironment, are constantly changing the composition and structure of the ECM - therefore, it is very important to maintain the native ultrastructure and composition of the ECM as much as possible [212] to present a native environment for the reseeded cells, e.g. decellularized arteries or veins for vascular cells. Most ECM scaffolds hereby primarily consist of collagen I, but also laminin, fibronectin and glycosaminoglycans (GAGs), as well as different growth factors and it is also known that the basement membrane, consisting of collagen IV and laminin, is retained after the decellularization process [212]. Another very important reason to maintain the ultrastructure of the tissue as good as possible is the influence on the attachment and phenotypic differentiation of cells, as well as migration [212, 217]. Therefore, the proper decellularization method, offering a cell-free scaffold while maintaining the ECM composition and ultrastructure, is the golden goal.

There are many different decellularization methods described, with combinations of physical and chemical methods being the most used ones. Physical treatments include pressure, freezing and thawing cycles, sonication and mechanical agitation using shakers or stir plates [24, 25]. However, they are only facilitating the decellularization process, but are not sufficient to fully remove all cells and cellular debris. Freezing of the tissue hereby disrupts the cell membranes through formation of ice crystals, whereas pressure application can only be used in tissues, which are not consisting of dense ECM like lungs or liver tissue to disrupt the cellular membranes. While being effective in lysing the membranes and therefore facilitating subsequent rinsing of cellular debris as well as retaining the ultrastructure of the ECM, these methods are still insufficient to obtain a completely cell-free scaffold. Therefore, physical treatment is followed by use of chemical agents like hypotonic and hypertonic solutions, detergents, alcohols or biologic agents like enzymes. Chemical agents include acid and alkaline treatments, which is disrupting cells and solubilizing cytoplasm components and furthermore removing ribonucleic acid (RNA) and DNA, while disinfecting the remaining tissue – however, they are also disrupting the ECM through dissociation of molecules like GAGs and damaging collagen [24, 25]. An extensively used agent is peracetic acid, which is known to efficiently remove cells and cellular debris, while just having a minimal effect on ECM structure and composition [24]. In contrast, treatment with hypotonic or hypertonic solutions efficiently lyses cells through osmotic shock but is not sufficient to remove all cellular residues within the tissue. One of the most used non-ionic detergents for decellularization is Triton-X. This agent is very suitable for thin tissues, disrupting lipid–lipid and lipid–protein interactions, but protein-protein interactions are left intact. However, the efficiency is dependent on the tissue, but it is less affecting the ultrastructure of the tissue in comparison to ionic detergents [218, 219]. These are also solubilizing cell membranes but are also known to denature proteins. Sodium dodecyl sulfate (SDS) is known to decellularize tissue more efficiently, in particular dense tissues, but it is also disrupting the native tissue structure, causing a loss of collagen integrity, decreasing the GAG concentration and removing growth factors from the tissue [24, 25]. In contrast, the efficacy of sodium dodecyl sulfate (SDC) is dependent on the tissue thickness. It removes the cells and cellular remnants efficiently but is disrupting the native tissue architecture and removing GAGs in combination with other zwitterionic detergents [24, 25]. Biologic agents include e.g., trypsin, which cleaves the peptide bonds on the C-side Arginin and Lysin, but with prolonged exposure, it can also disrupt the ECM ultrastructure and remove collagen, elastin, laminin, fibronectin and GAGs. However, in contrast to detergents, the GAG removal is slower [24, 25].

Taken together, it is clear that all treatments can have substantial effects on the extracellular matrix composition and therefore mechanical behavior and cell adhesion, migration and survival. Therefore, the development of a tissue- and application-specific decellularization protocol is of great interest. However, once optimized, the utilization of natural, decellularized scaffolds offers many advantages like the native ECM composition and ultrastructure and therefore excellent cell adhesion, differentiation and survival, as well as vascularized structures within the scaffold for engineering up to complete organs.

1.7.1.2 Biomaterials for Tissue Engineering

The field of biofabrication provides several techniques and possibilities to create 2D and 3D tissue models for *in vitro* testing and is defined as “the automated generation of biologically functional products with structural organization from living cells, bioactive molecules, biomaterials, cell aggregates such as micro-tissues, or hybrid cell-material constructs, through Bioprinting or Bioassembly and subsequent tissue maturation processes.”[220] By utilizing different fabrication methods like 3D printing in a biological context, biofabrication enables the generation of hierarchical structures including macro- and microstructural features of the ECM and the allocation of cells. As different tissues like muscle[221], cartilage[222] or the vasculature[223] exhibit distinctive ECM and cell hierarchies directly linked to their functionality, it is important to address these features during tissue generation to enable a high degree of tissue mimicry. Per definition, biomaterials are materials, which are exploited in contact with living tissues, organisms, or microorganisms [224]. Regarding TE, these biomaterials are utilized as an ECM for 2D or 3D cell culture and can be either natural materials like collagen or gelatin, or synthetic materials like polymers or ceramics. The most abundant biomaterials for TE are hydrogels, as they closely mimic the ECM of soft tissues and are designed to provide a 3D architecture for cell growth, including cell adhesion motifs, porosity, biodegradation and biocompatibility [225]. In this regard, artificial hydrogels based on biocompatible polymers like polyethylene glycol provide a suitable structure for cell survival. However, they do not provide means for cell adhesion and matrix degradation and are therefore not suitable for cell cultivation [226] without the addition of biocompatible modifications like peptides or protease cleavage sites. In contrast, natural hydrogels like collagen or modified natural biomaterials like methacrylated gelatin [227] intrinsically provide degradation and adhesion sites and are therefore directly usable in 3D cell culture. However, shrinking and natural batch-to-batch variations often lead to problems regarding handling and comparability of 3D tissues. Furthermore, these variations lead to problems in the formation of ordered or structured biomaterial constructs via means of biofabrication.

Biofabrication methods enabling the generation of hierarchical tissues can be divided into two categories[228] (see Figure 12):

1. Bioprinting or casting of bioinks, which directly include cells, hydrogels and other factors in the additive manufacturing process
2. the generation of scaffolds based on biomaterial inks, where cells can be seeded on previously fabricated scaffold structures based on biomaterials

In both cases, the artificial 3D matrix should enable good cell attachment, survival, proliferation and, in the best case, differentiation.

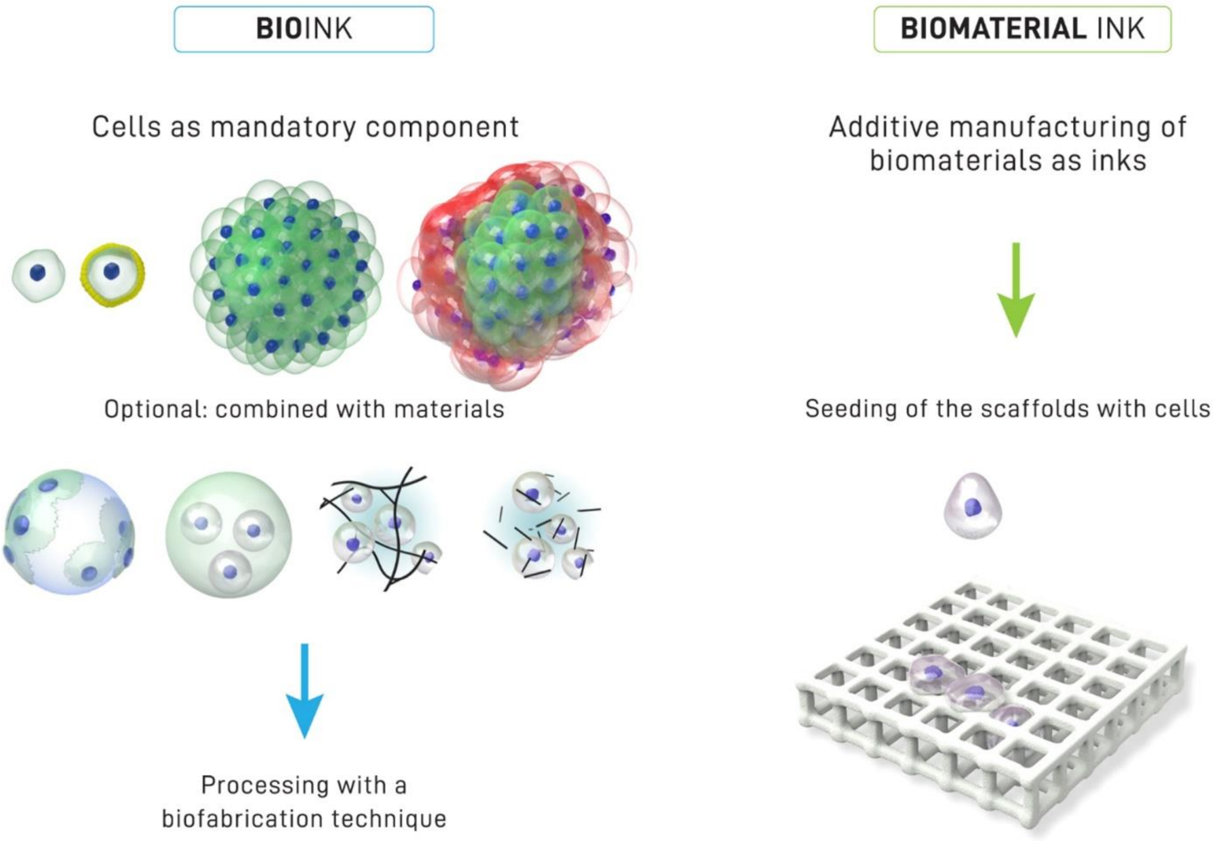

Figure 12: Bioinks and biomaterial inks. In Bioinks, cells are a mandatory component, optionally combinable with other materials, before being processed with a biofabrication technique. In contrast, Biomaterial Inks are fabricated from biomaterials as inks through additive manufacturing processes, resulting in a cell-free scaffold. This obtained scaffold is then seeded with cells. Image taken from Groll *et al.*: "A definition of bioinks and their distinction from biomaterial inks" [228].

In general, bioprinting utilizes common additive manufacturing methods like 3D printing and stereolithography and can be divided into several technologies. However, all techniques require biocompatible hydrogels as carrier material for cell printing. In this regard, hydrogels are very suitable, since they can be chemically or physically tuned according to the requirements and furthermore offer a permeable microenvironment [229].

Pressure-assisted printing systems are the most prominent methods due to their abundant availability and low cost.[230, 231]. Here, a syringe is filled with the bioink and extruded as a filament by applying pressure, enabling the generation of bigger construct via layer-by-layer deposition. The limiting factor for the resolution of this method is the cell viability, as shear stress increases with a decreasing nozzle diameter [232]. This technology can be further expanded by printing into support baths filled with hydrogels [233] or jammed microgels [234], which overcomes the resolution limitation and allows the generation of highly defined 3D structures. However, support bath printing is a very slow process, as fast printing-speeds can deform the initially printed structures. Furthermore, the printing device can be expanded by a coaxial nozzle, which allows the generation of filaments with an inner and outer shell [235].

Besides pressure-assisted systems, light-based bioprinting (stereolithography; SLA) is an emerging technology which uses light to crosslink hydrogels from a resin bath based on the precursor solution with cells. It includes slow but highly accurate methods like laser-based SLA [230] and two-photon polymerization [236] as well as faster, but slightly more inaccurate methods like digital light processing [237] or volumetric SLA [238]. However, the main disadvantage of these methods is the inability to control cell distribution, as the cells are mixed evenly in the precursor solution.

The second approach of biofabrication methods is the utilization of biomaterial inks. For example, cell-free, porous scaffolds can be fabricated, which can be post-seeded with cells. These scaffolds are fabricated within a cell hostile environment, e.g., high temperature or organic solvents. The most conventional and simplest way to create scaffolds is solvent casting/particle leaching. For example, dissolvable porogens like salt or gelatin is mixed within a matrix, e.g., a polymer dissolved in an organic solvent. After casting, the solvent evaporates and a composite of the matrix and the porogen is formed. The porogens can then be selectively removed by dissolution in a selective solvent, e.g., salt particles in water, leading to the creation of a porous scaffold [239].

Another category are fiber-based scaffolds, which are generated via extrusion of molten or dissolved polymers. Besides conventional 3D-printing, there are currently two main fabrication methods for the generation of fiber-based scaffolds: Solution electrospinning (SES) and melt electro writing (MEW). In SES, a dissolved polymer is filled in a syringe and extruded very slowly. An electrostatic force is applied to the resulting droplet at the tip of the syringe, which leads to the generation of a jet, that is collected on a flat or cylindrical collector to generate fibrous mats. During and after deposition, the solvent evaporates which leads to the creation of random or aligned polymeric nanofibers [240], which mimic the fibrous nature of the ECM and can be applied to several tissues like vascular, neural or tendon tissue. An important advantage is that not only synthetic materials like polycaprolactone [241] or poly(lactide-co-glycolide) [242] can be utilized, but even natural polymers like collagen [243] or hyaluronic acid [244] can be applied for electrospinning.

MEW is very similar to solution electrospinning; however, a polymer melt is used together with an applied high voltage to create a molten polymer jet. Compared to solution electrospinning, the jet is stable and can be directly deposited on a collector plate to create highly defined fibrous scaffolds [245]. This technology therefore allows the creation of porous geometries like box structures, sinusoidal architecures and even tubular scaffolds by printing on a cylindrical mandrel [246]. Since this method does not include solvents and works by melting the polymer, it increases the biocompatibility of the scaffolds and can be used with FDA-approved materials like polycaprolactone. However, natural polymers cannot be used with this technology, as they tend to degrade before melting can occur. Furthermore, pore size resolution (down to 40 µm [247]) is very low compared to the extruded filament diameter of down to 1 µm.

1.7.2 VASCULAR TISSUE ENGINEERING FOR *IN VITRO* ATHEROSCLEROSIS RESEARCH

Currently, in particular the field of biofabrication offer several methods and techniques for the generation of vascular 3D tissue models. The generation and utilization of these artery models has the potential to not only reduce animal trials, as the engineered arteries can meet the physical properties of natural ones. They furthermore provide a potent tool to study pathologies in a more controllable environment than *in vivo* studies, especially through application of controllable perfusion bioreactors [248].

As mentioned above, classical TE offers the utilization of decellularized scaffolds of different origin like decellularized xenografts [249]. These decellularized tissues provide a natural extracellular matrix (ECM), which is highly beneficial for cell adhesion and proliferation. Furthermore, by using human cells for reseeding of the structure, humanized arteries can be created from e.g. porcine arteries [250], which can also be expanded by the use of genetically modified cells to further understand specific interactions in the created model. However, an important disadvantage is that decellularization protocols include extensive physical, chemical or enzymatic treatment, which leads to a loss of structure and ECM components affecting mechanical stability and cell adhesion negatively [24-26]. It is therefore of great interest to generate a decellularization procedure, which on the one hand removes cells and all xenogenic remnants, except the matrix itself, and on the other hand keep the destruction of the matrix at a minimum, since the matrix plays an important role in the pathogenicity of atherosclerosis. Interestingly, despite all the advantages of native scaffolds, no *in vitro* atherosclerosis test model was described based on decellularized arteries until now.

Compared to unmodified scaffolds of natural origin based on classical TE, biofabrication offers several techniques to create tissue models utilizing synthetic and modified natural materials. Regarding the creation of vascular structures, it allows the bottom-up generation of channel structures from the size of microvessels to bigger ones in the size of arteries. However, the generation of the latter is challenging, since arteries consist of 3 different layers: The innermost layer (tunica intima), consists of a single layer of vascular endothelial cells surrounded by a basement membrane with elastic fibers. The second layer (tunica media) represents the thickest layer and consists of vascular smooth muscle cells embedded in between thick elastic fibers and collagenous fibers. The outermost tunica externa or tunica adventitia is composed of fibroblasts and dense collagenous and elastic fibers and connects the vessel to the surrounding tissue [251]. A biofabricated artery mimicking all important components of native arteries would be highly interesting in the field of biomedical research, leading to the development of several biofabrication strategies for the creation of these artificial arteries for the creation of *in vitro* disease models.

Among others, the most abundant biofabrication technologies are based on additive manufacturing (AM) approaches like 3D bioprinting, which is also being utilized to create vascular structures´[252-254]. In contrast to decellularized arteries, bioprinting is mainly independent of post-cell seeding, as the cells are already directly incorporated into the bioink. Moreover, a targeted and specific positioning of different cell types is possible, allowing the generation of multilayered constructs [253, 254]. However, cell survival is an ongoing issue because of the resulting high shear stress during the printing process, which also directly impairs the resolution [255]. Furthermore, to generate arteries via bioprinting, a minimum of 2 separate bioinks with their respective cells are needed to at least create the tunica and the adventitia in 3D printed artery models. Based on this prerequisite, at least two printheads are required to enable the creation of biofabricated arteries via bioprinting, meaning an advanced printing device is needed. Nevertheless, using 3D bioprinting, the successful creation of perfusable and functional three-layered artery models [253] with a drop-on-demand bioprinting technique combined with custom-built bioreactors and even atherosclerosis models [254] was reported. Here, a three-layered atherosclerosis model was created via in-bath coaxial cell printing with a triple coaxial nozzle. The endothelial cells (ECs), smooth muscle cells (SMCs) and the sacrificial Pluronic were printed directly in one step into a support bath which was filled with fibroblasts, resulting in a three-layered model with straight, curved and even stenotic arteries. The study further provides evidence that the EC-layer is reactive to TNF-alpha, LDL uptake and disturbed flow – furthermore, macrophage uptake and subsequent foam-cell formation was observed. Besides the inability to create bifurcations, this study provides a functional and useful artery model for the *in vitro* assessment of atherosclerotic conditions. However, the creation of these *in vitro* artery models is based on highly complex 3D printing technologies, which require high investments regarding devices and cannot be replicated by inexperienced users.

Besides bioprinting, another approach is the prefabrication of cell-free scaffolds, which can be seeded with cells afterwards [256, 257]. Since no cells are used during the process of scaffold creation, other materials like thermoplastics can be used, which are normally fabricated within cell hostile conditions like elevated temperatures above 37°C. Furthermore, sophisticated fabrication methods like solution electrospinning or melt electro writing can be used to mimic the fibrous composition of the ECM, which plays an important role for arterial functionality and integrity [251].

In this regard, vascular disease models were developed using prefabricated scaffolds [257]. In this work, a bi-layered atherosclerosis model based on nonwoven thermoplastic (polyglycolic acid) was developed and dynamically cultured. The functionality was furthermore validated by mimicking initial atherosclerotic processes like LDL and monocyte-uptake. The prefabrication of scaffolds and the subsequent cell seeding is therefore a good tool to achieve a physiologic, three-dimensional replication of arterial structures, which can be easily cultured under dynamic flow conditions. However, the main disadvantage of this method is the inability to create more complex structures like curvatures or bifurcations.

An option (besides bioprinting) to overcome this disadvantage is the utilization of casting methods, whereas cell-laden hydrogels can be casted into more complex structures and shapes. The first example for this technology is the generation of channel structures by casting and bonding of two fitting hydrogels, which provide grooves on both sides to generate the cylindrical channels after bonding [258-260], resulting in an endothelialized channel network in the hydrogel matrix. Based on this technique, Chen et al. developed an atherosclerosis model for the investigation of wall shear stress-induced endothelial dysfunction in a gelatin-patterned, endothelialized carotid artery model based on computational fluid dynamics. By utilizing the casting-method, round channels as well as more complex structures like curvatures and even exact models of the human carotid bifurcation [259] can be realized. However, this approach does not provide a sufficient solution to create multilayered constructs required for mimicking the structure of native arteries. To overcome this issue, multilayered structures can be created by targeted gelation of cell-laden hydrogels in the vicinity of preformed channels after filling of the mold with precursor solution. One possibility to achieve this is the incorporation of crosslinking ions into the channel walls. Via osmosis, the ions reach into the hydrogel, e.g., alginate, which leads to crosslinking of the gel in the vicinity of the channel [261, 262]. By elongation of the timeframe before flushing the leftover hydrogel precursor, the thickness of the hydrogel layer can be increased and vice versa. After seeding endothelial cells in the resulting lumen, bi-layered perfusable artery models are generated. However, alginate by itself is a biocompatible, but cell inert hydrogel and therefore requires modification like the addition of gelatin [263] or the functionalization with an RGD-peptide [264] to provide binding motifs for the attachment and spreading of the cells. Zhang et al. circumvented this issue by using two separate layers of collagen gels with SMCs and fibroblasts, formed by plastic compression and dehydration around mandrels, resulting in a functional three-layered artery model for atherosclerosis research [265]. The use of collagen hydrogel furthermore provides mechanical strength comparable to real arteries and excellent cellular adhesion and spreading, circumventing the disadvantages of cell inert hydrogels like alginate. After mechanical removal of the mandrels, endothelial cells were seeded by introduction into the channel, resulting in a circular, three-layered artery model. Key processes of atherogenesis were mimicked by LDL perfusion, leading to endothelial cell activation, monocyte accumulation and foam cell formation accompanied by the expression of pro-inflammatory cytokines [265]. However, the disadvantage of this method is the limited design freedom based on the mechanical removal of mandrels.

Another important method to achieve vascular-like structures is the utilization of sacrificial templates. Here, channel structures are either generated mechanically, e.g. via removable agarose templates [266], or chemically by using sacrificial scaffolds based on carbohydrates [267-270], gelatin [248] and alginate [271, 272] which can be dissolved via external stimuli like temperature or removal of ions. To generate scaffolds from these materials, 3D printing methods are commonly utilized. These scaffolds can then be integrated afterwards into hydrogels with subsequent crosslinking and dissolution. However, there are still several challenges that need to be overcome, like the need to precisely place the scaffold in the hydrogel and the manual error-prone connection to fluidic pumps after generation of the channel structures, which hindered the development of atherosclerosis or other disease models to this day.

Although a variety of biofabrication methodologies are available and have a high potential to be used as *in vitro* models, only few studies utilized this technology to investigate flow-related key processes of atherogenesis. E.g. one study used casted models of a human carotid artery bifurcation with two representative regions, which reflect the physiological and disturbed regions of WSS [259]. It was shown that endothelial cells expressed a disorganized inflammatory phenotype with increased permeability within the disturbed WSS region, proving the feasibility of *in vitro* models to investigate pathological fundamentals. Although structurally correct, these models did not represent the accurate mechanical behavior of native arteries as they were based on hydrogels. However, this study presented a simple but effective approach and biofabrication offers a variety of methods to improve and approach the *in vivo* situation. In this regard, especially magnetic resonance imaging (MRI) has the potential to evaluate these models non-invasively regarding disease development and progression modulated and initiated through altered hemodynamics. Up to now, however, the utilization of artery models for flow-related atherosclerosis research using high-resolution 4D-flow MRI, was not reported yet.

CHAPTER 2

Simultaneous Measurements of 3D Wall Shear Stress and Pulse Wave Velocity in the Murine Aortic Arch

Chapter 2 was published as original research article (Patrick Winter*, Kristina Andelovic*, Thomas Kampf, Jan Hansmann, Peter M. Jakob, Wolfgang R. Bauer, Alma Zernecke, Volker Herold: "Simultaneous Measurements of 3D Wall Shear Stress and Pulse Wave Velocity in the Murine Aortic Arch" in the Journal of Cardiovascular Magnetic Resonance (JCMR), Volume 23, Article number: 34 (2021), reproduced from [16] as open access article licensed under a Creative Commons Attribution 4.0 International License (https://creativecommons.org/licenses/by/4.0/) which permits use, sharing, adaptation, distribution and reproduction in any medium or format. The article is based on the collective work of the equal contributors Dr. Patrick Winter, who developed the radial flow encoding sequence and the author of this thesis Kristina Andelovic, who performed the experiments and statistical analysis. As the method described in this chapter is basis for the following *in vivo* studies and undividable into the sub-parts of the contributors without losing important information, this chapter was not split into the corresponding parts to improve understandability.

The original text was slightly modified to improve readability.

* Equal Contributors

The author contributions to the original research article are as follows:

Contributor	Contributions
Patrick Winter	Conceived the study, developed the radial flow-encoding sequence, analyzed the data, interpreted the results, prepared the original manuscript, reviewed the manuscript
Kristina Andelovic	Conceived the study, planned and conducted the experiments, analyzed the data, interpreted the results, prepared the original manuscript, reviewed the manuscript
Thomas Kampf	Interpreted the results, reviewed the manuscript
Jan Hansmann	Interpreted the results, provided funding, reviewed the manuscript
Peter Michael Jakob	Interpreted the results, reviewed the manuscript
Wolfgang Rudolf Bauer	Conceived the study, interpreted the results, provided funding, reviewed the manuscript
Alma Zernecke	Conceived the study, interpreted the results, provided funding, reviewed the manuscript
Volker Herold	Conceived the study, interpreted the results, provided funding, reviewed the manuscript

2.1 ABSTRACT

Purpose: Wall shear stress (WSS) and pulse wave velocity (PWV) are important parameters to characterize blood flow in the vessel wall. Their quantification with flow-sensitive phase-contrast (PC) cardiovascular magnetic resonance (CMR), however, is time-consuming. Furthermore, the measurement of WSS requires high spatial resolution, whereas high temporal resolution is necessary for PWV measurements. For these reasons, PWV and WSS are challenging to measure in one CMR session, making it difficult to directly compare these parameters. By using a retrospective approach with a flexible reconstruction framework, we here aimed to simultaneously assess both PWV and WSS in the murine aortic arch from the same 4D flow measurement.

Methods: Flow was measured in the aortic arch of 18-week-old wildtype (n = 5) and ApoE$^{-/-}$ mice (n = 5) with a self-navigated radial 4D-PC-CMR sequence. Retrospective data analysis was used to reconstruct the same dataset either at low spatial and high temporal resolution (PWV analysis) or high spatial and low temporal resolution (WSS analysis). To assess WSS, the aortic lumen was labeled by semi-automatically segmenting the reconstruction with high spatial resolution. WSS was determined from the spatial velocity gradients at the lumen surface. For calculation of the PWV, segmentation data was interpolated along the temporal dimension. Subsequently, PWV was quantified from the through-plane flow data using the multiple-points transit-time method. Reconstructions with varying frame rates and spatial resolutions were performed to investigate the influence of spatiotemporal resolution on the PWV and WSS quantification.

Results: 4D flow measurements were conducted in an acquisition time of only 35 min. Increased peak flow and peak WSS values and lower errors in PWV estimation were observed in the reconstructions with high temporal resolution. Aortic PWV was significantly increased in ApoE$^{-/-}$ mice compared to the control group (1.7 ± 0.2 versus 2.6 ± 0.2 m/s, $p < 0.001$). Mean WSS magnitude values averaged over the aortic arch were (1.17 ± 0.07) N/m^2 in wildtype mice and (1.27 ± 0.10) N/m^2 in ApoE$^{-/-}$ mice.

Conclusion: The post processing algorithm using the flexible reconstruction framework developed in this study permitted quantification of global PWV and 3D-WSS in a single acquisition. The possibility to assess both parameters in only 35 min will markedly improve the analyses and information content of *in vivo* measurements.

2.2 BACKGROUND

Atherosclerosis is a complex, chronic inflammatory disease of large and medium sized arteries, characterized by the formation of intimal lesions (atherosclerotic plaques) [273]. These plaques mainly occur at bifurcations, branching regions and in the inner curvature of the aortic arch, where the wall WSS is low and oscillatory [274-276]. Another main pathophysiological feature of atherosclerosis is the gradual arterial stiffening due to the loss of elastic fibers [9] and an increased collagen deposition during plaque development [167]. This increasing stiffness is one of the earliest markers of functional and structural changes and can be characterized by measuring the PWV, which is defined as the speed of arterial pressure waves travelling along the aorta and large arteries [277]. An altered WSS profile also appears to correlate with local elastic changes in the vasculature [2]. As hemodynamic parameters like the WSS play a key role in local plaque development [2], and as ultrasound-measurements indicate a possible link between higher PWV and lowered WSS [278], the simultaneous measurement of these two parameters is of great interest. In comparison to ultrasound, cardiovascular magnetic resonance (CMR) provides better tissue contrast and higher dimensional flow measurements. Therefore, quantifications of aortic PWV and WSS with flow sensitive 4D-phase contrast (PC) CMR are potential tools for preclinical research and early diagnosis of atherosclerosis. Ultimately, PWV and WSS may serve as CMR-based biomarkers of the vascular state and atherosclerotic lesion burden.

The widely used ApoE$^{-/-}$ mouse represents a good model for atherosclerosis research [279]. By feeding a high fat and cholesterol-rich diet, the development of atherosclerotic plaques can be accelerated to investigate the relationship of hemodynamic parameters like PWV and WSS in atherogenesis in a reasonable time frame. The simultaneous measurement of both WSS and PWV parameters, however, is challenging. While a high spatial resolution is required to determine the velocity gradients at the vessel wall for WSS quantification [60], high temporal resolution is needed to accurately capture the rapid propagation of the pulse wave [10, 11]. Thus, in most cases two separate measurements are conducted to measure both parameters, which prolongs acquisition time. For combined measurements of both cardiovascular parameters in swine, Wentland *et al.* developed an undersampled radial 4D-PC cine sequence with retrospective electrocardiogram (ECG) gating. It was shown that a single 4D-PC CMR measurement was sufficient to determine both PWV and WSS in a scan time in the order of 10 min [6]. The main challenges to adopt this method for measurements in murine models, however, are the small vessel dimensions (~ 10 times smaller) and the high heart rates (~ 5 times higher) compared to porcine models [4, 6]. Since the repetition times and relaxation times of CMR measurements in mice is on the same scale as for acquisitions in swine and cannot be shortened significantly, post processing techniques need to be adapted to fulfill the demands of PWV and WSS quantification in rodents. Zhao et al. presented a first approach to measure both parameters with a radial ECG- triggered technique in the abdominal aorta of mice [7], however, this technique relies on measuring flow in 2-dimensional planes. For a full coverage of flow dynamics in curved vessels such as the aortic arch, a full 3D measurement is needed [8]. Retrospective navigation and radial trajectories may be suitable for this task due to the highly flexible reconstruction framework [280]. For example, view-sharing reconstructions can be optimized to either reconstruct images at higher spatial resolution and lower frame rates or vice versa. Therefore, image reconstruction can be adjusted individually to the demands of a specific parameter. Recently we presented a radial 4D-PC cine CMR sequence for self-gated flow and WSS measurements in the murine aorta at high spatial and moderate temporal resolution [4]. The goal of this work is to further investigate the capabilities of the sequence and the retrospective reconstruction framework by modifying the post-processing algorithms to enable arbitrary frame rates and variable spatial resolutions. The new technique is utilized to extract both PWV and WSS from the same measurement and to investigate the influence of temporal and spatial resolution. Since both parameters are assessed in an acquisition time of only 35 min, the duration of *in vivo* scan protocols for preclinical studies is significantly reduced. This is demonstrated in an *in vivo* study using healthy wildtype and atherosclerotic ApoE$^{-/-}$ mice.

2.3 METHODS

2.3.1 ANIMAL HANDLING

Female wildtype (WT) C57BL/6 J mice (n = 5) and ApoE knock-out mice (ApoE$^{-/-}$, n = 5) (both 18 weeks old and from Charles River Laboratories, Sulzfeld, Germany) were fed a normal diet (WT) or a western type diet (ApoE$^{-/-}$: ssniff, Soest, Germany) for 14 weeks. Mice were anesthetized by a nose cone, applying 1.5% isoflurane in 2.0 Vol. % oxygen (2 L/min). A pressure-sensitive pneumatic balloon (Graseby Medical Ireland Limited, Dublin, Ireland) was used for cardiac and respiratory monitoring in real-time [4] by a custom-built ECG unit [281]. All animal experiments were approved by local authorities (Regierung von Unterfranken, Würzburg, Germany, reference number: 55.2-2531.01-427/17) to comply with German animal protection law.

2.3.2 DATA ACQUISITION AND PROCESSING

Measurements were performed with a 17.6 T vertical bore small animal MRI system (Bruker Avance 750 WB, Bruker BioSpin MRI GmbH, Rheinstetten, Germany) with a 1 T/m gradient system (diameter: 40 mm) and a custom-built single-channel transmit-receive electromagnetic (TEM) resonator (inner diameter: 24 mm). Flow was quantified in the aortic arch using a slab-selective non-triggered radial 4D-cine phase contrast sequence, as proposed recently [4]. Spatial encoding was performed using a 3D radial trajectory with an angular density adjusted to the anisotropic field of view (FOV) [282]. In addition, a 3D B_0 map was acquired for subsequent off-resonance correction [4]. All relevant scan parameters can be found in Table 1. Data processing and reconstruction was performed with Matlab (version 2016b, Mathworks, Inc., Natick, Massachusetts, USA). Self-navigation signals were extracted as proposed in [4, 15, 155].

Table 1: Scan parameters for the 4D-flow measurement. HS/LT: high spatial/low temporal. LS/HT: low spatial/high temporal

Parameter	HS/LT-res. reconstruction	LS/HT-res. reconstruction
Repetition Time [ms]	3.0	3.0
Echo Time [ms]	1.1	1.1
Flip Angle [°]	15	15
Number of Readout Points	140	140
Number of Projections	$1.6 \cdot 10^5$	$1.6 \cdot 10^5$
Number of Velocity Encoding Steps	4 (balanced 4-point encoding)	4 (balanced 4-point encoding)
Encoding Velocity [cm/s]	125	125
Field of View [mm^3]	25 x 25 x 4	25 x 25 x 4
Slab Thickness [mm]	4	4
Measurement Time [min]	32 (+ 3min for B_0 map)	32 (+ 3min for B_0 map)
Spatial resolution	100 µm	147 µm
N frames per cycle	20	200
Selection window	1/20	1/33

2.3.3 WSS ANALYSIS

2.3.3.1 Reconstruction

For the WSS *in vivo* study, 3D-cines were reconstructed retrospectively at high spatial and lower temporal resolution (HS/LT-res. reconstruction, see Figure 13A). To achieve maximum spatial resolution, all available radial k-space points were considered for reconstruction (see Figure 13B, red and blue points). The cardiac cycle was divided into 20 data selection intervals, corresponding to 20 relative phases in the heart cycle (see Figure 14A), as recently proposed [4]. The selection windows had a width of W = 1/20 of the full heart cycle, which corresponds to an average of 5–7 ms. Four 3D-cines (one flow-compensated and three flow-encoded) with an isotropic spatial resolution of 100 µm, respectively, were reconstructed with a Non-Uniform Fast Fourier Transform (NUFFT) [283, 284].

2.3.3.2 WSS Calculation

The lumen of the aortic arch was segmented with a semi-automatic labeling technique [12] and velocity was calculated from the phase differences of the four encoders [4]. A custom python software tool developed for Ensight 10.0.2 (Ansys, Inc., Canonsburg, Pennsylvania, USA) was used to calculate the WSS [4].

2.3.4 PWV ANALYSIS

2.3.4.1 Reconstruction

PWV was determined with the multiple-points transit-time method [7, 10], which requires higher frame rates in comparison to the WSS measurement [6]. Hence, the reconstruction algorithm was adapted to reconstruct the same 4D flow data at lower spatial and higher temporal resolution (LS/HT-res. reconstruction, see Figure 13A). Lower spatial resolution was chosen in order to minimize undersampling artifacts and noise. Therefore, only the inner 64.5% of the original data points (Figure 13B, red points) were used for reconstruction. The high effective frame rate (defined by the number of reconstructed frames covering the complete cardiac cycle) was achieved by applying overlapping sliding windows (see Figure 14B). Each window had a width of W = 1/33, which corresponds to 3–4 ms (approximately 1 × TR). Using this kind of data selection, the relative phases were divided into 200 intersecting intervals (relative distance between each interval: $\Delta = 1/200$ of the average heart cycle, or 0.5–0.7 ms). The associated projections within each interval were combined for image reconstruction. After rigid motion and off-resonance correction [4], a set of four 3D-cines (native spatial resolution 147 µm isotropic, 200 frames, respectively), was reconstructed and afterwards zero-filled to an isotropic spatial resolution of 74 µm.

2.3.4.2 PWV Calculation

The multiple-points transit-time method relies on accurately determining the timing of the upstrokes of through-plane flow curves. For analysis of velocity data, the segmentation was temporally interpolated with linear interpolation and re-gridded to the spatial resolution of the PWV reconstruction. The labeled data was used to set the velocity field outside the aorta to zero. Subsequently, the velocity data was smoothed with a 3-connectivity neighborhood spatial median filter and exported to EnSight. Using python software (Ansys, Inc), a centerline of the lumen segmentation was calculated.

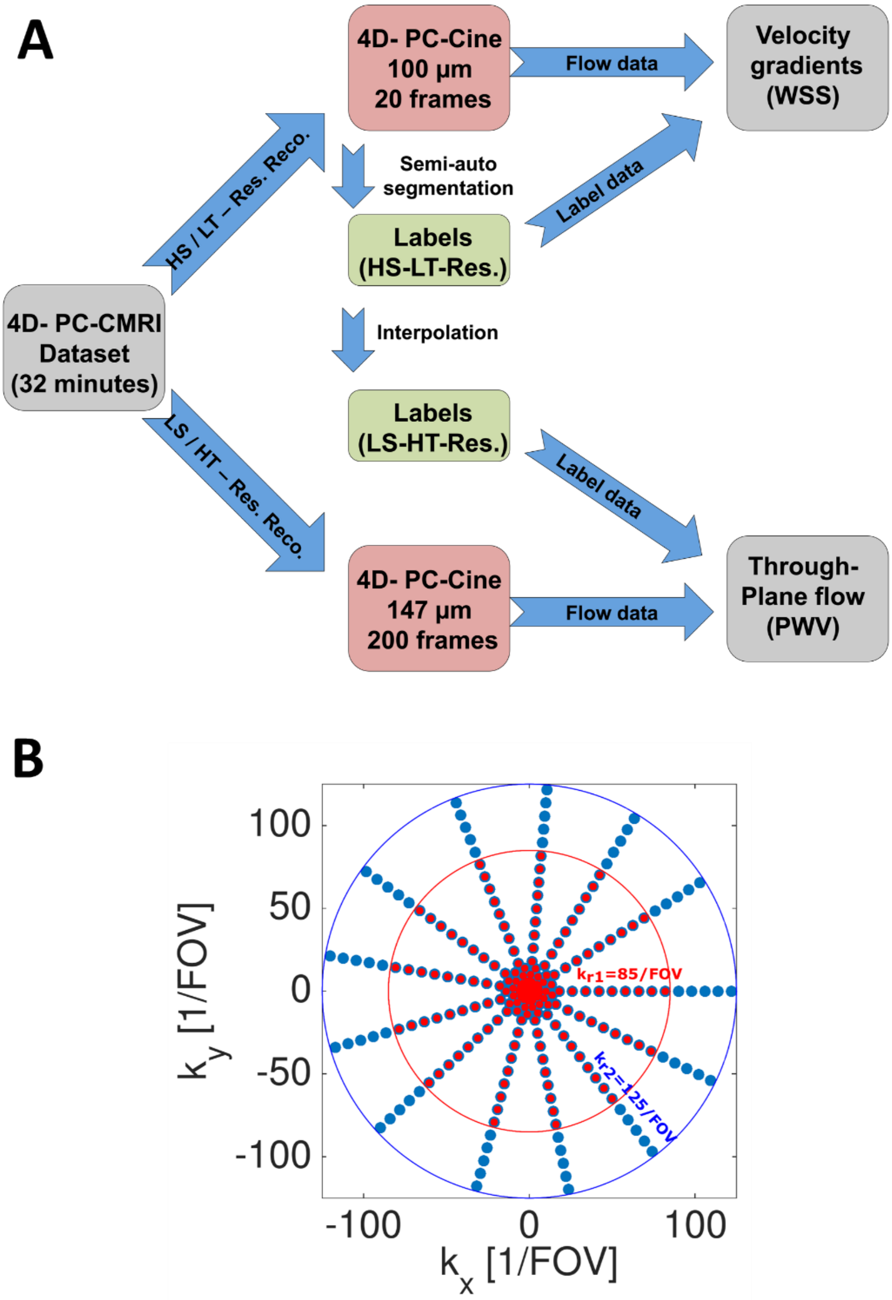

Figure 13: Illustration of the reconstruction process for the WSS- and PWV evaluation. A For WSS calculation, the 4D-PC data was reconstructed at high spatial and low temporal resolution (HS/LT-res. reconstruction, see top panels). The aortic lumen was labeled with semi-automatic segmentation. Using the flow and label data, velocity gradients were calculated. For PWV calculation, the 4D-PC data was reconstructed at low spatial and high temporal resolution (LS/HT-res. reconstruction, see bottom panels). The segmentation data obtained from the HS/LT-res. reconstruction was temporally interpolated. Using the interpolated label and flow data, through plane flow was determined at multiple locations. **B** For the LS/HT-res. reconstruction (PWV), only the inner k-space points with $k_r < 85/FOV$ were used (red points, shown in 2D for better illustration). The HS/LT-res. reconstruction uses all available k-space frequencies (red and blue points).

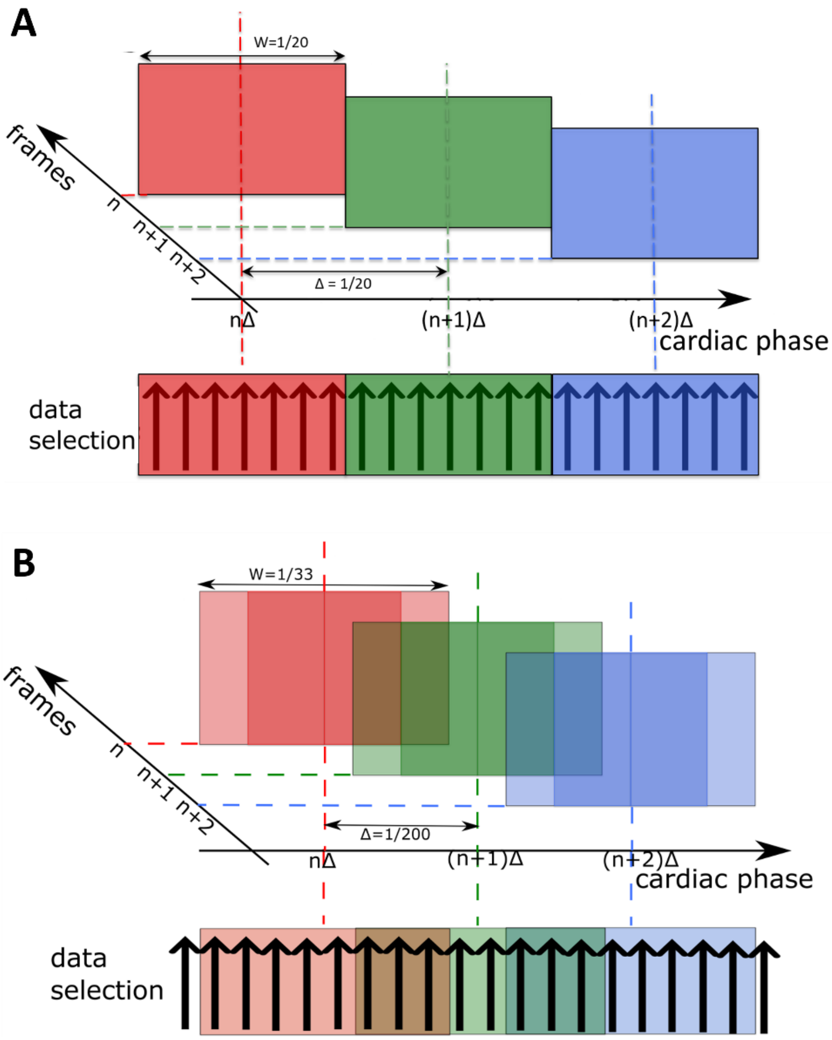

Figure 14: Sliding window selection of cardiac phases for the HS/LT-resolution reconstruction (illustrated for only 3 frames and unscaled for a better clarity). The selection window width of the average heart cycle was W = 1/20 and the distance between each window Δ = 1/20. **b** Sliding window selection of cardiac phases for the LS/HT- resolution reconstruction. Overlapping selection windows with a width of W = 1/33 and a distance of Δ = 1/200 of the average cardiac cycle were used. The lighter shadings at the left and right edges of the selection windows mark the overlapping areas (not at scale).

Through-plane flow was afterwards determined at approximately 50 equidistant locations (except regions close to the aortic branches) along the aortic arch and perpendicular to the centerline (see Figure 15A). Subsequently, the flow curves were imported to Matlab (Mathworks, Inc.) for further data processing. For each plane, the time point of the systolic upstroke of the volume flow was identified by measuring the intersection of a line fitted to the pre-systolic data points (baseline) and a line fitted to the upstroke of the early systolic pulse (Figure 15B). For more precise determination of the time point of the systolic upstroke, a tenfold linear interpolation was applied to the flow data prior to fitting. Subsequently, the distances of each plane Δx (relative to the proximal ascending aorta) were plotted against the time points of the systolic upstroke Δt (Figure 15C). For PWV calculation, a line was fitted to the plot. PWV was afterwards derived from the slope of this fit:

$$PWV = \frac{dx}{dt} \tag{1}$$

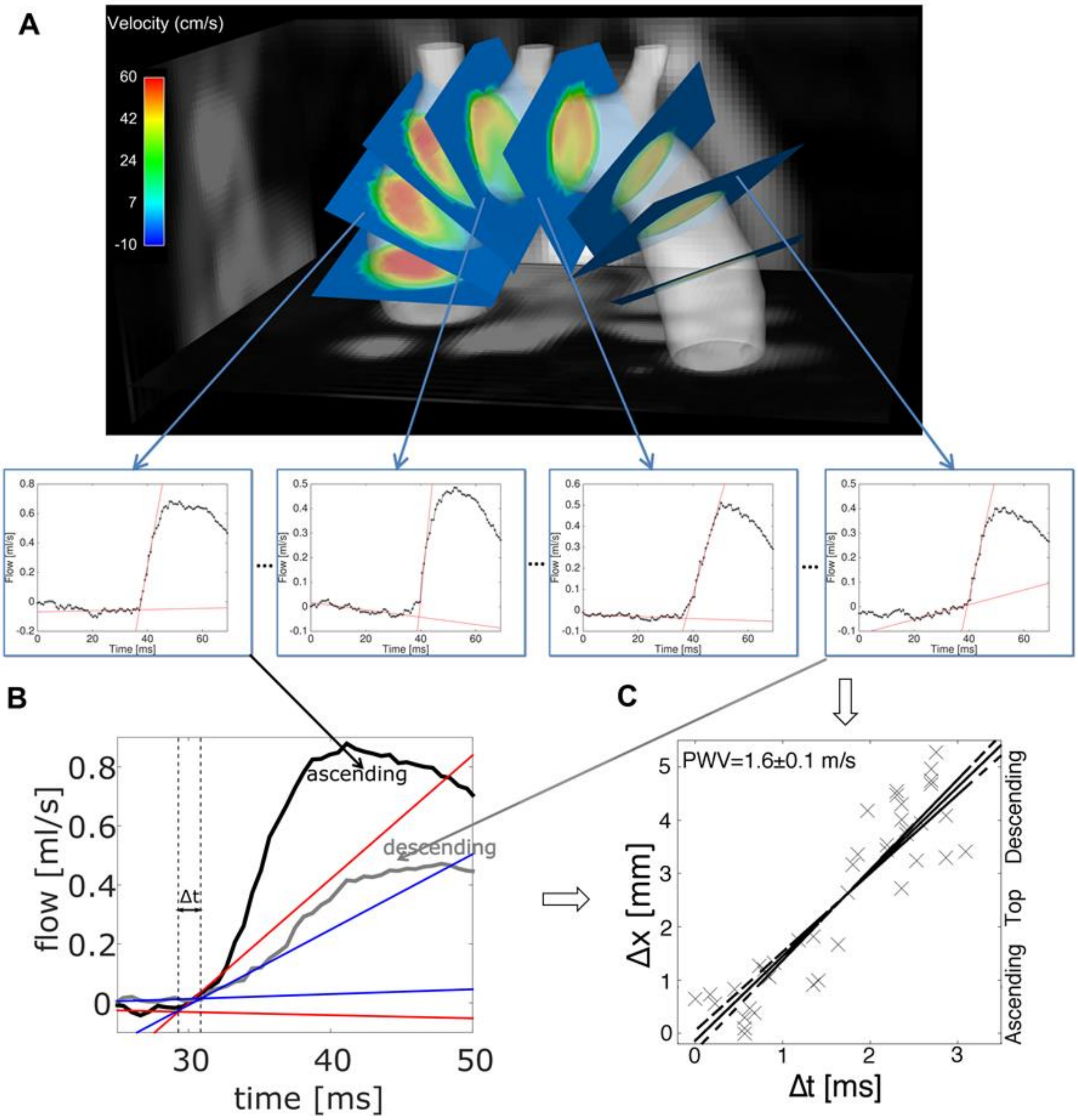

Figure 15: Illustration of the transit time pulse wave velocity (PWV) measurement. A Through-plane flow was determined at various positions along the aortic arch (for illustration only 8 planes are shown; in the experiment approx. 50 slices were used). **B** For each location (here shown for one plane in the ascending and descending aorta), the time point of the systolic upstroke was identified as the intersection of a line fitted to the pre-systolic data points and a line fitted to the upstroke of the early systolic pulse. **C** The distances Δx of each plane (relative to the proximal ascending aorta) were plotted against the time points of the systolic upstroke Δt (relative to the time point of the first plane). PWV was calculated from the slope of a line fitted to this plot.

2.3.5 YIELD, UNDERSAMPLING AND BLURRING

To assess the quality of self-navigation, the yield (i.e. the number of detected heartbeats N relative to the theoretically expected total number of heartbeats N_{th} occurring during a measurement time of 32 min) was calculated:

$$Yield\,[\%] = \frac{N}{N_{th}} \cdot 100 = \frac{N \,\cdot\, \overline{T}_{RR}}{32\,min} \cdot 100 \tag{2}$$

Hereby $\overline{T}_{RR}$ denotes the average cardiac period, which is determined with the self-navigation signal. Since the cardiac signal is affected by respiratory motion, the yield is usually smaller than 100%.

In order to estimate the degree of undersampling according to the Nyquist criterion, the theoretical number of projections N_{Nyq}, necessary to reconstruct an artifact-free image, was calculated. For an isotropic image matrix of the dimensions $J \times J \times J$, a field of view of $25 \times 25 \times 25$ mm^3 and a slab thickness of 4 mm, N_{Nyq} can be approximated as [285]:

$$N_{Nyq} \approx \pi \cdot J^2 \cdot \frac{4}{25}, \tag{3}$$

Since only a thin slab is excited and the trajectory is adjusted for reconstruction of an anisotropic FOV, the necessary number of projections is reduced by a factor of $\frac{4}{25}$. Equation (3) results into $N_{Nyq} \approx 1.4 \cdot 10^4$ for the LS/HT-res. reconstruction and $N_{Nyq} \approx 3.1 \cdot 10^4$ for the HS/LT-res. reconstruction, respectively. The undersampling factor can be afterwards calculated using:

$$us = \frac{N_{Nyq}}{\overline{N}_f}, \tag{4}$$

Where $\overline{N}_f$ is the average number of projections available to reconstruct a cine frame.

For the assessment of the temporal accuracy of the reconstructions, the standard deviations δ_p of the binned relative phases were estimated for each selection interval (Figure 14A and B). The temporal blurring is defined as $\delta t = \delta\bar{p} \cdot \overline{T}_{RR}$, where $\delta\bar{p}$ is the mean standard deviation of relative phases averaged over all selection intervals and $\overline{T}_{RR}$ the temporally averaged cardiac period.

2.3.6 TEMPORAL AND SPATIAL RESOLUTION

To investigate the influence of spatiotemporal resolution, one *in vivo* measurement was reconstructed at different frame rates (20–200 frames / heart cycle) and spatial resolutions (100 µm, 125 µm, 147 µm) as well as varying selection window widths (1/20–1/60), respectively. PWV and the time-dependent WSS magnitude values were assessed from these generated cines. Each PWV value was determined using the same analysis planes for the through-plane flow assessment as for the LS/HT-res. reconstruction. Prior to the PWV determination, each extracted through-plane flow curve was interpolated to the same effective temporal resolution as the 200 frames reconstruction using spline interpolation.

2.3.7 ERROR AND STATISTICS

All error and statistical analyses were performed in Matlab (version 2016b, Mathworks, Inc) and Prism 7 (GraphPad Software, San Diego, California, USA). In order to assess the PWV error, the standard deviation of the linear fit and the coefficient of determination R^2 were calculated. The Shapiro Wilk Normality Test was used for testing normal distribution. For normally distributed data, an unpaired sample t-test was utilized [286]. When normality test failed, a non-parametric Mann–Whitney-U test was performed. For analysis of the degree of correlation between heart rates with other parameters, the Pearson correlation coefficients were calculated. Differences of $p < 0.05$ were considered to be statistically significant.

2.4 RESULTS

2.4.1 STABILITY OF SELF-NAVIGATION

Self-navigation signals could be obtained from both the ApoE$^{-/-}$ and WT group. Figure 16A shows the results for the mean cardiac period $\overline{T}_{RR}$, averaged over all heartbeats detected during the 32 minutes of measurement. The standard deviations for the ApoE$^{-/-}$ and WT group are ±4 ms and ±8 ms, respectively. Heart rate variations are comparable in both animal groups. The total number of heartbeats N detected by the algorithm and the number of detected heartbeats relative to the expected theoretical number of heartbeat (Yield, see Equation (2)) were determined. The Yield was independent of the heart rate (p = 0.56, see Figure 17A). In average, approximately 20% of the data was omitted due to respiratory gating in both subsequent reconstructions.

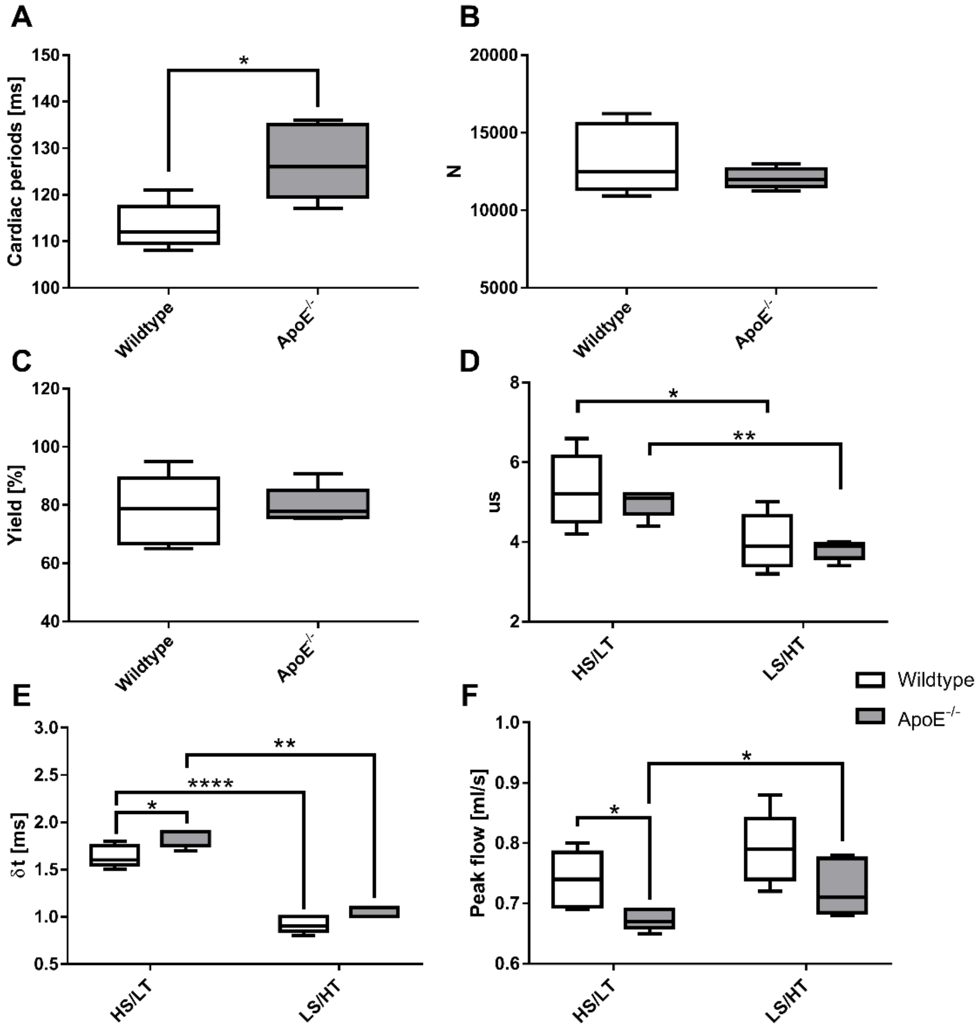

Figure 16: Stability of self-navigation, undersampling and temporal blurring. **A** Cardiac periods T_{RR} for wildtype and ApoE$^{-/-}$ mice. A slight significance was observed between both groups (*, $p = 0.01$). **B** No significant differences could be observed in the total number N of detected heartbeats. **C** Yield for both groups, showing no significant differences. **D** Undersampling factors for the high spatial/low temporal (HS/LT) and low spatial/high temporal (LS/HT) reconstructions in both animal groups (Wildtype: (HS/LT vs. LS/HT, *, $p = 0.03$. ApoE$^{-/-}$: HS/LT vs. LS/HT, **, $p < 0.01$). **E** Temporal blurring for the HS/LT and LS/HT reconstructions in both animal groups (HS/LT: Wildtype vs. ApoE$^{-/-}$ *, $p < 0.04$. Wildtype: HS/LT vs. LS/HT, ****, $p < 0.0001$. ApoE$^{-/-}$: HS/LT vs. LS/HT, **, $p < 0.01$). **F** Peak flow values for the HS/LT and LS/HT reconstructions in both animal groups (HS/LT: Wildtype vs. *Apoe*$^{-/-}$, *, $p = 0.02$. ApoE$^{-/-}$: HS/LT vs. LS/HT, *, $p = 0.05$)

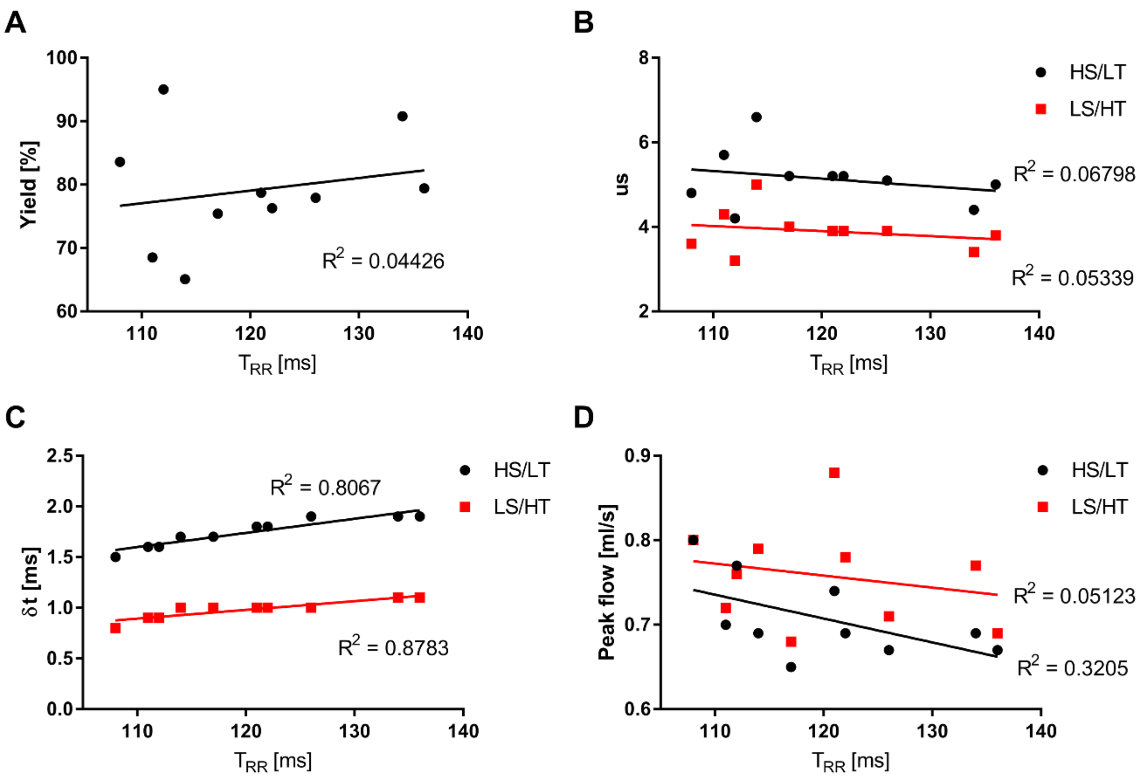

Figure 17: Correlation plots of cardiac periods with different parameters. **A** No dependency of the yield on the heart rate was observed ($p = 0.56$). **B** No correlation was observed between undersampling and heart rates (HS/LT: $p = 0.47$, LS/HT: $p = 0.52$). **C** A correlation was observed between the temporal blurring and the heart rate (HS/LT: $p < 0.0001$, LS/HT: $p < 0.001$) due to the relation of the width of the selection window with the cardiac periods. **D** In both reconstructions, no significant correlation between the cardiac periods and peak flow values was observed (HS/LT: $p = 0.09$, LS/HT: $p = 0.53$)

2.4.2 UNDERSAMPLING AND TEMPORAL BLURRING

Figure 16D displays the undersampling factors (see Equation (4)) for both types of reconstructions. In the HS/LT-res. reconstruction, the mean undersampling factor was 5.3 ± 0.9 for WT mice and 5.0 ± 0.4 for ApoE$^{-/-}$ mice, respectively. In the LS/HT-res. reconstruction, undersampling was 4.0 ± 0.7 for WT mice and 3.8 ± 0.2 for ApoE$^{-/-}$ mice. Less undersampling was achieved in the reconstruction with high temporal resolution due to the 32% lower spatial resolution. No correlation was observed between undersampling and heart rates (HS/LT: $p = 0.47$, LS/HT: $p = 0.52$, see Figure 17B).

Figure 16E and Figure 17C show the mean temporal blurring (see above) of the reconstructed 4D-PC-cine frames. In the HS/LT-res. reconstruction, the mean temporal width was 1.5–1.8 ms. In the LS/HT-res. reconstruction, the temporal blurring was 1.8–2 times smaller. Since the width of the selection windows is related to the cardiac period, a correlation was observed between the temporal blurring and the heart rate (HS/LT: $p < 0.001$, LS/HT: $p < 0.001$, see Figure 17C). Larger temporal blurring was detected in the HS/LT reconstruction of ApoE$^{-/-}$ mice ($p = 0.04$) due to the lower heart rate, however, no significant differences were found in the LS/HT reconstruction ($p = 0.08$, see Figure 16E).

2.4.3 FLOW VALUES

Figure 18A shows two reconstructions of through-plane flow in the ascending aorta of a representative ApoE$^{-/-}$ mouse, obtained from an LS/HT-res. and an HS/LT-res. reconstruction, respectively. Figure 18B displays the corresponding peak flow profiles. In the reconstruction with higher temporal resolution, the upstroke of the flow pulse is clearly recognizable and larger peak flow values are noticeable. Figure 16F shows the corresponding peak flow values for all animals. At higher temporal resolution, an increase in peak flow values is noticeable. In both reconstructions, no significant correlation between cardiac periods and peak flow values was observed (HS/LT: $p = 0.09$, LS/HT: $p = 0.53$, see Figure 17D).

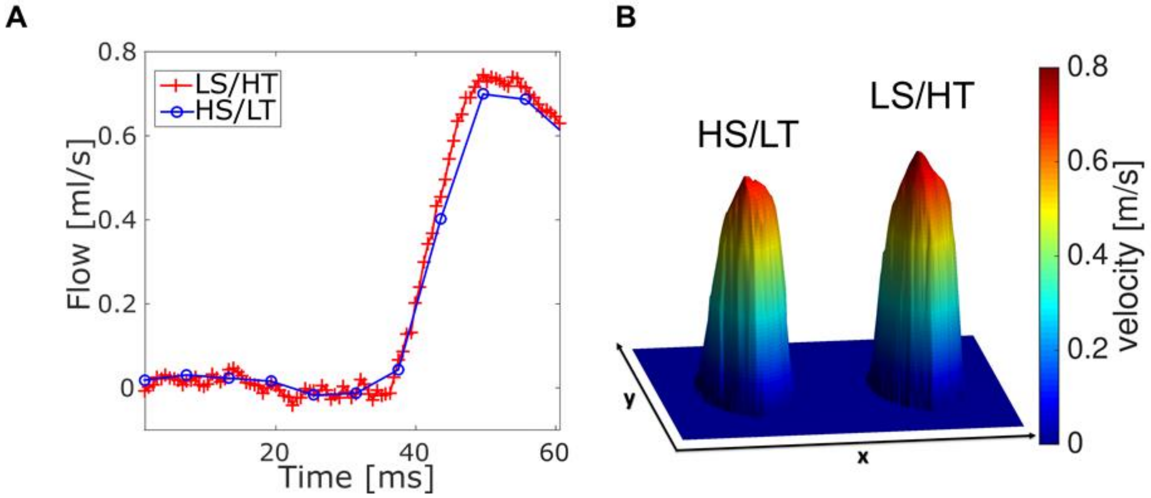

Figure 18: Through-plane flow and peak flow profiles for HS/LT and LS/HT reconstructions. **A** Through-plane flow in the ascending aorta of an ApoE$^{-/-}$ mouse, determined with the HS/LT-resolution (blue) and LS/HT-resolution (red) reconstruction. **B** Peak flow profile of the same plane (HS/LT and LS/HT reconstruction).

2.4.4 INFLUENCE OF TEMPORAL AND SPATIAL RESOLUTION

2.4.4.1 Pulse wave velocity

Table 2 displays the PWV values obtained from different reconstructions of the same *in vivo* experiment (see also Supplementary Figure 1-3 for the individual fits). In the first step, the frame rate of the LS/HT-res. reconstruction was artificially reduced to 100 and 50 frames by taking only every second and fourth frame of the reconstruction, respectively. The results suggest an increased PWV error and a lower R^2 value when only 50 frames are used (see Table 2, I). The 100 frames analysis already results in a much better accuracy of the fit and thus a lower PWV error. The PWV, however, is slightly underestimated in comparison to the full 200 frames dataset. In the next step, 4D flow cines were reconstructed using varying frame rates and window widths with a spatial resolution of 100 µm (see Table 2, II). The PWV value obtained from the cine with 20 frames and a 1/20 window width features a comparably large error relative to the LS/HT-res. reconstruction and a low coefficient of determination ($R^2 = 0.59$). A better accuracy was observed when larger frame rates and smaller selection windows were used. However, in the cine reconstructions with 50 frames or higher, severe undersampling artifacts occurred that precluded an accurate PWV measurement. The determination of a PWV value was not possible for a window width of 1/60 and an undersampling factor of more than 14. To further increase the frame rates, a cine with 60 overlapping frames and a window width of 1/20 was generated. The results indicated a lower PWV error in comparison to the 20 frames reconstruction but lower accuracy relative to the reconstructions with 100 frames or higher. Finally, 4D flow cines were generated at different spatial resolutions and 200 overlapping frames (window width: 1/33, see Table 2, **III**). While the results of the 125 µm reconstruction were similar to the 147 µm cine, a larger PWV error was observed in the 100 µm reconstruction due to more prominent undersampling artifacts.

Table 2: PWV estimation at different spatial resolutions, frame rates and selection window widths. OV reconstructions with overlapping frames. R^2: Coefficient of determination. us: undersampling factor. In bold: measurements used for the later PWV (LS/HT) and WSS (HS/LT) analysis. *No data evaluation possible. For the individual fits, see Supplementary Figure 1-3 in the supplement

Resolution	Frames	Width	PWV [m/s]	Error [m/s]	R^2	US
I. Influence of frame rates						
147	50 OV	1/33	1.50	0.13	0.77	3.6
147	100 OV	1/33	2.00	0.06	0.97	3.6
147	**200 OV**	1/33	2.44	0.10	0.93	3.6
I. Influence of window widths						
100	**20 (HS/LT)**	1/20	2.40	0.28	0.59	4.8
100	30	1/30	2.05	0.15	0.77	7.2
100	40	1/40	2.30	0.11	0.89	9.6
100	50	1/50	1.85	0.49	0.21	12.0
100	60	1/60	-	-	-	14.4
100	60 OV	1/20	1.66	0.16	0.68	4.8
I. Influence of spatial resolution						
100	200 OV	1/33	2.52	0.18	0.78	7.8
200	200 OV	1/33	2.20	0.08	0.93	5.0

2.4.4.2 Wall shear stress

The 100 µm 4D cine reconstructions (see Table 2, **II**) were used to investigate the influence of selection window widths and frame rates on WSS values. Figure 19A-E displays the time-dependent median WSS for different temporal resolutions (20–60 frames). In Figure 19F, boxplots of the WSS distribution over the cardiac cycle are shown. The results indicate a slight increase of the peak WSS compared to the 20 frames reconstruction when higher frame rates and smaller selection windows are used. However, for window widths of 1/50 and smaller, severe undersampling artifacts were observed. Figure 20 displays the results for reconstructions with overlapping selection windows for 60 overlapping (OV) frames (Figure 20B) and 200 overlapping frames (Figure 20C). For comparison, values from the HS/LT-res. reconstruction are shown (Figure 20A). The reconstruction with the highest frame rate (200 frames, W = 1/33) also features a slightly larger peak WSS (see Figure 20D).

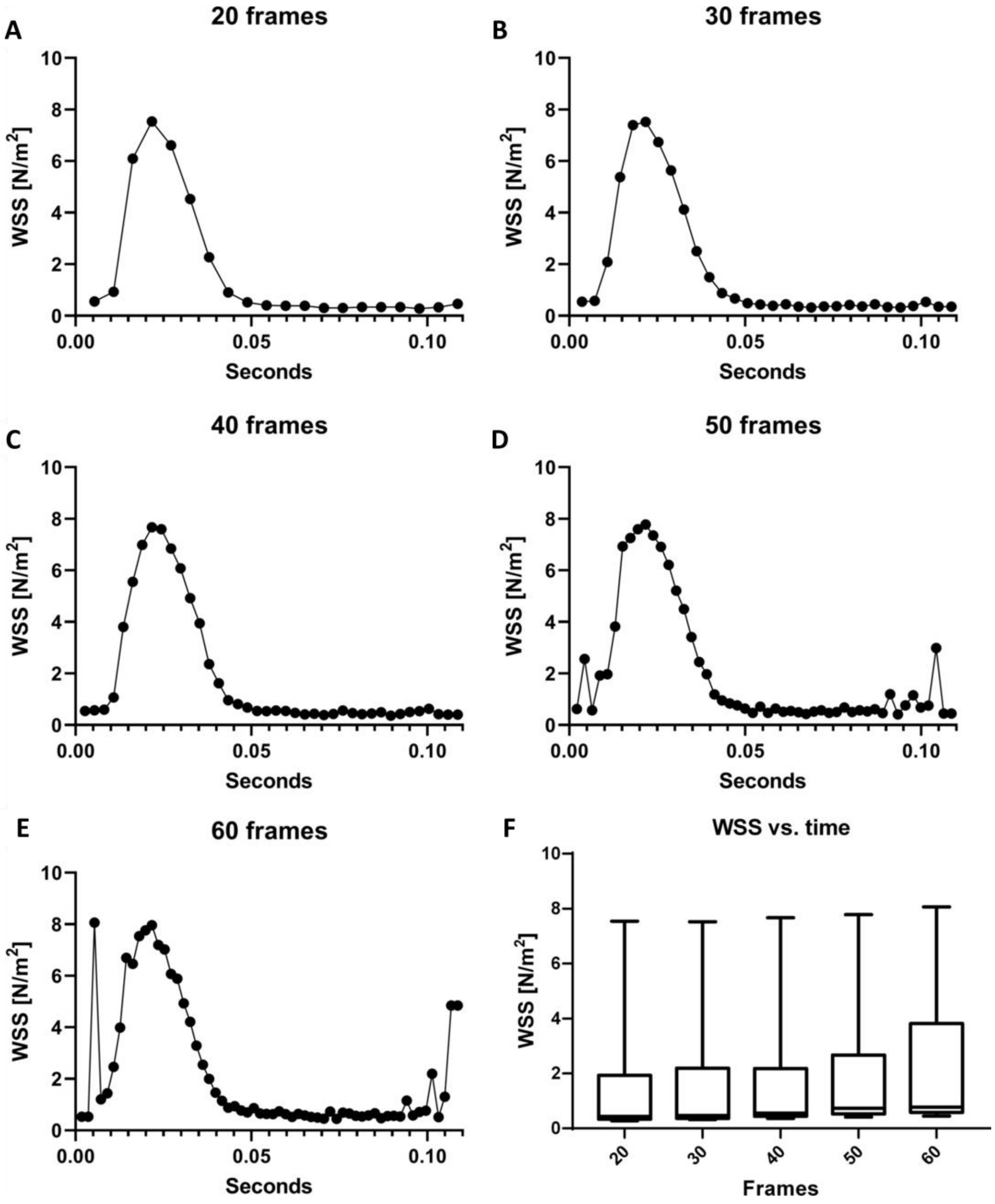

Figure 19: Time-dependent median WSS values for different temporal resolutions. **A** WSS values with 20 frames. **B** WSS values with 30 frames. **C** WSS values with 40 frames. **d** WSS values with 50 and 60 (**e**) frames. In **D** and **E**, severe undersampling factors are noticeable. **F** Boxplots of the WSS distribution over the cardiac cycle for all reconstructions. A slight increase of peak WSS values compared to the 20 frames reconstruction when using higher frame rates and smaller selection windows is observable.

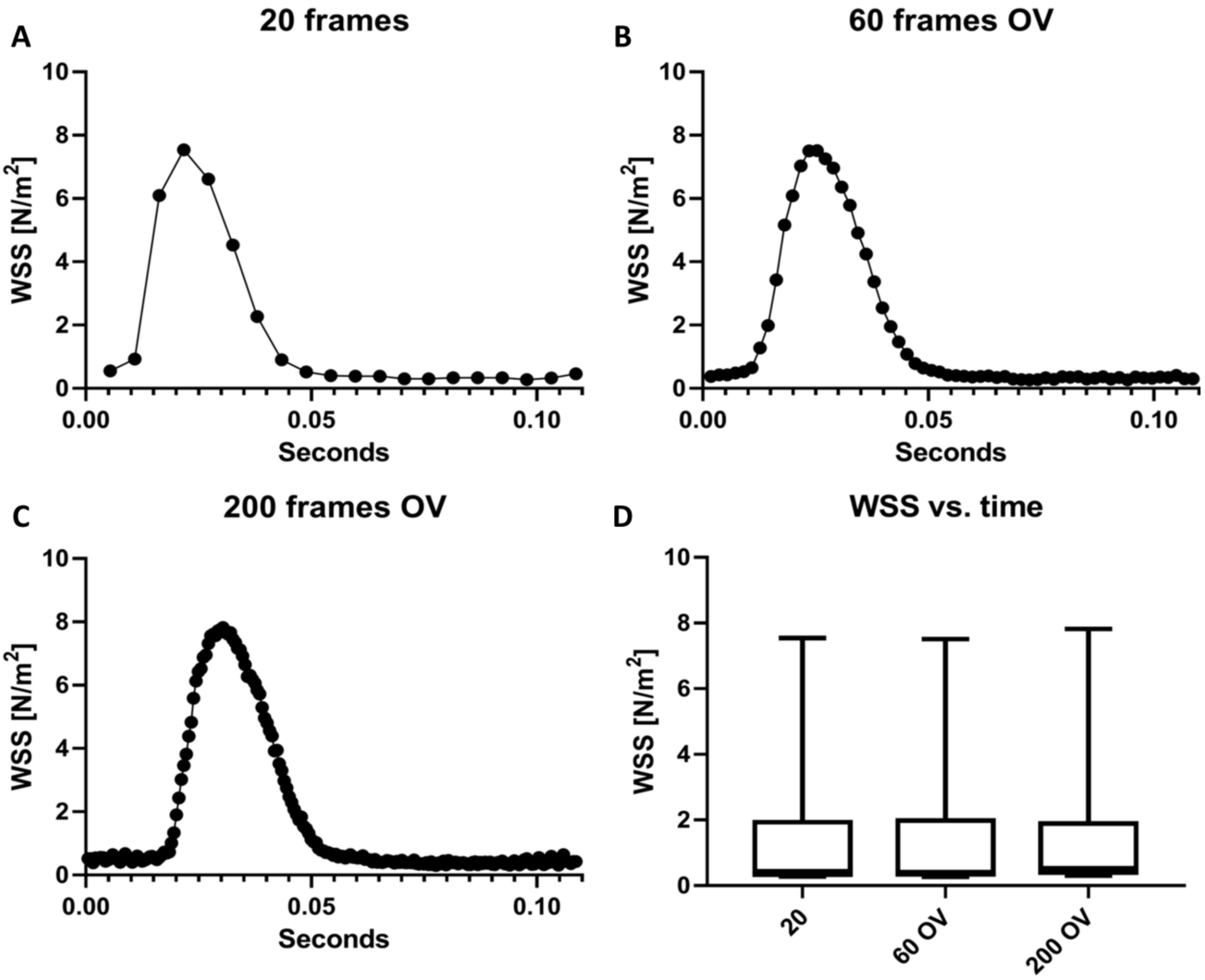

Figure 20: Time-dependent median WSS values for different temporal resolutions with overlapping selection windows. A WSS values with 20 frames. **B** WSS values with 60 overlapping (OV) frames. **C** WSS values with 200 overlapping (OV) frames. **D** Boxplots of the WSS distribution over the cardiac cycle for all reconstructions. The reconstruction with the highest frame rate (200 frames, W = 1/33) features a slightly larger peak WSS.

2.4.5 *IN VIVO* STUDY: WSS VALUES

Temporally averaged WSS magnitude values were calculated in the aortic arch of all wildtype and ApoE$^{-/-}$ mice using the HS/LT-res. reconstruction (20 frames). Figure 21 shows bulls-eye plots for the distribution of WSS magnitudes in three regions of interest (inner ring: ascending aorta (A), middle ring: top region (T), outer ring: descending aorta (D), see scheme in Figure 21A). Mean WSS values averaged over the whole aortic arch were (1.17 ± 0.07) N/m^2 (WT mice, see Figure 21B and (1.27 ± 0.10) N/m^2 (ApoE$^{-/-}$ mice, see Figure 21C). In both groups, a highly asymmetric distribution of WSS values in the ascending aorta is noticeable. Results also indicate a larger asymmetry of WSS distribution in the ApoE$^{-/-}$ group.

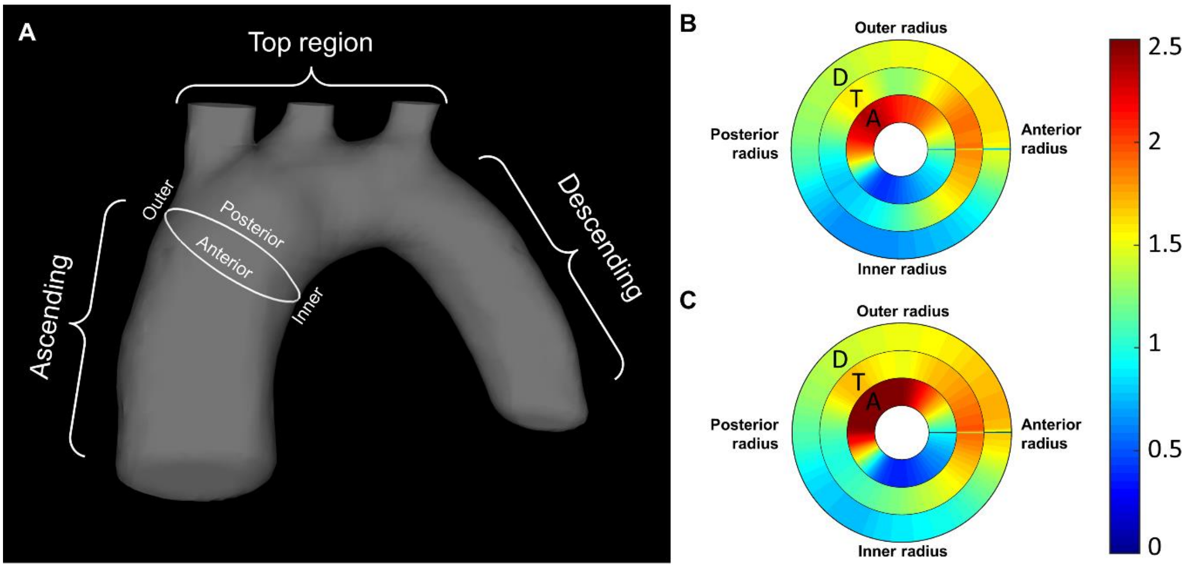

Figure 21: Regions of the aortic arch and corresponding WSS values. A Scheme of the aortic arch with the chosen regions: ascending (A), top region (T) and descending (D). White ring: Scheme of the inner, outer, anterior and posterior radius of the aorta. **B + C** Bulls-Eye plots for the temporal averaged WSS values (magnitude) for **B**: Wildtype and **C**: ApoE$^{-/-}$ mice. Inner ring: Ascending aorta (A). Middle ring: top region (T). Outer ring: descending aorta (D). Scale: N/m^2

2.4.6 *IN VIVO* STUDY: PWV VALUES

Aortic PWV was assessed in all 10 animals using the multiple-point transit time method and the LS/HT-res. reconstruction (200 frames). The PWV values are displayed in Figure 22. In the atherosclerotic ApoE$^{-/-}$ mouse model, significantly higher PWV values were observed compared to the WT control group ((2.6 ± 0.2) m/s versus (1.7 ± 0.2) m/s, $p < 0.001$).

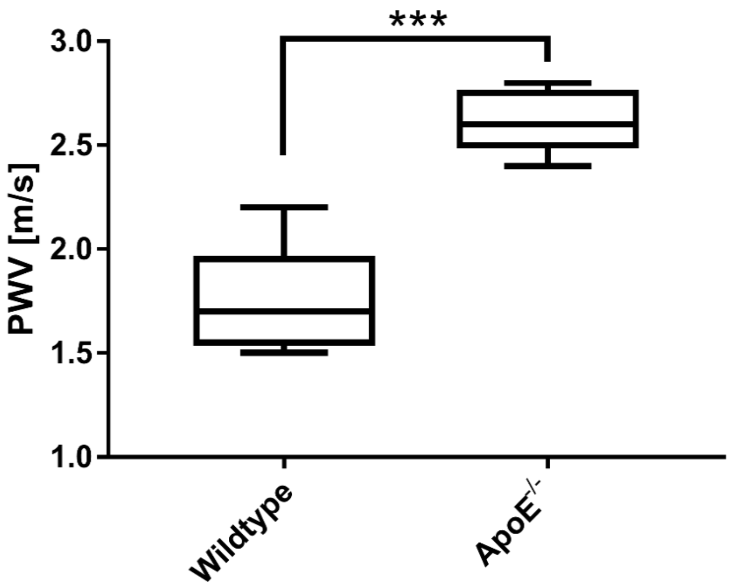

Figure 22: Pulse-wave velocities for wild-type and ApoE$^{-/-}$ mice. Data are presented as mean ± SD. Statistically significant differences are observable in ApoE$^{-/-}$ mice compared to the WT group (***, $p<0.001$).

2.5 DISCUSSION

2.5.1 SELF-GATING: STABILITY AND UNDERSAMPLING

Analysis of the self-navigation signals showed no significant differences in the heart rate variations as well as in the yield, which suggests no variations in stability between healthy WT and pathological subjects. In both groups, approximately 80% of the radial projections could be used for reconstruction. In the ApoE$^{-/-}$ group, the cardiac periods were slightly longer in comparison to the WT control group. The cause for these differences is unclear and will require further clarification. One possible reason might be that both animal groups were measured on two separate measurement days. For PWV as well as WSS quantification, no external cardiac or respiratory navigation signal was necessary, which strongly facilitates animal handling and reduces the influence of external disturbances, e.g. caused by interferences with the gradient system or a slipping of the sensor probes. Due to the large flip angle, short repetition times and a thin excitation slab, strong signal enhancement of inflowing blood and suppression of static tissue were achieved at the same time. Since the blood signal is orders of magnitudes larger than the signal of the surrounding tissue, undersampling artifacts such as streaking only slightly affect the quality of the reconstructed velocity maps [7]. This allows high acceleration factors with radial PC-MRI [287]. In the reconstruction used for PWV quantification, undersampling factors were between 3.8 and 4.0. In the WSS reconstruction, undersampling factors were larger due to the higher spatial resolution (5.0–5.3). Results were similar to findings reported for WSS measurements in 12-week-old WT mice [4].

2.5.2 FLOW VALUES AND SEGMENTATION

Peak flow values measured in this study ranged between 0.65 and 0.80 ml/s (HS/LT-res. reconstruction) and between 0.71 and 0.88 ml/s (LS/HT-res. reconstruction), respectively (see Figure 16F). The results are in good accordance with the values reported previously for 12-week-old WT mice (0.8–0.9 ml/s, [4]). In both animal groups, a 7% increase of peak flow was observed in the LS/HT-res. reconstruction, which can be attributed to the higher frame rate and the smaller selection windows. Furthermore, only the high frame rate reconstruction was capable of accurately detecting the upstroke of the systolic flow pulse. On the other side, only the high spatial resolution reconstruction enables accurate measurements of the velocity gradients and therefore WSS [60]. Thus, a combined analysis of flow at two different time scales and spatial resolutions provide better insight in the complex fluid dynamics of the aortic arch, which will be beneficial for future simulation-based CFD studies, especially in the context of atherogenesis [288-290].

For the LS/HT-resolution through-plane flow measurements, interpolated label data were used in order to reduce the time investment of the lumen segmentation. This was justified by the assumption that velocity values of voxels close to the aortic boundaries contribute only minimally to the flow integral [10]. This hypothesis should also be valid in vessels with large curvatures, since in case of laminar flow, flow profiles can still be modeled as asymmetric paraboloids [60]. In future studies, advanced segmentation techniques (e.g. based on machine learning) as a replacement of interpolation for more accurate vessel labeling (especially to further optimize WSS quantification) will be investigated.

2.5.3 WSS VALUES

Mean WSS values averaged over the aortic arch were (1.17 ± 0.07) N/m^2 in WT mice and (1.27 ± 0.10) N/m^2 in $ApoE^{-/-}$ mice. The results are in good accordance with previous studies in WT and $ApoE^{-/-}$ mice [4, 7, 8]. A strong asymmetric distribution of WSS values was observed in the ascending aorta. The results suggest an increase of WSS near the outer radius as well as a decrease near the inner radius of the ascending aorta in the atherosclerotic mouse model, indicating major hemodynamic and structural changes in this region, as expected [273]. Future studies could focus on detailed analyses of these interrelations.

2.5.4 PWV VALUES

Aortic PWV values of previous studies in 18 week-old mice obtained with CMR were 1.9 − 2.2 m/s for WT mice and 2.6 − 2.7 ml/s for $ApoE^{-/-}$ mice [9, 10], which is in range with the results found in this study (1.7 ± 0.2 m/s and 2.6 ± 0.2 m/s, respectively). In older $ApoE^{-/-}$ mice (8-9 months), larger PWV values of 3.00 − 5.84 m/s were found [7, 12, 13].

2.5.5 TEMPORAL AND SPATIAL RESOLUTION

The retrospective flow measurements presented in this work can be interpreted as a statistical process, since radial projections belonging to hundreds of heartbeats are combined to one dataset in order to reconstruct an image. The CMR signal (and therefore the self-navigation signal) is acquired with a repetition time of TR = 3 ms, thus the maximal achievable native temporal resolution is limited to this value. For the cine reconstructions, selection windows are used for the retrospective binning of projections. These windows were overlapped in order to realize a higher effective frame rate. Due to the finite width of the selection windows, each frame of the LS/HT-res. reconstruction had a temporal blurring of ± 0.8−1.1 ms (see Figure 16E), which is approximately 1.5−1.6 times the distance between two successive frames (approximately 0.6 ms). The selection windows act as a moving average filter that smoothens the flow curve [291]. The cut-off frequencies of these temporal low pass filters range between 220 and 650 Hz, depending on the used selection window size (see Supplementary Figure 4). In case of the LS/HT-res. reconstruction (W = 1/33), higher dynamic portions of the flow curve with frequencies above 350 Hz are suppressed. This might result in inaccuracies in the determination of the systolic upstroke. However, a Fourier analysis of triggered Cartesian through-plane flow measurements conducted at a native temporal resolution of 1 ms [15] revealed only small (< − 18 dB, see Supplementary Figure 5) contributions of frequency components above 300 Hz to the flow pulse. Therefore, applying a smoothing filter with a width of 1/33 only slightly affects the flow curve (see Supplementary Figure 6). Furthermore, since the temporal width of the selection windows is related to the average length of the cardiac period, temporal blurring depends on the heart rate. In this study, no significant correlation between the heart rate and peak flow values was observed. Future studies in animals with much slower heart rates ($T_{RR} > 150$ ms), however, should address this further.

Investigations of the fitting errors and R^2 values (see Table 2) indicated a reliable detection of PWV when window widths in the range of 1/30 to 1/40 (cut-off frequencies: 300–400 Hz, see Supplementary Figure 4) are used. Reconstructions with larger windows result in larger inaccuracies of the PWV measurement due to temporal blurring, even when higher frame rates with overlapping selection windows are utilized. On the other hand, reconstructions with window sizes of 1/50 and smaller exhibit large undersampling artifacts, which impede an accurate assessment of the PWV, thus limiting the minimum achievable temporal blurring. Regarding the frame rate, robust PWV detection was achieved for 40 frames or higher, however, the use of at least 100 frames is recommended in order to guarantee a large range of detectable PWV values. Especially in case of older ApoE$^{-/-}$ mice (8–9 months), PWV can be significantly increased to values of 4 m/s and higher [7, 12]. Hence, a very accurate sampling of the flow curves is required.

Regarding spatial resolution, a reliable PWV value was also found for the reconstruction with an isotropic resolution of 125 µm and an undersampling factor of 5. A further reduction to 100 µm and eightfold undersampling, however, lead to larger inaccuracies due to the more prominent undersampling artifacts. These might be reduced using k-t-acceleration techniques for reconstructions[12]. Since the best fitting results were obtained using window widths between 1/30 and 1/40, frame rates of at least 100 frames and slightly lower spatial resolution, cine reconstructions with 200 frames, window sizes of 1/33 and 147 µm spatial resolution were used for all the PWV evaluations in this *in vivo* study.

In case of the WSS measurement, an increase of peak WSS was detected when smaller window sizes and larger frame rates are utilized. Thus, the use of higher temporal resolution might be beneficial in order to gain a better understanding of the complex dynamics of wall shear stress. However, as an increase in frame rates leads into a much larger segmentation effort, more advanced segmentation techniques (e.g. using machine learning) need to be implemented first. Therefore, we used a frame rate of 20 frames/cycle for this *in vivo* WSS analysis.

2.5.6 LIMITATIONS

A possible error source of the transit-time method are local disturbances of the flow curves, e.g., caused by recirculating flow or signal cancellations due to off-resonances or accelerated flow. These are especially present in the ascending aorta, near the aortic branches and in the thoracic aorta close to the lung and can impede accurate detection of the systolic upstrokes. To address this issue, through-plane flow was measured in at least 50 locations along the aortic arch in order to minimize the influence of individual disturbed measurements. In general, transit-time techniques for PWV quantification are overall more robust than local PWV measurements since they rely more on the measurement of through-plane flow but less on accurate vessel segmentation [10, 11]. In spite of the small bias and the slightly varying temporal blurring (see section above), the presented method is capable of detecting quantitative differences in PWV between two groups with comparable accuracy as in previous studies [9, 10].

One further limitation of this study is the absence of a reference measurement to validate and further optimize the PWV and WSS measurements. Due to the time constraints in *in vivo* measurements, no additional triggered 3D flow measurement could be performed. In a previous study, however, our group has already successfully demonstrated the feasibility of the retrospective reconstruction framework for self-navigated local 2D PWV measurements [15]. The results were in very good agreement with triggered Cartesian and radial PWV measurements [11]. Regarding the WSS quantification, validation experiments have already been performed in a flow phantom [4].

2.5.7 ADVANTAGES

Measurements of PWV and WSS are challenging due to the different demands on spatial or temporal resolution. Up to now, usually two separate flow measurements are conducted in order to quantify both parameters in mice [8, 12]. Most PWV measurements rely on cardiac and respiratory gating with external trigger signals, which are prone to external disturbances and add several minutes to the already long acquisition time [10]. For local PWV measurements, k-t acceleration techniques as well as retrospective triggering using self-navigation are available [12, 15], however, local PWV cannot be estimated in the aortic arch due to the strong curvature and reflections near the aortic branches [154]. The highly flexible reconstruction framework presented in this study provides a possible solution to this problem, since both parameters can be derived from one single measurement. Furthermore, 3D PWV measurements allow the assessment of through-plane flow at an arbitrary number of analysis planes, in contrast to 2D-flow measurements, where the number of planes is restricted by the measurement time. This reduces the susceptibility to heart rate instabilities, B_0 inhomogeneities and flow artifacts [6]. Depending on the demands of the parameter of interest, the reconstructions can be optimized for either high temporal or high spatial resolution. The proposed data processing algorithms are easy to implement and do not require extensive computational efforts. Thus, the assessment of both 3D WSS and PWV in the aortic arch is possible in short measurement and computation times.

The *in vivo* study presented in this work was performed in a 17.6 T small animal CMR system. However, an adaptation of the radial 4D-PC CMR sequence to 7 T scanners with cryogenic receiver coils [118, 119] should be straightforward. Since the radial trajectory used in this method is susceptible to B_0 inhomogeneities, lower field strengths might be beneficial. Furthermore, the flexible reconstruction framework is not limited to small animal systems and has already been applied to measurements in humans [280, 292]. Ultimately, the flexible reconstruction might be also beneficial for the development of more realistic CFD models in humans and more efficient clinical routines, for example by addressing arrhythmias in greater detail and using dynamic spatiotemporal resolutions.

2.5.8 CONCLUSION

In this work, a new post processing method was presented to extract PWV and WSS from a single flow measurement. The proposed technique provides the assessment of both parameters in an acquisition time of only 35 min and was successfully applied to both healthy WT and atherosclerotic ApoE$^{-/-}$ mouse models. The results indicate no differences in robustness between healthy WT and in pathological mice.

With this new technique, high spatial and temporal resolution information can concurrently be obtained in short measurement and computation times to gain simultaneously insight into 3D WSS and PWV parameters in the aortic arch. This technique may enable new insights into the hemodynamic determinants of atherosclerosis. In particular, it will be interesting to apply WSS and PWV measurements in order to characterize the hemodynamics during plaque development and progression. Ultimately, these parameters may also contribute to monitoring of plaque stability and the identification of vulnerable plaques in the future, questions of high clinical relevance.

2.6 SUPPLEMENTARY FIGURES

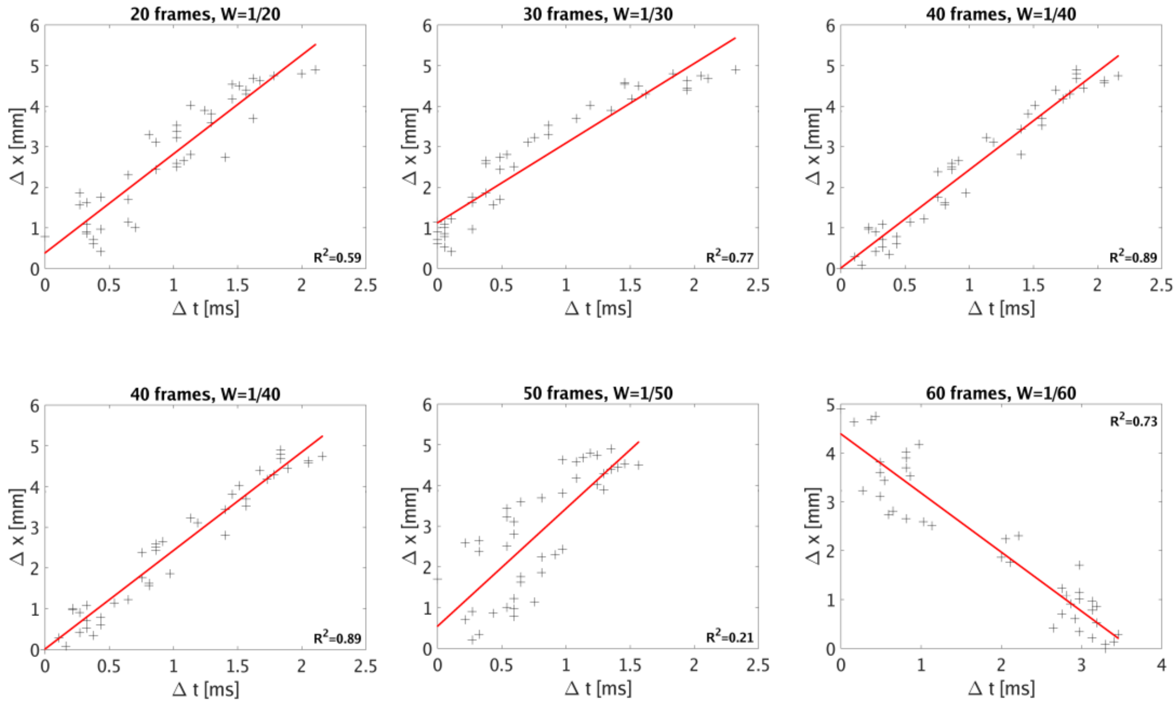

Supplementary Figure 1: Influence of window widths. Individual t-versus-x fits for the determination of PWV in order to investigate the influence of the window width.

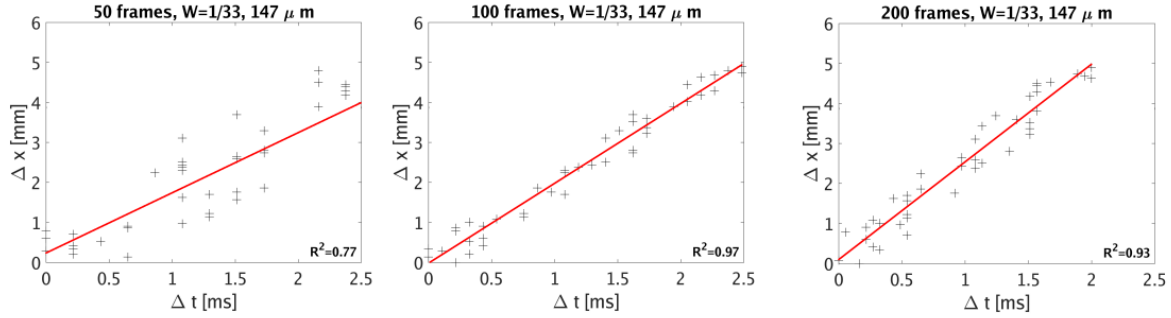

Supplementary Figure 2: Influence of frame rates. Individual t-versus-x fits for the determination of PWV in order to investigate the influence of the frame rate.

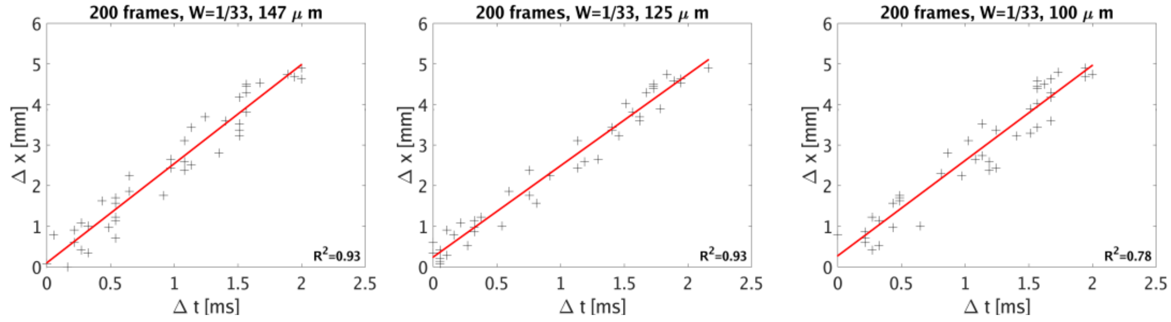

Supplementary Figure 3: Influence of spatial resolutions. Individual t-versus-x fits for the determination of PWV in order to investigate the influence of the spatial resolution.

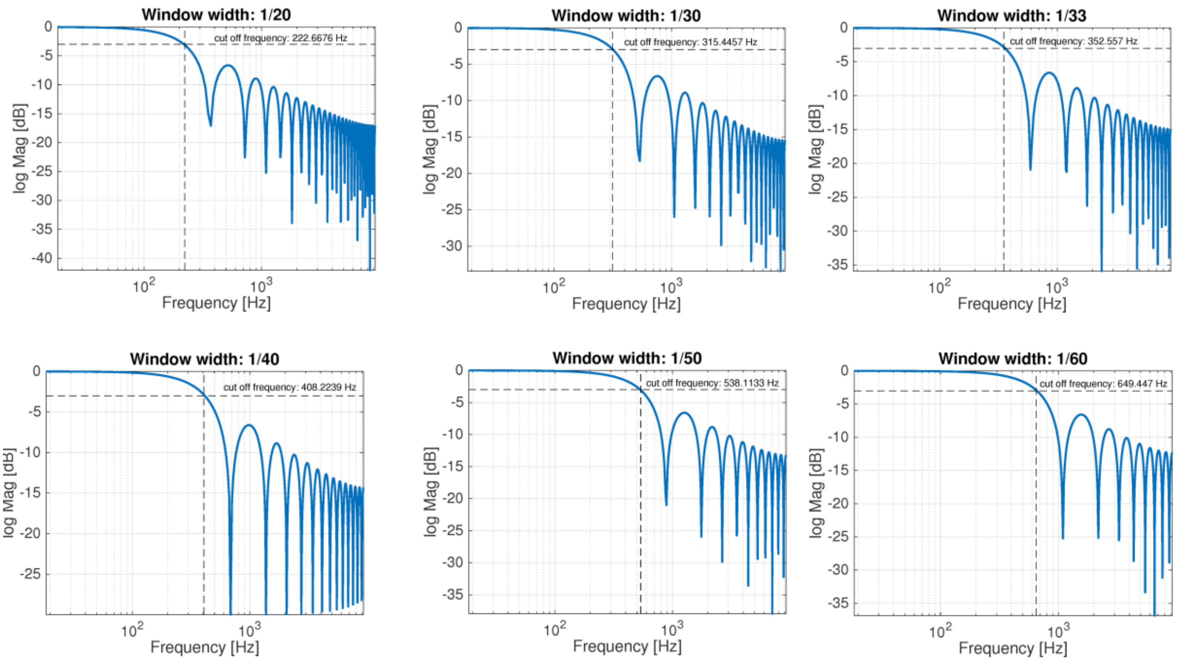

Supplementary Figure 4: Magnitude responses of the temporal filtering due to the retrospective binning of projections. The finite width of the selection window acts as a moving average filter that smoothens the flow curve and suppresses higher dynamic portions. The cut-of frequencies of these low pass filters depend on the window size and are in the range between 220 Hz (W=1/20) and 650 Hz (W=1/60).

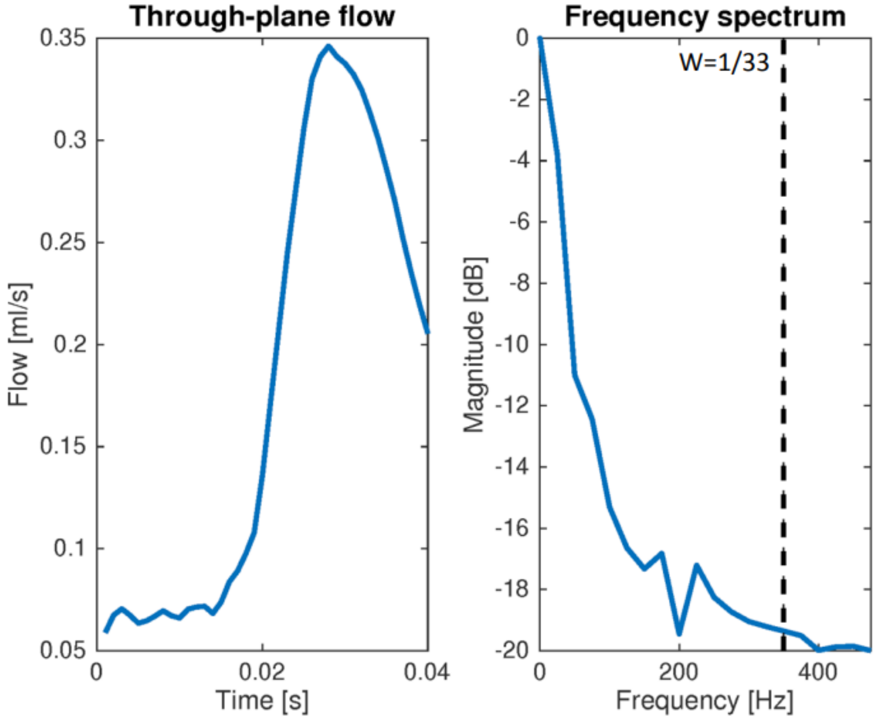

Supplementary Figure 5: Frequency analysis of a high-resolution (1 ms) flow measurement. The flow curve (left) was determined using a triggered Cartesian flow-encoding sequence. A Fourier analysis of the frequency spectrum (right) revealed only small contributions of frequency components >300 Hz. In dashed lines: Cut-of frequency for the 1/33 selection window (approximately 350 Hz). The CMR measurement used for these plots was originally published in 2013 [15].

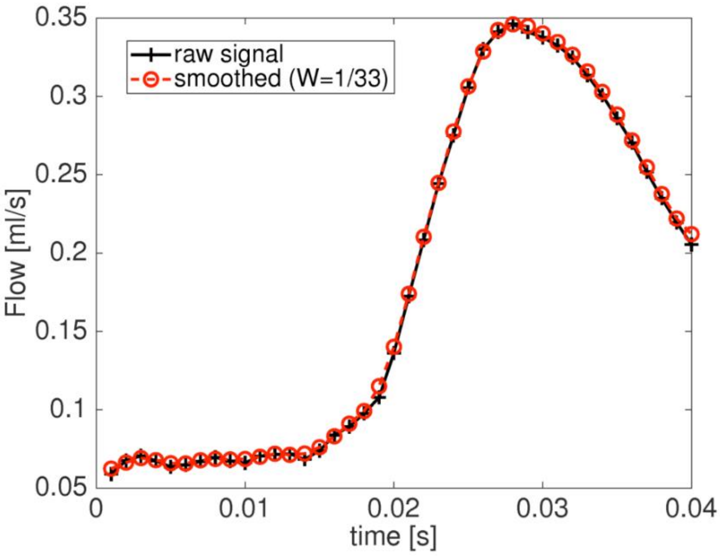

Supplementary Figure 6: Temporal filtering with a 1/33 window. The smoothing only slightly affects the flow curve. The CMR measurement used for these plots was originally published in 2013 [15].

CHAPTER 3

2D-Projection Maps of WSS and OSI Reveal Distinct Spatiotemporal Changes in Hemodynamics During Ageing and Atherosclerosis

Chapter 3 was published as original research article (Kristina Andelovic*, Patrick Winter*, Thomas Kampf, Anton Xu, Peter M. Jakob, Volker Herold, Wolfgang R. Bauer#, Alma Zernecke#: "2D-projection maps of WSS and OSI reveal distinct spatiotemporal changes in hemodynamics during ageing and atherosclerosis" in Biomedicines 2021, 9(12), 1856; reproduced from [5] as open access article distributed under the Creative Commons Attribution License which permits unrestricted use, distribution, and reproduction in any medium. The article is based on the work of the author of this thesis Kristina Andelovic, who designed the study and planned and conducted the experiments and analysis.

The original text was slightly modified to improve readability.

* and # Equal Contributors

The author contributions to the original research article are as follows:

Contributor	Contributions
Kristina Andelovic	Conceived the study, planned and conducted the experiments, analyzed the data, interpreted the results, prepared the original manuscript, reviewed the manuscript
Patrick Winter	Conceived the study, programmed the analysis scripts, analyzed the data, interpreted the results, reviewed the manuscript
Thomas Kampf	Idea for 2D projection maps, interpreted the results, reviewed the manuscript
Anton Xu	Helped with segmentation of MRI data sets, reviewed the manuscript
Peter Michael Jakob	Interpreted the results, reviewed the manuscript
Volker Herold	Conceived the study, provided funding, Interpreted the results, reviewed the manuscript
Wolfgang Rudolf Bauer	Conceived the study, interpreted the results, provided funding, Interpreted the results, reviewed the manuscript
Alma Zernecke	Conceived the study, interpreted the results, provided funding, Interpreted the results, prepared the original manuscript, reviewed the manuscript, supervised the project

3.1 ABSTRACT

Growth, ageing and atherosclerotic plaque development alter the biomechanical forces acting on the vessel wall. However, monitoring the detailed local changes in WSS at distinct sites of the murine aortic arch over time has been challenging. Here, we studied the temporal and spatial changes in flow, WSS, oscillatory shear index (OSI) and elastic properties of healthy wildtype (WT, $n = 5$) and atherosclerotic apolipoprotein E-deficient (*Apoe*$^{-/-}$, $n = 6$) mice during ageing and atherosclerosis using high-resolution 4D flow magnetic resonance imaging (MRI). Spatially resolved 2D projection maps of WSS and OSI of the complete aortic arch were generated, allowing the pixel-wise statistical analysis of inter- and intragroup hemodynamic changes over time and local correlations between WSS, PWV, plaque and vessel wall characteristics. The study revealed converse differences of local hemodynamic profiles in healthy WT and atherosclerotic *Apoe*$^{-/-}$ mice, and we identified the circumferential WSS as potential marker of plaque size and composition in advanced atherosclerosis and the radial strain as a potential marker for vascular elasticity. Two-dimensional (2D) projection maps of WSS and OSI, including statistical analysis provide a powerful tool to monitor local aortic hemodynamics during ageing and atherosclerosis. The correlation of spatially resolved hemodynamics and plaque characteristics could significantly improve our understanding of the impact of hemodynamics on atherosclerosis, which may be key to understand plaque progression towards vulnerability.

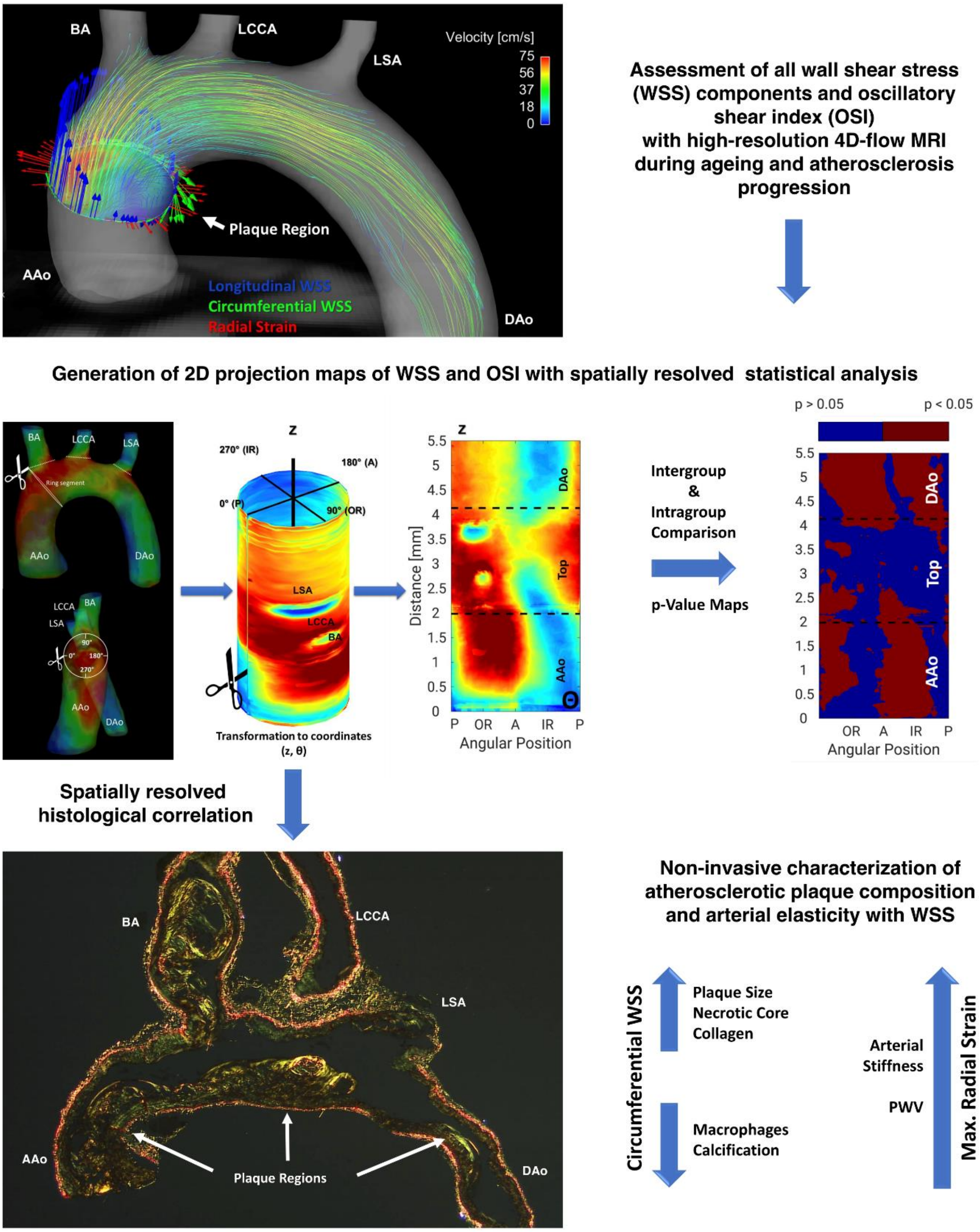

Figure 23: Graphical Abstract. Assessment of aortic flow, wall shear stress and oscillatory shear index was performed in the murine aortic arch of healthy wild-type and atherosclerotic *Apoe*$^{-/-}$ mice with high-resolution 4D-flow-MRI. The generation of 2D-projection maps of WSS and OSI with spatially resolved statistical analysis for intergroup and intragroup comparisons revealed distinct spatiotemporal changes in WSS and OSI profiles. 2D-projection maps furthermore allowed spatially resolved histological correlation with plaque parameters, identifying the circumferential WSS and radial strain as potential markers of plaque parameters and vascular elasticity.

3.2 BACKGROUND

Atherosclerosis is a complex inflammatory disease, characterized by the formation of fibrofatty lesions in the intimal layer of the artery wall (atherosclerotic plaques) [273]. Ruptures or erosions of these plaques are responsible for most of the cardiovascular events in the Western world, including myocardial infarction and stroke. Although cardiovascular risk factors, such as smoking, hypertension, hypercholesteremia and diabetes, can cause an endothelial dysfunction in the whole arterial tree, plaques develop mainly at predilection sites, such as curvatures, branch points and bifurcations [274, 276]. These regions are characterized by low and oscillatory wall shear stress (WSS) that cause an endothelial dysfunction, which, together with other processes, such as lipid deposition, determine the location of plaque development [62, 63]. The growing plaque furthermore leads to structural and mechanical changes in the vessel wall due to vascular remodeling and narrowing, enhancing disturbed flow patterns and affecting local WSS.

The endothelial WSS is a vector quantity, which consists of different components [60]; the longitudinal WSS (longWSS) points towards the direction of the flow. A second, circumferential component perpendicular to the longWSS can be attributed to helical flow and is orientated along the circumference of the vessel (circWSS). In addition, a third component, pointing towards the center of the vessel, can be derived, which is designated radial strain (radStrain) and can be attributed to the outwards blood pressure[4]. Besides low mean shear stress, which is mainly defined by the longitudinal WSS value, oscillatory shear stress is considered a pro-atherogenic hemodynamic parameter. It is caused by temporally oscillating flow and backflow and can be described by the oscillatory shear index (OSI). Various studies indicate a link between low and oscillatory shear stress and arterial remodeling [2, 278], leading to the gradual stiffening of the arteries due to increased collagen deposition [167] and fragmentation of elastic fibers [9]. This impairment of arterial compliance is a main pathophysiological feature of atherosclerosis, representing one of the earliest measurable markers of functional and structural changes during atherosclerosis development. The assessment of the arterial PWV with MRI enables the non-invasive characterization of arterial elasticity by measuring the speed of the pressure waves travelling through the arterial system, which is accelerated in stiffened arteries. For preclinical *in vivo* studies, several imaging techniques have been developed to assess the PWV globally [10] as well as at multiple local positions along the aorta [9, 12, 15].

To provide insight into the influence of hemodynamics on plaque progression, a detailed analysis of spatial and temporal changes in WSS and elasticity profiles over time is essential. Given local differences in plaque growth and phenotype [10, 12], the spatially resolved analysis of WSS, OSI and elasticity changes is of great interest; however, extracting these parameters in reasonable scan times remains challenging. Clinical studies demonstrated the capability of 4D flow MRI to spatially resolve WSS components in humans [293] and pixel-wise analyses have been used to detect differences between healthy subjects and Marfan patients [294]. However, preclinical applications in mice are still sparse due to technical limitations. In order to reduce errors caused by intra-observer variability and to minimize the burden on the laboratory animal, the assessment of both WSS and elasticity values in only one experimental session is desirable. In recent studies, 2D flow measurements [117], sophisticated electrocardiogram-triggered spiral and cartesian 4D flow MRI [8, 118] and accelerated radial 4D flow MRI [119] have been introduced for applications in mice. However, these techniques only allow the assessment of flow or the WSS, while a simultaneous measurement of flow, WSS and PWV could only be achieved in 2D [7]. Furthermore, most studies only focus on one single animal group and one measurement time point. One of the first studies describing the simultaneous assessment of WSS and elastic properties in preclinical models using 4D flow MRI was conducted by Wentland et al., who investigated atherosclerotic lesions in pigs with familial hypercholesterolemia[6]. Recently, we demonstrated that retrospectively gated 4D PC-MRI can also be used to simultaneously extract various parameters, including the PWV and all three components of the WSS in mice from only one 4D flow measurement [3, 4, 16].

Here, we present a longitudinal study that uses simultaneous assessments of flow, PWV, all WSS components and the OSI in the aortic arch, based on 4D phase contrast MRI (PC-MRI) [4, 16] for studying global and local hemodynamic changes in ageing wildtype (WT) and atherosclerosis-prone *Apoe*$^{-/-}$ mice during plaque progression. 2D projection maps are introduced to spatially resolve and visualize the distribution and temporal changes of hemodynamic profiles in the complete aortic arch. Pixel-wise statistical analysis for intra- and intergroup comparisons [105] revealed distinct spatiotemporal changes in WSS and OSI profiles. Correlations with elastic properties indicated that the radStrain could be of potential interest for the assessment of vascular elasticity. By correlating spatially resolved WSS and OSI values with atherosclerotic plaque parameters, we identified the circWSS as a promising new marker for advanced atherosclerotic plaque size and composition. The detailed analysis of local hemodynamics in healthy and atherosclerotic vessels will be the key to further understanding of the relationship of altered hemodynamics with atherosclerosis development and progression towards plaque vulnerability.

3.3 METHODS

3.3.1 ANIMAL HANDLING AND EXPERIMENTAL DESIGN

Female wildtype (WT) C57BL/6 J mice (*n* = 5) and *Apoe*$^{-/-}$ mice (*n* = 6) (Jackson Laboratory, Bar Harbor, ME, USA) were fed a normal diet (WT) or a Western diet (*Apoe*$^{-/-}$: ssniff, Soest, Germany) starting at the age of 4 weeks. One WT mouse died after the second measurement time point at 18 weeks due to unknown reasons. At the age of 12, 18 and 24 weeks, flow and WSS were measured using 17.6T MRI [4, 16] representing early (12 weeks) [105], intermediate (18 weeks) [9] and advanced atherosclerosis (24 weeks) [295], resulting in an equal time frame of 6 weeks in between the chosen time points. Histological analyses were performed after sacrifice at the age of 24 weeks (see Figure 24). Female mice were chosen in this study to enable keeping the animals together over the duration of 20 weeks. All animal experiments were approved by local authorities (Regierung von Unterfranken, Würzburg, Germany, 18 April 2017, reference number: 55.2-2531.01-427/17) to comply with German animal protection law.

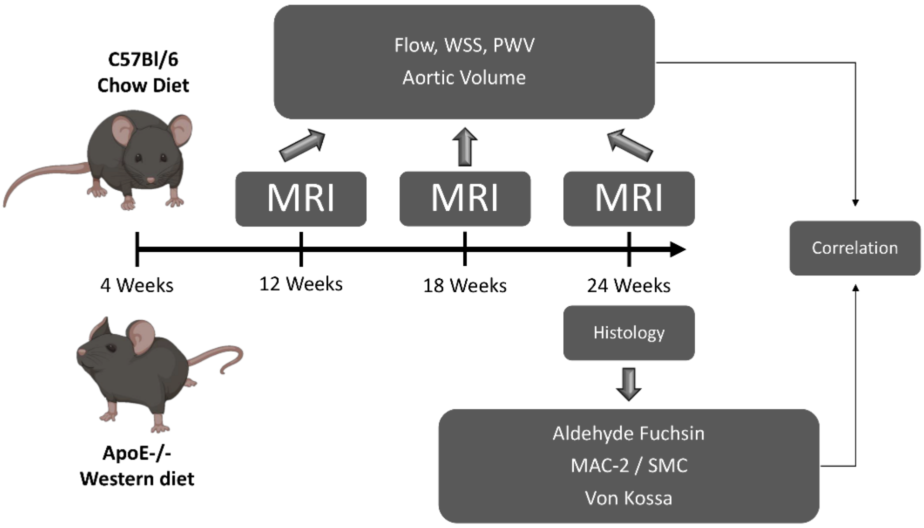

Figure 24: Study design. Study design. WT mice were fed a chow and *Apoe*$^{-/-}$ mice a Western diet starting at the age of 4 weeks. At 12, 18 and 24 weeks, flow and WSS were measured with 4D-PC MRI. After 24 weeks, aortas were analyzed histologically for collagen, SMC and MAC content, necrotic core size and calcification. Obtained data were correlated with spatially resolved WSS and OSI values.

3.3.2 MRI MEASUREMENTS

For MRI measurements, mice were anesthetized by applying 1.5% isoflurane in 2.0 Vol.% oxygen (2 L/min) via nose cone. A pressure-sensitive pneumatic balloon (Graseby Medical Limited, Watford, United Kingdom) was placed between the inner radio frequency resonator wall and the murine thorax to monitor vital functions (heartbeat and respiration) in real-time, by a custom-built ECG unit. Core body temperature was maintained at physiological 37 °C by adjusting the temperature of the gradient cooling unit. MRI measurements were performed using a 17.6 T vertical bore small animal MR system (Bruker Avance 750 WB, Bruker BioSpin MRI GmbH, Rheinstetten, Germany) with a 1 T/m gradient system with a diameter of 40 mm and a custom-built single-channel transmit–receive electromagnetic (TEM) resonator with an inner diameter of 24 mm. Flow was quantified in the aortic arch using a non-triggered, self-gated radial 4D-cine phase contrast sequence, as proposed recently [4, 16]. All data processing and reconstructions were performed with Matlab 2016b (The Mathworks, Inc., Natick, MA, USA). Cardiac and respiratory signals were extracted from the radial MRI signal and used for retrospective 3D cine reconstruction and cardiac and breath gating, as described previously [4, 16].

3.3.3 WSS CALCULATION

For WSS analysis, 3D cine were reconstructed at high spatial (100 µm isotropic) and moderate temporal resolution (20 frames per cardiac cycle) [4]. The lumen of the aortic arch was segmented, and a centerline of the lumen segmentation was calculated using Ensight (Ansys, Inc., Cannonsburg, PA, USA). Subsequently, the vectorial WSS $\vec{\tau}$ was derived from the 3D velocity gradients at the vessel wall, as described in [4]:

$$\vec{\tau} = 2\eta\dot{\varepsilon}\vec{n} \tag{5}$$

Where $\vec{n}$ denotes the lumen surface normal vector, η denotes the blood viscosity and $\dot{\varepsilon}$ denotes the 3×3 deformation tensor as follows:

$$\dot{\varepsilon}_{ij} = \frac{1}{2}\left(\frac{\partial v_i}{\partial x_j} + \frac{\partial v_j}{\partial x_i}\right), \tag{6}$$

where $v_{i,j}$ (i, j = 1,2,3) are the three velocity components and $x_{i,j}$ are the spatial coordinates. For the blood viscosity, a value of η = 0.004 Pa·s was assumed [16]. For the subsequent analysis, the WSS values were temporally averaged over the cardiac cycle.

3.3.3.1 Calculation of 2D-projection maps

To separate both WSS components and the radStrain, the averaged lumen segmentation, its centerline and the temporal averaged WSS vector were used (see Figure 25B). For each node on the lumen surface grid obtained from the segmentation, the component pointing towards the centerline (radStrain), in parallel to the centerline (longWSS) and perpendicular to the first two components (circWSS) were determined [4] (Figure 25A–C).

For generation of 2D projections of the 3D WSS maps, each data WSS point (x,y,z) on the lumen surface grid was transformed into coordinates (z, θ), where z is the position on the centerline (mm), relative to the beginning of the centerline (proximal ascending aorta) and θ the angle. Afterwards, WSS components were interpolated on a WSS (z, θ) map (see Figure 25D,F). The chosen convention was θ = 90° for the outer radius (OR) of the aorta and θ = 270° for the inner radius (IR) of the aorta. Therefore, θ = 0° marks the posterior side (P) and θ = 180° the anterior side (A) (Figure 25D,E). The grid size of the interpolated maps was 0.5° in the angular direction and 1µm in longitudinal direction.

The calculation of 2D projection maps enabled a pixel-wise analysis of the WSS distribution for each individual animal as well as all groups and timepoints. For the subsequent statistical analysis, the group mean value (averaged over all animals corresponding to a specific group and time point), and the corresponding standard deviation and *p*-value was calculated for each pixel. Afterwards, 2D difference maps (e.g., control–diseased) as well as maps of the statistical significance of these differences (*p*-value), similar to those described in [294], were computed for each parameter. In the significance maps, *p*-values of $p < 0.05$ are marked in red and values of $p > 0.05$ are marked in blue, respectively. Values obtained from the 2D projection maps were correlated with PWV measurements and histological findings (Figure 25G).

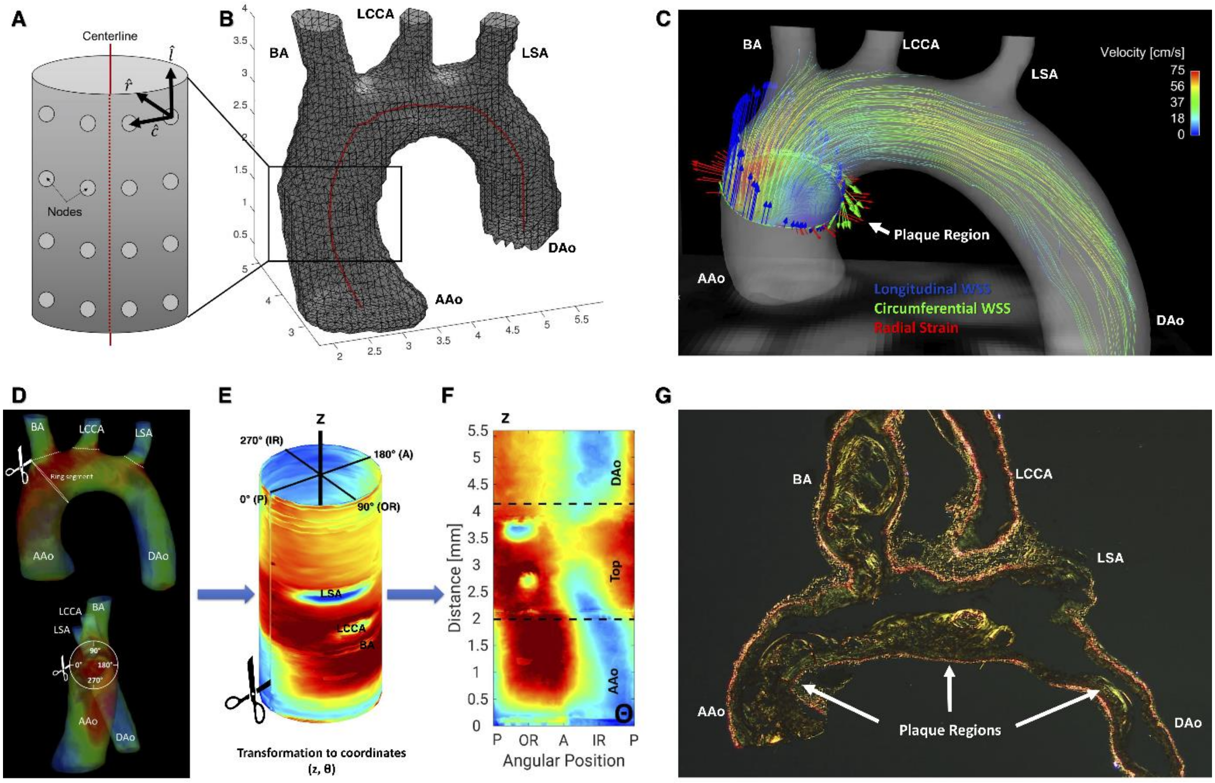

Figure 25: Lumen surface grid and 2D-projection map generation. **A** Schematic zoom of an aortic segment from (B). For each node, WSS components ($\hat{l}$:longitudinal, $\hat{c}$:circumferential and $\hat{r}$:radial) were determined. **B** Lumen surface grid of the aorta with centerline (red). **C** Aortic arch of an *Apoe*$^{-/-}$ mouse with streamlines and WSS components. Blue arrows: LongWSS. Green arrows: CircWSS. Red arrows: RadStrain. **D** Anterior (top) and frontal (bottom) view of the aorta with mean WSS values and a schematic ring segment. **E** Branches are cut off, aorta is opened on the posterior side at 0° and the WSS is projected to the coordinates (z,θ). Convention: θ=0°: Posterior side (P). **F** 2D projection map of WSS values of the arch. WSS and OSI values of the exact plaque position in the inner radius were used for histological correlation (**G).** AAo: Ascending aorta; BA: brachiocephalic artery; LCCA: left common carotid artery; LSA: left subclavian artery; DAo: descending aorta.

3.3.3.2 Calculation of the Oscillatory Shear Index (OSI)

The OSI is a marker for temporally varying shear stress values, therefore indicating oscillating flow and backflow. It is derived from the time dependent WSS vector $\vec{\tau}(t)$ using the following relation:

$$OSI\ [\%] = \frac{1}{2}\left(1 - \frac{|\sum_{i=1}^{n} \vec{\tau}(i)|}{\sum_{i=1}^{n} |\vec{\tau}(i)|}\right) \cdot 100. \qquad (7)$$

Here, $\sum_{i=1}^{n}$ indicates a summation over all time frames with n=20 and $i = 1, 2, \ldots, 20$ the frame index. The OSI is minimal when the WSS does not change direction or magnitude over time. On the other hand, the OSI reaches its maximum value when strong periodical variations or even sign changes occur [4].

3.3.4 PWV ANALYSIS

PWV was estimated with the multiple-points transit-time method [7, 10]. The same 4D flow data set was reconstructed at lower spatial (147 µm isotropic) and higher temporal resolution (200 frames per heart cycle). Through-plane flow was determined at approximately 50 equidistant locations along the aortic arch, as recently proposed [6]. The time point of the systolic upstroke of the volume flow was identified for each plane by measuring the intersection of a line fitted to the upstroke of the early systolic pulse and one line to the pre-systolic data points (baseline). Subsequently, the plane positions Δx (relative to the proximal ascending aorta) were plotted against the time points of the systolic upstrokes Δt. A line was fitted to the plot for PWV calculation and the PWV was afterwards derived from the slope of this fit, as follows:

$$PWV = \frac{\Delta x}{\Delta t} \tag{8}$$

For the PWV measurements at 18 weeks, we incorporated results that were originally published in [16] (see also Chapter 2).

3.3.5 AORTIC VOLUME QUANTIFICATION

To determine the aortic volume, the time dependent lumen segmentations of the 4D flow measurement were used. First, all segmentations were normalized to the same length by defining the center between the brachiocephalic artery and the left subclavian artery as a landmark (Figure 25B). Starting from this orientation point and using the centerline as length measure, all aortas were cut to a total length of 7 mm (3 mm along the centerline towards the proximal ascending aorta and 4 mm towards the distal descending aorta). Subsequently, the time-dependent aortic volumes were determined for all time frames by summation of the segmented voxels. The three aortic branches were excluded in order to reduce the error of the volume calculations. For the later analysis, the temporal mean, maximum and minimum values, as well as the difference between maximum and minimum volumes, were examined.

3.3.6 ATHEROSCLEROTIC LESION QUANTIFICATION

Aortas were removed, cleaned from fat and connective tissue and fixed in 4% paraformaldehyde PFA overnight, embedded in paraffin and cut longitudinally into 5 µm sections. Sections from the center of the inner curvature of aortic arch (corresponding to 270° in the corresponding WSS maps) were used for further analysis. For the assessment of plaque size and collagen content, sections were stained with Gabe's aldehyde fuchsin. In brief, sections were deparaffinized, rehydrated and stained for 15 min in aldehyde fuchsin solution to visualize elastic fibers. After 5× dipping in 70% Ethanol (EtOH), collagen was stained with picrosirius red solution for 90 min. For calcification analysis, adjacent sections were stained with Silvering after KOSSA (Morphisto, Offenbach am Main, HE, Germany) according to the manufacturer's protocol. After dehydration, sections were embedded with Vectamount mounting medium (Vector laboratories, Burlingame, CA, USA). Immunofluorescence staining of macrophages by Mac-2 (rat anti-mouse, CL8942AP, Cedarlane, Burlington, ON, Canada) and smooth muscle cells (SMCs) by aSMA (mouse anti-mouse, C6198, Sigma) were used to analyze plaque cellular content. After heat-mediated antigen retrieval (pH = 6), slides were blocked with 5% goat serum (Sigma Aldrich), incubated with primary antibody overnight at 4 °C, followed by secondary antibody Alexa Fluor 488-conjugated antibody (Molecular Probes, Life Technologies, Germany). Sections were mounted with 4',6-Diamidino-2-phenylindol (DAPI)-containing Vectashield mounting medium (Vector laboratories, Burlingame, CA, USA). Images were taken with a Leica DM 4000B fluorescence microscope and JVC KY-F75U camera. Plaque position, size, collagen content and cellular content were quantified by computerized image analysis (Diskus Software, Hilgers, Königswinter, NRW, Germany).

For correlations of histological findings with the MRI measurements, the WSS, radStrain and OSI values were assessed from the 2D projection maps using a strip located along the inner radius of the aortic arch (location: (270 ± 30)°). Spatial averages were computed for the corresponding plaque region in the inner curvature of the ascending and descending aorta and the top region, respectively.

3.3.7 STATISTICAL ANALYSIS

Data are presented as mean ± SEM. All error and statistical analyses were performed in Matlab 2016b (The Mathworks, Inc., Natick, MA, USA) and GraphPad Prism 8 (GraphPad Software, San Diego, CA, USA). Outlier exclusion was performed by using the Grubbs' test. Normal distribution was tested with the Shapiro–Wilk normality test. For normally distributed data, an unpaired t-test or an analysis of variance (ANOVA) was performed. When normality test failed, a non-parametric Mann–Whitney U test or a Kruskal–Wallis test was performed. For analysis of the degree of correlation, the Pearson correlation coefficients were calculated. For statistical analysis of the 2D projection maps, the difference values (e.g., *Apoe*$^{-/-}$ - WT) and the corresponding p-values were derived for each point (z, θ). Differences with $p < 0.05$ were considered statistically significant. In addition, a pixel-wise computation of the inter animal standard deviation was performed. As measure of accuracy, the spatial median as well as the lower and upper quartile values of the standard deviations were calculated.

3.4 RESULTS

3.4.1 AORTIC VOLUME DECREASES AND AORTIC FLOW AND PULSE-WAVE VELOCITY INCREASES IN ATHEROSCLEROTIC *APOE*$^{-/-}$ MICE

Weight, heart rates, aortic volumes and through-plane flow were assessed in 12-, 18- and 24-week-old wildtype (WT) and *Apoe*$^{-/-}$ mice. While the weight of WT mice increased over time, no significant changes were observed in *Apoe*$^{-/-}$ mice, with no significant differences between the groups (Supplementary Figure 7A). Heart periods did not change in either WT or *Apoe*$^{-/-}$ mice over time, but *Apoe*$^{-/-}$ mice featured longer heart periods compared to WT mice at 12 weeks (Supplementary Figure 7B).

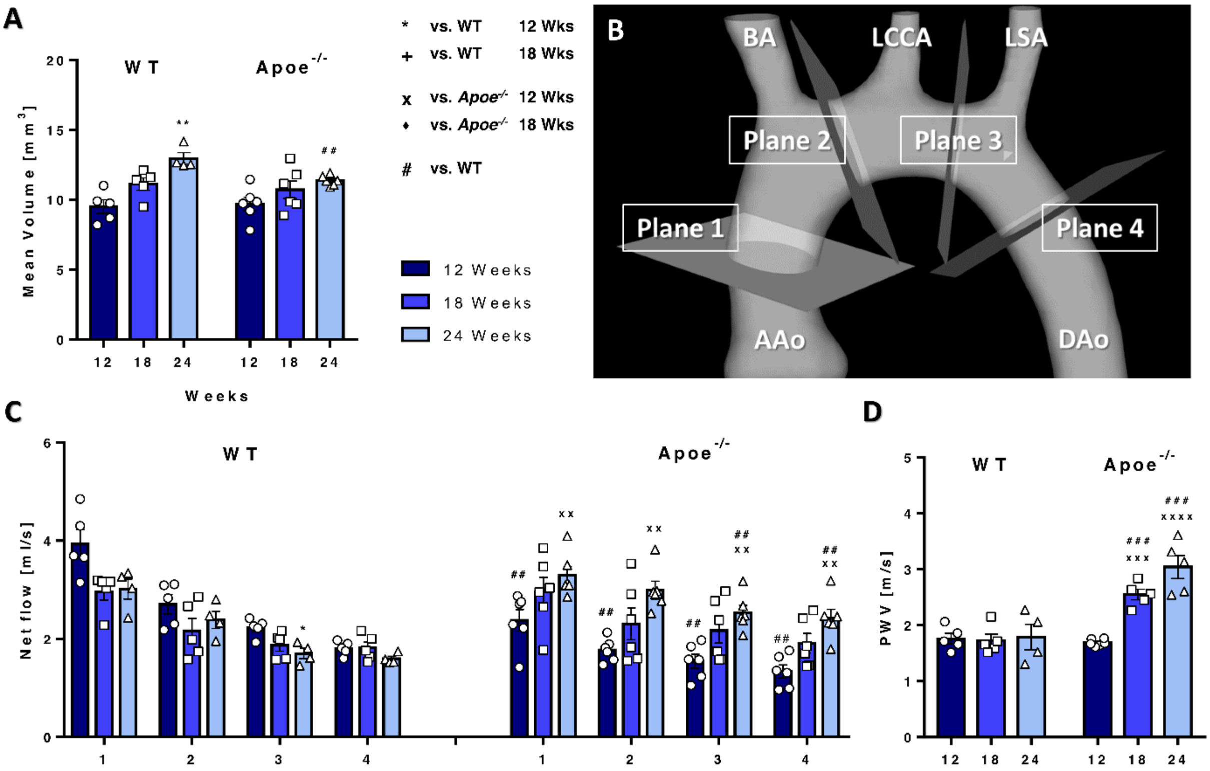

Figure 26: Aortic volumes are decreased and aortic flow and PWV are increased in atherosclerotic *Apoe*$^{-/-}$ mice. Mean aortic volumes were significantly larger in WT compared with *Apoe*$^{-/-}$ mice at 24 weeks. **B** Scheme of the analyzed planes. Plane 1: Inflow into the ascending part of the aortic arch. Plane 2: Residual flow after the BA. Plane 3: Residual flow after the LCCA. Plane 4: Residual flow after the LSA. **C** Net flow in the 4 analysis planes. WT mice showed a decrease, whereas *Apoe*$^{-/-}$ mice showed an increase in net flow over the course of the study. **D** PWV values. In contrast to WT mice, *Apoe*$^{-/-}$ mice displayed an increase in PWV over time. * vs. WT 12 weeks, $p < 0.05$; ** vs. WT 12 weeks, $p < 0.01$; $^{+}$ vs. WT 18 weeks, $p < 0.05$; ^{x} vs. *Apoe*$^{-/-}$ 12 weeks, $p < 0.05$; ^{xx} vs. *Apoe*$^{-/-}$ 12 weeks, $p < 0.01$; ^{xxx} vs. *Apoe*$^{-/-}$ 12 weeks, $p < 0.001$; ^{xxxx} vs. *Apoe*$^{-/-}$ 12 weeks, $p < 0.0001$; $^{\blacklozenge}$ vs. *Apoe*$^{-/-}$ 18 weeks, $p < 0.05$; $^{\#}$ vs. WT, $p < 0.05$; $^{\#\#}$ vs. WT, $p < 0.01$; $^{\#\#\#}$ vs. WT, $p < 0.001$.

Both mouse groups showed an increase in aortic volumes over time; however, 24-week-old *Apoe*$^{-/-}$ mice featured significantly smaller mean volumes compared with the control group (Figure 26A). Maximum (systolic) and minimum (diastolic) aortic volumes were also significantly smaller in atherosclerotic *Apoe*$^{-/-}$ mice compared with WT mice (Supplementary Figure 7). Furthermore, WT mice showed a stronger increase in maximum and minimum aortic volumes compared with *Apoe*$^{-/-}$ mice over time (Supplementary Figure 7C,D). In line, differences between systolic and diastolic volumes were smaller compared with WT mice, indicating an impaired dilatability during atherosclerotic plaque progression (Supplementary Figure 7). Net flow over the cardiac cycle increased over time in *Apoe*$^{-/-}$ but remained constant in WT mice (Figure 26B,C). Consistently elevated flow values were found in atherosclerotic mice at 24 weeks. Peak flow over the cardiac cycle was quantified in four analysis planes (Figure 26B). In line with the net flow, a trend towards decreased peak flow along the aorta was observed. In WT mice, no significant changes in peak flow values were noted over time (Supplementary Figure 7F). In *Apoe*$^{-/-}$ mice, however, peak flow significantly increased over time, resulting in significant differences in analysis planes 2–4 (Supplementary Figure 7F). While no significant changes in PWV values were observed in WT mice over time, PWV increased in *Apoe*$^{-/-}$ mice exhibiting significant differences, indicative of aortic stiffening (Figure 26D).

3.4.2 LONGITUDINAL WSS INCREASES IN *APOE*$^{-/-}$ MICE DURING ATHEROSCLEROSIS PROGRESSION BUT DECREASES IN WT MICE OVER TIME

The spatial mean and maximum values provide global information on WSS differences in the aortic arch. However, both the development of plaques and WSS locally affect the aorta, revealing strong differences of longWSS in the 3D visualization, in particular in the ascending aorta (AAo) and posterior side of the aorta, when comparing WT with *Apoe*$^{-/-}$ mice, where a much stronger WSS gradient was observed (Figure 27A). In WT mice, a continuous, significant decrease in spatial mean and maximum longWSS was measured over time. Mean (Figure 27B) and maximum (Supplementary Figure 8A) values were significantly lower in *Apoe*$^{-/-}$ compared with WT mice, but a significant increase was observed during atherosclerosis progression. As a result, 24-week-old *Apoe*$^{-/-}$ mice featured significantly higher values compared with respective WT mice, suggesting an increased WSS due to elevated flow, plaque growth and lumen narrowing). Spatially resolved WSS values were visualized by generating 2D projection maps of the whole aortic arch for each time point. In all measurements, an asymmetric distribution with highest values near the outer radius (OR) and lowest values near the inner radius (IR) was observed (Figure 27C,D). For error estimation, the spatial median values of the inter animal standard deviations were calculated for all groups and timepoints. The results indicate maximum median values of 0.34Pa and 0.39Pa in WT and *Apoe*$^{-/-}$ mice, respectively (see bold values in Supplementary Table 1 and Supplementary Table 2 and upper quartile values of 0.45Pa and 0.54Pa, respectively. The subsequent statistical analysis showed a significant decrease in longitudinal WSS values throughout the aorta of WT mice over time, leading to a decreased WSS gradient when comparing OR and IR (Figure 27C). In atherosclerotic *Apoe*$^{-/-}$ mice, however, a significant increase in longWSS in the top region and descending aorta (DAo) and a significant decrease around the IR of the AAo was observed (Figure 27D), resulting in an increasing WSS gradient over time (Figure 27D). When comparing both mouse models, *Apoe*$^{-/-}$ mice feature significantly lower longWSS mostly in the AAo and top region at 12 weeks and show gradually increased values over time and significantly higher longWSS in the top region and descending aorta (DAo) as well as in the OR of the AAo at 24 weeks, confirming a stronger WSS gradient compared with WT mice (Supplementary Figure 9).

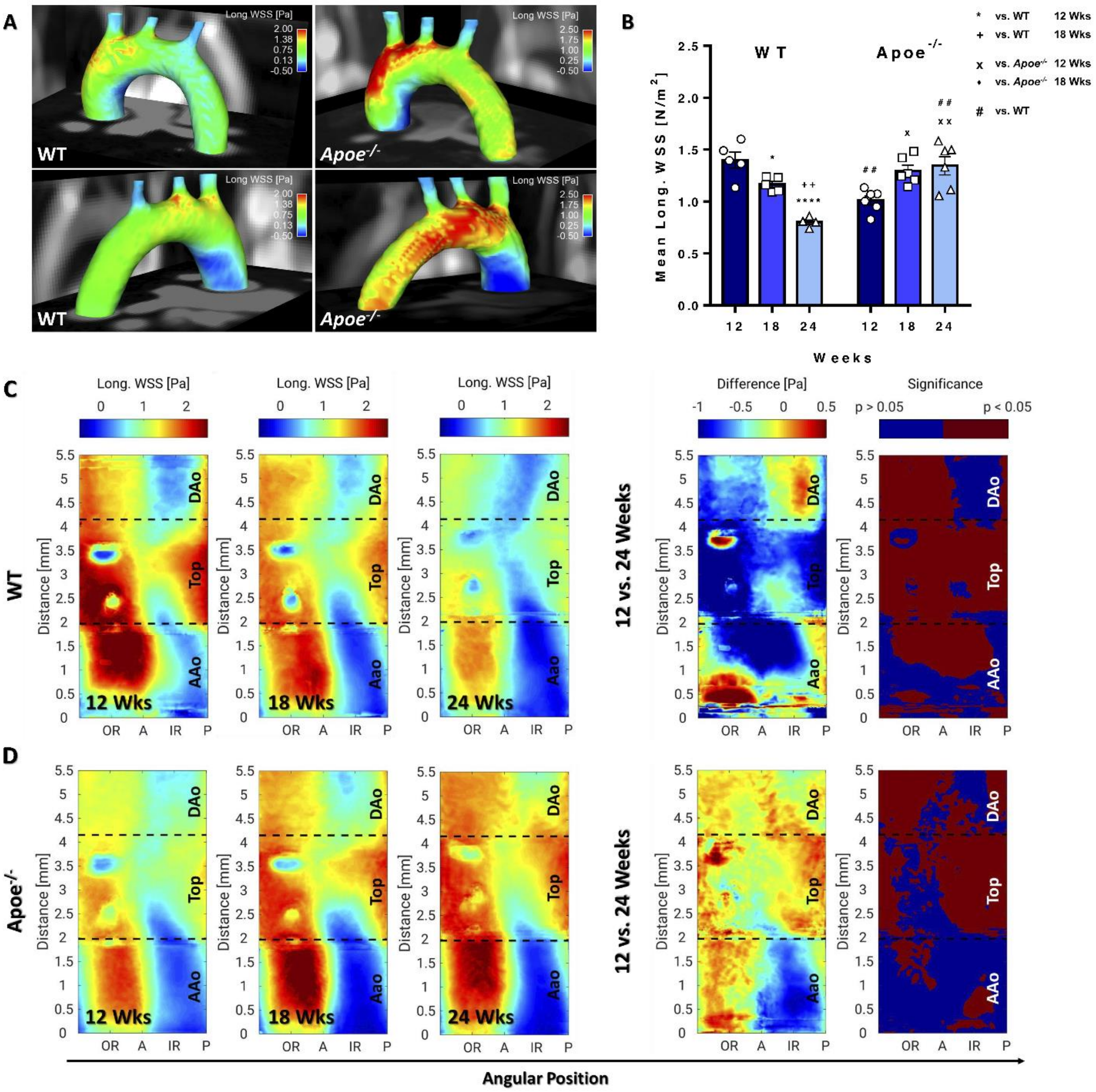

Figure 27: LongWSS increases in *Apoe*$^{-/-}$ mice during atherosclerosis progression but decreases in WT mice over time. **A** Three-dimensional longWSS map of a 24-week-old WT (left) and *Apoe*$^{-/-}$ mouse (right) from anterior and posterior view. A stronger WSS gradient was observed in *Apoe*$^{-/-}$ compared with WT mice and in the IR, lowered WSS is observable (dark blue spots). **B** Mean longWSS was decreasing in WT and increasing in *Apoe*$^{-/-}$ mice over time. * vs. WT 12 weeks, $p < 0.05$; **** vs. WT 12 weeks, $p < 0.0001$; $^{++}$ vs. WT 18 weeks, $p < 0.01$; ^{x} vs. *Apoe*$^{-/-}$ 12 weeks, $p < 0.05$; ^{xx} vs. *Apoe*$^{-/-}$ 12 weeks; $^{\#}$ vs. WT, $p < 0.05$; $^{\#\#}$ vs. WT, $p < 0.01$. **C** LongWSS maps of WT mice (group average) for all measurement time points and statistical intragroup comparison of longWSS values (12 vs. 24 weeks), showing the difference maps of longWSS values and significance maps. **D** LongWSS Maps of *Apoe*$^{-/-}$ mice.

3.4.3 CIRCUMFERENTIAL WSS SHOWS INVERSE CHANGES IN *APOE*$^{-/-}$ AND WT MICE, WHEREAS RADIAL STRAIN ONLY SHOWS LOCAL CHANGES

The 3D visualization of circWSS revealed high values around the posterior side of the AAo in the *Apoe*$^{-/-}$ mouse in comparison with WT mice (Figure 28A). Mean circWSS showed a similar pattern as longWSS in WT mice, decreasing significantly over time (Figure 28B). In *Apoe*$^{-/-}$ mice, a non-

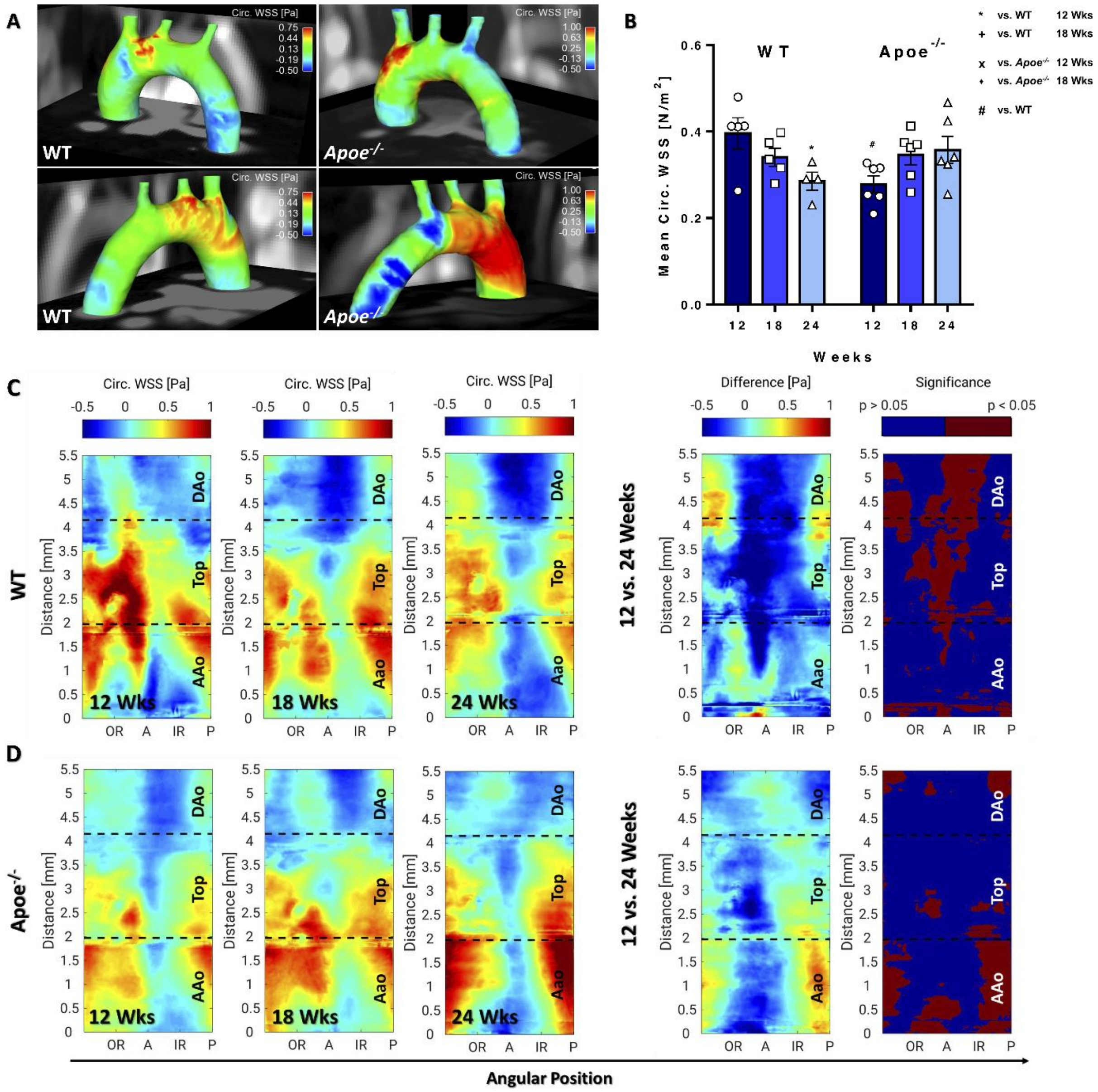

Figure 28: CircWSS shows inverse changes in *Apoe*$^{-/-}$ and WT mice. A Three-dimensional circWSS map of a 24-week-old WT mouse (left) and an *Apoe*$^{-/-}$ mouse (right) from anterior and posterior view. In comparison with the WT, high circWSS is visible in the posterior side of the AAo in the *Apoe*$^{-/-}$ mouse (red area in bottom right image). **B** Mean circWSS. WT mice showed significantly higher values at 12 compared to 24 weeks and compared with age-matched *Apoe*$^{-/-}$ mice. * vs. WT 12 weeks, $p < 0.05$; $^{\#}$ vs. WT, $p < 0.05$. **C** CircWSS maps of WT mice (group average) for all measurement time points and statistical intragroup comparison of circWSS values (12 vs. 24 weeks), showing the difference maps of circWSS values and significance maps. **D** CircWSS maps of *Apoe*$^{-/-}$ mice.

significant trend towards increased mean circWSS, and a significant increase in maximum values were observed (Figure 28B and Supplementary Figure 10). While *Apoe*$^{-/-}$ mice showed a decreased circWSS at 12 weeks compared with WT mice, both groups featured similar mean circWSS values at 18 and 24 weeks (Figure 28B and Supplementary Figure 10). At 24 weeks, however, maximum values were elevated in *Apoe*$^{-/-}$ relative to WT mice (Supplementary Figure 10).

2D projection maps of WT mice revealed a significantly decreasing circWSS around the anterior region and IR of the top and descending aorta during ageing (Figure 28C). In *Apoe*$^{-/-}$ mice, only mild changes were found during atheroprogression, with significantly increased values in the IR of the AAo, indicative of plaque growth (Figure 28D). Compared with WT mice, the most significant changes were noted at 24 weeks (Supplementary Figure 10), with increased values in the IR and posterior side of the AAo, and between the anterior and IR of the DAo in *Apoe*$^{-/-}$ mice, suggestive of increased helical flow in this area. In contrast, circWSS values were partially decreased in the OR. A corresponding analysis of the inter animal deviations revealed maximum median values of 0.30Pa and 0.25Pa (see bold values in Supplementary Table 1 and Supplementary Table 2) and upper quartile values of 0.40Pa and 0.35Pa in WT and *Apoe*$^{-/-}$ mice, respectively.

The 3D visualization of radStrain showed large areas with negative magnitude values near the outer radius of the AAo and Dao in the *Apoe*$^{-/-}$ mice (Supplementary Figure 11A). The WT mice, on the other hand, featured a significantly different pattern and positive values around the IR of the AAo. Mean radStrain did not change over time in WT and *Apoe*$^{-/-}$ mice, but significantly lower values were observed in 12-week-old *Apoe*$^{-/-}$ compared with age-matched WT mice (Supplementary Figure 11B). Similarly, peak radStrain values were lower in *Apoe*$^{-/-}$ mice and a significant decrease in peak radStrain was observed in WT mice over time (Supplementary Figure 8C and Supplementary Figure 12). In *Apoe*$^{-/-}$ mice, no clear trend was observed (Supplementary Figure 8C). However, local changes of radStrain were revealed by the 2D projection maps. In WT mice, a steady increase in radStrain was observed around the OR of the top and descending aorta, and a decrease around the IR of the same region (Supplementary Figure 11C). In contrast, *Apoe*$^{-/-}$ mice featured significantly decreased values around the IR of the AAo and top region, indicative of arterial stiffening (Supplementary Figure 11C). Comparisons of WT and *Apoe*$^{-/-}$ mice revealed drastic local changes of radStrain throughout the complete aortic arch during the course of the study (Supplementary Figure 12). In comparison with WT mice, *Apoe*$^{-/-}$ mice featured significantly decreased values around the IR of the AAo and OR of the DAo. A corresponding increase was observed around the OR of the AAo and the IR of the DAo. The analysis of the inter-animal standard deviations yielded maximum median values of 0.47Pa and 0.50Pa (see bold values in Supplementary Table 1 and Supplementary Table 2) and upper quartile values of 0.67Pa and 0.71Pa in WT and *Apoe*$^{-/-}$ mice, respectively.

3.4.4 OSI DECREASES IN *APOE*$^{-/-}$ MICE DURING ATHEROSCLEROSIS PROGRESSION BUT INCREASES IN WT MICE DURING AGEING

3D visualization of OSI values revealed elevated OSI values throughout the IR of the aorta in WT mice, whereas in *Apoe*$^{-/-}$ mice, elevated levels were only found in the IR of the AAo (red spot, Figure 29A). Mean OSI increased in WT mice over time, reaching high statistical significance at 24 compared with 12 weeks (Figure 29B). Conversely, a decrease in mean OSI was noted in *Apoe*$^{-/-}$ mice with significant changes after 24 weeks, leading to significantly lower values compared with WT mice. However, no differences in maximum OSI values were noted between the genotypes and time-points (Supplementary Figure 8D).

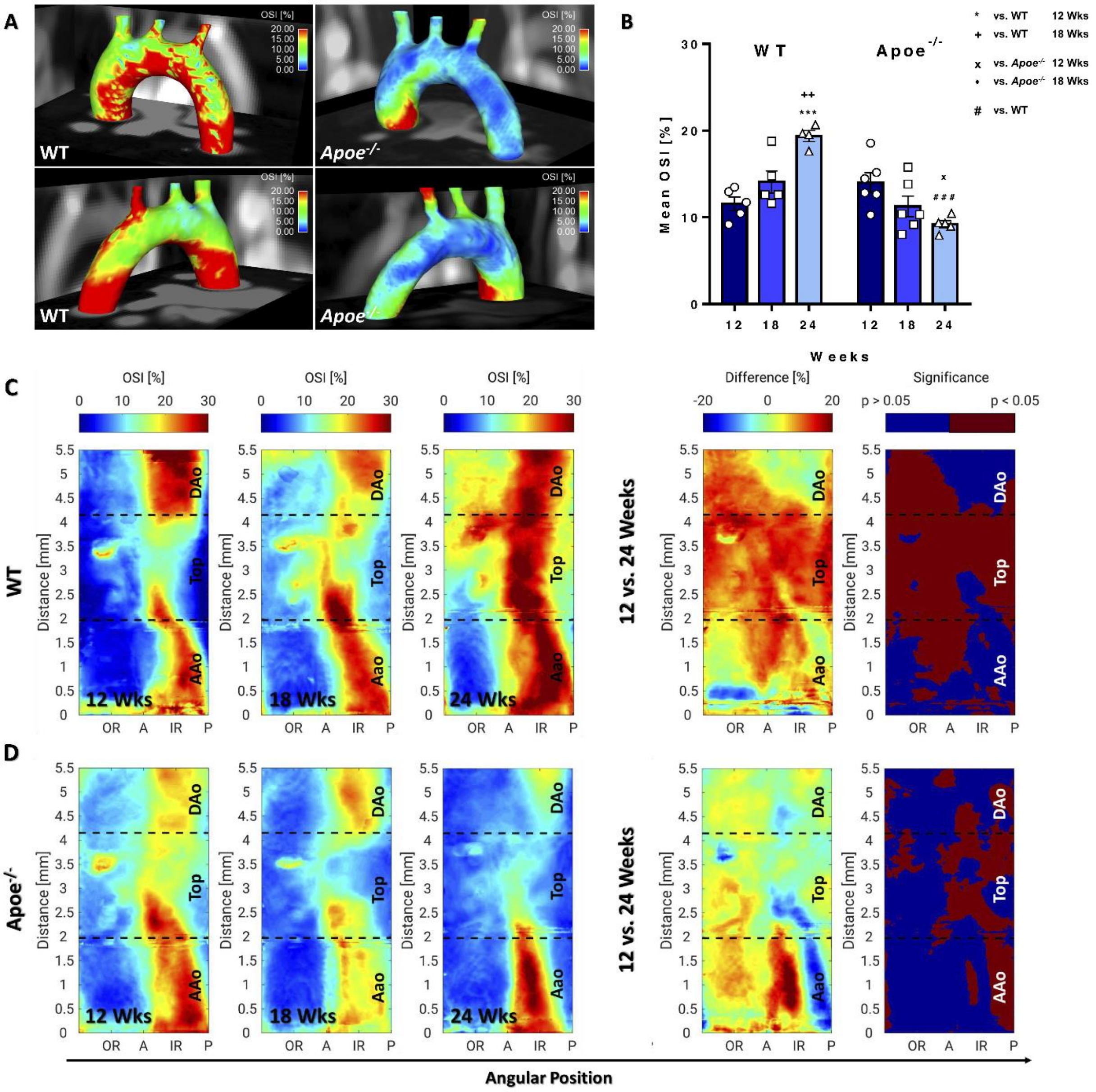

Figure 29: OSI decreases in *Apoe*$^{-/-}$ mice during atherosclerosis progression but increases in WT mice during ageing. A Three-dimensional OSI map of a 24-week-old WT mouse (left) and *Apoe*$^{-/-}$ mouse (right) from anterior and posterior view. The WT mouse showed high OSI values throughout the IR of the complete aorta, whereas in the *Apoe*$^{-/-}$ mouse, values were only elevated in the IR of the AAo (see red spot). **B** Mean OSI: Values significantly increased in WT and decreased in *Apoe*$^{-/-}$ mice. *** vs. WT 12 weeks, $p < 0.001$; $^{++}$ vs. WT 18 weeks, $p < 0.01$; ^{x} vs. *Apoe*$^{-/-}$ 12 weeks, $p < 0.05$; $^{\#\#\#}$ vs. WT, $p < 0.001$. **C** OSI maps of WT mice (group average) for all measurement time points and statistical intragroup comparison of OSI values (12 vs. 24 weeks), showing the difference maps of OSI values and significance maps. **D** OSI maps of *Apoe*$^{-/-}$ mice.

2D projection maps demonstrated that the OSI increased in large areas throughout the aortic arch in WT mice over time (Figure 29C), in particular in the outer top region of the arch, extending to the DAo at 24 weeks. In contrast, *Apoe*$^{-/-}$ mice showed significantly decreased OSI values around the IR and posterior side of the complete aortic arch over time (Figure 29D). Comparing WT and *Apoe*$^{-/-}$ mice, OSI values were regionally increased in *Apoe*$^{-/-}$ mice at 12 weeks and significantly decreased in the complete top and DAo. However, in the AAo, a significant, regional decrease was found around the posterior and anterior region (Supplementary Figure 13). The corresponding analysis of the inter animal standard deviations resulted in maximum median values of 5.8% and 6.3% (see bold values in Supplementary Table 1 and Supplementary Table 2) and respective upper quartile values of 8.4% and 7.8% in WT and *Apoe*$^{-/-}$ mice, respectively.

3.4.5 PLAQUE CHARACTERISTICS CORRELATE WITH WSS

WSS may have distinct and different impact on atherosclerotic lesion formation and growth; therefore, we examined lesion size and characteristics in *Apoe*$^{-/-}$ mice upon sacrifice after 24 weeks (Supplementary Figure 14) in correlation with WSS and OSI values. Plaque size was significantly smaller in the DAo compared with the AAo and negatively correlated with longWSS values. An increase in plaque size was observed with increasing circWSS values, but no correlations were found with OSI values (Figure 30A). Analysis of the plaque macrophage content revealed a tendency towards higher relative ratios in the DAo compared with the AAo and negatively correlated with circWSS (Figure 29B). Smooth muscle cell (SMC) content was higher in the top region compared with the DAo, but no correlations of SMC content with WSS or OSI was detected (Figure 29C). Relative necrotic core area showed no regional differences, but a positive correlation with circWSS (Figure 29D).

Plaque collagen content showed no area-specific differences, but a negative correlation with longWSS was observed (Figure 29E). For circWSS, however, a trend towards higher plaque collagen content with increasing WSS was visible. Media thickness was significantly increased in *Apoe*$^{-/-}$ compared with WT mice but showed no correlation with WSS values (Figure 29F). However, a positive trend towards increased media thickness with higher OSI values was noticeable. Calcified plaque regions were found in the AAo and top region but not in the Dao and we observed a negative correlation with circWSS and a positive correlation with the OSI (Figure 29G).

3.4.6 PWV CORRELATES WITH WSS AND VESSEL WALL CHARACTERISTICS

The development of large plaques throughout the complete aortic arch, leading to a loss of elasticity [9] and a constriction of the aortic lumen may result in increased PWV and longWSS values. Correlative analyses indeed demonstrated an increase in longWSS and circWSS with increasing PWV in all mice (Figure 31A,B). Furthermore, a significant correlation of maximum radStrain and PWV was observed (Figure 31C). In contrast, increasing OSI values negatively correlated with PWV (Figure 31D). Media thickness showed no changes in both groups across the AAo, the top region or the DAo over time, although media thickness was significantly increased in the AAo and top region of *Apoe*$^{-/-}$ compared with WT mice (Figure 31E). Interestingly, mean values of the media thickness correlated with PWV values (Figure 31F). Collagen content in the vessel wall was similar throughout the regions and between genotypes (Figure 31G), but a strong trend towards increased PWV values was noted in arteries with higher collagen content (Figure 31H).

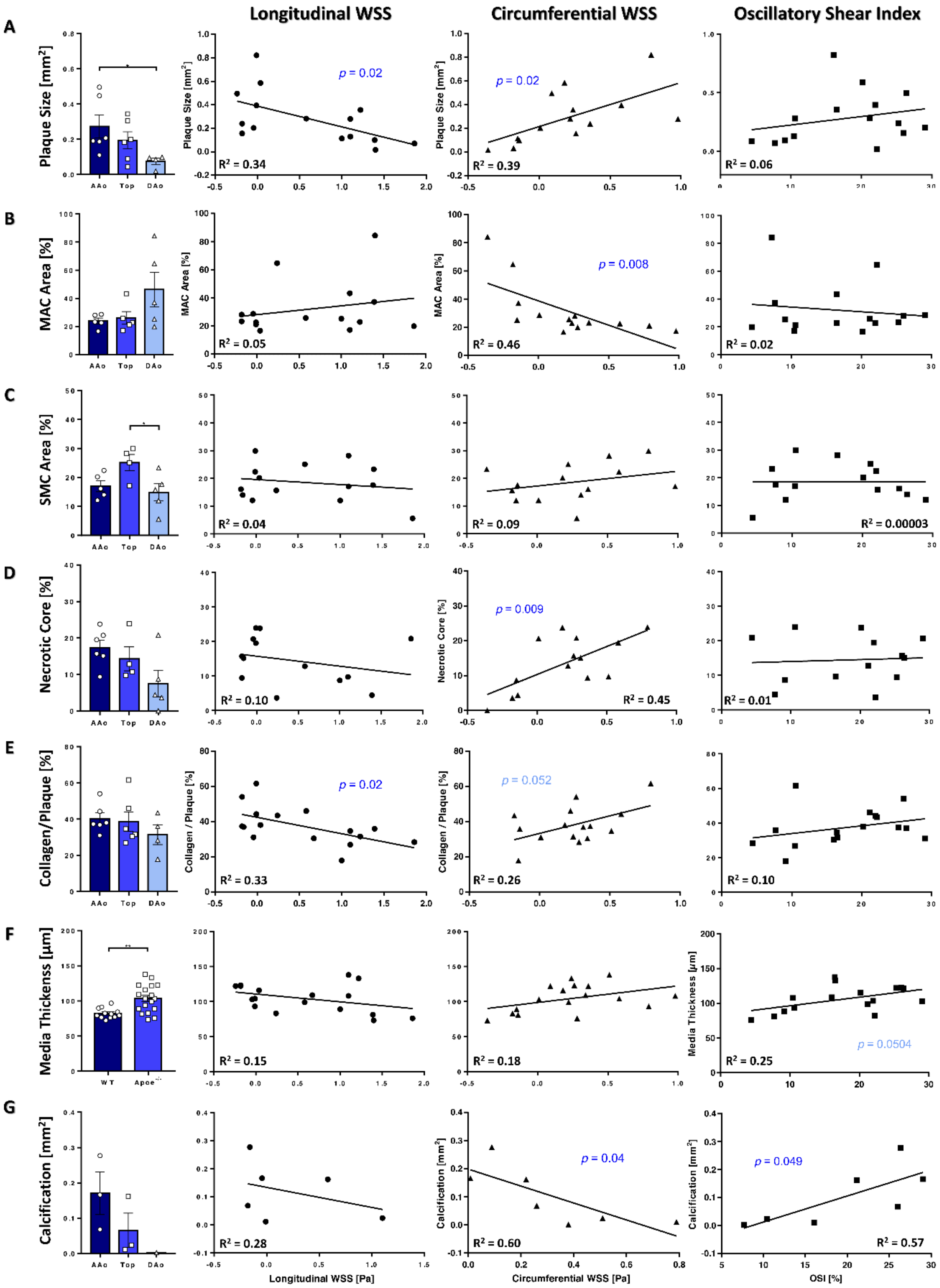

Figure 30: Plaque characteristics correlate with WSS values. **A** Plaque size was significantly smaller in the DAo compared with the AAo ($p < 0.05$, *). A correlation was found with longWSS and circWSS. **B** Relative MAC area. A correlation with circWSS was observed. **C** SMC area in atherosclerotic plaques. In the top region, a significantly higher SMC content was observed compared with the DAo ($p < 0.05$, *), but no correlation with WSS was found. **D** Necrotic core area showed no regional differences but positively correlated with circWSS. **E** Collagen analysis in atherosclerotic plaques. A correlation with longWSS was found. **F** Media thickness was significantly increased in *Apoe*$^{-/-}$ mice ($p < 0.01$, **), but no significant correlation with WSS was found. **G** Calcification: Larger areas were found in the AAo. A negative correlation was found with circWSS and a positive correlation with OSI.

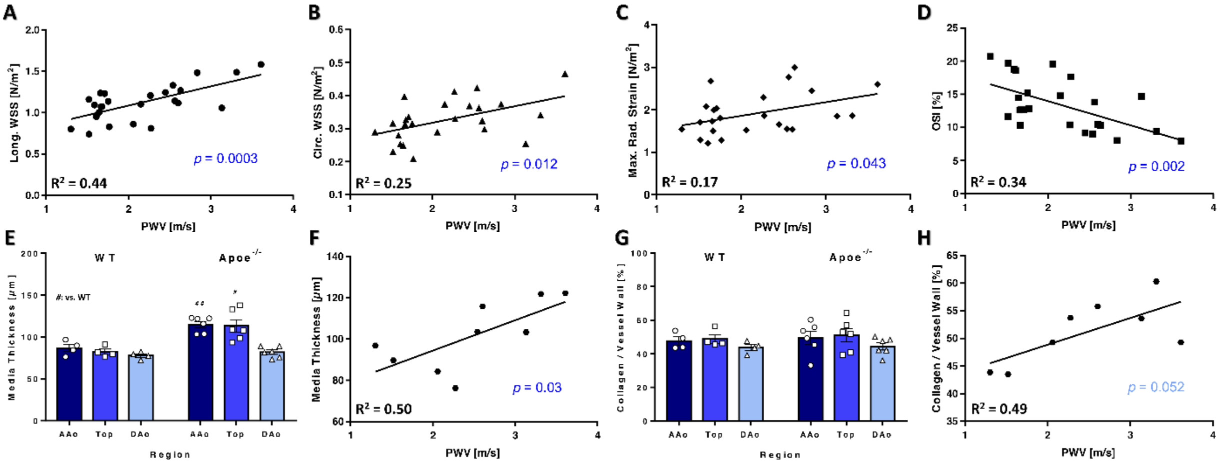

Figure 31: PWV correlates with WSS and vessel wall characteristics. **A** Correlation with longWSS. **B** Correlation with circWSS. **C** Correlation with maximum radStrain. **D** Correlation with OSI. **E** Media thickness: Significantly higher values were found in the AAo and top region of *Apoe*$^{-/-}$ compared with WT mice. **F** Correlation with media thickness. Media thickening increases PWV. **G** Collagen content of the vessel wall. No differences were observed. **H** Correlation with collagen content in the vessel wall. $^{\#}$ vs. WT, $p < 0.05$; vs. WT, $^{\#\#}$ $p < 0.01$.

3.5 DISCUSSION

Although altered WSS, elasticity and inflammation are closely intertwined and critical for plaque development, their growth and progression towards vulnerability, preclinical investigations still mostly focus on the two-dimensional analysis of only one of these parameters. Here, we applied high-resolution 4D PC-MRI as a powerful, non-invasive imaging modality [4, 16] for the simultaneous evaluation of hemodynamic profiles and elasticity in healthy WT and atherosclerotic *Apoe*$^{-/-}$ mice. Visualization of all WSS components and OSI and the statistical evaluation of spatiotemporal changes using 2D projection maps was revealed to be a potent tool allowing their spatially resolved correlation with histological parameters.

In *Apoe*$^{-/-}$ mice, hemodynamic profiles were evaluated during early atherosclerosis with beginning plaque formation at 12 weeks of age (corresponding to 8 weeks of Western diet) [197], intermediate atherosclerosis with measurable arterial stiffening at 18 weeks of age (corresponding to 14 weeks of diet) [9] and advanced atherosclerosis at 24 weeks of age (corresponding to 20 weeks of diet), resulting in progressive aortic atherosclerotic plaques [295]. The aging process in WT mice was observed in parallel at the same time points. The study revealed a contrary development of various hemodynamic parameters during ageing and atherosclerosis progression. Net flow was lower in *Apoe*$^{-/-}$ mice compared with WT mice, increasing over time in the atherosclerotic mouse group, but decreasing in WT mice. Both results are in good accordance with ultrasound measurements conducted in *Apoe*$^{-/-}$ and WT mice on normal diet [296], and in line with previous observations of elevated aortic flow in the ascending and abdominal aorta of 8 months old *Apoe*$^{-/-}$ mice [11, 297]. In addition, *Apoe*$^{-/-}$ mice showed reduced aortic volumes, in line with prior observations [297], attributable to plaque development constricting the lumen, as additionally confirmed by histology.

Furthermore, the difference between the maximum (systolic) and minimum (diastolic) aortic volume was decreased in *Apoe*$^{-/-}$ mice, indicating an impaired dilatability due to an increased stiffness of the aorta. This notion is also supported by the aortic PWV values, which significantly increased in *Apoe*$^{-/-}$ mice but stayed constant in the control group, in agreement with previous results [9, 13]. The PWV was shown to serve as a surrogate marker for early atherosclerotic vessel wall changes such as loss of arterial compliance due to elastin fragmentation [9]. Here, we provide evidence that PWV also correlates with media thickness and possibly collagen content, which may become even more apparent with an increased group size. Interestingly, PWV also correlated with maximum radStrain, indicating that this parameter could be a further possible marker of arterial compliance. *Apoe*$^{-/-}$ mice revealed significantly lower local radStrain values in the AAo, attributable to increased local stiffness. Our previous work already pointed out a possible connection between radStrain and the radial dilatability of the vessel [4]. Hence, we conclude that mapping of this parameter may describe vascular elasticity locally. However, this needs further investigation and confirmation through correlations with other elasticity measurements and CFD [12].

Not only elasticity is an important factor in atherosclerosis development; local shear stress conditions are also relevant to understand the connection between altered hemodynamics and atherosclerosis.

However, mean WSS values only provide global information about differences between healthy and diseased mice. Generating 2D projection maps allowed us to spatially resolve and visualize information about all WSS components and OSI during ageing and atherosclerosis. Here, changes in the longitudinal WSS profile over time also showed a contrary behavior, resulting in a steadily decreasing WSS gradient during ageing, attributable to increasing aortic volumes but constant net flow and elasticity. In contrast, during atherosclerosis progression, an increasing WSS gradient in particular in the ascending aorta was observed, attributable to an increased flow through smaller and stiffer vessels, resulting in steeper flow profiles and therefore elevated WSS values in *Apoe*$^{-/-}$ mice. These results are in agreement with values reported in previous studies [7, 8]. Furthermore, another study showed a drastic increase in vessel wall thickness due to plaque development in *Apoe*$^{-/-}$ mice, resulting in lumen narrowing and a consequent loss of arterial compliance [9], which is in line with the observed correlation of increasing longWSS and PWV. The significant drop in longWSS observed in WT mice, however, might be explained by increasing lumen volumes due to growth. Additionally, constant net flow was found in all analysis planes except plane 3, which together results in less steep flow profiles and, in consequence, lower longitudinal WSS values. Circumferential WSS, on the other hand, significantly increased over time during plaque growth in the ascending aorta of atherosclerotic mice, where the largest plaque burden was found. In WT mice, however, the circWSS decreased globally and locally in the top and descending aorta, similar to the longWSS component, which may be connected to the increasing aortic volumes.

A well-established marker for the characterization of oscillating flow and back-flow is the OSI. High OSI values mark large temporal varying changes in these specific regions, whereas low OSI values are found in regions of unidirectional, laminar flow. Our intergroup comparison revealed significantly elevated OSI values in the AAo, top region and DAo of 12-week-old atherosclerotic mice in comparison with WT mice. In the following, however, OSI decreased in *Apoe*$^{-/-}$ mice, and only the region near the inner curvature of the AAo featured large OSI values, where the largest plaque burden was observed. The drop of OSI values in atherosclerotic mice might thus be explained by structural changes of the vessel wall during plaque development. While longWSS increases, the fraction of temporally oscillating flow decreases, which consequently may lead to significantly lower OSI values in stiffened and constricted arteries. In WT mice on the other hand, OSI increased over time, attributable to increasing lumen volumes during ageing.

Furthermore, WSS is connected to plaque size, as revealed by correlations with histological analyses. Higher longWSS was observed in aortas with smaller plaque size, which is in line with results reported for models of cuff-induced plaque formation [72, 73]. For the circWSS, a converse relation was found, supporting the assumption that low longWSS and high circWSS, attributable to high helical flow, are pro-atherogenic factors causing plaque growth and progression. An increased collagen production is known to impact on arterial elasticity. Collagen content in the media did not differ significantly between healthy and atherosclerotic mice. However, collagen is also found in atherosclerotic plaques (20–60% collagen), which may have contributed to the increase in PWV in *Apoe*$^{-/-}$ compared with WT mice. Interestingly, plaque collagen content showed no regional differences, but significantly smaller plaques were found in the DAo compared with the AAo and a decreased collagen content was found in areas with higher longWSS. During atherosclerosis, SMCs migrate into the intima, where they proliferate and produce extracellular matrix components, including collagen, to form the fibrous cap [47]. Furthermore, laminar shear stress was shown to inhibit [78], while oscillatory shear stress stimulates SMC proliferation [77]. A lower SMC-derived collagen content within plaques may thus be in line with increased longWSS. Importantly, increased WSS values were reported to be associated with plaque rupture [92], whereas vortices causing oscillatory shear stress induce more stable plaques with higher SMC and collagen content [72, 73].

Monocytes/macrophages play key roles in the formation of atherosclerotic plaques, and monocyte recruitment is initiated through the dysfunction and activation of the vascular endothelium, a process intricately linked to local hemodynamics [298]. We noted a tendency towards lower macrophage but larger necrotic core content in the AAo compared with the DAo, in line with larger and more advanced lesions in the AAo, where atherosclerotic lesions form earlier than in the descending aorta. Interestingly, macrophages were significantly reduced in areas with high circWSS. This observation is in line with findings by Xing et al., who observed a greater accumulation of macrophages in plaques exposed to lower WSS in mice [73]. Although a high OSI environment was identified to correlate with plaque composition [72, 73], and even erosion [299], we only found a correlation with plaque calcification. We cannot exclude the possibility that this could have been caused by decreased SNR in regions with high OSI and low WSS values [4].

In our study, circWSS correlated with different parameters, including plaque size, macrophage content, calcification and necrotic core area. Elevated circWSS values indicate alterations of helical flow, presumably related to the changes in the vessel wall morphology and were detected in atheroprone regions [8]. Moreover, studies in humans have demonstrated that circWSS, as assessed by MRI, could serve as a parameter to study multidirectional flow in complex geometries [300, 301]. We thus propose the circWSS component as a potential parameter to non-invasively evaluate plaque characteristics in advanced atherosclerosis.

3.5.1 ACCURACY

The reproducibility as well as the stability of the 4D flow measurement have been examined in detail in a previous study in wildtype mice, showing good reproducibility of the WSS components [4, 16]. The stability of the measurement, assessed by using subsampling, revealed a measurement error in the order of 0.1 Pa for the WSS components and the radial strain [4, 16]. For a further investigation of the measurement error present in this study, the inter-animal standard deviations were analyzed in both wildtype and *Apoe*$^{-/-}$ mice (Supplementary Table 1 and Supplementary Table 2). We observed larger deviation values in comparison with the error of a single measurement. This is most likely due to natural variations between individual animals, differences in slice positioning, shim, etc. However, these deviations were lower than the observed inter group differences (see for example the difference map in Figure 27C, where difference values of more than 1 Pa were observable).

3.5.2 LIMITATIONS

The 2D analysis of histological sections does not reflect the 3D properties of the aortic arch and regional characteristics of the plaque. Therefore, a three-dimensional assessment of plaque characteristics, such as morphological measurements with MRI [170] or utilization of light sheet microscopy techniques [302], combined with spatially resolved WSS mapping, should be applied to further uncover the interrelationship of hemodynamics and atherosclerosis development and progression in the future. The results of this study furthermore point to a possible link between radStrain and radial aortic dilatability. In future studies, these results need to be correlated with local PWV measurements [10, 12] in order to investigate if radStrain indeed is capable of spatially resolving vessel wall elasticity. More thorough investigations, e.g., through CFD, need to be conducted in the future to exclude all possible sources of measurement errors, e.g., caused by displacement artifacts [303]. A further limitation is the relatively small sample size of the animal groups. While the study presented in this work already reveals interesting results, such as the correlation of WSS with plaque size, and previous studies already demonstrated good reproducibility and stability [4, 16], larger sample sizes and the investigation of earlier time points in atherogenesis will be necessary to further resolve possible correlations between plaque characteristics and OSI. Moreover, in order to prove the feasibility to quantify local differences in WSS and OSI profiles in mice, the study was conducted in female mice. Findings in humans already underline gender-specific differences in atherosclerosis, whereas conflicting results are reported in mice, as recently reviewed by Man *et al.* [304]. Interestingly, a recent study conducted by Crouch *et al.* [117] pointed out sex- and age-related differences of flow and WSS values in different locations of the murine vascular tree. Therefore, it will be important to compare female and male mice in future studies to investigate spatially resolved hemodynamics, including correlations with plaque size and composition and direct statistical comparison of the different sexes.

3.5.3 CONCLUSION AND FUTURE PERSPECTIVES

We demonstrate the feasibility and utility of high-resolution 4D flow MRI to spatially resolve (100 µm) all hemodynamic parameters in healthy and atherosclerotic mice over time, using 2D projection maps as a promising and powerful tool to enable local correlations of hemodynamics with plaque characteristics. The detailed mapping and statistical evaluation of all three WSS components and OSI in the complete aortic arch provide unprecedented insight into flow-dependent changes during the natural course of ageing and atherosclerotic disease progression and could contribute to an improved understanding of the association between altered hemodynamics and plaque progression. In future studies, early atherosclerotic lesion development could be investigated in order to reveal the relationship of altered hemodynamics and early vascular inflammation driving plaque development. Furthermore, efforts should be made to further characterize cellular plaque composition and plaque characteristics in a three-dimensional manner. The detailed, spatially resolved 3D-analysis of functional and structural plaque and vessel parameters, in combination with the spatially resolved 2D projection maps, could significantly improve preclinical atherosclerosis research. Moreover, our flexible reconstruction frameworks, developed in a preclinical application, could straightforwardly be applied to flow measurements in whole body MRI scanners [292], adapted to human applications and may even be utilized to map WSS and OSI in smaller arteries. As all hemodynamic parameters are assessed from one single measurement, an application in the clinic could be achieved in short examination times. The combined measurement of PWV and all WSS components may be a powerful tool to investigate local hemodynamics and plaque characteristics non-invasively to guide diagnosis and therapy in the future.

3.6 SUPPLEMENTARY FILES

3.6.1 SUPPLEMENTARY FIGURES

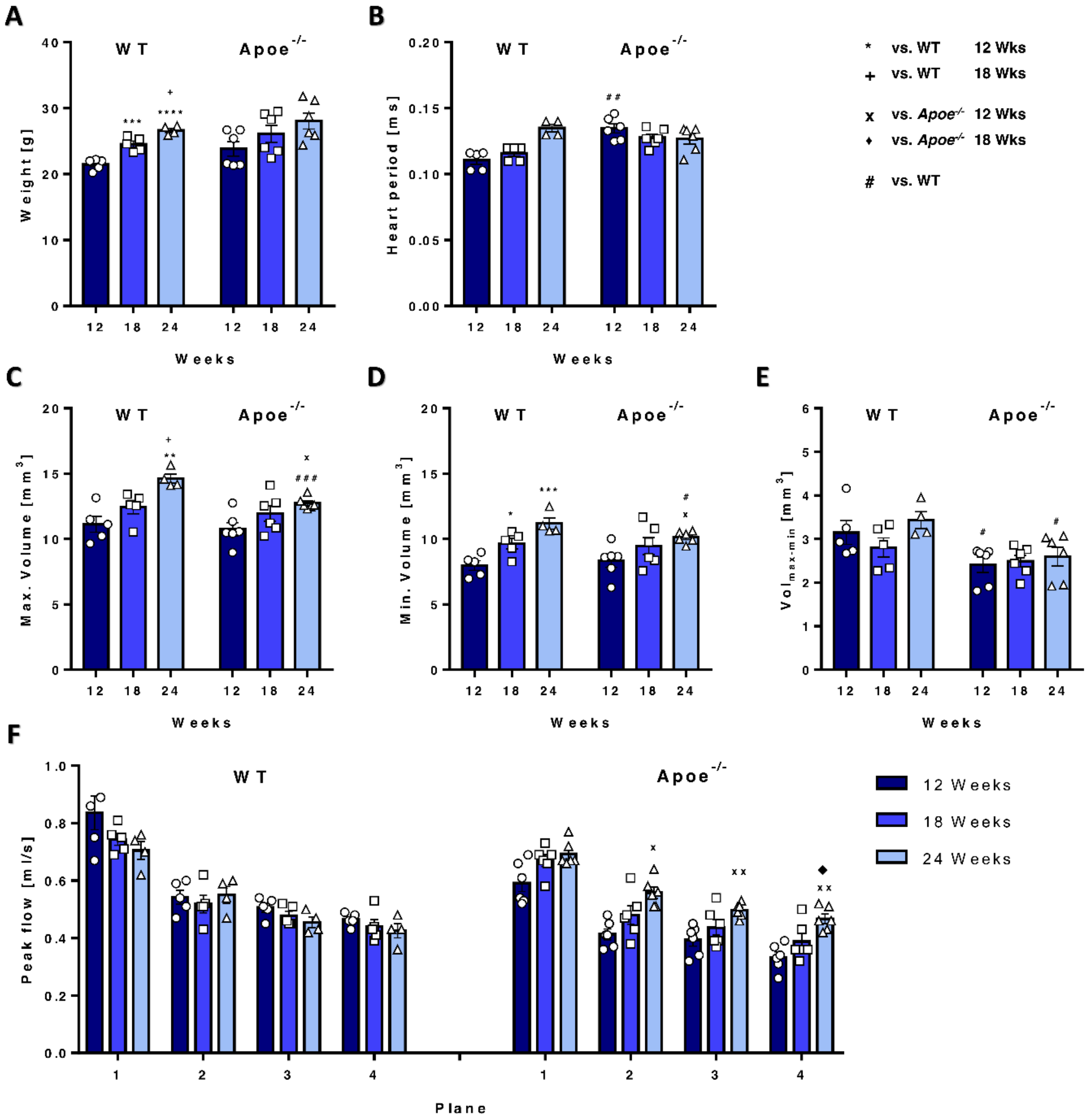

Supplementary Figure 7: Weight, heart periods, aortic volumes and peak flow of wild type and *Apoe*$^{-/-}$ mice for all measurement timepoints. **A** WT mice show a significant increase in weight for each time point. No significant increase is observable in the *Apoe*$^{-/-}$ group as well as in comparison to the wildtype group. **B** Heart periods are only different for the first measurement time point at 12 weeks. **C** Maximum aortic volumes. WT mice show a stronger increase in maximum aortic volume over time and significantly larger maximum volumes at 24 weeks compared to *Apoe*$^{-/-}$ mice. **D** Minimum aortic volume. Wildtype mice have a higher increase in minimum aortic volume over time and significantly larger minimum volumes at 24 weeks compared to *Apoe*$^{-/-}$ mice. **E** Difference between maximum and minimum aortic volumes. Significant differences can be found at the age of 12 and 24 weeks. **F** Peak flow values in wildtype mice stay constant over time, whereas *Apoe*$^{-/-}$ mice show a significant increase in peak flow over time for analysis planes 2-4. * vs. WT 12 weeks, * $p < 0.05$; ** $p < 0.01$; *** $p < 0.001$ and **** $p < 0.0001$; $^{+}$ vs. WT 18 weeks, $p < 0.05$; ^{x} vs. *Apoe*$^{-/-}$ 12 weeks, $p < 0.05$; ♦ vs. *Apoe*$^{-/-}$ 18 weeks, $p < 0.05$; $^{\#}$ vs. WT, $^{\#}$ $p < 0.05$; $^{\#\#\,p}$ < 0.01 and $^{\#\#\#}$ $p < 0.001$.

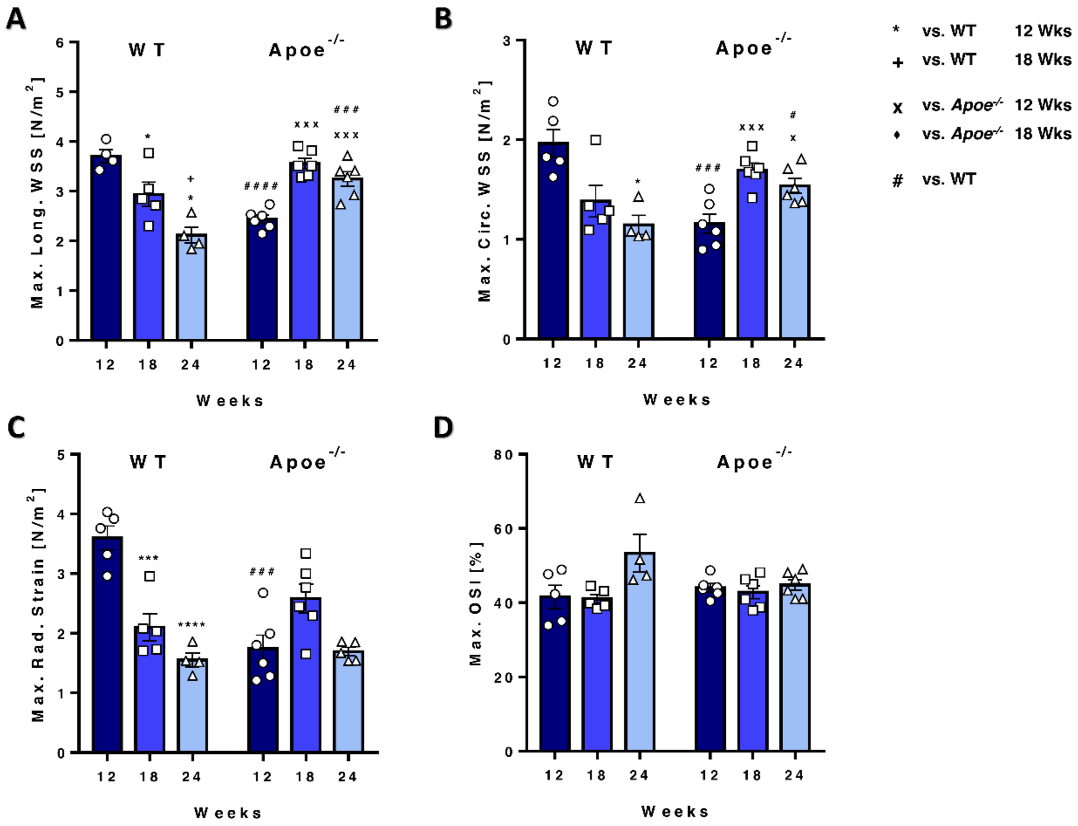

Supplementary Figure 8: Maximum WSS and OSI values for wild type and *Apoe*$^{-/-}$ mice over time. A Maximum longWSS values. WT mice show a significant decrease over time, whereas *Apoe*$^{-/-}$ mice show an increase. Maximum values are furthermore strongly decreased in *Apoe*$^{-/-}$ mice at 12 weeks and increased at 24 weeks compared to WT mice. (**B**) Maximum circWSS values over time. WT mice show a significant decrease over time, whereas Apoe$^{-/-}$ mice show an increase in maximum values over time. Maximum values are furthermore decreased in *Apoe*$^{-/-}$ mice at 12 weeks and increased at 24 weeks compared to WT mice. (**C**) Maximum radStrain values for all measurement time points. In WT mice, a significant decrease over time is observable, whereas *Apoe*$^{-/-}$ mice show no significant changes. RadStrain values are furthermore significantly decreased in *Apoe*$^{-/-}$ mice at 12 weeks compared to WT mice. (**D**) Maximum OSI values for all measurement time points. No significant differences are observable. * vs. WT 12 weeks, *** $p < 0.001$ and **** $p < 0.0001$; $^{+}$ vs. WT 18 weeks, $p < 0.05$; ^{x} vs. *Apoe*$^{-/-}$ 12 weeks, $p < 0.05$ and ^{xxx} $p < 0.001$; $^{\#}$ vs. WT, $^{\#}$ $p < 0.05$, $^{\#\#\#}$ $p < 0.001$ and $^{\#\#\#\#}$ $p < 0.001$.

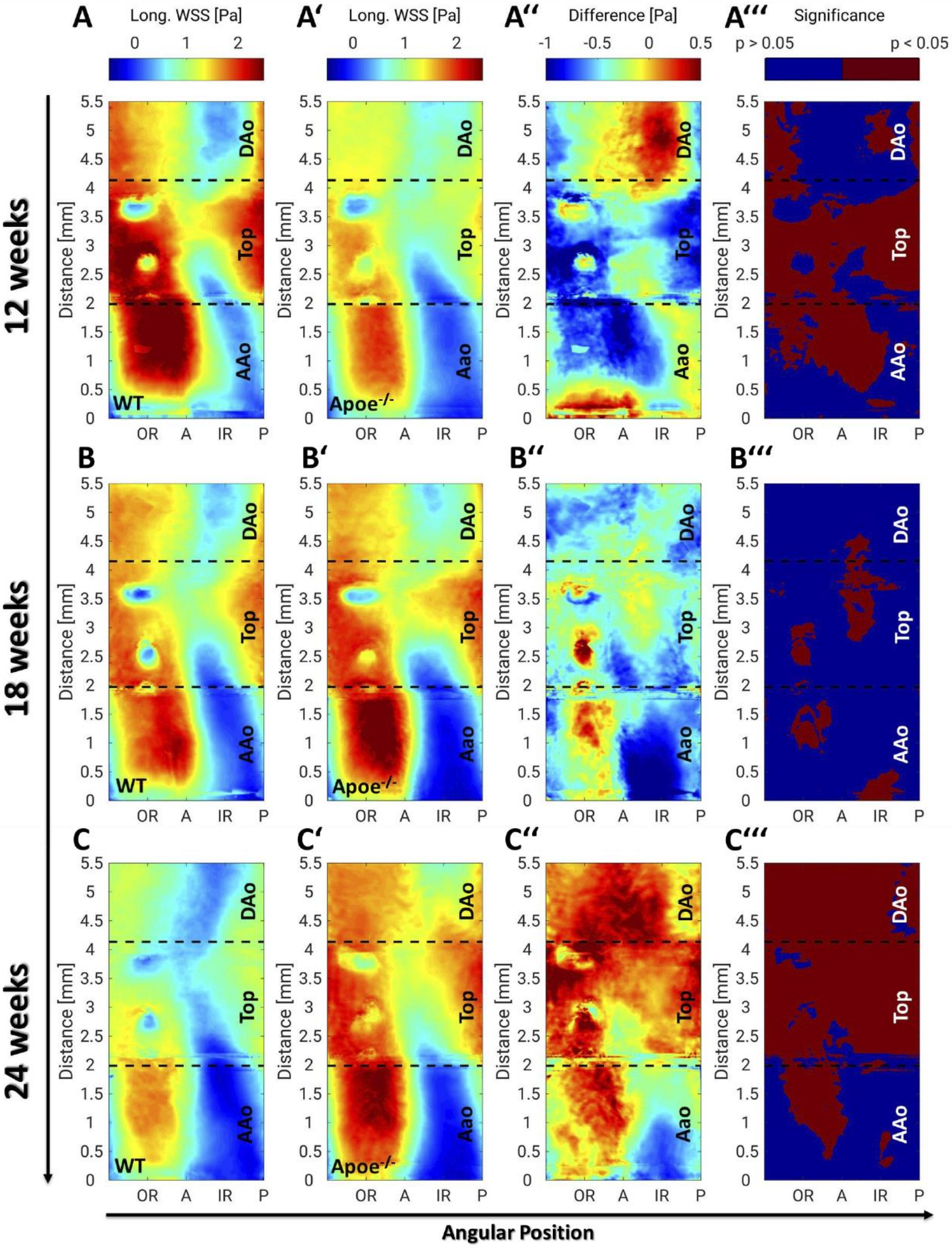

Supplementary Figure 9: LongWSS maps for both genotypes and all measurement time points. **A** LongWSS map for 12-week-old WT mice and (**A'**) for *Apoe*$^{-/-}$ mice (group average). **A''** Difference map (*Apoe*$^{-/-}$ - WT). **A'''** Significance map. WSS values are significantly increased in the top region, the upper part of the AAo and the posterior side of the DAo in WT mice. A significant difference was also observed near the IR of the DAo. **B** LongWSS map for 18-week-old WT mice and **B'** *Apoe*$^{-/-}$ mice. **B''** Difference map (*Apoe*$^{-/-}$ - WT). **B'''** Significance map. Both genotypes show a similar distribution across the arch. **C** LongWSS map for 24-week-old wildtype mice and **C'** for *Apoe*$^{-/-}$ mice. **C''** Difference map (*Apoe*$^{-/-}$ - WT). **C'''** Significance map. *Apoe*$^{-/-}$ mice show an overall increase of LongWSS values in the complete top region and DAo.

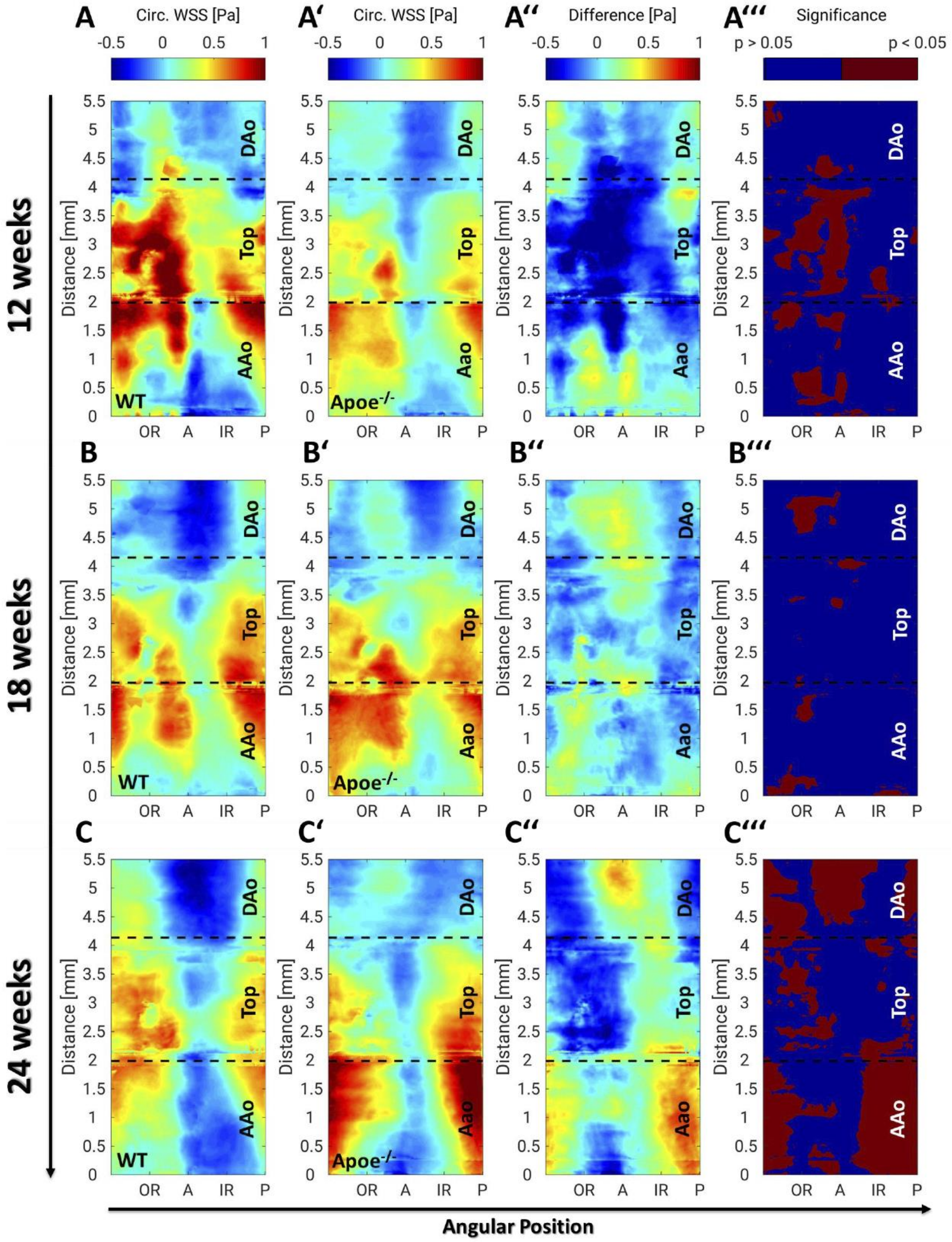

Supplementary Figure 10: CircWSS maps for both genotypes and all measurement time points. **A** CircWSS map for 12-week-old wildtype mice and **A'** for *Apoe*$^{-/-}$ mice (group average). **A''** Difference map (*Apoe*$^{-/-}$ - WT). **A'''** Significance map. CircWSS values of WT mice are significantly increased in the AAo and Top region (from OR to A). **B** CircWSS map for 18-week-old WT mice and **B'** for *Apoe*$^{-/-}$ mice. **B''** Difference map. **B'''** Significance map. Both genotypes show a similar distribution of WSS values across the arch. **C** CircWSS map for 24-week-old WT mice and **C'** for *Apoe*$^{-/-}$ mice. **C''** Difference map. **C'''** Significance map. CircWSS is significantly decreased in WT mice and increased in *Apoe*$^{-/-}$ mice.

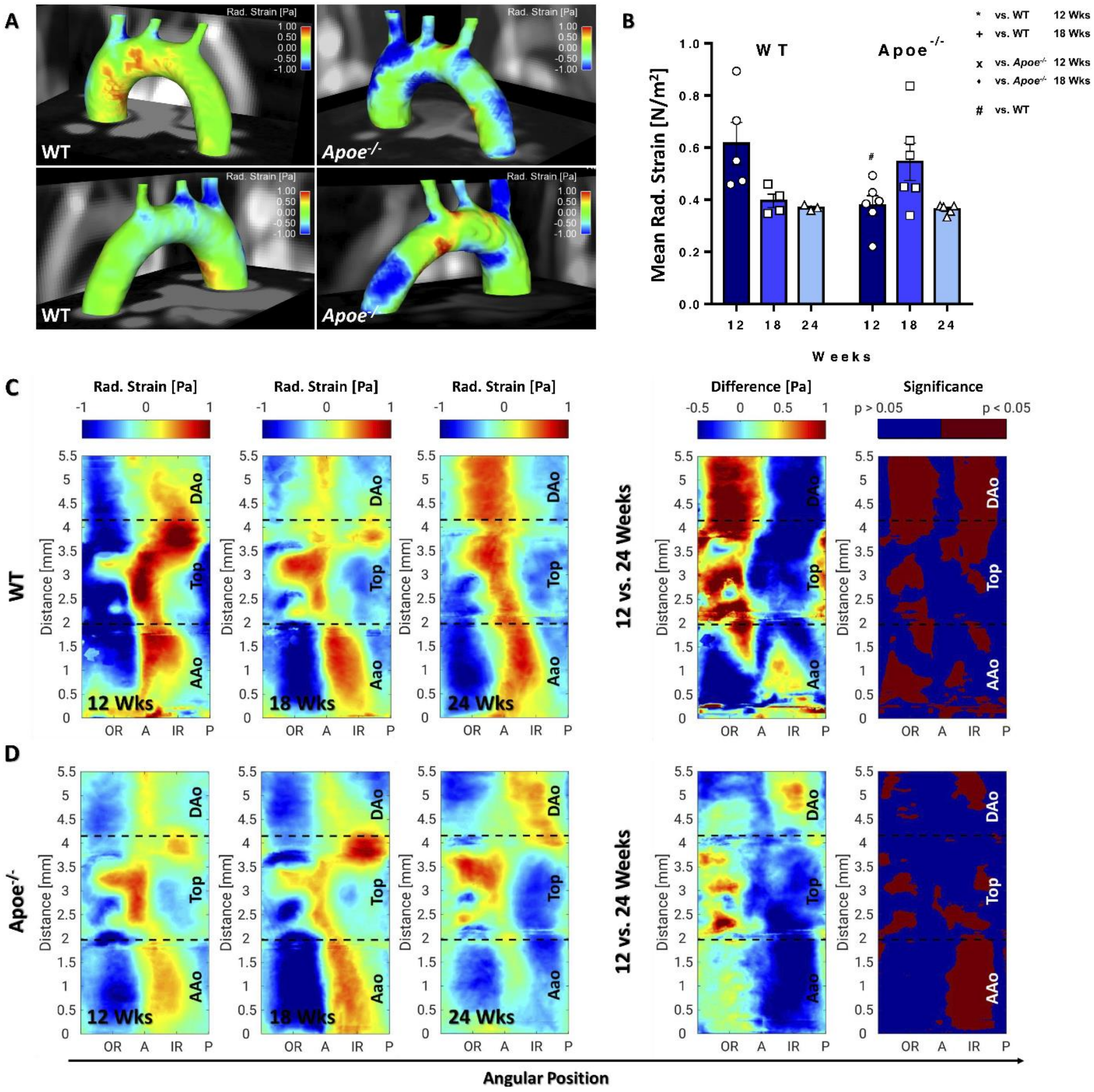

Supplementary Figure 11: Radial strain shows modest changes in *Apoe*$^{-/-}$ and WT mice over time. **A** Three-dimensional radStrain map of a 24-week-old WT mouse (left) and *Apoe*$^{-/-}$ mouse (right) from anterior and posterior view. The WT and *Apoe*$^{-/-}$ mouse feature significantly different radStrain patterns, especially around the IR and OR of the ascending aorta. **B** Mean radStrain values. Compared to WT mice, a significant decrease in radStrain is observable in *Apoe*$^{-/-}$ mice at 12 weeks. **C** RadStrain maps of WT mice (group average) for all measurement time points and statistical intragroup comparison of radStrain values (12 vs. 24 weeks), showing the difference maps of radStrain values and significance maps. D RadStrain Maps of *Apoe*$^{-/-}$ mice. $^{\#}$ vs. WT, $p < 0.05$.

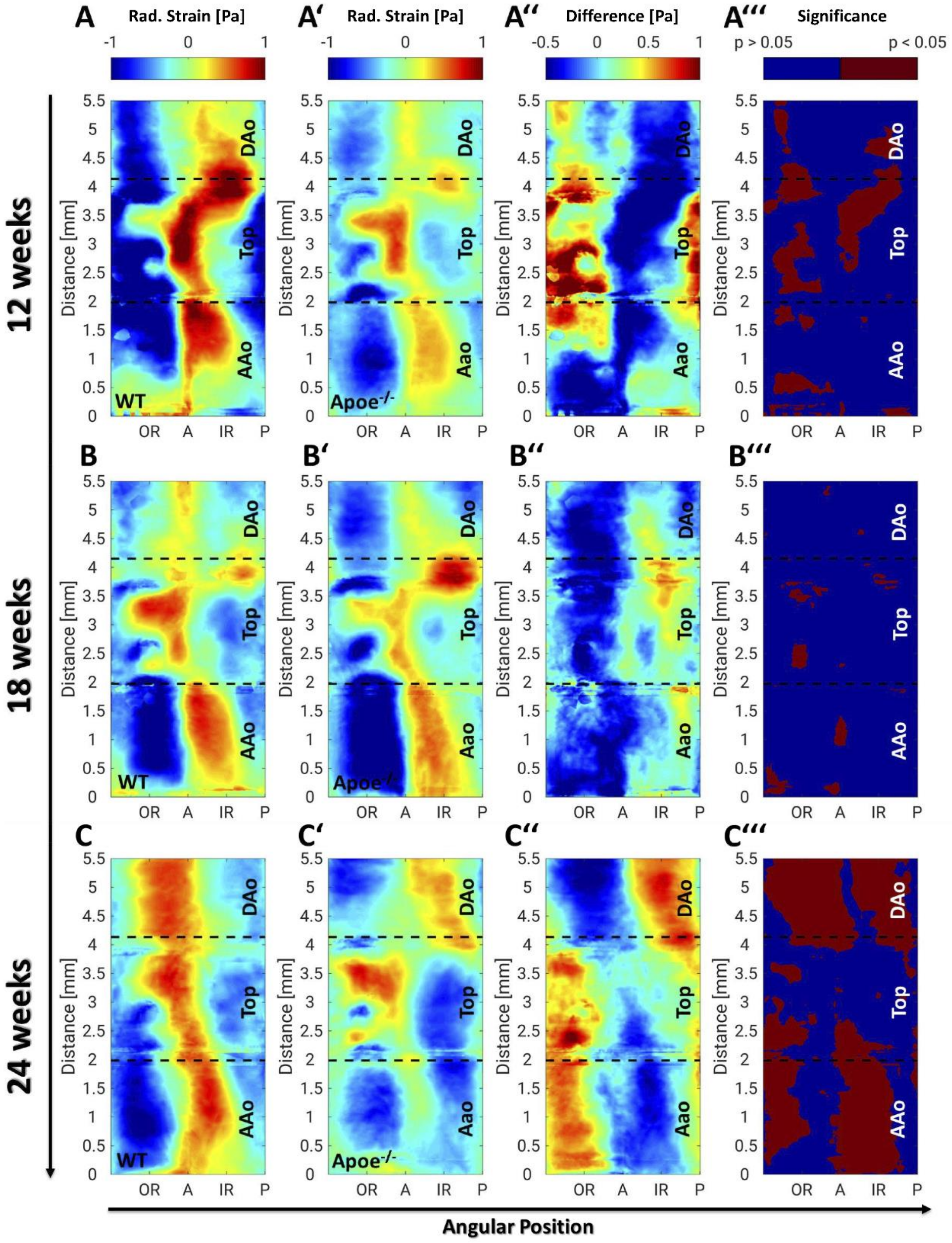

Supplementary Figure 12: Intergroup comparison of radial strain for all measurement time points. RadStrain map for 12-week-old WT mice and **A'** for *Apoe*$^{-/-}$ mice (group average). **A''** Difference map (*Apoe*$^{-/-}$ - WT). **A'''** Significance map. In *Apoe*$^{-/-}$ mice, a significant decrease is visible in the inner and outer radius of the top region. **B** RadStrain map for 18-week-old WT mice and **B'** for *Apoe*$^{-/-}$ mice. **B''** Difference map. **B'''** Significance map. Both genotypes show a similar distribution of radStrain values across the arch. **C** RadStrain map for 24-week-old WT mice and **C'** *Apoe*$^{-/-}$ mice **C''** Difference map. **C'''** Significance map. Large areas of significant differences are visible throughout the complete aortic arch.

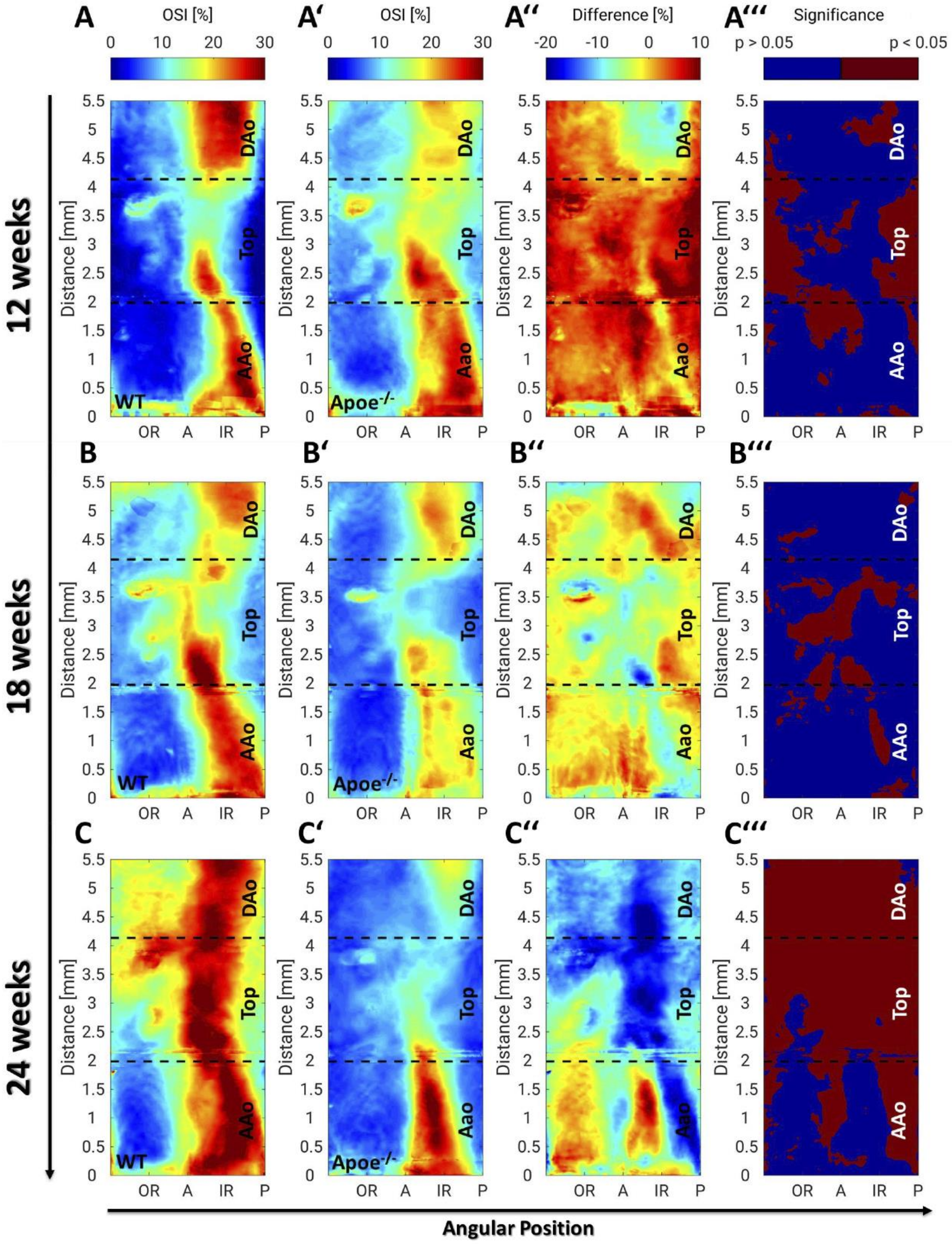

Supplementary Figure 13: Intergroup comparison of OSI for all measurement time points. A OSI map for 12-week-old WT mice and **A'** *Apoe$^{-/-}$* mice (group average). **A''** Difference map (*Apoe$^{-/-}$* - WT). **A'''** Significance map. OSI values are mostly elevated in atherosclerotic mice. **B** OSI map for 18-week-old WT mice and **B'** *Apoe$^{-/-}$* mice. **B''** Difference map. **B'''** Significance map. OSI values are elevated around the inner radius of WT mice and significantly lower near the inner radius of atherosclerotic mice. **C** OSI map for 24-week-old WT mice and **C'** *Apoe$^{-/-}$* mice. **C''** Difference map. **C'''** Significance map. A significant decrease in OSI values can be observed in the top region and descending aorta in *Apoe$^{-/-}$* mice.

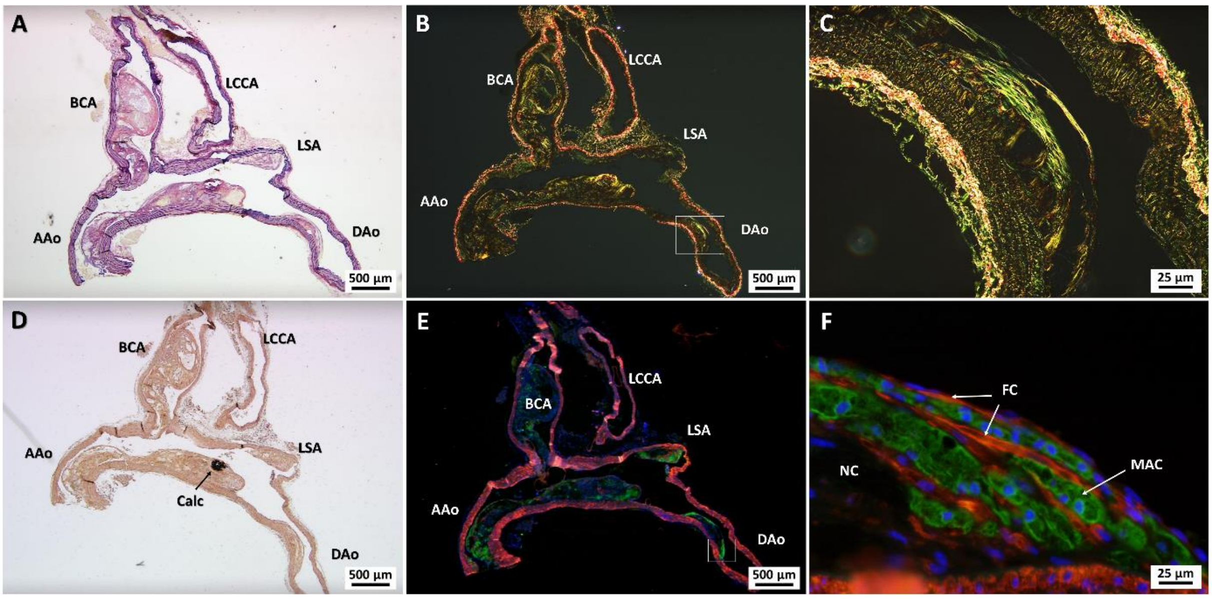

Supplementary Figure 14: Histological stainings of longitudinal sections of an exemplary atherosclerotic *Apoe*$^{-/-}$ mouse. **A** Aldehyde-Fuchsin overview staining. **B** Picro-siriusred staining under polarized light for collagen analysis. **C** Enlarged view of **B** (see white Box). **D** Silvering after Kossa staining for calcification analysis (see black arrow). **E** Immunofluorescence staining of MAC-2 for macrophages (green) and aSMA for smooth muscle cells (red). Nuclei are counterstained with DAPI (blue). **F** Enlarged view of **E** (see white box) with visible fibrous cap (FC), formed by SMCs, necrotic core (NC) and foam cells (MAC).

3.6.2 SUPPLEMENTARY TABLES

Supplementary Table 1: Spatial median, lower quartile and upper quartile values of the intragroup standard deviations (STD) in wild type mice. Values were determined from the pixel values of the 2D projection maps. The respective highest median values are marked in bold.

Long. WSS STD	**Median value [Pa]**	**Lower Quartile [Pa]**	**Upper Quartile [Pa]**
Weeks			
12	**0.34**	0.25	0.45
18	0.29	0.22	0.39
24	0.19	0.13	0.26
Circ. WSS STD	**Median value [Pa]**	**Lower Quartile [Pa]**	**Upper Quartile [Pa]**
Weeks			
12	**0.30**	0.19	0.40
18	0.29	0.22	0.39
24	0.12	0,08	0.17
Rad Strain STD	**Median value [Pa]**	**Lower Quartile [Pa]**	**Upper Quartile [Pa]**
Weeks			
12	**0.47**	0.33	0.67
18	0.29	0.22	0.39
24	0.23	0.14	0.35
OSI STD	**Median value [%]**	**Lower Quartile [%]**	**Upper Quartile [%]**
Weeks			
12	4.6	3.2	6.6
18	**5.8**	3.7	8.4
24	4.4	2.4	6.8

Supplementary Table 2: Spatial median, lower quartile and upper quartile values of the intra group standard deviations (STD) in *Apoe*$^{-/-}$ mice. Values were determined from the pixel values of the 2D projection maps. The respective highest median values are marked in bold.

Long. WSS STD	Median value [Pa]	Lower Quartile [Pa]	Upper Quartile [Pa]
Weeks			
12	0.27	0.20	0.36
18	**0.39**	0.28	0.54
24	0.33	0.23	0.47

Circ. WSS STD	Median value [Pa]	Lower Quartile [Pa]	Upper Quartile [Pa]
Weeks			
12	0.20	0.16	0.26
18	**0.25**	0.16	0.35
24	0.21	0.12	0.30

Rad Strain STD	Median value [Pa]	Lower Quartile [Pa]	Upper Quartile [Pa]
Weeks			
12	0.33	0.26	0.42
18	**0.50**	0.34	0.71
24	0.29	0.20	0.38

OSI STD	Median value [%]	Lower Quartile [%]	Upper Quartile [%]
Weeks			
12	**6.3**	4.8	7.8
18	5.5	3.4	7.9
24	3.4	2.1	6.2

CHAPTER 4

Local Hemodynamic Profiles in the Atherosclerotic *Ldlr*$^{-/-}$ and *Apoe*$^{-/-}$ Mouse Model Arise from Distinct Geometric Properties of the Aortic Arch

-

A Longitudinal Study Describing Hemodynamic Profiles During Early Atherosclerosis in Atherosclerotic *Ldlr*$^{-/-}$ and *Apoe*$^{-/-}$ Mice

Chapter 4 will be divided into two articles and submitted as original research articles (Kristina Andelovic, Patrick Winter, Thomas Kampf, Peter M. Jakob, Volker Herold, Wolfgang R. Bauer and Alma Zernecke) in a scientific journal. This chapter is based on the work of the author of this thesis Kristina Andelovic, who designed the study and planned and performed the experiments and analysis. The final publications will be supplemented with CFD-simulations by other collaborators and are in preparation at the time of handing in this thesis.

4.1 BACKGROUND

Atherosclerosis is the major underlying cause for most cardiovascular diseases like stroke and myocardial infarction, which are the major causes of death worldwide [1]. The pathogenesis of atherosclerosis, resulting in a chronic, inflammatory disease of large and medium sized arteries, is driven by the accumulation of lipoproteins and the subsequent infiltration of monocytes into the subendothelial intima. The activated endothelium responds through an increased expression of adhesion molecules, leading to the enhanced recruitment of immune cells like monocytes, which then differentiate into macrophages and ingest modified intimal lipoproteins and become foam cells, further driving the proinflammatory processes. Vascular smooth muscle cells (vSMCs) that migrate from the media into the intimal layer, proliferate and dedifferentiate to produce extracellular matrix, and form the fibrous cap, leading to a steady growth of the atherosclerotic plaque [47]. These processes entail a loss in arterial elasticity and increased stiffness, resulting in an elevated arterial PWV. In *Apoe*$^{-/-}$ mice receiving a Western Diet, an increase in the aortic PWV was observed, accompanied by an increased elastic fiber fragmentation [9].

Plaques mostly develop at predilection sites like the inner curvature of the aortic arch, branches and bifurcations [305]. These regions are characterized by low and oscillatory WSS, which is proportional to the friction force of the blood flow acting on the endothelium and influencing its inflammatory status, contributing to plaque development, progression, and even rupture and erosion [3]. WSS and PWV are thus important flow-related parameters, which may be used to characterize the vessel wall during atherosclerotic plaque development and progression [3, 4, 9, 12, 16]. For preclinical applications in mice, we have developed a technique that allows the assessment of the different components of the WSS [60], the radStrain and OSI values, as well as elasticity properties in a single measurement [3, 4, 16] (see also Chapters 2 and 3).

Among other factors such as blood pressure and viscosity, which strongly depend on the hematocrit [306], WSS is strongly dependent on geometrical parameters of the aorta such as the diameter of the vessel or its curvature. Feintuch *et al.* performed a CFD study in C57BL/6 mice and observed that changing the shape of the flow profiles qualitatively altered the velocity and WSS patterns in the proximal aorta, whereas almost no changes were observed in the arch and descending aorta (DAo) [17]. CFD simulations also demonstrated that the WSS distribution in the aortic arch is less dependent on the inlet flow condition but rather on the inhomogeneities in lesion prevalence [18]. Another *in silico* study performed by Choudhury *et al.* observed a strong interdependency of WSS and lumen surface concentration (LSC) of LDL in an abdominal aortic aneurysm model [19]. Here, CFD were simulated numerically in different aneurysm geometries using the Navier-Stokes and transport equations. Among other findings, strong peaks of LSC were observed at locations where temporal averaged WSS changes sign, which was attributed to regions of flow separation or flow reattachment. Furthermore, the height and width of the simulated aneurysms strongly affected the WSS and concentration of LDL, pointing out a close relationship between WSS and lipid accumulation, linked to local fluid-flow patterns.

The multifactorial nature of atherogenesis and progression, therefore, not only include chronic inflammatory processes and lipid metabolism acting together, but also altered hemodynamics. Hence, the investigation of these mechanisms requires suitable animal models for studying the underlying basic mechanisms. Different mouse models of atherosclerosis are widely used, in particular the *Apoe*$^{-/-}$ mouse model independently introduced by Zhang *et al.* and Plump *et al.* [49, 50] and the low-density lipoprotein receptor (*Ldlr*$^{-/-}$) mouse model generated by model by Ishibashi *et al.* [51]. Although in both models atherogenesis is driven by non-HDL hyperlipidemia, there are certain differences, e.g., in plasma lipoproteins, consisting of predominantly of chylomicrons and very low-density lipoproteins (vLDL) in *Apoe*$^{-/-}$ mice, whereas the predominant lipoprotein in *Ldlr*$^{-/-}$ mice is LDL, better reflecting the human lipoprotein profile. In *Apoe*$^{-/-}$ mice, complex vascular lesions comparable to human plaques develop spontaneously, even when fed a standard chow diet [55]. In contrast, very slow atherosclerosis progression is observed in *Ldlr*$^{-/-}$ mice without dietary induction. However, atherosclerosis can be accelerated in both models by feeding a Western type diet enriched in fat and cholesterol.

Interestingly, most studies were conducted in just one model, and only few studies report the investigation of atherosclerosis-related mechanisms in both models under the same conditions [55, 59], with the majority of studies focusing on lipid metabolism and inflammation. Up to now, however, no preclinical flow-sensitive MRI studies have been performed to study model-specific differences in hemodynamic patterns and PWV in these different atherosclerotic animal models.

We therefore present for the first time a study of local hemodynamic parameters including WSS, OSI and the PWV in the aortic arch of WT, *Apoe*$^{-/-}$ and *Ldlr*$^{-/-}$ mice at baseline levels and during early atherosclerosis progression using high-resolution 4D-flow MRI [4, 16]. While the basal characterization only showed typical differences in lipid profiles, the aortic arches of the atherosclerotic mouse models showed characteristic geometric properties in *Ldlr*$^{-/-}$ mice. Spatially resolved 2D projection maps including statistical analyses [5] furthermore revealed coherent, distinct flow and WSS profiles in the atherosclerotic *Ldlr*$^{-/-}$ mouse model. However, analysis of lipid profiles during early atherosclerosis progression showed an unexpectedly higher atherogenic risk in *Ldlr*$^{-/-}$ mice, whereas *Apoe*$^{-/-}$ mice featured more atherogenic WSS profiles and an increased plaque burden, indicating that the basal WSS profile could potentially have a higher impact on atherosclerosis than the lipid profile.

4.2 METHODS

4.2.1 ANIMAL HANDLING

Female wild type (WT) C57BL/6 J mice (n = 5), Ldlr knock-out mice (*Ldlr*$^{-/-}$, n = 10) and ApoE knock-out mice (*Apoe*$^{-/-}$, n = 10) (both C57BL/6J background, Charles River) were fed a normal diet (WT) or a Western type diet (ssniff, Soest, Germany) for 4 and 8 weeks, starting at the age of 4 weeks (see Figure 32). All animal experiments were approved by local authorities (Regierung von Unterfranken, Würzburg, Germany, reference number: 55.2-2531.01-427/17) to comply with German animal protection law.

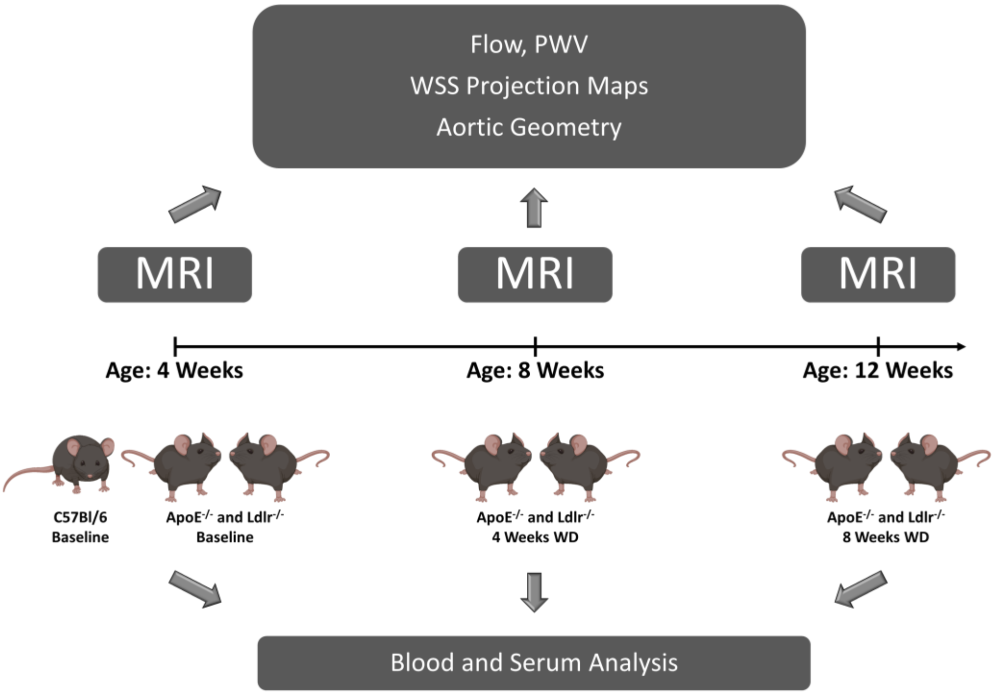

Figure 32: Study Design. For basal characterization, blood and serum analysis as well as flow, PWV, WSS and aortic geometry was assessed via 4D-flow MRI in Wildtype, *Apoe*$^{-/-}$ and *Ldlr*$^{-/-}$ mice at baseline levels at the age of 4 weeks. After receiving a western type diet starting at the age of 4 weeks, the same parameters were measured in the atherosclerotic mouse models after 4 weeks and 8 weeks of western diet for the investigation of time-dependend hemodynamic changes during atherosclerosis development.

4.2.2 MRI MEASUREMENTS

For MRI measurements, mice were anesthetized by applying 1.5 % isoflurane in 2.0 Vol. % oxygen (2 L/min) via nose cone. A pressure-sensitive pneumatic balloon (Graseby Medical Limited, Watford, United Kingdom) was placed between the inner radio frequency (RF) resonator wall and the murine thorax to monitor vital functions (heartbeat and respiration) in real-time by a custom-built ECG unit [281]. Core body temperature was maintained at physiological 37 °C by adjusting the temperature of the gradient cooling unit.

4.2.2.1 Data acquisition and reconstruction

All experiments were conducted using a 17.6T small animal MRI scanner (Bruker Avance 750 WB, Bruker BioSpin MRI GmbH, Rheinstetten, Germany), a 1T/m gradient system with an inner diameter of 40mm and a custom-built single-channel transmit-receive coil. For flow quantification, a retrospective radial 4D-PC cine MRI sequence was used, as introduced recently [4, 16] (see also Chapter 2). Cardiac and respiratory gating signals were assessed from the center k-space signal and used for retrospective motion synchronization, as proposed recently [4, 16]. All image reconstruction, post-processing and data analysis were performed with Matlab 2016b (The Mathworks, Inc., Natick, Massachusetts, USA). All relevant scan parameters can be found in Chapter 2 and [16].

4.2.3 WSS ANALYSIS

3D-cine frames were reconstructed at high spatial (100 µm isotropic) and moderate temporal resolution (20 frames per cardiac cycle) [4]. Using the magnitude data of the cine reconstruction, voxels of the lumen were selected using the magnitude data and semi-automatic segmentation. Subsequently, a centerline of the lumen segmentation was calculated with a python software tool (Ansys, Inc., USA.) Using the 3D velocity fields and the surface normal vectors of the lumen segmentation, WSS was derived, as described in [4]. For all examinations, a blood viscosity value of $\eta = 0.004$ Pa·s was assumed [7].

4.2.3.1 Calculation of 2D projection maps

Calculation of 2D WSS Maps was performed as described in [5] and Chapter 3. In short, a centerline was used for separation of both WSS components and the radStrain. For each point on the segmented lumen surface, the vector component parallel to the centerline (longWSS), in circumferential direction (circWSS) and pointing towards the centerline (radStrain) were computed. Afterwards, WSS values $\vec{\tau}(x, y, z)$ were transformed into coordinates $\vec{\tau}(z, \theta)$, where z defines the position on the centerline [mm] relative to the proximal ascending aorta and θ the angular direction. WSS components were subsequently re-gridded on a $\tau_i(z, \theta)$ map (with i representing one of the three vectorial components). As convention, $\theta=0°$ was defined as posterior side (P), $\theta=180°$ as anterior side (A), $\theta=90°$ as outer radius (OR) and $\theta=270°$ as inner radius.

4.2.4 PWV ANALYSIS

The multiple-points transit-time method was used for calculation of the aortic PWV [7, 10]. Hereby, the data processing algorithm was adapted to reconstruct images at higher temporal resolution (200 frames per heart cycle). First, through-plane flow was determined at approximately 50 equally spaced locations along the aorta. Subsequently, the time point of the early-systolic upstroke of the flow pulse was calculated for each analysis plane. In the following, the locations of the analysis planes were plotted against the time points of the systolic upstrokes. By fitting a line to this plot, PWV can be assessed from the slope of the linear fit:

$$PWV = \frac{dx}{dt} \tag{9}$$

4.2.5 QUANTIFICATION OF AORTIC GEOMETRY

4.2.5.1 Aortic curvature

The aortic curvature (see Figure 33) was assessed by using a polynomial fit to the centerline in order to generate a “smoother” (differentiable) curve. For each point on the smoothed curve, the radius of the circle that approximates best the curve at this point was calculated. The curvature coefficient k_r is the reciprocal value of its radius.

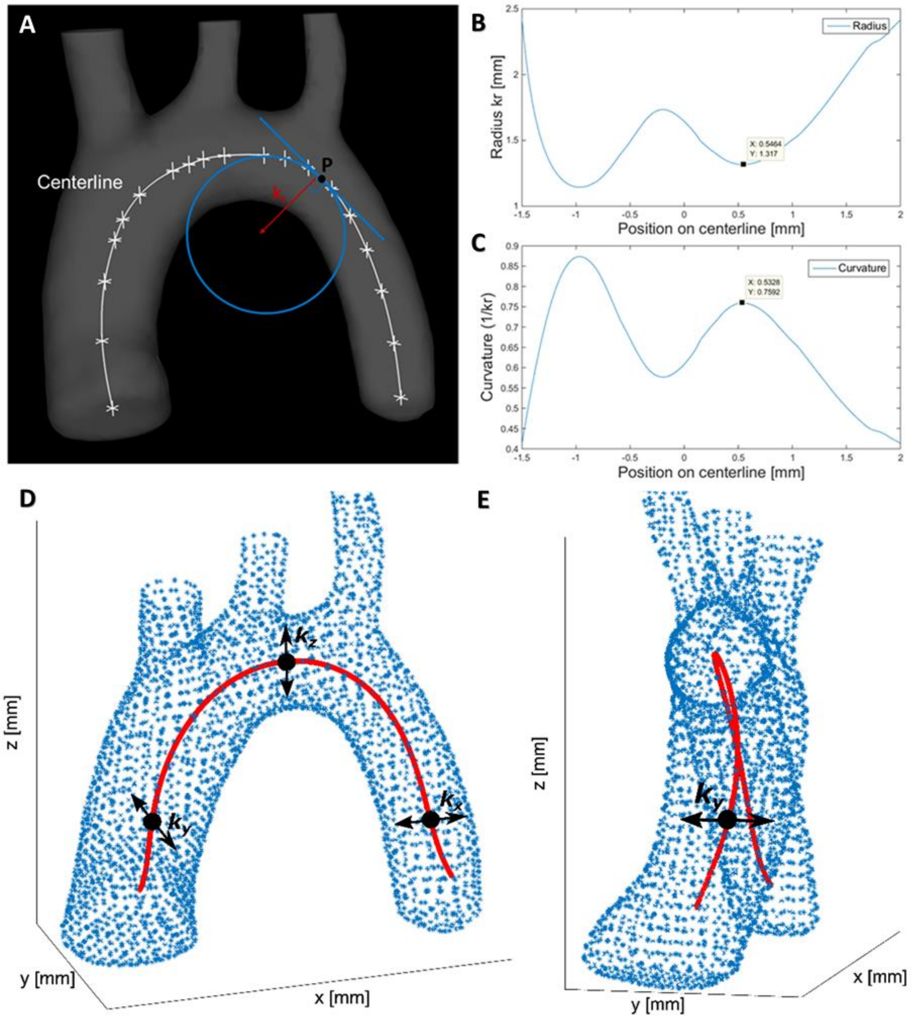

Figure 33: Scheme of the aortic curvature calculation and segmentation and centerline to illustrate the three curvature components. **A** For each point P on the centerline, a circle was calculated, which matches best the curvature at this point. Aorta with centerline (white) and the corresponding calculated circle (blue) and the radius k_r (red). **B** Radius k_r over the length of the aorta. **C** The reciprocal value of the radius k_r is the curvature ($1/k_r$), shown over the length of the centerline. One minimum of the radius k_r and the corresponding maximum of the curvature coefficient k ($1/k_r$) are marked as black points. **D** side view and **E** frontal view of the aorta illustrate the three curvature components. k_x is the component parallel to arch and is predominant in the lower ascending and descending aorta. k_y is the component perpendicular to the arch. It is mostly influenced by the shear between the trunks of the ascending and descending aorta. k_z is the orientation along the height of the aorta and has the highest values in the top region. The more the arch is pointed, the higher is the k_z value.

$$k_r = \frac{\frac{d^2y}{dx^2}}{\left(1+\left(\frac{dy}{dx}\right)^2\right)^{\frac{3}{2}}} \tag{10}$$

For a detailed derivation of (10), please see Supplementary Methods.

For a more detailed analysis of aortic curvature, the curvature values were split into three components. Schemes to illustrate the meaning of components k_x, k_y and k_z can be found in Figure 33D and E, respectively. k_x is the curvature in parallel to the aortic arch. It usually reaches its highest values in the ascending and descending aorta, near the transition from a straight aortic trunk towards a curved vessel. k_y means the curvature perpendicular to the aorta. It is largely dependent on the shear between the trunks of the ascending and descending aorta (Figure 33E). Finally, a third component, k_z along the height of the aorta can be described. This value reaches the highest values near the top region of the aorta. The higher k_z, the more the arch is pointed.

4.2.5.2 Aortic radius

The centerline and the temporally averaged segmentation without bifurcations were used for the calculation of the aortic radius. The minimum distance to the segmented lumen surface was calculated for each point on the centerline to obtain the radius.

4.2.5.3 Aortic volumes

Aortic volumes were calculated using the lumen segmentations of the 4D flow measurement, as described in [5] and Chapter 3. First, a normalization of the segmentations was performed by using the center between the left subclavian artery and brachiocephalic artery as landmark. Using this orientation point, all aortas were cut to the same length of 7 mm. Afterwards, all segmented voxels were added up to obtain aortic volumes. In order to reduce the error, the three aortic branches were excluded from the calculations.

4.2.6 CHARACTERIZATION OF FLOW PROFILES

For a more detailed characterization of all three phenotypes, the steepness of the diastolic flow profiles was assessed for all animals. First, the distance to the brachiocephalic artery was used as a landmark to measure the volume flow in the same position in the ascending aorta in all animals. Afterwards, the incline angles α were calculated by fitting lines to the flank of the diastolic flow profile (Figure 34A). The incline angle α can be assessed from the slope of the fit, m, by using the formula $\alpha = \tan^{-1}(m)$. Calculating the incline angles for all angular directions results in a slope profile (Figure 34B). Subsequently, histograms of all three angular distributions were computed. Mean values and standard deviations of the incline angles as well as the skewness (i.e., the deviation of the distribution from a normal distribution) were computed and compared.

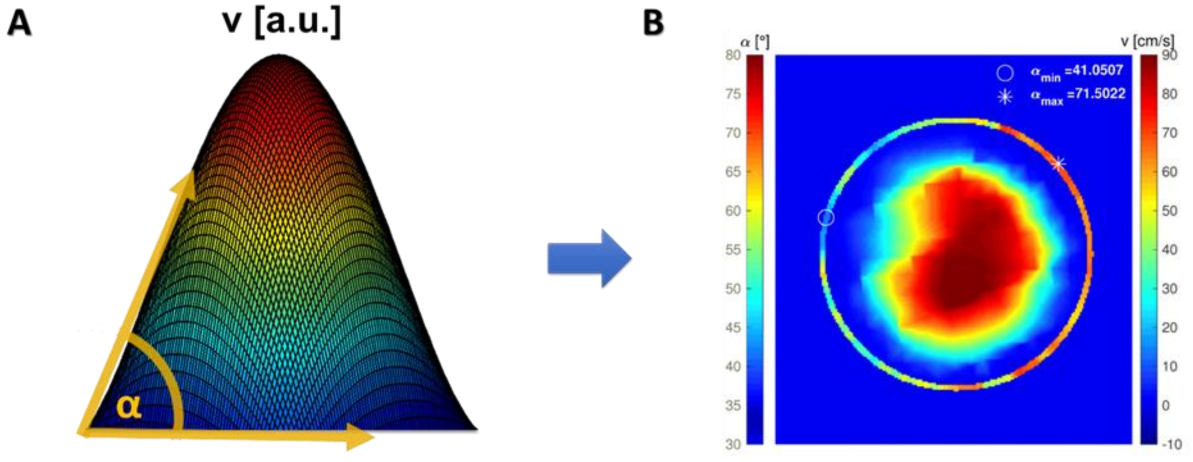

Figure 34: Characterization of flow profiles. **A** The incline angle of the flow profile was assessed from the slope of a line fitted to the flank of the flow profile. **B** Calculating the incline angles for all angular directions results in a slope profile, revealing the maximum (α_{max}) and minimum steepness (α_{min}).

4.2.7 ATHEROSCLEROTIC LESION QUANTIFICATION

After *in situ* perfusion of the arteries with phosphate-buffered saline (PBS), followed by 4% paraformaldehyde (PFA; Sigma Aldrich, USA), aortas were removed, cleaned from fat and connective tissue and post-fixed in 4% PFA overnight. For analysis of the extent of atherosclerosis throughout the aortic arch, the aorta was opened longitudinally, and the adventitia was stripped off. Tissue was stained for lipid depositions with Oil-red-O (ORO) and embedded in glycerol gelatin. The percentage of lipid deposition was calculated by dividing the stained area by the total aortic surface by computerized image analysis (Diskus Software, Hilgers, Germany). All images were recorded with a Leica DM 4000B fluorescence microscope and JVC KY-F75U camera.

4.2.8 BLOOD ANALYSIS, SERUM CHOLESTEROL AND TRIGLYCERIDE MEASUREMENTS

Blood was taken by heart puncture after sacrifice and analyzed using an automated hematology analyzer (XP300, Sysmex, Germany). Serum was analyzed for total cholesterol (Cobas Total Cholesterol Assay, Roche) and triglycerides (Cobas Triglyceride Assay, Roche) according to the manufacturer´s instructions.

4.2.9 SERUM LIPOPROTEIN PROFILE

Serum lipoprotein profile was assessed by size exclusion chromatography. Fractioning was performed with 2-5 µl of serum (depending on diet length) by utilizing a Superose 6 3.2/300 gel filtration column from GE Healthcare (Uppsala, Sweden) and PBS, pH 7.4 as elution buffer, which was delivered at a flow rate of 50 µl/min by a first pump (Waters 1525 binary pump, Eschborn, Germany). The separated lipoproteins were mixed in a T-tube with 50 µl/min cholesterol reagent (Roche, Mannheim, Germany), delivered by a second pump (Waters 1515 pump). The mixture was pumped through a 500 µl reaction coil PEEP tubing (internal diameter 0.75mm) at 37˚C into a post column reaction oven (Waters

Temperature Control Module II). Absorption was then measured with an UV-VIS detector at 500nm (Waters 2489 UV7Visible Detector). A total run time of 60 min was performed for each sample. Integration of the chromatograms was performed with the Waters Empower 3 software. Very low density lipoprotein (VLDL), low density lipoprotein (LDL) and high density lipoprotein (HDL) concentrations were calculated as products of the area percent of total cholesterol.

4.2.10 STATISTICAL ANALYSIS

Data are represented as mean ± SEM. All error and statistical analyses were performed in Matlab 2016b (The Mathworks, Inc., Natick, Massachusetts, USA) and GraphPad Prism 8 (GraphPad Software, San Diego, USA). For testing normal distribution, the Shapiro Wilk Normality Test was used. An unpaired t-test or an ANOVA was performed for normally distributed data. A non-parametric Mann-Whitney-U test or a Kruskal-Wallis test was performed when normality test failed. Pearson correlation coefficients were calculated for analysis of the degree of correlation. Differences of $p<0.05$ were considered as statistically significant.

4.3 RESULTS

4.3.1 BASAL CHARACTERIZATION OF WT, *APOE*$^{-/-}$ AND *LDLR*$^{-/-}$ MICE REVEALS DIFFERENCES IN LIPID PROFILES ONLY

Weight, cardiac periods, heart rates, blood and serum composition were assessed in 4-week-old wild type (WT), *Apoe*$^{-/-}$ and *Ldlr*$^{-/-}$ mice. No differences were observed in the weight, cardiac periods as well or heart rates between the different groups (Supplementary Figure 15A-C). Blood analysis furthermore revealed no difference in blood cell count and hematocrit (Supplementary Figure 15D). However, serum analysis at baseline levels showed increased cholesterol and triglyceride concentrations in *Apoe*$^{-/-}$ and *Ldlr*$^{-/-}$ compared to WT mice and differences in the lipoprotein profile (Supplementary Figure 15 and Supplementary Figure 20), as described previously [59]. The atherogenic index of plasma (AIP) was not significantly elevated in *Apoe*$^{-/-}$ and *Ldlr*$^{-/-}$ mice compared to WT mice at baseline (Supplementary Figure 15).

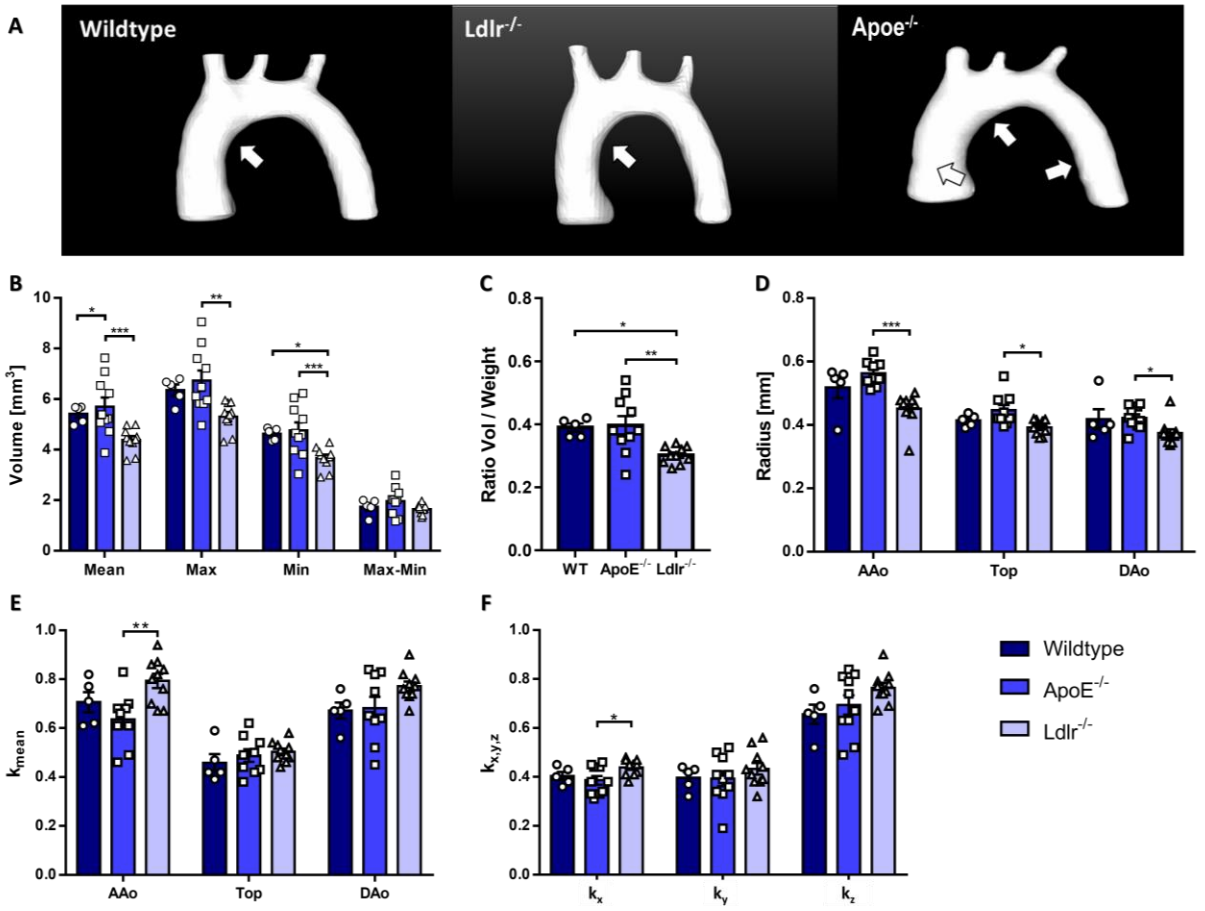

Figure 35: Aortic arches of WT, *Apoe*$^{-/-}$ and *Ldlr*$^{-/-}$ mice show characteristic geometric properties. **A** Aortic lumen segmentation of each genotype, showing characteristic differences in geometry (see white arrows). **B** Aortic volumes. Mean volume was significantly higher in *Apoe*$^{-/-}$ compared to WT (*, $p<0.05$) and *Ldlr*$^{-/-}$ mice (***, $p<0.001$). Maximum volume was highest in *Apoe*$^{-/-}$ compared to *Ldlr*$^{-/-}$ mice (**, $p<0.01$) and minimum volume was lowest in *Ldlr*$^{-/-}$ compared to WT (*, $p<0.05$) and *Apoe*$^{-/-}$ mice (***, $p<0.001$). Difference (max-min) showed no significant differences. **C** Ratio of aortic volume to body weight showed lowest values in *Ldlr*$^{-/-}$ compared to WT (*, $p<0.05$) and *Apoe*$^{-/-}$ mice (***, $p<0.001$). **D** Aortic radius is significantly decreased in all regions in *Ldlr*$^{-/-}$ compared to *Apoe*$^{-/-}$ mice (AAo: ***, $p<0.001$; Top: *, $p<0.05$; Dao: *, $p<0.05$). **E** Mean curvature coefficient k is significantly higher in the AAo in *Ldlr*$^{-/-}$ compared to *Apoe*$^{-/-}$ mice (**, $p<0.01$). **F** Curvature coefficient k_x is higher in *Ldlr*$^{-/-}$ compared to *Apoe*$^{-/-}$ mice. Data are presented as mean ± SEM.

4.3.2 AORTIC ARCHES OF WT, *APOE*$^{-/-}$ AND *LDLR*$^{-/-}$ MICE SHOW CHARACTERISTIC GEOMETRIC PROPERTIES

For flow and WSS quantification, the accurate segmentation of the aortic lumen is a prerequisite. Interestingly, segmentation data of the three genotypes revealed characteristic geometric properties (Figure 35A). Whereas WT and *Apoe*$^{-/-}$ mice showed a similar geometry, the aortic arch of the *Ldlr*$^{-/-}$ mouse displayed differences, in particular when compared to *Apoe*$^{-/-}$ mice, in several properties. *Apoe*$^{-/-}$ mice demonstrated the largest aortic volumes compared to WT and *Ldlr*$^{-/-}$ mice, with the latter showing the smallest volumes (Figure 35B). Calculation of the aortic volume to bodyweight ratio similarly revealed a significantly smaller ratio in *Ldlr*$^{-/-}$ compared to *Apoe*$^{-/-}$ and WT mice (Figure 35C). Both maximum (systolic) and minimum (diastolic) volumes were lower in *Ldlr*$^{-/-}$ compared to *Apoe*$^{-/-}$ mice; the difference (maximum – minimum values, however, were unaltered between the genotypes (Figure 35B).

The aortic radius was significantly smaller in *Ldlr*$^{-/-}$ mice compared to *Apoe*$^{-/-}$ mice in three defined regions of the aortic arch, with the greatest differences in the ascending aorta (Figure 35D). Moreover, aortic curvature was quantified by calculating the curvature coefficient, which was significantly greater in *Ldlr*$^{-/-}$ compared to *Apoe*$^{-/-}$ mice (Figure 35E), fitting to the impression evoked by the aortic lumen segmentations (Figure 35A). For a deeper characterization, the curvature coefficient k was split into the spatial components (k_x, k_y, k_z). Here, only k_x showed significantly higher values in *Ldlr*$^{-/-}$ compared to *Apoe*$^{-/-}$ mice, indicating a more abrupt transition between the ascending aorta and the curved top region in *Ldlr*$^{-/-}$ mice (Figure 35F).

4.3.3 FLOW PROFILES BUT NOT INFLOW AND ELASTIC PROPERTIES DIFFER IN WT, *APOE*$^{-/-}$ AND *LDLR*$^{-/-}$ MICE

Not only the geometry, but also the aortic flow profiles showed characteristic differences, resulting in a circular profile in *Ldlr*$^{-/-}$ mice in contrast to the asymmetric flow profiles found in WT and *Apoe*$^{-/-}$ mice (see Figure 36A, B).

Therefore, aortic flow values were quantified in four analysis planes throughout the aortic arch (plane 1: ascending aorta; plane 2: between brachiocephalic artery and left carotid artery; plane 3: between left carotid artery and left subclavian artery; plane 4: between left subclavian artery and descending aorta) [5]. While aortic inflow (corresponding to plane 1) was similar in all three genotypes, as reflected by the peak flow (Figure 36C), the net flow (Figure 36D) and volume flow, normalized to cardiac periods (Figure 36E), differences were observable in the other planes (Supplementary Figure 16). The peak flow showed significantly higher values in plane 4 in *Apoe*$^{-/-}$ mice compared to the other two genotypes (Supplementary Figure 16A), and net flow was elevated in all 3 residual planes (Supplementary Figure 16B). Moreover, volume flow was elevated in plane 2 in *Apoe*$^{-/-}$ mice compared to WT mice, and in plane 4 in comparison to both genotypes (Supplementary Figure 16C), indicating an elevated blood flow into the thoracic aorta in *Apoe*$^{-/-}$ mice.

The aortic PWV, defined by the velocity at which the blood pressure pulse travels through the arterial system, showed no significant differences (Figure 36F), indicating similar aortic compliance in all three genotypes.

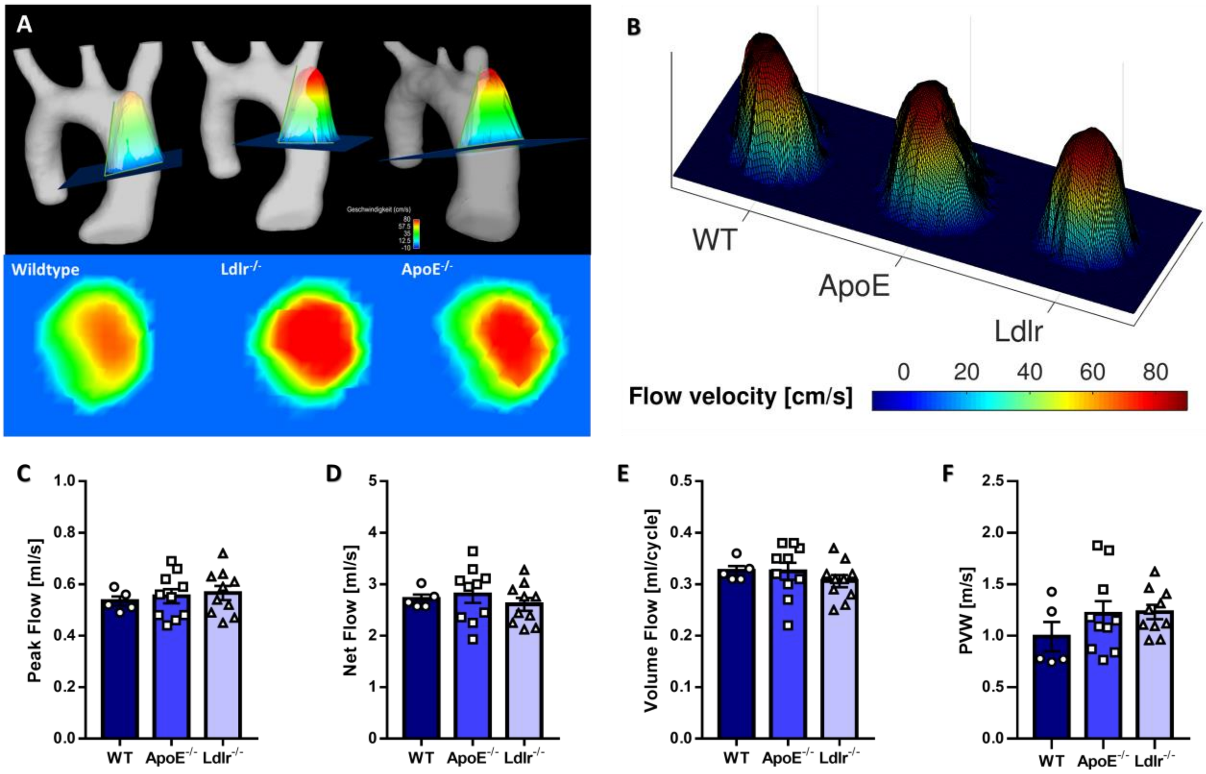

Figure 36: Flow profiles but not elastic properties differ in WT, *Apoe$^{-/-}$* and *Ldlr$^{-/-}$* mice. **A** Illustration of the 3D flow profile in the aortic arches of the three genotypes in one exemplary plane in the ascending aorta (upper image) and the corresponding 2D flow profile (lower image). **B** 3D flow profiles for each genotype, showing the asymmetric flow profiles of WT and *Apoe$^{-/-}$* mice and the circular flow profile of the *Ldlr$^{-/-}$* mouse. **C-E** Flow values for plane 1, reflecting the blood inflow into the aorta. **C** Peak flow values are similar in all three genotypes. **D** No differences are observed for net flow values. **E** Volume flow is not significantly different. **F** PWV values are similar in all genotypes. Data are presented as mean ± SEM.

To further characterize the flow profiles, the distribution of incline angles of the diastolic flow profile α was assessed in the ascending aorta. WT and *Apoe$^{-/-}$* mice feature similar mean values and standard deviations of the incline angle (Figure 37A, B and D) and a comparable skewness value κ (Figure 37A, B), indicative of an equally steep, asymmetric flow profile. *Ldlr$^{-/-}$* mice, however, exhibit a significant larger mean value of α, indicating a steeper flow profile (Figure 37C, D). A plot of the differences between the maximum and minimum incline angle revealed much larger differences in *Apoe$^{-/-}$* mice in comparison to *Ldlr$^{-/-}$* mice (Figure 37E), as also reflected by the most symmetric angle distribution and the smallest range of angle variations relative to the other two groups (Figure 37F).

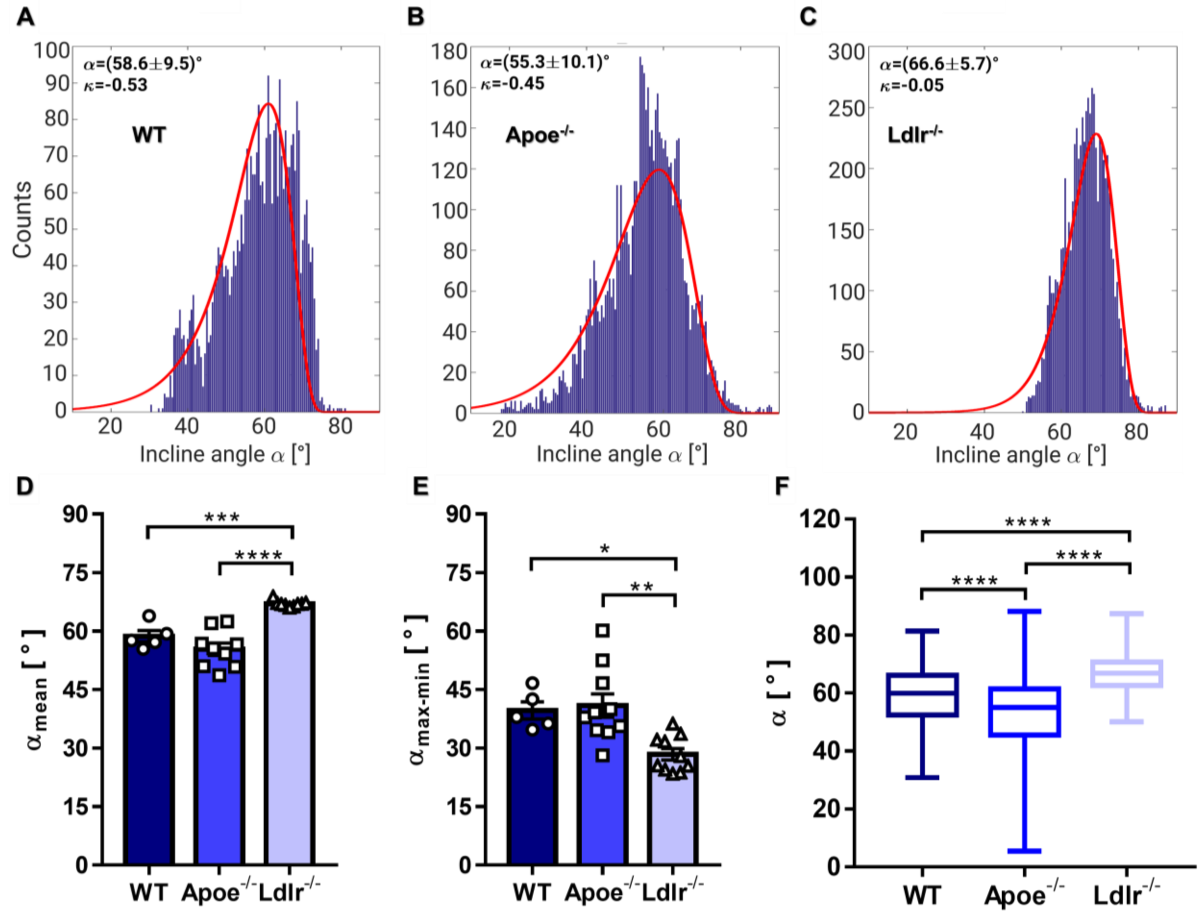

Figure 37: Distributions of incline angles reveal steeper and more symmetric flow profiles in *Ldlr*$^{-/-}$ mice. **A** WT and **B** *Apoe*$^{-/-}$ mice exhibit analogous distributions of incline angles with a similar skewness κ, indicating comparable flow profiles. **C** The distribution of *Ldlr*$^{-/-}$ mice features elevated incline angles with a significantly larger skewness, indicative of steeper and more symmetric flow profiles (red lines: log normal fits of the histograms). **D** Mean steepness angle. *Ldlr*$^{-/-}$ mice show the highest values, indicative of the steepest flow profile (***, $p<0.001$; ****, $p<0.0001$). **E** Difference of maximum and minimum steepness angles. *Ldlr*$^{-/-}$ mice feature significantly less difference, indicating a more symmetric distribution of incline angles (*, $p<0.05$; **, $p<0.01$). **F** Whiskers plots of the mean incline angles, indicating the steepest flow profiles in *Ldlr*$^{-/-}$ mice (****, $p<0.0001$). Data are presented as mean ± SEM.

4.3.4 *LDLR*$^{-/-}$ MICE SHOW LOCAL DIFFERENCES IN WSS PROFILES COMPARED TO WT AND *APOE*$^{-/-}$ MICE

The WSS is highly dependent on the flow profile. Therefore, global WSS and OSI values were evaluated in the aortic arch of WT, *Apoe*$^{-/-}$ and *Ldlr*$^{-/-}$ mice. Although a different flow profile was observed in *Ldlr*$^{-/-}$ mice, the resulting mean (Figure 38A) and maximum (Figure 38C) longWSS, circWSS and radStrain was similar in all genotypes. In addition, no differences could be detected for mean (Figure 38B) and maximum (Figure 38C) OSI values.

In order to further investigate the impact of the flow profiles on the local WSS and OSI characteristics, 2D projection maps of WSS and OSI [5] were generated, followed by the pixel-wise statistical analyses of local differences. LongWSS profiles were similar in *Apoe*$^{-/-}$ and WT mice, as reflected by only small areas of significance in the three aortic regions (Figure 39A). In contrast, *Ldlr*$^{-/-}$ mice revealed significantly decreased WSS values in particular in the inner radius of the ascending aorta, and significantly increased longWSS around the inner radius of the descending aorta compared to WT mice (Figure 39B), and even more pronounced when compared to *Apoe*$^{-/-}$ mice (Figure 39C).

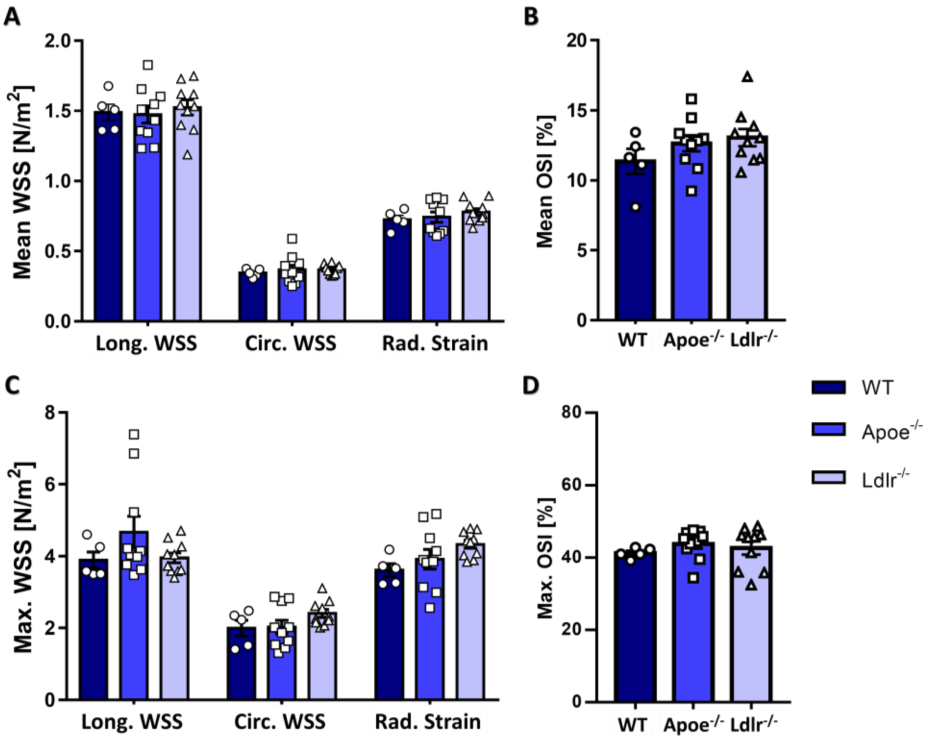

Figure 38: Global WSS and OSI Values do not differ in the three genotypes. A Mean WSS values for all genotypes. No significant differences are observable. **B** Mean OSI values are not significantly different. **C** Maximum WSS values. No significances are noticeable. **D** Maximum OSI values show no significant differences at baseline levels. Data are presented as mean ± SEM.

Also the circWSS was rather similar in *Apoe*$^{-/-}$ and WT mice (Figure 39D), whereas larger areas of significantly decreased circWSS were observed around the inner radius of *Ldlr*$^{-/-}$ mice throughout the aortic arch (Figure 39E), and increased circWSS was noted in the anterior and the inner radius of the ascending aorta (Figure 39F).

In line with the WSS profile, analysis of the radStrain profile revealed strong similarities between *Apoe*$^{-/-}$ and WT mice with only smaller areas of significance in the inner radius of the ascending and descending aorta in *Apoe*$^{-/-}$ mice (Figure 40A). *Ldlr*$^{-/-}$ mice showed a significant increase in the radStrain around the inner radius and a decrease around the outer radius in the top region and descending aorta compared to WT mice (Figure 40B). When comparing *Ldlr*$^{-/-}$ and *Apoe*$^{-/-}$ mice, decreased radStrain values were noted around the inner radius of the ascending aorta, whereas an increase was observed in the inner radius of ascending aorta (Figure 40C).

OSI values were significantly increased in the region between the inner radius and anterior side of the ascending aorta in *Apoe*$^{-/-}$ compared to WT mice (Figure 40D), whereas *Ldlr*$^{-/-}$ mice displayed elevated OSI values in the whole descending aorta compared to WT mice (Figure 40E). Interestingly, the comparison between *Ldlr*$^{-/-}$ and *Apoe*$^{-/-}$ mice revealed significantly higher OSI values in the inner radius of the ascending aorta in *Apoe*$^{-/-}$ mice. In contrast to this, *Ldlr*$^{-/-}$ mice displayed a large area of increased OSI values in the inner radius of the whole descending aorta (Figure 40F).

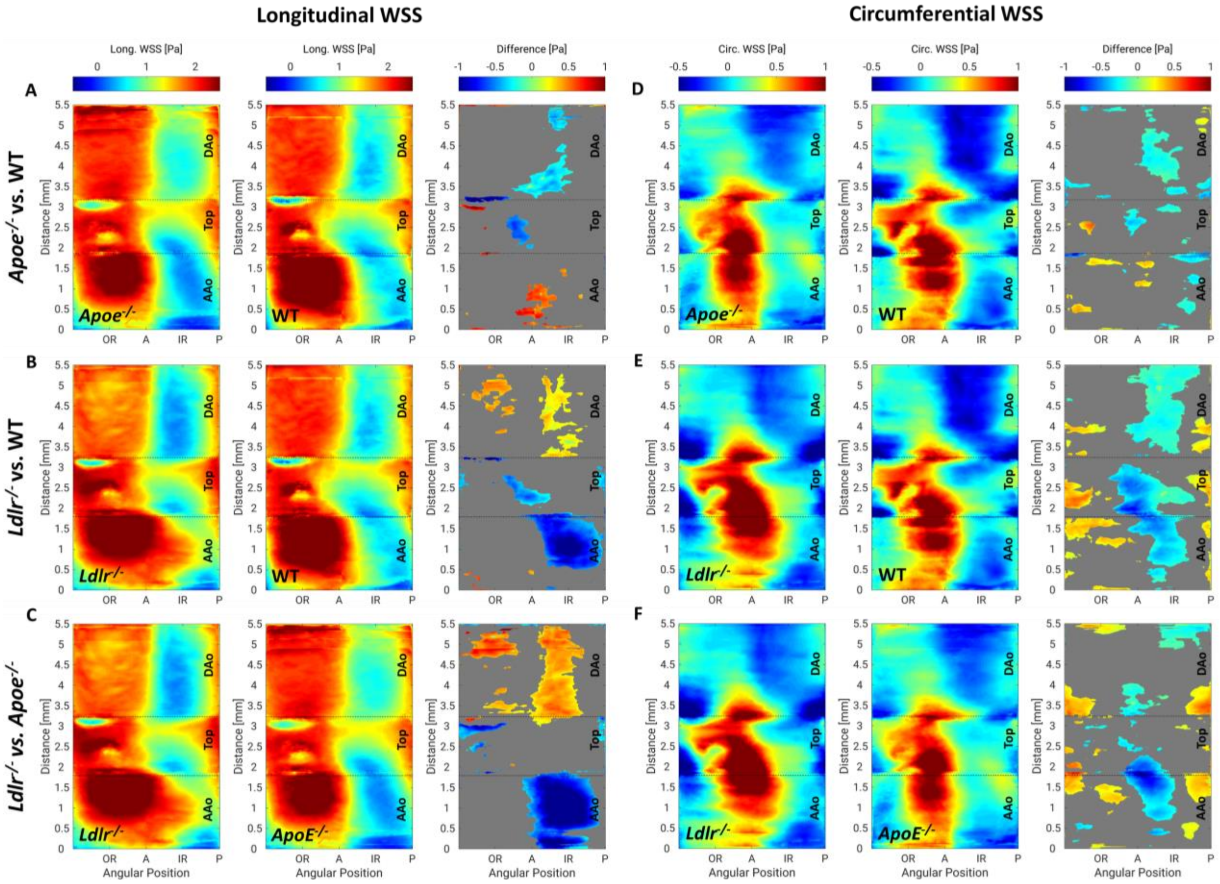

Figure 39: 2D-projection maps reveal local, characteristic differences in longitudinal and circumferential WSS profiles. **A-C** LongWSS profiles. **A** Comparison of *Apoe*$^{-/-}$ to WT mice. Only small differences are observable. **B** Comparison of *Ldlr*$^{-/-}$ to WT mice. Differences are observed in particular in the IR of the AAo and DAo. **C** Comparison of *Ldlr*$^{-/-}$ to *Apoe*$^{-/-}$ mice. Strong differences are observed around the IR in the AAo and DAo. **D-F** CircWSS profiles. **D** Comparison of *Apoe*$^{-/-}$ to WT mice. Only small differences in particular in the IR of the DAo are observable. **E** Comparison of *Ldlr*$^{-/-}$ to WT mice. Differences are observed around the IR of the whole aortic arch. **F** Comparison of *Ldlr*$^{-/-}$ to *Apoe*$^{-/-}$ mice. Strong differences are observed in particular around the IR in the AAo and P of the DAo.

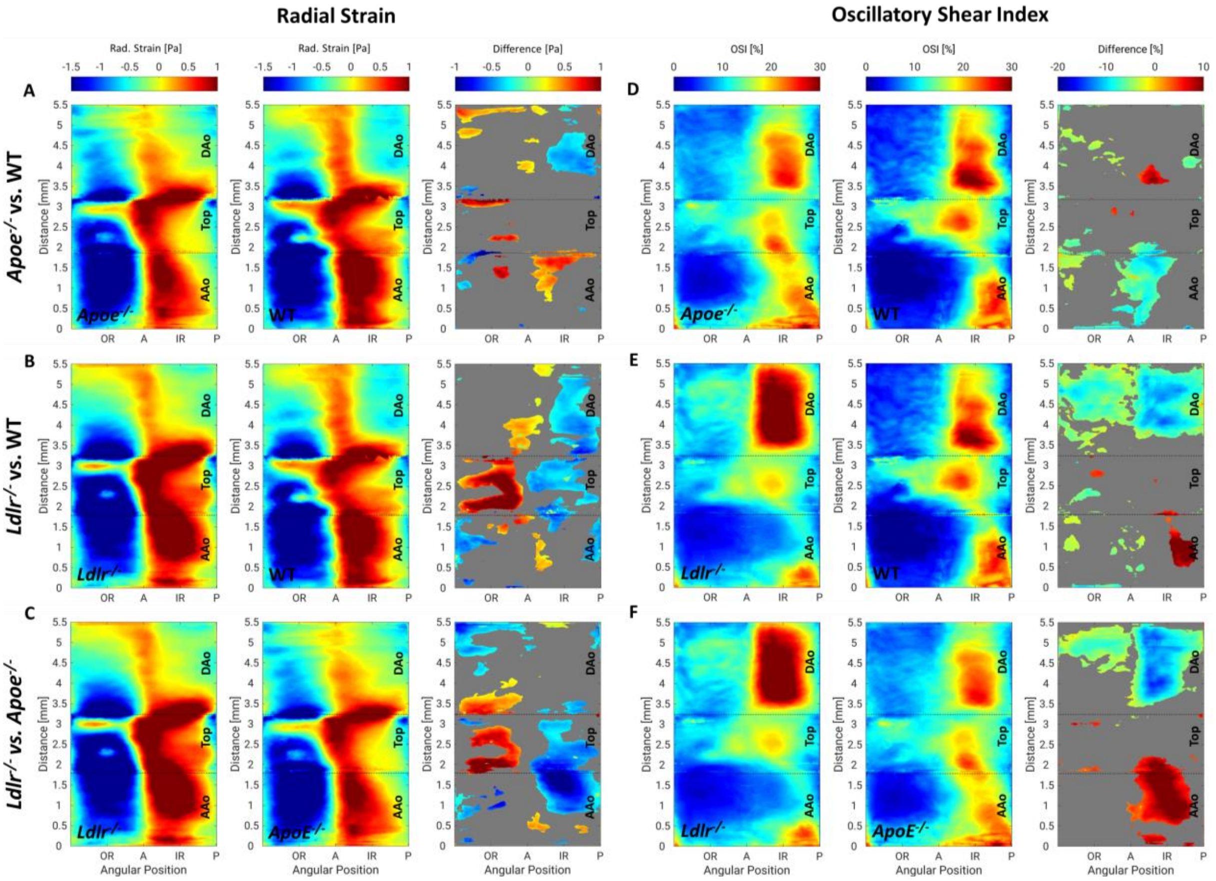

Figure 40: 2D-projection maps reveal local, characteristic differences in radStrain and OSI profiles. A-C RadStrain profiles. **A** Comparison of *Apoe*$^{-/-}$ to WT mice. Only small differences are observable. **B** Comparison of *Ldlr*$^{-/-}$ to WT mice. Differences are observed throughout the aorta. **C** Comparison of *Ldlr*$^{-/-}$ to *Apoe*$^{-/-}$ mice. Differences are observed throughout the aorta. **D-F** OSI profiles. **D** Comparison of *Apoe*$^{-/-}$ to WT mice. Only small differences in particular in the A to IR region of the Aao are observable. **E** Comparison of *Ldlr*$^{-/-}$ to WT mice. Strong differences are observed in the whole DAo. **F** Comparison of *Ldlr*$^{-/-}$ to *Apoe*$^{-/-}$ mice. Strong differences are observed in particular around the IR in the AAo and DAo.

4.3.5 AORTIC GEOMETRY CHANGES DURING ATHEROSCLEROSIS PROGRESSION

After receiving a Western diet (WD) for 4 and 8 weeks, hemodynamic parameters in *Apoe*$^{-/-}$ and *Ldlr*$^{-/-}$ mice were again characterized. As expected, both *Apoe*$^{-/-}$ and *Ldlr*$^{-/-}$ mice showed an increase in weight during the observation period, with *Ldlr*$^{-/-}$ mice exhibited a significantly lower bodyweight compared to *Apoe*$^{-/-}$ mice at both timepoints (Supplementary Table 3). Interestingly, assessment of the aortic geometry revealed an equalization of the aortic radius in both mouse models during atherosclerosis progression. The aortic radius was increased all regions in *Apoe*$^{-/-}$ and *Ldlr*$^{-/-}$ mice after 4 weeks of WD and did not further increase after 8 weeks of WD, leading to an overall alignment of aortic radius in both groups (Figure 41A). A similar trend was observed in the aortic volumes, which increased significantly in both groups of mice after 4 weeks of WD (Figure 41B). The mean aortic curvature remained constant in all regions of *Apoe*$^{-/-}$ mice during atherosclerosis progression, whereas a diminution in the mean curvature was observed in *Ldlr*$^{-/-}$ mice, leading to an alignment of valued in both groups except in the AAo after 8 weeks of WD, where a still significantly greater mean curvature was noticed compared to *Apoe*$^{-/-}$ mice (Figure 41C).

In *Apoe*$^{-/-}$ mice, no changes in the curvature were observed in the x- and y-direction after 8 weeks of WD, but an increase in z-curvature was noticed after 8 weeks of WD, indicative of a more pointed arch geometry. In *Ldlr*$^{-/-}$ mice, a significantly decreased curvature was seen in the x-,y- and z-direction after 4 weeks of WD, and in the y- and z-direction after 8 weeks of WD, compared to *Apoe*$^{-/-}$ mice. Hence, the mean aortic curvature aligns during atherosclerosis progression in both mouse models, with the curvature components showing model-specific changes (Figure 41D). In *Apoe*$^{-/-}$ mice, k_x remained constant and k_y increased between 4 weeks and 8 weeks of WD, indicating a slightly larger shear between the trunks of the ascending and descending aorta. An even larger increase was noticeable for the k_z component due to an increasing tapering of the aortic arch. In *Ldlr*$^{-/-}$ mice, however, k_x and k_y remained constant while a slight increase of k_z was observable.

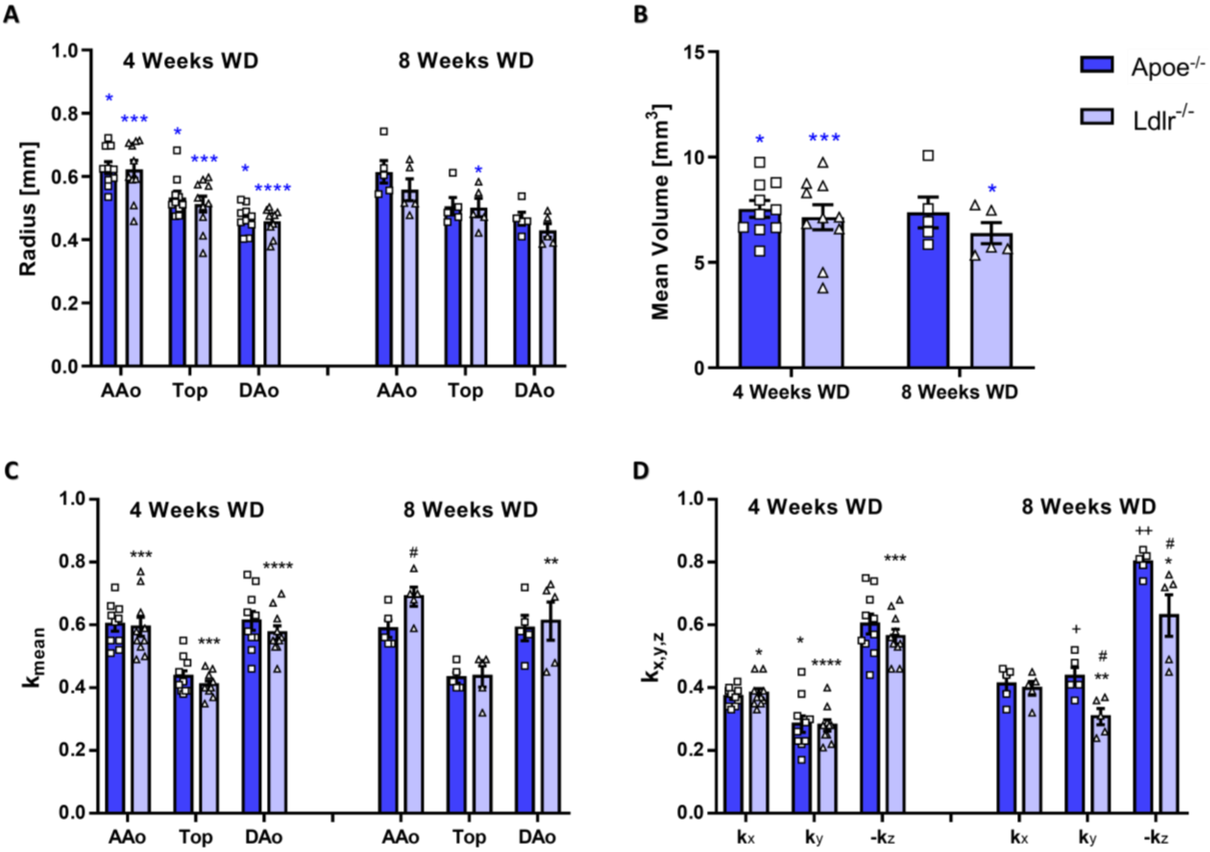

Figure 41: Aortic geometry changes during atherosclerosis progression. **A** Aortic radius slightly increases in *Apoe*$^{-/-}$ mice in all aortic regions and strongly increases in *Ldlr*$^{-/-}$ mice in all aortic regions after 4 weeks of WD. **B** Mean aortic volume slightly increases in *Apoe*$^{-/-}$ mice and strongly increases in *Ldlr*$^{-/-}$ mice after 4 weeks of WD. **C** Mean aortic curvature stays constant in all regions of Apoe$^{-/-}$ mice during atherosclerosis progression. In *Ldlr*$^{-/-}$ mice, a decreased curvature is observed in all regions, but compared to *Apoe*$^{-/-}$ mice, a significantly greater curvature is noticed in the AAo after 8 weeks of WD. **D** Aortic curvature k in x-,y- and z-direction. *Ldlr*$^{-/-}$ mice show a significant decrease of curvature in all directions after 4 weeks of WD. In *Apoe*$^{-/-}$ mice, no changes are observed in x- and y-direction after 8 weeks of WD, but an increase in z-curvature is noticed after 8 weeks of WD. After 8 weeks of WD, *Ldlr*$^{-/-}$ mice show a decreased curvature in y- and z-direction compared to *Apoe*$^{-/-}$ mice. Data are presented as mean ± SEM**.** Significances to baseline are marked with * (lower) and * (higher), to 4 Weeks WD with $^{+}$ and to *Apoe*$^{-/-}$ with $^{\#}$.

4.3.6 AORTIC INFLOW REMAINS CONSTANT, BUT FLOW PROFILES, AORTIC ELASTICITY AND GLOBAL WSS CHANGE DURING ATHEROSCLEROSIS PROGRESSION

Due to the influence of aortic geometry on the flow (and WSS) profiles, we furthermore characterized the aortic inflow, the flow profiles as well as changes in aortic elasticity during atherosclerosis progression.

Peak flow values were elevated in *Apoe*$^{-/-}$ mice compared to baseline levels and to *Ldlr*$^{-/-}$ mice after 4 weeks of WD, but no changes were observed with ongoing diet. Furthermore, no differences were noted in net flow and volume flow levels, indicating no changes in aortic inflow during atherosclerosis development (Figure 42A-C). When comparing flow values of *Apoe*$^{-/-}$ and *Ldlr*$^{-/-}$ mice in planes 2-4, peak- and net flow values were significantly elevated in *Apoe*$^{-/-}$ mice in all planes after 4 weeks of WD. However, after 8 weeks of WD, peak- and net flow values equalized. Interestingly, volume flow remained elevated in *Apoe*$^{-/-}$ mice in plane 2 and 3 even after 8 weeks of WD (Supplementary Figure 16). Furthermore, elevated PWV values were noted in both models, indicative of decreased aortic elasticity (Figure 42D) and positively correlated with differences between minimum and maximum aortic volumes (Figure 42E). *Apoe*$^{-/-}$ mice developed an even more asymmetric shape of the flow profile during atherosclerosis progression, which may be due to the increasing shear and the more pointed arch, whereas in *Ldlr*$^{-/-}$ mice, flow profiles remained steeper and more symmetric than in the *Apoe*$^{-/-}$ mouse model (Figure 42F).

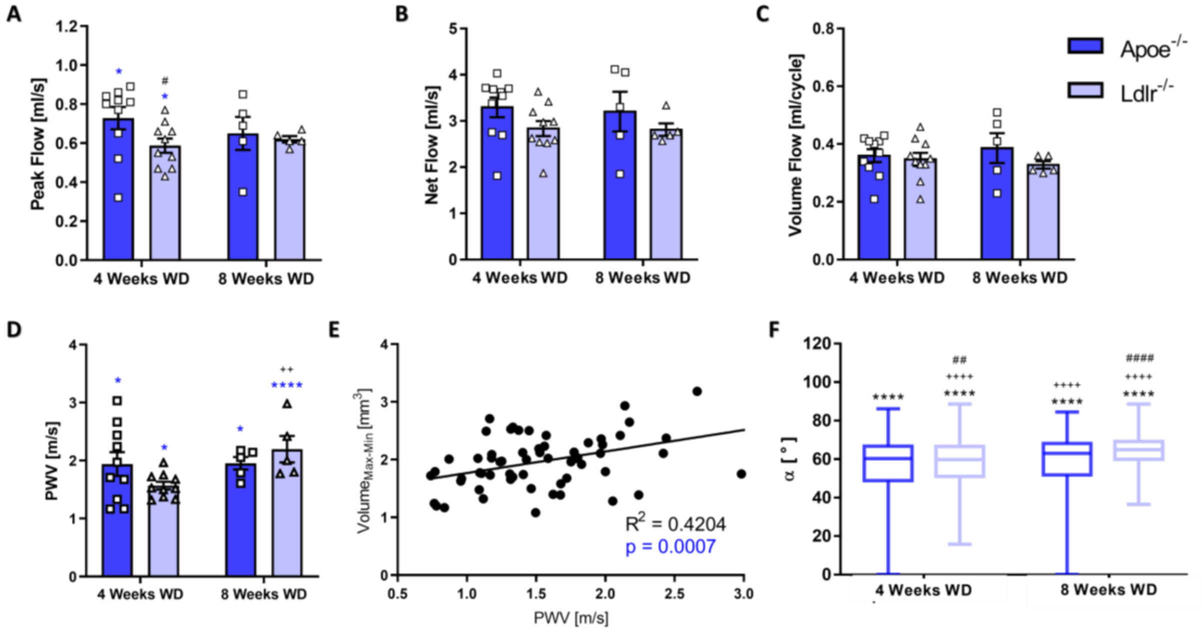

Figure 42: Flow profiles and aortic elasticity change during atherosclerosis progression. **A** Peak flow, **B** Net flow and **C** Volume flow for plane 1 in the aortic arch of *Apoe*$^{-/-}$ and *Ldlr*$^{-/-}$ mice after 4 and 8 weeks of WD. Only peak flow values are elevated in *Apoe*$^{-/-}$ compared to baseline levels and to *Ldlr*$^{-/-}$ mice after 4 weeks of WD. **D** PWV increases over time in both models but shows no significant differences between the models. **E** Analysis of the flow profile in both mouse models. Flow profiles differ significantly between the groups, showing steeper and more symmetric flow profiles in *Ldlr*$^{-/-}$ mice compared to *Apoe*$^{-/-}$ mice even during atherosclerosis progression. Data are presented as mean ± SEM**.** Significances to baseline are marked with * (lower) and * (higher), to 4 Weeks WD with $^{+}$ and to *Apoe*$^{-/-}$ with $^{\#}$.

4.3.7 2D PROJECTION MAPS REVEAL TIME-DEPENDENT, LOCAL CHANGES IN THE WSS PROFILE OF *APOE*$^{-/-}$ AND *LDLR*$^{-/-}$ MICE DURING ATHEROSCLEROSIS PROGRESSION

Despite differences in flow profiles, global longWSS and OSI values did not change during atherosclerosis progression in both groups (Figure 43A, Supplementary Table 5). The global circWSS values in *Ldlr*$^{-/-}$ mice, however, showed a significant decrease after 4 weeks of WD compared to baseline levels, whereas levels in *Apoe*$^{-/-}$ mice remained constant. Moreover, values were significantly decreased in *Ldlr*$^{-/-}$ mice compared to *Apoe*$^{-/-}$ mice at both time points (Figure 43A, Supplementary Table 5). Analysis of global radStrain values indicated the same trend over the course of the study. RadStrain in *Apoe*$^{-/-}$ mice remained constant over time, whereas values in *Ldlr*$^{-/-}$ mice decreased significantly at 4 weeks of diet compared to baseline levels. Compared to *Apoe*$^{-/-}$ mice, radStrain was significantly decreased in *Ldlr*$^{-/-}$ mice at both time points (Figure 43C, Supplementary Table 5).

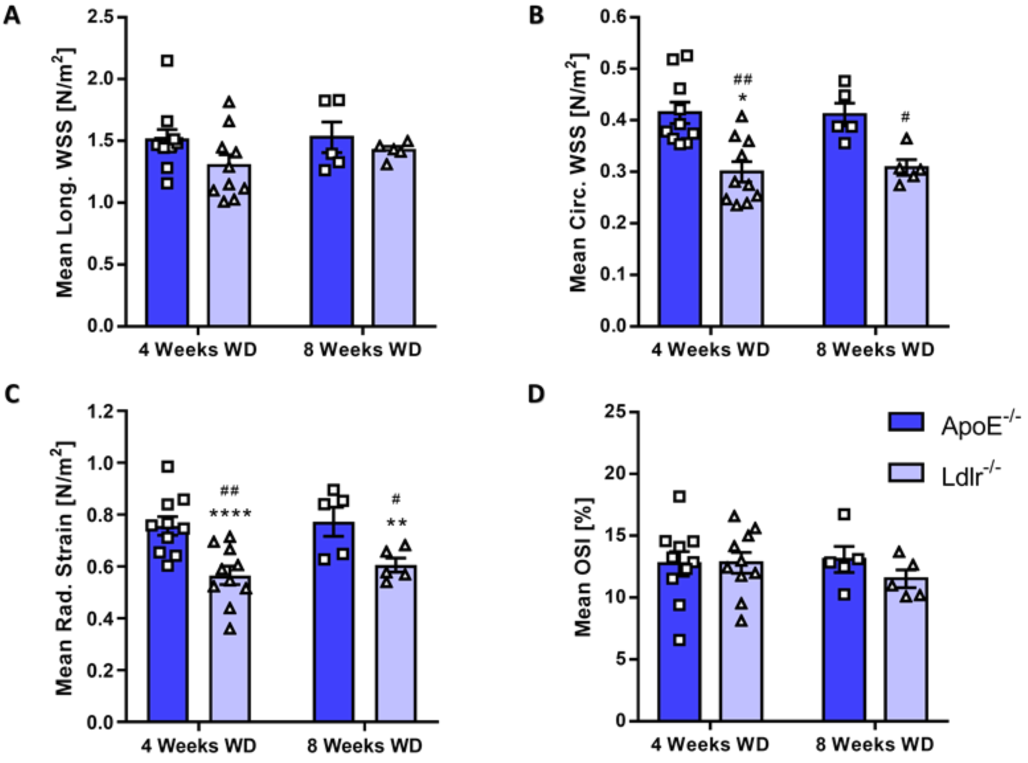

Figure 43: Global WSS values of *Apoe*$^{-/-}$ and *Ldlr*$^{-/-}$ mice after 4 and 8 weeks of WD. **A** Global values of longWSS are not changing during atherosclerosis progression. **B** CircWSS is significantly decreased in *Ldlr*$^{-/-}$ mice after 4 and 8 weeks of WD compared to *Apoe*$^{-/-}$ mice. **C** RadStrain is significantly decreased in *Ldlr*$^{-/-}$ mice after 4 and 8 weeks of WD compared to *Apoe*$^{-/-}$ mice. Data are presented as mean ± SEM**.** Significances to baseline are marked with * (lower) and * (higher), to 4 Weeks WD with $^{+}$ and to *Apoe*$^{-/-}$ with $^{\#}$.

Evaluating local WSS, both atherosclerotic mouse models exhibit distinct changes after 4 weeks of WD, suggestive of morphological changes in the aortic arch. In *Apoe*$^{-/-}$ mice, significantly elevated longWSS values in large regions of the aortic arch were noted compared to *Ldlr*$^{-/-}$ mice, whereas in the IR of the DAo, negative longWSS values indicate a larger amount of backflow around this area (Figure 44A). Interestingly, after 8 weeks of diet, the measurement indicates an alignment of longWSS values (Figure 44B). Comparing changes in the intergroup profile over time, longWSS in *Ldlr*$^{-/-}$ mice elevated around the IR of the top DAo (Supplementary Figure 18A). *Apoe*$^{-/-}$ mice, on the other hand, exhibited a region of larger negative longWSS values around the IR of the DAo but spots with elevated values in the other parts after 8 weeks of diet (Supplementary Figure 18B).

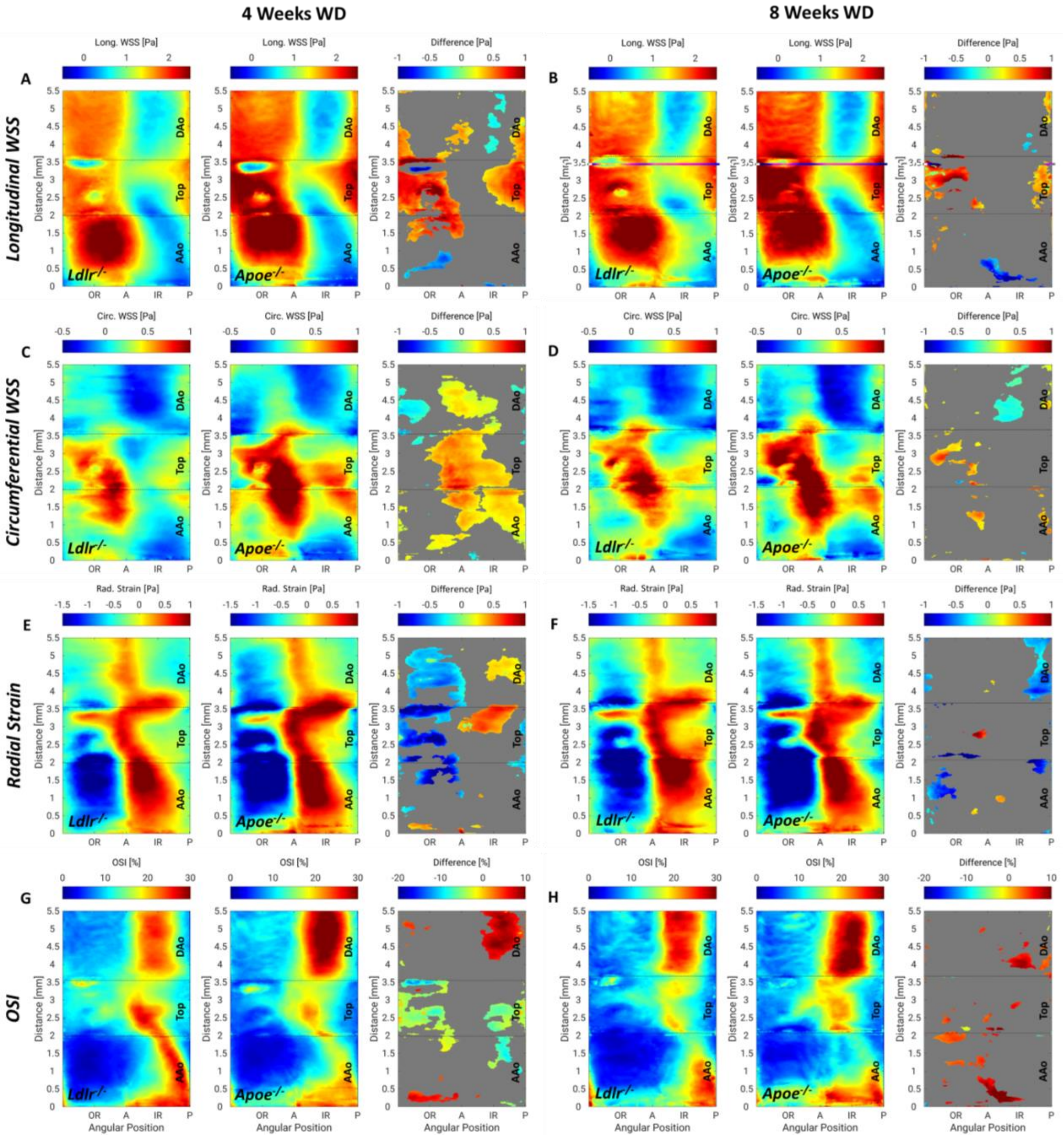

Figure 44: 2D-projection maps reveal time-dependent, local changes in the WSS profile of *Apoe*$^{-/-}$ and *Ldlr*$^{-/-}$ mice during atherosclerosis progression. A, C, E, G: Intergroup comparison of WSS and OSI profiles after 4 weeks of diet. **B, D, F, H:** Intergroup comparison after 8 weeks of diet**. A** LongWSS. *Apoe*$^{-/-}$ mice show elevated regions of longWSS compared to *Ldlr*$^{-/-}$ mice. **B** With ongoing diet, longWSS profile aligns. **C** CircWSS. *Apoe*$^{-/-}$ mice show large areas of elevated circWSS throughout the aorta compared to *Ldlr*$^{-/-}$ mice after 4 weeks of diet. **D** With ongoing diet, circWSS profile aligns. **E** RadStrain. *Apoe*$^{-/-}$ mice show large areas of reduced values in the OR and elevated spots in the IR compared to *Ldlr*$^{-/-}$ mice after 4 weeks of diet. **E** With ongoing diet, radStrain profile aligns. **F** OSI. *Apoe*$^{-/-}$ mice show a highly elevated region in the IR of the DAo compared to *Ldlr*$^{-/-}$ mice after 4 weeks of diet. **E** With ongoing diet, OSI profile aligns.

Moreover, *Apoe*$^{-/-}$ mice showed large areas of elevated circWSS compared to *Ldlr*$^{-/-}$ mice throughout the aortic arch (Figure 44C), indicating a larger amount of helical flow.

However, with ongoing diet, an alignment of the circWSS similar to the longWSS was observed (Figure 44D). Intragroup comparisons revealed an elevation of circWSS values around the IR of the AAo in *Ldlr*$^{-/-}$ mice over time (Supplementary Figure 18C), whereas in *Apoe*$^{-/-}$ mice, elevated values were found around the IR and posterior side and large areas of reduced values around the anterior side (Supplementary Figure 18D).

Regarding radStrain, *Apoe*$^{-/-}$ mice featured larger negative values around the OR of the arch and larger positive values around the IR of the top region after 4 weeks of diet (Figure 44E). In accordance with the observations of the longWSS and circWSS profile, an alignment of radStrain values was observed after 8 weeks of diet (Figure 44F). Intragroup comparisons revealed drastic changes in the radStrain profile around the outer and IR in *Ldlr*$^{-/-}$ mice during atherosclerosis progression (Supplementary Figure 18E), whereas in *Apoe*$^{-/-}$ mice, the radStrain profile remained unchanged over time (Supplementary Figure 18F). OSI values were significantly elevated in *Apoe*$^{-/-}$ mice in the IR of the DAo, indicating a larger amount of oscillating flow and backflow compared to *Ldlr*$^{-/-}$ mice (Figure 44G), which aligned after 8 weeks of diet (Figure 44H). During atherosclerosis progression, *Ldlr*$^{-/-}$ mice revealed a moderate reduction of OSI around the IR of the DAo and small reductions of OSI in the other parts of the aorta (Supplementary Figure 18G). In *Apoe*$^{-/-}$ mice, on the other hand, an increase of OSI was detected in the DAo and a small reduction in the AAo and top region (Supplementary Figure 18H).

4.3.8 THE SHEAR STRESS PROFILE, BUT NOT THE ATHEROGENIC INDEX OF PLASMA PREDICTS PLAQUE BURDEN

Analysis of the basal WSS profile in both mouse models revealed a more atherogenic flow and WSS profile in *Apoe*$^{-/-}$ compared to *Ldlr*$^{-/-}$ mice with no differences in the atherogenic index of plasma despite differences in serum lipoprotein profile. Therefore, after analysis of changes in the WSS and OSI profiles, changes in blood and serum parameters as well as the atherogenic index of plasma were again examined during atherosclerosis progression (Supplementary Figure 19, Supplementary Figure 20). Notably, hematocrit levels were significantly elevated in *Apoe*$^{-/-}$ compared to *Ldlr*$^{-/-}$ mice after 8 weeks of WD, in line with higher leukocyte counts in blood (Supplementary Figure 19A). Moreover, cholesterol levels increased significantly in both mouse models in response to Western diet feeding, with no further alterations in *Apoe*$^{-/-}$ mice but an additional increase in cholesterol levels in *Ldlr*$^{-/-}$ mice at 8 weeks compared to 4 weeks of diet (Supplementary Figure 19B). Serum triglyceride levels slightly increased in *Apoe*$^{-/-}$ mice after 8 weeks of diet, and in *Ldlr*$^{-/-}$ mice, an increase was noted when compared to baseline levels and to *Apoe*$^{-/-}$ mice at both time points (Supplementary Figure 19C). Serum lipoprotein concentrations (Supplementary Figure 19D) and proportions (Supplementary Figure 19G, Supplementary Figure 20) of vLDL typically increased higher in *Apoe*$^{-/-}$ mice compared to *Ldlr*$^{-/-}$ mice, whereas serum LDL was significantly higher in *Ldlr*$^{-/-}$ mice (Supplementary Figure 19E, H). The HDL fraction showed a steady, significant decrease over time in both models (Supplementary Figure 19F, I). The AIP was calculated from serum triglyceride and HDL concentrations, resulting in an unexpectedly higher atherogenic risk in *Ldlr*$^{-/-}$ mice after 4 weeks of WD (Figure 45C). Furthermore, plaque burden was examined in the aortic arch of *Apoe*$^{-/-}$ and *Ldlr*$^{-/-}$ mice, resulting in significantly higher plaque areas in *Apoe*$^{-/-}$ compared to *Ldlr*$^{-/-}$ mice after 8 weeks of diet, indicating that baseline flow and WSS profiles could be more crucial for atherosclerotic plaque burden than the serum composition (Figure 45A, B).

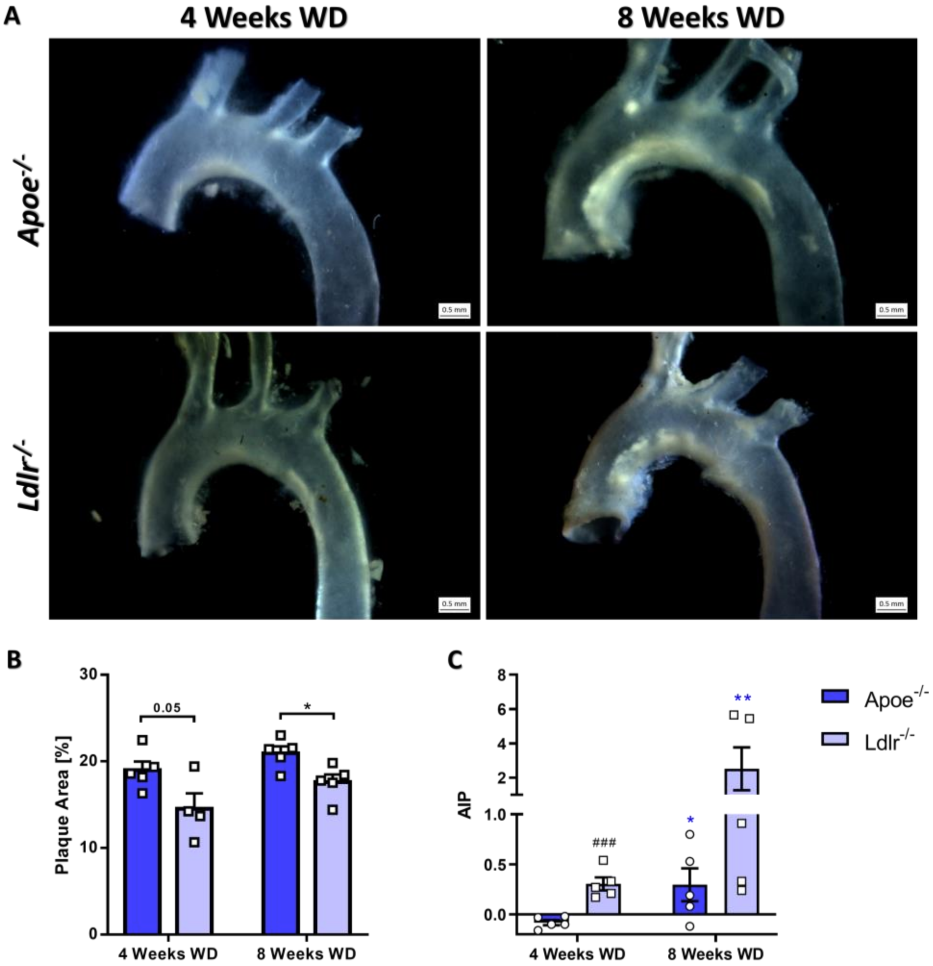

Figure 45: The WSS profile, but not the atherogenic index of plasma predicts plaque burden. **A** Stereomicroscopic images of the aortic arches of exemplary *Apoe*$^{-/-}$ and *Ldlr*$^{-/-}$ mice after 4 and 8 weeks of diet. **B** Analysis of the plaque area in the aortic arch after ORO staining. *Apoe*$^{-/-}$ mice show significantly higher plaque area after 8 weeks of diet. **C** Atherogenic index of plasma. *Ldlr*$^{-/-}$ mice have significantly higher risk compared to *Apoe*$^{-/-}$ mice at both timepoints. Significances to baseline are marked with * (lower) and * (higher), to 4 Weeks WD with $^{+}$ and to *Apoe*$^{-/-}$ with $^{\#}$.

4.4 DISCUSSION

Atherosclerosis is of multifactorial nature, including chronic inflammation processes and lipid metabolism acting together [28], but also altered hemodynamics [32, 307]. Low and oscillatory WSS play a central role in atherosclerosis development and progression as well as plaque composition, favoring endothelial cell activation, inflammation and influencing local lipid deposition [19, 308]. In particular the *Apoe*$^{-/-}$ and the *Ldlr*$^{-/-}$ mouse are well-established models in basic and preclinical atherosclerosis research. However, the underlying mechanism causing atherosclerosis differs between these models, and there are certain other differences regarding inflammation, lipid profile and plaque development described [39, 54, 55, 59], but studies incorporating both models are still rare. Despite the well-known relationship of altered hemodynamics and atherosclerosis and the lipid profile resembling the human one, the *Ldlr*$^{-/-}$ mouse is still neglected in studies of flow and WSS. Therefore, we aimed to characterize the aortic geometry and hemodynamic changes in both models at baseline levels and during atherosclerosis progression.

We here show for the first time significant differences between the examined genotypes at baseline levels. This covers, inter alia: Significantly smaller aortic volumes (max, min, mean) and aortic radii (ascending, top, descending) in *Ldlr*$^{-/-}$ mice in comparison to *Apoe*$^{-/-}$ mice. In contrast, *Apoe*$^{-/-}$ mice feature the largest aortic volumes and radii. The results for the aortic radiii are in good agreement with previous results published for 6 weeks old mice (e.g. *Apoe*$^{-/-}$: AAo 0.70mm, DAo 0.54mm [9]. Interestingly, significant differences were also observed for the ratio between the aortic volume and the body weight of the animals, where the aortic volume was normalized to the body weight. Here again, *Ldlr*$^{-/-}$ mice exhibited the smallest values, in particular in comparison to the *Apoe*$^{-/-}$ group. Moreover, analysis of the aortic curvature revealed that *Ldlr*$^{-/-}$ mice have significantly elevated curvature values in the ascending aorta relative to the *Apoe*$^{-/-}$ mouse model at baseline levels. This significant difference is indicative of a more abrupt transition between the straight trunk of the AAo and the aortic arch in *Ldlr*$^{-/-}$ mice. In *Apoe*$^{-/-}$ mice, on the other hand, a smoother transition between the AAo and aortic arch was noticeable. This conclusion is also supported by the k_x value, which was significantly higher in *Ldlr*$^{-/-}$ mice. Interestingly, after 4 weeks of diet, an alignment of mean aortic curvature was noticeable, which also results in less significant differences in the distribution of steepness angles. In *Ldlr*$^{-/-}$ mice, all curvature components significantly decreased. which may be explained by the growth of the animals and thus, to significant structural changes. In *Apoe*$^{-/-}$ mice, on the other hand, no changes of the curvature components are noticeable between the baseline and 4 weeks. After 8 weeks, however, the k_y and k_z components are significantly higher in *Apoe*$^{-/-}$ mice, indicating a larger shear and a more pointed aortic arch in comparison to *Ldlr*$^{-/-}$ mice. Overall, the examinations indicate that in particular the two atherosclerotic mouse models feature significantly different initial geometric conditions at baseline levels.

At baseline levels, no significant differences between peak flow, net flow and volume flow were observed between the three genotypes, indicating no differences in aortic inflow. Therefore, an impact of different inflow rates on the resulting flow profiles can be excluded. However, much steeper and more symmetric flow profiles were detected in the *Ldlr*$^{-/-}$ group, which can most likely be explained by the much smaller aortic radii and the differences in aortic curvature. Due to the more curved aortic arch, a straighter trunk is observable in *Ldlr*$^{-/-}$ mice, which results in more symmetric flow profiles in comparison to the other atherosclerotic mouse group. *Apoe*$^{-/-}$ mice, on the other hand, feature the largest variance and much larger skewness of the steepness angles in comparison to the other two mouse groups, indicating significantly more asymmetric flow profiles compared to *Ldlr*$^{-/-}$ mice. These noticeable differences are still present, however less significant after 4 weeks of WD, which may be explainable by the alignment of aortic curvature in both mouse groups due to growth (see above) and are also observable after 8 weeks of WD. In conclusion, the results indicate that the shape of the flow profiles is more likely influenced by the aortic geometry rather than the input flow, as significantly different geometric features were observed but no differences in flow rates.

Aortic PWV revealed no significant differences in aortic elasticity between the three genotypes at baseline level. PWV values were lower compared to studies performed at later measurement days (in *Apoe*$^{-/-}$ mice: 1.2±0.4 m/s versus 1.7±0.1 m/s at 6 weeks [9] and 2.6±0.1 m/s at 18 weeks [16]. The results indicate higher arterial elasticity at a very young age. During growth and the development of plaques, the aorta becomes equally stiffer in both models, resulting in higher PWV values.

Next to loss of arterial elasticity and therefore increasing PWV during atherosclerosis progression, the local hemodynamic conditions are relevant to understand the interplay of altered WSS profiles and atherogenesis. When comparing the spatially and temporally averaged values of the WSS components, no significant differences could be observed between the three genotypes at baseline levels. However, only global information about differences in hemodynamics is provided by the analysis of mean WSS values, which provides reliable information about hemodynamic conditions in advanced atherosclerosis. This was recently shown in a study between healthy wild type and atherosclerotic *Apoe*$^{-/-}$ mice, where the subsequent generation of 2D-projection maps localized the spatially resolved information about significant changes in all WSS components and OSI during ageing and atherosclerosis [5], see also Chapter 3. Interestingly, despite showing no significant differences in aortic global WSS in all three genotypes, the more detailed analysis of the 2D-projection maps revealed large significant spots in the presented study, where the *Ldlr*$^{-/-}$ mouse markedly deviates from the two other genotypes, pointing out the importance of spatially resolved WSS and OSI analysis. When comparing *Apoe*$^{-/-}$ with *Ldlr*$^{-/-}$ mice, decreased longWSS values were observable especially around the inner radius of the DAo in *Ldlr*$^{-/-}$ mice, whereas much lower values and a much steeper WSS gradient between outer and inner radius were detected in the AAo of *Apoe*$^{-/-}$ mice, which is most likely due to the more asymmetric flow profiles. The deviations are similar, however, slightly less significant when comparing *Ldlr*$^{-/-}$ mice with the wild type control group. Moreover, only small spots of significant differences were observed when *Apoe*$^{-/-}$ and WT mice are compared, indicating a similar aortic WSS profile, which most likely results from the similar geometry between these two genotypes. Since this study revealed large differences in aortic volumes, radii and curvature but no deviations in the flow rates, the genotype-specific differences in the longWSS profiles are more likely caused by the different geometric features rather than the input flow. After four weeks of western diet, differences between both atherosclerotic mouse models are mostly observed in the top region of the aorta. Here, *Apoe*$^{-/-}$ mice featured significantly elevated longWSS values around the anterior and posterior side as well as the outer radius relative to *Ldlr*$^{-/-}$ mice. However, after eight weeks of western diet, less deviations between the two atherosclerotic mouse models were observed. This may be explained by the completed growth process of the mice or even due to plaque growth, which alters the vascular geometry. However, to clarify this, further investigation is needed.

Regarding circWSS, the comparison of both atherosclerotic mouse models revealed reduced values between the anterior side and inner radius of the ascending aorta in *Apoe*$^{-/-}$ mice, indicating more helical flow in *Ldlr*$^{-/-}$ mice. The deviations are even larger when *Ldlr*$^{-/-}$ mice are compared with WT mice. Here, the difference map indicated that circWSS was elevated in the AAo and top region near the inner radius in the *Ldlr*$^{-/-}$ model. In the DAo, on the other hand, smaller negative circWSS were detected. In conclusion, *Ldlr*$^{-/-}$ mice featured the largest amount of positive helical flow in the AAo of all genotypes. The control group, on the other hand, exhibited the largest negative helical flow in the DAo compared to the other two groups. Analogues to the longitudinal component, the observed deviations in circWSS are most likely caused by the differences in the aortic radius and, at least in the AAo, by the differences in curvature. After four weeks of western diet, significant differences between both atherosclerotic groups were observed, especially around the inner radius and the anterior and posterior side. Interestingly, *Apoe*$^{-/-}$ mice featured larger circWSS values relative to *Ldlr*$^{-/-}$ mice, indicating large hemodynamic changes between four and eight weeks and a converse development of helical flow in both atherosclerotic mouse models. After 8 weeks of WD and similar to the development of the longitudinal component, an adjustment of circWSS values between both atherosclerotic mouse groups is noticeable.

Similar to the WSS, no significant differences in spatially averaged OSI values could be observed. The detailed 2D-comparison between the two atherosclerotic mouse models, however, revealed significantly reduced OSI in the AAo and significantly elevated OSI in the DAo of *Ldlr*$^{-/-}$ mice. When comparing *Apoe*$^{-/-}$ with WT mice, the control group featured the smallest values. These differences between genotypes may be explained as well by the differences in geometry and the shape of the flow profiles. As shown above, the *Apoe*$^{-/-}$ group exhibited the larges aortic radii and the largest skewness of flow profiles, which may result in more recirculating and temporally oscillating flow in the region around the AAo. *Ldlr*$^{-/-}$ mice, on the other hand, featured more steeper and symmetric flow profiles, leading to a more straightforward flow direction. After four weeks of western diet, large differences of OSI between both atherosclerotic groups were observed in the descending aorta. Interestingly, *Apoe*$^{-/-}$ mice showed the largest OSI values. Similar to the temporal development of the WSS components, an adjustment of OSI values became apparent after eight weeks of western diet. These observations as well as the temporal development of the longWSS and circWSS suggest that the natural growth process plays an important role in the characteristics of the flow profiles and that the influence of plaque distribution on the WSS values may only become predominant in later time points [3]. The inner curvature of the aorta is a highly atherosusceptible region, as low and oscillatory WSS conditions predominate. The different shear stress and OSI profiles, with *Apoe*$^{-/-}$ mice having decreased longWSS and increased OSI values in the AAo and *Ldlr*$^{-/-}$ mice in the DAo, suggest an influence of distinct basal aortic geometries in both models on the resulting plaque development.

Next to the geometry, blood hematocrit is known to strongly correlate with blood viscosity [309] – a parameter also influencing the WSS and atherosclerosis [61]. Examination of hematocrit baseline levels revealed similar blood viscosity in all models, therefore an influence on the basal WSS profiles can be excluded. However, with atherosclerosis progression and consequently elevated circulating immune cells in the blood due to inflammation, hematocrit levels increased significantly in both atherosclerotic mouse models over time, with *Apoe*$^{-/-}$ mice having significantly higher values than *Ldlr*$^{-/-}$ mice after 8 weeks of diet. A study conducted in *Apoe*$^{-/-}$ mice by Tous *et al.* revealed that elevated circulating blood cells enhance atherosclerosis, whereas decreased circulating blood cells attenuate atherosclerosis progression, pointing out the role of hemorheology in disease progression [309]. Together with the significantly increased plaque area in *Apoe*$^{-/-}$ mice after 8 weeks of diet, these results indicate an interplay between altered shear stress due to elevated hematocrit levels and the rate of atherosclerosis progression. However, WSS profiles were similar between the atherosclerotic models at this time point. A correction of the WSS calculation with hematocrit levels and therefore blood viscosity [306] should be conducted in future studies to further clarify the role of altered viscosity and WSS in atherosclerosis to potentially reveal viscosity-dependent differences in regional WSS profiles.

Risk factors of atherosclerosis furthermore include high triglyceride and cholesterol and levels. At baseline levels, triglyceride levels were elevated in both atherosclerotic mouse models compared to the control group, but lower than values found for 8-week-old *Apoe*$^{-/-}$ and *Ldlr*$^{-/-}$ mice on normal chow ([310]), which may be explained by the younger age and different food composition in this study. Interestingly, during diet application and atherosclerosis development, *Ldlr*$^{-/-}$ mice featured significantly higher triglyceride levels than *Apoe*$^{-/-}$ mice at both time points. Analysis of basal cholesterol levels in all genotypes showed strongly elevated cholesterol levels in both atherosclerosis models compared to the control group and slightly elevated levels in *Ldlr*$^{-/-}$ mice compared to *Apoe*$^{-/-}$ mice, with values corresponding well with literature [310]. On Western diet, cholesterol levels increased, with *Ldlr*$^{-/-}$ mice having slightly higher values than *Apoe*$^{-/-}$ mice [311]. The *Apoe*$^{-/-}$ and *Ldlr*$^{-/-}$ mouse model are furthermore known to have different basal lipid profiles, resulting from the underlying mechanisms causing atherosclerosis initiation and progression. We therefore investigated basal lipid profiles as well as changes in lipid profiles during atheroprogression, showing typical model-related distributions of lipoproteins being comparable to literature [59]. To predict the basal and changing risk during diet application of both atherosclerotic mouse models, the atherogenic index of plasma (AIP) was calculated, which is a logarithmically transformed ratio of triglyceride concentration to HDL-cholesterol and a well-established marker for assessing the risk of CVD [312], revealing no significant differences in risk at baseline levels in all genotypes. Surprisingly, with ongoing diet and atherosclerosis progression, the *Ldlr*$^{-/-}$ mouse featured a significantly increased risk already after 4 weeks of diet, despite higher HDL-fractions compared to *Apoe*$^{-/-}$ mice. This is most likely caused by the highly increased triglyceride levels found in *Ldlr*$^{-/-}$ mice. Despite the differences in blood and serum lipid composition, both models are described to develop plaques at the same positions in the vascular tree, namely the inner curvature of the aorta, branch points and bifurcations [54], sharing the same hemodynamic characteristics: Regions of low and oscillatory WSS, and pointing out the importance and major role of hemodynamics in atherosclerosis development and progression. However, they are also known to differ in terms of plaque development rate and size [39, 54, 55, 59]. Nevertheless, until now the exact reason is still not clear and investigations of plaque composition in different regions of the aortic arch in both models are missing. In our study, examination of aortic atherosclerotic plaque burden revealed significantly larger plaque areas in *Apoe*$^{-/-}$ mice compared to *Ldlr*$^{-/-}$ mice after 8 weeks of diet, despite the significantly higher risk assessed through the AIP in *Ldlr*$^{-/-}$ mice, therefore suggesting that the basal WSS profile could have a more determinant role in atherosclerosis than the lipid profile.

Taken together, our data show that the atherosclerotic *Apoe*$^{-/-}$ and *Ldlr*$^{-/-}$ mouse models feature significantly different aortic geometries at baseline levels, resulting in more symmetric flow profiles in the *Ldlr*$^{-/-}$ mouse and more asymmetric flow profiles in *Apoe*$^{-/-}$ mice. As various parameters possibly influencing the WSS were similar in all models at baseline levels, there is strong evidence that the aortic geometry plays a significant role in the resulting flow- and WSS profiles, leading to a stronger WSS gradient in the inner curvature of the ascending aorta in the *Apoe*$^{-/-}$ mouse and in the descending aorta in the *Ldlr*$^{-/-}$ mouse. Moreover, these regions of low WSS simultaneously feature high OSI values - Both hemodynamic conditions are known to drive plaque development and influence plaque composition. Therefore, together with the higher AIP in *Ldlr*$^{-/-}$ mice but the larger plaque areas in *Apoe*$^{-/-}$ mice, there is evidence that both models feature distinct patterns and/or rates of plaque development, with *Apoe*$^{-/-}$ mice being more atherosusceptible in the ascending aorta and *Ldlr*$^{-/-}$ mice in the descending aorta.

However, these potential coherences need to be clarified in future studies. CFD is a powerful tool to model atherosclerosis and to set up experiments, which cannot or only hardly be performed *in vivo*. The main differences found in this study are the distinct aortic geometry, influencing the WSS profile and the model-specific lipid profile in the atherosclerotic mouse models. Therefore, experiments with combinations of all different parameters (e.g., aortic geometry of the *Ldlr*$^{-/-}$ mouse with the lipid profile of the *Apoe*$^{-/-}$ mouse) simulating the resulting plaque development and composition would be desirable. Thon *et al.* have done pioneering work by developing a quantitative model of early atherosclerotic plaques using *in vitro* experiments as input-parameters, including inflammatory, lipid and macrophage dynamics in early atherosclerotic plaques [288] and also incorporated the influence of the pulsatile blood flow and the compliance of the artery wall to the atherosclerotic process, revealing pulsatile flow to be crucial, whereas compliance only has a minor influence [289]. Moreover, they found out that regions in arteries with an approximate wall shear stress exposure below 20% of the average exposure and their surroundings are potential regions where progression-prone atherosclerotic plaques develop [290]. However, most of the input parameters were taken from literature. Measurements of biological input parameters like cholesterol, lipid profile etc., combined with WSS profiles measured in the same mice could even further improve this model and help to unravel the complex interplay between WSS profiles, lipids and atherogenesis.

4.5 SUPPLEMENTARY FILES

4.5.1 SUPPLEMENTARY METHODS

4.5.1.1 Aortic Curvature

For a curve given as function $f\colon \mathbb{R} \to \mathbb{R}, y = f(x)$, the angle of its slope, α, is given as

$$\frac{dy}{dx} = \tan\alpha \qquad (1)$$

Hence, according to the chain rule of differentiation, the second derivation is:

$$\frac{d^2y}{dx^2} = (1 + \tan\alpha^2)\frac{d\alpha}{dx} \qquad (2)$$

Combining (1) and (2) leads to:

$$\frac{d^2y}{dx^2} = \left(1 + \left(\frac{dy}{dx}\right)^2\right)\frac{d\alpha}{dx} \qquad (3)$$

The infinitesimal arc length of the curve, *ds,* is defined as:

$$ds^2 = dx^2 + dy^2 \qquad (4)$$

Therefore:

$$\frac{ds}{dx} = \sqrt{1 + \left(\frac{dy^2}{dx^2}\right)} \qquad (5)$$

The curvature k_r, is defined as $k_r = \frac{d\alpha}{ds}$. Using (3) + (5), this results into:

$$k_r = \frac{d\alpha}{ds} = \frac{\frac{d\alpha}{dx}}{\frac{ds}{dx}} = \frac{\frac{d^2y}{dx^2}}{\left(1 + \left(\frac{dy}{dx}\right)^2\right)^{\frac{3}{2}}} \qquad (6)$$

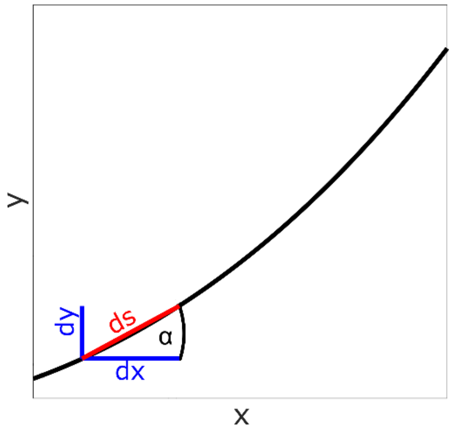

Illustration of the calculation of aortic curvature (in 2D for more simplicity). Black curve: Section of centerline. $\mathrm{ds} = \sqrt{\mathrm{dx}^2 + \mathrm{dy}^2}$

4.5.2 SUPPLEMENTARY FIGURES

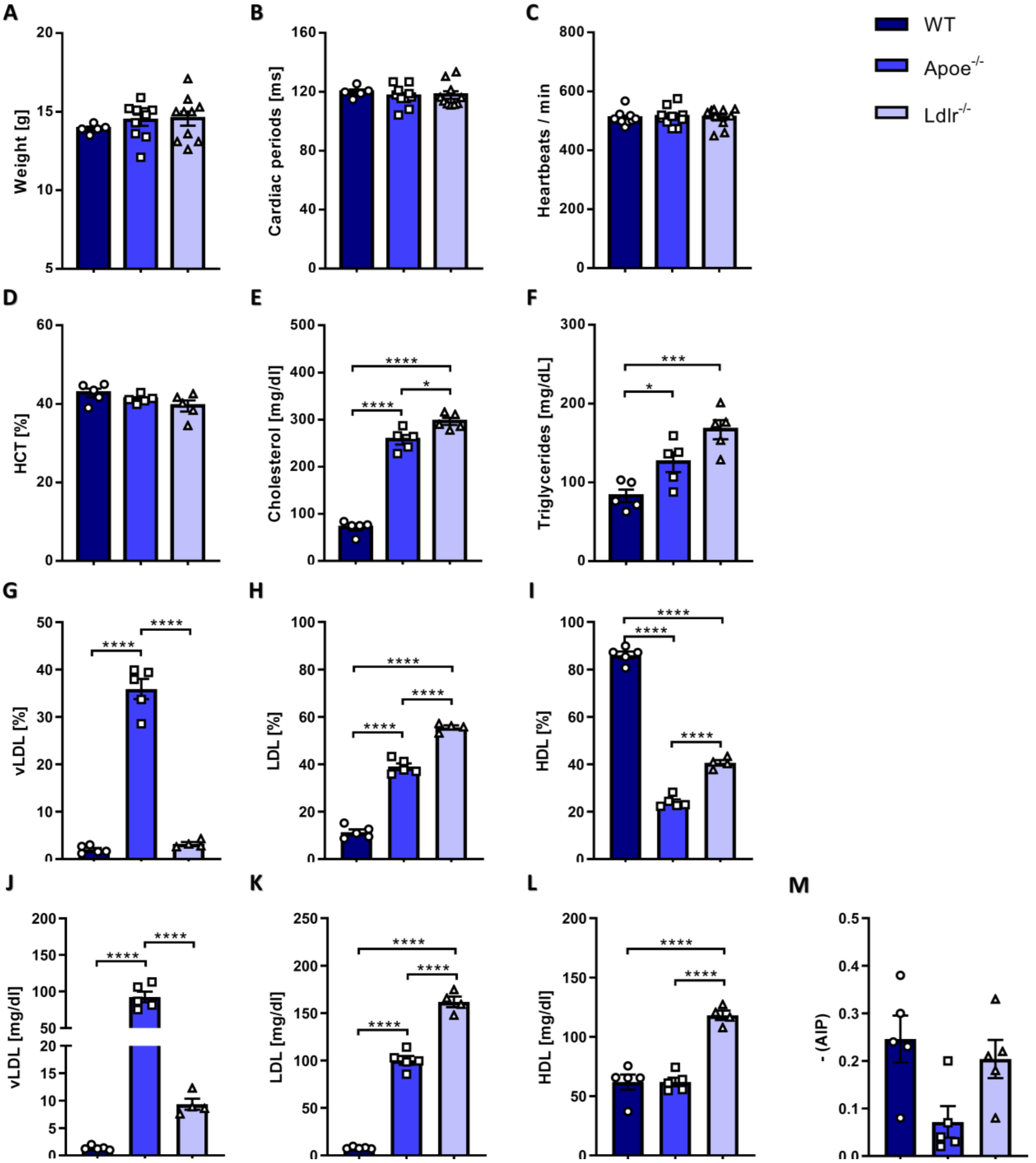

Supplementary Figure 15: Basal characterization of WT, *Apoe*$^{-/-}$ and *Ldlr*$^{-/-}$ mice only reveals differences in lipid profiles. **A** Weight of all genotypes showed no differences. **B** Cardiac periods and **C** heartrates are similar in all genotypes. **D** Hematocrit analysis reveals no differences between the genotypes. **E** Serum cholesterol is significantly increased in *Apoe*$^{-/-}$ and *Ldlr*$^{-/-}$ Mice compared to WT mice and significantly higher in *Ldlr*$^{-/-}$ compared to *Apoe*$^{-/-}$ mice. **F** Serum triglycerides are significantly increased in *Apoe*$^{-/-}$ and *Ldlr*$^{-/-}$ mice compared to WT mice. **G-I** Serum lipoprotein proportions and **J-L** concentrations. **G, J** vLDL is significantly increased in *Apoe*$^{-/-}$ mice. **H, K** LDL is significantly elevated in *Apoe*$^{-/-}$ and *Ldlr*$^{-/-}$ compared to WT mice and in *Apoe*$^{-/-}$ compared to *Ldlr*$^{-/-}$ mice. **I, L** HDL proportion is highest in WT mice, but concentration is elevated in *Ldlr*$^{-/-}$ compared to WT and *Apoe*$^{-/-}$ mice. **J** Atherogenic index of plasma (AIP) shows no significant differences.

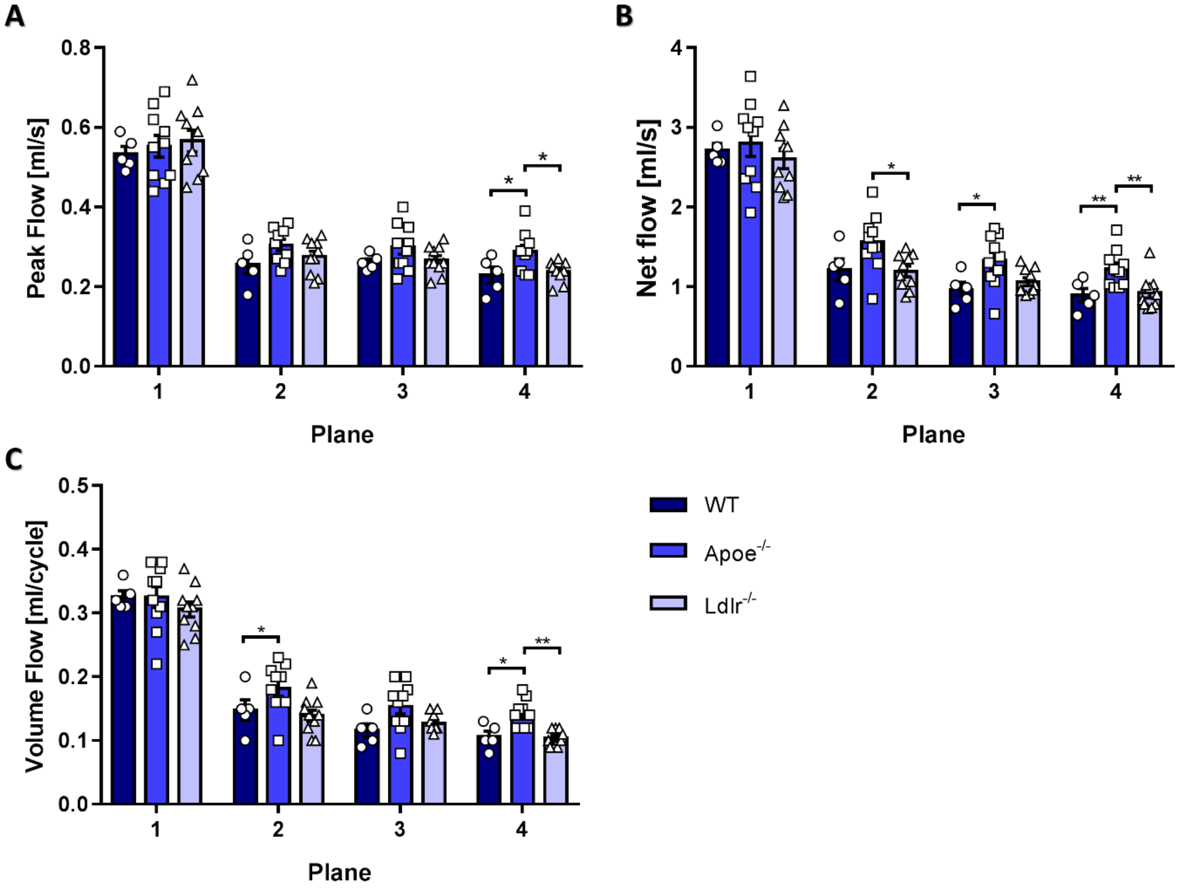

Supplementary Figure 16: Peak flow, net flow and volume flow in WT, *Apoe*$^{-/-}$ and *Ldlr*$^{-/-}$ mice at baseline levels. **A** Peak flow in all analysis planes. Peak flow values are significantly higher in *Apoe*$^{-/-}$ compared to *Ldlr*$^{-/-}$ and WT mice in plane 4. **B** Net flow is increased in *Apoe*$^{-/-}$ compared to *Ldlr*$^{-/-}$ in plane 2 and 4 and to WT in plane 3. **C** Volume flow is increased in *Apoe*$^{-/-}$ compared to WT in plane 2 and in plane 4 compared to WT and *Ldlr*$^{-/-}$.

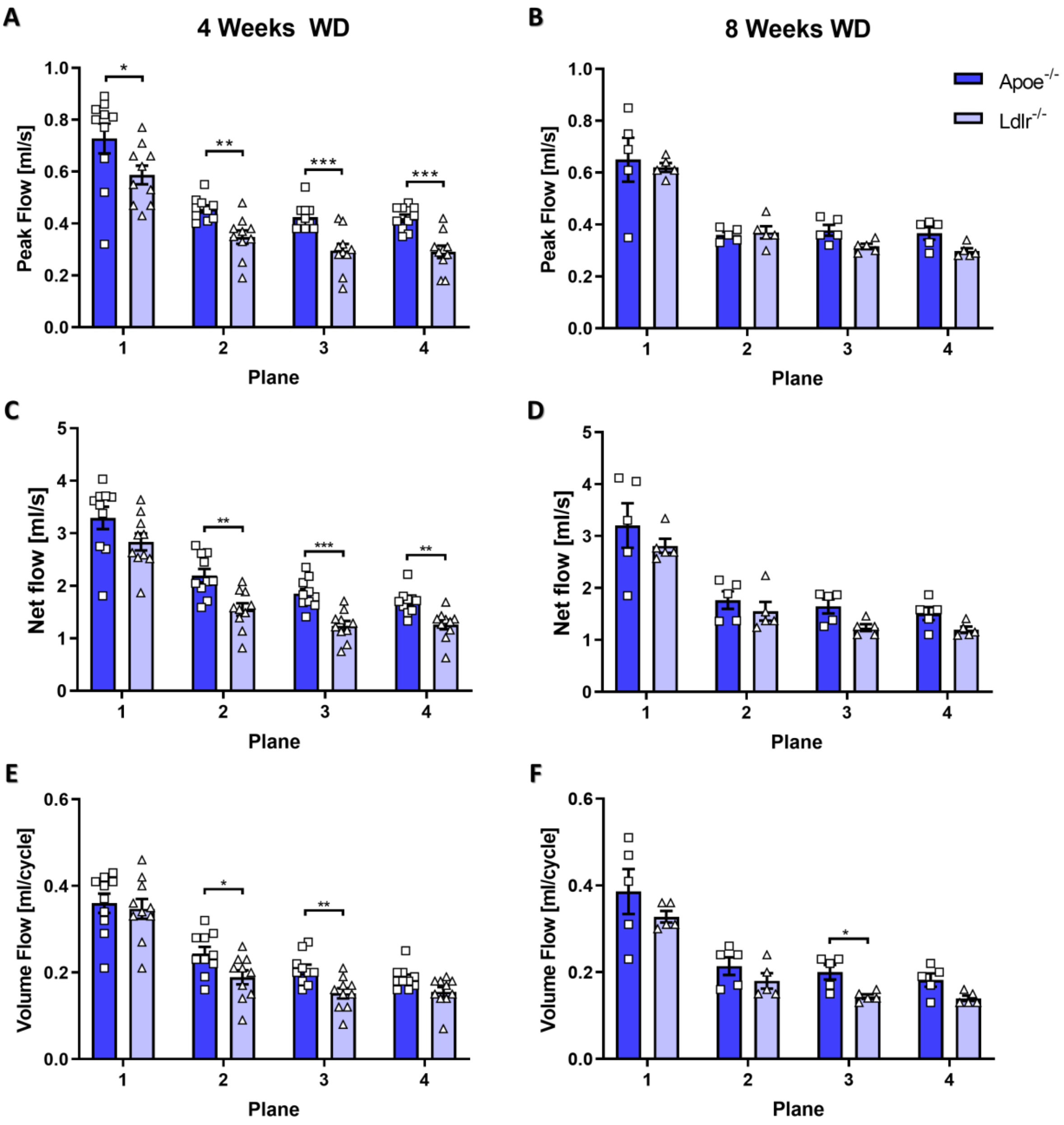

Supplementary Figure 17: Peak flow, net flow and volume flow of *Apoe*$^{-/-}$ and *Ldlr*$^{-/-}$ mice after 4 and 8 weeks of WD. A Peak flow after 4 weeks and **B** 8 weeks of WD. Peak flow is significantly elevated in all planes in *Apoe*$^{-/-}$ mice after 4 weeks of WD, but aligns with *Ldlr*$^{-/-}$ mice after 8 weeks of WD. **C** Net flow after 4 weeks and **D** 8 weeks of WD. Net flow is significantly elevated in planes 2-4 in *Apoe*$^{-/-}$ mice after 4 weeks of WD, but aligns with *Ldlr*$^{-/-}$ mice after 8 weeks of WD. **E** Net flow after 4 weeks and **F** 8 weeks of WD. Volume flow is significantly elevated in planes 2 and 3 in *Apoe*$^{-/-}$ mice at both time points.

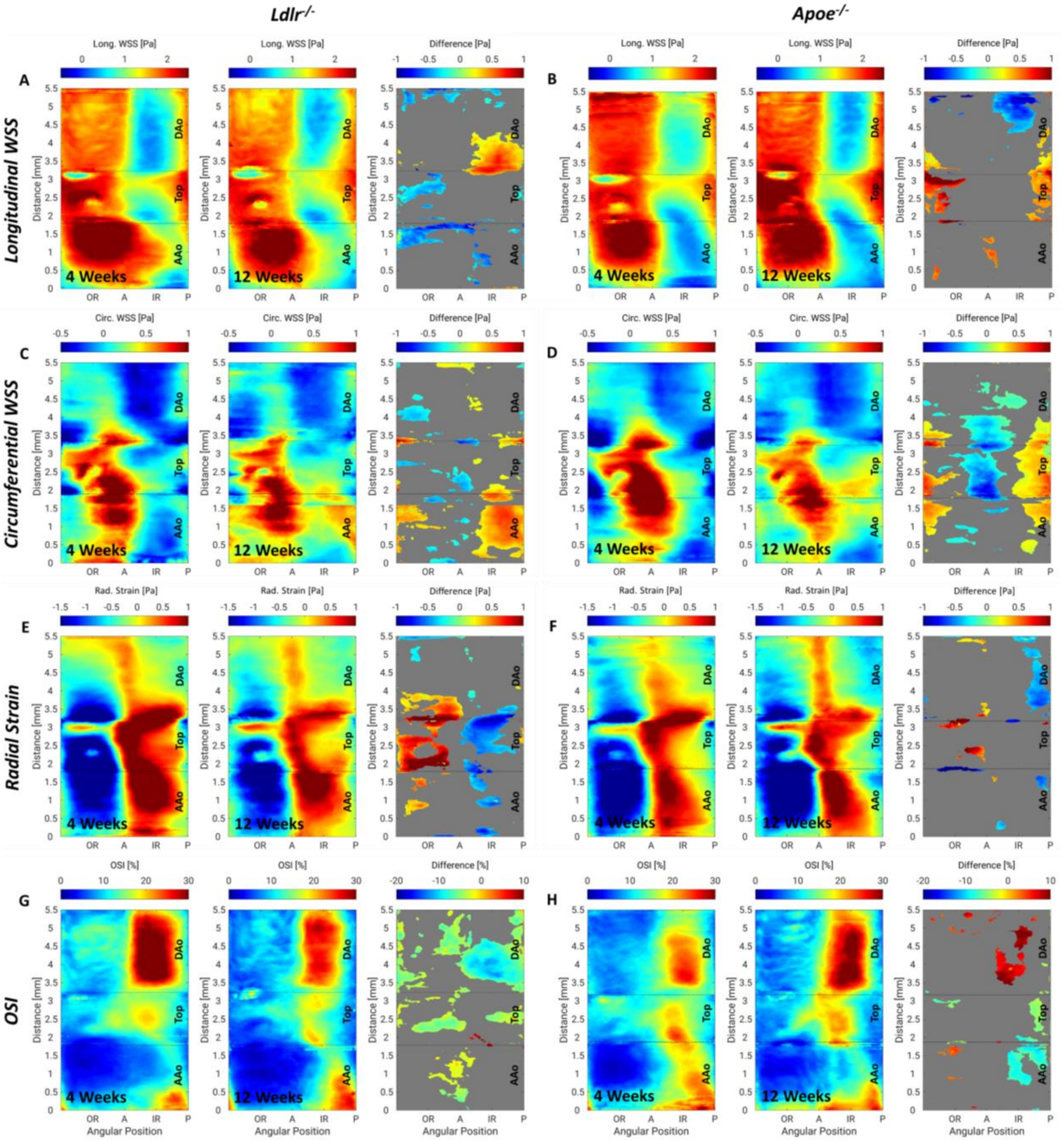

Supplementary Figure 18: Intragroup comparison of changes in the WSS and OSI profile of *Apoe*$^{-/-}$ and *Ldlr*$^{-/-}$ mice during atherosclerosis progression. **A** Changes in longWSS profile of *Ldlr*$^{-/-}$ and **B** *Apoe*$^{-/-}$ mice during 8 weeks of WD. Only smaller significant areas of changes are observed. **C** Changes in circWSS profile of *Ldlr*$^{-/-}$ and **D** *Apoe*$^{-/-}$ mice during 8 weeks of WD. Changes are observed throughout the aortic arch. **E** Changes in radStrain profile of *Ldlr*$^{-/-}$ and **F** *Apoe*$^{-/-}$ mice during 8 weeks of WD. *Ldlr*$^{-/-}$ mice show strong changes of radStrain values. **G** Changes in OSI profile of *Ldlr*$^{-/-}$ and **H** *Apoe*$^{-/-}$ mice during 8 weeks of WD. *Ldlr*$^{-/-}$ mice show larger areas of changing OSI values, whereas *Apoe*$^{-/-}$ mice show stronger changes.

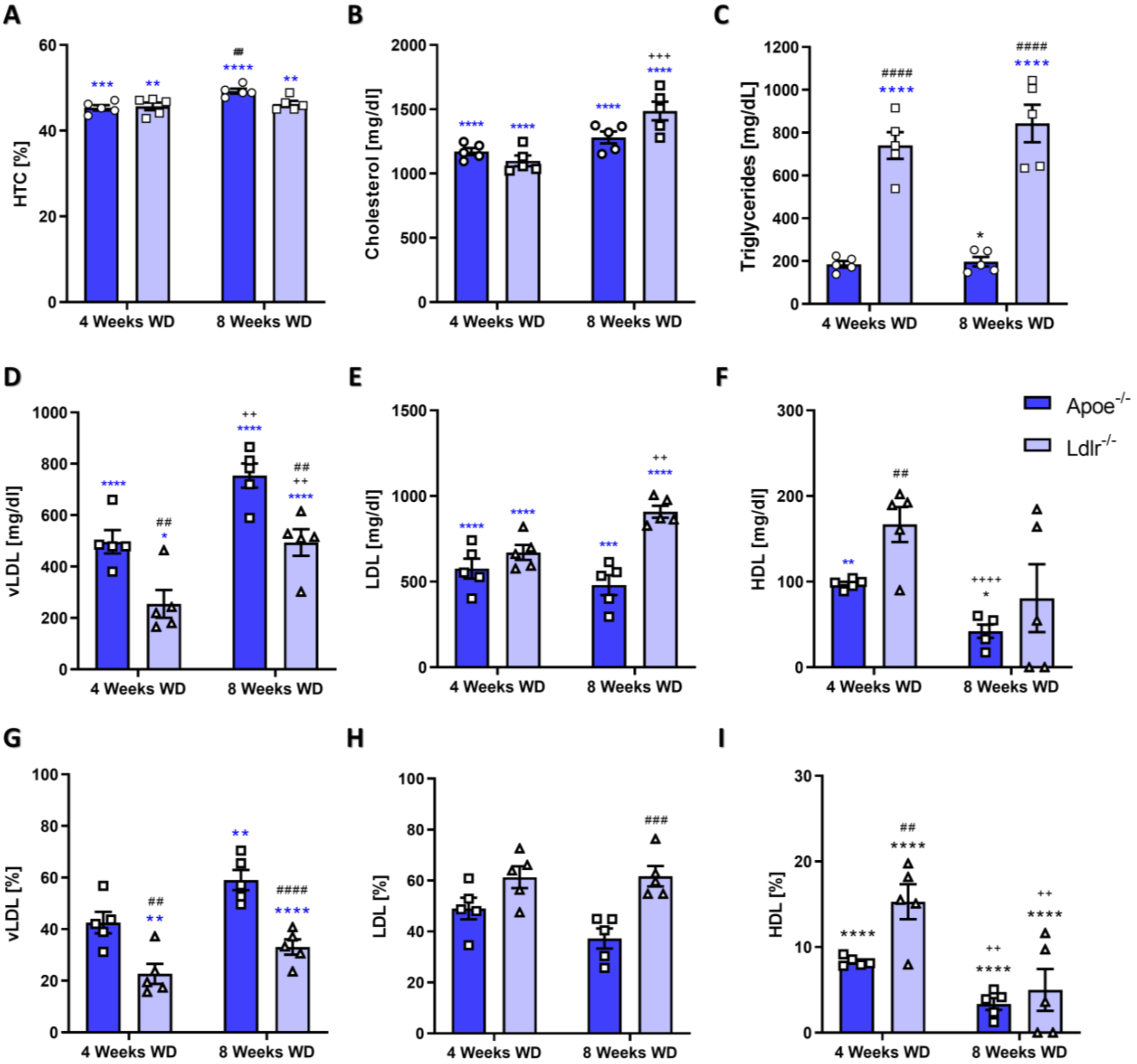

Supplementary Figure 19: Blood and serum parameters of *Ldlr*$^{-/-}$ and *Apoe*$^{-/-}$ mice during atherosclerosis progression. **A** Hematocrit is elevated in *Apoe*$^{-/-}$ mice compared to *Ldlr*$^{-/-}$ mice after 8 weeks of WD. **B** Cholesterol remains on a constant level in *Apoe*$^{-/-}$ mice during diet, whereas in *Ldlr*$^{-/-}$ mice, a significant increase is noticed from 4 to 8 weeks of WD. **C** Triglyceride level slightly increases in *Apoe*$^{-/-}$ mice after 8 weeks of diet. In *Ldlr*$^{-/-}$ mice, a high significant increase is noticed compared to baseline levels and to *Apoe*$^{-/-}$ mice. **D** vLDL concentration significantly increases in both mouse models but is higher in *Apoe*$^{-/-}$ mice. **E** LDL significantly increases over time in both mouse models, whereas HDL concentration (**F**) decreases. G vLDL proportion is significantly higher in *Apoe*$^{-/-}$ mice after western diet. H LDL proportion significantly increases in *Ldlr*$^{-/-}$ mice. **I** HDL fraction shows a steady, significant decrease over time in both models. After 8 weeks of diet, *Apoe*$^{-/-}$ mice show significantly less HDL compared to *Ldlr*$^{-/-}$ mice. Data are presented as mean ± SEM**.** Significances to baseline are marked with * (lower) and * (higher), to 4 Weeks WD with $^{+}$ and to *Apoe*$^{-/-}$ with $^{\#}$.

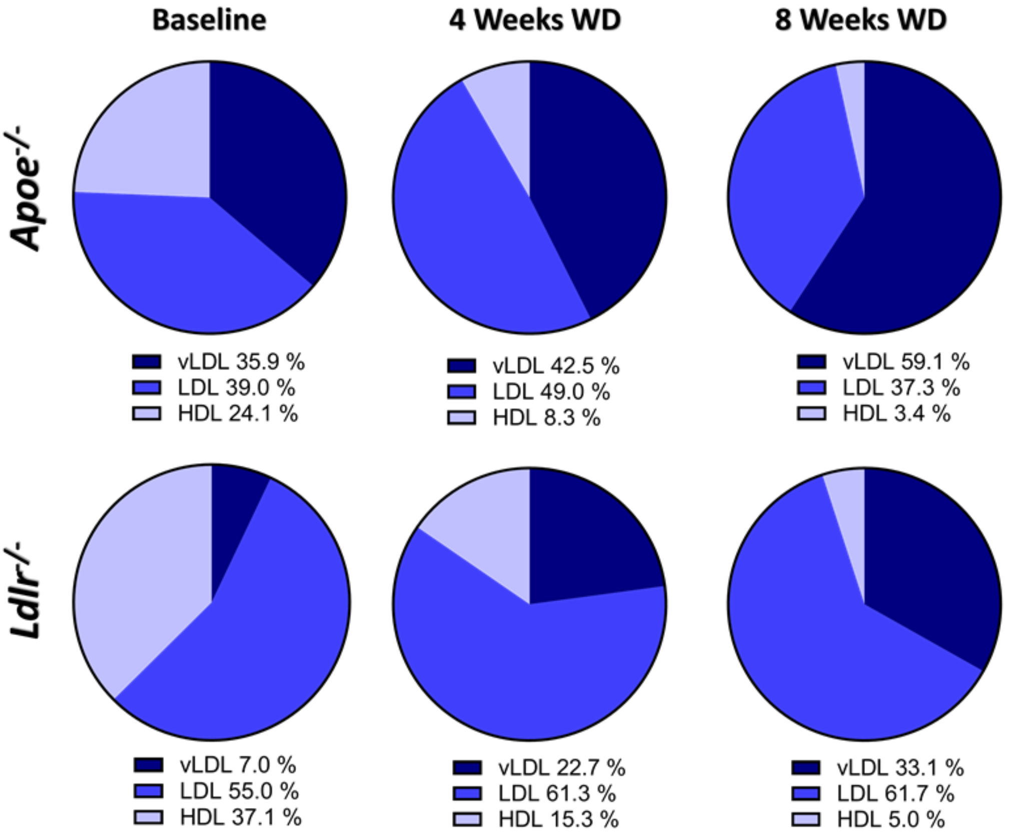

Supplementary Figure 20: Relative serum lipoprotein distribution *Apoe*$^{-/-}$ and *Ldlr*$^{-/-}$ mice at baseline and during atherosclerosis progression.

4.5.3 SUPPLEMENTARY TABLES

Supplementary Table 3: Basal Characterization of *Apoe*$^{-/-}$ and *Ldlr*$^{-/-}$ mice over time. Data are presented as mean ± SD**.** Significances to baseline are marked with * (lower) and * (higher), to 4 Weeks WD with $^{+}$ and to *Apoe*$^{-/-}$ with $^{\#}$.

	***Apoe*$^{-/-}$**	***Ldlr*$^{-/-}$**
Weight [g]		
Baseline	14.5 ± 1.2	14.6 ± 1.4
4 Weeks WD	22.3 ± 1.6 ****	19.7 ± 1.6 ****, $^{\#\#}$
8 Weeks WD	24.3 ± 2.3 ****	21.1 ± 1.2 ****, $^{\#}$
Cardiac Periods [ms]		
Baseline	117.1 ± 7.1	117.8 ± 8.1
4 Weeks WD	110.5 ± 6.4	121.7 ± 11.4 $^{\#}$
8 Weeks WD	120.6 ± 4.4 $^{+}$	117.2 ± 8.5
Heartbeats / min		
Baseline	514.2 ± 32	511.5 ± 33.1
4 Weeks WD	544.7 ± 33.8	497 ± 48.3 $^{\#}$
8 Weeks WD	498.1 ± 18.5 $^{+}$	514.1 ± 35.7

Supplementary Table 4: Basal characterization of flow and WSS in WT, *Apoe*$^{-/-}$ and *Ldlr*$^{-/-}$ mice. Data are presented as mean ± SD. Significances to WT are marked with * and to *Apoe*$^{-/-}$ mice with $^{\#}$.

	Wild type	***Apoe*$^{-/-}$**	***Ldlr*$^{-/-}$**
Aortic inflow (Plane 1)			
Peak Flow [ml/s]	0.53 ± 0.04	0.55 ± 0.09	0.57 ± 0.09
Net Flow [ml/s]	2.72 ± 0.19	2.81 ± 0.53	2.61 ± 0.40
Volume Flow [ml/cycle]	0.33 ± 0.02	0.33 ± 0.05	0.31 ± 0.04
Pulse Wave Velocity	0.99 ± 0.32	1.21 ± 0.39	1.23 ± 0.22
Wall Shear Stress			
Mean Values			
Longitudinal WSS [N/m^2]	1.49 ± 0.13	1.48 ± 0.19	1.53 ± 0.17
Circumferential WSS [N/m^2]	0.35 ± 0.03	0.37 ± 0.10	0.37 ± 0.04
Radial Strain [N/m^2]	0.73 ± 0.07	0.74 ± 0.12	0.78 ± 0.07
Oscillatory Shear Index [%]	11.34 ± 2.01	12.64 ± 1.83	13.05 ± 1.94
Maximum Values			
Longitudinal WSS [N/m^2]	3.89 ± 0.51	4.67 ± 1.38	3.95 ± 0.44
Circumferential WSS [N/m^2]	2.00 ± 0.50	2.03 ± 0.60	2.41 ± 0.34
Radial Strain [N/m^2]	3.61 ± 0.40	3.92 ± 0.86	4.33 ± 0.35
Oscillatory Shear Index [%]	41.21 ± 1.43	43.27 ± 4.07	42.60 ± 5.80

Supplementary Table 5: Global WSS analysis of *Apoe*$^{-/-}$ and *Ldlr*$^{-/-}$ mice for all time points. Data are presented as mean ± SD. Significances to baseline levels are marked with * (lower) or * (higher), to 4 weeks WD with $^{+}$ and to *Apoe*$^{-/-}$ mice with $^{\#}$.

	Apoe$^{-/-}$	*Ldlr*$^{-/-}$
Mean Values		
Longitudinal WSS [N/m^2]		
Baseline	1.48 ± 0.19	1.53 ± 0.17
4 Weeks WD	1.51 ± 0.26	1.30 ± 0.28
8 Weeks WD	1.53 ± 0.28	1.42 ± 0.07
Circumferential WSS [N/m^2]		
Baseline	0.37 ± 0.10	0.37 ± 0.04
4 Weeks WD	0.41 ± 0.07	0.30 ± 0.06 $^{*, \#\#}$
8 Weeks WD	0.41 ± 0.05	0.31 ± 0.03 $^{\#}$
Radial Strain [N/m^2]		
Baseline	0.74 ± 0.12	0.78 ± 0.07
4 Weeks WD	0.76 ± 0.12	0.57 ± 0.11 $^{****, \#\#}$
8 Weeks WD	0.77 ± 0.13	0.61 ± 0.06 $^{**, \#}$
OSI [%]		
Baseline	12.64 ± 1.83	13.05 ± 1.94
4 Weeks WD	12.73 ± 3.14	12.82 ± 2.66
8 Weeks WD	13.09 ± 2.34	11.52 ± 1.59
Maximum Values		
Longitudinal WSS [N/m^2]		
Baseline	3.47 ± 1.38	3.95 ± 0.44
4 Weeks WD	4.83 ± 0.92	3.30 ± 0.49 $^{\#\#}$
8 Weeks WD	5.08 ± 1.15	3.92 ± 0.99
Circumferential WSS [N/m^2]		
Baseline	2.03 ± 0.59	2.41 ± 0.34
4 Weeks WD	2.25 ± 0.56	1.48 ± 0.35 $^{****, \#\#}$
8 Weeks WD	2.27 ± 0.50	1.86 ± 0.32 *
Radial Strain [N/m^2]		
Baseline	3.92 ± 0.86	4.33 ± 0.35
4 Weeks WD	4.18 ± 1.25	3.00 ± 0.70 $^{****, \#}$
8 Weeks WD	4.70 ± 1.28	3.56 ± 0.49 *
OSI [%]		
Baseline	43.72 ± 4.07	42.60 ± 5.80
4 Weeks WD	45.75 ± 2.31	42.92 ± 5.29
8 Weeks WD	44.52 ± 2.65	48.42 ± 10.28

CHAPTER 5

Native And Decellularized Carotid Artery Models For Flow-Related *In Vitro* Atherosclerosis Research

Chapter 5 is planned to be submitted as original research article (Kristina Andelovic, Patrick Winter, Thomas Schwarz, Wolfgang R. Bauer, Volker Herold, Jan Hansmann and Alma Zernecke: "Native and Decellularized Porcine Carotid Artery Models for *in vitro* Atherosclerosis Research". The article is based on the work of the author of this thesis, Kristina Andelovic, who designed the study and planned and performed all experiments and data analysis. The final publication will be supplemented by collaborators and is in preparation at the time of handing in this thesis.

5.1 ABSTRACT

Mouse models of vascular diseases like e.g., atherosclerosis, are well established and frequently used for the investigation of vascular disease development and progression as well as to guide clinical therapy. However, a reduction of animal experiments due to animal welfare is desirable. Moreover, these models are costly and time-consuming while only offering a limited possibility to investigate hemodynamic-related disease development in a controllable manner. To better understand flow-related vascular disease development and progression, *in vitro* artery models reflecting the mechanical and structural properties of native arteries offer a great potential. Here, we report the development of an *in vitro* artery model based on decellularized porcine carotid artery scaffolds, which shows complete acellularity while maintaining the overall ultrastructure, extracellular matrix composition and mechanical strength and offering good cellular adhesion and proliferation. Histological, immunohistochemical, and electron microscopic analyses of the decellularized scaffolds demonstrated the formation of a tight endothelial layer and the presence of collagen and elastin. Subsequently, an MRI-suitable bioreactor setup was established to assess high-resolution 4D hemodynamics in artery models. The results obtained prove the feasibility to quantify arterial volume flow, the vectorial WSS with all three components as well as the PWV in native and tissue-engineered artery models, with all parameters relevant for flow-related disease research. Furthermore, the three-dimensional assessment of the vessel wall morphology was achieved to pave the way for the identification of first atherosclerotic processes like vessel wall thickening in *in vitro* vascular disease models. Therefore, the proposed artery model can be used together with the MRI-suitable bioreactor system to non-invasively study the role of arterial hemodynamics in vascular diseases as well as the effect of new therapeutic drugs on specific vascular functions in a fully controllable hemodynamic environment.

5.2 BACKGROUND

Cardiovascular diseases, such as atherosclerosis, are the most common direct and indirect leading cause of death worldwide [313]. Therefore, there is a significant demand for the investigation of the fundamental processes underlying disease development and progression in order to prevent the evolution of atherosclerotic plaques formation as well as to find new therapeutic targets. The pathogenesis of atherosclerosis is initiated by a dysfunctional, activated endothelium and the subsequent accumulation of lipoproteins into the intimal layer, which is followed by a chronic inflammatory response due to immune cell infiltration [314]. Risk factors like smoking, hypertension and diabetes can cause this endothelial dysfunction throughout the whole arterial tree - however, plaques preferentially develop at curvatures, branchings and bifurcations – regions, which are characterized by low and oscillatory WSS, therefore suggesting a close relationship between altered hemodynamics and atherogenesis [62, 63]. The shear stress is proportional to the friction force of the blood flow acting on the vessel wall, influencing the inflammatory status of the endothelium in early-stage atherosclerosis [62, 63] and plaque rupture [91, 92, 299] and erosion [299] in late-stage atherosclerosis.

On the cellular level, studies already showed various indications that pathologic hemodynamic conditions influence vascular remodeling. For example, structural and morphological adaptions of the vessel wall were observed *ex vivo* in the porcine *arteria basilaris*, compensating for the higher circumferential stress due to hypertonia through increased collagen content and number of smooth muscle cells and therefore leading to an increased wall thickness [120]. Furthermore, Gotschy et al. discovered that the PWV, a marker for vascular elasticity, is elevated even before morphological changes in the vascular wall occur, which was accompanied by increased elastin fragmentation [9]. It was furthermore observed that low WSS induced intimal thickening, while large WSS variations and inflammation induced medial thinning [164], pointing out the close relationship of WSS and arterial elasticity in atherosclerosis. Therefore, the knowledge of the correlation between arterial PWV and endothelial WSS is of great relevance to understand the interaction of arterial stiffness with pathologic flow patterns [3].

Mouse models of vascular diseases like e.g., atherosclerosis, are well established and widely used for the investigation of fundamental processes causing disease development and progression as well as for testing of new therapeutical targets [315]. However, the generation and utilization of these mouse models is time-consuming and expensive. Moreover, *in vivo* it is challenging to exactly determine local effects of hemodynamics and to change them in a controllable manner in order to examine the influence on variable biological parameters, as the *in vivo* model only allows limited control over arterial hemodynamics through complicated operations [20, 21] or the utilization of drugs [22].

At this point, vascular tissue engineering offers a promising alternative to conventional *in vivo* studies using animal models, since tissue-engineered arteries have similar physical properties than native arteries and enable the study of pathologies with conditions of lower complexity in a fully controllable environment when cultured in suitable bioreactor systems [23]. To generate tissue engineered arteries, there are various approaches described using biofabrication methods [316] as well as native biological materials, namely decellularized scaffolds of different origin like autologous sources and decellularized xenografts [249]. However, decellularized scaffolds provide a natural extracellular matrix (ECM) environment to cells and therefore promote excellent cell adhesion and growth [27]. The golden goal of decellularization is the efficient removal of the cells from the tissue, but simultaneously preserving the complex mixture of structural and functional proteins comprising the extracellular matrix (ECM) to minimize effects on the mechanical stability. However, most protocols include extensive physical, chemical or enzymatic treatment, leading to a loss of structure and ECM components and consequently leading to an impaired mechanical stability and cell adhesion [24-26]. Therefore, there is still a need for a fast and gentle decellularization method concerning transplantation models as well as the generation of *in vitro* test systems for vascular disease and therapy, as the mechanical integrity is a prerequisite for a good artery model in order to investigate early, fundamental atherosclerotic processes. The big advantage of tissue-engineered arteries is the freedom of choosing any cell source for reseeding, therefore it is simple to generate e.g., humanized arteries from porcine scaffolds [250]. Furthermore, specific genetically modified cells can be used in order to understand the crosstalk between e.g., specific proteins, enzymes or receptors with hemodynamics in a controllable environment.

Previous studies have already reported the successful generation of *in vitro* disease models like e.g., atherosclerosis, using different approaches based on biofabrication methods [254, 257, 259, 265, 317, 318]. One approach to reproduce the complexity of the arterial wall in an autologous *in vitro* model within a controllable environment to recreate fundamental processes in atherogenesis was the establishment of a static coculture system of human endothelial cells and vascular smooth muscle cells on a modified fibrin gel [317]. Here, the *in vitro* accumulation of low-density lipoprotein (LDL) and immune cells into the subendothelial matrix could be demonstrated for the first time [317, 318]. However, in this model, the three-dimensional circular structure as well as the physiologic hemodynamic conditions of native arteries was lacking. Therefore, a further step to the development of an adequate *in vitro* artery model was to use synthetic, tubular structures and the seeding of human vascular cells in order to achieve a physiologic, three-dimensional replication of arterial structures under pulsatile flow conditions [257]. Initial processes of atherosclerosis like the intimal accumulation of LDL and high-density lipoprotein (HDL) as well as the adhesion and transmigration of monocytes could be shown in this model [257]. Furthermore, the successful creation of a functional and perfusable, three-layered atherosclerosis model [254] with straight, curved and even stenotic arteries using 3D bioprinting was reported. Another functional, three-layered atherosclerosis model based on casting was introduced by Zhang et al. [265]. However, only a few studies were investigating the flow-related key processes of atherogenesis [259]. Here, a model of the human carotid artery bifurcation was created by casting and two representative regions, reflecting physiological and disturbed regions of WSS, were chosen based on computational fluid dynamics. Endothelial cells in the disturbed WSS region showed a disorganized, inflammatory phenotype with higher permeability, whereas endothelial cells in the physiologic WSS region showed a normal phenotype. Therefore, the investigation of flow-related disease processes in artery models is feasible. However, all these models are based on biofabricated scaffolds or casted hydrogels, not reflecting the native arterial extracellular matrix and especially the mechanical behavior, which plays a very important role for the flow-related investigation of atherogenesis. For these investigations, MRI is a powerful tool since it allows the non-invasive, serial measurement of disease development and progression regarding altered hemodynamics like WSS [4, 16], PWV [13, 15, 16, 200] as well as changes in the vascular morphology [201] and inflammation processes [197, 198]. However, these techniques are mainly used in humans and rodents, although the measurement of these parameters *in vivo* are challenging due to the long measurement times and the limited spatiotemporal resolution. Only a few studies were reporting the utilization of artificial vessels, which can indeed meet the elastic properties on an artery [13, 202]. However, since they are of artificial nature, these models are missing the ability to mimic native vascular aspects like the presence of cells and the crosstalk between them and their environmental surrounding. To our knowledge, the utilization of artery models for flow-related disease research using high-resolution 4D-flow MRI was not reported yet.

In this study, we therefore present for the first time a suitable setup for studying arterial hemodynamics in native and tissue engineered artery models under fully controllable hemodynamic conditions. The artery model, cultured in a suitable bioreactor platform [23], shows good extracellular matrix preservation and mechanical integrity, as well as excellent cell adhesion and vitality, and provides the assessment of flow related parameters under controlled environments. Moreover, the utilization of native and tissue engineered arteries offers a great potential to study flow dynamics and morphology in healthy and pathological cases, which could significantly improve our understanding of the key mechanisms in atherogenesis.

5.3 METHODS

5.3.1 ANIMAL WELFARE COMPLIANCE

Animal research was performed according to the German law and institutional guidelines approved by the Ethics Committee of the District of Unterfranken, Würzburg, Germany (approval number: 55.2-2532-2-256). Porcine carotid arteries were obtained from 15 to 25 kg German Landrace pigs (6 to 8 weeks old). The animals received human care in compliance with the Guide for Care and Use of Laboratory Animals published by the National Institutes of Health (NIH publication No. 85-23, revised 1996) after approval from the institutional animal protection board. Surgeries were conducted in compliance with the German Animal Protection Laws (§4 Abs. 3) and the institute's animal protection officer regularly informed the responsible authorities.

5.3.2 GRAFT HARVESTING AND DECELLULARIZATION

Following euthanasia, carotid arteries were explanted, transferred into Phosphate Buffered Saline without Ca^{2+} and Mg^{2+} (PBS^{-}, Merck) and freed from connective tissue and fat. After three washing steps in PBS^{-} containing 1% Penicillin/Streptomycin (P/S, Sigma), cleaned carotid arteries were frozen at -80°C until further usage.

For decellularization, carotid arteries were thawed, connected to peristaltic pumps and perfused at a constant flow rate of 20 ml/min with ddH_20 for 1h, followed by continuous perfusion with either 4% (w/v) Sodium Deoxycholate (SDC, Sigma) for 4h or 1% (w/v) Sodium Dodecyl Sulfate (SDS, Sigma) for 2h at room temperature (RT, see Figure 46A). For establishment of the optimal duration of ionic detergent decellularization, samples were taken at 24, 48 and 72h and from 1-5h. After flushing three times with phosphate-buffered saline ($PBS^{-)}$ for 1h, the decellularized scaffold was placed in PBS^{-} with 1% penicillin-streptomycin (P/S) on a rocking shaker overnight and washed 3x with PBS^{-} with 1% P/S for 1h. To remove residual DNA, the scaffolds were treated with 1 mg/ml DNAse I (Roche) dissolved in PBS with Ca^{2+} and Mg^{2+} (PBS^{+}, Sigma) for 2h at 37°C. Subsequently, the scaffolds were washed three times in PBS^{-} with 1% P/S on a rocking shaker for 1h (see Figure 46B).

Decellularized scaffolds were sterilized by 25 kGy gamma-irradiation (BBF steriXpert, Kernen-Rommelshausen, Germany) and stored in PBS^{-} at 4°C until further use (see Figure 46C).

5.3.3 DNA-CONTENT

Residual DNA content and fragment length was assessed using the DNeasy Blood and Tissue Kit (Qiagen, Hilden, Germany). Lyophilized native and decellularized tissues were weighed and digested with Proteinase K for 4 h at 56 °C and DNA was isolated according to the manufacturer's instructions.

DNA content was quantified with the Quant-iT™ PicoGreen™ dsDNA Assay Kit (ThermoFisher Scientific). Measurements were performed at an excitation of 480 nm and an emission of 525 nm using an Infinite M200 Plate Reader (Tecan). For qualitative analysis, extracted DNA was separated by gel electrophoresis on a 1.5 % Agarose Gel at 150 V and maximum current.

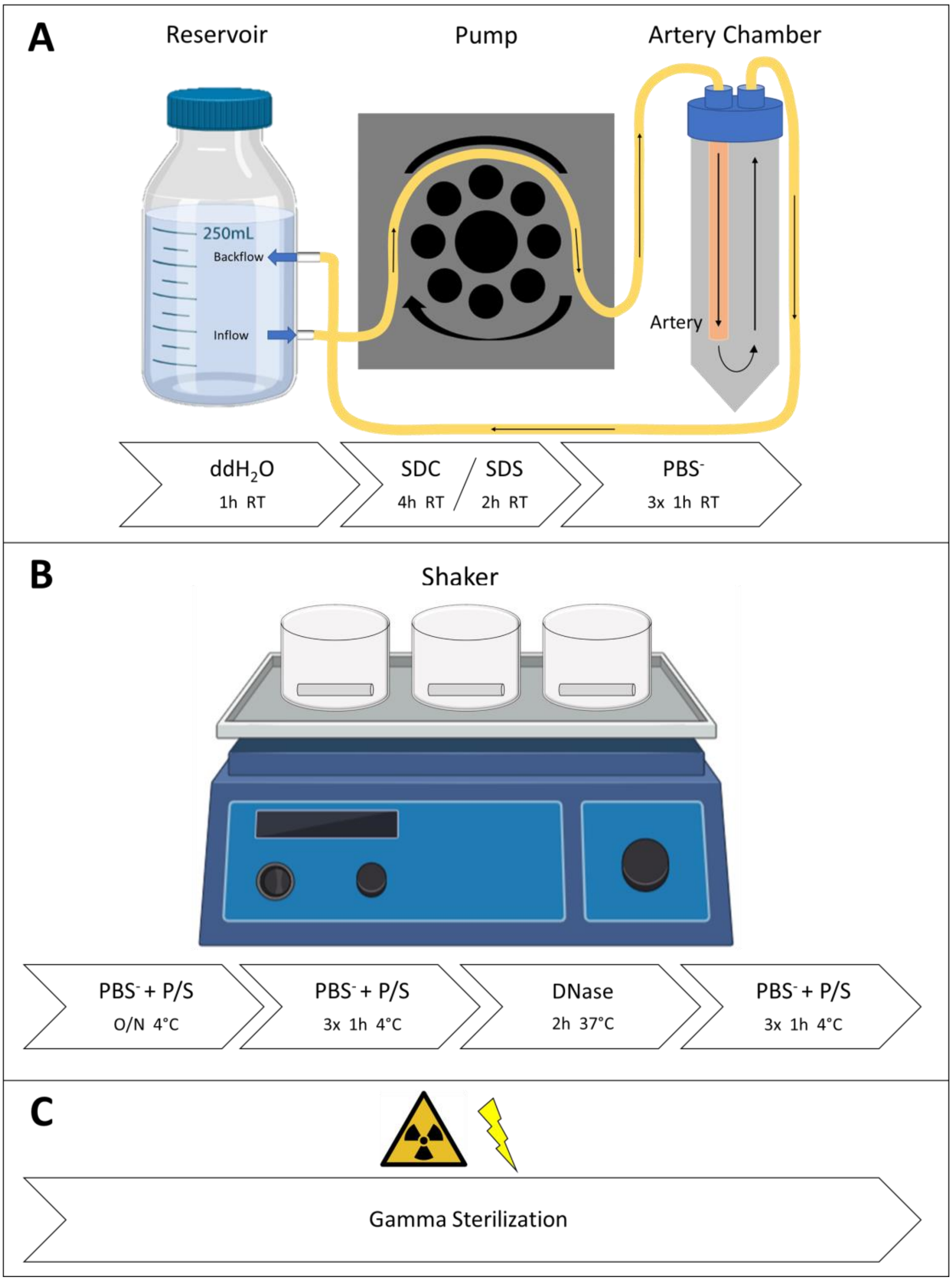

Figure 46: Scheme of the decellularization protocol for porcine carotid arteries. **A** Scheme of the osmotic shock and ionic detergent decellularization steps. Thawed arteries were connected to a custom-built artery chamber and a peristaltic pump system with solvent reservoir. After 1h perfusion with ddH_2O, decellularization solution was perfused (either 1 % SDS for 1 h or 4 % SDC for 4 h) for an efficient removal of cells and cellular debris. Residual decellularization solvent was removed by washing with PBS^- . **B** Enzymatic treatment. After washing in PBS^- + P/S on a shaker, DNAse I digestion was performed for 2 h to remove residual DNA. C Gamma sterilization was performed to obtain sterile decellularized scaffolds. The succession of used agents as well as temperature and duration are illustrated in the timeline below. Subfigures taken from BioRender.com

5.3.4 HISTOLOGY

Native and decellularized arteries were fixed with Histofix (Roth) for 2 h at RT or overnight at 4°C. Samples were embedded in paraffin and cut into 5 µm sections. Prior to staining, paraffin-sections were deparaffinized and rehydrated. Efficiency of decellularization and overall tissue structure was examined qualitatively with Hematoxylin and Eosin staining (Morphisto) and Feulgen Staining (Merck). The presence of extracellular matrix (ECM) was visualized with Masson's Trichrome (Morphisto) and Picro-Siriusred (Morphisto) for Collagen and Elastica van Gieson (Morphisto) for Elastin. Staining was performed according to the manufacturer's instructions. Sections were dehydrated and embedded in Entellan (Merck).

5.3.5 COLLAGEN ANALYSIS

Hydroxyproline content of native and decellularized arteries (each n = 5) was quantified by the method of Edwards and O'Brien [319] with small modifications. Lyophilized samples were weighted, and tissue was hydrolyzed in 6 N HCl at 90°C overnight. HCl was allowed to evaporate at 80°C for 4-6 h under the fume hood until the samples were completely dry. Samples were dissolved in pH-6 Buffer (18.08g sodium acetate (water free), 11.5g citric acid (aqueous), 3ml acetic acid, 8.5 g NaOH (all from Sigma) in 250ml ddH_20). 100 µl of each standard (from a 1mg/ml Hydroxyproline-stock (Sigma) and sample were mixed with 50 µl of Chloramine-T solution (70.5 mg Chloramine-T, solved in 4 ml pH-6 Buffer and 0.5 ml Isopropanol) and incubated for 20 min. 50 µl Ehrlich's reagent (750 mg DAB in 3 ml Isopropanol, 1.3 ml 60% perchloric acid) was added to each well, mixed and incubated for 30min at 65°C. Measurements were performed at 570 nm performed with an Infinite M200 Plate Reader (Tecan). Total collagen was afterwards calculated from the hydroxyproline content with a conversion factor of 7.46 [320].

5.3.6 ELECTRON MICROSCOPY

Native, decellularized matrices and cell-seeded scaffolds were fixed overnight at 4 °C in 6.25 % glutaraldehyde (Sigma). Fixed samples were washed five times in PBS and dried with the critical point method after dehydration in acetone. Sample preparation and imaging microscopy was done in collaboration with Prof. Krohne (Biocenter Imaging Core Facility, University of Würzburg). In brief, samples were coated with 10–20 nm gold/palladium (80/20) in an argon bath using a BAL-TEC SCD 005 Sputter Coater (Leica Microsystems). Imaging was examined using a JEOL JSM 7500F scanning electron microscope (Jeol Ltd.) at 5 kV.

5.3.7 BIOMECHANICAL TESTING

To evaluate biomechanical properties of the native and decellularized scaffolds, tensile strength and rheological properties were determined.

5.3.7.1 Tensile Strength

Tensile strength test was performed to determine the maximum force the tissue can withstand before rupture. Native (n = 10) and decellularized carotid arteries (SDS: n = 6, SDC: n = 6) were fixed on the connector of the mechanical tester (Z2.3, Zwick/Roell, Ulm, Germany). Tissues were pulled with a cross head speed of 1 mm/s and a starting length L_0 of 23,74 mm at room temperature. Tensile forces were applied until rupture.

5.3.7.2 Rheology

Rheological properties were assessed using an Anton Paar (Ostfildern, Germany) Physica MCR 301 system in collaboration with Dr. Thomas Lorson (Chair for Advanced Materials Synthesis, University of Würzburg University of Würzburg). To investigate the viscoelastic properties, the linear viscoelastic (LVE) region was obtained by performing amplitude sweeps from 0.01% to 100% strain deformation with an angular frequency of 10 rad/s. Afterwards, frequency sweeps from 0.1 to 100 rad/s were measured with 0.5% strain deformation.

5.3.8 TOTAL BILE ACID ASSAY

Depletion of the decellularization reagent (SDC) was assessed by measuring the remaining bile acid using the total bile acid kit (Diazyme). Samples were taken from the supernatant after γ-sterilization and treated according to the manufacturer's instructions. Samples and standard controls were measured in triplicates at 0 s (E0), 60 s (E1) and 120 s (E2) after beginning of the reaction. ΔE = E2 - E1 was calculated and bile acid concentration determined from a given calibrator (50 µmol/L).

5.3.9 RESEEDING OF SCAFFOLDS AND CULTIVATION

5.3.9.1 Isolation of Blood Outgrowth Endothelial Cells (BOECs)

Human Blood Outgrowth Endothelial Cells (BOECs) were isolated from fresh blood according to established protocols with minor modifications [321, 322]. In brief, 60ml of blood was collected by venipuncture in sodium citrate tubes and diluted 1:1 with Dulbecco's Phosphate-Buffered Saline without Ca^{2+} and Mg^{2+} (PBS^-, Gibco). Six 50ml conical tubes with 15ml of density gradient centrifugation medium (Ficoll-Paque Premium, 1.077 g/ml, GE Healthcare) were prepared and 20 ml of diluted blood was gradually added on top of the medium. Samples were centrifuged at 400 x g for 35 min at room temperature (RT) with accelerator and brake off. Buffy coat layer was collected and the mononuclear cell suspension was diluted 1:1 in PBS^- before washing at RT for 20 min at 300 x g. Medium used for BOECs generation was prepared by supplementing endothelial basal medium (EGM-2, Lonza) with the growth factor supplements provided by the manufacturer without serum. For preparation of 15ml of BOECs generation medium, 2.5ml of FCS (Sigma Aldrich) were added to 12.5ml of EGM-2. The entire cell suspension was plated into a single, collagen I coated T75 cell culture Flask (Greiner Bio-One) and medium was carefully changed after 24h. After 7 to 14 days of culture, outgrowth colonies appeared between 7 and 14 days of culture, which were allowed to grow to approximately 1000 to 2000 cells per colony before passaging.

5.3.9.2 Culture of BOECs

After passage 2, BOECs were cultured in EGM-2 (Lonza) supplemented with 10% fetal calf serum (FCS). Medium was changed every 2-3 days. After reaching 90% confluency, cells were incubated with PBS/ Ethylenediaminetetraacetic acid (EDTA) (0.45 M EDTA) for 5 minutes and afterwards trypsinized with 0.05% Trypsin-EDTA 1X (Thermo Fischer Scientific). Cells were seeded with an initial seeding density of minimum 10000 cells/cm^2.

5.3.9.3 Characterization of BOECs

Immunofluorescence and flowcytometric analysis for BOECs markers was performed to identify the phenotype of isolated BOECs as described previously [321, 322]. For immunofluorescence staining, cells were cultured in chamber slides (ibidi) until confluency. Permeabilization and was performed for 5min with 0.2% TritonX (Sigma) in PBS$^-$ (Gibco). Samples were incubated with 5% (v/v) goat serum (Sigma) diluted in antibody diluting solution (DCS, innovative diagnostic systems) for 30min at RT prior to incubation with primary antibodies for 1h at RT or overnight at 4 °C. Afterwards, cells were washed three times with 0.5% Tween 20 (Sigma) in PBS$^-$ (PBST) and samples were incubated with secondary antibodies diluted in antibody diluting solution for 1h at RT (list of antibodies in Supplementary Table 6). Stained samples were washed three times with PBST and embedded in Vectashield containing DAPI (Vectorlabs) to visualize nuclei.

For flowcytometric analysis, cells were washed at 4°C and 400xg for 5 min before incubation for 10 min with F_c Block (BD Biosciences), diluted 1:50 in PBS supplemented with 2% FCS (PBS/FCS). Subsequently, cells were washed in PBS/FCS and stained in 50µl antibody suspension and incubated for 30min at 4°C in the dark. After washing two times, cells were analyzed with a FACS Canto (BD Biosciences).

5.3.9.4 Static Culture

Sterile scaffolds were cut into appropriate pieces and clamped into cell crowns. Before each experiment, scaffolds were incubated in cell culture medium overnight. For cell seeding, medium was aspirated and 1 x 10^6 cells / cm^2 were added to the inner compartment of the cell crown.

5.3.9.5 Dynamic culture

Seeding of the artery was performed by tying up one end of the artery with sterile surgical threads and filling the lumen with endothelial cell suspension with a concentration of 3x10^6 cells/ml). After sealing the other end, the construct was turned around every 15min for 3h to allow uniform cell attachment. On the next day, the artery was opened. Cells were allowed to adhere and proliferate for 5 days during static culture before dynamic cultivation.

Bioreactors were assembled before autoclaving. Arteries were placed in the bioreactors and cultured under a pressure of approximately 120/80 mmHg for 3 weeks. Medium was changed every 7 days. After the experiment, scaffolds were removed and washed in PBS. A small piece of the Scaffold was embedded in paraffin for hematoxylin and eosin (HE)- and immunofluorescence (IF)-staining. The remaining scaffold cut into appropriate pieces and clamped in sterile cell crowns (48-well) for further analysis (3-(4,5-dimethylthiazol-2-yl)-2,5-diphenyltetrazolium bromide (MTT)Assay, Transepithelial electrical resistance (TEER), Fluorescein (FITC) Dextrane analysis).

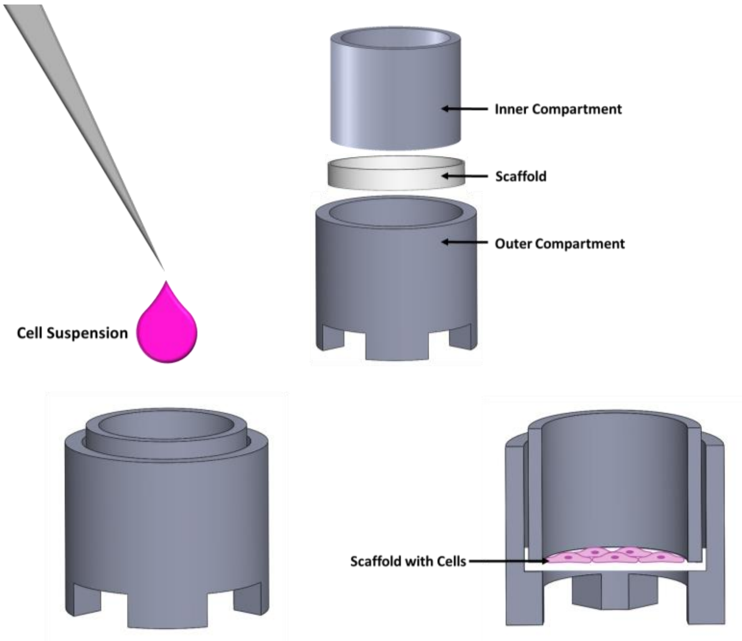

Figure 47: Scheme of cell crowns used for static culture. Cell crowns consist of two compartments. The scaffold is placed between the inner and outer compartment. After application of the cell suspension into the inner compartment, cells grow on the scaffold. Image recreated and adapted from [323].

5.3.10 CELL VIABILITY AND FUNCTIONALITY

5.3.10.1 MTT-Assay

MTT solution (Sigma) was diluted in culture medium (1 mg/ml) and applied to the cell crowns. Samples were incubated 3 h at 37 °C. The scaffolds were removed from the cell crowns, washed with PBS- and the seeded area was punched out and incubated in a 1,5ml tube with 1ml Isopropanol on a shaker at 4°C overnight. Extractions were vortexed and Absorption at 570nm was measured in Triplicates. Measurements were performed with an Infinite M200 Plate Reader (Tecan).

5.3.11 MRI-MEASUREMENTS

Measurements were conducted on a 17.6T MRI scanner (Bruker Avance 750 WB, with a 1 T/m gradient system and a 24 mm birdcage coil. For flow measurements radial 2D- and 4D-PC MRI sequences were used. The scan parameters were: V_{ENC}=150 cm/s (2D) and 167 cm/s (4D). TR/TE = 3.0/1.1ms, FOV = 25x25x10 mm^3 (4D). Morphology was imaged with a flow compensated radial 3D-FLASH sequence (TR/TE = 4/1.5ms, FOV = 25x25x10 mm^3). Total measurement time was 2.4 minutes (2D), 32 minutes (4D) for flow measurements and 4 minutes for the morphology measurement. Self-navigation signals extracted from the radial MR signal were used for retrospective reconstructions, as described previously [4]. Flow cines were reconstructed with a frame rate of 120 frames (2D) and 20 frames (4D) per pump cycle. The spatial resolution was 100µm (isotropic) for the flow measurements and 98µm (isotropic) for morphology measurement. All reconstructions were conducted with MATLAB (The MathWorks, Inc., Natick, USA). The local PWV was determined from the 2D flow measurements using the Q-A method described previously [11, 15], see also Chapter 2-4. Using the data points of the early upstroke of the flow pulse, the PWV value can be assessed as the slope of a linear fit of the Q(A) curve, where Q(t) represents the volume flow and A(t) is the cross-sectional area of the artery. WSS was calculated from the 3D-velocity derivations at the vessel wall, which were determined with the 4D flow measurement using EnSight (Ansys, USA) for data processing [4].

5.3.12 STATISTICAL ANALYSIS

All statistical analyses were performed in GraphPad Prism 8 (GraphPad Software, San Diego, USA). For testing normal distribution, the Shapiro Wilk Normality Test was used. Statistical comparisons between different groups were performed using either an unpaired t-test or ANOVA for normally distributed data. When normality test failed, a non-parametric Mann-Whitney-U test or a Kruskal-Wallis test was performed. All data are graphically represented as mean ± standard deviation of the mean (SEM) unless stated otherwise. P-values of < 0.05 were considered statistically significant.

5.4 RESULTS

5.4.1 DECELLULARIZATION OF PORCINE CAROTID ARTERIES RESULTS IN AN EFFICIENT CELL REMOVAL

The goal of decellularization is the efficient removal of all cellular and nuclear components, however, simultaneously retaining overall composition and mechanical properties of the tissue, and strongly depends on the particular tissue properties and later application [24, 25]. Therefore, a protocol was established, which combines physical treatment, osmotic shock, chemical treatment by ionic detergents and enzymatic treatment (see Figure 46A) to guarantee efficient cell removal and preservation of extracellular matrix. The multi-step, perfusion-based decellularization resulted in a macroscopically cleared, acellular extracellular matrix scaffold with both decellularization protocols (data not shown).

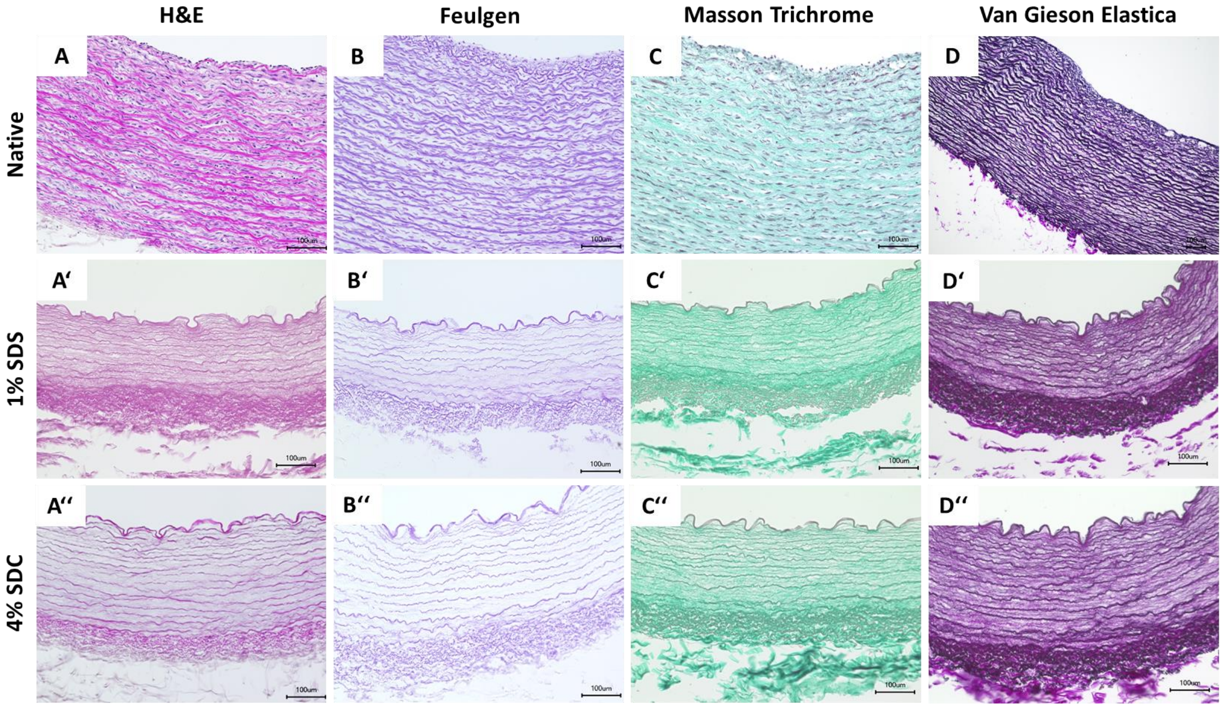

Figure 48: Decellularization process efficiently removes cellular components, while ECM components and macrostructure are retained. Representative images of histological stainings of a native carotid artery (A–D) and decellularized arteries with 1% SDS (A'–D') and 4% SDC (A''–D''), as shown by Hematoxylin & Eosin (A - A''), Feulgen for DNA (B – B''), Masson Trichrome for collagen (C – C'') and van Gieson Elastica staining for elastic fibers (D - D''). In both decellularization methods, no cellular components can be detected.

To further assess the overall efficiency of the developed decellularization protocol, histological analysis, residual DNA-content, DNA fragment size distribution and bile-acid concentration was performed. Histological analysis indicated that the structural matrix integrity remained intact (see Figure 48). However, in contrast to native carotid arteries, where excessive nuclei are present (see Figure 48A), the optimized decellularization protocol resulted in acellular scaffolds for 1% SDS after 2h (see Figure 48A') and for 4% SDC after 4h (see Figure 48A''). Furthermore, no DNA was detected by Feulgen DNA staining for both protocols (see Figure 48B' for SDS and Figure 48B'' for SDC), whereas DNA is clearly visible in native carotid arteries (see Figure 48B). Conservation of collagens was indicated by Masson

Trichrome staining (see Figure 48C-C’’) and elastin by Van Gieson Elastica staining (see Figure 48D-D’’) in both, native and decellularized arteries.

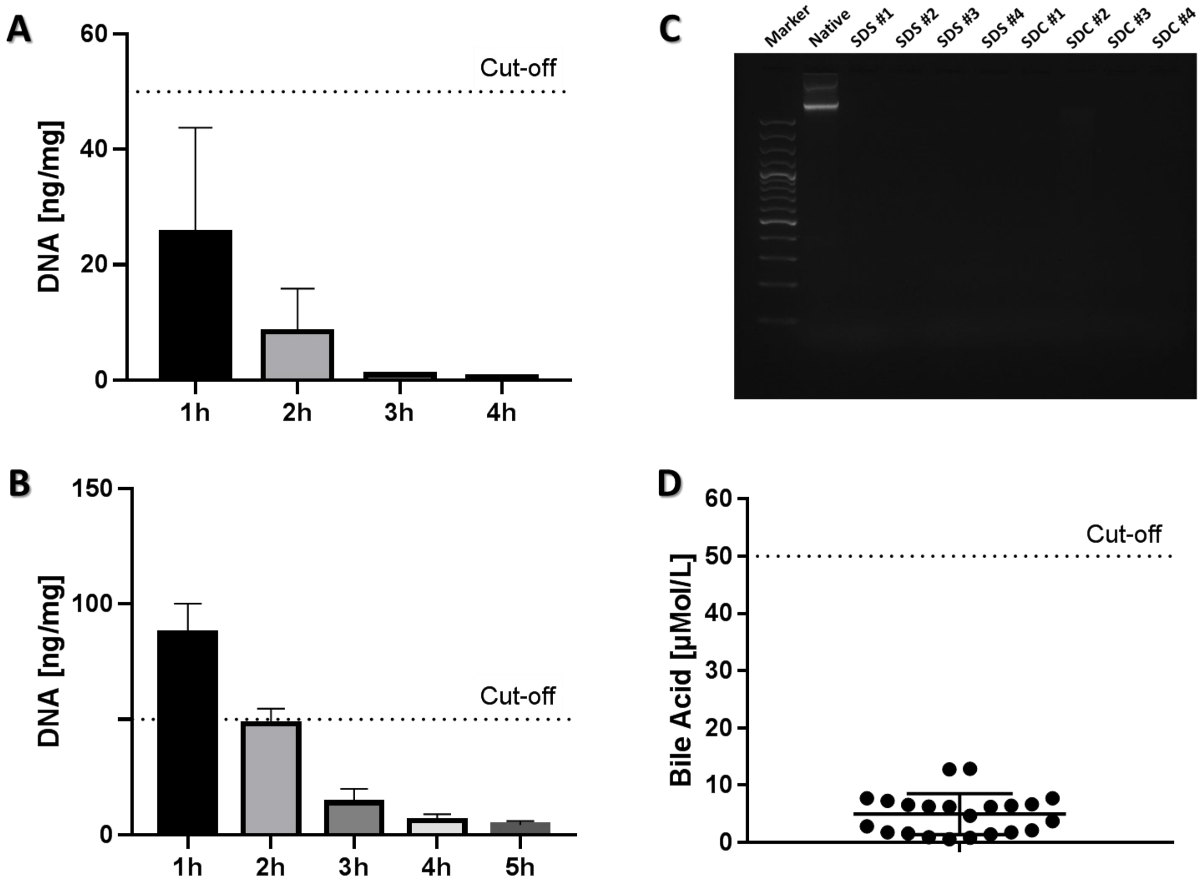

Figure 49: Optimized decellularization protocol efficiently removes DNA and bile acid residuals. **A** Time-dependent residual DNA content of decellularized arteries with 1% SDS. **B** Residual DNA content for arteries decellularized with 4% SDC. The cut-off value for DNA residues is defined as 50ng DNA per 1mg tissue. Data are represented as mean ± SEM. **C** Gel-electrophoresis image of isolated DNA from native and decellularized arteries shows no big DNA-fragments after decellularization. **D** Residual bile acid after the decellularization and washing process is clearly under the cut-off value of 50µMol bile acid per 1L.

However, not only the lack of visible nuclei in histological sections determines a successful decellularization meeting the described criteria [24]. As a direct correlation between nucleic material and adverse host reactions exists [324, 325], the residual double-stranded DNA (dsDNA) content should be under 50 ng dsDNA per 1mg of dry tissue [24]. Therefore, the residual DNA was quantitatively assessed for both decellularization methods (see Figure 49A+B). Samples were taken after 1-4 h of detergent treatment with SDS and 1-5 h for treatment with SDC. For SDS, the residual DNA content was already found under the given cut-off value after 2h of decellularization (8.4±22.4 ng/mg, see Figure 49A). For the decellularization with SDC, the residual DNA content was found to be under the cut-off value after 3h (13.9±12.1 ng/mg, see Figure 49B). Nevertheless, the final protocol was decided to be with 4h of detergent treatment (6.0±5.8 ng/mg, see Figure 49B) to be more in the range of the values obtained with SDS.

Furthermore, the DNA removal was qualitatively confirmed by determination of the fragment size length by agarose gel electrophoresis (see Figure 49C) with a cut-off value of 200bp [324, 325]. The extracted DNA from the native porcine carotid artery tissue showed a strong band with low electrophoretic mobility, corresponding to undigested genomic DNA (see Native in Figure 49C). In contrast, no DNA bands were observable after decellularization with both protocols, indicating the absence of genomic DNA fragments. To avoid cell death after reseeding due to toxic bile acid remnants, coming from the decellularization detergent, the depletion of the decellularization reagent was assessed by measuring the remaining bile acid concentration (see Figure 49D). A concentration of 5.0±3.6 µMol/L confirmed a successful washing procedure with values below the cut-off value of 50 µMol/L.

5.4.2 DECELLULARIZATION OF PORCINE CAROTID ARTERIES RESULTS IN AN INTACT ULTRASTRUCTURE AND PRESERVED EXTRACELLULAR MATRIX

Not only the efficient removal of cells and cellular remnants is an important benchmark for a good decellularization protocol, but also the micro- and ultrastructural matrix integrity and extracellular matrix preservation. Therefore, the ultrastructure of native and decellularized porcine carotid arteries was analyzed with scanning electron microscopy (SEM).

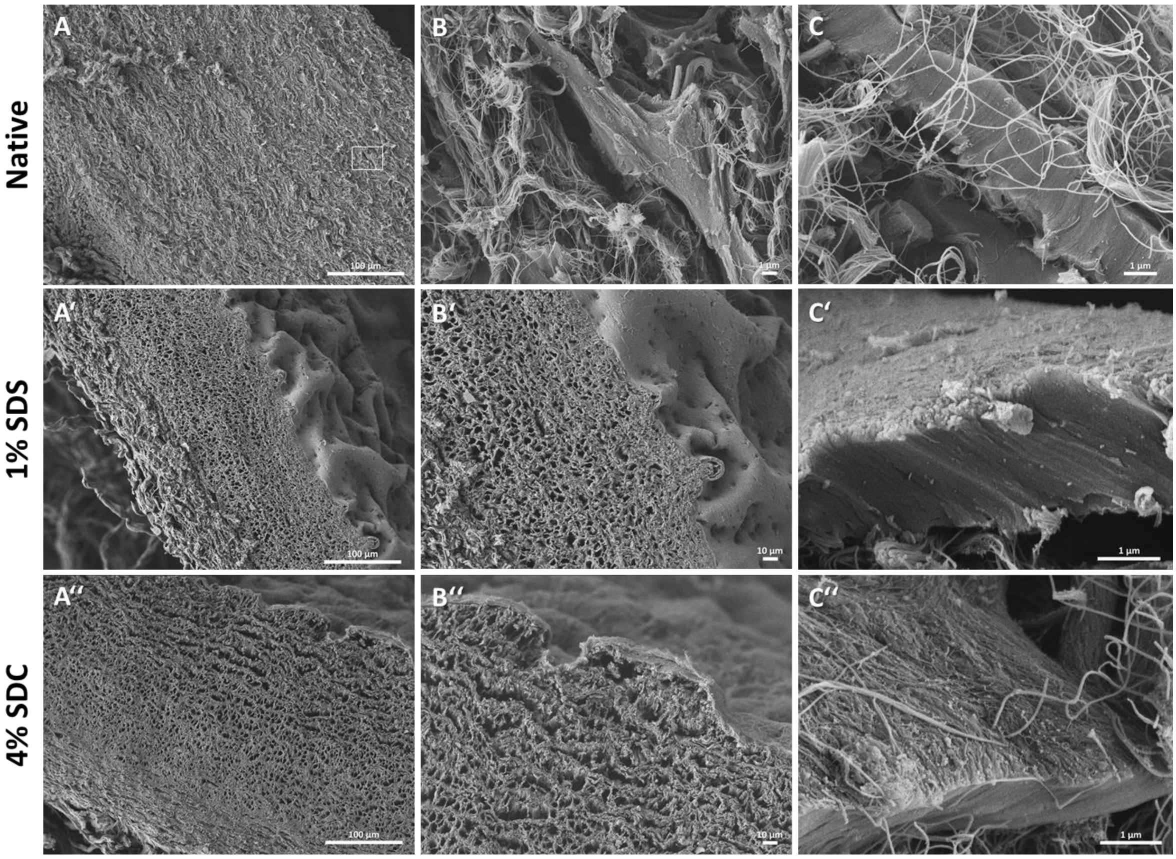

Figure 50: Scanning electron microscope images of the media of porcine carotid arteries shows clear accellularity. A-A’’ Cross-sections of the medial layer of native and decellularized carotid arteries. **B-B’’** Enlarged view of the cross sections from A-A’’. **B** Smooth muscle cells embedded in the dense ECM of native arteries are clearly visible. **B’** and **B’’** In both types of decellularized arteries, no SMCs can be found (see white arrows). **C-C’’** Enlarged view on the elastic fibers of native and decellularized arteries. **C** In native arteries, thick elastic fibers are covered by dense ECM fibers. **C’** Nearly no ECM fibers are visible (see white arrow). **C’’** A layer of ECM fibers is visible (see white arrow).

Figure 50 shows the cross section of native (A-C) and decellularized porcine carotid arteries (SDS: A'-C' and SDC: A''-C''). Compared to decellularized arteries, the native artery demonstrates a dense ECM with embedded smooth muscle cells (see white arrow in Figure 50B) throughout the medial layer. However, in decellularized arteries, holes are clearly visible where the smooth muscle cells were embedded before (see white arrows in Figure 50B' and B''), proving complete acellularity in the tunica media. Furthermore, elastic laminae are densely covered in native arteries (see Figure 50C), followed by arteries decellularized with 4% SDC (see Figure 50C'') whereas arteries decellularized with 1% SDS showed a loss in collagenous ECM covering the elastic laminae (see white arrow in Figure 50C'). In the intimal layer, endothelial cells are clearly present in native porcine carotid arteries (see Figure 51 A-C). In contrast, complete acellularity is confirmed in decellularized arteries (see A'-C' for SDS and A''-C'' for SDC). However, a dense ECM fiber structure is only visible on the intimal layer of arteries decellularized with 4% SDC (Figure 51C''), whereas SDS shows significantly less ECM fibers and fiber bundles covering the internal elastic lamina (see white arrow in Figure 51C').

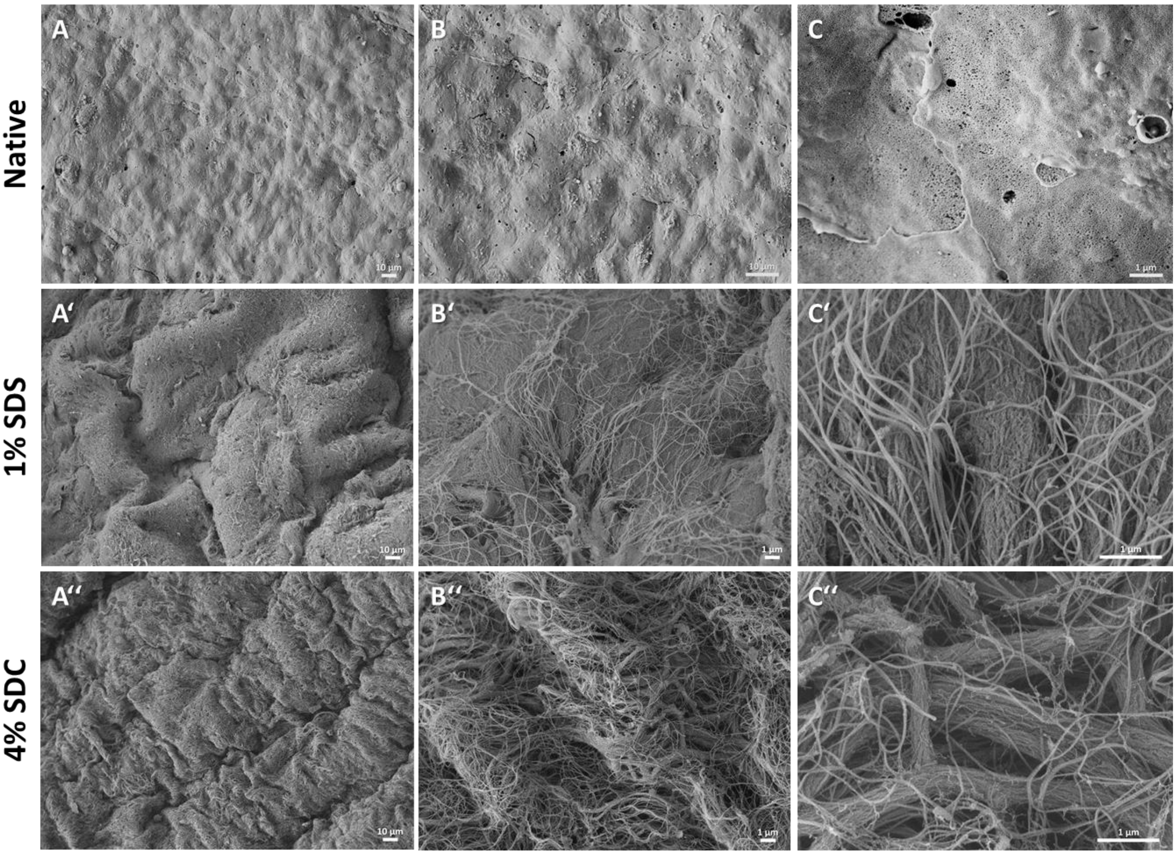

Figure 51: Scanning electron microscope images of the intima of porcine carotid arteries. A-A'' Intimal layer of native and decellularized carotid arteries. **B-B''** Enlarged view of the intimal layer from A-A''. **C-C''** Enlarged view of B-B''. In contrast to the native intima, no endotheial cells are present in decellularized arteries, where the basal lamina is exposed. A clear reduction of ECM fibers is visible in arteries decellularized with SDS.

The ultrastructure of collagen bundles is furthermore shown in Figure 52. Here, a clear similarity is observable between fiber bundles from native arteries (Figure 52A) and arteries decellularized with 4% SDC (Figure 52C). However, SDS seems to destroy the ultrastructure of collagenous fibers (see Figure

52B). Taken together, the presence of collagen was confirmed by histology (Figure 48 C-C'') and SEM analysis (see Figure 52).

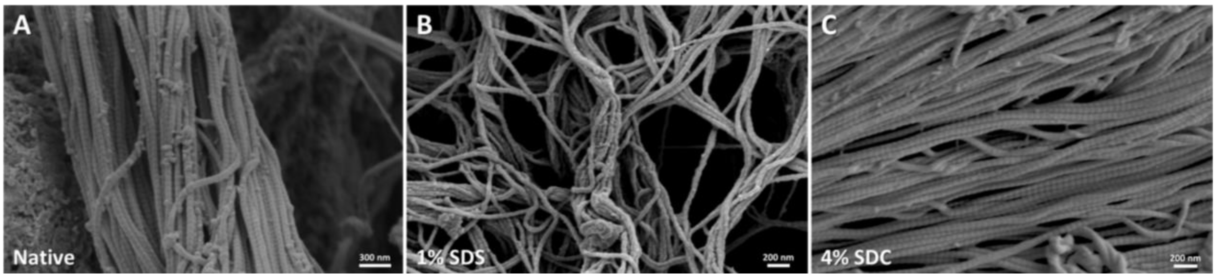

Figure 52: Scanning electron microscope images of collagenous fibers from native and decellularized porcine carotid arteries. **A** Collagen fiber bundle from native carotid arteries. **B** Collagenous fibers from arteries decellularized with 1% SDS. **C** Collagenous fibers from arteries decellularized with 4% SDC.

However, to state a clear assertion, quantitative measurements of hydroxyproline (HYP) content, an amino acid predominantly found in collagen [320], were performed in native and decellularized arteries. Measurements of the HYP content revealed a significant increase in HYP in decellularized arteries compared to native arteries (see Figure 53A). However, the enrichment was the strongest in arteries decellularized with 4% SDC compared to native arteries (103.4±19.4 µg/mg vs. 64.0±12.0 µg/mg, **, p<0.01) and arteries decellularized with SDS (103.4.7±19.4 µg/mg vs. 74.0±12.8 µg/mg, *, p<0.05, see Figure 53A). However, no significant difference in HYP content was found between native and decellularized arteries with SDS (see Figure 53A).

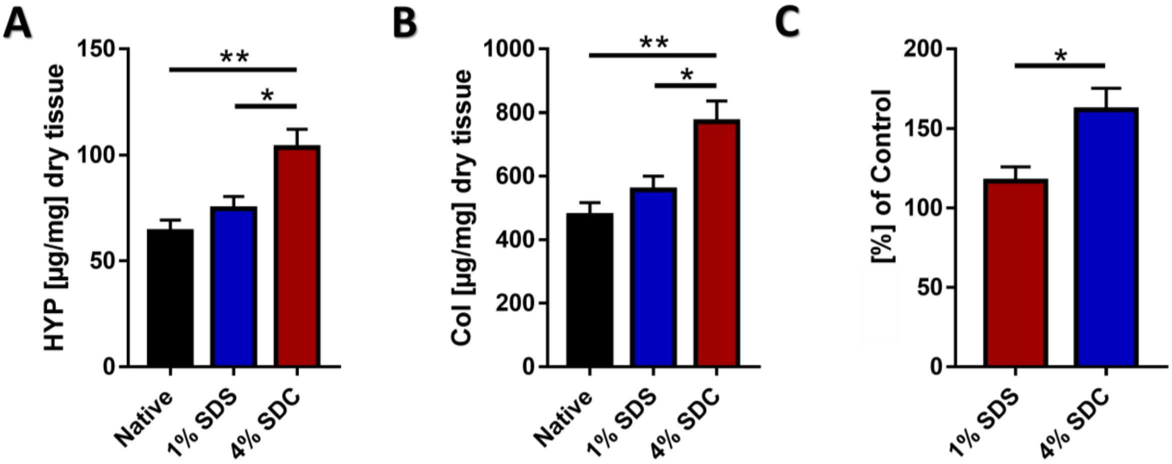

Figure 53: Hydroxyproline is enriched in arteries decellularized with 4%SDC. **A** Measured HYP content in native and decellularized arteries. **B** Calculated collagen content in native and decellularized arteries. **C** Relative enrichment of collagen in decellularized arteries compared to native arteries. An enrichment of collagen was found in arteries decellularized with 4% SDC. Data are represented as mean ± SEM.

Total collagen was calculated from the hydroxyproline content and revealed an enrichment of total collagen in arteries decellularized with 4% SDC compared to native arteries (771.6±144.5 µg/mg vs. 476.9±89.8 µg/mg, **, p<0.01) and arteries decellularized with SDS (771.6±144.5 µg/mg vs. 557.0±95.3

µg/mg, **, p<0.05, see Figure 53B). In conclusion, an overall enrichment of 161,8±30.3% collagen in arteries decellularized with SDC was found (see Figure 53C).

Additionally, picrosirius red stainings (Figure 54A) of native and decellularized arteries were analyzed for the relative collagen content per area under polarized light (see Figure 54B). Here, analysis revealed significantly less collagen in arteries decellularized with SDS compared to native arteries (44.3±7.2% vs. 58.0±1.6%, **, p<0.01), whereas no difference was observable between native arteries and arteries decellularized with SDC (58.0±1.6% vs. 50.1±9.4%) as well as between both decellularization protocols (SDS vs. SDC: 44.3±7.2% vs. 50.1±9.4%, see Figure 54A). The reduction of collagen content in arteries decellularized with SDS therefore amounts to 23.5% and in arteries decellularized with SDC to 13.6% (see Figure 54B).

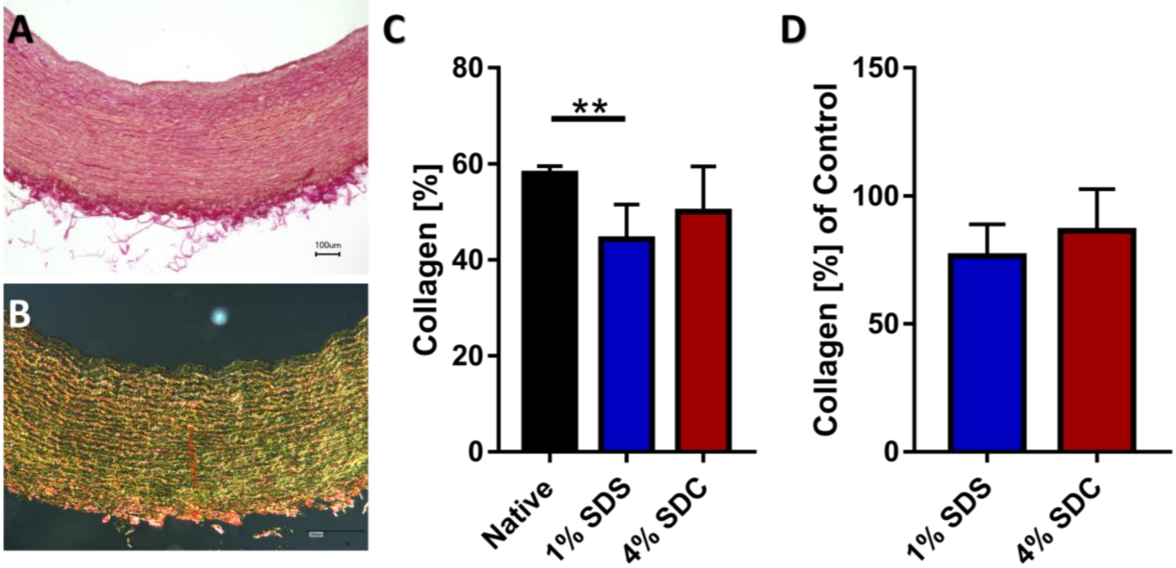

Figure 54: Arteries decellularized with SDS have significantly less collagen than native arteries. **A** Exemplary Image of a native porcine carotid artery stained with picrosirius red. B Same section under polarized light. **C** Relative collagen content of native and decellularized arteries. **B** Relative collagen content of native and decellularized arteries normalized to native collagen content. Arteries decellularized with SDS show significantly less collagen than native arteries and arteries decellularized with SDC.

Taken together, both established decellularization protocols resulted in an efficient cell- and cellular remnant removal with values of residual DNA-content, fragment length and bile acid remnants being below the described cut-off values. Furthermore, the macroscopic and ultrastructural analyses revealed better preserved ECM in arteries decellularized with SDC, which was furthermore confirmed by collagen content analysis.

5.4.3 MECHANICAL PROPERTIES ARE RETAINED IN DECELLULARIZED ARTERIES

Next to structural and compositional characteristics of decellularized scaffolds, mechanical cues are known to contribute largely to normal functionality. The extracellular matrix provides structural support to the arteries during physiological function. Elastic lamellae and interconnecting fibers support the initial lower loads, whereas collagen fibers accommodate deformations encountered at higher pressures due to the over 100x higher stiffness [326]. To draw conclusions about the integrity of the mechanical properties after decellularization of the arteries, uniaxial tensile strength tests and rheological measurements were performed.

5.4.3.1 Decellularization does not affect the ultimate strength of the tissue

A sudden drop in the stress-strain curve of arteries provides insight into the ultimate strength of the tissue. Figure 55A shows the maximum tensile strength σ_M of native and decellularized arteries, obtained from the stress-strain curves. Mean values were 2.02±0.93 N/mm^2 for native arteries, whereas decellularized arteries had a tendency towards higher maximum tensile strength (SDS: 2.51±0.52 N/mm^2 and SDC: 2.36±0.45 N/mm^2), indicating a slightly, but not significantly higher stiffness of native arteries. The corresponding force needed to disrupt the arteries is shown in Figure 55B. Values obtained for native porcine carotid arteries were 9.26±2.89 N, whereas decellularized arteries showed corresponding higher values of 11.59±1.80 N for SDS and 10.77±2.56 N. Taken together, both decellularization protocols did not significantly affect the tensile strength of arteries.

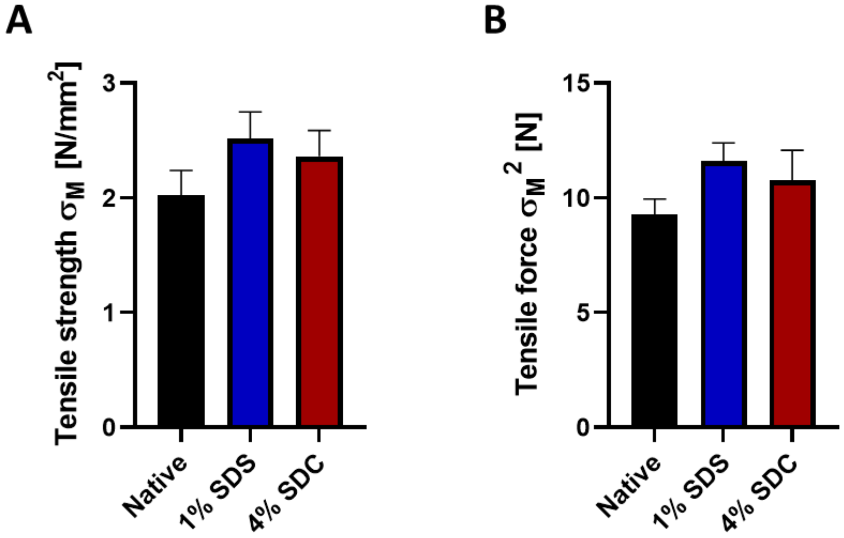

Figure 55: Uniaxial tensile strength of native and decellularized arteries shows no significant impairment of strength. A Maximum tensile strength σ_M of native (black) and decellularized arteries with 1% SDS (blue) and 4% SDC (red). **B** Corresponding tensile force σ_M^2. Data are represented as mean ± SEM. Statistical analysis was performed with a non-parametric Kruskal-Wallis test. No significant differences were observed between the different matrices.

5.4.3.2 Decellularization with SDS results in softer matrices

To further explore the mechanical properties of the decellularized arteries, oscillatory rheological analysis was performed using a plate-to-plate setup. Measurements were performed with PBS$^-$-soaked scaffolds to mimick circumstances found in cell culture. Before measurement, the optimal gap width was determined for the subsequent test series. Strain sweep measurements revealed a significantly higher storage and loss modulus (G' and G'') in the linear viscoelastic (LVE) region of arteries decellularized with 4% SDC (1408 ± 158,5 Pa and 148,2 ± 13,5 Pa) compared to 1% SDS (652,3 ± 72,2 Pa and 57,7 ± 9,8 Pa), indicating a weaker viscoelastic strength of the arteries decellularized with 1% SDS (see

Figure 56A, C and D). Furthermore, arteries decellularized with 4% SDC exhibited an earlier flow point (G’ = G’’) than with 4% SDS, correlating with a lower structural resistance against shear forces.

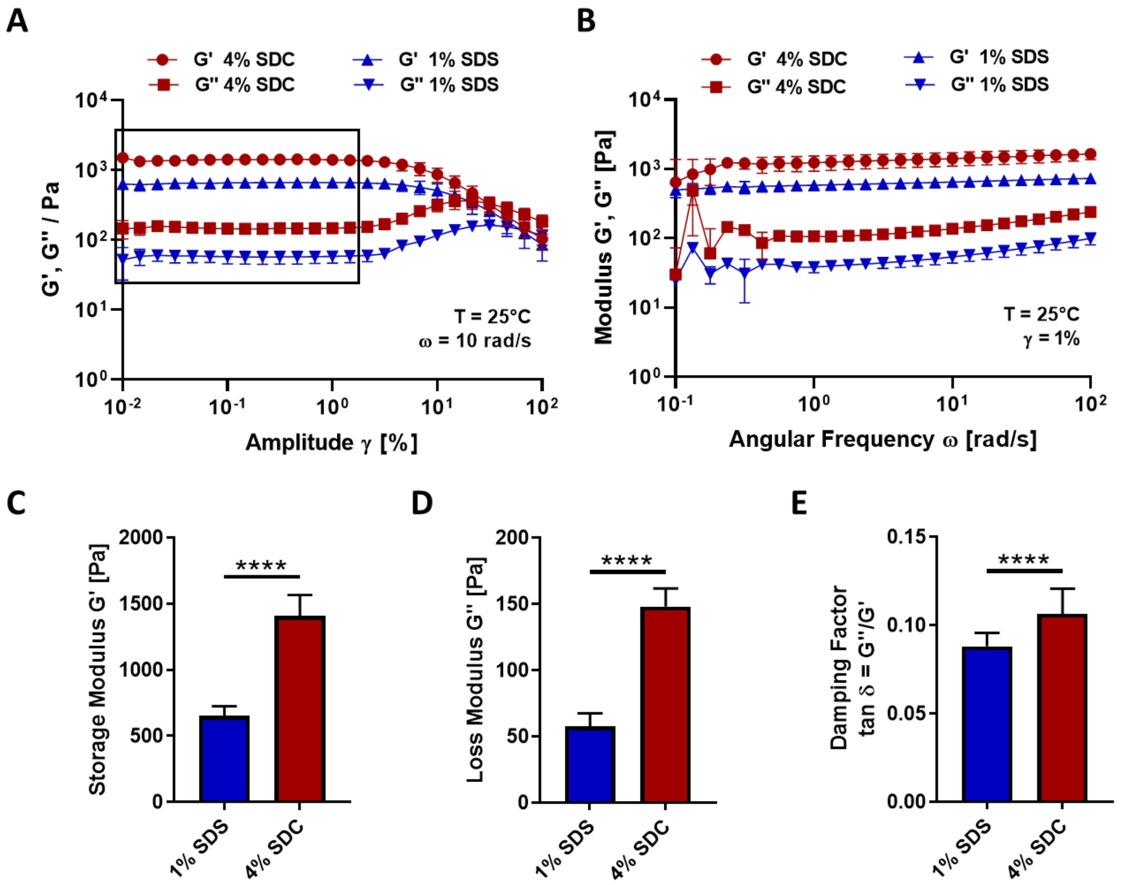

Figure 56: Rheological measurements of decellularized arteries. **A, B** Data plots of oscillatory rheological measurements. Storage modulus G’ (blue), and loss modulus, G’’ (red) of both scaffolds were determined in dependency on the strain deformation (**A**; ω = 10 rad/s, T = 25 °C), and frequency (**B**; γ = 0.5%, T = 25 °C). Data are represented as mean ± SD (n = 3). **C-E** Mean values of measured parameters for both scaffolds. Mean storage and loss modulus as well as the damping factor were calculated from values in the linear viscoelastic region (black box). Data are represented as mean ± SD (n = 3). ****p < 0.0001, calculated with an unpaired Mann-Whitney-U test.

Both scaffolds showed damping factors (tan δ = G’’/G’) of tan δ > 1 in the LVE region indicating a viscoelastic solid behavior. However, the damping factor of 4% SDC (0.11 ± 0.01) was significantly higher compared to 1% SDS (0.09 ± 0.008), proving arteries decellularized with 4% SDC to be more viscous (Figure 56E). Frequency sweeps revealed that the viscoelastic properties are rather indifferent over a large range of frequencies and revealed a decreased shear modulus for 1% SDS, confirming its softer structure compared to 4% SDC (see Figure 56B). In summary, these data prove viscoelastic solid-like properties for both matrices, whereby the arteries decellularized with 1% SDS exhibited lower stiffness compared to 4% SDC, corroborating specific mechanical properties of ECMs depending on the decellularization method. Taken together, the SDC-based decellularization protocol resulted in a better overall performance concerning ultrastructure, preservation of the extracellular matrix (in particular collagen) and consequently better retained mechanical properties and was therefore chosen for the following experiments.

5.4.4 STATIC CULTIVATION

5.4.4.1 BOECs express typical endothelial markers

Blood outgrowth endothelial cells (BOECs) are mature endothelial cells isolated from human blood with typical endothelial character and high proliferation capability, making them potentially useful in vascular tissue engineering approaches using easily available, autologous cells [321, 322]. Therefore, this cell type was chosen for the generation of the artery model. To identify the isolated cells as BOECs, immunofluorescence staining and flow cytometric analysis for typical endothelial cell markers was performed.

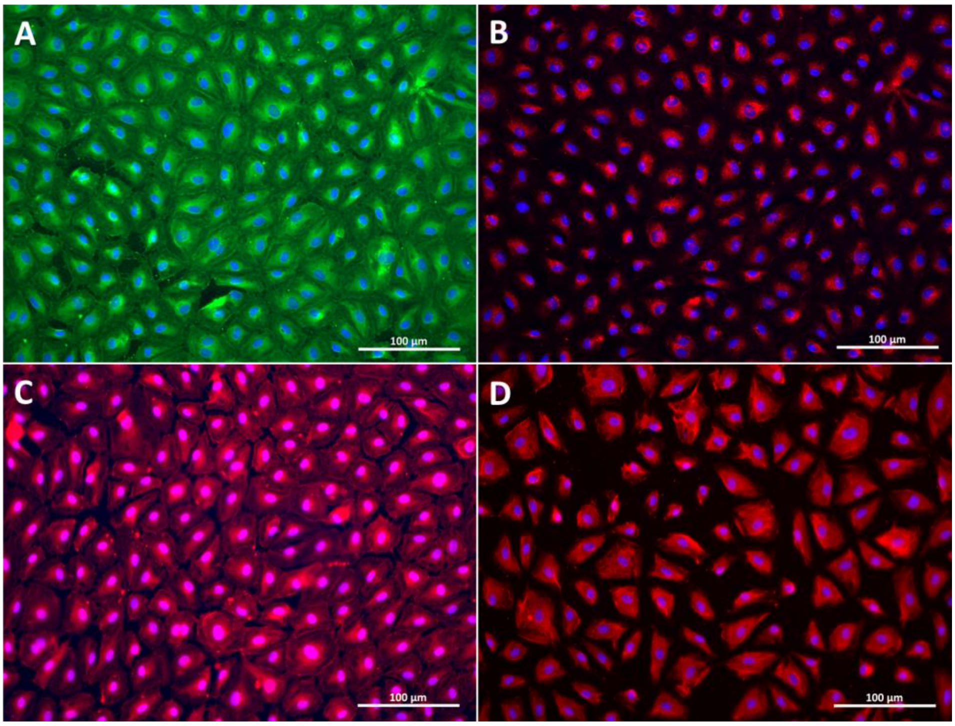

Figure 57: Isolated BOECs express typical markers as revealed by immunofluorescence staining. **A** CD31 is expressed in isolated and cultured BOECs. **B** BOECs are positive for von-Willebrand factor. **C** VE-Cadherin staining shows a positive signal in BOECs. **D** BOECs are also positive for VEGFR-2.

Immunofluorescence staining revealed an expression of the typical endothelial surface markers CD31 (Figure 57A), CD144 (Figure 57C) and VEGFR2 (Figure 57D) and the existence of Weibel-Palade bodies with Von Willebrand Factor (vWF) as punctate cytoplasmic staining (Figure 57B). These findings were furthermore confirmed by flow cytometric analysis, where a clear expression of CD31 (Figure 58A), CD144 (Figure 58B) and VEGFR2 (Figure 58C) was found. Moreover, isolated BOECs were positive for the progenitor and activation marker CD34 (Figure 58D) and negative for the monocytic marker CD14 (Figure 58E) as well as the inflammatory activation marker VCAM-1 (Figure 58F). Taken together, pure cell populations of BOECs expressing multiple endothelial cell markers were obtained with the described isolation method.

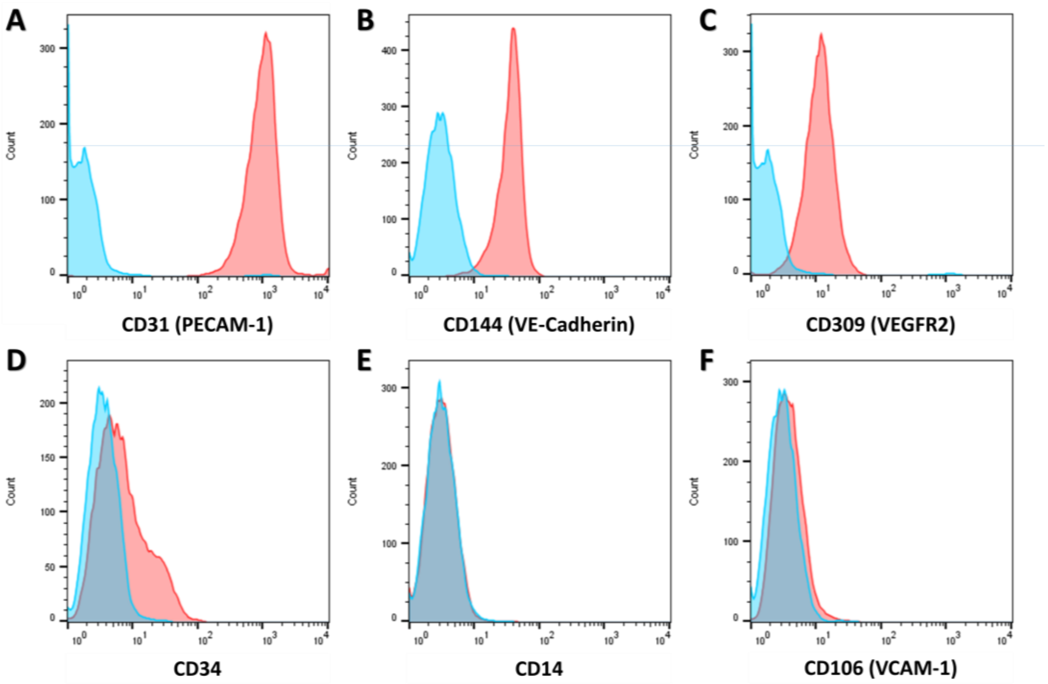

Figure 58: Isolated BOECs express typical markers as revealed by flowcytometric analysis. A BOECs are positive for CD31**. B** All BOECs express CD144 (VE-Cadherin) and **C** VEGFR2 (CD309). **D** CD34 is differentially expressed on BOECs. E BOECs are negative for CD14. **F** BOECs are not expressing VCAM-1 in standard culture. Red: Stained cell population for the indicated marker. Blue: Corresponding Isotype control.

5.4.4.2 Decellularized scaffolds provide good cell adhesion, proliferation, and vitality

To further test the performance of the decellularized carotid arteries regarding cell viability, adhesion and proliferation, isolated BOECs were seeded onto the scaffolds in static culture experiments using cell crowns (see Figure 47) and HE-stainings and SEM analysis was performed for the visualization of cells on the scaffold as well as an MTT test for viability and proliferation were performed after 3 and 7 days of culture (see Figure 59). After 3d of culture, nuclei of seeded BOECs visibly adhered on the scaffold, as revealed by H&E staining. However, no continuous endothelium was formed after 3d (see black arrows in Figure 59A+B). The corresponding SEM image of the intimal layer shows a clear presence of BOECs, but due to the not fully formed layer, the underlying basal lamina is visible (see white arrows in Figure 59C). However, after 7d of culture, a continuous, tight layer of BOECs was found (see Figure 59D+E), which was furthermore confirmed by SEM analysis of the intima (see Figure 59F) and the cross section of the scaffold with a visible, tight layer of endothelium on top (see white arrow in Figure 59H), proving a good adhesion and proliferation of seeded BOECs on the scaffolds. Viability and proliferation was furthermore confirmed by an MTT assay of BOECs cultured on decellularized scaffolds for 3d and 7d. Here, a significant increase in absorption was found after 7d of culture (0.09 ± 0.02 vs. 0.16 ± 0.02, *, $p<0.05$).

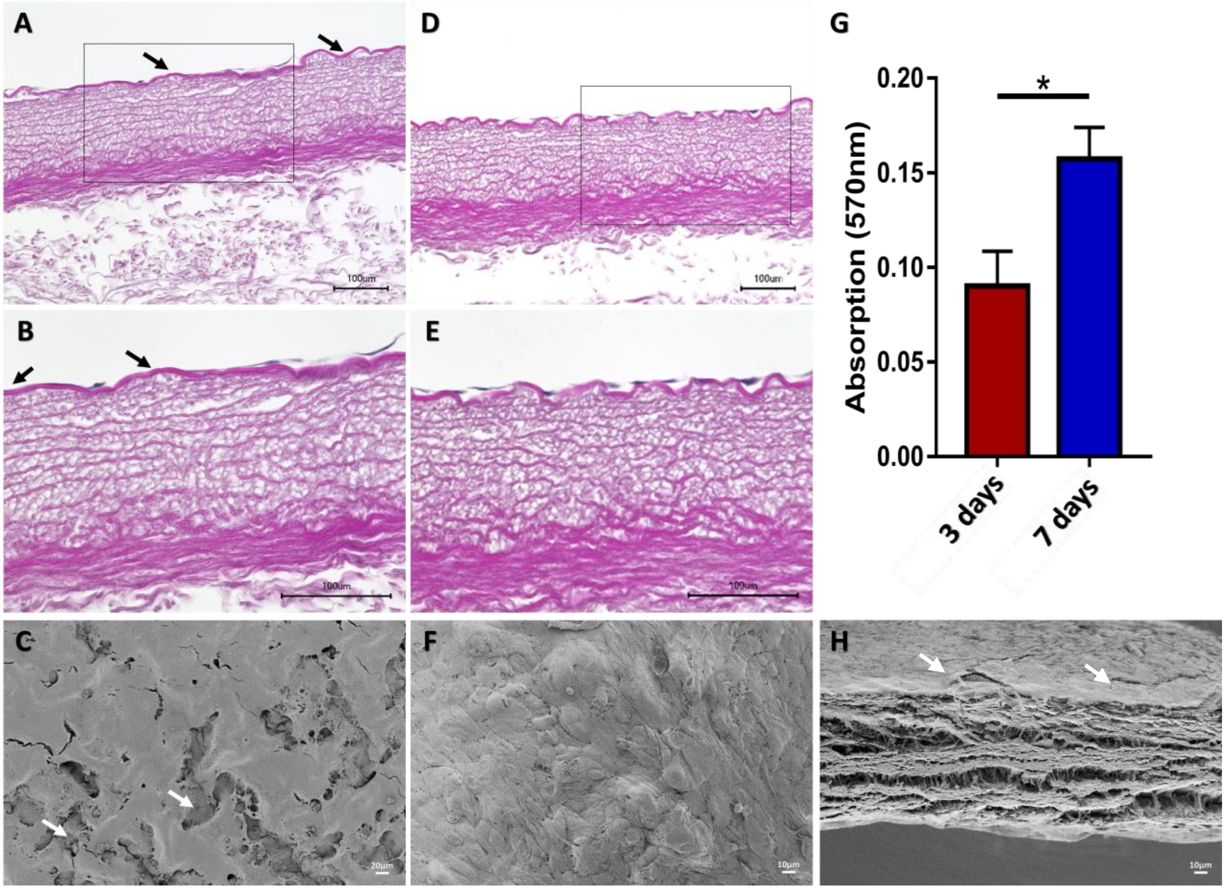

Figure 59: Decellularized scaffolds provide good cell adhesion, proliferation, and vitality. **A** HE-staining of BOECs cultured on the decellularized scaffold for 3d. **B** Enlarged view of A (see black square). Cell nuclei of BOECs are clearly visible, but no continuous endothelium is present (see black arrows). **C** Corresponding SEM image of the intimal layer. Endothelial cells are present, but no continuous layer was formed (see white arrows). **D** HE-staining of BOECs cultured on the decellularized scaffold for 7d. **E** Enlarged view of D (see black square). A Continuous endothelium is clearly visible. **F** Corresponding SEM image of the intimal layer and **H** the cross section. A tight endothelial layer is present. **G** MTT assay of BOECs cultured on decellularized scaffold for 3d and 7d. A significant increase in absorption was found (*, $p<0.05$).

5.4.5 DYNAMIC CULTIVATION OF ARTERY MODELS

5.4.5.1 Bioreactor platform and custom-fit artery chamber

Generating tissue engineered arteries for *in vitro* research not only requires complete acellularity, good mechanical stability and good cell survival and adhesion, but also complex, pulsatile culturing conditions. To meet these requirements, an air driven, generic modular bioreactor platform [23] was used for the dynamic cultivation of artery models (see Figure 60B). The schematic functionality of the air-driven perfusion pump (4) to provide pulsatile flow is depicted in Figure 60A. Due to the applied air pressure, one bag is filled with air, squeezing the medium out of the other bag into the tubing system. Alternate air filling of the two air bags therefore results in controllable and adjustable pulsatile flow conditions. Via the user interface (1), all experimental conditions, e.g., dynamic flow rates, dynamic pressures or oxygen concentration can be accessed and varied, which are sensed by a flow (6) and pressure sensor (7). Furthermore, a robust control of culture processes like the gas exchange (2), heating (4) and the trapping of air bubbles (7) is given, before the medium is pumped into the artery chamber with the artery model (8, see also Figure 60C-F).

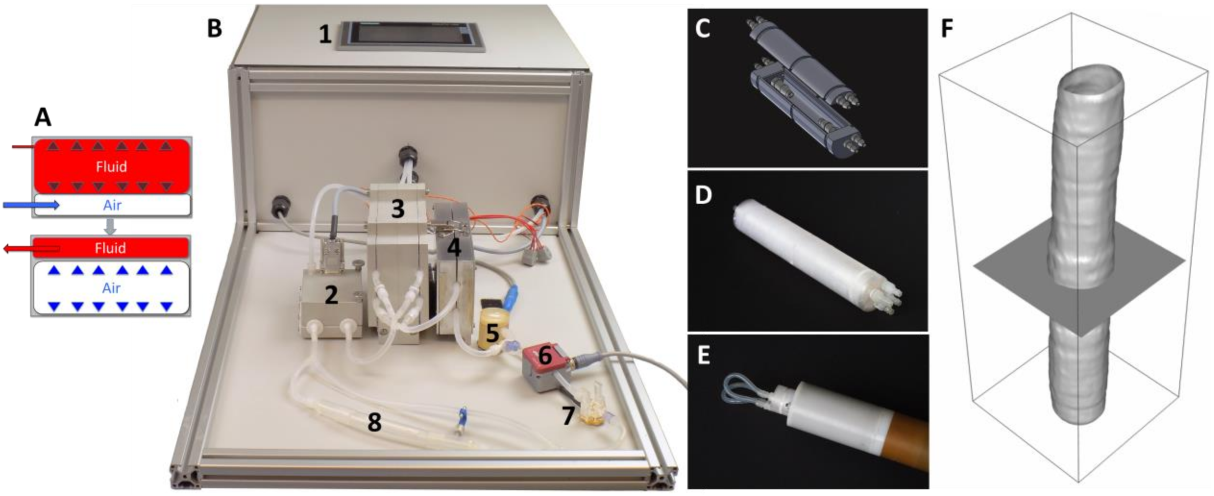

Figure 60: Modular Bioreactor platform and artery chamber for long-term culture and MRI measurements of arteries with pulsatile flow application. **A** Schematic functionality of the air-driven perfusion pump to provide pulsatile flow. **B** Modular bioreactor platform. Via user interface (1), all experimental conditions, e.g., dynamic flow rates, dynamic pressures or oxygen concentration can be accessed. (2) Gas exchanger, (3) air-driven bag pump, (4) heat exchanger, (5) bubble trap module, (6) flow sensor, (7) pressure sensor, (8) tissue chamber with artery model. **C** CAD-image of the custom-fit, MRI-suitable artery chamber. **D** 3D-printed artery chamber, designed and printed by Thomas Schwarz, Fraunhofer-Translationszentrum für Regenerative Therapien TLZ-RT, Würzburg, Germany. **E** Artery chamber positioned in the birdcage coil for MRI measurements. **F** 3D Isosurface of an artery model measured in the artery chamber via MRI.

A custom-built, form-fit and MRI-compatible artery chamber was furthermore specifically designed for the simultaneous long-term culture and high resolution 4D-flow MRI measurements of the artery models (see Figure 60C-E). Additionally, the backflow channels are integrated into the chamber lid (see Figure 60C), guaranteeing the form-fit integration into the birdcage coil (Figure 60E). Taken together, this setup is suitable for the culture and investigation of flow-related processes in native and tissue engineered artery models within a fully controllable environment.

5.4.6 ESTABLISHMENT OF 4D-FLOW MRI MEASUREMENTS IN ARTERY MODELS

5.4.6.1 High-resolution 4D-flow and WSS measurements are feasible in the artery model

To test the performance of the bioreactor system (see Figure 60) in combination with our previously published 4D flow sequence [4] (see also Chapter 2), we extracted the self-navigation signal and measured volume flow, WSS as well as PWV and morphology in native artery models under physiologic, pulsatile flow conditions.

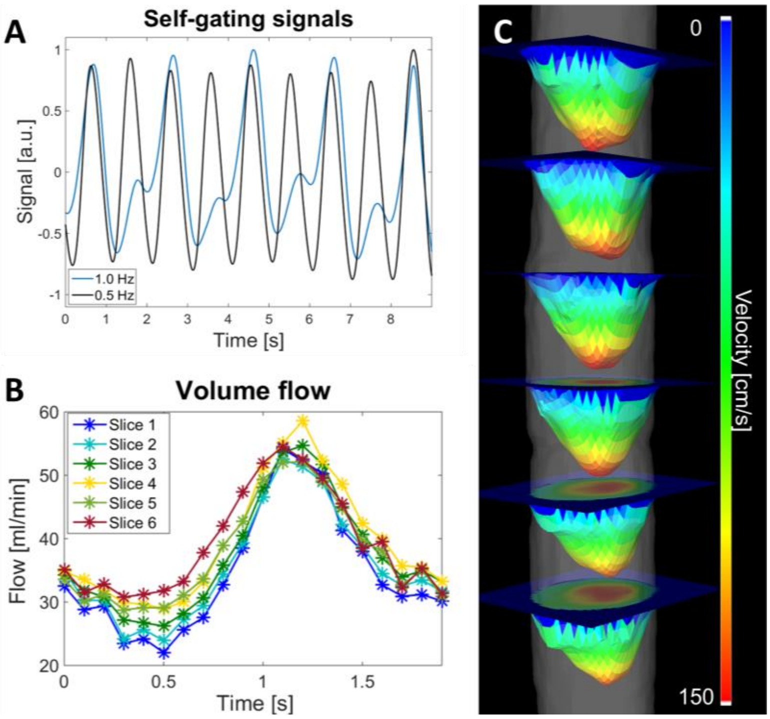

Figure 61: Ex vivo dynamic flow measurements of the carotid artery model. A MR self-gating signals, extracted from the 4D flow measurements, for two different pump frequencies (black: 0.5 Hz / blue: 1 Hz). The strong modulations can be referred to the pulsatile behavior of the perfusion pump. The signals extracted from the radial DC signal were used for retrospective reconstructions. **B** Measured volume flow [ml/s] through 6 analysis planes of the 4D flow measurement (see Figure 61C) as a function of time. **C** 3D flow profiles at the highest flow values of the corresponding 6 analysis planes perpendicular to the artery.

Self-navigation signals could successfully be extracted from the radial DC signal of the *ex vivo* measurements of the native porcine carotid artery model. Figure 61A shows exemplary signals acquired during the 4D flow measurements at 2 different pump frequencies of 0.5 Hz (black line) and 1 Hz (blue line). The strong modulations due to the pulsatile flow are clearly visible, guaranteeing successful navigation without the need for an external connection of the MRI scanner to the pump system. The pulsatile behavior is furthermore reflected by the results of the 4D flow measurements (see Figure 61B+C). Figure 61B shows the volume flow through 6 exemplary planes in the native carotid artery. As expected, a clearly parabolic flow profile predominates in the straight vessel.

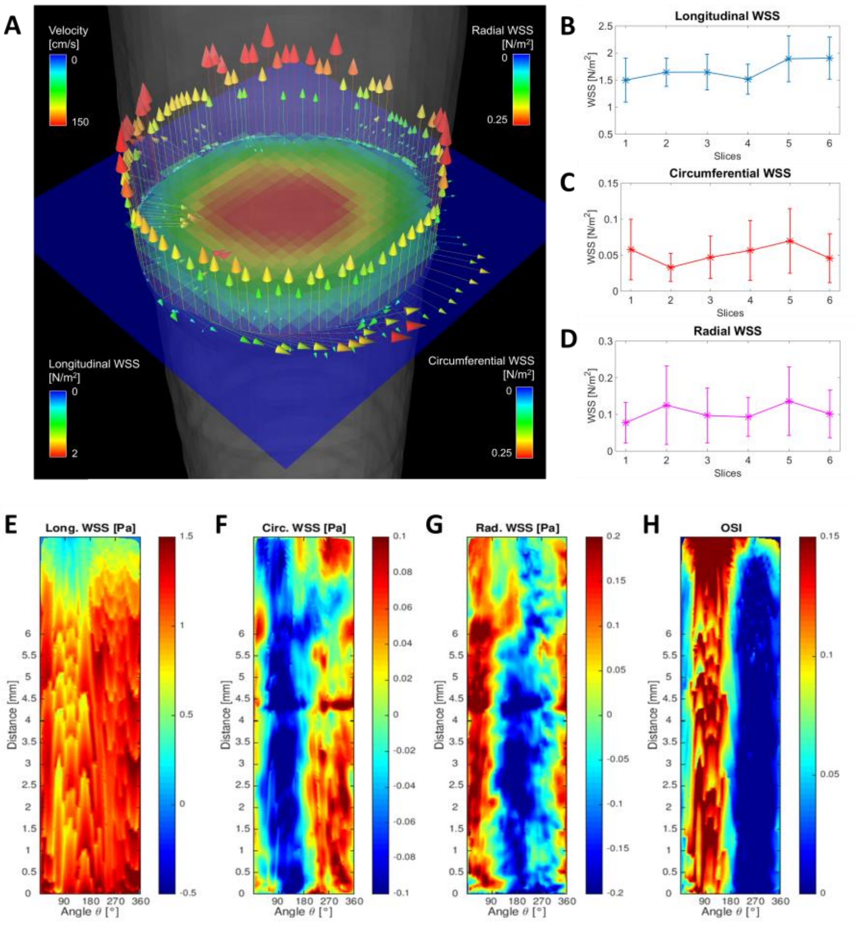

Figure 62: Analysis of wall shear stress in the artery model. **A** Vector illustration of longitudinal and circumferential components of the WSS as well as the radStrain, calculated from the 4D flow measurement. **B-D** Calculated mean values (±SD) of the two WSS components and the radStrain. **E** 2D projection map [3] of longitudinal, **F** circumferential WSS, **G** radial strain and **H** OSI in the native artery model.

In a next step, the longitudinal and circumferential WSS as well as the radial strain were successfully calculated from the 3D velocity gradients of the 4D flow measurement (shown for one exemplary 2D plane in Figure 62A and the plots of the corresponding WSS components in Figure 62B-D). Furthermore, the generation of 2D-projection maps to fully resolve values of all WSS components, consisting of longitudinal WSS (Figure 62E), circumferential WSS (Figure 62F), radial strain (Figure 62G) and OSI (Figure 62H) in the complete carotid artery was feasible.

5.4.6.2 Determination of the local PWV

The determination of the PWV is a good tool to non-invasively assess the arterial stiffness, which is an important marker in early and late atherosclerosis. Therefore, the local PWV was calculated at 4 different locations of the artery using the Q(A)-method [11] (see Figure 63). For the determination of the local PWV, the cross-sectional area changes A (Figure 63A) and the time-dependent volume flow Q (Figure 63B) was measured. The PWV value was assessed by fitting a line to the data points of the Q-A curve (Figure 63C) corresponding to the early upstroke of the flow pulse (see red marks). The mean PWV value over all slices was 5.7±0.5 m/s.

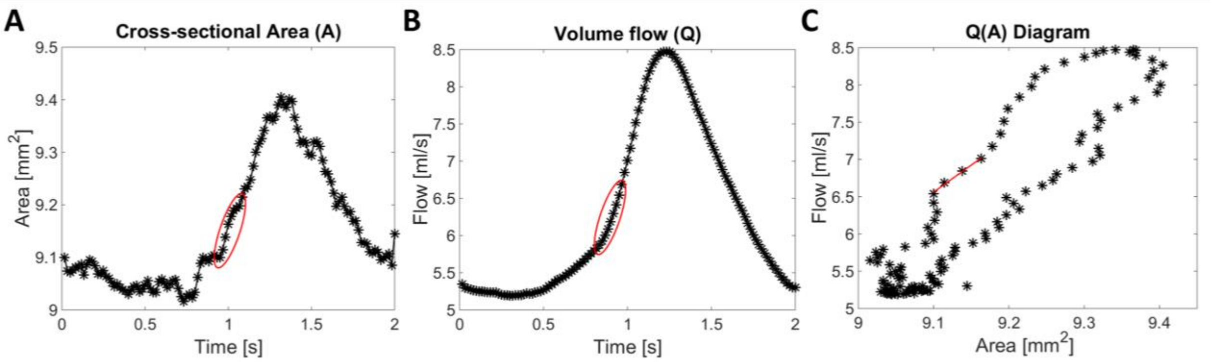

Figure 63: *Ex vivo* measurement of the local PWV in the porcine carotid artery model. **A** Measured volume flow (Q) pulse as a function of time. **B** Measured changes of the cross-sectional area (A). **C** Q-A diagram for calculations of the local pulse wave velocity. The data points during the early upstroke of the flow pulse (marked red) were used for linear fit (red line).

5.4.6.3 3D Morphology

Changes in arterial elasticity come along and correlate with morphological changes of the vessel wall. Therefore, the determination of the vessel morphology and wall thickness is of great importance. To test a fast, three-dimensional assessment of the vessel wall morphology, a threshold-based segmentation was applied to the 4D cine reconstruction of the morphology measurement. After subtraction of the lumen signal, the segmented data was exported to the data viewing tool OsiriX (PIXMEO Sarl, Swiss). Figure 64 displays the successful measurement of the vessel morphology, showing a cut through a 3D volume rendering of the segmented vessel.

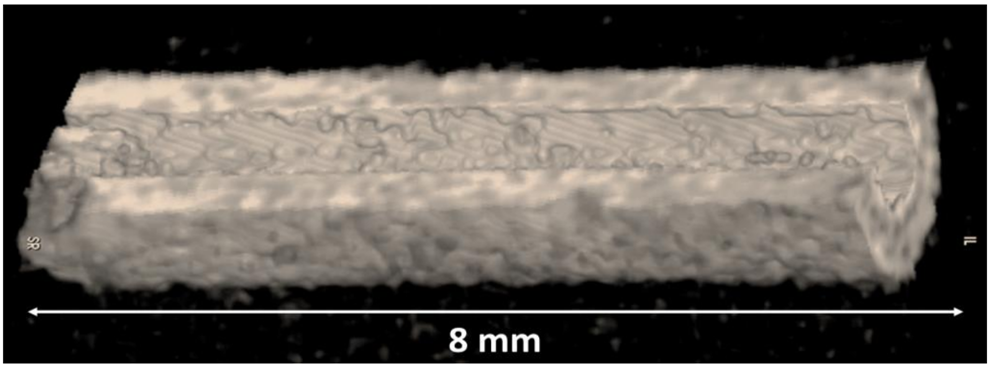

Figure 64: Cut through a 3D volume rendering of the vessel wall of the native artery model. This image data was acquired with a flow compensated radial 3D sequence and visualized with the 3D data viewing tool OsiriX (PIXMEO Sarl, Swiss).

Taken together, we successfully established an MRI-suitable setup for high-resolution 4D-flow measurements, proving the feasibility of assessing 4D flow dynamics, wall shear stress and pulse wave velocity as well as a fast, three-dimensional visualization of vascular morphology in artery models cultured under physiologic, pulsatile flow conditions.

5.5 DISCUSSION

Biological artery models, cultured in a bioreactor-platform with adjustable pulsatile flow conditions [23], represent a potential *in vitro* test system for atherosclerosis research and provide a suitable tool for the development of new flow quantification techniques as well as studies of arterial elasticity and flow dynamics [13, 202]. However, artificial vessel phantoms can meet the elastic properties of the blood vessels but are not excellently suitable for the development of *in vitro* test systems due to their synthetic nature. At this point, tissue engineering poses a potential alternative to conventional flow phantoms since tissue-engineered arteries have similar physical properties than native arteries and enable the study of pathologies in defined environments, offering the possibility for controlled biological (cellular) and physical (hemodynamic) modifications.

In this study, we therefore developed a gentle decellularization method for porcine carotid arteries, preserving the ultrastructure, ECM composition, mechanical stability, and showing complete acellularity meeting the described good manufacturing practice (GMP) standards [24, 25]. Reseeding of the carotid artery scaffolds showed excellent cell adhesion and proliferation, resulting in a tight endothelial cell layer. Furthermore, an MRI suitable setup was established, comprised of a modular bioreactor platform for a fully controllable hemodynamic environment [23] and a custom-fit artery chamber for the development and application of high-resolution 4D-flow MRI [4, 16], including WSS quantification in the complete artery and the investigation of arterial stiffness through PWV measurements and morphological imaging.

However, the most relevant criterion for the development of a suitable *in vitro* atherosclerosis test system for the investigation of flow-related disease development and progression is the preservation of the native mechanical stability, which is mostly influenced by the extracellular matrix [327]. Therefore, the development of an optimal decellularization protocol, resulting in efficient cell removal while minimizing the effects on architecture, ultrastructure, ECM composition and therefore mechanical properties is of great relevance. Ineffective decellularization can furthermore not only cause a strong inflammatory response in transplantation studies [216], but also affect cell survival, adhesion and proliferation and furthermore cause a significant loss in mechanical stability due to excessive ECM damage and loss of ultrastructure. Non-ionic detergents are suitable for the decellularization of thin tissues, preserving glycosaminoglycans (GAGs) and less affecting ultrastructure in comparison to ionic detergents [218, 219]. In contrast, ionic detergents are suitable for the efficient cell and cytoplasmatic protein removal in thick tissues, however, they are known to affect GAGs, remove growth factors and are also known to damage collagen [24, 328]. In order to find the optimal decellularization protocol, we therefore tested two different decellularization approaches, based on the ionic detergents sodium deoxycholate (SDC) and sodium deoxycholate (SDS) to solubilize cytoplasmic and nuclear components, combined with preceding osmotic shock to lyse the cell membranes, and following enzymatic treatment for the digestion of residual host DNA [24, 25]. In comparison to other detergents, SDS is known to decellularize tissue more efficiently, however, it is also disrupting the native tissue structure, causing a loss of collagen integrity and decreasing the GAG concentration [24, 25]. In contrast, SDC also removes the cells and cellular remnants efficiently, but is known for a greater disruption of the native tissue architecture in combination with other zwitterionic detergents [24, 25]. To our knowledge, the effect of SDC alone on the remaining ECM of arteries has not been reported yet. Both protocols showed an efficient cellular removal after a short time period of 2h for SDS and 4h for SDC, resulting in a very fast protocol compared to other published techniques of arterial decellularization [329]. Complete acellularity was confirmed by the absence of cell nuclei and visible DNA in respective histology as well as by DNA extraction and measurement, resulting in a sufficient reduction to < 50 ng/mg dry weight and a residual fragment length of <200 bp [24].

Concerning architecture and ultrastructure, both protocols showed a good preservation of the overall arterial structure, with the presence of thick elastic lamellae and collagen bundles and fibers. However, decellularization with SDS is known to strongly affect ECM structure [24, 25, 212], which was clearly visible in scaffolds decellularized with SDS, showing damaged collagen bundles and less collagen fibers on the basal lamina, whereas in arteries decellularized with SDC, a dense ECM fiber network is present on the basal lamina and the collagen bundles strongly resemble the native status. This was furthermore reflected by measurements of the hydroxyproline content in native and decellularized arteries, revealing a significant enrichment of hydroxyproline and therefore collagen in arteries decellularized with SDC, and consequently indicating a loss of collagen in arteries decellularized with SDS. The obtained values furthermore correspond well with literature [330]. However, due to the weight of the present cell nuclei in native arteries, the obtained values are not fully comparable to decellularized arteries. Therefore, the collagen content was determined through histological analysis of picrosirius red staining under polarized light, revealing significantly less collagen in arteries decellularized with SDS in comparison to native arteries. These findings were furthermore underlined by rheological analysis, where the softer structure of arteries decellularized with SDS was confirmed, indicating damaged collagenous tissue due to the decellularization process with SDS. However, not only the collagen content is crucial for mechanical stability, but also the elastin content. To draw conclusions on the elasticity of the arteries, the ultimate tensile strength of native and decellularized arteries was determined. Here, a considerably similar mechanical integrity in comparison to native arteries was found for both decellularization protocols. Decellularized arteries showed a statistically insignificant increase in ultimate strength compared to native arteries, which may be explained by minor disruptions of mainly collagen fibers [24] in native arteries. As collagen is less present in decellularized arteries due to the decellularization process, a slightly higher elasticity is observed.

Considering the preservation of mechanical properties and ECM, the proposed SDC-based decellularization and sterilization process seems to be favorable. The decellularized artery closely mimics the native ultrastructure and shows no potential cytotoxicity through bile acid remnants. We therefore achieved a good balance between efficient cell removal and the disruption of the extracellular matrix structure with SDC-based decellularization. Furthermore, SDS is known to show reduced recellularization capability through excessive ECM-modification [331], which was not observed in decellularized arteries with SDC. Here, we achieved a good proliferation, adhesion, and vitality of cells on the decellularized carotid artery scaffold. Moreover, the choice for blood outgrowth endothelial cells (BOECs), also called endothelial colony forming cells (ECFCs) or (late) outgrowth endothelial cells (OECs), paves the way for not only creating a suitable *in vitro* artery and atherosclerosis model, but also the creation of vascular grafts based on the presented scaffolds with autologous cells from patients in future studies. These cells are a very suitable source due to their very high proliferation and expansion rate and their easy availability through venipuncture [321, 322] and show a typical endothelial phenotype [332, 333] and gene expression [332, 334, 335] compared to endothelial progenitor cells (EPCs), which show a more hematopoietic character, proving the relation of BOECs to large vessel–derived as well as microvascular endothelial cells [334, 335].

With BOECs being also suitable for viral transduction [336, 337] and therefore the investigation of specific target genes or proteins in atherosclerosis, we created a biologically controllable artery model, which can be further modified by e.g., using additional smooth muscle cells for medial layer formation or calcifying medium for the induction of vascular stiffness [338], which will be the focus in future studies.

However, to create a potential *in vitro* test system for flow-related atherosclerosis research, there is also a need for a fully controllable environment, which enables the controlled application of physiologic and pathologic hemodynamic conditions to the artery models. A modular bioreactor platform with a pulsatile perfusion pump [23] was used to mimic the *in vivo* blood circulation and equipped with a custom-fit, MRI-compatible artery chamber to assess of flow-related parameters like WSS and PWV using 4D-flow MRI [4, 16] and the performance of the setup was successfully tested in subsequent measurements with native artery models. Radial acquisitions and self-navigation were successfully applied for retrospective cine reconstructions, showing strong modulations in the radial DC signal, which could be clearly attributed to the applied pulsatile flow through the artery. Therefore, with this setup, MRI measurements are enabled without the need for a direct connection of the bioreactor platform with the MRI scanner, strongly facilitating the measurement process. Consequently, the proposed setup is easy to implement in all types of scanners including whole body MRI systems, with no constraints to measurement times, leading to higher resolutions, better signal-to-noise ratio (SNR) as well as a higher reproducibility. Furthermore, with this setup, the overall handling is significantly improved, as in contrast to *in vivo* measurements, no anaesthesia and monitoring of vital functions is required. Moreover, the segmentation process of the measured arteries is significantly accelerated and improved, as no disturbing background signal from the surrounding tissue is present. However, the application of conventional prospectively triggered cine techniques is also straightforward and can be easily achieved by using pressure sensors to tap the pressure pulse.

To further test the suitability of the setup in the investigation of flow-related disease processes, high-resolution 4D-flow MRI measurements [4, 16] were performed, including volume flow, WSS and PWV measurements [10, 15]. PWV values obtained from the measurements correspond well with literature [6]. Furthermore, WSS values are in good accordance with the results reported previously for porcine carotid arteries *in vivo* [6, 164]. Moreover, in the same session, a fast assessment of 3D morphology was performed, which could potentially identify and localize eventual arterial thickening processes during atherosclerosis development and progression in the artery models.

Taken together, the proposed setup together with the native and tissue engineered artery models offers a great potential to study flow dynamics and morphology in healthy and pathological cases under a fully controllable biologic (cellular) and physical (hemodynamic) environment, which could significantly improve basic atherosclerosis research and could help to identify and understand key mechanisms in disease development.

5.6 CONCLUSION

Mouse models of vascular diseases like e.g., atherosclerosis only offer a limited possibility to investigate hemodynamic-related disease development in a controllable manner. To better understand flow-related disease development and progression in e.g., atherosclerosis, *in vitro* artery models offer a great potential. We here present for the first time a suitable setup for studying arterial hemodynamics in native and tissue engineered artery models under fully controllable conditions. The described tissue-engineered artery model constitutes a model system; however, it possesses all relevant components for the extension to an atherosclerosis model. Furthermore, it allows the controlled reconstruction of physiologic and pathologic conditions and therefore enables the targeted investigation of disease-relevant key processes. In comparison to the *in vivo* situation, the utilization of *in vitro* artery models offers conditions of lower complexity with controllable influencing factors. Therefore, in combination with biological and physical methods, these models offer the opportunity to contribute to the fundamental reconnaissance of the interrelationship between increased pulse wave velocity, altered shear profiles and inflammation processes.

5.7 SUPPLEMENTARY FILES

5.7.1 LIST OF ANTIBODIES FOR IMMUNOHISTOLOGY

Supplementary Table 6: List of Antibodies for Immunohistology.

Antigen	Dilution	Company	Catalogue #
CD31 (PECAM-1)	1:20	abcam	ab28364
Von Willebrandt Factor (vWF)	1:250	abcam	ab154193
CD144 (VE-Cadherin)	1 µg/ml	abcam	ab33168
CD309 (VEGFR-2)	1:200	Invitrogen	MA5-15157

5.7.2 LIST OF ANTIBODIES FOR FLOWCYTOMETRY

Supplementary Table 7: List of Antibodies for flow cytometry.

Antigen	Fluorophore	Company	Catalogue #
CD31 (PECAM-1)	APC	Miltenyi Biotec	130-098-174
CD34 (Mucosialin)	FITC	Miltenyi Biotec	130-113-740
CD144 (VE-Cadherin)	FITC	Miltenyi Biotec	130-100-713
CD309 (VEGFR-2)	APC	Miltenyi Biotec	130-098-910
CD106 (VCAM-1)	FITC	Miltenyi Biotec	130-104-162
CD14	APC	Miltenyi Biotec	130-110-578

Supplementary Table 8: List of Isotype controls for flow cytometry.

Antigen	Fluorophore	Company	Catalogue #
IgG1κ	APC	Miltenyi Biotec	130-098-846
IgG2aκ	FITC	Miltenyi Biotec	130-098-877
REA (S)	FITC	Miltenyi Biotec	130-104-610

CHAPTER 6

An Easy-To-Prepare Hydrogel-Based Artery Model For Flow-Related *In Vitro* Atherosclerosis Research

Chapter 6 is planned to be submitted as a modified version in a scientific journal as an original research article (Kristina Andelovic, Matthias Ryma, Celine Frank, Jürgen Groll and Alma Zernecke: "An Easy-To-Prepare Hydrogel-Based Artery Model For Flow-Related *In Vitro* Atherosclerosis Research". This chapter is based on the work of the author of the thesis, Kristina Andelovic, who designed the study and performed all experiments and data analysis. The final publication will be supplemented with additional experiments and is in preparation at the time of handing in this thesis.

6.1 ABSTRACT

The field of biofabrication provides several techniques to mimic the vasculature with its multi-layered structure as accurately as possible. However, current methods mostly rely on prefabricated scaffold designs, or need special equipment or even complex multi-step procedures to achieve more complex geometries like bifurcations or even a model of the aortic arch. In particular for *in vitro* models of vascular diseases, where flow dynamics often play an important role, the development of functional and design-specific perfusion chambers for the controllable, dynamic cultivation of these models is crucial.

Therefore, we developed an easy-to-prepare, low cost and fully customizable artery model based on thermoresponsive sacrificial scaffolds, processed with the technique of Melt Electro Writing. The biomimetic shape of the scaffold was chosen to resemble both, bifurcations and curvatures to mimic the geometric properties of the aortic arch. This sacrificial scaffold was embedded into a gelatin-hydrogel, crosslinked with bacterial transglutaminase and mixed with vascular smooth muscle cells (vSMCs), followed by dissolution and flushing of the sacrificial scaffold. Endothelial cells (ECs) were seeded into the remaining channel and grown to confluency under dynamic flow conditions. The custom-built and highly adaptable perfusion chamber was designed specifically for the scaffold structure, enabling a one-step creation and simultaneous dynamic cultivation of the artery models. It was furthermore shown that vascular smooth muscle cells were migrating towards the channel and maintained cell viability. With this, a hydrogel-based artery model with both crucial cell types, namely SMCs and ECs, was successfully given, making it an excellent basis for the development of *in vitro* disease test systems for e.g., atherosclerosis research.

6.2 BACKGROUND

3D artery models for the development of *in vitro* test systems are of great importance in the biomedical research field, as they offer a simplified environment in comparison to the *in vivo* situation, yet more controllable. Therefore, they are a powerful tool to gain new insights into homeostasis as well as key processes of disease development and progression. The field of biofabrication offers several techniques allowing the generation of channel structures ranging from channels in the size of microvessels to bigger ones in the size of arteries. However, mimicking the structure of arteries is challenging, as the arterial wall consists of three different layers: The innermost layer (tunica intima) consists of a single layer of vascular endothelial cells surrounded by a basement membrane with elastic fibers. The second layer (tunica media) represents the thickest layer and consists of vascular smooth muscle cells embedded in between thick elastic fibers and collagenous fibers. The outermost tunica externa or tunica adventitia is composed of fibroblasts and dense collagenous and elastic fibers and connects the vessel to the surrounding tissue [251]. *In vitro* vascular tissue models mimicking all important components of native arteries are of great importance and utility especially in the field of biomedical research, but simple and effective strategies for their creation are still under development.

In this regard, Additive Manufacturing (AM) approaches like 3D bioprinting techniques gained much attention in recent years. It has already been shown that vascular structures can be directly bioprinted via 3D printing techniques [252-254]. However, since bioprinting is an additive manufacturing technique, where each layer provides the structural integrity for the upcoming one, generation of perfusable tissues require printing of one stable and one sacrificial bioink (for the later channel) with suitable rheology – as direct printing of overhangs is not possible. Therefore, the minimum setup is a 3D printing device which supports at least two printheads for the application of these two bioinks, which also must be highly adapted to enable precise deposition of the gel while maintaining stability after printing. Another approach to generate vascular structures is the prefabrication of scaffolds with subsequent cell seeding [256, 257]. The advantage of this scaffold prefabrication with biomaterials compared to bioprinting is the ability to mimic the fibrous composition of the ECM and to further adapt the mechanical properties, which play an important role for arterial functionality and integrity [251]. However, since the fabrication processes are requiring non-physiological parameters like elevated temperature or the application of organic solvents, cells cannot be incorporated during the fabrication process of the scaffold. Additionally, this method does not allow the creation of more complex structures like curvatures or bifurcations and outer cell seeding is difficult to manage due to the round structure.

Nevertheless, this disadvantage can be avoided by utilizing casting-methods, where cell-laden hydrogels can be casted into more complex structures and shapes. There have been several approaches to make use of and further develop the casting approach for creating simple channels or sophisticated channel networks, which can be roughly categorized into 3 methodologies:

1. The generation of channel structures by casting and bonding of two fitting hydrogels, which provide grooves on both sides to generate cylindrical channels after bonding [258-260], resulting in a perfusable channel network in the hydrogel matrix.

2. Creation of multilayered structures by targeted gelation of cell-laden hydrogels in the vicinity of preformed channels after filling of the mold with precursor solution. This can be achieved by incorporating crosslinking ions into the channel walls, which lead to the gelation of the hydrogel, e.g., alginate [261, 262]. This results in a tunable thickness of the medial layer by elongated exposure to the ions in the channel wall and the subsequent flushing of uncrosslinked precursor solution. After endothelial cell seeding into the resulting lumen, bi-layered, perfusable artery models are created.
3. Successive casting of hydrogel layers around mandrels. Removal of the mandrels and subsequent introduction of endothelial cells into the channels resulted in a functional three-layered artery model for atherosclerosis research [265].

However, the main disadvantage of these techniques is the manual application of accurate multi-step procedures, which leads to a low reproducibility and time-intensive assembly.

The sacrificial template technology is another method to achieve vascular-like structures. Besides channel creation with mechanically removable agarose templates [266], the application of sacrificial scaffolds, such as carbohydrates [267-270], gelatin [248] and alginate [271, 272], which can be embedded into hydrogels and dissolved by external stimuli, can be used to generate channels or sophisticated channel networks. These sacrificial scaffolds can be generated via 3D printing methods and were mainly shown with carbohydrate-based scaffolds [267-270], improving the design freedom of vascular networks drastically. However, this technique has several challenges that need to be addressed before becoming an easy-to-use technology. First, the specific positioning and embedment of sacrificial structures into hydrogels is challenging, and the structure is usually fully emersed in the hydrogel. This leads to the necessity of a manual post-establishment of the fluid connections with needles or cannulas since the inlet and outlets are initially blocked by the hydrogel. Therefore, the establishment of a leakage-free perfusion loop is imprecise and prone to error. Furthermore, sacrificial structures based on carbohydrates dissolve directly in aqueous solution, so it is hardly possible for hydrogel gelation to occur in time to create perfusable channels. Therefore, post-processing like coating with PLGA, hydrogel or other materials is needed to increase the timeframe for gelation, which is time- and cost-intensive and increases in difficulty when fabricating more complex structures [267, 339]. Besides carbohydrates, another study featured the creation of highly complex perfusable channel networks by utilizing a complex multi-casting approach based on selective dissolution of thermoplastic material [340]. However, it requires the utilization of several materials and is neither cost- nor time-efficient because of the elongated timeframe.

Despite the variety of methodologies for creating functional artery (and vascular disease) models, there is still a big gap between mimicking the native structure of arteries with all cellular components in a precise way and simultaneously reducing the complexity of the fabrication process - yet establishing a method to achieve leakage-free perfusability for the application of physiologic and / or pathologic hemodynamic conditions.

Therefore, our goal in this study was to overcome all the disadvantages of the mentioned techniques and combine sacrificial scaffold utilization with simultaneous casting into custom-designed perfusion chambers for the direct creation and dynamic cultivation of standardized, customizable artery models with natural bifurcations for *in vitro* research of vascular diseases. For this, we used the thermoresponsive polymer poly(2-cyclopropyl-2-oxazoline) (PcycloPrOx or PcPrOx), fabricated via melt electrowriting [341] to create the bifurcating sacrificial fiber scaffolds. Its swelling behavior in aqueous solutions like hydrogels leads to fiber fusion and thus creates interconnected channel networks after dissolution via temperature decrease below 25°C. To enable targeted casting of hydrogel around the scaffolds, we furthermore developed customizable perfusion chambers, where the scaffolds are prefixated - enabling leakage-free and simple casting of the hydrogel into the perfusion chamber and leading to a direct connection between the channels and the tubing system of the perfusion pump after dissolution of the polymer. This resulted in a fast, one-step creation of ready-to-use artery models with natural bifurcations. We further show that a continuous endothelial layer was rapidly created inside the channels and that smooth muscle cells were spreading and migrating towards the channel, forming a media-like structure. The adaptable channel and hydrogel designs in combination with the customizable perfusion chambers represent an important milestone in developing *in vitro* vascular disease models.

6.3 METHODS

6.3.1 SCAFFOLD PREPARATION

6.3.1.1 Synthesis of PcycloPrOx

All chemicals were purchased from Sigma Aldrich (Munich, Germany). PcycloPrOx was synthesized as described in literature [342] and was kindly provided by Julia Blöhbaum, Department for Functional Materials in Medicine and Dentistry (FMZ, Würzburg, Germany).

6.3.1.2 Production of MEW fibers/scaffolds fabricated with PcycloPrOx

For the process of Melt Electrowriting, a custom-built device, already described elsewhere [343], was used. In order to produce homogenous fibers, the MEW device was equipped with one heating zone at the syringe and another one at the nozzle. For MEW of P*c*PrOx, a 22G needle was used. The temperature of the syringe was set to 210°C while the temperature of the nozzle was set to 225°C. The distance between nozzle and collector plate was 2 mm and the pneumatic pressure was set to 2 bar. Production of the scaffolds was performed by Matthias Ryma, Department for Functional Materials in Medicine and Dentistry (FMZ, Würzburg, Germany). Before application in cell culture, scaffolds were sterilized by UV-treatment (254 nm) with an UV-lamp (VL-4.LC, Vilber Lourmat, Essen, Germany) for 30min.

6.3.2 CELL CULTURE

6.3.2.1 Primary human vascular cells

Primary human microvascular endothelial cells (hmECs, PCS-110-010) and primary human aortic smooth muscle cells (HAoSMCs, PCS-100-012) were purchased from ATCC (Manassas, Virginia, USA) and cultured in Vascular Cell Basal Medium (PCS-100-030) with the Microvascular Endothelial Cell Growth Kit-VEGF (PCS-110-041) for hmECs and the Vascular Smooth Muscle Cell Growth Kit (PCS-100-042) for HAoSMCs. After reaching confluency, cells were incubated with PBS/EDTA (0.45 M EDTA) for 5 minutes (for hmECs) and afterward trypsinized with 0.05% Trypsin-EDTA 1X (Thermo Fischer Scientific, Waltham, Massachusetts, USA). Cells were seeded with an initial seeding density of 8.000 cells/cm².

6.3.2.2 Isolation of primary murine vascular cells

Primary murine vascular endothelial cells (mAECs) and smooth muscle cells (mASMCs) were isolated from the aorta of 6-10-week-old mice. After opening the chest, the heart and aorta was flushed with PBS^{-} (Gibco) with 1000 U/ml heparine (Roche, Basel, Switzerland) to avoid blood clotting. Aorta was cut out and washed 3x in cold HBSS (Gibco) with 1% PenStrep (Gibco), 1% Amphotericin B (Gibco) and 1% Gentamycin (Gibco). Afterwards, the tissue was digested with an enzyme-mix (Collagenase II 1 mg/ml, Trypsine-inhibitor 1 mg/ml and Elastase 0,744 U/ml, dissolved in HBSS; all from Worthington Biochemical, Lakewood, NJ) for 10 min at 37°C.

Enzyme mix was washed away with DMEM-F12 medium (Gibco) and the adventitia was stripped off to remove fibroblasts. The remaining aorta was cut into small pieces and digested for 1h at 37°C in the enzyme mix. Cell suspension was centrifuged and washed in DMEM-F12. Afterwards, cells were seeded onto gelatin-coated cell culture flasks with a density of 2 aortas per 25cm^2 and cultured in DMEM-F12 with 20% FCS and 1% PenStrep until confluency. After passage 3, serum was reduced to 10%.

6.3.2.2.1 Separation and purification of murine vascular cells

At passage 2, cells were incubated with PBS/EDTA (0.45 M EDTA) for 5 minutes and afterwards detached with StemPro Accutase (Thermo Fisher). Separation and purification of mAECs and mASMCs was conducted with the CD31 MicroBeads, mouse kit (Miltenyi Biotec, Bergisch Gladbach, Germany) according to the manufacturers protocol. In brief, cells were magnetically labelled with CD31 Microbeads and loaded onto a MACS column, which was placed in the magnetic field of a MACS Separator. Labeled CD31-positive mAECs were retained in the column, whereas unlabeled mASMCs ran through. Both cell fractions were washed and seeded separately into gelatin-coated cell culture flasks. mASMCs were cultured in DMEM-F12 with 10% FCS and 1% PenStrep, mAECs were cultured in DMEM-F12 with 10% FCS, and 1% PenStrep, supplemented with 5mg/ml bovine ECGS (Sigma) and 500 U/ml heparin (Roche).

6.3.2.3 Murine cell lines

Murine endothelial cell line C166 (CRL-2581) and aortic smooth muscle cell line MOVAS (CRL-2797) were purchased from ATCC and cultured in DMEM High Glucose (Gibco) supplemented with 10% FCS and 1% PenStrep. Cells were cultured until 80 – 90% confluence and passaged according to the manufacturer’s instructions.

6.3.2.4 Characterization of murine ECs and SMCs

6.3.2.4.1 Immunocytochemistry

For immunocytochemical analysis of isolated murine vascular cells, cells at passage 3 were grown in chamber slides (ibidi) until confluency. After washing with PBS-, fixation was performed in 4% PFA for 10min. Samples were blocked with 5% goat serum (Sigma Aldrich), incubated with primary antibody (all from abcam, see Table 3) overnight at 4˚C, and fluorescence-conjugated secondary antibody (1:400, all from Molecular Probes, Life Technologies, Carlsbad, CA, USA). Samples were mounted with DAPI-containing Vectashield mounting medium (Vector labs, Burlingame, CA, USA) to counterstain nuclei.

Table 3: Primary antibodies used for cell characterization.

Catalogue number	Antigen	Host	Dilution
Ab28364	CD31	Rb	1:50
Ab7817	aSMA	Ms	1:100
Ab53219	SM-MHC	Rb	1:50
Ab46794	Calponin	Rb	1:100
Ab90395	Col I	Ms	1:2000
Ab7778	Col III	Rb	1:100

Ab6586	Col IV	Rb	1:200
Ab21610	Elastin	Rb	1:200

6.3.2.4.2 *Flow cytometry*

For FACS-analysis, cells were detached with Accutase, washed in PBS$^-$ with 1% FCS and 2mM EDTA (PBS/FCS) and 500.000 cell per sample were incubated with Fc-Block (Firma, 1:50 dilution in PBS/FCS) for 10min at RT. Live/Dead solution was prepared by diluting the eBioscience Fixable Viability Dye eFluor 450 in PBS/FCS (1:1000). After washing in PBS/FCS, surface staining of endothelial cells with CD31 (1:100, Miltenyi Biotec) and CD144 (1:10, Miltenyi Biotec) was performed in a volume of 50µl of Live/Dead solution per sample for 30min at 4°C. Samples were washed, resuspended in PBS/FCS and kept on ice until measurement. For flow-cytometric analysis of smooth muscle cells, cells were first stained in Live/Dead solution for 30min at 4°C. Subsequently, intracellular staining was performed using the BD Cytofix/Cytoperm fixation and permeabilization solution kit (BD Biosciences, Franklin Lakes, NJ, USA) according to the manufacturer's instructions, before incubation with aSMA antibody (1:200, Invitrogen). Samples were read with a FACS Celesta Flow Cytometer (BD Biosciences), using FACS Diva software (BD Biosciences) and analyzed with FlowJo (LLC, BD Biosciences).

6.3.3 HYDROGEL PREPARATION

6.3.3.1 Gelatin/Ruthenium hydrogels

For preparation of gelatin hydrogels with Ruthenium (tris(2,2-bipyridyl)dichlororuthenium(**II**) hexahydrate, Sigma) [344], 13wt% gelatin (from porcine skin powder, gel strength ~300 g Bloom, Type A, Sigma) was dissolved in specific cell culture medium and sterile filtered at 50°C. As initiator for the radical chain reaction, a sterile filtered, 2mM Ruthenium stock solution (Sigma), dissolved in PBS$^-$ (Gibco) was prepared. Additionally, a stock solution of 20mM sodium persulfate (SPS, Sigma), dissolved in PBS$^-$ at 80°C for 10-15 min, was prepared as crosslinking agent. For a final concentration of 10% gelatin hydrogel, the following pipetting scheme was used for the preparation of 1ml volume (see Table 4):

Table 4: Used substances and concentrations for Gelatin/Ruthenium hydrogels.

Substance	Stock Concentration	Volume	Final Concentration
Gelatin	14%	700µl	10%
Cell suspension	-	100µl	Variable
Ruthenium	2mM	100µl	0.2mM
SPS	20mM	100µl	2mM

The used cell number varied depending on the experiment. After adding the cell suspension, the gel was gently mixed with the pipet tip to avoid shear forces during pipetting and therefore cell death. Photo-initiated crosslinking was performed with visible light by utilization of a LED dental curing lamp for 5min until complete gelation.

6.3.3.2 Gelatin-Methacryloyl (GelMA) hydrogels

For the creation of GelMA hydrogels, 11 wt% GelMA (Bloom 300, Sigma) was dissolved in cell culture medium and sterile filtered. Irgacure stock solution (Irgacure 2959, BASF) was prepared by dissolving 5 wt% in PBS$^-$ at 80°C for 30min before sterile filtering. A cell pellet with defined cell number was prepared and resuspended in GelMA, before the Irgacure stock solution was diluted 1:10 in GelMA to obtain a final concentration of 0.5% prior to photo-initiated crosslinking with an UV-lamp (VL-4.LC, Vilber Lourmat, Essen, Germany) at 365nm for 10min until complete gelation.

6.3.3.3 Microbacterial transglutaminase (mTG) hydrogels

For hydrogel preparation of gelatin hydrogels, enzymatically crosslinked with microbacterial transglutaminase (mTG), 12 wt% gelatin was dissolved in cell culture media and sterile filtered at 50°C. Stock solution of 10 wt% microbial transglutaminase (100 U/g) (Würzteufel GmbH, B06XCJF1QJ) was prepared by dissolving in PBS$^-$ and sterile filtering at 37°C. For gelation of the gelatin, 100µl of the mTG stock solution as well as 100µl of cell suspension with defined cell number was applied per 1ml hydrogel and incubated for 1-2h at 37°C until complete gelation.

6.3.4 HYDROGEL TESTING

The different hydrogel systems were furthermore tested in static cultures for the evaluation of proliferation, spreading and vitality of encapsulated primary human cells (hmECs and HAoSMCs). For this, hydrogels were prepared as described in chapter 6.3.3 with a final cell concentration of $1x10^6$ cells/ml and kept at 37°C to avoid untimely gelation. Transwells (Corning) were added to 24-well plates and 100µl of each hydrogel system with either hmECs or HAoSMCs was added into one transwell. Hydrogel was crosslinked in and covered in cell specific medium. Microscopic evaluation was performed at day 3,7,10 and 14. Furthermore, stereomicroscopical examination with a Discovery V20 (Zeiss) was performed at day 14. For this, hydrogels were cut in half and the cross-section was examined for cell distribution and thickness. Afterwards, a Live/Dead staining was performed to evaluate cell viability. With the remaining half, cell distribution was confirmed with an H&E-staining and marker expression was checked with immunofluorescence staining.

6.3.5 HYDROGEL STAININGS

6.3.5.1 Live/Dead staining

To visualize and distinguish between live and dead cells in the hydrogel constructs, a live/dead staining was performed with the LIVE/DEAD Viability/Cytotoxicity Kit, for mammalian cells (Thermo Fisher Scientific) according to the manufacturer’s instructions. In brief, samples were washed in PBS and incubated for 30min in PBS with 2 µM Calcein for visualization of living cells and 1 µM Ethidium Homodimer-1, marking dead cells. After one washing step in PBS$^-$, analysis was performed with a standard fluorescence microscope.

6.3.5.2 Visualization of Cells with CellTracker Green

Visualization of cells was performed with CellTracker Green CMFDA Dye (Invitrogen) according to the manufacturer's instructions. In brief, 0.5µl CellTracker Green was added per ml cell culture medium and samples were incubated for 30min at 37°C. For visualization of smooth muscle cells, the whole hydrogel construct was incubated. For visualization of the endothelialized channel, solution was directly applied into the channel. Analysis was performed with a standard fluorescence microscope.

6.3.6 HISTOLOGY

6.3.6.1 Fixation and embedding

For histological examination of hydrogel constructs, samples were washed 3x with PBS^- and fixed with 4% PFA (Roth) over night at 4°C. For cryoprotection of the hydrogels, the constructs were incubated in 30% sucrose solution, dissolved in ddH_20, for additional 24h, before incubation in TissueTek O.C.T. compound (Hartenstein) over night. In the following, snap-freezing in liquid nitrogen was performed for 30 seconds per sample in order to avoid water crystallization, leading to destruction of the samples. Samples were cut with a cryotome with a thickness of 10µm per section.

6.3.6.2 Histological staining

For a general overview staining, sections were stained with hematoxylin / eosin (H&E, Morphisto) according to the manufacturer's instructions. In brief, sections were rehydrated for 5min in PBS^- and stained for 6min in hematoxylin solution and afterwards incubated in H_2O (tap water) for 5 min to stain cell nuclei. Subsequently, extracellular matrix and cytoplasm was stained for 6min in eosin solution and washed in ddH_2O. After dehydration, sections were embedded with Vectamount mounting medium (Vector laboratories).

6.3.6.3 Immunofluorescence staining

Immunofluorescence staining of endothelial cells by anti-CD31 and smooth muscle cells (SMCs) by anti-aSMA (see Table 3) were used to visualize the cells encapsulated in the different gel systems. After heat-mediated antigen retrieval (citrate buffer, pH = 6), slides were blocked with 5% goat serum (Sigma Aldrich), incubated with primary antibody overnight at 4˚C, followed by fluorescence-conjugated secondary antibody (1:400, all from Molecular Probes, Life Technologies. Sections were mounted with DAPI-containing Vectashield mounting medium (Vector laboratories, Burlingame, USA).

All images were recorded with a Leica DM 4000B fluorescence microscope with a JVC KY-F75U camera, or an Axio Observer (Zeiss) equipped with epi fluorescence optics and a MRm camera.

6.3.7 RAPID PROTOTYPING OF SILICONE MOLDS AND PERFUSION CHAMBERS

Solid Works 2018 Educational (Dassault Systemes, Vélizy-Villacoublay, France) was used for designing the negatives for the silicone molds and the perfusion chambers (STL files in attachment). The .stl files were created with Magics Envisiontec Base 20.2 and printed with an EnvisionTec DLP printer with E-shell 600 resin, after conversion and slicing with the corresponding software (Perfactory RP 3.2.337). 3D-Printing of the perfusion chamber prototypes was performed by Matthias Ryma, Department for Functional Materials in Medicine and Dentistry (FMZ, Würzburg, Germany). After printing, the prototypes were cleaned with Isopropanol and sonicated for 15 minutes in Isopropanol. Furthermore, the dried molds and chambers were illuminated with the Otoflash G171 light-curing unit (NK-Optik GmbH, Germany) to introduce final crosslinking to the resin. Luer locks or threads were directly printed and commercially availible luer locks were screwed into the perfusion chamber. As an alternative, perfusion chambers were created with the Ember Autodesk DLP printer (Autodesk, San Rafael, USA). Here, FotoDent® guide 405 nm resin (Dreve Dentamid GmbH, Unna, Germany) was used because of an increased stability of the prototypes. For this, the .stl files were converted with the Autodesk Print Studio Software (Autodesk, San Rafael, USA) for DLP-printing. Silicone molds and lids were created from the printed negatives by mixing one part of the green Dublisil 15 (addition-vulcanising vinyl-polysiloxane, Dreve Dentamid, Germany) component and 1 part of the white component. The mixture was filled into the negatives and allowed to crosslink for 30min before removal.

6.3.8 CREATION AND DYNAMIC CULTIVATION OF BIOENGINEERED ARTERY MODELS

6.3.8.1 Three-layered artery model

A volume of 80 µl Gelatin/Ruthenium hydrogel containing $1x10^5$ murine vascular smooth muscle cells (MOVAS) was pipetted into the silicone mold for the SMC-layer (see Figure 69G). The construct was covered in 170 µl of hydrogel containing $2,5x10^5$ murine fibroblasts (L929, ATCC) in the silicone mold for the fibroblast layer (see Figure 69H). C166 endothelial cell suspension with a concentration of $1x10^6$ cells/ml was prepared and injected into the channel after dissolution of the polymer. Dynamic cultivation was conducted with a OB1 MK3+ MICROFLUIDIC FLOW CONTROLLER (Elveflow) with a pressure of 20 mbar for 7-14 days.

6.3.8.2 Double layered artery model

For the double-layered artery model, a volume of 600µl containing $5x10^5$ smooth muscle cells was used. Endothelial cell suspension with a concentration of $1x10^6$ cells/ml was prepared and injected into the channel after dissolution of the polymer. Dynamic cultivation was performed using the ibidi pump system (ibidi, see Figure 65) with a pressure of 10 mbar for 7-14 days.

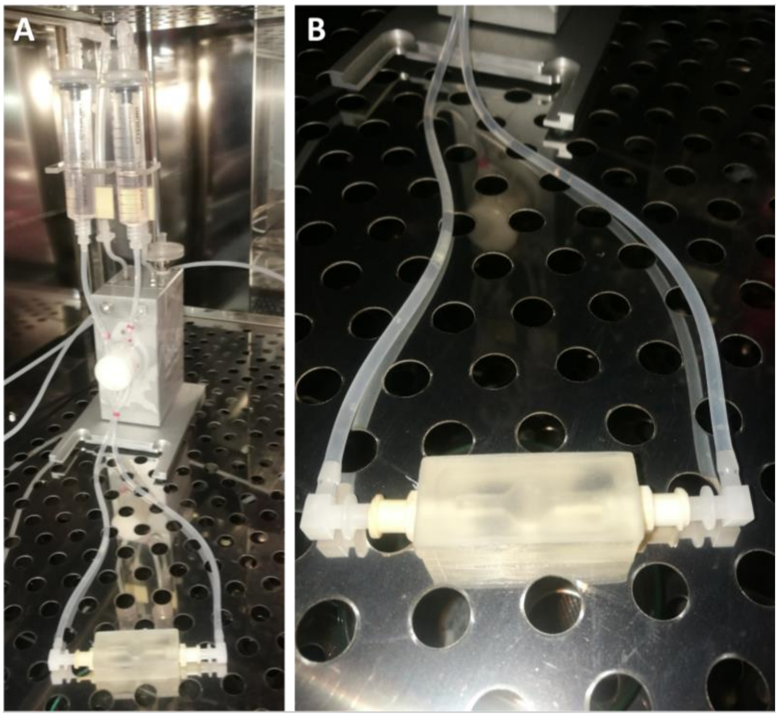

Figure 65: ibidi pump system for the dynamic cultivation of bi-layered artery models. **A** Image of the fluidic unit of the perfusion pump with one exemplary perfusion chamber containing a bi-layered artery model. **B** Enlarged view of the perfusion chamber, connected through the luer lock system with the tubing of the pump.

6.4 RESULTS

6.4.1 CHARACTERIZATION OF ISOLATED MURINE VASCULAR CELLS

6.4.1.1 Murine aortic endothelial cells (mECs)

For the characterization of isolated murine vascular cells and analysis of the purity of the two obtained cell fractions, the expression of cell-specific markers was analyzed via immunofluorescence stainings and flow cytometry. To confirm the endothelial cell type of the isolated cell fraction, cells were analyzed for the CD31 (PECAM-1) and CD144 (VE-Cadherin) expression. Figure 66A-C shows the gating strategy of the flow cytometric analysis, consisting of doublet exclusion (Figure 66B) and dead cell exclusion (Figure 66C). To distinguish between the positive and negative population, the gate was set with an unstained control. A clear expression of both endothelial pan markers CD31 (PECAM-1) and CD144 (VE-Cadherin) was observed, confirming a good purity of 95,1% of the endothelial cell population after MACS sorting and cultivation (see Figure 66D). Furthermore, cells were positive for CD31 in immunocytological stainings, showing the typical cobblestone-morphology of endothelial cells (Figure 66E and Figure 67B).

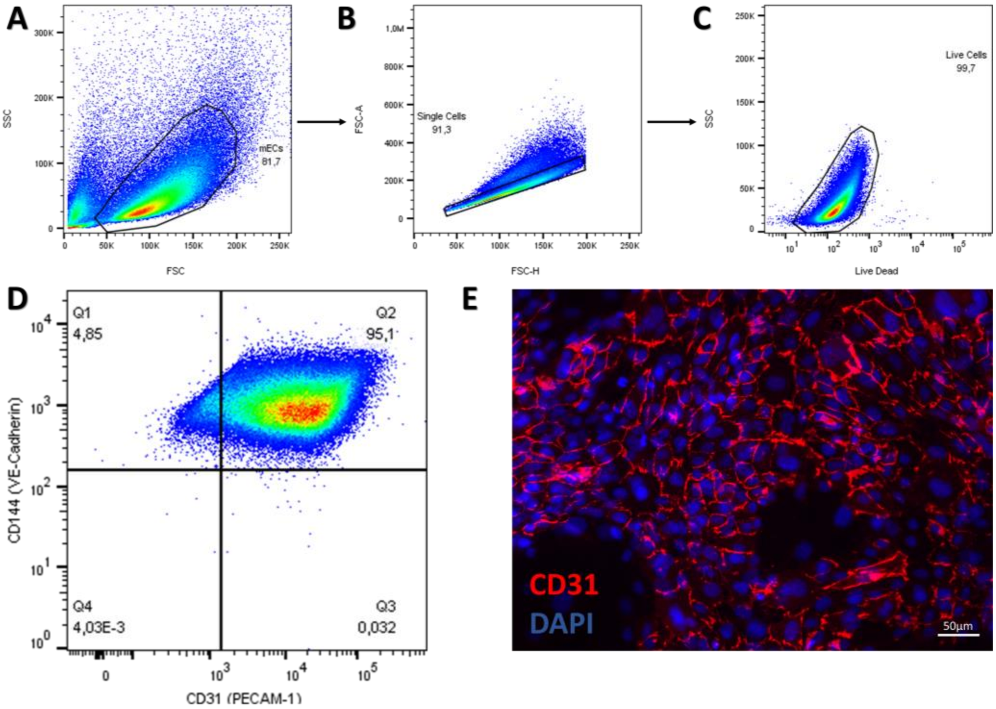

Figure 66: Characterization of isolated murine aortic endothelial cells. **A** Gating strategy for the subsequent flow-cytometric analysis, containing doublet exclusion and dead cell exclusion. **B** Double staining of the pan-markers CD31 and CD144 revealed a purity of 95.1% endothelial cells. To distinguish between the positive and negative population, the gate was set with an unstained control. **C** Immunofluorescent staining of CD31 shows the typical cobblestone morphology of mECs.

6.4.1.2 Murine aortic smooth muscle cells

Furthermore, the smooth muscle cell fraction was analyzed for the purity, defined smooth muscle cell markers and extracellular matrix production to confirm the cell type on the one hand and the ability to synthesize their own ECM on the other hand. mSMCs show the typical morphology of SMCs - in contrast to ECs from the same isolation, which show the typical endothelial cobblestone-morphology (Figure 67B). The gating strategy of the flow cytometric analysis was performed as shown for mECs in Figure 66A-C, consisting of doublet exclusion and dead cell exclusion. To distinguish between the positive and negative population, the gate was set with an unstained control as shown in Figure 67C. A clear expression of the typical smooth muscle cell marker alpha smooth muscle actin (aSMA, see Figure 67D) was observed, confirming a good purity of 99% of the vascular smooth muscle cell population.

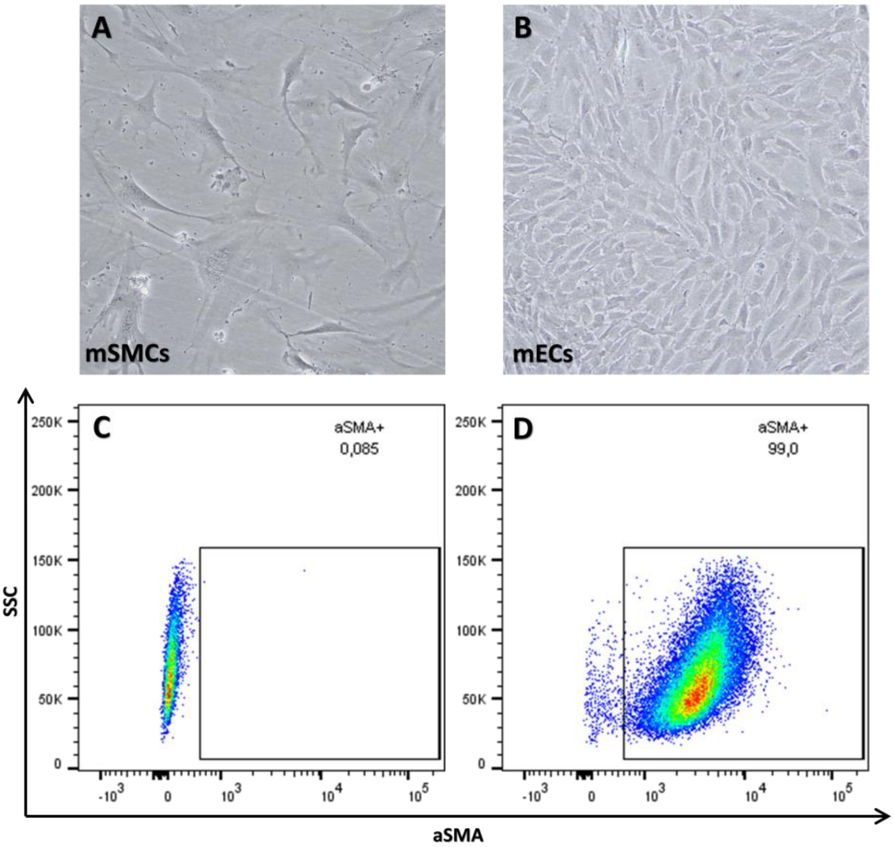

Figure 67: Characterization of isolated and cultured murine aortic smooth muscle cells. **A** Cells show the typical morphology of SMCs. **B** In Contrast, mECs from the same isolation show the typical endothelial morphology. **C** Negative control of mSMCs shows no positive Signal for aSMA. **D** mSMCs are 99 % positive for aSMA. FACS measurement was performed and data was kindly provided by Celine Frank.

Furthermore, cells were stained for various smooth mucle cell markers, including alpha smooth muscle actin (see Figure 68A), Calponin (Figure 68B) and smooth mucle myosin heavy chain (SM-MHC, see Figure 68C). The ability to synthesize ECM-components was furthermore confirmed by immunocytological staining of various extracellular matrix proteins like collagen III (Figure 68D), collagen IV (Figure 68E) and elastin (Figure 68F), confirming the smooth muscle cell identity of isolated and cultured murine aortic cells and their ability to synthesize extracellular matrix.

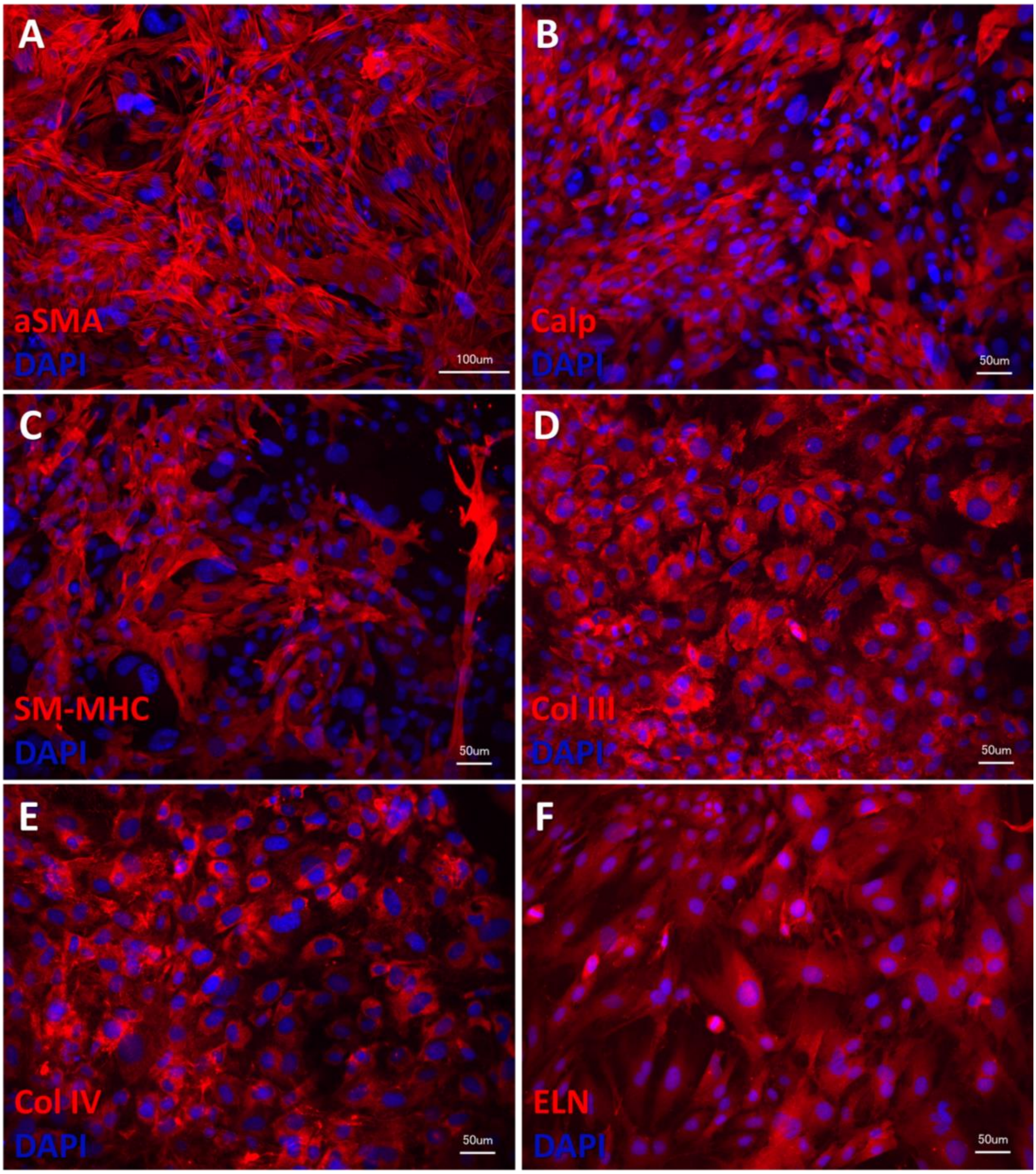

Figure 68: Immunocytological characterization of isolated and cultured murine aortic smooth muscle cells. A Immunofluorescent staining of aSMA shows a strong positive signal in all cells. **B** A strong signal was also observed for Calponin. C mSMCs are also positive for smooth muscle myosin heavy chain (SM-SMHC). **D** mSMCs produce Collagen III as well as **E** Collagen IV and **F** Elastin.

6.4.2 THREE-LAYERED HYDROGEL-BASED ARTERY MODEL

6.4.2.1 Scaffold generation and molding

The sacrificial PcPrOx scaffolds were created via MEW and naturally designed as a network with two bifurcations with a fiber diameter of 400-500 µm thickness (see Figure 69A and B). To create multiple layers of different cells around the sacrificial scaffolds, they were coated in succession. For this, molds for casting of PDMS (Figure 69C-F) were specifically designed for the scaffolds, which were afterwards used as molds for embedding the scaffolds with a thin layer of hydrogel. In brief, the scaffolds were added to the initial PDMS mold (Figure 69G) and hydrogel was casted around the scaffold. After gelation, the embedded scaffold was removed and introduced into the second PDMS mold (Figure 69H) for casting of another hydrogel layer.

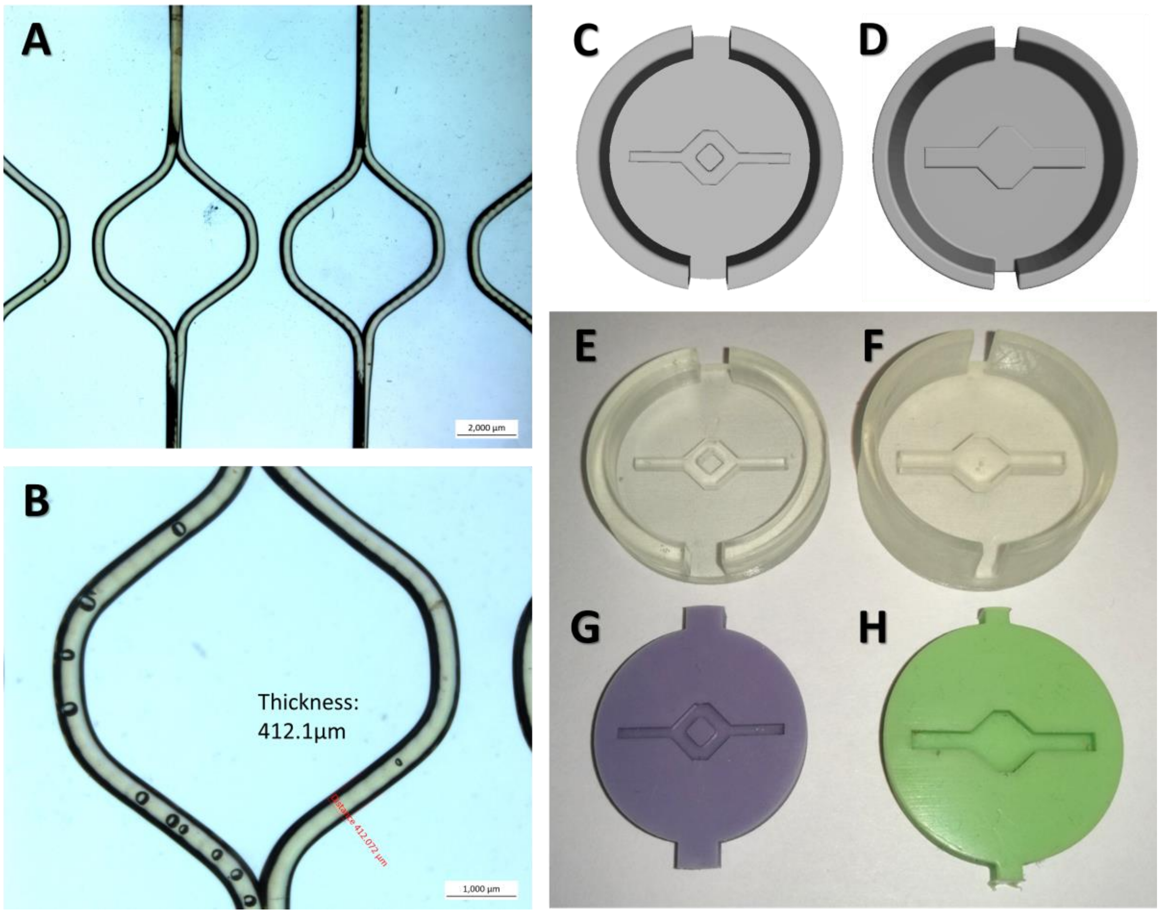

Figure 69: Sacrificial PcPrOx Scaffolds and casting molds for the generation of a three-layered artery model. A Stereomicroscopic picture of melt electrowritten sacrificial PcPrOx scaffolds. **B** Enlarged view of the scaffold with a fiber diameter of 400-500µm. **C** CAD-image of the mold for the SMC-layer, where the sacrificial scaffold is embedded into a hydrogel containing smooth muscle cells. D CAD-image of the mold for the fibroblast-layer, where the hydrogel containing smooth muscle cells is embedded into a hydrogel containing fibroblasts to create the three-layered model. **E** 3D-printed mold of the SMC-layer cast and **F** the fibroblast-layer cast. **G** Silicone cast for the generation of the SMC-layer and **H** of the fibroblast-layer.

In order to generate a three-layered hydrogel-based artery model, a workflow containing two subsequent casting steps was established and optimized. The whole procedure is illustrated in Figure 70. The sacrifical PcPrOx scaffolds, generated via Melt Electrowriting (MEW), were sterilized under UV light for 30 min. Silicone-molds were filled with hydrogel containing smooth muscle cells and the sacrificial scaffold was positioned carefully into the center for the later creation of the channel for the endothelial cell layer. After gel-specific cross-linking and gelation of the gel, the construct was removed carefully with sterile forceps and covered with medium to avoid dehydration. In this time, the fibroblasts were added to the second hydrogel and the smooth muscle cell layer was embedded into the second mold, filled with the second hydrogel to achieve a bi-layered hydrogel around the scaffolds (see Figure 70F).

After gelation, the artery model was carefully removed and covered in medium. Subsequently, the model was introduced into the previously described, specific perfusion chambers. After dissolution of the polymer by temperature decrease, a channel throughout the hydrogel construct was created and endothelial cells were seeded into the channels to create the three-layered construct (see Figure 72), consisting of an endothelialized channel (mimicking the intima), a smooth muscle cell layer (mimicking the media) and a fibroblast layer (mimicking the adventitia).

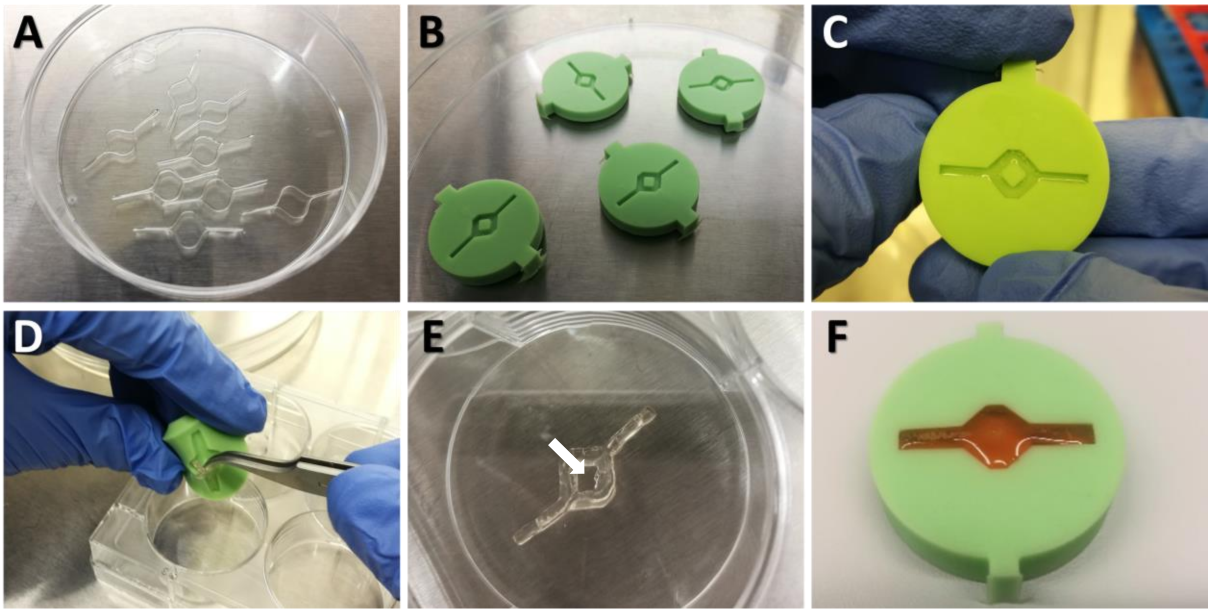

Figure 70: Established workflow for generating the three-layered artery model. **A** Sacrifical PcPrOx scaffolds generated via MEW. **B** Sterilized silicone-molds for the creation of the channel surrounded by a smooth muscle cell layer. **C** PcPrOx scaffold (white arrow) embedded in a hydrogel containing smooth muscle cells. **D** After cross-linking and gelation of the gel, construct was removed carefully with sterile forceps. **E** Smooth muscle cell layer containing the sacrificial scaffold for channel generation and subsequent endothelialization. **F** Smooth muscle cell layer was embedded into another mold and surrounded by hydrogel containing fibroblasts. After gelation, artery model was removed as shown in **D**.

6.4.2.2 Perfusion chamber design for the three-layered artery model

Dynamic cultivation of artery models requires a bioreactor with direct and leakage-free connection to pump systems in order to apply continuous or pulsatile flow for the generation of a natural arterial environment. Therefore, several development and optimization steps for the bioreactors were established, with Figure 71 showing the first approach of a perfusion chamber design. Here, the created artery model was added into the main chamber, which is connected to the outside by small holes (see Figure 71A and B). The artery model was covered in cell-specific medium before the channels of the artery model were connected with plastic cannulas through the holes in the chamber to enable the dissolution of the polymer and the subsequent injection of the endothelial cell suspension into the created channels as well as to furthermore establish a connection for perfusion systems. The chamber was closed by a PDMS lid, which was casted into the forms shown in Figure 71C and D (CAD-image) and Figure 71E and F (cast version of the silicone lid). The PDMS used for the creation was chosen to be transparent in order to enable microscopic evaluation of the model. However, connecting the endothelial channel with the cannulas manually was not consistently feasible and therefore not easily reproducible. Furthermore, the fluid connections were prone to leakage (data not shown).

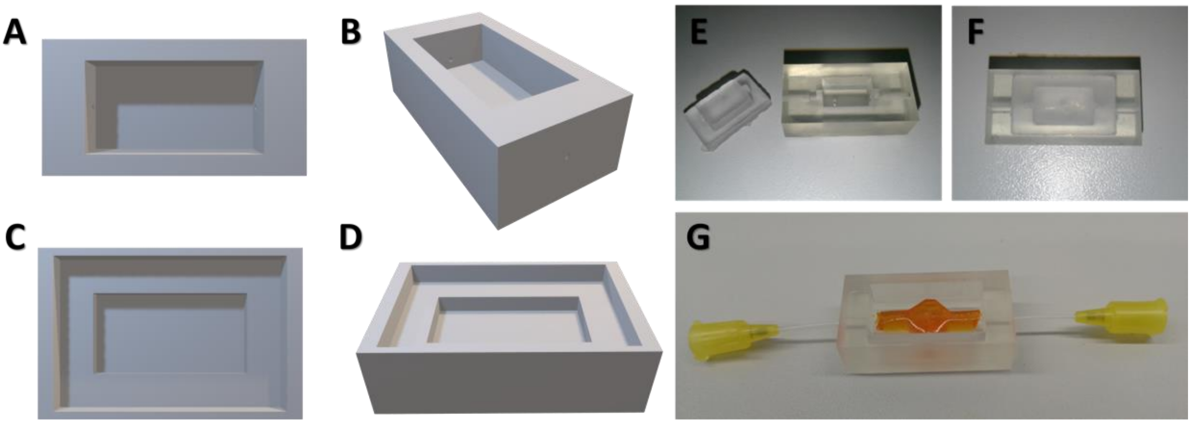

Figure 71: Perfusion chamber design for the dynamic cultivation of the three-layered artery model. A CAD-image of the designed perfusion chamber (top view) and **B** (trimetric projection). **C** CAD-image of the designed negative for the silicone lid (top view) and **D** (tilted view). **E** 3D-printed perfusion chamber with casted silicone lid (open view) and **F** (closed view). **G** Perfusion chamber with embedded three-layered artery model, connected to cannulas for connection to a perfusion pump and subsequent dynamic cultivation.

Therefore, the perfusion chamber was redesigned and adapted to circumvent these issues. The next version of the reactor (see Figure 73) was designed with a form-fit chamber design, where the hydrogel could be fitted in a more accurate way. However, the main challenge was to find the right size for the hydrogel chamber, as the Ruthenium/gelatin hydrogels tend to swell [344]. For this, swelling experiments were performed (data not shown) in order to achieve the right dimensions for the design of the chamber. Additionally, female luer lock connectors were introduced to both sides of the bioreactor for the connection to standardized tubing systems, which guarantees a better leak-tightness (see Figure 73D, E and F). Another approach was to implement screw threads into the chamber (see Figure 73C) to allow the usage of commercially available luer locks, where the screw threads were sealed with teflon tape before they were turned into the threads of the chamber, which would furthermore improve the leak-tightness of the connection to the tubing system of the pump. However, for the sake of simplicity, chambers with directly printed luer locks were used for the experiments (see Figure 73D).

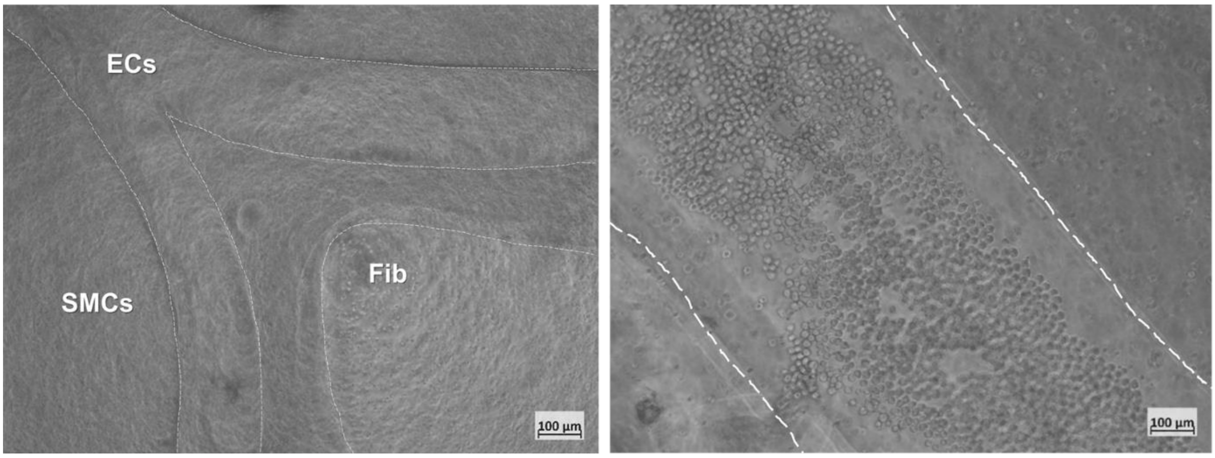

Figure 72: Three-layered artery model. A Microscopic image of the model with its three layers, consisting of the endothelialized channel (ECs), the surrounding medial layer of SMCs embedded in hydrogel (SMCs) and the third adventitial layer of fibroblasts (Fib). White linings mark the border between the different layers. **B** Enlarged view of the endothelial channel after seeding with C166 endothelial cells. The cell suspension in the cannel is clearly visible. Borders to the SMC layer are marked by white lines.

This perfusion chamber was furthermore designed to allow a perfusion through the created channels after dissolving of the sacrificial polymer scaffold without directly connecting the endothelialized channel. Therefore, endothelialization was performed via injection into the channel with a syringe filled with cell suspension.

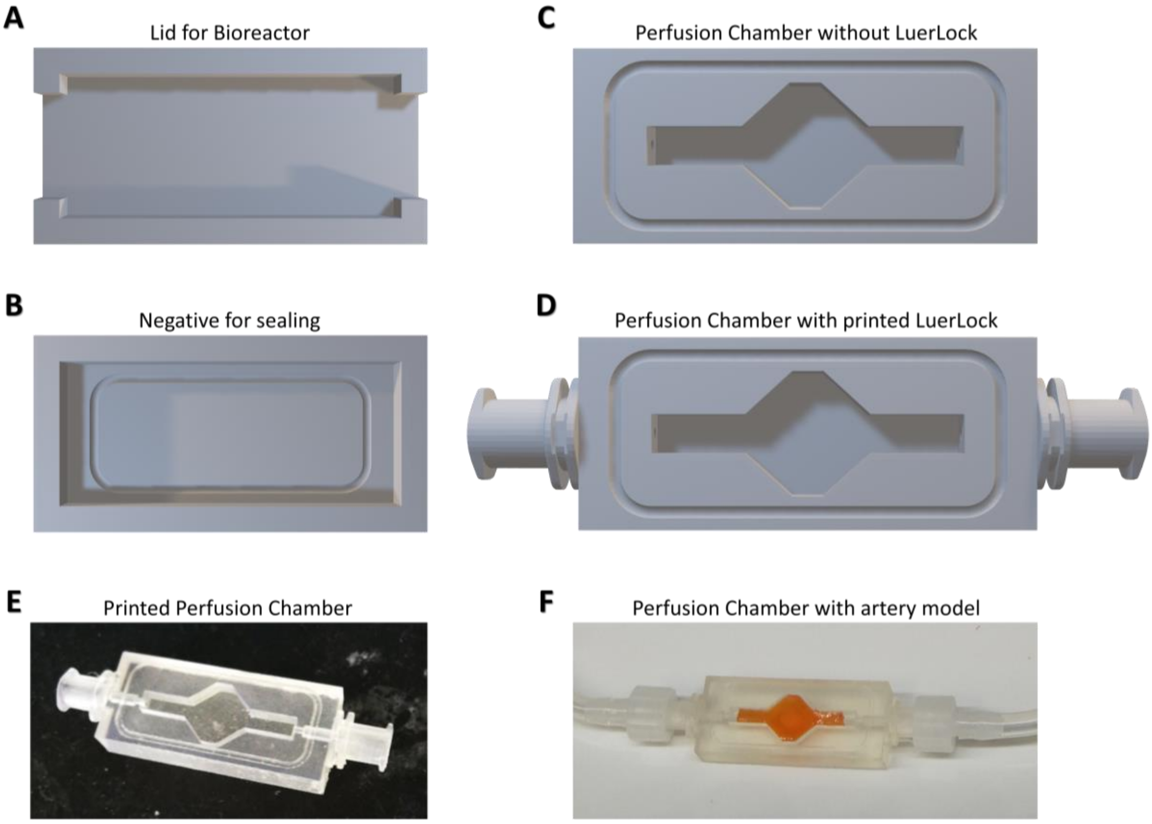

Figure 73: Optimized perfusion chamber for the cultivation of a three-layered artery model. **A** CAD-image of the lid for the perfusion chamber. **B** CAD-image of the negative for creating the silicone sealing for a leakage-free cultivation. **C** CAD image of the perfusion chamber without printed LuerLocks. In this model, screw threads were printed into the chamber, allowing the usage of commercially available LuerLocks and sealing with teflon tape. **D** CAD image of the perfusion chamber with implemented LuerLocks for the connection to standardized tubings of the perfusion pump. **E** 3D-printed perfusion chamber without artery model and **F** with artery model, connected to the perfusion pump.

Microscopic images directly after generation of the model show the successful establishment of the artery model with its three layers, consisting of the created channel for the endothelial cells (ECs), the surrounding medial layer of SMCs embedded in hydrogel (SMCs) and the third adventitial layer of fibroblasts (Fib) embedded in a second hydrogel (see Figure 72A). Furthermore, after dissolution of the sacrificial scaffold by temperature decrease, no residues of the polymer were found. Furthermore, after injection of the endothelial cell suspension, endothelial cells were present in the channel, proving the feasibility of post-endothelialization via direct injection (see Figure 72B).

6.4.2.3 Dynamic cultivation of three-layered artery models

For the improved cultivation of the artery models, the hydrogels were embedded in the fit-form chamber and closed with the lid, sealed by the casted silicone forms and tightened with cable ties to improve the leak-tightness. Furthermore, for enabling of dynamic cultivation of several artery models, parallel and series connections of several perfusion chambers were examined for functionality (see Figure 74A and B). However, cultivation of the models in parallel connection (Figure 74A) did not guarantee a uniform perfusion of all models, despite using the exact tubing length for all chamber connections. Therefore, for the subsequent cultivation, series connection of the chambers containing the three-layered artery model was used (Figure 74B). However, connecting the tubing system of the perfusion pump to the luer locks of the perfusion chamber revealed stability issues with the resin used for 3D printing of the chambers, as the luer locks were too brittle and broke after connection to the tubing system (see black arrow in Figure 74C). Moreover, sterilization of the silicone sealings with either 70% ethanol or autoclaving led to shrinkage in both cases (see black arrows in Figure 74D).

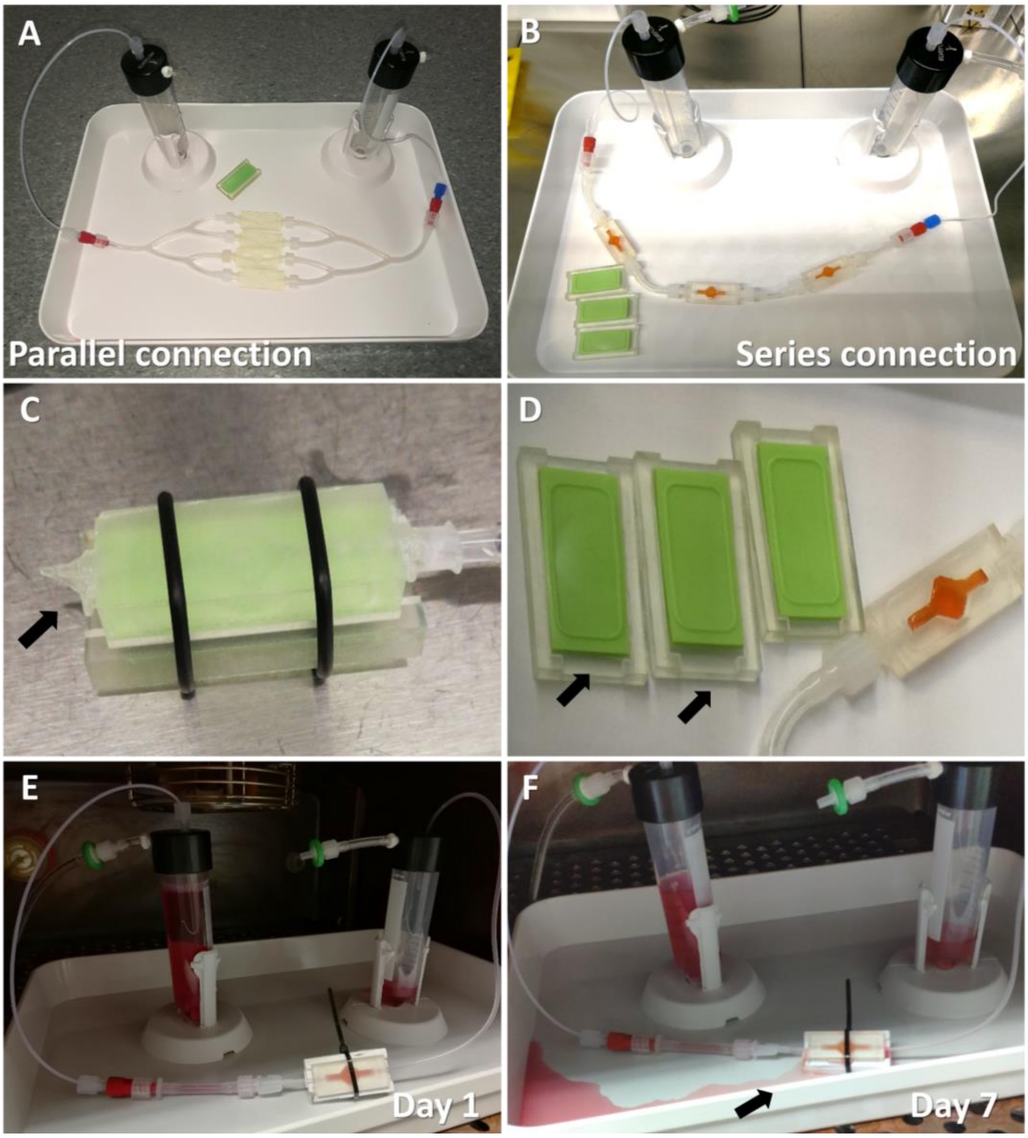

Figure 74: Dynamic cultivation of the three-layered artery model. A Parallel connection of 4 perfusion chambers connected to the perfusion system to achieve parallel cultivation of several models. **B** Series connection of 4 perfusion chambers connected to the perfusion system. **C** The used resin for 3D-prinitng of the chambers showed brittle properties, leading to breaking off of the printed luer locks (see black arrows). **D** The casted silicone sealing for the printed lids showed a shrinking behaviour after sterilization with either 70% ethanol or autoclaving (see black arrows). **E** Dynamically cultured artery model after one day of culture. No leakage was observed. **F** After 7 days of dynamic culture, the perfusion chamber showed leakage (see black arrow).

After 1 day of dynamic cultivation, no leakage was observed in the system (Figure 74E). However, after a prolonged perfusion time, sealing of the chamber system failed and leakage was observed at day 7 (Figure 74F).

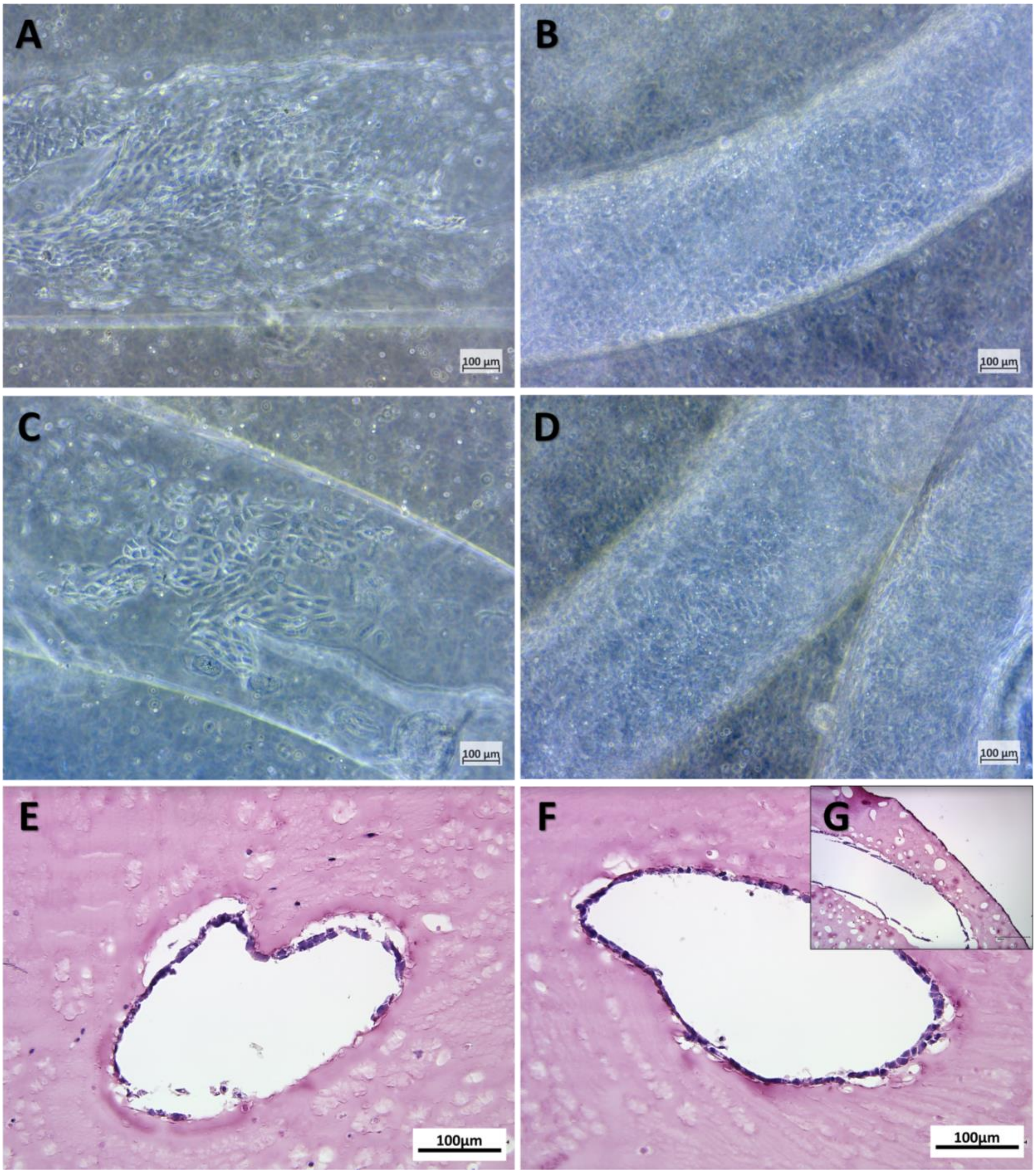

Figure 75: Three-layered artery model after 7d of cultivation. **A, C** Microscopic images of statically cultivated artery model. After 7d of culture, channels in the hydrogel model were not fully endothelialized. **B, D** Microscopic images of dynamically cultivated artery model. In these models, channels were fully endothelialized after 7d of culture. **E** H&E-staining of the cross-section of statically cultured models confirm the incomplete endothelialization. **F** H&E-staining of dynamically cultured artery models in cross-sections and **G** in longitudinal sections confirm the complete endothelialization of dynamically cultured artery models throughout the model.

However, microscopic and histological examination of the models cultured under static and dynamic conditions indicate a successful perfusion in dynamically cultured models, visible through a full endothelialization of the channels (see Figure 75B and D). This was moreover confirmed by H&E-stainings of cross-sections (Figure 75F) and longitudinal sections (Figure 75G) of the models. In contrast, in the static control, channels were not fully endothelialized after 7d of culture (see Figure 75A and C), as additionally visualized by H&E-stainings (Figure 75E). Overall structure of the model (see Figure 77) was furthermore visualized by light-sheet microscopy (see Figure 76), showing the existence of the channels throughout the whole constructs and confirming abundant cellular content by autofluorescence.

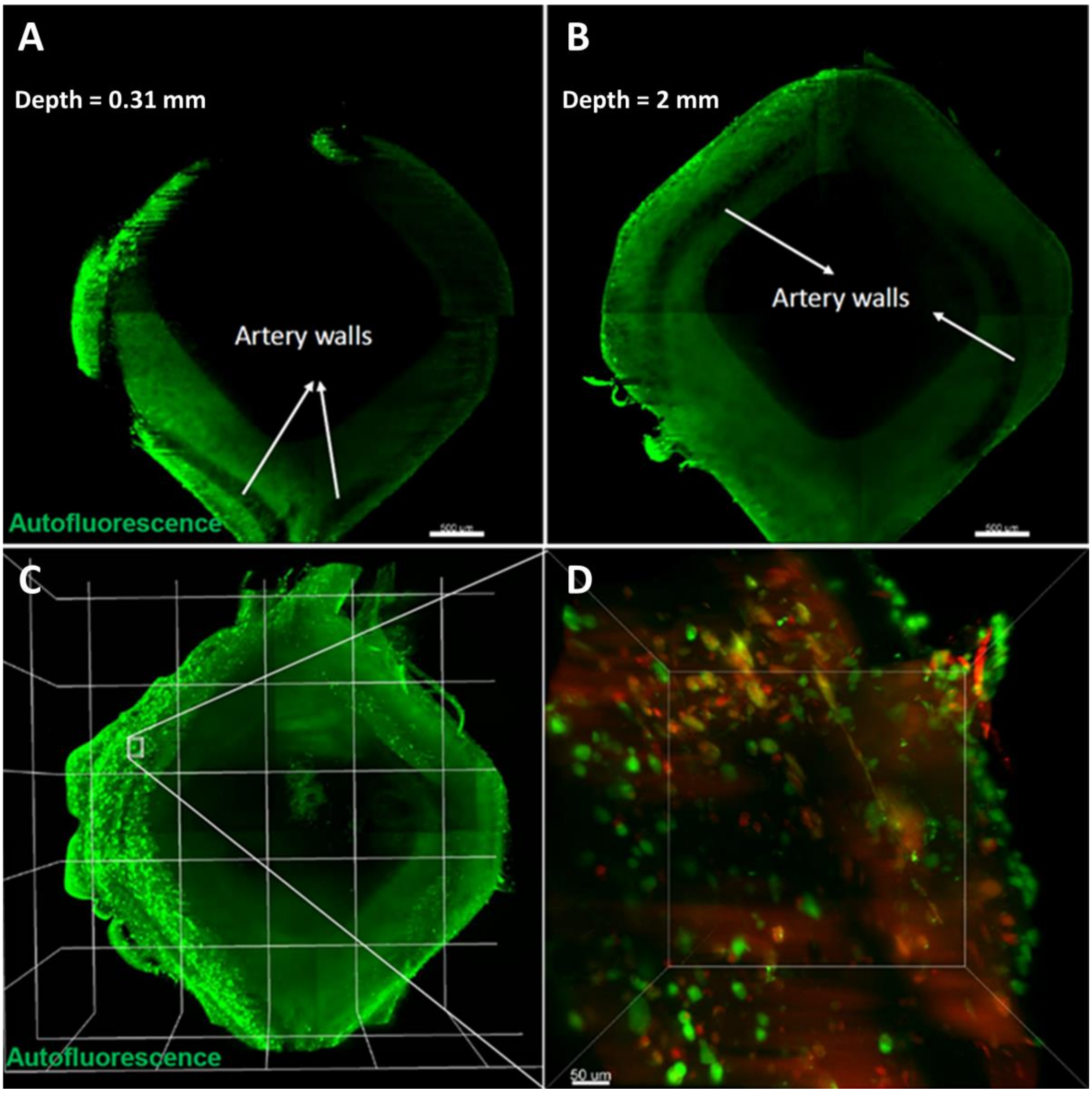

Figure 76: Light-sheet microscopy image of a three-layered artery model. **A** 2D optical section from the construct with a depth of 0.31 mm and **B** with a depth of 2mm, showing the existence of channels throughout the whole model. **C** 3D mapping of the biofabricated artery model with cellular resolution. **D** Enlarged view of C, showing embedded cells in the hydrogel matrix. Image was kindly provided by Zeinab Mokhtariasl.

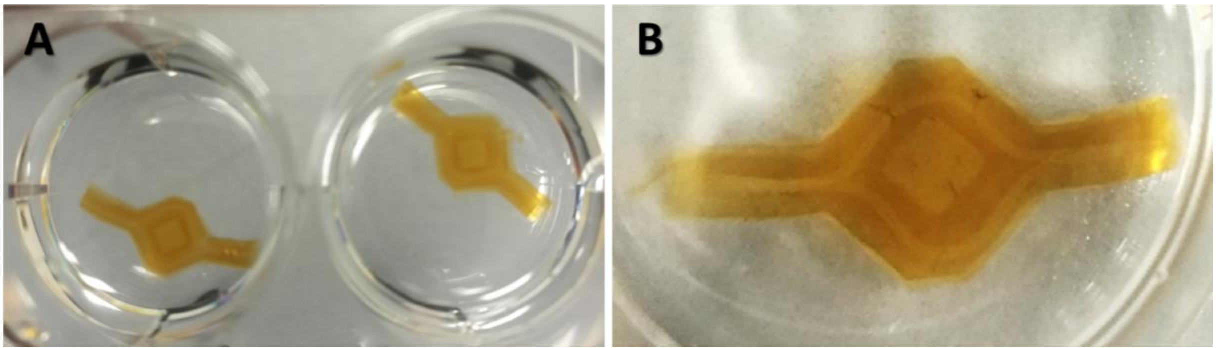

Figure 77: Three-layered biofabricated artery model generated with the casting method. The endothelialized channels created through dissolution of the sacrificial scaffold and subsequent injection of endothelial cells are clearly visible.

6.4.3 BI-LAYERED HYDROGEL-BASED ARTERY MODEL

6.4.3.1 Perfusion chamber design for the bi-layered artery model

To further improve the simplicity of generating biofabricated artery models and the subsequent dynamic cultivation, the perfusion chamber was redesigned in order to enable a direct generation of bi-layered models in the chambers, consisting of smooth muscle cells and endothelial cells (see Figure 78).

For the direct generation of a bi-layered artery model in the perfusion chamber, a new workflow was established, as shown in Figure 78C-E. The main chamber consists of a pillar, which on the one side reduces the amount of hydrogel needed for chamber filling, and on the other side provides a more natural bifurcation design for the bi-layered hydrogel models (See Figure 78A). To circumvent leakage out of the printed, brittle luer locks (see Figure 74C and F), screw threads for commercially available luer locks were introduced into the design, which were furthermore sealed by using teflon tape around the threads of the luer locks (see Figure 78B). Moreover, the scaffold was fixed into the apertures of the luer locks in order to guarantee the connection of the later created channels with the tubing system (see Figure 78C). The apertures were sealed with PcPrOx-glue, consisting of 50% PcPrOx dissolved in water, by carefully pipetting the glue into the aperture, where the scaffold is positioned. After drying of the glue, the whole construct was sterilized under UV-light to exclude possible contaminations by threading the scaffold into the chamber system. In a next step, hydrogel with smooth muscle cells was prepared and directly pipetted into the chamber, surrounding the sacrificial scaffold and sealing the connections between scaffold and luer lock, therefore creating a direct channel from the luer locks throughout the model (see Figure 78D). After gelation of the hydrogel, an easy dissolution of the polymer scaffold and the glue was enabled by simply flushing the channels with cold PBS with a syringe connected to the luer locks. Moreover, endothelial cell seeding was improved with this design, as a syringe filled with cell suspension could be connected directly to the luer locks for injection.

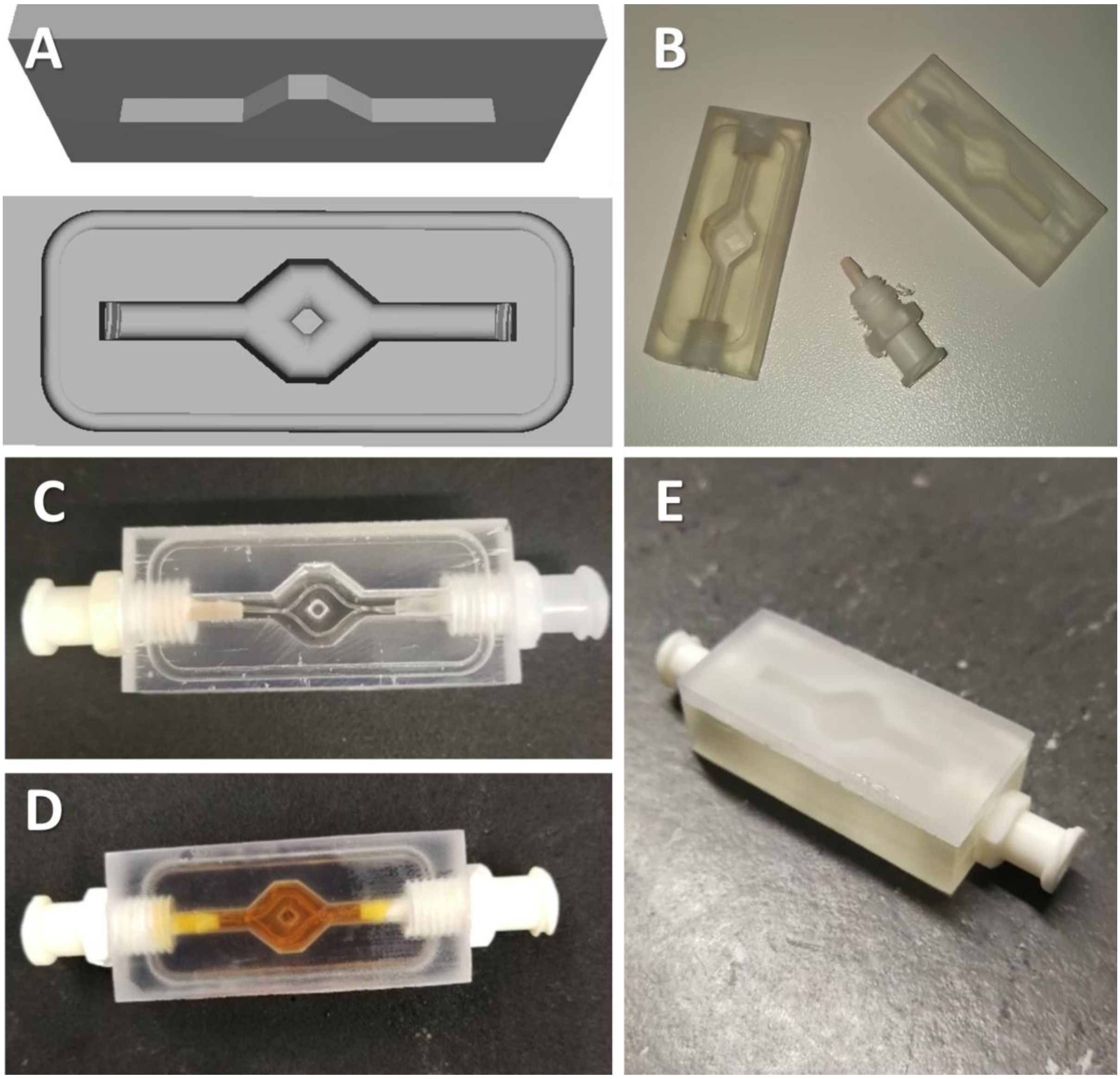

Figure 78: Designed perfusion chamber for the direct generation of bi-layered artery models. **A** CAD-image of the perfusion chamber (bottom) and custom-fit lid (top). **B** 3D-printed perfusion chamber with screw threads for commercially available luer locks and the lid. **C** Assembled perfusion chamber with fixed PcPrOx scaffold. **D** Bi-layered artery model was generated by pipetting SMC-containing hydrogel into the chamber. **E** Closed perfusion chamber containing the artery model.

6.4.3.2 Dynamic cultivation of bi-layered artery models

After injection of endothelial cells into the channel, cells were allowed to adhere before connection to the pump system. Models were cultured under continuous flow with 10mbar pressure and analyzed for cell viability after 7d of culture. Complete endothelialization with viable cells was observed in the linear region (see Figure 79A) as well as at the bifurcation region (see Figure 79B). However, at some spots of the channel, constriction of the lumen could be observed (see white arrows in Figure 79).

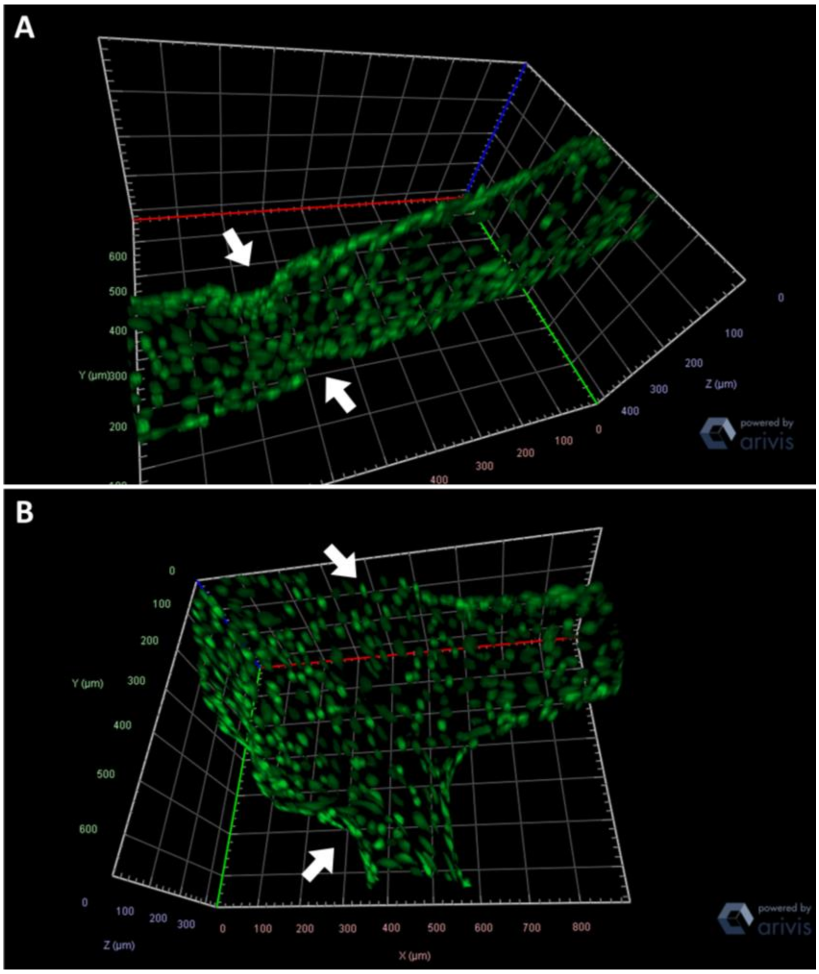

Figure 79: Z-stack images of bi-layered artery models cultured under dynamic conditions, perfused with CellTracker Green. A Image of the linear region of the scaffold shows complete endothelialization (visualized with CellTracker, perfused through the channel) and spots of constriction due to gel swelling (see white arrows). B The bifurcation region of the channel is densely endothelialized with spots of constriction due to gel swelling (see white arrows).

Moreover, in some experiments, leaking problems occurred (see Figure 80A), leading to complete dehydration of the scaffold in some cases (see Figure 80C). Interestingly, leakage did not occur through the luer locks connecting the tubing system of the perfusion pump to the chambers, but from the model itself.

Figure 80: Problems of the usage of Gelatin/Ruthenium hydrogels for dynamically cultivated bi-layered artery models. A After a certain culture period, strong leakage was observed in the models. **B** Gelatin/Ruthenium hydrogels were sticking to the chamber walls, destroying the models during removal from the chamber. **C** Leakage of the perfusion system furthermore destroyed the models by dehydration.

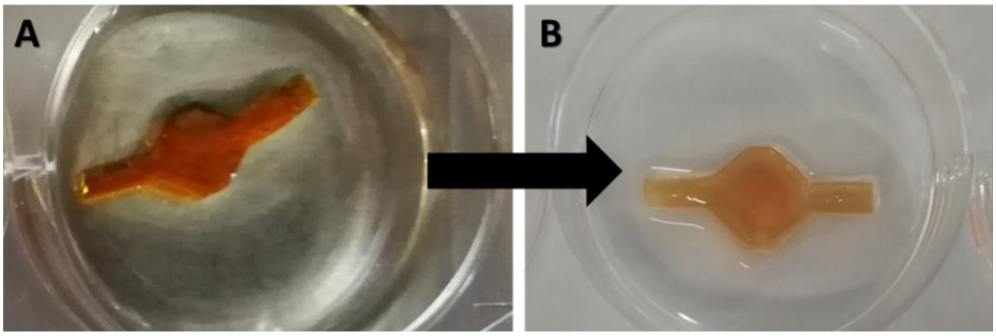

Figure 81: Swelling behavior of Gelatin/Ruthenium hydrogels. **A** Artery model removed from the perfusion chamber after dynamic cultivation for 7d. **B** After 1d of static culture, the gel was visibly swelling.

To test this, the model was carefully flushed directly with PBS filled in a syringe connected to the luer locks. The fluid could not pass through the channel until failure of the model, revealing clogging of the channels due to swelling of the gel. This was furthermore confirmed by observation of dynamically cultured models, which were removed from the perfusion chamber and cultured statically for 1 day (see Figure 81). After this short culture period, a visible swelling was already observed. Moreover, in some cases, Gelatin/Ruthenium hydrogels were sticking to the form-fit perfusion chamber, leading to destruction of the model while removing the construct (Figure 80B).

6.4.4 OPTIMIZATION OF THE HYDROGEL SYSTEM

Due to swelling problems with Gelatin/Ruthenium hydrogels, several gel systems were tested in the next step for cell viability, proliferation and spreading in order to find the optimal gel system for the creation of hydrogel-based artery models. The tested gel systems consisted of the commercially available Gelatin-Methacryloyl (GelMA) hydrogel system, crosslinked via UV-light with Irgacure as photo initiator, Gelatin hydrogel crosslinked with Ruthenium as photo initiator (Ruthenium), and Gelatin enzymatically crosslinked with micro bacterial transglutaminase (mTG). For these tests, primary human microvascular endothelial cells (hmECs) and primary human aortic smooth muscle cells (HAoSMCs) were used in order to choose cell types, which are more sensitive to their environment than cell lines.

6.4.4.1 Microscopical evaluation of proliferation and spreading

Microscopical evaluation of proliferation and spreading was performed after day 3 (see Figure 82), day 7 (not shown) and day 10 of static culture (see Figure 83). Spheroids encapsulated in 10% (Figure 82E) and 8% mTG hydrogel (Figure 82G) showed similar growth as in 10% GelMA. In contrast, smooth muscle cell growth and spreading was different in the gel systems. HAoSMCs grown in 10% GelMA showed the strongest spreading (Figure 82B), followed by 8% mTG gel (Figure 82H). A slight spreading was observed in HAoSMCs cultured in 10% mTG (Figure 82F). However, in 10% Ruthenium gel, HAoSMCs still showed a roundish appearance (Figure 82D). In the 10% GelMA hydrogel, growth of ECs in spheroids was observable already after 3d of culture (Figure 82A), whereas in the Ruthenium hydrogel, less and smaller spheroids were found (Figure 82C).

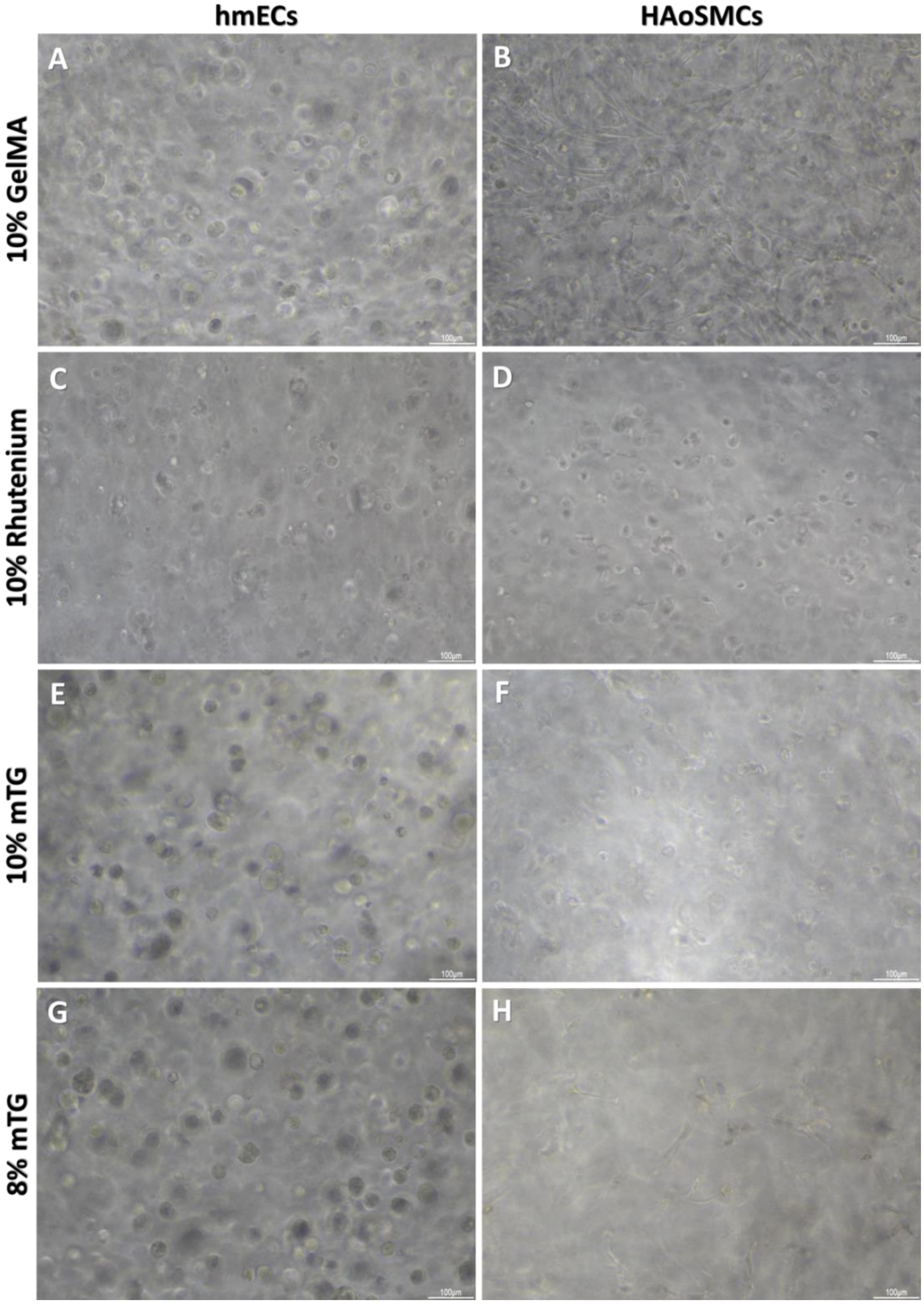

Figure 82: Microscopic evaluation of cell growth and spreading of primary human cells encapsulated in different hydrogel systems after 3 days of static culture. **A** hmECs in 10% GelMA. Growth of ECs in spheroids is observable. **B** HAoSMCs in 10% GelMA. Spreading of the cells is observable. **C** hmECs in 10% Ruthenium gel. Growth of ECs in small spheroids is observable. **D** HAoSMCs in 10% Ruthenium gel. Slight spreading of the cells is observable. **E** hmECs in 10% mTG. Growth of ECs in spheroids is observable. **F** HAoSMCs in 10% mTG. Slight spreading of the cells is observable. **G** hmECs in 10% mTG. Growth of ECs in spheroids is observable. **H** HAoSMCs in 10% mTG. Spreading of the cells is observable.

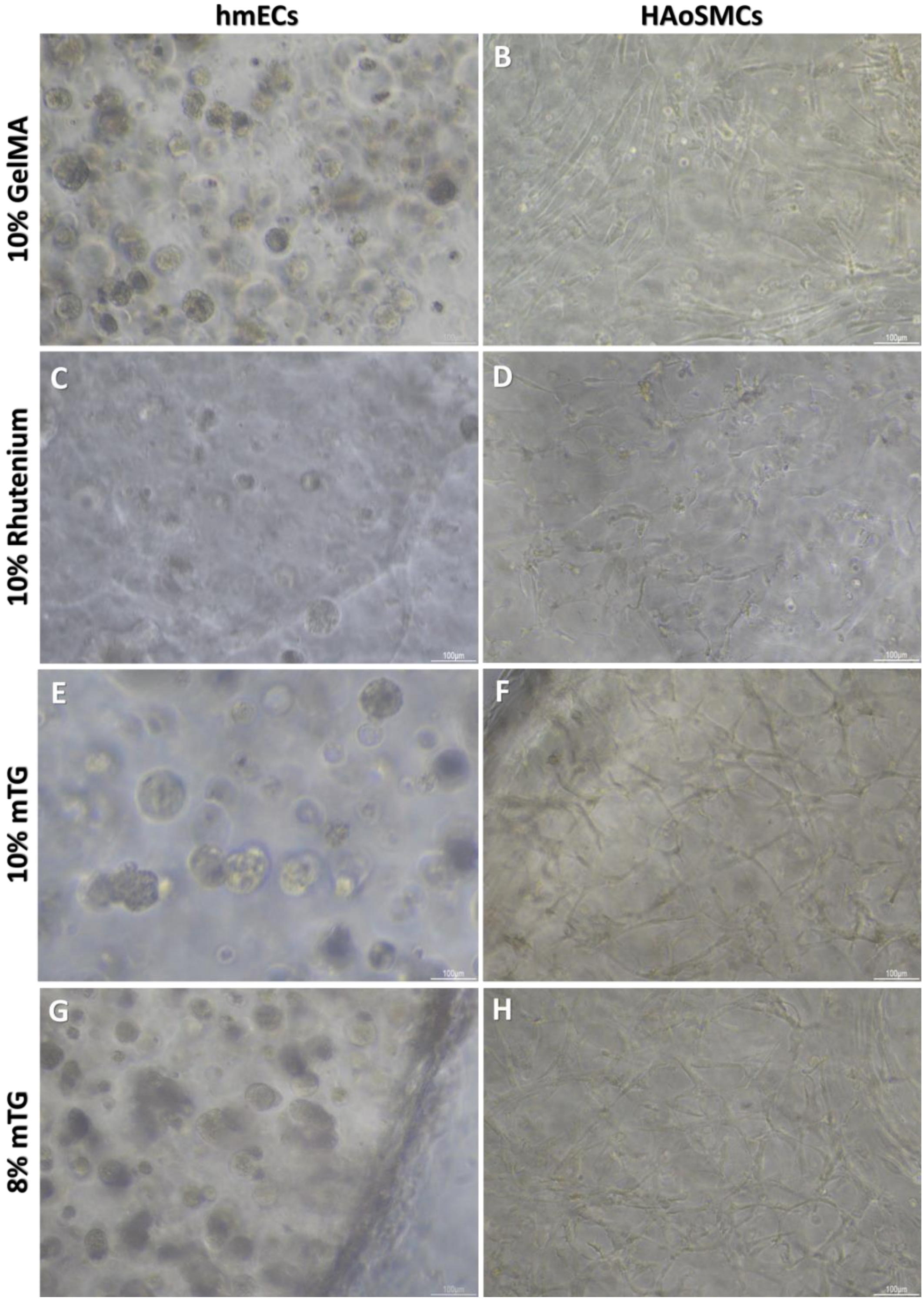

Figure 83: Microscopic evaluation of cell growth and spreading of primary human cells encapsulated in different hydrogel systems after 10 days of static culture. **A** hmECs in 10% GelMA. Strong growth of ECs in spheroids is observable. **B** HAoSMCs in 10% GelMA. Spreading of the cells is observable. **C** hmECs in 10% Ruthenium gel. Only very small spheroids are observable. **D** HAoSMCs in 10% Ruthenium gel. Only few cells are observable. **E** hmECs in 10% mTG. Growth of ECs in spheroids is observable. **F** HAoSMCs in 10% mTG. Spreading of the cells is observable. **G** hmECs in 10% mTG. Growth of ECs in spheroids is observable. **H** HAoSMCs in 10% mTG. Spreading of the cells is observable.

After 10 days of culture, ECs encapsulated in 10% GelMA hydrogel (Figure 83A) as well as in 10% mTG (Figure 83E) and 8% mTG (Figure 83G) showed an increased growth of spheroids in contrast to 10% Ruthenium, where less and smaller spheroids were found (Figure 83C). However, ECs cultured in 10% mTG hydrogel (Figure 83E) exhibited the largest spheroids. For the SMCs, an equal growth and spreading was observed in 10% GelMA (Figure 83B), 10% mTG (Figure 83F) and 8% mTG hydrogel (Figure 83H). However, in Ruthenium hydrogels, a reduced spreading of SMCs was found (Figure 83D).

6.4.4.2 Evaluation of cell distribution

To evaluate the cell distribution within the hydrogel, the cultured hydrogels were cut in half and imaged with a stereomicroscope to visualize the encapsulated cells in the cross-section (see Figure 84). Endothelial cells (hmECs) growing in spheroids were equally distributed throughout the complete cross-section of the gel in GelMA (Figure 84A), 10% mTG (Figure 84C) and 8% mTG (Figure 84D), whereby GelMA hydrogels showed the densest population due to the smaller thickness of the gel itself. However, Ruthenium hydrogels contained smaller spheroids throughout the gel with only few, unequally distributed larger spheroids (Figure 84B).

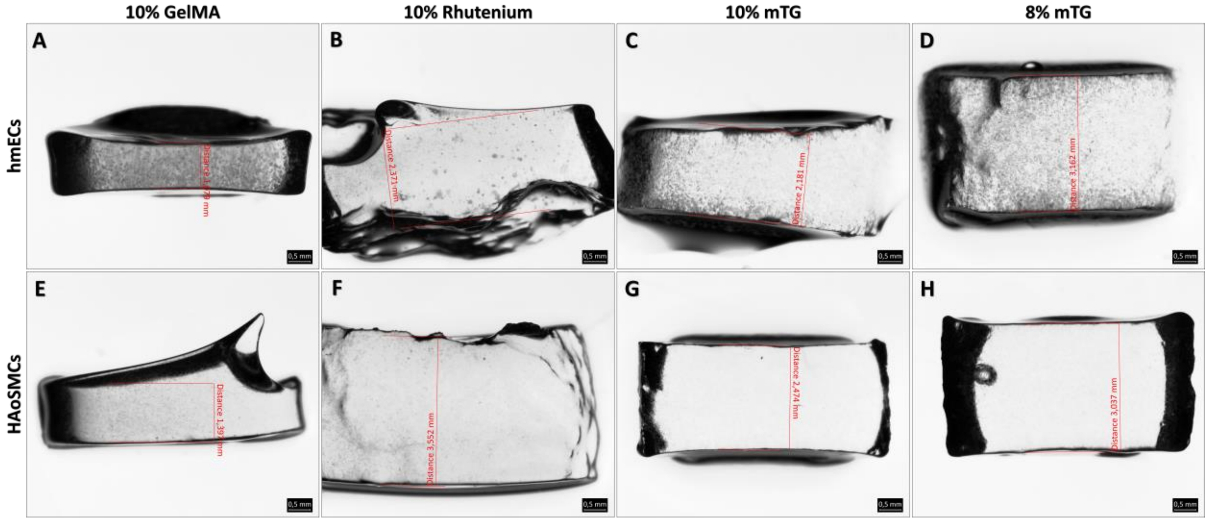

Figure 84: Stereomicroscopic images of hydrogels containing hmECs and HAoSMCs after 10 days of static culture. A hmECs cultured in 10% GelMA. Equal distribution of large spheroids is observable. **B** hmECs in 10% Ruthenium gel. Small spheroids are observable throughout the gel with only few, unequally distributed larger spheroids. **C** hmECs in 10% mTG. Equal distribution of spheroids throughout the gel is noticeable. **D** hmECs in 8% mTG. Equal distribution of spheroids throughout the gel is noticeable. **E** HAoSMCs in 10% GelMA. Equal distribution of cells throughout the gel is noticeable. **F** HAoSMCs in 10% Ruthenium gel. An equal distribution of cells throughout the gel was found. **G** HAoSMCs in 10% mTG. Cells are distributed equally. **H** HAoSMCs in 8% mTG. An equal distribution of the cells was found.

Smooth muscle cell population was found to be equally distributed in all gel systems (see Figure 84E-H). Interestingly, the gel thickness differed strongly among the different conditions (see Table 5), although an equal volume of all gels was pipetted into the transwell systems to obtain a gel thickness around 1mm in previous tests (data not shown). Furthermore, Ruthenium gels were sticking to the transwell system, leading to a slight destruction of the gel while removing (see Figure 84B and F).

Table 5: Measured gel thickness. Thickness was assessed by measurements of the cross section from stereo microscopical images.

	10% GelMA	**10% Ruthenium**	**10% mTG**	**8% mTG**
hmECs	1,1mm	2,4mm	2,2mm	3,2mm
HAoSMCs	1,4mm	3,6mm	2,5mm	3,0mm

6.4.4.3 Evaluation of cell viability and cell-specific marker expression

To further evaluate the cell viability in the different gel systems, a live/dead staining was performed, and hydrogel slices of cross-sections were analyzed via fluorescence microscopy (see Figure 85). Living, green fluorescent endothelial spheroids were found in all conditions, however, cells cultured in 10% GelMA (Figure 85A) and 8% mTG (Figure 85G) included the lowest number of dead spheroids, marked by red fluorescence, followed by 10% mTG (Figure 85E). Ruthenium gels showed the highest number of dead hmECs (Figure 85C). In contrast, dead smooth muscle cells were found in all conditions. The highest number of living smooth mucle cells with an elongated morphology were found in 8% mTG hydrogels (Figure 85H), followed by 10% GelMA (Figure 85B) and 10% mTG (Figure 85F). Ruthenium gels showed less dead SMCs compared to the other conditions, however, SMC number was decreased, and an elongated morphology was missing (Figure 85D).

Furthermore, cell-specific marker expression was checked with immunofluorescence staining in histological sections (see Figure 86). Endothelial cell specific CD31 marker expression was found in all culture conditions (Figure 86A, C, E and G). However, less and smaller spheroids were found in sections of 10% Ruthenium hydrogel (Figure 86C). Smooth muscle cells were stained via aSMA and were also found in all conditions (see Figure 86B, D, F and H). However, visualizing encapsulated smooth muscle cells in histological sections, which are growing in single cells, was difficult in contrast to the endothelial spheroids with a greater size. This is even better visible when looking at exemplary H&E-stainings of GelMA hydrogels (see Figure 87). Endothelial spheroids are clearly visible due to their size (Figure 87A-C), whereas SMCs are only visible as small blue dots Figure 87D-F).

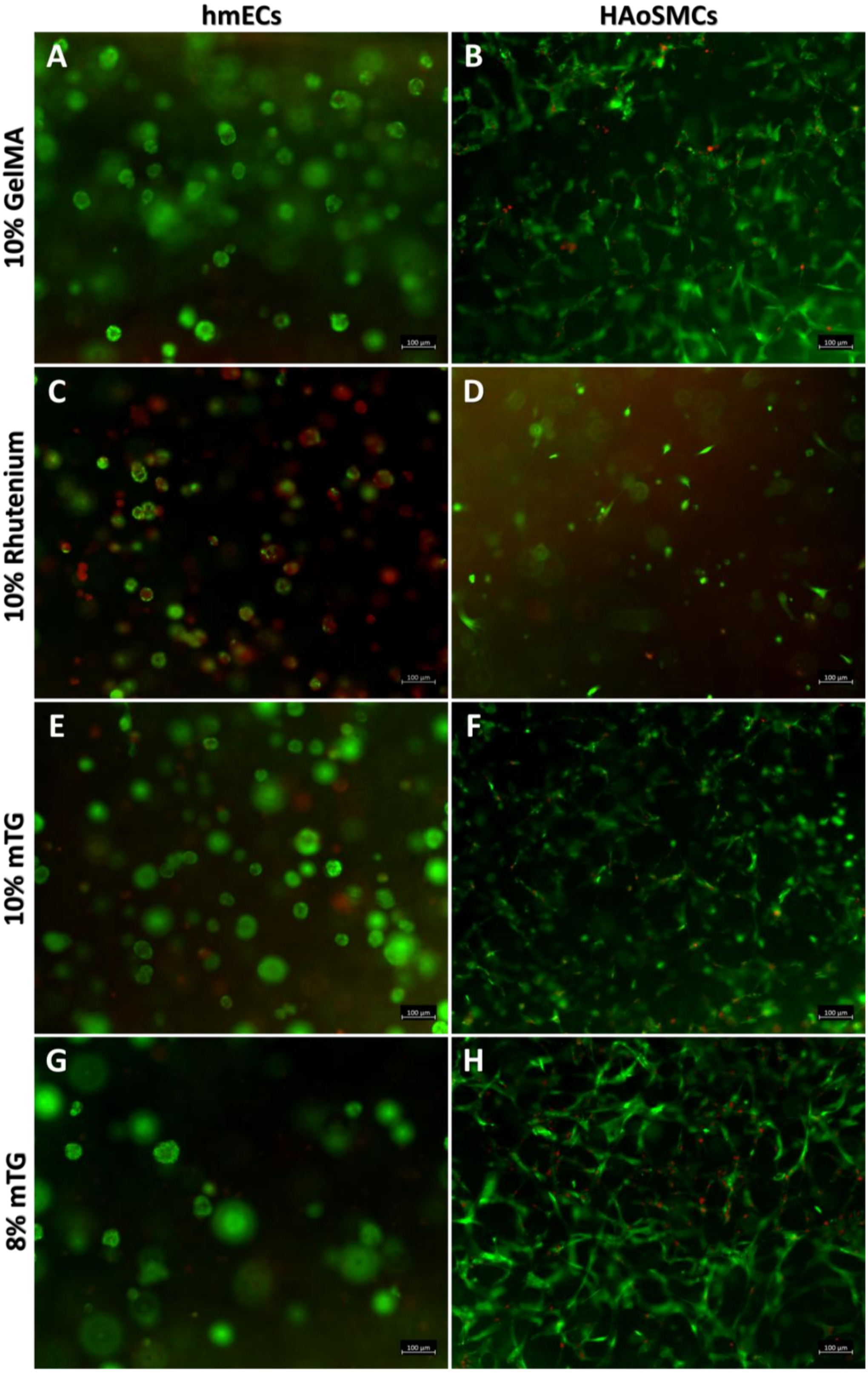

Figure 85: Live/Dead staining of primary human cells encapsulated in different hydrogel systems after 14 days of static culture. **A** hmECs in 10% GelMA. **B** HAoSMCs in 10% GelMA. **C** hmECs in 10% Ruthenium gel. **D** HAoSMCs in 10% Ruthenium gel. **E** hmECs in 10% mTG. **F** HAoSMCs in 10% mTG. **G** hmECs in 10% mTG. **H** HAoSMCs in 10% mTG. Live cells are visualized in green, dead cells in red.

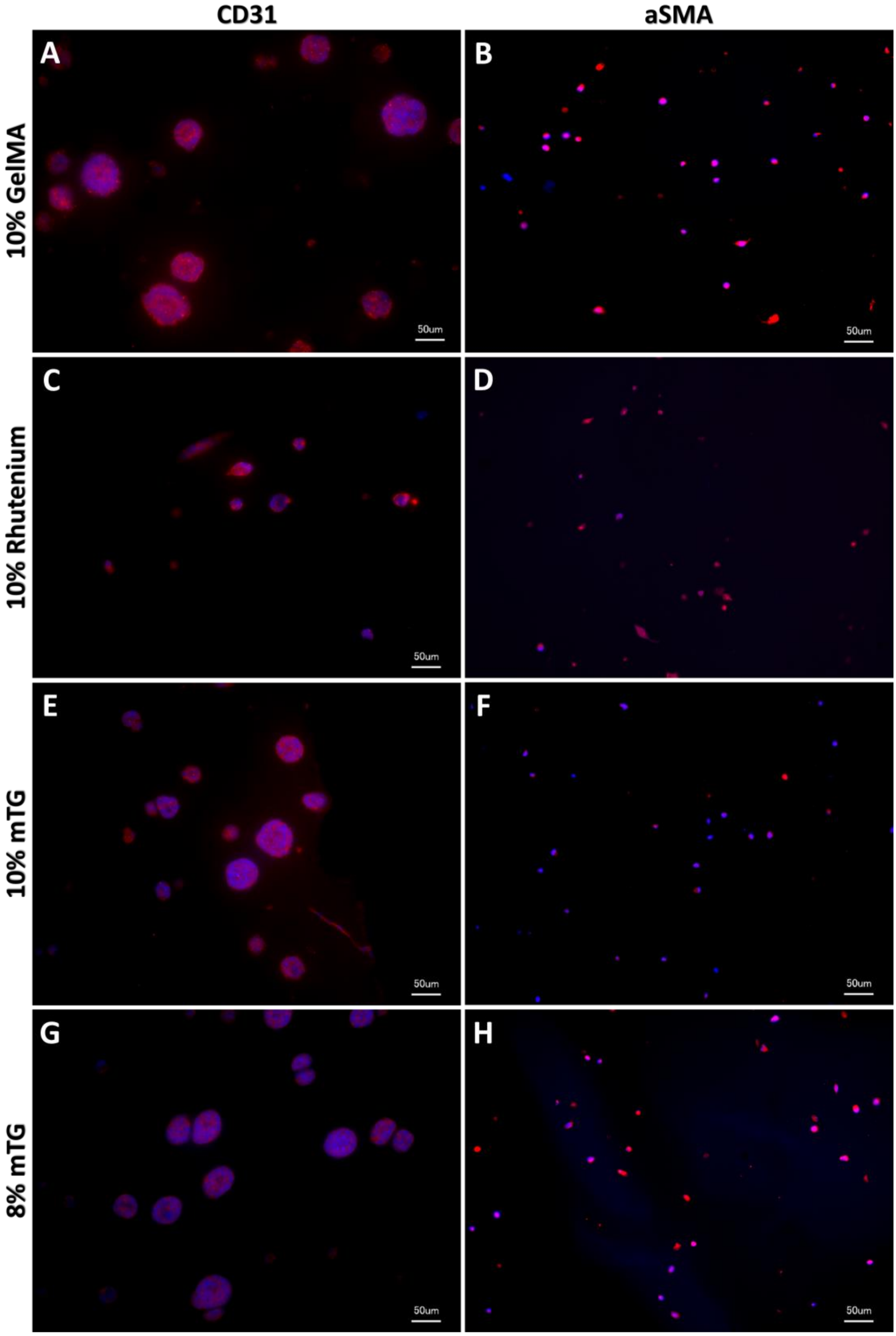

Figure 86: Immunofluorescence staining of primary human cells encapsulated in different hydrogel systems after 14 days of static culture. **A** CD31-staining of hmECs in 10% GelMA. **B** aSMA-staining of HAoSMCs in 10% GelMA. **C** CD31-staining of hmECs in 10% Ruthenium gel. **D** aSMA-staining of HAoSMCs in 10% Ruthenium gel. **E** CD31-staining of hmECs in 10% mTG. **F** aSMA-staining of HAoSMCs in 10% mTG. **G** CD31-staining of hmECs in 10% mTG. **H** aSMA-staining of HAoSMCs in 10% mTG. Nuclei are counterstained with DAPI (blue).

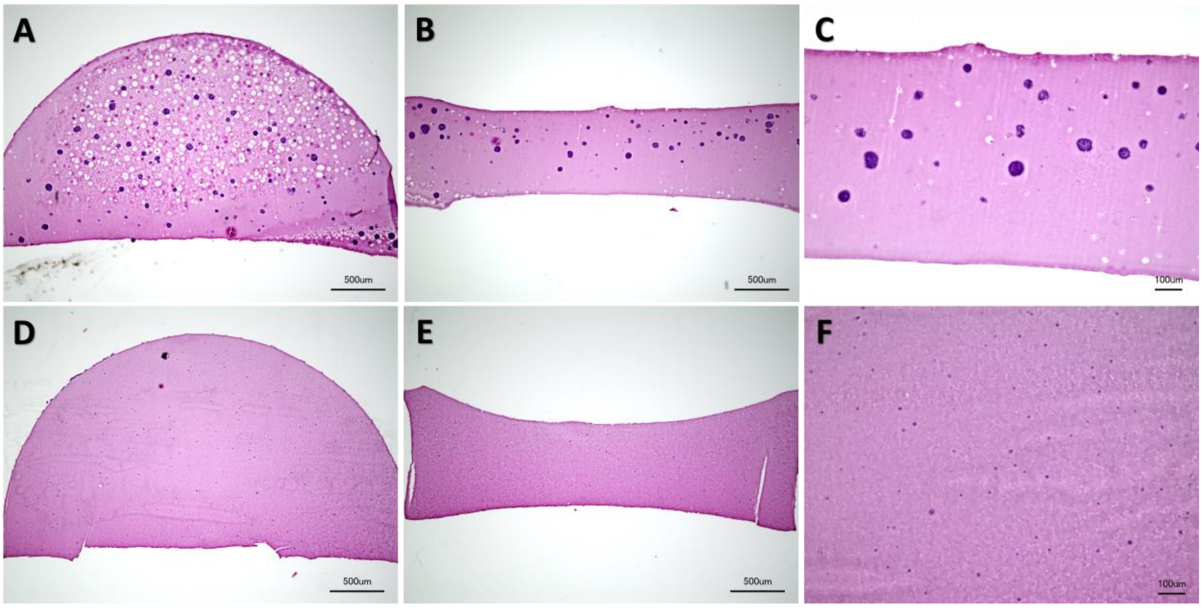

Figure 87: H&E-staining of longitudinal and cross-sections of cells encapsulated in 10% GelMA after 14d of culture. A Longitudinal section and **B** Cross-Section of GelMA hydrogel containing hmECs. **C** Enlarged view of B. Spheroids are cleary visible. **D** Longitudinal section and **E** Cross-Section of GelMA hydrogel containing HAoSMCs. **F** Enlarged view of D. Nuclei are only visible as small blue dots.

6.4.4.4 Suitability of the hydrogel systems in the creation of artery models

In summary, both, GelMA and mTG hydrogels are suitable for culturing endothelial cells as well as smooth muscle cells for a prolonged cultivation time, guaranteeing cell vitality, spreading and proliferation. However, the gel systems were only tested in Transwells during static culture. To test the feasibility of creating artery models with both hydrogel systems, artery models were built with either 10% GelMA or 10% mTG hydrogel according to the work flow described previously and in Figure 78 in the 3D-printed perfusion chambers. Both gels were casted around the scaffolds and in both cases channel creation was observed.

However, commercially available GelMA exhibits a low viscosity, leading to leakage of the precursor solution through the luer lock channels out of the perfusion chamber before gelation can occur (see white arrows in Figure 88A and B). The higher viscosity and the natural and fast thermoresponsive gelation of the gelatin in mTG hydrogels lead to the instant inhibition of leakage and an easy channel creation was possible. However, artery models created with mTG hydrogels adhered strongly to the chamber walls, which impaired the intact removal of the gels in contrast to models created with GelMA (see Figure 88C), which did not occur when using GelMA hydrogels.

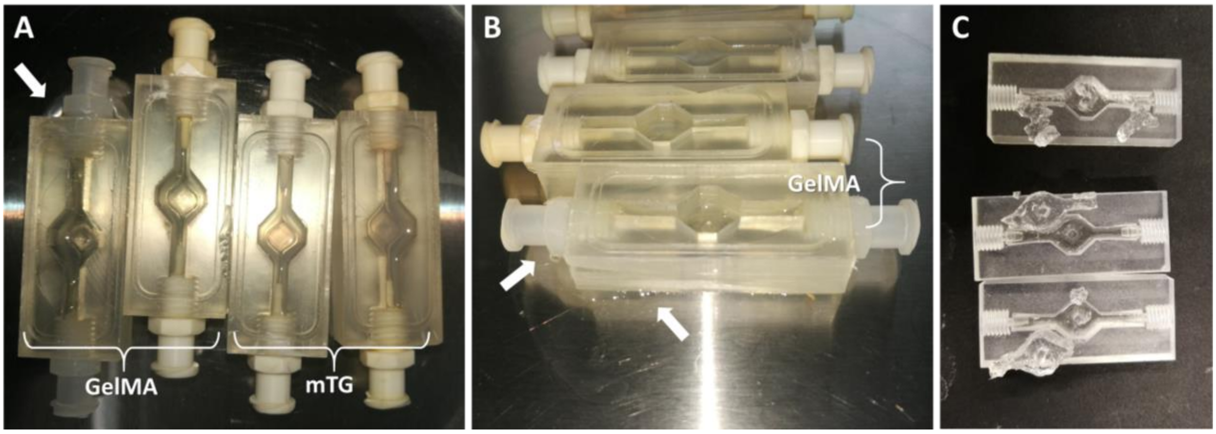

Figure 88: Creation of artery models with GelMA and mTG hydrogels. **A** Perfusion chambers with sacrificial scaffolds covered in GelMA and mTG hydrogel. **B** Enlarged view of perfusion chambers filled with GelMA hydrogel. Due to its lower viscosity, GelMA leaked out of the perfusion chambers through the luer locks (see white arrows). **C** Some artery models created with mTG hydrogel were destroyed during removal.

6.4.5 OPTIMIZATION OF BI-LAYERED HYDROGEL-BASED ARTERY MODELS

6.4.5.1 Optimized perfusion chamber design

After optimization of the gel system used for the creation of the artery models, the perfusion chamber was further customized and optimized, allowing the scaffolds to be prefixed between the main chamber (hydrogel mold) of the perfusion chamber. Therefore, cone-shaped fixation structures were printed into the main chamber ahead of the luer lock connections for the tubing system of the pump. Three combinations of closed and opened fixation structures were tested for insertion of the scaffolds: 2 closed cones (see Figure 89A and F), 1 closed and one opened cone (see Figure 89B) and 2 opened structures (see Figure 89C and G), which were all tested for the simplest and most reproducible way of fixating the scaffolds. Here, the closed structures often led to breaking of the scaffold during handling, as some scaffolds were too thick at the ends due to the printing process. The simplest handling was observed with both opened structures, as the ends of the scaffolds could be simply added into the fixation structures (see Figure 89C and H). To fixate the scaffold and furthermore initially block the fluid connection during hydrogel application into the main chamber, an adhesive based on a 50% PcycloPrOx/water mixture was dropped on the ends of the scaffolds positioned into the cone-shaped fixation structures.

Furthermore, the pillar in the middle of the main chamber was maintained, allowing the reduction of the amount of hydrogel needed and providing a more natural bifurcation design for the artery models. As a further addition, the lid consists of a groove for the implementation of an O-ring and a hole for an air filter (see Figure 89D and E), allowing pressure reduction in the main chamber when pressing the lid against the perfusion chamber for optimum leak-tightness. Furthermore, the usage of a sterile filter allows better gas exchange during culture. Since the hydrogel strongly adhered to the perfusion chamber, leading to complications when removing the model after cultivation (see Figure 80B and Figure 88C), the chamber was coated with a thin layer of PDMS (Sylgard, see Figure 90A), which was manually added with a brush to avoid sticking of the hydrogel (see Figure 90B).

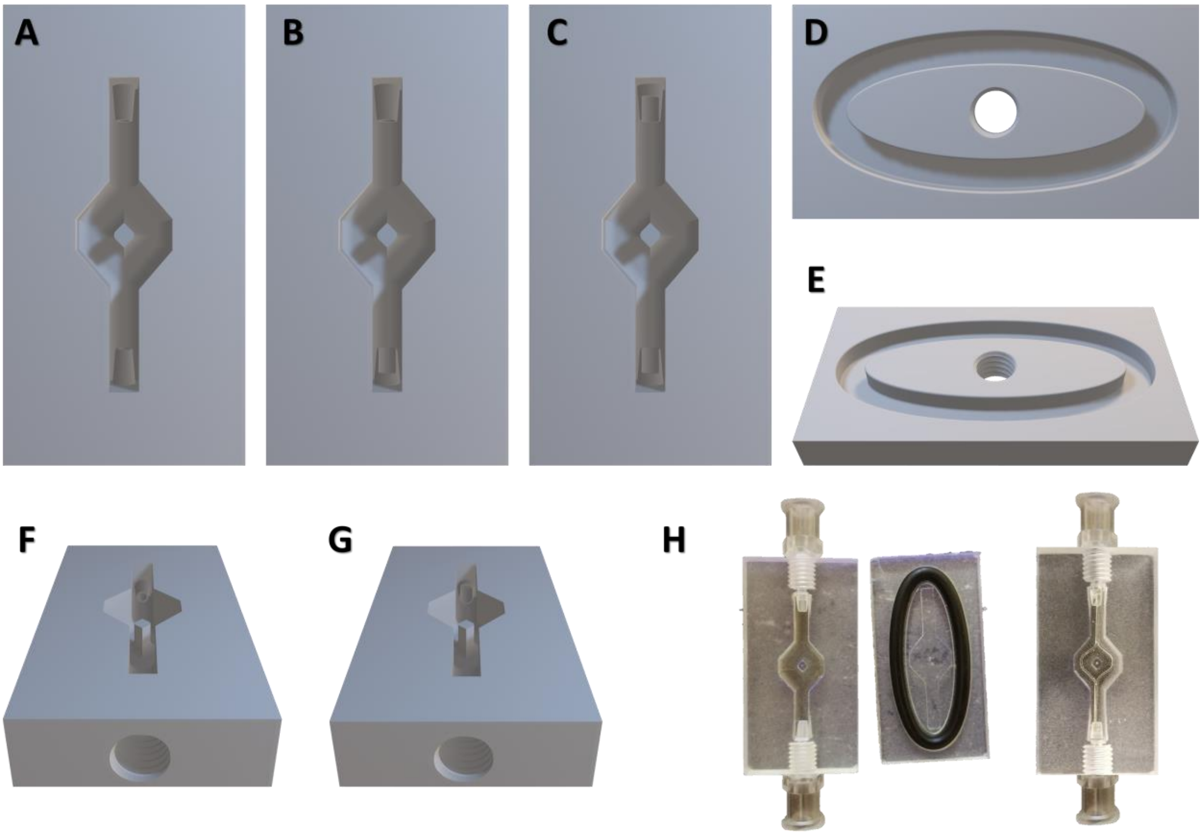

Figure 89: Optimized perfusion chamber design for bi-layered artery models. **A** Version 1of the optimized perfusion chamber with 2 closed cones for the direkt fixation of the scaffold into the chamber (top view). **B** Version 2 of the perfusion chamber with one opened cone and one closed cone (top view). **C** Version 3 of the perfusion chamber with two opened cones (top view). **D** Lid of the perfusion chamber (top view) and **E** (tilted view) with groove for O-ring application and hole for an air filter for improved gas exchange. **F** Tilted view of a perfusion chamber with closed cones and **G** opened cones . **H** 3D-printed perfusion chamber with fixed scaffold and lid.

6.4.5.2 Dynamic cultivation of optimized bi-layered artery models

The feasibility of culturing the artery models in the optimized perfusion chambers (see Figure 89C) was tested and supervised within the framework of the bachelor thesis of Celine Frank. For these experiments, the murine vascular smooth muscle cell line MOVAS (CRL-2797) was used, encapsulated in 8% mTG hydrogel. For the subsequent endothelialization of the created channels, the murine C166 cell line was utilized and the artery models were created as described previously. Furthermore, after dissolution of the sacrificial scaffold, models were first connected to the perfusion pump and cultured over night to nourish the smooth muscle cells in the hydrogel layer and to simultaneously guarantee the complete removal of the residual PcPrOx and the perfusability. Subsequently, endothelial cells were seeded as described before and allowed to adhere for 1 day during periodical rotation of the perfusion chamber. Models were divided in statically cultured models and dynamically cultured models under continuous flow with 10mbar pressure for 14 days, resulting in 1.0 – 1.5 ml/sec flow.

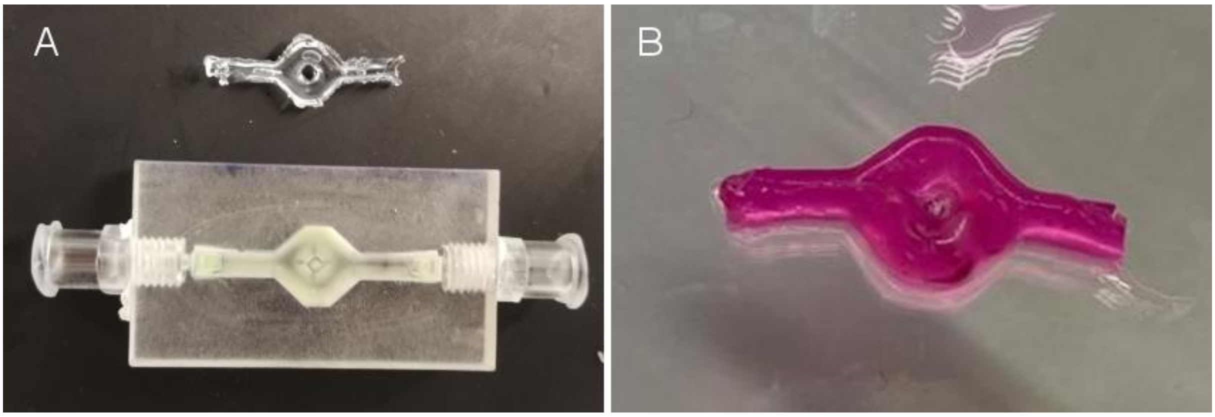

Figure 90: Optimized bi-layered artery model creation and cultivation. A Bottom side view of the perfusion chamber, showing the PDMS coating in the main chamber and the cultured and removed artery model on the top side. **B** Cultured artery models are easily removable without destroying the model. This image was kindly provided by Celine Frank.

Removal of the hydrogel succeeded without complications or destruction of the gel (see Figure 90). The removal was furthermore optimized by cooling down the perfusion chamber for 5 min on ice, leading to a slight shrinkage of the hydrogel and therefore already a slight detachment from the walls. Combined with the newly introduced PDMS coating, an easy removal of the model was guaranteed.

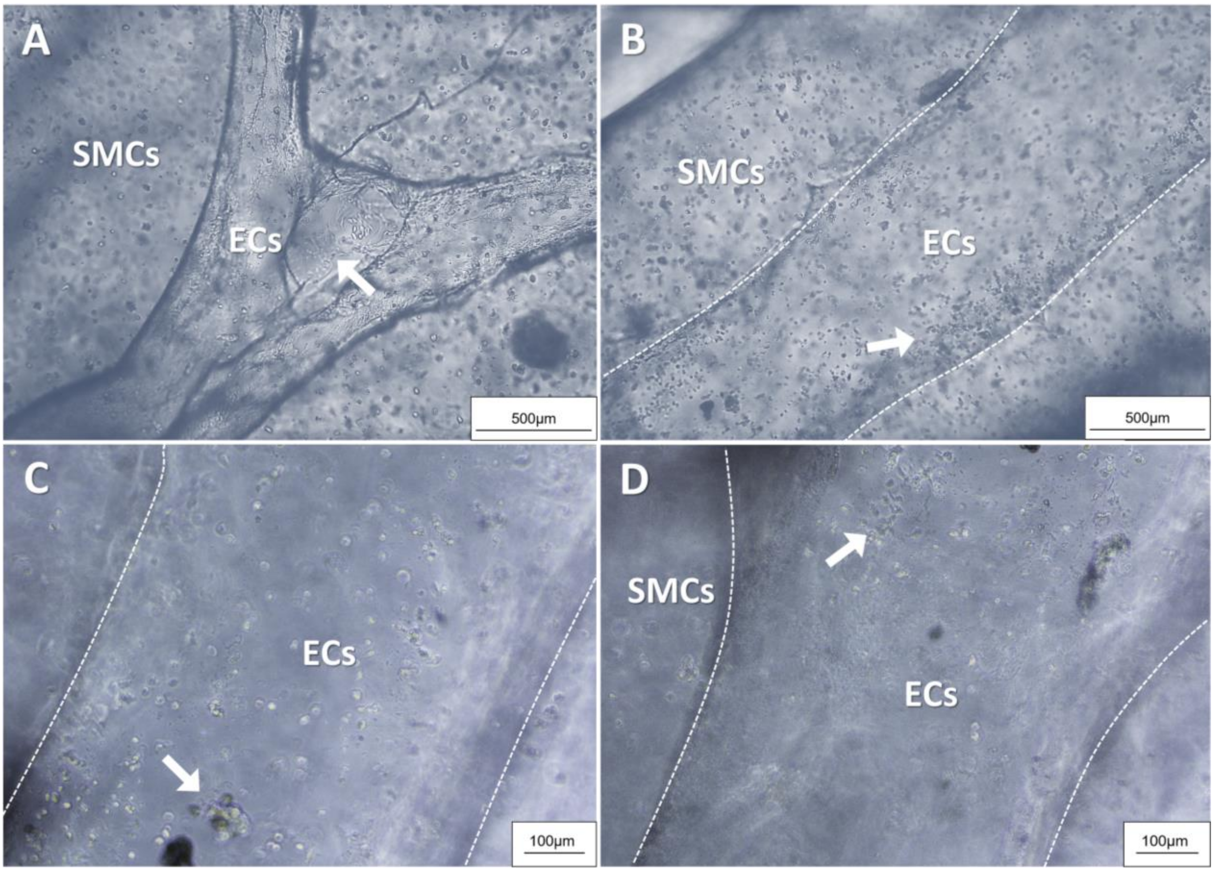

Figure 91: Microscopical evaluation of statically cultured artery models in 8% mTG hydrogel and optimized perfusion chambers. A Bifurcation region of the artery model. **B** Linear region of the artery. **C** Enlarged view of the linear region. **D** Enlarged view of the bifurcation region. Only few adherent ECs are observable, whereas most ECs and SMCs show a roundish morphology. Borders between the endothelialized channel and the smooth muscle cell layer are marked by white lines. SMCs: smooth mucle cells. ECs: Endothelial cells. Images were kindly provided by Celine Frank and adapted.

Furthermore, vitality, adhesion, proliferation and spreading were controlled after 14 days of culture by microscopic evaluation (see Figure 91 and Figure 92) and Live/Dead staining (data not shown). Additionally, the arrangement and alignment of smooth muscle cells in the hydrogel, the endothelial cells in the channel and along the vascular wall were analyzed. The static culture served as control for the dynamic cultivation. In statically cultured models, both cell types showed mainly a roundish morphology in all regions of the model (see white arrows in Figure 91A-D), indicating cell death due to a lack of nourishment, which was furthermore confirmed by Live/Dead analysis (data not shown). Endothelial cells were not evenly distributed in the channel and were found to build small aggregates (see white arrow in Figure 91C). However, smooth muscle cells were uniformly distributed throughout the gel. In contrast to the roundish morphology of ECs in statically cultured models, the dynamically cultured models showed a complete endothelialization throughout the whole model with the typical cobblestone morphology of adherent endothelial cells. The bifurcation region (see Figure 92A and B) showed a dense layer of adherent ECs and surrounding SMCs as well as the linear region (see white arrows in Figure 92C). Furthermore, smooth muscle cells showed a spreaded morphology in contrast to the static control and migration towards the endothelialized channel (see white arrow in Figure 92D), proving the necessity of flow for cell survival and proliferation.

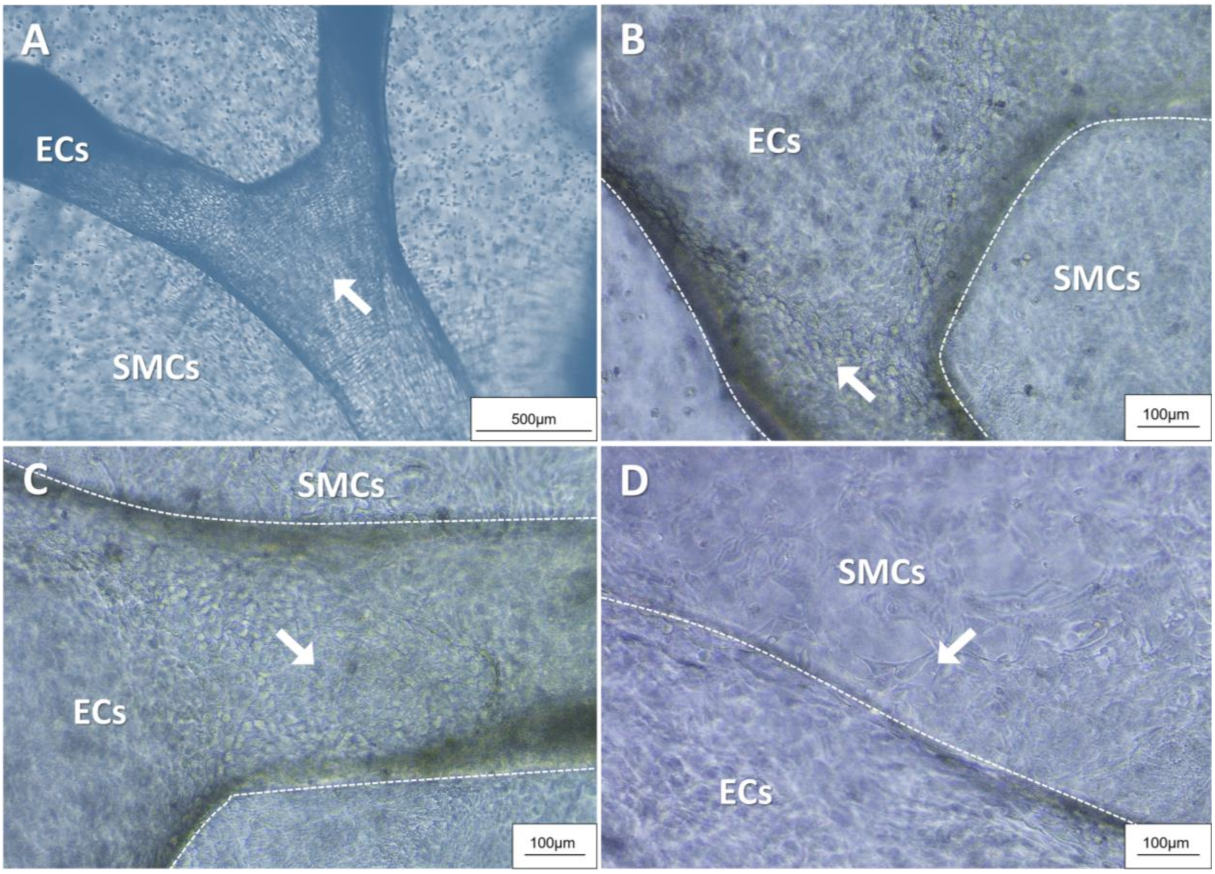

Figure 92: Microscopical evaluation of dynamically cultured artery models in 8% mTG hydrogel and optimized perfusion chambers. **A** Bifurcation region of the artery model. **B** Enlarged view of the bifurcation region of the artery. **C** Enlarged view of the linear region ahead of the bifurcation. **D** Enlarged view of the linear region. Complete endothelialization is observable throughout the model. Smooth muscle cells are spreading in the hydrogel and showing a migration towards the channel. Borders between the endothelialized channel and the smooth muscle cell layer are marked by white lines. SMCs: smooth mucle cells. ECs: Endothelial cells. Images were kindly provided by Celine Frank and adapted.

The redesign of the perfusion chambers in combination with an alternative gel system led to a significant optimization of the creation and cultivation of hydrogel-based artery models. However, microscopical evaluation of the models was not possible during the culture period due to the thickness of the perfusion chamber itself, prohibiting the observation of the endothelialization process. Furthermore, to avoid dehydration of the hydrogel surface of the models, the perfusion chambers had to be regularly opened and humidified with medium, which is a possible source for eventual contaminations. Leak-tightness was guaranteed in this model; however, the process was still laborious as clamps were used for fixation.

6.4.5.3 Final perfusion chamber design for the creation and culture of bi-layered artery models

To address the aforementioned drawbacks and further optimize the design of the perfusion chamber, the final design consisted of an improved, cone-shaped fixation structure design for the sacrificial scaffolds, reaching the ground of the chamber in order to avoid breaking during handling and addition of the scaffolds (see Figure 93B). Additionally, the bottom of the main chamber was designed to implement the adhesion of standard glass cover slips with PDMS (see Figure 93A), which allows an easy observation of cell growth, adhesion and proliferation during and after cultivation, and furthermore facilitating the removal of the models in combination with the PDMS coating of the inner walls. The height of the perfusion chamber was also extended to include a medium reservoir on top of the hydrogel mold to avoid dehydration of the hydrogel (see Figure 93A). Therefore, the nourishment of the model is guaranteed not only from the perfused channel, but also from the surface.

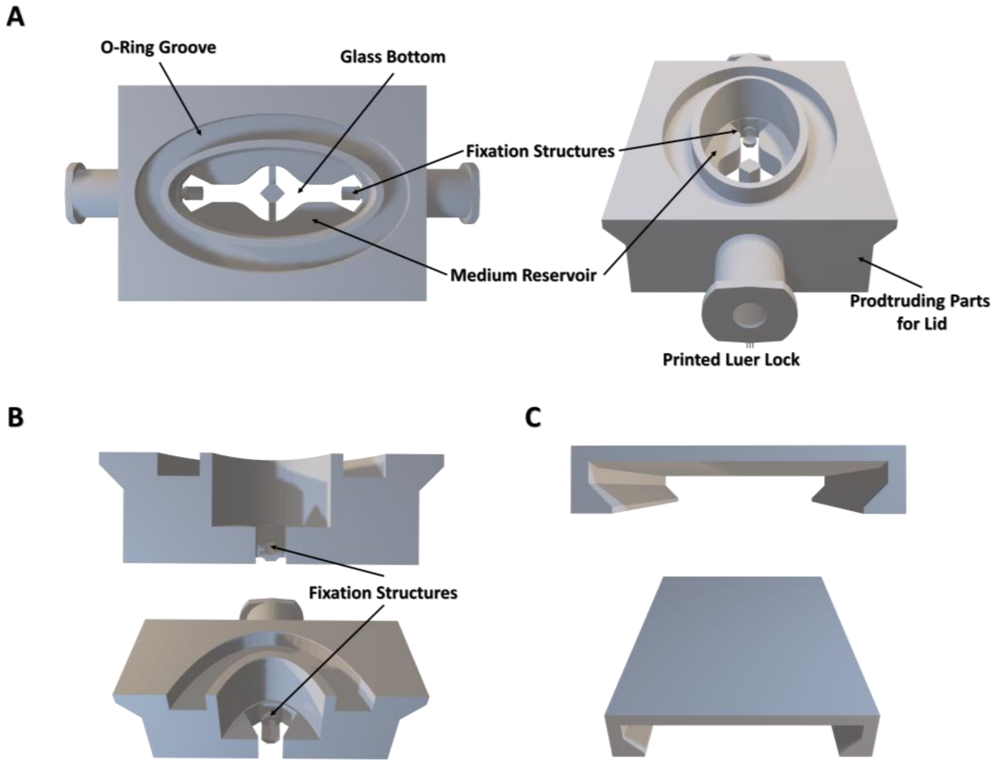

Figure 93: CAD-images of the final perfusion chamber design for the creation and culture of bi-layered artery models. A Final design with the implemented O-ring groove for improved sealing, a glass bottom for microscopical evaluation during culture, the improved fixation structures for the sacrificial scaffolds and the protruding parts for the new lid design. **B** Cut-through the perfusion chamber, revealing the new design of the fixation structures. **C** New sliding lid design, custom-fit for the perfusion chambers.

Furthermore, the groove for the O-ring was added to the chamber itself to introduce a new lid design (see Figure 93C). For this, the main chamber provides two protruding parts at the left and right side (see Figure 93A). The lid was designed to allow sliding onto these protruding parts of the chamber for sealing, facilitating the sealing process on the one hand and the opening and closing of the chambers for medium exchange on the other hand. To improve sliding, the protruding parts were furthermore coated with a lubricant. For the final perfusion chamber design, FotoDent® guide 405 nm resin was used for printing of the chambers, entailing a better stability and less britlleness, including an overall smoother structure, therefore avoiding strong sticking of the gel.

6.4.5.4 Dynamic cultivation of the final bi-layered artery model

To test the performance and leak-tightness of the final perfusion chamber design and to furthermore confirm the vitality of the cells during culture, dynamic cultivation experiments were performed with either human primary endothelial cells (hmECs, see Figure 94) or human aortic smooth muscle cells (HAoSMCs, see Figure 95) for 7 days in order to distinguish between both cell types. Comparison of static and dynamic culture conditions after 7 days of culture revealed better adherence and proliferation of endothelial cells in all regions of the artery model (bifurcation region see Figure 94C and linear region see Figure 94D), resulting in a confluent endothelium in the complete channel. In contrast, no continuous endothelium was observed in both region during 7 days of static culture (Figure 94A+B). Interestingly, HAoSMCs showed spreading and migration towards the channel in all regions, forming a media-like structure around the channels (see white arrows in Figure 95). However, it remains to be investigated weather this media-like structure forming would be enhanced through previous endothelialization of the channel.

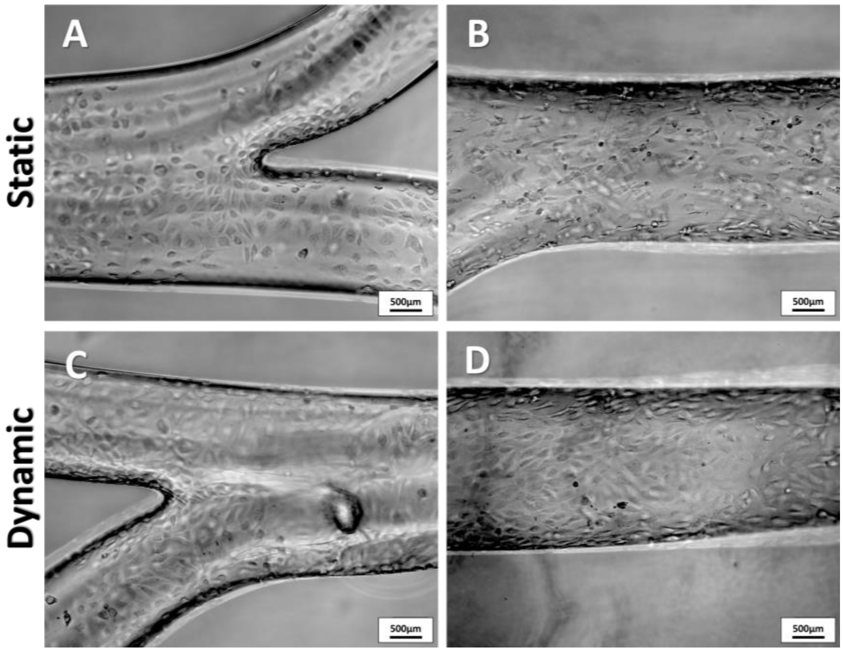

Figure 94: Cultivation of artery models with hmECs after 7 days of culture. A Bifurcation region of the static culture control. B Linear region of the static culture control. hmECs are adherent in all regions, but no tight endothelial layer formed after 7 days of culture. **C** Bifurcation region of the model after dynamic culture. **D** Linear region of the model after dynamic culture. hmECs are adherent in all regions, but in contrast to the static culture, a confluent endothelial layer formed after 7 days of culture.

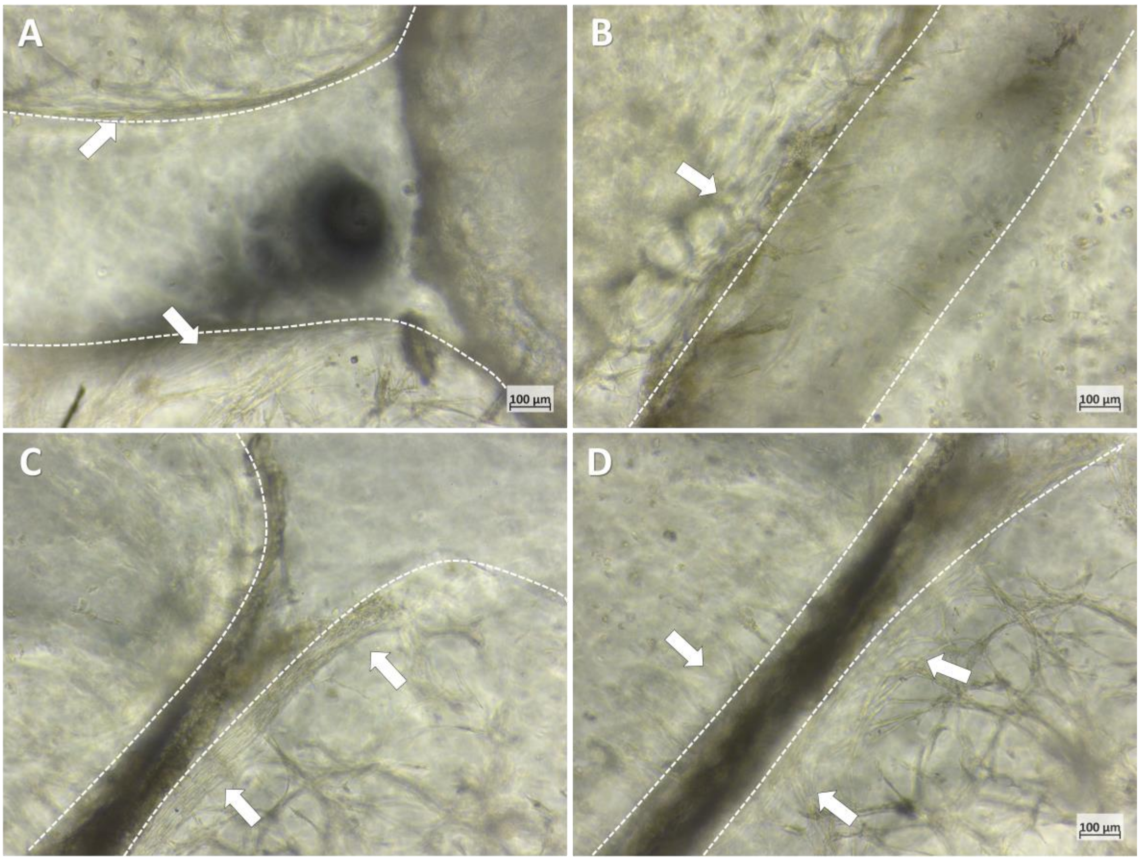

Figure 95: Cultivation of artery models with HAoSMCs. A + B Center region after the bifurcation of the artery model. HAoSMCs are spreading in the hydrogel and migrating towards the channel (see white arrows). **C + D** Linear region before the bifurcation of the artery model. Also here, HAoSMCs are spreading in the hydrogel and migrating towards the channel, forming a media-like structure (see white arrows).

6.4.6 PROOF-OF-CONCEPT FOR THE GENERATION OF AN AORTIC ARTERY MODEL

To test the generation of more complex structures with the sacrificial scaffold method, scaffolds were furthermore printed in an aortic shape, embedded in hydrogel and dissolved, resulting in a perfusable channel-system resembling the structure of an aorta. Therefore, the generation of more complex structures with this method is feasible. Custom-fit perfusion chambers for aortic artery models will be designed in the future.

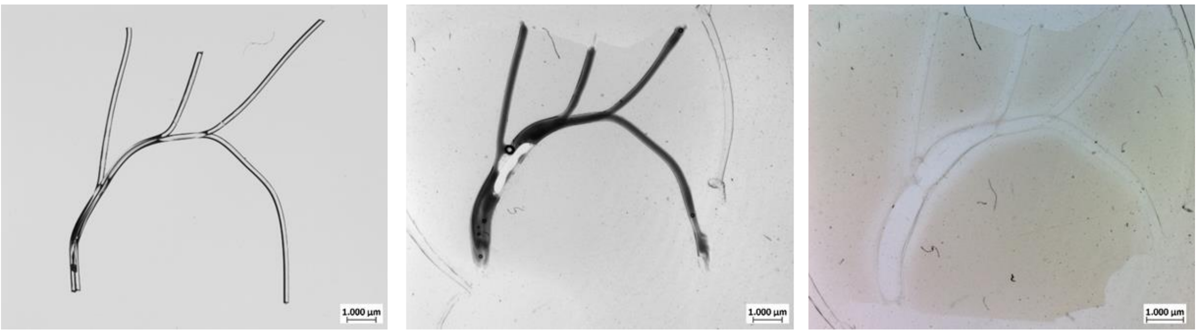

Figure 96: Proof-of-concept for the generation of an aortic artery model . A Printed POx scaffold in the shape of an aorta. **B** Scaffold embedded in 8% mTG-hydrogel before dissolution of the polymer and **C** after dissolution of the polymer, creating an aortic-like channel structure in the hydrogel.

6.5 DISCUSSION

3D artery models for the development of *in vitro* test systems are of great importance in the biomedical research field, as they offer a simplified environment to the *in vivo* situation, yet more controllable. Therefore, they are a powerful tool to gain new insights into homeostasis as well as key processes of disease development and progression. In this study, an artery tissue model based on sacrificial template technology, customizable perfusion reactors and hydrogels was developed. PcPrOx scaffolds created via MEW were used as sacrificial structures for the creation of perfusable constructs, which can be easily dissolved by simple temperature reduction within physiological range [345]. Furthermore, the usage of PcPrOx as sacrificial material for channel generation in hydrogels offers many additional advantages like biocompatibility [346] and stability in aqueous solutions, enabling casting of hydrogel solution around the scaffold while retaining the initial shape of the sacrificial scaffolds. This furthermore enables the usage of natural, non-synthetic hydrogel systems like gelatin hydrogels, enzymatically crosslinked with microbacterial transglutaminase [259, 347-349]. These natural hydrogel systems provide many advantages like excellent cell adhesion, proliferation and spreading. However, the enzymatically driven crosslinking process takes time in comparison to chemical crosslinking methods, which is not posing a problem when using PcPrOx scaffolds due to its described physical properties. Moreover, in contrast to conventional carbohydrate-based scaffolds [350], PcPrOx scaffolds can easily be stored at room temperature after the printing process without loss or alteration of the initial shape, facilitating overall handling and enabling high-throughput approaches. Therefore, post-modifications of the scaffolds like various coating-procedures described for carbohydrate-based scaffolds to increase the stability [351, 352] during storage or gelation of the used hydrogel are not needed.

Compared to conventional MEW, which is mainly used for the creation of fibrous scaffolds with diameters below 100µm [246], scaffolds based on fiber diameters of approximately 500µm were printed in this study. With this, bigger perfusable structures in the range of large murine arteries or small human arteries can be created by embedment in a crosslinkable hydrogel. Furthermore, this MEW-based approach of scaffold creation allows the generation of naturally branched scaffolds due to the initial swelling behavior of PcPrOx in aqueous solutions, leading to fusion of the stacked fibers, which is a natural consequence of the MEW process. Therefore, the generation of natural bifurcations according to Murray’s Law [353] are enabled. However, with the process of MEW, several geometries of initial scaffold structures [354] like the shape and size of a murine aorta can be created and mimicked, leading to unlimited possibilities of *in vitro* test model development and therefore animal experiment reductions.

This is an excellent basis for the investigation of key processes in diseased arteries and offers the advantage, to be directly compared to the *in vivo* situation. However, to achieve this, the model should be established with primary murine vascular cells. Therefore, the isolation of these cells was the first step, resulting in a very high purity of aortic endothelial and smooth muscle cells, identified by a clear pan-marker expression. Furthermore, the aortic smooth muscle cells showed the ability to synthesize extracellular matrix components - properties, which are good to enrich the hydrogel with these components during cultivation.

From the inside to the outside, the artery contains the endothelial layer (tunica intima), the thick tunica media consisting of vascular SMCs and the adventital layer with fibroblasts (tunica externa or tunica adventitia) [251]. Therefore, the first approach was to recreate these three layers by embedding the scaffolds in two layers of gelatin crosslinked with ruthenium, with encapsulated SMCs to mimic the tunica media and fibroblasts to mimic the tunica adventitia. After dissolution of the polymer by temperature decrease, a monolayer of ECs after channel creation was added in order to imitate the tunica intima. While the creation of the three-layered approach with the developed method was easy and simple to achieve, the connection to the perfusion system in simple rectangular perfusion chambers via cannulas was not consistently feasible and therefore not easily reproducible, as the scaffolds were completely surrounded by the hydrogel, blocking the access points to the fluid connections. Therefore, the connections to the perfusion system had to be established manually, leading to eventual damage of the hydrogel and therefore not guaranteeing a leakage-free perfusion. In order to circumvent this issue, the main chamber of the perfusion chamber was adapted to the form of the biofabricated tissue. Here, the slight swelling of the photocrosslinkable Ruthenium/Gelatin hydrogels [344] was counteracted by estimating the final size of the construct and adapting the main chamber size. Additionally, luer locks were used as a connection that allowed perfusion through the created channels after dissolution of the sacrificial polymer scaffold without direct connection to the endothelialized channel. For the biological characterization of the artery model system, murine endothelial cells, smooth muscle cells and fibroblasts were used. Endothelial cell seeding was performed by short-term static cell culture to allow initial cell adhesion and attachment, followed by dynamic cultivation with continuous flow. However, during dynamic cultivation of the created models, leakage of the perfusion chambers was observed because of several reasons. The main issue resulted from the missing direct connection of the endothelialized channels to the perfusion chamber, causing the flow to not be fully directed into the channels.

Despite these issues, the successful creation of three-layered artery models in a short time of around 20-30 min, providing three cellular layers mimicking the morphology of an artery [251] and including a highly confluent endothelial layer compared to the static cultivation was shown after a short culture period of 7 days, as confirmed by microscopical and histological evaluation. Therefore, a fast and simple creation of three-layered artery models was established, with no need for special and expensive equipment. This method furthermore allows the generation of many models in parallel, enabling for example high-throughput drug-screening or the generation of *in vitro* disease models, which can be cultured under many different conditions in parallel. The next steps should include the optimization of the perfusion chamber, consisting of a direct connection between the endothelialized channel and the perfusion chamber in order to enable a leakage-free dynamic cultivation. In combination with the simple and cost-effective creation of the three-layered artery models, this method opens the door for the development of specific flow-related disease-models like an *in vitro* atherosclerosis test system. This vascular disease highly depends on the vascular geometry and the flow dynamics, causing disease development and progression at special vascular sites like curvatures and branch points [305, 355]. The special environment needed for the atherogenic stimuli can be mimicked and highly controlled by the applied flow and therefore shear stress and the variable scaffold geometry, which can be achieved and varied by printing different geometries with MEW and the corresponding hydrogel geometry, which is simply variable in form, size and thickness to mimick various types of arteries.

The generation of functional, three-layered artery [253] and even atherosclerosis models [254, 265] was also shown with complex 3D bioprinting techniques. Schöneberg et al. used drop-on-demand bioprinting combined with casting to obtain three-layered constructs with different hydrogel compositions per layer and good viability [253]. Gao et al. even developed a functional atherosclerosis model with highly complex in-bath coaxial cell printing, creating straight, curved and stenotic vessels [254]. Moreover, another three-layered atherosclerosis models was developed by Zhang et al. by a multi-casting method [265]. However, these techniques are all limited in the geometry design freedom. Here, no bifurcations or even a replicate of an aorta can be created – a prerequisite for the investigation of flow-related disease development and progression [305, 355] in *in vitro* models.

Although a three-layered model reflects the *in vivo* situation in a more accurate way, and the adventitial layer has many functions and effects regarding vascular stability, repair and remodeling [356], the existence of an adventitial layer in an *in vitro* artery model is of secondary importance. However, the endothelium, which serves as a barrier between the blood and the tissue and which is controlling nutrient exchange [251, 357, 358] as well as the medial layer, consisting of smooth muscle cells and being responsible for vasoconstriction and dilatation to regulate hemodynamics [251] and providing vascular stability, play a more important role, especially when mimicking key processes of vascular diseases [359]. Therefore, this led to the decision to create a simplified bi-layered artery model with the intimal, endothelial cell layer and the tunica media consisting of smooth muscle cells. This furthermore opened up the possibility to cast the smooth muscle cell containing hydrogel gel directly around a prefixated scaffold in the perfusion chamber. To avoid instability of the printed luer locks, commercial screw-in luer locks were used, which also served as the prefixation point for the scaffold, further simplifying the creation process of the model. However, casting of Ruthenium/Gelatin revealed that the swelling of the Rhutenium/Gelatin hydrogel [344] gradually blocked the fluid connections during cultivation, preventing perfusion and leading to leakage due to pressure overload in the chamber.

In order to find the optimal hydrogel system for the creation of the biofabricated artery models, additional crosslinkable hydrogel materials were evaluated with primary human vascular cells. The additionally tested gel systems consisted of the commercially available Gelatin-Methacryloyl (GelMA) hydrogel system [227, 360, 361], crosslinked via UV-light with Irgacure as photo initiator, and Gelatin enzymatically crosslinked with micro bacterial transglutaminase (mTG) [259, 347-349]. Cell viability experiments using the described systems revealed that cell survival and proliferation showed better results in GelMA and mTG hydrogels compared to Ruthenium/Gelatin hydrogels. In general, gelatin-based hydrogels offer many advantages, as they are based on the natural matrix component collagen, which is a main component of the artery [251]. Furthermore, these hydrogel systems are biocompatible, and provide excellent cell adhesion, vitality and proliferation [349]. The functionalized Gelatin of GelMA hydrogels provide the same advantages, additionally yielding the benefit of a low viscosity [360, 362, 363] compared to standard gelatin, preventing high shear forces acting on the cells during pipetting and improving overall handling. GelMA is furthermore commercially available and extensively described in literature, however, this gel system is very expensive compared to standard gelatin. Moreover, casting of the non-viscous GelMA into the perfusion chambers led to leakage through the fluid connections and therefore clogging of the channels after the crosslinking process, which was not observed with other gelatin-based hydrogels.

To counteract these drawbacks and to guarantee a leakage-free perfusion of the endothelialized channel, the perfusion chamber design was therefore advanced to include novel, cone-shaped fixation points for the scaffolds, enabling the precise positioning and fixation for the inflow and outflow of the biofabricated model. For the subsequent fixation of the scaffold and the simultaneous blocking of the fluid connection, a drop of an adhesive based on an aqueous solution of PcPrOx was added into the fixation points and dried afterwards. Apart from fixation of the scaffold, this process furthermore facilitates the introduction of the hydrogel into the main chamber, avoiding clogging of the fluid connections due to unintended inflowing hydrogel, which in turn enables the utilization of various low-viscosity hydrogel systems. Furthermore, dissolution of the scaffold and the release of the fluid connections is achieved in a one-step process by simple temperature decrease [342] and subsequent flushing of the model via the luer locks, which can be connected by any commercially available syringe to apply cold fluid into the channels. Therefore, a direct connection between the generated channels and the fluid connection of the perfusion chamber to the tubing system of the pump was generated, enabling the direct creation of artery models in the chamber, followed by an easy endothelialization through simple injection of the cell suspension into the channels and simultaneously a direct, leakage-free perfusion of the artery models. Furthermore, the cost-effective and easy-to-prepare PDMS coating was shown to avoid destruction of the biofabricated models during removal and furthermore, to enable the utilization of more adhesive hydrogels like gelatin crosslinked with microbacterial transglutaminase [259, 347-349]. The described hydrogel system was furthermore chosen as preferential system as it provides gentle crosslinking via enzymatic reaction through transglutaminase, a natural enzyme found across several organisms. Additionally, this gel system is very cost-effective compared to commercially available gel systems like GelMA, nevertheless, entailing the same advantages.

The feasibility of creating and culturing hydrogel-based bi-layered artery models in the optimized, custom-fit perfusion chamber was successfully shown by dynamic cultivation experiments. However, one remaining drawback was the missing possibility to microscopically evaluate cell spreading, proliferation and endothelial cell layer formation during culture and to apply other optical analysis methods. Therefore, the final design of the perfusion chamber exhibits an open bottom, which is sealed with a glass coverslip to introduce transparency and therefore to enable efficient microscopy during and after endothelization. Furthermore, the main chamber provides an elevated design, acting as a medium reservoir for the addition of media on top of the hydrogel construct, as well as protruding parts to introduce a sliding lid design for the simplification of a tight sealing. The resin chosen for the final design of the perfusion chamber furthermore provides better material stability and therefore enables the direct implementation and printing of luer lock connections. Dynamic culture experiments with the final perfusion chamber design proved the feasibility of directly generating and culturing hydrogel-based artery models with vital smooth muscle cells embedded in a natural hydrogel based on collagen, circumferentially shaped around a tight layer of endothelial cells, mimicking all relevant components of a native artery [251].

Several *in vitro* disease models like e.g., atherosclerosis models have been developed based on bi- or three-layered artery models [254, 257, 259, 265], describing successful induction of atherosclerotic key processes like endothelial activation through TNF-alpha, monocyte- and LDL uptake and even foam cell formation, which can be easily transferred to the proposed artery model. However, this artery model offers the advantage to entail geometrical design freedom and therefore could act as an excellent model for the investigation of flow-related disease progression.

In summary, we here present an easy-to-prepare artery model, which is excellent for the *in vitro* research of vascular function and various diseases like e.g. atherosclerosis. This model can be prepared at very low cost and in a short timeframe of only 5-30 min, depending on the gelation time of the used hydrogel system. Furthermore, an even closer mimicking of the vascular microenvironment is possible by utilizing arterial extracellular matrix, processed into hydrogels [254, 364] or a mixture of GelMA and Gelatin hydrogel, which was shown to promote cell functionalization in a vessel-on a chip model [258]. Furthermore, this given flexibility in using any desired hydrogel system, with tunable stiffness and extracellular matrix components paves the way for the development of not only various artery models like natural bifurcations or even the aorta, but also various tissues like e.g., vascularized heart, muscle or even a blood-brain barrier model, depending on the number of layers and types of cells used. The presented system also offers the generation of a fully customizable *in vitro* test system for various vascular diseases, as cells of any species can be used without limitation, which was shown in this study for human and murine vascular cells. This furthermore offers the opportunity to utilize e.g. distinct knock-out cells to examine the functionality or the interrelation of certain genes or proteins with other cell types incorporated into this system or being perfused through the channels and the hemodynamics, being enabled by a fully controlled hemodynamic environment when using perfusion pumps. When using the murine system in particular, a validation and direct comparison to the *in vivo* situation is possible, leading to a reduction of animal experiments when used for pre-experiments or even animal experiment replacement.

6.6 CONCLUSION

The study presents the development of an easy-to-prepare, low cost and fully customizable artery model, which paves the way for the development of *in vitro* disease test systems or even more complex 3D tissue models. The utilization of the thermoresponsive polymer PcPrOx, processed with the technique of Melt Electro Writing, allows a biomimetic fabrication of sacrificial scaffolds resembling the structure of native arteries, including curvatures and bifurcations up to even more complex vessel structures like the aorta. Due to the excellent physical properties of PcPrOx, the scaffold remains stable even in aqueous solutions like hydrogels, resulting in accurate channel generation. The custom-fit perfusion chamber design allows the simultaneous one-step creation, dynamic cultivation and microscopic observation of the biofabricated models, furthermore, providing a fully controllable hemodynamic environment and enabling an easily achievable adaption to various scaffold and surrounding hydrogel dimensions and forms, depending on the desired vascular structure. Vascular cells were shown to remain vital, spread and proliferate. Endothelial cells formed a confluent monolyer within a very short time and smooth muscle cells were observed to migrate towards the channel, forming media-like structures. Moreover, the possibility to create custom-tailored artery models according to individual requirements by adapting the shape and size and using different vascular structures, cells of various tissues or species as well as different hydrogel systems, mimicking the extracellular matrix environment from the target vessels, makes it an excellent basis for the development of *in vitro* disease test systems for e.g., atherosclerosis research.

CHAPTER 7

Summary and Future Perspectives

-

Zusammenfassung und Ausblick

7.1 SUMMARY AND FUTURE PERSPECTIVES

Within this thesis, three main approaches for the assessment and investigation of altered hemodynamics like wall shear stress, oscillatory shear index and the arterial pulse wave velocity in atherosclerosis development and progression were conducted:

1. The establishment of a fast method for the simultaneous assessment of 3D WSS and PWV in the complete murine aortic arch via high-resolution 4D-flow MRI
2. The utilization of serial *in vivo* measurements in atherosclerotic mouse models using high-resolution 4D-flow MRI, which were divided into studies describing altered hemodynamics in late and early atherosclerosis
3. The development of tissue-engineered artery models for the controllable application and variation of hemodynamic and biologic parameters, divided in native artery models and biofabricated artery models, aiming for the investigation of the relationship between atherogenesis and hemodynamics

Chapter 2 describes the establishment of a method for the simultaneous measurement of 3D WSS and PWV in the murine aortic arch at, using ultra high-field MRI at 17.6T [16], based on the previously published method for fast, self-navigated wall shear stress measurements in the murine aortic arch using radial 4D-phase contrast MRI at 17.6 T [4]. This work is based on the collective work of Dr. Patrick Winter, who developed the method and the author of this thesis, Kristina Andelovic, who performed the experiments and statistical analyses. As the method described in this chapter is basis for the following *in vivo* studies and undividable into the sub-parts of the contributors without losing important information, this chapter was not split into the single parts to provide fundamental information about the measurement and analysis methods and therefore better understandability for the following studies. The main challenge in this chapter was to overcome the issue of the need for a high spatial resolution to determine the velocity gradients at the vascular wall for the WSS quantification and a high temporal resolution for the assessment of the PWV without prolonging the acquisition time due to the need for two separate measurements. Moreover, for a full coverage of the hemodynamics in the murine aortic arch, a 3D measurement is needed, which was achieved by utilization of retrospective navigation and radial trajectories, enabling a highly flexible reconstruction framework to either reconstruct images at lower spatial resolution and higher frame rates for the acquisition of the PWV or higher spatial resolution and lower frame rates for the acquisition of the 3D WSS in a reasonable measurement time of only 35 minutes. This enabled the *in vivo* assessment of all relevant hemodynamic parameters related to atherosclerosis development and progression in one experimental session. This method was validated in healthy wild type and atherosclerotic *Apoe*$^{-/-}$ mice, indicating no differences in robustness between pathological and healthy mice.

The heterogeneous distribution of plaque development and arterial stiffening in atherosclerosis [10, 12], however, points out the importance of local PWV measurements. Therefore, future studies should focus on the 3D acquisition of the local PWV in the murine aortic arch based on the presented method, in order to enable spatially resolved correlations of local arterial stiffness with other hemodynamic parameters and plaque composition.

In **Chapter 3**, the previously established methods were used for the investigation of changing aortic hemodynamics during ageing and atherosclerosis in healthy wild type and atherosclerotic *Apoe*$^{-/-}$ mice using the previously established methods [4, 16] based on high-resolution 4D-flow MRI. In this work, serial measurements of healthy and atherosclerotic mice were conducted to track all changes in hemodynamics in the complete aortic arch over time. Moreover, spatially resolved 2D projection maps of WSS and OSI of the complete aortic arch were generated. This important feature allowed for the pixel-wise statistical analysis of inter- and intragroup hemodynamic changes over time and most importantly – at a glance. The study revealed converse differences of local hemodynamic profiles in healthy WT and atherosclerotic *Apoe*$^{-/-}$ mice, with decreasing longWSS and increasing OSI, while showing constant PWV in healthy mice and increasing longWSS and decreasing OSI, while showing increased PWV in diseased mice. Moreover, spatially resolved correlations between WSS, PWV, plaque and vessel wall characteristics were enabled, giving detailed insights into coherences between hemodynamics and plaque composition. Here, the circWSS was identified as a potential marker of plaque size and composition in advanced atherosclerosis. Moreover, correlations with PWV values identified the maximum radStrain could serve as a potential marker for vascular elasticity. This study demonstrated the feasibility and utility of high-resolution 4D flow MRI to spatially resolve, visualize and analyze statistical differences in all relevant hemodynamic parameters over time and between healthy and diseased mice, which could significantly improve our understanding of plaque progression towards vulnerability. In future studies the relation of vascular elasticity and radial strain should be further investigated and validated with local PWV measurements and CFD.

Moreover, the 2D histological datasets were not reflecting the 3D properties and regional characteristics of the atherosclerotic plaques. Therefore, future studies will include 3D plaque volume and composition analysis like morphological measurements with MRI or light-sheet microscopy to further improve the analysis of the relationship between hemodynamics and atherosclerosis.

Chapter 4 aimed at the description and investigation of hemodynamics in early stages of atherosclerosis. Moreover, this study included measurements of hemodynamics at baseline levels in healthy WT and atherosclerotic mouse models. Due to the lack of hemodynamic-related studies in *Ldlr*$^{-/-}$ mice, which are the most used mouse models in atherosclerosis research together with the *Apoe*$^{-/-}$ mouse model, this model was included in this study to describe changing hemodynamics in the aortic arch at baseline levels and during early atherosclerosis development and progression for the first time. In this study, distinct differences in aortic geometries of these mouse models at baseline levels were described for the first time, which result in significantly different flow- and WSS profiles in the *Ldlr*$^{-/-}$ mouse model. Further basal characterization of different parameters revealed only characteristic differences in lipid profiles, proving that the geometry is highly influencing the local WSS in these models. Most interestingly, calculation of the atherogenic index of plasma revealed a significantly higher risk in *Ldlr*$^{-/-}$ mice with ongoing atherosclerosis development, but significantly greater plaque areas in the aortic arch of *Apoe*$^{-/-}$ mice. Due to the given basal WSS and OSI profile in these two mouse models

– two parameters highly influencing plaque development and progression – there is evidence that the regional plaque development differs between these mouse models during very early atherogenesis.

Therefore, future studies should focus on the spatiotemporal evaluation of plaque development and composition in the three defined aortic regions using morphological measurements with MRI or 3D histological analyses like LSFM. Moreover, this study offers an excellent basis for future studies incorporating CFD simulations, analyzing the different measured parameter combinations (e.g., aortic geometry of the *Ldlr*$^{-/-}$ mouse with the lipid profile of the *Apoe*$^{-/-}$ mouse), simulating the resulting plaque development and composition. This could help to understand the complex interplay between altered hemodynamics, serum lipids and atherosclerosis and significantly improve our basic understanding of key factors initiating atherosclerosis development.

Chapter 5 describes the establishment of a tissue-engineered artery model, which is based on native, decellularized porcine carotid artery scaffolds, cultured in a MRI-suitable bioreactor-system [23] for the investigation of hemodynamic-related atherosclerosis development in a controllable manner, using the previously established methods for WSS and PWV assessment [4, 16]. This *in vitro* artery model aimed for the reduction of animal experiments, while simultaneously offering a simplified, but completely controllable physical and biological environment. For this, a very fast and gentle decellularization protocol was established in a first step, which resulted in porcine carotid artery scaffolds showing complete acellularity while maintaining the extracellular matrix composition, overall ultrastructure and mechanical strength of native arteries. Moreover, a good cellular adhesion and proliferation was achieved, which was evaluated with isolated human blood outgrowth endothelial cells. Most importantly, an MRI-suitable artery chamber was designed for the simultaneous cultivation and assessment of high-resolution 4D hemodynamics in the described artery models. Using high-resolution 4D-flow MRI, the bioreactor system was proven to be suitable to quantify the volume flow, the two components of the WSS and the radStrain as well as the PWV in artery models, with obtained values being comparable to values found in literature for *in vivo* measurements. Moreover, the identification of first atherosclerotic processes like intimal thickening is achievable by three-dimensional assessment of the vessel wall morphology in the *in vitro* models. However, one limitation is the lack of a medial smooth muscle cell layer due to the dense ECM. Here, the utilization of the laser-cutting technology for the generation of holes and / or pits on a microscale, eventually enabling seeding of the media with SMCs showed promising results in a first try and should be further investigated in future studies. Therefore, the proposed artery model possesses all relevant components for the extension to an atherosclerosis model which may pave the way towards a significant improvement of our understanding of the key mechanisms in atherogenesis.

Chapter 6 describes the development of an easy-to-prepare, low cost and fully customizable artery model based on biomaterials. Here, thermoresponsive sacrificial scaffolds, processed with the technique of MEW were used for the creation of variable, biomimetic shapes to mimic the geometric properties of the aortic arch, consisting of both, bifurcations and curvatures. After embedding the sacrificial scaffold into a gelatin-hydrogel containing SMCs, it was crosslinked with bacterial transglutaminase before dissolution and flushing of the sacrificial scaffold. The hereby generated channel was subsequently seeded with ECs, resulting in an easy-to-prepare, fast and low-cost artery model. In contrast to the native artery model, this model is therefore more variable in size and shape and offers the possibility to include smooth muscle cells from the beginning. Moreover, a custom-built and highly adaptable perfusion chamber was designed specifically for the scaffold structure, which enabled a one-step creation and simultaneously offering the possibility for dynamic cultivation of the artery models, making it an excellent basis for the development of *in vitro* disease test systems for e.g., flow-related atherosclerosis research. Due to time constraints, the extension to an atherosclerosis model could not be achieved within the scope of this thesis. Therefore, future studies will focus on the development and validation of an *in vitro* atherosclerosis model based on the proposed bi- and three-layered artery models.

In conclusion, this thesis paved the way for a fast acquisition and detailed analyses of changing hemodynamics during atherosclerosis development and progression, including spatially resolved analyses of all relevant hemodynamic parameters over time and in between different groups. Moreover, to reduce animal experiments, while gaining control over various parameters influencing atherosclerosis development, promising artery models were established, which have the potential to serve as a new platform for basic atherosclerosis research.

7.2 ZUSAMMENFASSUNG UND AUSBLICK

Im Rahmen dieser Arbeit wurden drei Hauptansätze zur Bewertung und Untersuchung der veränderten Hämodynamik wie Wandschubspannung, des oszillatorischen Scherindex und der arteriellen Pulswellengeschwindigkeit bei der Entwicklung und Progression der Atherosklerose durchgeführt:

1. Die Etablierung einer schnellen Methode zur gleichzeitigen Bestimmung der 3D-Wandschubspannung und der Pulswellengeschwindigkeit im gesamten Aortenbogen der Maus mittels hochauflösender 4D-Fluss-MRT
2. Die Verwendung von seriellen *in vivo* Messungen in atherosklerotischen Mausmodellen mittels hochauflösender 4D-Fluss-MRT, die in Studien zur Beschreibung der veränderten Hämodynamik bei später und früher Atherosklerose aufgeteilt wurden
3. Die Entwicklung von tissue-engineerten Arterienmodellen für die kontrollierte Anwendung und Variation von hämodynamischen und biologischen Parametern, unterteilt in native Arterienmodelle und biofabrizierte Arterienmodelle, mit dem Ziel, die Beziehung zwischen Atherogenese und veränderter Hämodynamik zu untersuchen

Kapitel 2 beschreibt die Etablierung einer Methode zur gleichzeitigen Messung von 3D-Wandschubspannung und Pulswellengeschwindigkeit im Aortenbogen der Maus unter Verwendung der Ultrahochfeld-MRT bei 17,6T [16], die auf der zuvor veröffentlichten Methode zur schnellen, selbstnavigierten Messung der Wandschubspannung im Aortenbogen der Maus unter Verwendung der radialen 4D-Phasenkontrast-MRT bei 17,6T [4] basiert. Dieses Projekt basiert auf der gemeinsamen Arbeit von Dr. Patrick Winter, der diese Methode entwickelt hat, und der Autorin dieser Thesis, Kristina Andelovic, die die Experimente und statistischen Analysen durchgeführt hat. Da die in diesem Kapitel beschriebene Methode die Grundlage für die folgenden *in vivo* Studien darstellt und sich nicht in die einzelnen Beiträge der Autoren aufteilen lässt, ohne dass wichtige Informationen verloren gehen, wurde dieses Kapitel nicht in die einzelnen Teile aufgeteilt, um grundlegende Informationen über die Mess- und Analysemethoden zu liefern und somit eine bessere Verständlichkeit für die folgenden Studien zu gewährleisten. Die größte Herausforderung in diesem Kapitel bestand darin, die Anforderung an eine hohe räumliche Auflösung zur Bestimmung der Geschwindigkeitsgradienten an der Gefäßwand für die WSS-Quantifizierung und an eine hohe zeitliche Auflösung für die Bestimmung der Pulswellengeschwindigkeit zu erfüllen, ohne die Messzeit aufgrund der Notwendigkeit von zwei separaten Messungen zu verlängern. Darüber hinaus ist für eine vollständige Erfassung der Hämodynamik im murinen Aortenbogen eine vollständige 3D-Messung des Aortenbogens erforderlich, die durch die Nutzung der retrospektiven Navigation und radialen Trajektorien erreicht wurde.

Dies wurde durch ein hoch flexibles Rekonstruktionssystem ermöglicht, das entweder Bilder mit geringerer räumlicher Auflösung und höheren Bildraten für die Erfassung der Pulswellengeschwindigkeit oder mit höherer räumlicher Auflösung und niedrigeren Bildraten für die Erfassung der 3D-WSS in einer angemessenen Messzeit von nur 35 Minuten rekonstruieren konnte. Die *in vivo*-Bestimmung aller relevanter hämodynamischen Parameter, die mit der Entwicklung und dem Fortschreiten der Atherosklerose zusammenhängen, wurde somit in einer einzigen experimentellen Sitzung ermöglicht.

Die Methode wurde an gesunden Wildtyp- und atherosklerotischen *Apoe*$^{-/-}$ Mäusen validiert, wobei keine Unterschiede in der Robustheit der Messungen zwischen pathologischen und gesunden Mäusen festgestellt werden konnten.

Die heterogene Verteilung der Plaqueentwicklung und Arterienversteifung in der Atherosklerose [10, 12] weist jedoch auf die Wichtigkeit lokaler PWV-Messungen hin. Zukünftige Studien sollten sich daher auf die 3D-Erfassung der lokalen PWV im murinen Aortenbogen auf Grundlage der vorgestellten Methode konzentrieren, um räumlich aufgelöste Korrelationen der lokalen arteriellen Steifigkeit mit anderen hämodynamischen Parametern und der Plaquezusammensetzung zu ermöglichen.

In **Kapitel 3** wurden die zuvor etablierten Methoden zur Untersuchung der sich verändernden Hämodynamik in der Aorta während des Alterns und der Atherosklerose bei gesunden Wildtyp- und atherosklerotischen *Apoe*$^{-/-}$ Mäusen verwendet [4, 16], die auf hochauflösender 4D-Fluss MRT basieren. In dieser Arbeit wurden serielle Messungen an gesunden und atherosklerotischen Mäusen durchgeführt, um alle Veränderungen der Hämodynamik im gesamten Aortenbogen über die Zeit zu verfolgen. Zudem wurden in dieser Arbeit räumlich aufgelöste 2D-Projektionskarten der WSS und des OSI des gesamten Aortenbogens generiert. Diese Methode ermöglichte die pixelweise statistische Analyse der Unterschiede und hämodynamischen Veränderungen zwischen und innerhalb von Gruppen im Zeitverlauf und die Visualisierung auf einen Blick. Die Studie ergab sich gegensätzlich entwickelnde lokale hämodynamische Profile bei gesunden WT- und atherosklerotischen *Apoe*$^{-/-}$ Mäusen, wobei die longWSS über die Zeit abnahm und der OSI zunahm, während die PWV bei gesunden Mäusen konstant blieb. Im Gegensatz nahm die longWSS zu und der OSI bei kranken Mäusen ab, während die PWV über die Zeit zunahm. Darüber hinaus wurden räumlich aufgelöste Korrelationen zwischen WSS, PWV, Plaque und Gefäßwandeigenschaften ermöglicht, die detaillierte Einblicke in die Zusammenhänge zwischen Hämodynamik und Plaquezusammensetzung in der Atherosklerose bieten. Dabei wurde die zirkumferentielle WSS als potenzieller Marker für die Plaquegröße und -zusammensetzung bei fortgeschrittener Atherosklerose identifiziert. Darüber hinaus ergaben Korrelationen mit der PWV, dass der maximale radiale Druck als potenzieller Marker für die vaskuläre Elastizität dienen könnte. Zusammengefasst demonstriert diese Studie die Nützlichkeit der hochauflösenden 4D-Fluss MRT zur räumlichen Auflösung, Visualisierung und Analyse statistischer Unterschiede in allen relevanten hämodynamischen Parametern im Zeitverlauf und zwischen gesunden und erkrankten Mäusen, was unser Verständnis der Plaqueprogression in Richtung Vulnerabilität erheblich verbessern könnte.

In zukünftigen Studien sollte jedoch der Zusammenhang zwischen Gefäßelastizität und radialem Druck weiter untersucht und mit lokalen PWV-Messungen und CFD validiert werden. Darüber hinaus spiegelten die histologischen 2D-Datensätze nicht die 3D-Eigenschaften und regionalen Charakteristika der atherosklerotischen Plaques wider. Daher sollten künftige Studien eine Analyse des 3D-Plaquevolumens und der 3D-Plaquenzusammensetzung sowie morphologische Messungen mittels MRT oder der Lichtblattmikroskopie mit einbeziehen, um das fundamentale Verständnis der Beziehung zwischen veränderter Hämodynamik und der Atherosklerose weiter zu verbessern.

In **Kapitel 4** ging es um die Beschreibung und Untersuchung der Hämodynamik in frühen Stadien der Atherosklerose. Darüber hinaus umfasste diese Studie zum ersten Mal Messungen der basalen

Hämodynamik in gesunden WT- und atherosklerotischen Mausmodellen. Aufgrund des Mangels an Studien, die die Hämodynamik in *Ldlr*$^{-/-}$ Mäusen beschreiben, die zusammen mit dem *Apoe*$^{-/-}$ Mausmodell die am häufigsten verwendeten Mausmodelle in der Atheroskleroseforschung sind, wurde dieses Modell in diese Studie integriert, um erstmals die sich verändernde Hämodynamik im Aortenbogen zu Beginn und während der Entwicklung und Progression der frühen Atherosklerose zu beschreiben. In dieser Studie wurden erstmals deutliche Unterschiede in den basalen Aortengeometrien dieser Mausmodelle identifiziert, die zu signifikant unterschiedlichen Fluss- und WSS-Profilen im *Ldlr*$^{-/-}$ Mausmodell führen. Eine weitere basale Charakterisierung verschiedener Parameter ergab nur modell-charakteristische Unterschiede in den Lipidprofilen, was beweist, dass die Geometrie die lokale WSS in diesen Modellen stark beeinflusst. Interessanterweise ergab die Berechnung des atherogenen Plasma-Indexes ein signifikant höheres Risiko bei *Ldlr*$^{-/-}$ Mäusen mit fortschreitender Atheroskleroseentwicklung, aber signifikant größere Plaqueflächen im Aortenbogen der *Apoe*$^{-/-}$ Mäuse.

Aufgrund des gegebenen basalen WSS- und OSI-Profils in diesen beiden Mausmodellen - zwei Parameter, die die Plaque-Entwicklung und -Progression stark beeinflussen - gibt es Hinweise darauf, dass sich die regionale Plaque-Entwicklung zwischen diesen Mausmodellen während der Atherogenese stark unterscheidet. Daher sollten sich künftige Studien auf die räumlich-zeitliche Bewertung der Plaqueentwicklung und -Zusammensetzung in den drei definierten Aortenregionen konzentrieren, wobei morphologische Messungen mittels MRT oder histologische 3D-Analysen wie LSFM zum Einsatz kommen. Darüber hinaus bietet diese Studie eine hervorragende Grundlage für künftige Studien mit CFD-Simulationen, in denen die verschiedenen gemessenen Parameterkombinationen (z. B. die Aortengeometrie der *Ldlr*$^{-/-}$Maus mit dem Lipidprofil der *Apoe*$^{-/-}$ Maus) analysiert und die daraus resultierende Plaqueentwicklung und -Zusammensetzung simuliert werden. Dies könnte zum Verständnis des komplexen Zusammenspiels zwischen veränderter Hämodynamik, Serumlipiden und Atherosklerose beitragen und unser grundlegendes Verständnis der Schlüsselfaktoren für die Entstehung von Atherosklerose deutlich verbessern.

In **Kapitel 5** wird die Etablierung eines tissue-engineerten Arterienmodells beschrieben, das auf nativen, von Schweinehalsschlagadern hergestellten, dezellularisierten Gerüststrukturen basiert. Diese wurden zudem in einem MRT-geeigneten Bioreaktorsystem [23] kultiviert, um die hämodynamisch bedingte Atheroskleroseentwicklung auf kontrollierbare Weise zu untersuchen, wobei hierfür die zuvor etablierten Methoden zur WSS- und PWV-Bewertung [4, 16] verwendet wurden. Dieses *in vitro* Arterienmodell zielte auf die Reduzierung von Tierversuchen ab und bot gleichzeitig eine vereinfachte, aber vollständig kontrollierbare physikalische und biologische Umgebung. Zu diesem Zweck wurde in einem ersten Schritt ein sehr schnelles und schonendes Dezellularisierungsverfahren etabliert, das zu Gerüststrukturen basierend auf Schweinehalsschlagadern führte, die eine vollständige Azellularität aufwiesen, wobei gleichzeitig die Zusammensetzung der extrazellulären Matrix, die allgemeine Ultrastruktur und die mechanischen Eigenschaften der nativen Arterien erhalten blieben. Darüber hinaus wurde eine gute Zelladhäsion und -proliferation erreicht, die mit isolierten menschlichen Endothelzellen aus humanem Vollblut untersucht wurde. Darüber hinaus wurde zum ersten Mal eine MRT-geeignete Arterienkammer für die gleichzeitige Kultivierung der generierten Modelle und der Untersuchung der hochauflösenden 4D-Hämodynamik in diesen Arterienmodellen entwickelt. Unter

Verwendung der hochauflösenden 4D-Fluss-MRT erwies sich das Bioreaktorsystem als sehr geeignet, den Volumenstrom, die beiden Komponenten der WSS inklusive dem radialen Druck und die PWV in den Arterienmodellen zu quantifizieren, wobei die erhaltenen Werte sehr gut mit den in der Literatur gefundenen Werten für *in vivo*-Messungen vergleichbar sind. Darüber hinaus lassen sich durch die dreidimensionale Untersuchung der Gefäßwandmorphologie in den *in vitro*-Modellen erste atherosklerotische Prozesse wie die Verdickung der Intima erkennen. Eine Einschränkung ist jedoch das Fehlen einer medialen glatten Muskelzellschicht aufgrund der dichten ECM des Gewebegerüsts. Die Verwendung der Laserschneidetechnik zur Erzeugung von Löchern und / oder Gruben im Mikrometerbereich, die eine Besiedlung des Mediums mit SMCs ermöglichen, zeigte in einem ersten Versuch vielversprechende Ergebnisse und sollte in zukünftigen Studien daher dringend weiter untersucht werden. Das präsentierte Arterienmodell verfügt somit über alle relevanten Komponenten für die Erweiterung zu einem Atherosklerosemodell und ebnet den Weg für ein deutlich besseres Verständnis der Schlüsselmechanismen in der Atherogenese.

Kapitel 6 beschreibt die Entwicklung eines einfach herzustellenden, kostengünstigen und vollständig an gegebene Bedürfnisse anpassbaren Arterienmodells auf Grundlage von Biomaterialien. Hier wurden thermoresponsive Opfergerüststrukturen, die mit der MEW-Technik hergestellt wurden, zur Herstellung variabler, biomimetischer Formen verwendet, um die geometrischen Eigenschaften des Aortenbogens, bestehend aus Verzweigungen und Krümmungen, zu imitieren. Nach der Einbettung der Opfergerüststruktur in ein Gelatin-Hydrogel, das zudem SMCs enthält, wurde es mit bakterieller Transglutaminase vernetzt, bevor es aufgelöst und gespült wurde. Der so entstandene Hydrogelkanal wurde anschließend mit Endothelzellen besiedelt, wodurch ein einfach zu erstellendes, schnelles und kostengünstiges Arterienmodell entstand. Im Gegensatz zum nativen Arterienmodell ist dieses Modell daher deutlich variabler in Größe und Form und bietet die wichtige Möglichkeit, von Anfang an glatte Muskelzellen mit einzubringen. Darüber hinaus wurde speziell für die gegebene Gerüststruktur eine maßgeschneiderte und hochgradig anpassungsfähige Perfusionskammer entwickelt, die eine sehr schnelle und einstufige Herstellung des Arterienmodells ermöglicht und gleichzeitig die Möglichkeit zur dynamischen Kultivierung der Modelle bietet, was eine hervorragende Grundlage für die Entwicklung von *in vitro* Krankheits-Testsystemen für z.B. die Atheroskleroseforschung im Zusammenhang mit der Hämodynamik darstellt. Aus Zeitgründen konnte die Ausweitung auf ein Atherosklerosemodell jedoch im Rahmen dieser Arbeit nicht realisiert werden. Daher werden sich zukünftige Studien auf die Entwicklung und Validierung eines *in vitro*-Atherosklerosemodells konzentrieren, das auf den hier entwickelten zwei- und dreischichtigen Arterienmodellen basiert.

Zusammenfassend lässt sich sagen, dass diese Arbeit den Weg für eine schnelle Erfassung und detaillierte Analyse der sich verändernden Hämodynamik während der Entwicklung und der Progression der Atherosklerose geebnet hat, einschließlich räumlich aufgelöster Analysen aller relevanten hämodynamischen Parameter im Zeitverlauf innerhalb einer Gruppe und zwischen verschiedenen Gruppen. Darüber hinaus wurden vielversprechende Arterienmodelle etabliert, die das Potenzial haben, als neue Plattform für die Atherosklerose-Grundlagenforschung zu dienen, um Tierversuche zu minimieren und gleichzeitig die Kontrolle über verschiedene Parameter zu erlangen, die die Atheroskleroseentwicklung beeinflussen.

REFERENCES

1. (WHO), W.H.O. *Cardiovascular diseases (CVDs) - Fact Sheet 2021*. 2021 11.06.2021; Available from: https://www.who.int/news-room/fact-sheets/detail/cardiovascular-diseases-(cvds), accessed 01.12.2021.

2. Harloff, A., et al., *In vivo assessment of wall shear stress in the atherosclerotic aorta using flow-sensitive 4D MRI.* Magn Reson Med, 2010. **63**(6): p. 1529-36.

3. Andelovic, K., et al., *Evaluation of Plaque Characteristics and Inflammation Using Magnetic Resonance Imaging.* Biomedicines, 2021. **9**(2).

4. Winter, P., et al., *Fast self-navigated wall shear stress measurements in the murine aortic arch using radial 4D-phase contrast cardiovascular magnetic resonance at 17.6 T.* J Cardiovasc Magn Reson, 2019. **21**(1): p. 64.

5. Andelovic, K., et al., *2D Projection Maps of WSS and OSI Reveal Distinct Spatiotemporal Changes in Hemodynamics in the Murine Aorta during Ageing and Atherosclerosis.* Biomedicines, 2021. **9**(12): p. 1856.

6. Wentland, A.L., et al., *Measurements of wall shear stress and aortic pulse wave velocity in swine with familial hypercholesterolemia.* J Magn Reson Imaging, 2015. **41**(5): p. 1475-85.

7. Zhao, X., R. Pratt, and J. Wansapura, *Quantification of aortic compliance in mice using radial phase contrast MRI.* J Magn Reson Imaging, 2009. **30**(2): p. 286-91.

8. Janiczek, R.L., et al., *Three-Dimensional Phase Contrast Angiography of the Mouse Aortic Arch Using Spiral MRI.* Magnetic Resonance in Medicine, 2011. **66**(5): p. 1382-1390.

9. Gotschy, A., et al., *Local arterial stiffening assessed by MRI precedes atherosclerotic plaque formation.* Circ Cardiovasc Imaging, 2013. **6**(6): p. 916-23.

10. Gotschy, A., et al., *Local versus global aortic pulse wave velocity in early atherosclerosis: An animal study in ApoE-/--mice using ultrahigh field MRI.* PLoS One, 2017. **12**(2): p. e0171603.

11. Herold, V., et al., *In vivo measurement of local aortic pulse-wave velocity in mice with MR microscopy at 17.6 Tesla.* Magn Reson Med, 2009. **61**(6): p. 1293-9.

12. Herold, V., et al., *Assessment of local pulse wave velocity distribution in mice using k-t BLAST PC-CMR with semi-automatic area segmentation.* J Cardiovasc Magn Reson, 2017. **19**(1): p. 77.

13. Parczyk, M., et al., *Regional in vivo transit time measurements of aortic pulse wave velocity in mice with high-field CMR at 17.6 Tesla.* J Cardiovasc Magn Reson, 2010. **12**: p. 72.

14. Wentland, A.L., et al., *Aortic pulse wave velocity measurements with undersampled 4D flow-sensitive MRI: comparison with 2D and algorithm determination.* Journal of Magnetic Resonance Imaging, 2013. **37**(4): p. 853-859.

15. Winter, P., et al., *Fast retrospectively triggered local pulse-wave velocity measurements in mice with CMR-microscopy using a radial trajectory.* J Cardiovasc Magn Reson, 2013. **15**: p. 88.

16. Winter, P., et al., *Simultaneous measurements of 3D wall shear stress and pulse wave velocity in the murine aortic arch.* J Cardiovasc Magn Reson, 2021. **23**(1): p. 34.

17. Feintuch, A., et al., *Hemodynamics in the mouse aortic arch as assessed by MRI, ultrasound, and numerical modeling.* American Journal of Physiology-Heart and Circulatory Physiology, 2007. **292**(2): p. H884-H892.

18. Van Doormaal, M.A., et al., *Haemodynamics in the mouse aortic arch computed from MRI-derived velocities at the aortic root.* Journal of the Royal Society Interface, 2012. **9**(76): p. 2834-2844.

19. Choudhury, S., K. Anupindi, and B.S.V. Patnaik, *Influence of wall shear stress and geometry on the lumen surface concentration of low density lipoprotein in a model abdominal aortic aneurysm.* 2019. **31**(1): p. 011901.

20. Bosch, L., et al., *The transverse aortic constriction heart failure animal model: a systematic review and meta-analysis.* Heart Failure Reviews, 2020.

21. Kuhlmann, M.T., et al., *Implantation of a carotid cuff for triggering shear-stress induced atherosclerosis in mice.* Journal of visualized experiments : JoVE, 2012(59): p. 3308.

22. Luong, L., et al., *Heart rate reduction with ivabradine promotes shear stress-dependent anti-inflammatory mechanisms in arteries.* Thromb Haemost, 2016. **116**(1): p. 181-90.

23. Schuerlein, S., et al., *A versatile modular bioreactor platform for Tissue Engineering.* Biotechnol J, 2017. **12**(2).

24. Crapo, P.M., T.W. Gilbert, and S.F. Badylak, *An overview of tissue and whole organ decellularization processes.* Biomaterials, 2011. **32**(12): p. 3233-43.

25. Gilbert, T.W., T.L. Sellaro, and S.F. Badylak, *Decellularization of tissues and organs.* Biomaterials, 2006. **27**(19): p. 3675-83.

26. Mendibil, U., et al., *Tissue-Specific Decellularization Methods: Rationale and Strategies to Achieve Regenerative Compounds.* Int J Mol Sci, 2020. **21**(15).

27. Massaro, M.S., et al., *Decellularized xenogeneic scaffolds in transplantation and tissue engineering: Immunogenicity versus positive cell stimulation.* Materials Science and Engineering: C, 2021. **127**: p. 112203.

28. Linton, M.F., et al., *The Role of Lipids and Lipoproteins in Atherosclerosis*, in *Endotext*, K.R. Feingold, et al., Editors. 2000, MDText.com, Inc.Copyright © 2000-2021, MDText.com, Inc.: South Dartmouth (MA).

29. Mundi, S., et al., *Endothelial permeability, LDL deposition, and cardiovascular risk factors-a review.* Cardiovascular research, 2018. **114**(1): p. 35-52.

30. Goldstein, J.L. and M.S. Brown, *The low-density lipoprotein pathway and its relation to atherosclerosis.* Annu Rev Biochem, 1977. **46**: p. 897-930.

31. Mahmood, S.S., et al., *The Framingham Heart Study and the epidemiology of cardiovascular disease: a historical perspective.* Lancet (London, England), 2014. **383**(9921): p. 999-1008.

32. Cunningham, K.S. and A.I. Gotlieb, *The role of shear stress in the pathogenesis of atherosclerosis.* Nature: Laboratory Investigation, 2004. **85**: p. 9-23.

33. Ungvari, Z., M.S. Wolin, and A. Csiszar, *Mechanosensitive production of reactive oxygen species in endothelial and smooth muscle cells: role in microvascular remodeling?* Antioxid Redox Signal, 2006. **8**(7-8): p. 1121-9.

34. Huang, L., et al., *SR-B1 drives endothelial cell LDL transcytosis via DOCK4 to promote atherosclerosis.* Nature, 2019. **569**(7757): p. 565-569.

35. Glass, C.K. and J.L. Witztum, *Atherosclerosis: The Road Ahead.* Cell, 2001. **104**(4): p. 503-516.

36. Galkina, E. and K. Ley, *Vascular adhesion molecules in atherosclerosis.* Arterioscler Thromb Vasc Biol, 2007. **27**(11): p. 2292-301.

37. Gisterå, A. and G.K. Hansson, *The immunology of atherosclerosis.* Nature Reviews Nephrology, 2017. **13**(6): p. 368-380.

38. Doran, A.C., N. Meller, and C.A. McNamara, *Role of Smooth Muscle Cells in the Initiation and Early Progression of Atherosclerosis.* Arteriosclerosis, Thrombosis, and Vascular Biology, 2008. **28**(5): p. 812-819.

39. Getz, G.S. and C.A. Reardon, *Use of Mouse Models in Atherosclerosis Research.* Methods Mol Biol, 2015. **1339**: p. 1-16.

40. Swirski, F.K., et al., *Ly-6Chi monocytes dominate hypercholesterolemia-associated monocytosis and give rise to macrophages in atheromata.* J Clin Invest, 2007. **117**(1): p. 195-205.

41. Mills, C.D., et al., *M-1/M-2 macrophages and the Th1/Th2 paradigm.* J Immunol, 2000. **164**(12): p. 6166-73.

42. Chinetti-Gbaguidi, G., et al., *Human atherosclerotic plaque alternative macrophages display low cholesterol handling but high phagocytosis because of distinct activities of the PPARγ and LXRα pathways.* Circ Res, 2011. **108**(8): p. 985-95.

43. Bennett, M.R., S. Sinha, and G.K. Owens, *Vascular Smooth Muscle Cells in Atherosclerosis.* Circulation research, 2016. **118**(4): p. 692-702.

44. Feil, S., et al., *Transdifferentiation of vascular smooth muscle cells to macrophage-like cells during atherogenesis.* Circ Res, 2014. **115**(7): p. 662-7.

45. Allahverdian, S., et al., *Contribution of intimal smooth muscle cells to cholesterol accumulation and macrophage-like cells in human atherosclerosis.* Circulation, 2014. **129**(15): p. 1551-9.

46. Korshunov, V.A., S.M. Schwartz, and B.C. Berk, *Vascular Remodeling.* Arteriosclerosis, Thrombosis, and Vascular Biology, 2007. **27**(8): p. 1722-1728.

47. Basatemur, G.L., et al., *Vascular smooth muscle cells in atherosclerosis.* Nature Reviews Cardiology, 2019. **16**(12): p. 727-744.

48. Fahed, A.C. and I.-K. Jang, *Plaque erosion and acute coronary syndromes: phenotype, molecular characteristics and future directions.* Nature Reviews Cardiology, 2021. **18**(10): p. 724-734.

49. Zhang, S.H., et al., *Spontaneous hypercholesterolemia and arterial lesions in mice lacking apolipoprotein E.* Science, 1992. **258**(5081): p. 468-71.

50. Plump, A.S., et al., *Severe hypercholesterolemia and atherosclerosis in apolipoprotein E-deficient mice created by homologous recombination in ES cells.* Cell, 1992. **71**(2): p. 343-53.

51. Ishibashi, S., et al., *Hypercholesterolemia in low density lipoprotein receptor knockout mice and its reversal by adenovirus-mediated gene delivery.* J Clin Invest, 1993. **92**(2): p. 883-93.

52. De Wilde, D., et al., *Vulnerable plaque detection and quantification with gold particle-enhanced computed tomography in atherosclerotic mouse models.* Mol Imaging, 2015. **14**.

53. Meir, K.S. and E. Leitersdorf, *Atherosclerosis in the Apolipoprotein E–Deficient Mouse.* 2004. **24**(6): p. 1006-1014.

54. Emini Veseli, B., et al., *Animal models of atherosclerosis.* Eur J Pharmacol, 2017. **816**: p. 3-13.

55. Getz, G.S. and C.A. Reardon, *Animal Models of Atherosclerosis.* 2012. **32**(5): p. 1104-1115.

56. Nakashima, Y., et al., *ApoE-deficient mice develop lesions of all phases of atherosclerosis throughout the arterial tree.* Arterioscler Thromb, 1994. **14**(1): p. 133-40.

57. Getz, G.S. and C.A. Reardon, *Apoprotein E as a lipid transport and signaling protein in the blood, liver, and artery wall.* J Lipid Res, 2009. **50 Suppl**(Suppl): p. S156-61.

58. Poznyak, A.V., et al., *Animal models of human atherosclerosis: current progress.* Brazilian journal of medical and biological research = Revista brasileira de pesquisas medicas e biologicas, 2020. **53**(6): p. e9557-e9557.

59. Getz, G.S. and C.A. Reardon, *Do the Apoe-/- and Ldlr-/- Mice Yield the Same Insight on Atherogenesis?* Arteriosclerosis, thrombosis, and vascular biology, 2016. **36**(9): p. 1734-1741.

60. Stalder, A.F., et al., *Quantitative 2D and 3D Phase Contrast MRI: Optimized Analysis of Blood Flow and Vessel Wall Parameters.* Magnetic Resonance in Medicine, 2008. **60**(5): p. 1218-1231.

61. Cho, Y.I., D.J. Cho, and R.S. Rosenson, *Endothelial shear stress and blood viscosity in peripheral arterial disease.* Curr Atheroscler Rep, 2014. **16**(4): p. 404.

62. Hoogendoorn, A., et al., *Multidirectional wall shear stress promotes advanced coronary plaque development: comparing five shear stress metrics.* Cardiovasc Res, 2020. **116**(6): p. 1136-1146.

63. Evans, P.C., et al., *Shear stress: the dark energy of atherosclerotic plaques.* Cardiovascular Research, 2020.

64. Frydrychowicz, A., et al., *Three-dimensional analysis of segmental wall shear stress in the aorta by flow-sensitive four-dimensional-MRI.* Journal of Magnetic Resonance Imaging, 2009. **30**(1): p. 77-84.

65. Chatzizisis, Y.S., et al., *Role of endothelial shear stress in the natural history of coronary atherosclerosis and vascular remodeling: molecular, cellular, and vascular behavior.* J Am Coll Cardiol, 2007. **49**(25): p. 2379-93.

66. Pedrigi, R.M., et al., *Thin-cap fibroatheroma rupture is associated with a fine interplay of shear and wall stress.* Arterioscler Thromb Vasc Biol, 2014. **34**(10): p. 2224-31.

67. Thondapu, V., et al., *Biomechanical stress in coronary atherosclerosis: emerging insights from computational modelling.* Eur Heart J, 2017. **38**(2): p. 81-92.

68. Kadam, A.A., et al., *Inflammatory monocyte response due to altered wall shear stress in an isolated femoral artery model.* J Biol Methods, 2019. **6**(1): p. e109.

69. Gijsen, F., et al., *Expert recommendations on the assessment of wall shear stress in human coronary arteries: existing methodologies, technical considerations, and clinical applications.* Eur Heart J, 2019. **40**(41): p. 3421-3433.

70. Cheng, C., et al., *Atherosclerotic lesion size and vulnerability are determined by patterns of fluid shear stress.* Circulation, 2006. **113**(23): p. 2744-53.

71. Cheng, C., et al., *Shear stress-induced changes in atherosclerotic plaque composition are modulated by chemokines.* J Clin Invest, 2007. **117**(3): p. 616-26.

72. Pedrigi, R.M., et al., *Influence of shear stress magnitude and direction on atherosclerotic plaque composition.* R Soc Open Sci, 2016. **3**(10): p. 160588.

73. Xing, R., et al., *Temporal and spatial changes in wall shear stress during atherosclerotic plaque progression in mice.* R Soc Open Sci, 2018. **5**(3): p. 171447.

74. Seneviratne, A.N., et al., *Low shear stress induces M1 macrophage polarization in murine thin-cap atherosclerotic plaques.* J Mol Cell Cardiol, 2015. **89**(Pt B): p. 168-72.

75. Seifert, R., et al., *Molecular imaging of MMP activity discriminates unstable from stable plaque phenotypes in shear-stress induced murine atherosclerosis.* PLoS One, 2018. **13**(10): p. e0204305.

76. Matlung, H.L., et al., *Transglutaminase activity regulates atherosclerotic plaque composition at locations exposed to oscillatory shear stress.* Atherosclerosis, 2012. **224**(2): p. 355-62.

77. Haga, M., et al., *Oscillatory shear stress increases smooth muscle cell proliferation and Akt phosphorylation.* J Vasc Surg, 2003. **37**(6): p. 1277-84.

78. Kim, S.A., et al., *Laminar shear stress suppresses vascular smooth muscle cell proliferation through nitric oxide-AMPK pathway.* Biochem Biophys Res Commun, 2017. **490**(4): p. 1369-1374.

79. Xu, J., et al., *Oscillatory Shear Stress Induces Endothelial Dysfunction through the Activation of P2Y12.* Molecular & Cellular Biomechanics, 2019. **16**: p. 142.

80. Hsu, P.-L., et al., *Shear-Induced CCN1 Promotes Atheroprone Endothelial Phenotypes and Atherosclerosis.* Circulation, 2019. **139**(25): p. 2877-2891.

81. Sun, Z., et al., *Activation of GPR81 by lactate inhibits oscillatory shear stress-induced endothelial inflammation by activating the expression of KLF2.* IUBMB Life, 2019. **71**(12): p. 2010-2019.

82. Wang, Z., et al., *Oscillatory Shear Stress Induces Oxidative Stress via TLR4 Activation in Endothelial Cells.* Mediators of Inflammation, 2019. **2019**: p. 7162976.

83. van Hoof, R.H.M., et al., *Heart rate lowering treatment leads to a reduction in vulnerable plaque features in atherosclerotic rabbits.* PLOS ONE, 2017. **12**(6): p. e0179024.

84. Alfaidi, M.A., et al., *Dietary Docosahexaenoic Acid Reduces Oscillatory Wall Shear Stress, Atherosclerosis, and Hypertension, Most Likely Mediated via an IL-1-Mediated Mechanism.* J Am Heart Assoc, 2018. **7**(13).

85. Brunner, G., et al., *Associations Between Carotid Artery Plaque Burden, Plaque Characteristics, and Cardiovascular Events: The ARIC Carotid Magnetic Resonance Imaging Study.* JAMA Cardiol, 2020.

86. Leistner, D.M., et al., *Differential immunological signature at the culprit site distinguishes acute coronary syndrome with intact from acute coronary syndrome with ruptured fibrous cap: results from the prospective translational OPTICO-ACS study.* Eur Heart J, 2020. **41**(37): p. 3549-3560.

87. Cicha, I., et al., *Carotid plaque vulnerability: a positive feedback between hemodynamic and biochemical mechanisms.* Stroke, 2011. **42**(12): p. 3502-10.

88. de Weert, T.T., et al., *Atherosclerotic plaque surface morphology in the carotid bifurcation assessed with multidetector computed tomography angiography.* Stroke, 2009. **40**(4): p. 1334-40.

89. Murata, N., et al., *High shear stress on the coronary arterial wall is related to computed tomography-derived high-risk plaque: a three-dimensional computed tomography and color-coded tissue-characterizing intravascular ultrasonography study.* Heart and Vessels, 2019. **34**(9): p. 1429-1439.

90. Wang, Y., et al., *High shear stress induces atherosclerotic vulnerable plaque formation through angiogenesis.* Regenerative biomaterials, 2016. **3**(4): p. 257-267.

91. Fukumoto, Y., et al., *Localized elevation of shear stress is related to coronary plaque rupture: a 3-dimensional intravascular ultrasound study with in-vivo color mapping of shear stress distribution.* J Am Coll Cardiol, 2008. **51**(6): p. 645-50.

92. Kojima, K., et al., *High Wall Shear Stress Is Related to Atherosclerotic Plaque Rupture in the Aortic Arch of Patients with Cardiovascular Disease: A Study with Computational Fluid Dynamics Model and Non-Obstructive General Angioscopy.* Journal of Atherosclerosis and Thrombosis, 2020. **advpub**.

93. Han, D., et al., *Relationship Between Endothelial Wall Shear Stress and High-Risk Atherosclerotic Plaque Characteristics for Identification of Coronary Lesions That Cause Ischemia: A Direct Comparison With Fractional Flow Reserve.* J Am Heart Assoc, 2016. **5**(12).

94. Thondapu, V., et al., *High Spatial Endothelial Shear Stress Gradient Independently Predicts Site of Acute Coronary Plaque Rupture and Erosion.* Cardiovasc Res, 2020.

95. Stone, P.H., et al., *Role of Low Endothelial Shear Stress and Plaque Characteristics in the Prediction of Nonculprit Major Adverse Cardiac Events.* JACC: Cardiovascular Imaging, 2018. **11**(3): p. 462-471.

96. Chatzizisis, Y.S., et al., *Association of global and local low endothelial shear stress with high-risk plaque using intracoronary 3D optical coherence tomography: Introduction of 'shear stress score'.* European Heart Journal - Cardiovascular Imaging, 2016. **18**(8): p. 888-897.

97. Vergallo, R., et al., *Endothelial shear stress and coronary plaque characteristics in humans: combined frequency-domain optical coherence tomography and computational fluid dynamics study.* Circ Cardiovasc Imaging, 2014. **7**(6): p. 905-11.

98. Eshtehardi, P., et al., *Association of coronary wall shear stress with atherosclerotic plaque burden, composition, and distribution in patients with coronary artery disease.* J Am Heart Assoc, 2012. **1**(4): p. e002543.

99. Papafaklis, M.I., et al., *Effect of the local hemodynamic environment on the de novo development and progression of eccentric coronary atherosclerosis in humans: insights from PREDICTION.* Atherosclerosis, 2015. **240**(1): p. 205-11.

100. Timmins, L.H., et al., *Oscillatory wall shear stress is a dominant flow characteristic affecting lesion progression patterns and plaque vulnerability in patients with coronary artery disease.* J R Soc Interface, 2017. **14**(127).

101. Chatzizisis, Y.S., et al., *Prediction of the localization of high-risk coronary atherosclerotic plaques on the basis of low endothelial shear stress: an intravascular ultrasound and histopathology natural history study.* Circulation, 2008. **117**(8): p. 993-1002.

102. Koskinas, K.C., et al., *Thin-capped atheromata with reduced collagen content in pigs develop in coronary arterial regions exposed to persistently low endothelial shear stress.* Arterioscler Thromb Vasc Biol, 2013. **33**(7): p. 1494-504.

103. Stone, P.H., et al., *Role of Low Endothelial Shear Stress and Plaque Characteristics in the Prediction of Nonculprit Major Adverse Cardiac Events: The PROSPECT Study.* JACC Cardiovasc Imaging, 2018. **11**(3): p. 462-471.

104. Moore, J.E., et al., *Fluid Wall Shear-Stress Measurements in a Model of the Human Abdominal-Aorta - Oscillatory Behavior and Relationship to Atherosclerosis.* Atherosclerosis, 1994. **110**(2): p. 225-240.

105. van Ooij, P., et al., *Characterization of Abnormal Wall Shear Stress Using 4D Flow MRI in Human Bicuspid Aortopathy.* Annals of Biomedical Engineering, 2015. **43**(6): p. 1385-1397.

106. Szajer, J. and K. Ho-Shon, *A comparison of 4D flow MRI-derived wall shear stress with computational fluid dynamics methods for intracranial aneurysms and carotid bifurcations - A review.* Magnetic Resonance Imaging, 2018. **48**: p. 62-69.

107. Cibis, M., et al., *Relation between wall shear stress and carotid artery wall thickening MRI versus CFD.* Journal of Biomechanics, 2016. **49**(5): p. 735-741.

108. Peper, E.S., et al., *Highly accelerated 4D flow cardiovascular magnetic resonance using a pseudo-spiral Cartesian acquisition and compressed sensing reconstruction for carotid flow and wall shear stress.* J Cardiovasc Magn Reson, 2020. **22**(1): p. 7.

109. Greve, J.M., et al., *Allometric scaling of wall shear stress from mice to humans: quantification using cine phase-contrast MRI and computational fluid dynamics.* American Journal of Physiology-Heart and Circulatory Physiology, 2006. **291**(4): p. H1700-H1708.

110. Weinberg, P.D. and C.R. Ethier, *Twenty-fold difference in hemodynamic wall shear stress between murine and human aortas.* Journal of Biomechanics, 2007. **40**(7): p. 1594-1598.

111. Barakat, G.C.a.A.K.a.H.R.d.B.a.A., *Influence of pulsatile blood flow on allometry of aortic wall shear stress.* arXiv, 2018. **1802.03722**.

112. Molony, D., et al., *Bulk Flow and Near Wall Hemodynamics of the Rabbit Aortic Arch: A 4D PC-MRI Derived CFD Study.* J Biomech Eng, 2018.

113. Cibis, M., et al., *The Effect of Spatial and Temporal Resolution of Cine Phase Contrast MRI on Wall Shear Stress and Oscillatory Shear Index Assessment.* PLoS One, 2016. **11**(9): p. e0163316.

114. Karim, A., et al. *In Vivo MRI quantification of circumferential wall shear stress in atherosclerotic-prone mouse aorta*. in *2007 IEEE 33rd Annual Northeast Bioengineering Conference*. 2007.

115. van Bochove, G.S., et al., *MRI-determined carotid artery flow velocities and wall shear stress in a mouse model of vulnerable and stable atherosclerotic plaque.* MAGMA, 2010. **23**(2): p. 77-84.

116. Peng, S.L., et al., *Optimized analysis of blood flow and wall shear stress in the common carotid artery of rat model by phase-contrast MRI.* Sci Rep, 2017. **7**(1): p. 5253.

117. Crouch, A.C., et al., *In Vivo MRI Assessment of Blood Flow in Arteries and Veins from Head-to-Toe Across Age and Sex in C57BL/6 Mice.* Ann Biomed Eng, 2020. **48**(1): p. 329-341.

118. Braig, M., et al., *Preclinical 4D-flow magnetic resonance phase contrast imaging of the murine aortic arch.* PLOS ONE, 2017. **12**(11).

119. Braig, M., et al., *Analysis of accelerated 4D flow MRI in the murine aorta by radial acquisition and compressed sensing reconstruction.* NMR Biomed, 2020. **33**(11): p. e4394.

120. Hu, J.J., et al., *Biomechanics of the porcine basilar artery in hypertension.* Ann Biomed Eng, 2007. **35**(1): p. 19-29.

121. Grote, K., et al., *Mechanical stretch enhances mRNA expression and proenzyme release of matrix metalloproteinase-2 (MMP-2) via NAD(P)H oxidase-derived reactive oxygen species.* Circ Res, 2003. **92**(11): p. e80-6.

122. Rodriguez, A.I., et al., *MEF2B-Nox1 signaling is critical for stretch-induced phenotypic modulation of vascular smooth muscle cells.* Arterioscler Thromb Vasc Biol, 2015. **35**(2): p. 430-8.

123. Chesler, N.C., D.N. Ku, and Z.S. Galis, *Transmural pressure induces matrix-degrading activity in porcine arteries ex vivo.* Am J Physiol, 1999. **277**(5): p. H2002-9.

124. Maedeker, J.A., et al., *Hypertension and decreased aortic compliance due to reduced elastin amounts do not increase atherosclerotic plaque accumulation in Ldlr-/- mice.* Atherosclerosis, 2016. **249**: p. 22-9.

125. Liu, S.L., et al., *Cardiovascular protection in females linked to estrogen-dependent inhibition of arterial stiffening and macrophage MMP12.* JCI Insight, 2019. **4**(1).

126. van Popele, N.M., et al., *Association between arterial stiffness and atherosclerosis: the Rotterdam Study.* Stroke, 2001. **32**(2): p. 454-60.

127. Ohyama, Y., et al., *Aortic Arch Pulse Wave Velocity Assessed by Magnetic Resonance Imaging as a Predictor of Incident Cardiovascular Events: The MESA (Multi-Ethnic Study of Atherosclerosis).* Hypertension, 2017. **70**(3): p. 524-530.

128. Harbaoui, B., et al., *Development of Coronary Pulse Wave Velocity: New Pathophysiological Insight Into Coronary Artery Disease.* J Am Heart Assoc, 2017. **6**(2).

129. Korteweg, D.J., *Ueber die Fortpflanzungsgeschwindigkeit des Schalles in elastischen Röhren.* Annalen der Physik, 1878. **241**(12): p. 525-542.

130. Doupis, J., et al., *Pulse Wave Analysis by Applanation Tonometry for the Measurement of Arterial Stiffness.* Open Cardiovasc Med J, 2016. **10**: p. 188-95.

131. Apostolakis, I.Z., et al., *Adaptive Pulse Wave Imaging: Automated Spatial Vessel Wall Inhomogeneity Detection in Phantoms and in-Vivo.* IEEE Trans Med Imaging, 2020. **39**(1): p. 259-269.

132. Tang, C.J., et al., *Measurement of local pulse wave velocity for carotid artery by using an ultrasound-based method.* Ultrasonics, 2020. **102**.

133. Karageorgos, G.M., et al., *Arterial wall mechanical inhomogeneity detection and atherosclerotic plaque characterization using high frame rate pulse wave imaging in carotid artery disease patients in vivo.* Phys Med Biol, 2020. **65**(2): p. 025010.

134. Negoita, M., et al., *A method for determining local pulse wave velocity in human ascending aorta from sequential ultrasound measurements of diameter and velocity.* Physiol Meas, 2018. **39**(11): p. 114009.

135. Wang, Z., et al., *A novel methodology for rat aortic pulse wave velocity assessment by Doppler ultrasound: validation against invasive measurements.* Am J Physiol Heart Circ Physiol, 2019. **317**(6): p. H1376-H1387.

136. Di Lascio, N., et al., *Alterations in Carotid Parameters in Apoe-/- Mice Treated with a High-Fat Diet: A Micro-Ultrasound Analysis.* Ultrasound in Medicine and Biology, 2019. **45**(4): p. 980-988.

137. Leow, C.H. and M.X. Tang, *Spatio-Temporal Flow and Wall Shear Stress Mapping Based on Incoherent Ensemble-Correlation of Ultrafast Contrast Enhanced Ultrasound Images.* Ultrasound Med Biol, 2018. **44**(1): p. 134-152.

138. Xing, R., et al., *Contrast-enhanced micro-CT imaging in murine carotid arteries: a new protocol for computing wall shear stress.* Biomed Eng Online, 2016. **15**(Suppl 2): p. 156.

139. Lo Vercio, L., et al., *Assessment of image features for vessel wall segmentation in intravascular ultrasound images.* Int J Comput Assist Radiol Surg, 2016. **11**(8): p. 1397-407.

140. Wentland, A.L., T.M. Grist, and O. Wieben, *Review of MRI-based measurements of pulse wave velocity: a biomarker of arterial stiffness.* Cardiovascular Diagnosis and Therapy, 2014. **4**(2): p. 193-206.

141. Huang, C., et al., *Comparison of Different Pulse Waveforms for Local Pulse Wave Velocity Measurement in Healthy and Hypertensive Common Carotid Arteries in Vivo.* Ultrasound Med Biol, 2016. **42**(5): p. 1111-23.

142. Pereira, T., C. Correia, and J. Cardoso, *Novel Methods for Pulse Wave Velocity Measurement.* J Med Biol Eng, 2015. **35**(5): p. 555-565.

143. Zhu, Z.Q., et al., *Carotid stiffness and atherosclerotic risk: non-invasive quantification with ultrafast ultrasound pulse wave velocity.* European Radiology, 2019. **29**(3): p. 1507-1517.

144. Wang, Z., et al., *Noninvasive method for measuring local pulse wave velocity by dual pulse wave Doppler: in vitro and in vivo studies.* PLoS One, 2015. **10**(3): p. e0120482.

145. Di Lascio, N., et al., *Ultrasound-based Pulse Wave Velocity Evaluation in Mice.* Jove-Journal of Visualized Experiments, 2017(120).

146. Williams, R., et al., *Noninvasive ultrasonic measurement of regional and local pulse-wave velocity in mice.* Ultrasound in Medicine and Biology, 2007. **33**(9): p. 1368-1375.

147. Weir-McCall, J.R., et al., *Effects of inaccuracies in arterial path length measurement on differences in MRI and tonometry measured pulse wave velocity.* Bmc Cardiovascular Disorders, 2017. **17**.

148. Hrabak-Paar, M., et al., *Variability of MRI Aortic Stiffness Measurements in a Multicenter Clinical Trial Setting: Intraobserver, Interobserver, and Intracenter Variability of Pulse Wave Velocity and Aortic Strain Measurement.* 2020. **2**(2): p. e190090.

149. Mohiaddin, R.H. and D.B. Longmore, *Mri Studies of Atherosclerotic Vascular-Disease - Structural Evaluation and Physiological Measurements.* British Medical Bulletin, 1989. **45**(4): p. 968-990.

150. Kenyhercz, W.E., et al., *Quantification of aortic stiffness using magnetic resonance elastography: Measurement reproducibility, pulse wave velocity comparison, changes over cardiac cycle, and relationship with age.* Magn Reson Med, 2016. **75**(5): p. 1920-6.

151. Singh, A., et al., *Aortic stiffness in aortic stenosis assessed by cardiovascular MRI: a comparison between bicuspid and tricuspid valves.* European Radiology, 2019. **29**(5): p. 2340-2349.

152. Peper, E.S., et al., *Regional assessment of carotid artery pulse wave velocity using compressed sensing accelerated high temporal resolution 2D CINE phase contrast cardiovascular magnetic resonance.* J Cardiovasc Magn Reson, 2018. **20**(1): p. 86.

153. Roberts, P.A., et al., *Real-time aortic pulse wave velocity measurement during exercise stress testing.* Journal of Cardiovascular Magnetic Resonance, 2015. **17**.

154. Vulliémoz, S., N. Stergiopulos, and R. Meuli, *Estimation of Local Aortic Elastic Properties With MRI.* Magnetic Resonance in Medicine, 2002. **47**(47): p. 649-654.

155. Winter, P., et al., *Self-navigation under non-steady-state conditions: Cardiac and respiratory self-gating of inversion recovery snapshot FLASH acquisitions in mice.* Magn Reson Med, 2016. **76**(6): p. 1887-1894.

156. Markl, M., et al., *Estimation of Global Aortic Pulse Wave Velocity by Flow-Sensitive 4D MRI.* Magnetic Resonance in Medicine, 2010. **63**(6): p. 1575-1582.

157. Ruesink, T., et al., *In Vitro Validation of 4D Flow MRI for Local Pulse Wave Velocity Estimation.* Cardiovascular Engineering and Technology, 2018. **9**(4): p. 674-687.

158. Markl, M., et al., *Analysis of pulse wave velocity in the thoracic aorta by flow-sensitive four-dimensional MRI: Reproducibility and correlation with characteristics in patients with aortic atherosclerosis.* Journal of Magnetic Resonance Imaging, 2012. **35**(5): p. 1162-1168.

159. Houriez-Gombaud-Saintonge, S., et al., *Comparison of different methods for the estimation of aortic pulse wave velocity from 4D flow cardiovascular magnetic resonance.* J Cardiovasc Magn Reson, 2019. **21**(1): p. 75.

160. Juffermans, J.F., et al., *The effects of age at correction of aortic coarctation and recurrent obstruction on adolescent patients: MRI evaluation of wall shear stress and pulse wave velocity.* Eur Radiol Exp, 2019. **3**(1): p. 24.

161. Hope, M.D., T. Sedlic, and P. Dyverfeldt, *Cardiothoracic magnetic resonance flow imaging.* J Thorac Imaging, 2013. **28**(4): p. 217-30.

162. Winter, P., et al., *Simultaneous Measurements of 3D Wall Shear Stress and Pulse Wave Velocity in the Murine Aortic Arch.* J. Cardiovasc. Magn. Reson., 2021, doi: 10.1186/s12968-021-00725-4.

163. Palombo, C. and M. Kozakova, *Arterial stiffness, atherosclerosis and cardiovascular risk: Pathophysiologic mechanisms and emerging clinical indications.* Vascul Pharmacol, 2016. **77**: p. 1-7.

164. Millon, A., et al., *Low WSS Induces Intimal Thickening, while Large WSS Variation and Inflammation Induce Medial Thinning, in an Animal Model of Atherosclerosis.* PLOS ONE, 2015. **10**(11): p. e0141880.

165. Kohn, J.C., et al., *Cooperative effects of matrix stiffness and fluid shear stress on endothelial cell behavior.* Biophys J, 2015. **108**(3): p. 471-8.

166. Kim, C.W., et al., *Disturbed Flow Promotes Arterial Stiffening Through Thrombospondin-1.* Circulation, 2017. **136**(13): p. 1217-1232.

167. Diez, J., *Arterial stiffness and extracellular matrix.* Adv Cardiol, 2007. **44**: p. 76-95.

168. Jiang, Y., et al., *Ex-vivo imaging and plaque type classification of intracranial atherosclerotic plaque using high resolution MRI.* Atherosclerosis, 2016. **249**: p. 10-6.

169. Kuroiwa, Y., et al., *Coronary high-signal-intensity plaques on T1-weighted magnetic resonance imaging reflect intraplaque hemorrhage.* Cardiovasc Pathol, 2019. **40**: p. 24-31.

170. Truong, M., et al., *Classifications of atherosclerotic plaque components with T1 and T2* mapping in 11.7 T MRI.* European Journal of Radiology Open, 2021. **8**: p. 100323.

171. Harteveld, A.A., et al., *Quantitative Intracranial Atherosclerotic Plaque Characterization at 7T MRI: An Ex Vivo Study with Histologic Validation.* AJNR Am J Neuroradiol, 2016. **37**(5): p. 802-10.

172. Okuchi, S., et al., *Visualization of carotid vessel wall and atherosclerotic plaque: T1-SPACE vs. compressed sensing T1-SPACE.* Eur Radiol, 2019. **29**(8): p. 4114-4122.

173. Chai, J.T., et al., *Quantification of Lipid-Rich Core in Carotid Atherosclerosis Using Magnetic Resonance T(2) Mapping: Relation to Clinical Presentation.* JACC Cardiovasc Imaging, 2017. **10**(7): p. 747-756.

174. Alkhalil, M., et al., *T2 mapping MRI technique quantifies carotid plaque lipid, and its depletion after statin initiation, following acute myocardial infarction.* Atherosclerosis, 2018. **279**: p. 100-106.

175. Calcagno, C., et al., *Combined PET/DCE-MRI in a Rabbit Model of Atherosclerosis: Integrated Quantification of Plaque Inflammation, Permeability, and Burden During Treatment With a Leukotriene A4 Hydrolase Inhibitor.* JACC Cardiovasc Imaging, 2018. **11**(2 Pt 2): p. 291-301.

176. Hombach, V., Grebe, O. and Botnar, R.M. , *Kardiovaskuläre Magnetresonanztomografie.* Schattauer, Berlin, 2005.

177. Libby, P., et al., *Inflammation in atherosclerosis: from pathophysiology to practice.* J Am Coll Cardiol, 2009. **54**(23): p. 2129-38.

178. Bäck, M., et al., *Inflammation and its resolution in atherosclerosis: mediators and therapeutic opportunities.* Nature Reviews Cardiology, 2019. **16**(7): p. 389-406.

179. Wolf, D. and K. Ley, *Immunity and Inflammation in Atherosclerosis.* Circ Res, 2019. **124**(2): p. 315-327.

180. Moriya, J., *Critical roles of inflammation in atherosclerosis.* J Cardiol, 2019. **73**(1): p. 22-27.

181. Ridker, P.M., et al., *Antiinflammatory Therapy with Canakinumab for Atherosclerotic Disease.* N Engl J Med, 2017. **377**(12): p. 1119-1131.

182. Nidorf, S.M., et al., *Colchicine in Patients with Chronic Coronary Disease.* N Engl J Med, 2020. **383**(19): p. 1838-1847.

183. Vöö, S., et al., *Imaging Intraplaque Inflammation in Carotid Atherosclerosis With 18F-Fluorocholine Positron Emission Tomography-Computed Tomography: Prospective Study on Vulnerable Atheroma With Immunohistochemical Validation.* Circ Cardiovasc Imaging, 2016. **9**(5).

184. Li, X., et al., *68Ga-DOTATATE PET/CT for the detection of inflammation of large arteries: correlation with18F-FDG, calcium burden and risk factors.* EJNMMI Res, 2012. **2**(1): p. 52.

185. Nahrendorf, M., et al., *18F-4V for PET-CT imaging of VCAM-1 expression in atherosclerosis.* JACC Cardiovasc Imaging, 2009. **2**(10): p. 1213-22.

186. Meletta, R., et al., *CD80 Is Upregulated in a Mouse Model with Shear Stress-Induced Atherosclerosis and Allows for Evaluating CD80-Targeting PET Tracers.* Mol Imaging Biol, 2017. **19**(1): p. 90-99.

187. Aizaz, M., et al., *PET/MRI of atherosclerosis.* Cardiovascular diagnosis and therapy, 2020. **10**(4): p. 1120-1139.

188. Li, X., et al., *Targeting P-selectin by gallium-68-labeled fucoidan positron emission tomography for noninvasive characterization of vulnerable plaques: correlation with in vivo 17.6T MRI.* Arterioscler Thromb Vasc Biol, 2014. **34**(8): p. 1661-7.

189. Fernandez-Friera, L., et al., *Vascular Inflammation in Subclinical Atherosclerosis Detected by Hybrid PET/MRI.* J Am Coll Cardiol, 2019. **73**(12): p. 1371-1382.

190. Smits, L.P., et al., *Evaluation of ultrasmall superparamagnetic iron-oxide (USPIO) enhanced MRI with ferumoxytol to quantify arterial wall inflammation.* Atherosclerosis, 2017. **263**: p. 211-218.

191. Kooi, M.E., et al., *Accumulation of Ultrasmall Superparamagnetic Particles of Iron Oxide in Human Atherosclerotic Plaques Can Be Detected by In Vivo Magnetic Resonance Imaging.* Circulation, 2003. **107**(19): p. 2453-2458.

192. Briley-Saebo, K.C., et al., *Targeted iron oxide particles for in vivo magnetic resonance detection of atherosclerotic lesions with antibodies directed to oxidation-specific epitopes.* J Am Coll Cardiol, 2011. **57**(3): p. 337-47.

193. Wen, S., et al., *OxLDL-targeted iron oxide nanoparticles for in vivo MRI detection of perivascular carotid collar induced atherosclerotic lesions in ApoE-deficient mice.* J Lipid Res, 2012. **53**(5): p. 829-38.

194. Segers, F.M., et al., *Scavenger receptor-AI-targeted iron oxide nanoparticles for in vivo MRI detection of atherosclerotic lesions.* Arterioscler Thromb Vasc Biol, 2013. **33**(8): p. 1812-9.

195. Nahrendorf, M., et al., *Noninvasive vascular cell adhesion molecule-1 imaging identifies inflammatory activation of cells in atherosclerosis.* Circulation, 2006. **114**(14): p. 1504-11.

196. Chan, J.M.S., et al., *Imaging vulnerable plaques by targeting inflammation in atherosclerosis using fluorescent-labeled dual-ligand microparticles of iron oxide and magnetic resonance imaging.* J Vasc Surg, 2018. **67**(5): p. 1571-1583 e3.

197. Michalska, M., et al., *Visualization of vascular inflammation in the atherosclerotic mouse by ultrasmall superparamagnetic iron oxide vascular cell adhesion molecule-1-specific nanoparticles.* Arterioscler Thromb Vasc Biol, 2012. **32**(10): p. 2350-7.

198. Andelovic, K., et al., *3D visualization of Vascular Cell Adhesion Molecule-1 (VCAM-1) specific Ultrasmall Superparamagnetic Iron Oxide (USPIO) nanoparticles in the atherosclerotic mouse with accelerated self-navigated radial 4D-MRI.* Proceedings of the ISMRM, 2017. **25: 2778**.

199. Higashi, Y., et al., *Insulin-Like Growth Factor-1 Receptor Deficiency in Macrophages Accelerates Atherosclerosis and Induces an Unstable Plaque Phenotype in Apolipoprotein E-Deficient Mice.* Circulation, 2016. **133**(23): p. 2263-78.

200. Volker, H., et al., *Assessment of Local Pulse Wave Velocity Distribution in Mice using k-t BLAST PC-MRI with Semi-Automatic Area Segmentation.* Journal of Cardiovascular Magnetic Resonance, 2017.

201. Coolen, B.F., et al., *Vessel wall characterization using quantitative MRI: what's in a number?* Magnetic Resonance Materials in Physics, Biology and Medicine, 2018. **31**(1): p. 201-222.

202. Zimmermann, J., et al., *On the impact of vessel wall stiffness on quantitative flow dynamics in a synthetic model of the thoracic aorta.* Scientific Reports, 2021. **11**(1): p. 6703.

203. Langer, R. and J.P. Vacanti, *Tissue engineering.* Science, 1993. **260**(5110): p. 920.

204. Saba, N., R. Abraham, and A. Keating, *Overview of autologous stem cell transplantation.* Crit Rev Oncol Hematol, 2000. **36**(1): p. 27-48.

205. Manji, R.A., W. Lee, and D.K.C. Cooper, *Xenograft bioprosthetic heart valves: Past, present and future.* International Journal of Surgery, 2015. **23**: p. 280-284.

206. Baker, B.M. and C.S. Chen, *Deconstructing the third dimension - how 3D culture microenvironments alter cellular cues.* Journal of Cell Science, 2012. **125**(13): p. 3015-3024.

207. Duval, K., et al., *Modeling Physiological Events in 2D vs. 3D Cell Culture.* Physiology (Bethesda), 2017. **32**(4): p. 266-277.

208. Asadian, M., et al., *Fabrication and Plasma Modification of Nanofibrous Tissue Engineering Scaffolds.* Nanomaterials, 2020. **10**(1): p. 119.

209. Fioretta, E.S., et al., *Next-generation tissue-engineered heart valves with repair, remodelling and regeneration capacity.* Nature Reviews Cardiology, 2021. **18**(2): p. 92-116.

210. Devillard, C.D. and C.A. Marquette, *Vascular Tissue Engineering: Challenges and Requirements for an Ideal Large Scale Blood Vessel.* Frontiers in Bioengineering and Biotechnology, 2021. **9**(913).

211. Yu, J.R., et al., *Current and Future Perspectives on Skin Tissue Engineering: Key Features of Biomedical Research, Translational Assessment, and Clinical Application.* Advanced Healthcare Materials, 2019. **8**(5): p. 1801471.

212. Badylak, S.F., D. Taylor, and K. Uygun, *Whole-organ tissue engineering: decellularization and recellularization of three-dimensional matrix scaffolds.* Annu Rev Biomed Eng, 2011. **13**: p. 27-53.

213. Grimes, D.R., et al., *A method for estimating the oxygen consumption rate in multicellular tumour spheroids.* Journal of the Royal Society Interface, 2014. **11**(92).

214. Chang, W.G. and L.E. Niklason, *A short discourse on vascular tissue engineering.* NPJ Regen Med, 2017. **2**.

215. Asakawa, N., et al., *Pre-vascularization of in vitro three-dimensional tissues created by cell sheet engineering.* Biomaterials, 2010. **31**(14): p. 3903-9.

216. Keane, T.J., et al., *Consequences of ineffective decellularization of biologic scaffolds on the host response.* Biomaterials, 2012. **33**(6): p. 1771-81.

217. Cortiella, J., et al., *Influence of acellular natural lung matrix on murine embryonic stem cell differentiation and tissue formation.* Tissue Eng Part A, 2010. **16**(8): p. 2565-80.

218. Faulk, D.M., et al., *The effect of detergents on the basement membrane complex of a biologic scaffold material.* Acta Biomater, 2014. **10**(1): p. 183-93.

219. Vavken, P., S. Joshi, and M.M. Murray, *TRITON-X is most effective among three decellularization agents for ACL tissue engineering.* J Orthop Res, 2009. **27**(12): p. 1612-8.

220. Groll, J., et al., *Biofabrication: reappraising the definition of an evolving field.* Biofabrication, 2016. **8**(1): p. 013001.

221. Tsang, H.H. and S. Raza, *Impact energy absorption of bio-inspired tubular sections with structural hierarchy.* Composite Structures, 2018. **195**: p. 199-210.

222. Mansfield, J.C., et al., *Collagen reorganization in cartilage under strain probed by polarization sensitive second harmonic generation microscopy.* Journal of the Royal Society Interface, 2019. **16**(150).

223. Yang, G., et al., *Vascularization in tissue engineering: fundamentals and state-of-art.* Progress in Biomedical Engineering, 2020. **2**(1): p. 012002.

224. Vert, M., et al., *Terminology for biorelated polymers and applications (IUPAC Recommendations 2012).* Pure and Applied Chemistry, 2012. **84**(2): p. 377-410.

225. El-Sherbiny, I.M. and M.H. Yacoub, *Hydrogel scaffolds for tissue engineering: Progress and challenges.* Global cardiology science & practice, 2013. **2013**(3): p. 316-342.

226. Elisseeff, J., et al., *Photoencapsulation of chondrocytes in poly(ethylene oxide)-based semi-interpenetrating networks.* J Biomed Mater Res, 2000. **51**(2): p. 164-71.

227. Yue, K., et al., *Synthesis, properties, and biomedical applications of gelatin methacryloyl (GelMA) hydrogels.* Biomaterials, 2015. **73**: p. 254-271.

228. Groll, J., et al., *A definition of bioinks and their distinction from biomaterial inks.* Biofabrication, 2018. **11**(1): p. 013001.

229. GEHRKE, S.H., et al., *Factors Determining Hydrogel Permeability.* Annals of the New York Academy of Sciences, 1997. **831**(1): p. 179-184.

230. Mota, C., et al., *Additive manufacturing techniques for the production of tissue engineering constructs.* J Tissue Eng Regen Med, 2015. **9**(3): p. 174-90.

231. Choudhury, D., S. Anand, and M.W. Naing, *The Arrival of Commercial Bioprinters - Towards 3D Bioprinting Revolution!* 2018, 2018. **4**(2).

232. Moroni, L., et al., *Biofabrication strategies for 3D in vitro models and regenerative medicine.* Nature reviews. Materials, 2018. **3**(5): p. 21-37.

233. Hinton, T.J., et al., *Three-dimensional printing of complex biological structures by freeform reversible embedding of suspended hydrogels.* Sci Adv, 2015. **1**(9): p. e1500758.

234. Highley, C.B., et al., *Jammed Microgel Inks for 3D Printing Applications.* Adv Sci (Weinh), 2019. **6**(1): p. 1801076.

235. Kjar, A., et al., *Engineering of tissue constructs using coaxial bioprinting.* Bioactive Materials, 2021. **6**(2): p. 460-471.

236. Xing, J.F., M.L. Zheng, and X.M. Duan, *Two-photon polymerization microfabrication of hydrogels: an advanced 3D printing technology for tissue engineering and drug delivery.* Chem Soc Rev, 2015. **44**(15): p. 5031-9.

237. Ma, X., et al., *Deterministically patterned biomimetic human iPSC-derived hepatic model via rapid 3D bioprinting.* Proc Natl Acad Sci U S A, 2016. **113**(8): p. 2206-11.

238. Bernal, P.N., et al., *Volumetric Bioprinting of Complex Living-Tissue Constructs within Seconds.* Adv Mater, 2019. **31**(42): p. e1904209.

239. Aram, E. and S. Mehdipour-Ataei, *A review on the micro- and nanoporous polymeric foams: Preparation and properties.* International Journal of Polymeric Materials and Polymeric Biomaterials, 2016. **65**(7): p. 358-375.

240. Ganan-Calvo, A.M., J. Davila, and A. Barrero, *Current and droplet size in the electrospraying of liquids. Scaling laws.* Journal of Aerosol Science, 1997. **28**(2): p. 249-275.

241. Jana, S., A. Bhagia, and A. Lerman, *Optimization of polycaprolactone fibrous scaffold for heart valve tissue engineering.* Biomed Mater, 2019. **14**(6): p. 065014.

242. Russo, V., et al., *Tendon Biomimetic Electrospun PLGA Fleeces Induce an Early Epithelial-Mesenchymal Transition and Tenogenic Differentiation on Amniotic Epithelial Stem Cells.* Cells, 2020. **9**(2).

243. Law, J.X., et al., *Electrospun Collagen Nanofibers and Their Applications in Skin Tissue Engineering.* Tissue Engineering and Regenerative Medicine, 2017. **14**(6): p. 699-718.

244. Snetkov, P., et al., *Hyaluronan-Based Nanofibers: Fabrication, Characterization and Application.* Polymers, 2019. **11**(12).

245. Brown, T.D., P.D. Dalton, and D.W. Hutmacher, *Direct writing by way of melt electrospinning.* Adv Mater, 2011. **23**(47): p. 5651-7.

246. Robinson, T.M., D.W. Hutmacher, and P.D. Dalton, *The Next Frontier in Melt Electrospinning: Taming the Jet.* Advanced Functional Materials, 2019. **29**(44).

247. Tylek, T., et al., *Precisely defined fiber scaffolds with 40 mum porosity induce elongation driven M2-like polarization of human macrophages.* Biofabrication, 2020. **12**(2): p. 025007.

248. Wu, W., et al., *Direct-write assembly of biomimetic microvascular networks for efficient fluid transport.* Soft Matter, 2010. **6**(4): p. 739-742.

249. Lin, C.-H., et al., *In Vivo Performance of Decellularized Vascular Grafts: A Review Article.* International journal of molecular sciences, 2018. **19**(7): p. 2101.

250. Pellegata, A.F., et al., *Arterial Decellularized Scaffolds Produced Using an Innovative Automatic System.* Cells Tissues Organs, 2014. **200**(6): p. 363-373.

251. Krams, R. and M. Bäck, *The ESC Textbook of Vascular Biology*. 2017: Oxford University Press.

252. Datta, P., B. Ayan, and I.T. Ozbolat, *Bioprinting for vascular and vascularized tissue biofabrication.* Acta Biomaterialia, 2017. **51**: p. 1-20.

253. Schöneberg, J., et al., *Engineering biofunctional in vitro vessel models using a multilayer bioprinting technique.* Scientific Reports, 2018. **8**(1): p. 10430.

254. Gao, G., et al., *Construction of a Novel In Vitro Atherosclerotic Model from Geometry-Tunable Artery Equivalents Engineered via In-Bath Coaxial Cell Printing.* Advanced Functional Materials, 2021. **31**(10): p. 2008878.

255. Moroni, L., et al., *Biofabrication strategies for 3D in vitro models and regenerative medicine.* Nature Reviews Materials, 2018. **3**(5): p. 21-37.

256. Jungst, T., et al., *Heterotypic Scaffold Design Orchestrates Primary Cell Organization and Phenotypes in Cocultured Small Diameter Vascular Grafts.* Advanced Functional Materials, 2019. **29**(43): p. 1905987.

257. Robert, J., et al., *A three-dimensional engineered artery model for in vitro atherosclerosis research.* PLoS One, 2013. **8**(11): p. e79821.

258. Nie, J., et al., *Vessel-on-a-chip with Hydrogel-based Microfluidics.* Small, 2018. **14**(45): p. 1802368.

259. Chen, R., et al., *Gelatin-based perfusable, endothelial carotid artery model for the study of atherosclerosis.* BioMedical Engineering OnLine, 2019. **18**(1): p. 87.

260. He, J., et al., *Fabrication of circular microfluidic network in enzymatically-crosslinked gelatin hydrogel.* Mater Sci Eng C Mater Biol Appl, 2016. **59**: p. 53-60.

261. Fukushi, M., et al., *Formation of pressurizable hydrogel-based vascular tissue models by selective gelation in composite PDMS channels.* RSC Advances, 2019. **9**(16): p. 9136-9144.

262. Kinoshita, K., et al., *Fabrication of multilayered vascular tissues using microfluidic agarose hydrogel platforms.* Biotechnol J, 2016. **11**(11): p. 1415-1423.

263. Bociaga, D., et al., *Sodium Alginate/Gelatine Hydrogels for Direct Bioprinting—The Effect of Composition Selection and Applied Solvents on the Bioink Properties.* Materials, 2019. **12**(17): p. 2669.

264. Sandvig, I., et al., *RGD-peptide modified alginate by a chemoenzymatic strategy for tissue engineering applications.* Journal of Biomedical Materials Research Part A, 2015. **103**(3): p. 896-906.

265. Zhang, X., et al., *Modeling early stage atherosclerosis in a primary human vascular microphysiological system.* Nature Communications, 2020. **11**(1): p. 5426.

266. Bertassoni, L.E., et al., *Hydrogel bioprinted microchannel networks for vascularization of tissue engineering constructs.* Lab on a Chip, 2014. **14**(13): p. 2202-2211.

267. Miller, J.S., et al., *Rapid casting of patterned vascular networks for perfusable engineered three-dimensional tissues.* Nature Materials, 2012. **11**(9): p. 768-774.

268. Ma, J.Y., Y.C. Wang, and J. Liu, *Bioprinting of 3D tissues/organs combined with microfluidics.* Rsc Advances, 2018. **8**(39): p. 21712-21727.

269. Gelber, M.K., et al., *Model-guided design and characterization of a high-precision 3D printing process for carbohydrate glass.* Additive Manufacturing, 2018. **22**: p. 38-50.

270. Pollet, A.M.A.O., et al., *3D Sugar Printing of Networks Mimicking the Vasculature.* Micromachines, 2020. **11**(1): p. 43.

271. Wu, W., A. DeConinck, and J.A. Lewis, *Omnidirectional printing of 3D microvascular networks.* Adv Mater, 2011. **23**(24): p. H178-83.

272. Lee, W., et al., *On-demand three-dimensional freeform fabrication of multi-layered hydrogel scaffold with fluidic channels.* Biotechnol Bioeng, 2010. **105**(6): p. 1178-86.

273. Cochain, C. and A. Zernecke, *Macrophages and immune cells in atherosclerosis: recent advances and novel concepts.* Basic Res Cardiol, 2015. **110**(4): p. 34.

274. Zarins, C.K., et al., *Carotid bifurcation atherosclerosis. Quantitative correlation of plaque localization with flow velocity profiles and wall shear stress.* Circ Res, 1983. **53**(4): p. 502-14.

275. Asakura, T. and T. Karino, *Flow patterns and spatial distribution of atherosclerotic lesions in human coronary arteries.* Circ Res, 1990. **66**(4): p. 1045-66.

276. Gnasso, A., et al., *In vivo association between low wall shear stress and plaque in subjects with asymmetrical carotid atherosclerosis.* Stroke, 1997. **28**(5): p. 993-8.

277. Callaghan, F.J., et al., *Relationship between pulse-wave velocity and arterial elasticity.* Med Biol Eng Comput, 1986. **24**(3): p. 248-54.

278. Yang, J.W., et al., *Wall shear stress in hypertensive patients is associated with carotid vascular deformation assessed by speckle tracking strain imaging.* Clin Hypertens, 2014. **20**: p. 10.

279. Lee, Y.T., et al., *Mouse models of atherosclerosis: a historical perspective and recent advances.* Lipids in Health and Disease, 2017. **16**(1): p. 12.

280. Herold, V., et al., *Free Breathing Self-Gated PC-MRI with Pseudo Random Sampled Kt-Sparse-Sense.* Proceedings of the International Society of Magnetic Resonance in Medicine, Singapore, 2016. **24**: p. 0466-0466.

281. Rommel, E., *A double trigger unit for ECG and breath triggered mouse heart imaging.* Proceedings of the Conference of the European Society of Magnetic Resonance in Medicine and Biology, 2000. **17**.

282. Larson, P.Z., P.T. Gurney, and D.G. Nishimura, *Anisotropic field-of-views in radial imaging.* IEEE Transactions on Medical Imaging, 2008. **27**(1): p. 47-57.

283. Fessler, J.A. and B.P. Sutton, *Nonuniform fast Fourier transform using minmax interpolation.* IEEE Transactions on Signal Processing, 2003. **51**(2): p. 560-574.

284. Fessler, J.A., *Image reconstruction toolbox*, in https://web.eecs.umich.edu/~fessler/. 2020.

285. Brown, R.W., et al., *Magnetic Resonance Imaging: Physical Principles and Sequence Design*. Vol. 2. 2014: John Wiley & Sons.

286. Kreyszig, E., *Introductory Mathematical Statistics*. 1970: John Wiley & Sons. 210-210.

287. Gu, T., et al., *PC VIPR: a high-speed 3D phase-contrast method for flow quantification and high-resolution angiography.* American Journal of Neuroradiology, 2005. **26**(4): p. 743-749.

288. Thon, M.P., et al., *A Quantitative Model of Early Atherosclerotic Plaques Parameterized Using In Vitro Experiments.* Bull Math Biol, 2018. **80**(1): p. 175-214.

289. Thon, M.P., et al., *A multiphysics approach for modeling early atherosclerosis.* Biomech Model Mechanobiol, 2018. **17**(3): p. 617-644.

290. Thon, M.P., M.R. Myerscough, and M.W. Gee, *A Spatially Resolved and Quantitative Model of Early Atherosclerosis.* Bull Math Biol, 2019. **81**(10): p. 4022-4068.

291. Smith, S.W., *The Scientist and Engineer's Guide to Digital Signal Processing*. Vol. 2. 1999: California Technical Publishing.

292. Winter, P., et al., *Fast self-navigated PC-MRI for human cardiac flow measurements using retrospective radial sampling.* Proceedings of the ISMRM, 2017. **25:3213**.

293. Sotelo, J., et al., *3D Quantification of Wall Shear Stress and Oscillatory Shear Index Using a Finite-Element Method in 3D CINE PC-MRI Data of the Thoracic Aorta.* IEEE Transactions on Medical Imaging, 2016. **35**(6): p. 1475-1487.

294. Guala, A., et al., *Decreased rotational flow and circumferential wall shear stress as early markers of descending aorta dilation in Marfan syndrome: a 4D flow CMR study.* Journal of Cardiovascular Magnetic Resonance, 2019. **21**(1): p. 63.

295. MacKinnon, A.C., et al., *Inhibition of galectin-3 reduces atherosclerosis in apolipoprotein E-deficient mice.* Glycobiology, 2013. **23**(6): p. 654-663.

296. Hartley, C.J., et al., *Hemodynamic changes in apolipoprotein E-knockout mice.* Am J Physiol Heart Circ Physiol, 2000. **279**(5): p. H2326-34.

297. Herold, V., et al., *In vivo comparison of atherosclerotic plaque progression with vessel wall strain and blood flow velocity in apoE(-/-) mice with MR microscopy at 17.6 T.* MAGMA, 2009. **22**(3): p. 159-66.

298. Cunningham, K.S. and A.I. Gotlieb, *The role of shear stress in the pathogenesis of atherosclerosis.* Laboratory Investigation, 2005. **85**(1): p. 9-23.

299. Thondapu, V., et al., *High Spatial Endothelial Shear Stress Gradient Independently Predicts Site of Acute Coronary Plaque Rupture and Erosion.* Cardiovasc Res, 2020.

300. Sotelo, J., et al., *3D axial and circumferential wall shear stress from 4D flow MRI data using a finite element method and a laplacian approach.* Magnetic Resonance in Medicine, 2018. **79**(5): p. 2816-2823.

301. Rodríguez-Palomares, J.F., et al., *Aortic flow patterns and wall shear stress maps by 4D-flow cardiovascular magnetic resonance in the assessment of aortic dilatation in bicuspid aortic valve disease.* J Cardiovasc Magn Reson, 2018. **20**(1): p. 28.

302. Becher, T., et al., *Three-Dimensional Imaging Provides Detailed Atherosclerotic Plaque Morphology and Reveals Angiogenesis After Carotid Artery Ligation.* Circ Res, 2020. **126**(5): p. 619-632.

303. Schmidt, S., et al., *The impact of 4D flow displacement artifacts on wall shear stress estimation.* Magnetic Resonance in Medicine, 2021. **85**(6): p. 3154-3168.

304. Man, J.J., J.A. Beckman, and I.Z. Jaffe, *Sex as a Biological Variable in Atherosclerosis.* Circulation Research, 2020. **126**(9): p. 1297-1319.

305. VanderLaan, P.A., C.A. Reardon, and G.S. Getz, *Site Specificity of Atherosclerosis.* Arteriosclerosis, Thrombosis, and Vascular Biology, 2004. **24**(1): p. 12-22.

306. Stark, H. and S. Schuster, *Comparison of various approaches to calculating the optimal hematocrit in vertebrates.* J Appl Physiol (1985), 2012. **113**(3): p. 355-67.

307. Heo, K.-S., K. Fujiwara, and J.-i. Abe, *Shear stress and atherosclerosis.* Molecules and cells, 2014. **37**(6): p. 435-440.

308. Venturini, G., et al., *Integrated proteomics and metabolomics analysis reveals differential lipid metabolism in human umbilical vein endothelial cells under high and low shear stress.* American Journal of Physiology-Cell Physiology, 2019. **317**(2): p. C326-C338.

309. Tous, M., et al., *Circulating blood cells modulate the atherosclerotic process in apolipoprotein E-deficient mice.* Metabolism, 2004. **53**(1): p. 95-100.

310. Laboratory, T.J. *PHENOTYPES OF LDLR AND APOE KNOCKOUT MICE*. 2021 15.12.2021]; Available from: https://www.jax.org/jax-mice-and-services/strain-data-sheet-pages/phenotype-information-for-002052-and-002207#.

311. Getz, G.S. and C.A. Reardon, *Diet and Murine Atherosclerosis.* 2006. **26**(2): p. 242-249.

312. Dobiásová, M., *[AIP--atherogenic index of plasma as a significant predictor of cardiovascular risk: from research to practice].* Vnitr Lek, 2006. **52**(1): p. 64-71.

313. Barquera, S., et al., *Global Overview of the Epidemiology of Atherosclerotic Cardiovascular Disease.* Arch Med Res, 2015. **46**(5): p. 328-38.

314. Libby, P., et al., *Atherosclerosis.* Nature Reviews Disease Primers, 2019. **5**(1): p. 56.

315. von Scheidt, M., et al., *Applications and Limitations of Mouse Models for Understanding Human Atherosclerosis.* Cell Metab, 2017. **25**(2): p. 248-261.

316. Zhang, Q., et al., *Biofabrication of tissue engineering vascular systems.* APL Bioeng, 2021. **5**(2): p. 021507.

317. Dorweiler, B., et al., *A novel in vitro model for the study of plaque development in atherosclerosis.* Thromb Haemost, 2006. **95**(1): p. 182-9.

318. Dorweiler, B., et al., *Subendothelial infiltration of neutrophil granulocytes and liberation of matrix-destabilizing enzymes in an experimental model of human neo-intima.* Thromb Haemost, 2008. **99**(2): p. 373-81.

319. Edwards, C.A. and W.D. O'Brien, Jr., *Modified assay for determination of hydroxyproline in a tissue hydrolyzate.* Clin Chim Acta, 1980. **104**(2): p. 161-7.

320. Neuman, R.E. and M.A. Logan, *THE DETERMINATION OF COLLAGEN AND ELASTIN IN TISSUES.* Journal of Biological Chemistry, 1950. **186**(2): p. 549-556.

321. Ormiston, M.L., et al., *Generation and Culture of Blood Outgrowth Endothelial Cells from Human Peripheral Blood.* Journal of visualized experiments : JoVE, 2015(106): p. e53384-e53384.

322. Martin-Ramirez, J., et al., *Establishment of outgrowth endothelial cells from peripheral blood.* Nature Protocols, 2012. **7**(9): p. 1709-1715.

323. Radakovic, D., et al., *A multilayered electrospun graft as vascular access for hemodialysis.* PLOS ONE, 2017. **12**(10): p. e0185916.

324. Nagata, S., R. Hanayama, and K. Kawane, *Autoimmunity and the clearance of dead cells.* Cell, 2010. **140**(5): p. 619-30.

325. Zheng, M.H., et al., *Porcine small intestine submucosa (SIS) is not an acellular collagenous matrix and contains porcine DNA: possible implications in human implantation.* J Biomed Mater Res B Appl Biomater, 2005. **73**(1): p. 61-7.

326. Black, L.D., et al., *Mechanical and failure properties of extracellular matrix sheets as a function of structural protein composition.* Biophys J, 2008. **94**(5): p. 1916-29.

327. Wagenseil, J.E. and R.P. Mecham, *Vascular extracellular matrix and arterial mechanics.* Physiological reviews, 2009. **89**(3): p. 957-989.

328. Woods, T. and P.F. Gratzer, *Effectiveness of three extraction techniques in the development of a decellularized bone-anterior cruciate ligament-bone graft.* Biomaterials, 2005. **26**(35): p. 7339-49.

329. Cheng, J., et al., *Decellularization of porcine carotid arteries using low-concentration sodium dodecyl sulfate.* Int J Artif Organs, 2020: p. 391398820975420.

330. Dahl, S.L.M., et al., *Decellularized Native and Engineered Arterial Scaffolds for Transplantation.* Cell Transplant, 2003. **12**(6): p. 659-666.

331. Gratzer, P.F., R.D. Harrison, and T. Woods, *Matrix alteration and not residual sodium dodecyl sulfate cytotoxicity affects the cellular repopulation of a decellularized matrix.* Tissue Eng, 2006. **12**(10): p. 2975-83.

332. Medina, R.J., et al., *Molecular analysis of endothelial progenitor cell (EPC) subtypes reveals two distinct cell populations with different identities.* BMC Med Genomics, 2010. **3**: p. 18.

333. Hirschi, K.K., D.A. Ingram, and M.C. Yoder, *Assessing Identity, Phenotype, and Fate of Endothelial Progenitor Cells.* Arteriosclerosis, Thrombosis, and Vascular Biology, 2008. **28**(9): p. 1584-1595.

334. Jiang, A., et al., *A practical question based on cross-platform microarray data normalization: are BOEC more like large vessel or microvascular endothelial cells or neither of them?* J Bioinform Comput Biol, 2007. **5**(4): p. 875-93.

335. Pan, W., et al., *Semi-supervised learning via penalized mixture model with application to microarray sample classification.* Bioinformatics, 2006. **22**(19): p. 2388-2395.

336. Lin, Y., et al., *Use of blood outgrowth endothelial cells for gene therapy for hemophilia A.* Blood, 2002. **99**(2): p. 457-62.

337. De Meyer, S.F., et al., *Phenotypic correction of von Willebrand disease type 3 blood-derived endothelial cells with lentiviral vectors expressing von Willebrand factor.* Blood, 2006. **107**(12): p. 4728-36.

338. Mune, S., et al., *Mechanism of phosphate-induced calcification in rat aortic tissue culture: possible involvement of Pit-1 and apoptosis.* Clin Exp Nephrol, 2009. **13**(6): p. 571-7.

339. Gryka, M.C., et al., *Controlled dissolution of freeform 3D printed carbohydrate glass scaffolds in hydrogels using a hydrophobic spray coating.* Additive Manufacturing, 2019. **26**: p. 193-201.

340. Justin, A.W., R.A. Brooks, and A.E. Markaki, *Multi-casting approach for vascular networks in cellularized hydrogels.* J R Soc Interface, 2016. **13**(125).

341. Hochleitner, G., et al., *High definition fibrous poly (2-ethyl-2-oxazoline) scaffolds through melt electrospinning writing.* Polymer, 2014. **55**(20): p. 5017-5023.

342. Bloksma, M.M., et al., *Poly(2-cyclopropyl-2-oxazoline): From Rate Acceleration by Cyclopropyl to Thermoresponsive Properties.* Macromolecules, 2011. **44**(11): p. 4057-4064.

343. Hochleitner, G., et al., *Additive manufacturing of scaffolds with sub-micron filaments via melt electrospinning writing.* Biofabrication, 2015. **7**(3): p. 035002.

344. Elvin, C.M., et al., *A highly elastic tissue sealant based on photopolymerised gelatin.* Biomaterials, 2010. **31**(32): p. 8323-31.

345. Bloksma, M.M., et al., *Poly(2-cyclopropyl-2-oxazoline): From Rate Acceleration by Cyclopropyl to Thermoresponsive Properties.* Macromolecules, 2011. **44**(11): p. 4057-4064.

346. Moreadith, R.W., et al., *Clinical development of a poly(2-oxazoline) (POZ) polymer therapeutic for the treatment of Parkinson's disease - Proof of concept of POZ as a versatile polymer platform for drug development in multiple therapeutic indications.* European Polymer Journal, 2017. **88**: p. 524-552.

347. Yung, C.W., et al., *Transglutaminase crosslinked gelatin as a tissue engineering scaffold.* J Biomed Mater Res A, 2007. **83**(4): p. 1039-46.

348. Gupta, D., J.W. Santoso, and M.L. McCain, *Characterization of Gelatin Hydrogels Cross-Linked with Microbial Transglutaminase as Engineered Skeletal Muscle Substrates.* Bioengineering, 2021. **8**(1): p. 6.

349. Yang, G., et al., *Enzymatically crosslinked gelatin hydrogel promotes the proliferation of adipose tissue-derived stromal cells.* PeerJ, 2016. **4**: p. e2497.

350. Pollet, A.M.A.O., et al., *3D Sugar Printing of Networks Mimicking the Vasculature.* Micromachines, 2020. **11**(1).

351. Miller, J.S., et al., *Rapid casting of patterned vascular networks for perfusable engineered three-dimensional tissues.* Nat Mater, 2012. **11**(9): p. 768-74.

352. Gryka, M.C., et al., *Controlled dissolution of freeform 3D printed carbohydrate glass scaffolds in hydrogels using a hydrophobic spray coating.* Additive Manufacturing, 2019. **26**: p. 193-201.

353. Barber, R., et al. *Using Murra™ s Law To Design ArtificialVascular Microfluidic Networks*. 2006.

354. Robinson, T.M., D.W. Hutmacher, and P.D. Dalton, *The Next Frontier in Melt Electrospinning: Taming the Jet.* Advanced Functional Materials, 2019. **29**(44): p. 1904664.

355. Wong, K.K.L., et al., *Coronary arteries hemodynamics: effect of arterial geometry on hemodynamic parameters causing atherosclerosis.* Medical & Biological Engineering & Computing, 2020. **58**(8): p. 1831-1843.

356. Majesky, M.W., et al., *The adventitia: a dynamic interface containing resident progenitor cells.* Arterioscler Thromb Vasc Biol, 2011. **31**(7): p. 1530-9.

357. Aird, W.C., *Endothelium in health and disease.* Pharmacological Reports, 2008. **60**(1): p. 139-143.

358. Pries, A.R., T.W. Secomb, and P. Gaehtgens, *The endothelial surface layer.* Pflugers Archiv-European Journal of Physiology, 2000. **440**(5): p. 653-666.

359. Lyle, A.N. and W.R. Taylor, *The pathophysiological basis of vascular disease.* Laboratory Investigation, 2019. **99**(3): p. 284-289.

360. Liu, T., et al., *Applications of Gelatin Methacryloyl (GelMA) Hydrogels in Microfluidic Technique-Assisted Tissue Engineering.* Molecules, 2020. **25**(22).

361. Zhu, M., et al., *Gelatin methacryloyl and its hydrogels with an exceptional degree of controllability and batch-to-batch consistency.* Scientific Reports, 2019. **9**(1): p. 6863.

362. Pepelanova, I., et al., *Gelatin-Methacryloyl (GelMA) Hydrogels with Defined Degree of Functionalization as a Versatile Toolkit for 3D Cell Culture and Extrusion Bioprinting.* Bioengineering (Basel), 2018. **5**(3).

363. Xie, M., et al., *Protocols of 3D Bioprinting of Gelatin Methacryloyl Hydrogel Based Bioinks.* J Vis Exp, 2019(154).

364. Davidov, T., et al., *Porcine arterial ECM hydrogel: Designing an in vitro angiogenesis model for long-term high-throughput research.* Faseb j, 2020. **34**(6): p. 7745-7758.

APPENDIX

A.1 ABBREVIATIONS

^{18}F-FCH	^{18}F-fluorocholine
2D	2-dimensional
3D	3-dimensional
4D	4-dimensional
AAo	Ascending Aorta
ABC	ATP binding cassette
ABCA-1	ABC transporter
ABCG-1	ATP-binding cassette sub-family G member 1
ANOVA	Analysis of variance
aoPWV	Aortic pulse wave velocity
ApoB^{100}	Apolipoprotein B-100
ApoE	Apolipoprotein E
ATP	Adenosin triphosphate
baPWV	Brachial-ankle pulse wave velocity
BOECs	Human Blood Outgrowth Endothelial Cells
CAD	Computer-aided design
CD	Cluster of differentiation
CFD	Computational fluid dynamics
cfPWV	Carotid-femoral pulse wave velocity
circWSS	Circumferential wall shear stress
coPWV	Coronary pulse wave velocity
CT	Computed tomography
CVD	Cardiovascular disease
DAo	Descending Aorta
DAPI	4',6-Diamidino-2-phenylindol
DNA	Deoxyribonucleic acid
dsDNA	Double-stranded DNA
E.g.	Example given
EC	Endothelial cell
ECFCs	Endothelial colony forming cells
ECG	Electrocardiogram
ECM	Extracellular matrix
EDTA	Ethylenediaminetetraacetic acid
EGF	Epidermal growth factor
ELN	Elastin
eNOS	Endothelial nitric oxide synthase
Et	Local elasticity
EtOH	Ethanol
FCS	Fetal calf serum
FDA	Food and Drug Administration
FGF	Fibroblast growth factor

FITC	Fluorescein
FOV	Field-of-view
GAG	Glycosaminoglycan
GelMA	Gelatin-Methacryloyl
GM-CSF	Granulocyte–macrophage colony stimulating factor
GMP	Good manufacturing practice
HAoSMCs	Primary human aortic smooth muscle cells
HB-EGF	Heparin-binding epidermal growth factor
HDL	High density lipoprotein
HE	Hematoxylin and eosin
hmECs	Primary human microvascular endothelial cells
HS/LT	High spatial / low temporal
HYP	Hydroxyproline
ICAM-1	Intercellular adhesion molecule 1
IF	Immunofluorescence
IFNγ	Interferon-γ
IL	Interleukin
IR	Inter radius
LDL	Low-density lipoprotein
Ldlr	Low-density lipoprotein receptor
longWSS	Longitudinal wall shear stress
LRP-1	LDLR related protein 1
LS/HT	Low spatial / high temporal
LSC	Lumen surface concentration
LVE	Linear viscoelastic (region)
Mac-2	Macrophage-2 antigen
mAECs	Primary murine vascular endothelial cells
mASMCs	Primary murine smooth muscle cells
MCP-1	Monocyte chemoattractant protein-1
M-CSF	Macrophage-colony stimulating factor
MEW	Melt electrowriting
MMP	Matrix metalloproteinase
MR	Magnetic resonance
MRI	Magnetic resonance imaging
mTG	Microbacterial transglutaminase
MTT	3-(4,5-dimethylthiazol-2-yl)-2,5-diphenyltetrazolium bromide
NF-kB	Nuclear factor kappa B
NO	Nitric oxide
Nox.1	NADPH-Oxidase Isoform 1
NUFFT	Non-uniform Fast Fourier Transform
OR	Outer radius
ORO	Oil-red-O
OSI	Oscillatory shear index
oxLDL	Oxidized LDL
P/S	Penicillin-streptomycin
PBS	Phosphate-buffered saline

PC	Phase-contrast
PCL	Polycaprolactone
PcPrOx	Poly(2-cyclopropyl-2-oxazoline)
PcycloPrOx	Poly(2-cyclopropyl-2-oxazoline)
PDGF	Platelet-derived growth factor
PDMS	Polydimethylsiloxan
PET	Positron emission tomography
PFA	Paraformaldehyde
PVV	Pulse wave velocity
radStrain	Radial Strain
RF	Radio frequency
RGD	Arginylglycylaspartic acid
RNA	Ribonucleic acid
ROS	Reactive oxygen species
RT	Room temperature
SDC	Sodium Deoxycholate
SDS	Sodium dodecyl sulfate
SEM	Scanning electron microscopy
SLA	Stereolithography
SM-MHC	Smooth muscle myosin heavy chain
SNR	Signal-to-noise ratio
SR	Scavenger receptors
SREBP	Sterol regulatory element-binding protein
STD	Standard deviation
TE	Tissue Engineering
TEER	Transepithelial electrical resistance
TEM	Transmit-receive electromagnetic
TGF	Transforming growth factor
TNF	Tumor necrosis factor
TT	Transit time
US	Ultrasound
USPIOs	Ultrasmall superparamagnetic iron oxide particles
UV-VIS	Ultraviolet–visible spectrophotometry
VCAM-1	Vascular cell adhesion protein 1
vLDL	Very low density lipoprotein
vSMC	Vascular smooth muscle cells
WD	Western type diet
WSS	Wall shear stress
WT	Wildtype
αSMA	α-smooth muscle actin

A.2 CURRICULUM VITAE

A.3 PUBLICATIONS AND CONFERENCE CONTRIBUTIONS

A.3.1 PUBLICATIONS AS FIRST AUTHOR

1. Patrick Winter*, **Kristina Andelovic***, Thomas Kampf, Fabian Tobias Gutjahr, Julius Heidenreich, Alma Zernecke, Wolfgang Rudolf Bauer, Peter Michael Jakob and Volker Herold: "*Fast self-navigated wall shear stress measurements in the murine aortic arch using radial 4D-phase contrast cardiovascular magnetic resonance at 17.6 T*". Journal of Cardiovascular Magnetic Resonance (JCMR), Issue 21, 64 (2019)

2. Patrick Winter*, **Kristina Andelovic***, Thomas Kampf, Jan Hansmann, Peter M. Jakob, Wolfgang R. Bauer, Alma Zernecke, Volker Herold: "*Simultaneous Measurements of 3D Wall Shear Stress and Pulse Wave Velocity in the Murine Aortic Arch*". Journal of Cardiovascular Magnetic Resonance (JCMR), Volume 23, Article number: 34 (2021)

3. **Kristina Andelovic***, Patrick Winter*, Wolfgang Rudolf Bauer, Peter Michael Jakob, Volker Herold and Alma Zernecke: "*Evaluation of plaque characteristics and inflammation using magnetic resonance imaging*". Special issue of Biomedicines: Molecular imaging of inflammation and immunity, Biomedicines 2021, 9(2), 185.

4. **Kristina Andelovic***, Patrick Winter*, Thomas Kampf, Anton Xu, Peter M. Jakob, Volker Herold, Wolfgang R. Bauer#, Alma Zernecke#: "*2D-projection maps of WSS and OSI reveal distinct spatiotemporal changes in hemodynamics during ageing and atherosclerosis*". Biomedicines 2021, 9(12), 1856

A.3.4 PUBLICATIONS AS FIRST AUTHOR IN PREPARATION

1. **Kristina Andelovic**, Patrick Winter, Wolfgang Rudolf Bauer, Peter Michael Jakob, Volker Herold and Alma Zernecke: "*Local hemodynamic profiles in the atherosclerotic Ldlr$^{-/-}$ and Apoe$^{-/-}$ mouse model arise from distinct geometric properties of the aortic arch*" – Baseline data

2. **Kristina Andelovic**, Patrick Winter, Wolfgang Rudolf Bauer, Peter Michael Jakob, Volker Herold and Alma Zernecke: "*A longitudinal study describing hemodynamic profiles during early atherosclerosis in atherosclerotic Ldlr$^{-/-}$ and Apoe$^{-/-}$ mice*" - 8 & 12 weeks data

3. **Kristina Andelovic**, Patrick Winter, Wolfgang Rudolf Bauer, Peter Michael Jakob, Volker Herold and Alma Zernecke: "*Native and Decellularized Carotid Artery Models for Flow-Related in vitro Atherosclerosis Research*"

4. **Kristina Andelovic**, Matthias Ryma, Celine Frank, Jürgen Groll and Alma Zernecke: "*An Easy-to-Prepare Hydrogel-based Artery Model for Flow-related in vitro Atherosclerosis Research*".

A.3.2 OTHER PUBLICATIONS

1. Volker Herold, Stefan Herz, Patrick Winter, Fabian Tobias Gutjahr, **Kristina Andelovic**, Wolfgang Rudolf Bauer, Peter Michael Jakob: „*Assessment of local pulse wave velocity distribution in mice using k-t BLAST PC-CMR with semi-automatic area segmentation*”. Journal of Cardiovascular Magnetic Resonance (JCMR), Volume 19, Article Number: 77 (2017)

A.3.3 SUBMITTED PUBLICATIONS

1. Matthias Ryma, Hatice Genc, Ali Nadernezhad, Ilona Paulus, Dominik Schneiderei, **Kristina Andelovic**, Oliver Friedrich, Stefan Lyer, Christoph Alexiou, Iwona Cicha and Jürgen Groll: “*Print-and-fuse strategy for sacrificial filaments enables biomimetically structured perfusable microvascular networks with functional endothelium inside 3D hydrogels*”. Advanced Materials, 2021

A.3.5 CONFERENCE CONTRIBUTIONS AS FIRST AUTHOR

1. **Kristina Andelovic**, Patrick Winter, Thomas Kampf, Volker Herold, Thomas Schwarz, Jan Hansmann, Peter Jakob, and Wolfgang Bauer: “*A novel platform to study hemodynamics and morphology in an ex vivo carotid artery model under pulsatile flow conditions*”. Proceedings of the ISMRM 2017, 2830. Annual Meeting of the International Society for Magnetic Resonance in Medicine (ISMRM), 2017, Hawaii, United States of America

2. **Kristina Andelovic**, Patrick Winter, Thomas Kampf, Volker Herold, Peter Jakob, and Wolfgang Bauer: „*3D visualization of Vascular Cell Adhesion Molecule-1 (VCAM-1) specific USPIO nanoparticles in the atherosclerotic mouse with accelerated self-navigated radial 4D-MRI*”. Proceedings of the ISMRM 2017, 2778. Annual Meeting of the International Society for Magnetic Resonance in Medicine (ISMRM), 2017, Hawaii, United States of America

3. **Kristina Andelovic**, Patrick Winter, Thomas Kampf, Volker Herold, Sebastian Schürlein, Jan Hansmann Peter Jakob and Wolfgang Bauer: „*Untersuchung arterieller Hämodynamiken und Morphologie unter variablen Flusskonditionen in einem ex vivo Arterienmodell*“. Clin. Res. Cardiol. 106, Suppl. 1. 83. Jahrestagung der Deutschen Gesellschaft für Kardiologie (DGK), 2017, Mannheim, Germany

4. **Kristina Andelovic**, Patrick Winter, Thomas Kampf, Peter Jakob, Wolfgang Bauer and Volker Herold: „*Quantifizierung der Wandschubspannung im murinen Aortenbogen mittels hochaufgelöster, radialer 4D-Phasenkontrast-MRT bei 17.6T*“. Clin. Res. Cardiol. 107, Suppl. 1. 84. Jahrestagung der Deutschen Gesellschaft für Kardiologie (DGK), 2018, Mannheim, Germany

5. **Kristina Andelovic**, Patrick Winter, Thomas Kampf, Peter Jakob, Wolfgang Bauer and Volker Herold: "*Fast Self-Navigated Wall Shear Stress Measurements in the Murine Aortic Arch Using Radial 4D-PC-MRI at 17.6T*". Proceedings of the ISMRM 2018, 4580. Annual Meeting of the International Society for Magnetic Resonance in Medicine (ISMRM), 2018, Paris, France

6. **Kristina Andelovic**, Patrick Winter, Thomas Kampf, Volker Herold, Jan Hansmann, Peter Jakob, and Wolfgang Bauer: "*A Platform to Study 4D Hemodynamics and Morphology in Artery Models Using Ultra-High Field MRI (17.6 T)*". 5th TERMIS World Congress 2018, Kyoto, Japan.

7. **Kristina Andelovic**, Patrick Winter, Thomas Kampf, Anton Xu, Peter Jakob, Wolfgang Bauer and Volker Herold: "*Self-Navigated Wall Shear Stress Measurements Using Radial 4D-PC-MRI at 17.6 T for Tissue Engineering Approaches*". 5th TERMIS World Congress 2018, Kyoto, Japan.

8. **Kristina Andelovic,** Patrick Winter, Thomas Kampf, Peter Jakob, Volker Herold, Alma Zernecke, and Wolfgang Bauer: "*4D Flow and Wall Shear Stress Measurements at 17.6T in the Murine Aortic Arch for Atherosclerosis Research*". DZHI/DZHK Joint Symposium "Heart Failure Interfaces", 2019, Wuerzburg, Germany

9. **Kristina Andelovic**, Matthias Ryma, Tobias Weigel, Patrick Winter, Jan Hansmann, Jürgen Groll and Alma Zernecke: "*A Platform to Study 4D Hemodynamics and Morphology in Artery Models Using Ultra-High Field MRI (17.6 T)*". 30th Annual Conference of the European Society for Biomaterials 2019, Dresden, Germany.

A.3.6 OTHER CONFERENCE CONTRIBUTIONS

1. Patrick Winter, **Kristina Andelovic**, Thomas Kampf, Peter Jakob, Wolfgang Bauer and Volker Herold: "*Fast self-gated 4D flow measurements in the murine aortic arch with retrospective radial sampling*". Proceedings of the ISMRM 2017, 3212. Annual Meeting of the International Society for Magnetic Resonance in Medicine (ISMRM), 2017, Hawaii, United States of America

2. Patrick Winter, **Kristina Andelovic**, Thomas Kampf, Peter Jakob, Wolfgang Bauer and Volker Herold: „*Fast self-navigated PC-MRI for human cardiac flow measurements using retrospective radial sampling*". Proceedings of the ISMRM 2017, 3213. Annual Meeting of the International Society for Magnetic Resonance in Medicine (ISMRM), 2017, Hawaii, United States of America

3. Volker Herold, Patrick Winter, Stefan Herz, Fabian Gutjahr, **Kristina Andelovic**, Wolfgang Rudolf Bauer and Peter Michael Jakob: „*Assessment of Local Pulse-Wave-Velocity Distribution in Mice using k-t BLAST MRI with Semi-Automatic Area Segmentation*". Proceedings of the ISMRM 2017, 2782. Annual Meeting of the International Society for Magnetic Resonance in Medicine (ISMRM), 2017, Hawaii, United States of America

4. Patrick Winter, **Kristina Andelovic**, Fabian Gutjahr, Peter Michael Jakob, Wolfgang Rudolf Bauer and Volker Herold: „*Selbstnavigierte Phasenkontrast (PC) - Cine MRT zur schnellen Flussbildgebung im menschlichen Herzen*“. 83. Jahrestagung der Deutschen Gesellschaft für Kardiologie (DGK), 2017, Mannheim, Germany

5. Anton Xu, Michael Anton Seethaler, **Kristina Andelovic**, Peter Michael Jakob and Wolfgang Bauer: „*^{19}F Magnetic Resonance Imaging of Tissue Inflammation and T1 Imaging of Fibrosis after Myocardial Infarction in Rats*”. 5th TERMIS World Congress 2018, Kyoto, Japan.

6. Tobias Weigel, Tobias Schmitz, **Kristina Andelovic**, Maren Jannasch, Sebastian Schürlein and Jan Hansmann: “*3D nano fiber scaffolds for the generation of tissue models*”. 30th Annual Conference of the European Society for Biomaterials 2019, Dresden, Germany.

7. Patrick Winter, Michael Seeg, Teresa Reichl, Thomas Kampf, Stefan Herz, **Kristina Andelovic**, Wolfgang Bauer, Peter Jakob, Volker Herold and Patrick Vogel: „*A novel phantom for realistic dynamic flow and wall shear stress measurements in a human aneurysm model.*” 23. Jahrestagung der Deutschen Sektion der ISMRM e.V., Zürich, Switzerland, 2021.

8. Teresa Reichl, Patrick Winter, **Kristina Andelovic**, Wolfgang Rudolf Bauer, Peter Michael Jakob, Thorsten Bley, Volker Herold, Volker Christian Behr, Stefan Herz and Patrick Vogel: „*Highly Flexible Human Aneurysm Models for Realistic Flow Experiments with MPI and MRI*“. 11th International Workshop on Magnetic Particle Imaging (IWMPI), Würzburg, Germany, 2022.

9. Patrick Winter, **Kristina Andelovic**, Thomas Kampf, Susanne Schnell, Alma Zernecke, Wolfgang Rudolf Bauer, Peter Michael Jakob and Volker Herold: „ *Local and Global aortic pulse wave velocity in the murine aortic arch assessed by 4D flow magnetic resonance imaging.*“ Annual Meeting of the International Society for Magnetic Resonance in Medicine (ISMRM), London, England, UK, 2022.

A.4 ACKNOWLEDGEMENTS / DANKSAGUNG

An erster Stelle möchte ich mich herzlich bei Prof. Dr. Alma Zernecke bedanken, welche mir die Möglichkeit gab, dass ich meine Dissertation am Lehrstuhl für Experimentelle Biomedizin II unter ihrer Betreuung absolvieren konnte. Produktive Besprechungen und interessante Diskussionen lieferten mir immer wieder neue Anreize und Ideen für meine Arbeiten. Danke für die Möglichkeit, auf vielen Ebenen interdisziplinär und frei arbeiten zu können, sowohl im Bereich der Physik als auch im Bereich des Tissue Engineering und der Biofabrikation. Danke für die großartigen Büros, Labore und die Ausstattung und dass ich mir viele Sachen, die ich ausprobieren wollte, bestellen und versuchen konnte. Weiterhin danke ich ihr, dass sie bei Fragen immer da war, mich und meine Vorhaben immer unterstützt und mir sehr viel Freiraum in meiner Arbeit gelassen hat, damit ich mich wissenschaftlich entfalten konnte. Das eigenverantwortliche Arbeiten und Forschen hat mir wirklich sehr viel Spaß gemacht.

Weiterhin möchte ich mich herzlich bei Prof. Dr. Dr. Wolfgang Bauer bedanken, der mich in den ersten Jahren meiner Dissertation begleitet hat und mir die interdisziplinäre Arbeit zwischen der Physik und der Biologie ermöglicht hat. Diese Interdisziplinarität hat mir sehr geholfen, über den Tellerrand hinaus zu blicken und einen tiefen Einblick in die physikalische MR-Methodenentwicklung und in die kardiovaskuläre Bildgebung zu gewinnen. Außerdem konnte ich mir dadurch ein sehr breit gefächertes Wissen über die MRT und deren wirklich vielseitige Möglichkeiten aneignen. Auch hier möchte ich mich natürlich herzlich für die Unterstützung, auf vielen Ebenen interdisziplinär arbeiten zu können, den Freiraum in meinen Tätigkeiten, den interessanten Diskussionen und das Ermöglichen der Teilnahme an nationalen und internationalen Konferenzen bedanken. Weiterhin danke ich ihm natürlich herzlich für die Betreuung als Zweitprüfer.

Bei Prof. Dr. Jan Hansmann möchte ich mich auch herzlich für die Betreuung als Drittprüfer und für die tolle Betreuung im Tissue Engineering bedanken. Auch hier haben viele interessante Diskussionen immer wieder neue, interessante Ideen für unsere gemeinsamen Projekte geliefert, die hoffentlich auch in Zukunft noch erfolgreich weitergeführt werden. In diesem Zuge möchte ich mich auch bei Tobias Weigel für die lustige Zusammenarbeit am Elektrospinner und in der Zellkultur bedanken. Auch wenn dieses Projekt aus Platzmangel nicht in die Thesis mit aufgenommen wurde, war es doch sehr erfolgreich!

Bei Prof. Dr. Peter Jakob möchte ich mich gern für die Möglichkeit bedanken, am Institut für Experimentelle Physik V zu arbeiten und alle Geräte und Räume zu nutzen. Weiterhin danke ich für die lustigen und interessanten Diskussionen und den wertvollen Input bei den Projekten.

Weiterhin danke ich dem Prüfungsvorsitzenden für die Bereitschaft zum Prüfungsvorsitz und der Deutschen Forschungsgemeinschaft (DFG) für die Förderung des Projektes „Hochaufgelöste MR-Flussbildgebung zur Charakterisierung der arteriellen Hämodynamik als Indikator zellulärer Pathomechanismen in der frühen Atherogenese“ (Projektnummer 396923792), die mir die Promotion am Lehrstuhl für Experimentelle Biomedizin II ermöglichte.

Im gleichen Zuge möchte ich mich auch nochmal bei unserem gesamten Team (bestehend aus Prof. Dr. Zernecke, Prof. Dr. Dr. Bauer, Prof. Dr. Hansmann, Dr. Herold und Dr. Winter), das an dem DFG Projekt beteiligt war, herzlich für die tolle Zusammenarbeit und die Unterstützung bedanken.

Ein ganz herzlicher und großer Dank geht an Sabine Voll, die bei allen Fragen und Problemen immer sofort eine Lösung parat hatte und die auch immer für ein nettes, kleines oder auch größeres Pläuschen zu haben war, egal ob lachend oder weinend. Sie hatte immer ein offenes Ohr und wirklich wertvolle Ratschläge. Ohne ihre außergewöhnlich große Hilfsbereitschaft und ihrem Management würde alles den Bach runtergehen!

Natürlich geht ein großer Dank auch an Dr. Patrick Winter, der eng mit mir zusammen an den MRT-Projekten gearbeitet hat. Danke für die die zahlreichen Erklärungen und die geduldige Hilfe beim Verstehen und Anwenden der MR-Techniken. Wir haben uns gegenseitig viel beigebracht, viel diskutiert, gelacht und ausgetüftelt. Gemeinsam haben wir wirklich sehr viel erreicht, und wir werden auch in Zukunft sicher noch einiges erreichen! Schließlich haben wir noch ein paar Paper in der Warteschlage :-D

Dem restlichen ehemaligen Büro A032 danke ich für die lustige Zeit, die gemeinsame Zeit beim Mittagessen, die Ablenkung von der Arbeit, dem Trashtalk und für die intensiven, schweißtreibenden Kicker-Matches!

Frau Silvia Schülein danke ich für die Koordination und Unterstützung bei allen allgemeinen Anliegen und die stetige Bereitschaft zu helfen.

Unserem Büro 106 in der Experimentellen Biomedizin, und hier ganz besonders Ivana und Giuseppe, danke ich ebenfalls für die wirklich tolle und lustige Zeit, die Ablenkung, die Hilfe und Unterstützung im Labor sowie in allen Lebenslagen und natürlich unseren Trashtalk-Sessions. Ohne euch wäre alles wirklich sehr langweilig und trist gewesen. Im selben Zug möchte ich auch Maja und Nuria für alles danken. Ihr seid alle wirklich sehr gute Freunde geworden, die mir sehr ans Herz gewachsen sind und die mich hoffentlich auch weiterhin in meinem Leben begleiten werden <3

Ein großer Dank geht auch an Celine Frank, die ich während ihrer Bachelorarbeit betreuen durfte. Die Zeit war wirklich toll, die Zusammenarbeit sehr erfolgreich und ich freue mich darauf, dich das nächste Mal als Masterandin betreuen zu dürfen.

Allen anderen nicht namentlich genannten Mitarbeitern des Lehrstuhls für Experimentelle Biomedizin II und der Experimentellen Physik V danke ich für ihre Hilfsbereitschaft und das sehr angenehme und lustige Arbeitsklima.

Herrn Prof. Dr. Groll möchte ich für die tollen Meetings und Diskussionen danken, die immer wieder interessante, neue Ideen für unser laufendes Projekt und auch zukünftige Projekte hervorbrachten. Weiterhin bedanke ich mich herzlich für die Unterstützung und die Möglichkeit, am FMZ als Postdoc arbeiten zu können, um die neuen Projektideen in die Tat umsetzen zu können.

Mein kleiner, aber starker Hase Matthias Ryma verdient einen besonders großen Dank. Du hast mich schon lange vor und auch während meiner Dissertation begleitet, mein Leben bereichert und warst immer für mich da, sowohl privat als auch beruflich. Du hast mich immer unterstützt, aufgebaut und Mut zugesprochen. Ich danke dir auch für die tolle Zusammenarbeit an unserem Arterienmodell, der Herstellung aller Materialien und den interessanten Diskussionen und dem wertvollen Input für das Grundprinzip und Design. Ohne dich wäre alles nur halb so schön und ich bin unendlich froh, dass ich dich habe! <3

Zuletzt möchte ich mich bei all meinen restlichen Freunden und meiner Familie für die Unterstützung in allen Lebenslagen bedanken. Vor allem meinen Eltern, meiner Schwester und dem kleinen Nicki verdanke ich sehr viel. In allen Lebenslagen bekam ich immer eure Unterstützung und viel Zuspruch. Ich habe immer euren Stolz gespürt und ich bin sehr froh, dass ich immer auf euch zählen kann! <3

A.5 AFFIDAVIT

I hereby confirm that my thesis entitled “Characterization of arterial hemodynamics using mouse models of atherosclerosis and tissue-engineered artery models” is the result of my own work. I did not receive any help or support from commercial consultants. All sources and / or materials applied are listed and specified in the thesis.

Furthermore, I confirm that this thesis has not yet been submitted as part of another examination process neither in identical nor in similar form.

Place, Date Signature

A.6 EIDESSTAATLICHE ERKLÄRUNG

Hiermit erkläre ich an Eides statt, die Dissertation „Charakterisierung arterieller Hämodynamiken in atherosklerotischen Mausmodellen und tissue-engineerten Arterienmodellen“ eigenständig, d.h. insbesondere selbständig und ohne Hilfe eines kommerziellen Promotionsberaters, angefertigt und keine anderen als die von mir angegebenen Quellen und Hilfsmittel verwendet zu haben.

Ich erkläre außerdem, dass die Dissertation weder in gleicher noch in ähnlicher Form bereits in einem anderen Prüfungsverfahren vorgelegen hat.

Ort, Datum Unterschrift